INSTITUTE OF THEORETICAL PHYSICS, WARSAW UNIVERSITY, WARSAW
INSTITUTE OF EXPERIMENTAL PHYSICS, WARSAW UNIVERSITY, WARSAW
INSTITUTE FOR NUCLEAR STUDIES, WARSAW

PHYSICS AT FUTURE ACCELERATORS

PROCEEDINGS OF THE X WARSAW SYMPOSIUM ON ELEMENTARY PARTICLE PHYSICS

KAZIMIERZ, POLAND, MAY 24 – 30 1987

WARSZAWA 1987

INSTITUTE OF THEORETICAL PHYSICS, WARSAW UNIVERSITY, WARSAW
INSTITUTE OF EXPERIMENTAL PHYSICS, WARSAW UNIVERSITY, WARSAW
INSTITUTE FOR NUCLEAR STUDIES, WARSAW

P H Y S I C S
A T F U T U R E A C C E L E R A T O R S

PROCEEDINGS OF THE X WARSAW SYMPOSIUM
ON ELEMENTARY PARTICLE PHYSICS
KAZIMIERZ, POLAND, MAY 24 - 30, 1987

Edited by Z. AJDUK

WARSZAWA 1987

O r g a n i z i n g   C o m m i t t e e

H. ABRAMOWICZ	S. POKORSKI
Z. AJDUK	R. SOSNOWSKI
G. BIAŁKOWSKI	A. WRÓBLEWSKI
D. KIEŁCZEWSKA	J. ZAKRZEWSKI

This is the tenth volume in the series of Proceedings:

1. Proceedings of the I International Symposium on Hadron Structure and Multiparticle Production, Kazimierz, 1977;
2. Proceedings of the II International Symposium on Hadron Structure and Multiparticle Production, Kazimierz, 1979;
3. Proceedings of the III Warsaw Symposium on Elementary Particle Physics, Jodłowy Dwór, 1980 (published in the journal "Nukleonika", 26, 147, 1095 (1981));
4. Proceedings of the IV Warsaw Symposium on Elementary Particle Physics, Kazimierz, 1981;
5. Proceedings of the V Warsaw Symposium on Elementary Particle Physics, Kazimierz, 1982;
6. Proceedings of the VI Warsaw Symposium on Elementary Particle Physics, Kazimierz, 1983;
7. Proceedings of the VII Warsaw Symposium on Elementary Particle Physics, Kazimierz, 1984;
8. Proceedings of the VIII Warsaw Symposium on Elementary Particle Physics, Kazimierz, 1985;
9. Proceedings of the IX Warsaw Symposium on Elementary Particle Physics, Kazimierz, 1986.

LIST OF PARTICIPANTS

1. H.Abramowicz - Warsaw
2. M.Adamus - Warsaw
3. Z.Ajduk - Warsaw
4. B.Badełek - Warsaw
5. G.Baranko - Stanford
6. A.Bassetto - Padua
7. A.V.Batunin - Protvino
8. H.Białkowska - Warsaw
9. D.Bloch - Strasbourg
10. A.Blondel - CERN Geneva
11. J.Blümlein - Zeuthen
12. W.de Boer - Hamburg
13. G.Bohm - Zeuthen
14. A.Breskin - Rehovot
15. R.Budzyński - Warsaw
16. P.Cenci - CERN Geneva
17. E.Cohen - Saclay
18. F.Csikor - Budapest
19. P.Danielewicz - Warsaw
20. J.P.Derendinger - Zurich
21. N.G.Deshpande - Eugene
22. A.Dubničkova - Bratislava
23. A.Filipkowski - Warsaw
24. L.Fluri - Neuchatel
25. G.E.Forden - Stony Brook
26. B.Foster - Bristol
27. J.M.Gaillard - Orsay
28. J.Gajewski - Warsaw
29. Ch.Geich-Gimbel - Bonn
30. K.Genser - Warsaw
31. M.Giler - Łódź
32. R.Gokieli - Warsaw
33. P.Górnicki - Warsaw
34. M.Górski - Warsaw
35. K.Hahn - Leipzig
36. W.Heck - CERN Geneva
37. T.Hofmokl - Warsaw
38. R.Hołyński - Cracow
39. D.Issler - Berne
40. F.Jewsky - Hamburg
41. E.M.Kabuss - Heidelberg
42. J.Kalinowski - Warsaw
43. M.Kalinowski - Warsaw
44. R.Karpiuk - Warsaw
45. J.Kempa - Łódź
46. J.Kempczyński - Warsaw
47. S.Klimek - Warsaw
48. K.Kołodziej - Katowice
49. J.Kosiec - Warsaw
50. U.O.Kötz - Hamburg
51. A.Krause - Berne
52. M.Krawczyk - Warsaw
53. P.Krawczyk - Warsaw
54. J.Królikowski - Warsaw
55. W.Królikowski - Warsaw
56. A.Kryś - Łódź

57.J.H.Kühn - Munich
58.A.Majewska - Warsaw
59.R.Mańka - Katowice
60.M.Markytan - Vienna
61.K.Meissner - Warsaw
62.Ta-Chung Meng - Berlin
63.D.Milewska - Warsaw
64.P.Minkowski - Berne
65.A.G.Minten - CERN Geneva
66.O.A.Mogilevski - Kiev
67.R.Nania - CERN Geneva
68.J.Nassalski - Warsaw
69.R.Nowak - Warsaw
70.J.Nowicka - Kielce
71.Yu.N.Obukhov - Warsaw
72.M.Olechowski - Warsaw
73.M.Palacz - Warsaw
74.J.Pawełczyk - Warsaw
75.M.Pawłowski - Warsaw
76.R.Peschanski - Warsaw
77.S.Pokorski - Warsaw
78.H.Roloff - Zeuthen
79.E.Rondio - Białystok
80.A.Roussarie - Saclay
81.A.Sandacz - Warsaw
82.L.Silverman - Orsay
83.Yu.M.Sinyukov - Kiev
84.S.N.Sokolov - Protvino
85.R.Sosnowski - Warsaw
86.M.Spaliński - Warsaw
87.M.Staszel - Warsaw
88.A.Stopczyński - Warsaw
89.H.Ströbele - CERN Geneva
90.M.Šumbera - Řež/Prague
91.M.Szczekowski - Warsaw
92.A.Szczepaniak - Warsaw
93.M.Szeptycka - Warsaw
94.R.Szwed - Warsaw
95.P.Szymański - Warsaw
96.M.Tamada - Łódź
97.A.Tsirou - Hamburg
98.T.Tymieniecka - Warsaw
99.M.Walczak - Łódź
100.R.Walczak - Warsaw
101.J.Wdowczyk - Łódź
102.R.Weiner - Marburg
103.G.Wilk - Warsaw
104.G.Wilquet - Warsaw
105.R.Windmolders - CERN Geneva
106.Z.Włodarczyk - Kielce
107.E.De Wolf - Antwerp
108.K.Woźniak - Cracow
109.A.Wróblewski - Warsaw
110.G.Wrochna - Warsaw
111.B.Yuldashev - Tashkent
112.J.Żakrzewski - Warsaw
113.S.Zylberajch - Saclay
114.A.Żarnecki - Warsaw

C O N T E N T S *

---

* **We list here the names of the speakers only.**
A complete list of the authors is given in the text of the talk.

HEAVY IONS. HEAVY FLAVORS

Chairmen: R.Windmolders , M.Markytan

EXPERIMENTAL TECHNIQUES AT FUTURE ACCELERATORS

Chairman: E.De Wolf

SUPERSTRINGS

Chairman: P.Minkowski

LATEST RESULTS ON EXPERIMENTAL TESTS OF THE ELECTROWEAK THEORY AT THE CERN $\bar{p}p$ COLLIDER

Patrizia Cenci
CERN, 1211 Geneva 23, Switzerland

ABSTRACT

The leptonic and hadronic decays of the Intermediate Vector Bosons (IVB) produced at the CERN $\bar{p}p$ collider have been studied by the UA1 and UA2 Collaborations. Results on IVB masses and branching ratios, on lepton universality and number of neutrinos species are presented and compared with the predictions of the Standard Model of unified electroweak theory. The UA1 and UA2 data are found to be in good agreement with each other and with theoretical calculations.

1. INTRODUCTION

The successful operation of the CERN $\bar{p}p$ Collider [1] has given the opportunity to observe experimentally the existence of the IVB predicted by the by the unified electroweak theory [2].
This paper describes some properties of the IVB decays into both leptonic and hadronic channels as measured by the UA1 and UA2 experiments.

The identification of leptons in the UA1 and UA2 detectors is discussed. The IVB masses and the production cross sections (times branching ratios) are measured for the different leptonic decays These data provide the first test of the universality of the weak couplings between IVB and leptons at $Q^2 = m_W^2$. A study of the number of light neutrino species as a function of the top mass is performed from the measured values of the $W^{\pm}$ and Z^0 decay widths. A study of IVB detection through their hadronic decays is presented and a signal of a statistical significance of 3.3 s.d. is reported. Finally, the measured Standard Model parameters and the theoretical calculations are compared.

The results presented correspond to the data collected by the UA1 and UA2 experiments during the whole operational period of the CERN $\bar{p}p$ Collider (1981/1985) at the center-of-mass energies of $\sqrt{s} = 546$ GeV and $\sqrt{s} = 630$ GeV. The data from the UA2 experiment [3] are final, whilst those from UA1 are the latest available at the time of writing [4] but some numbers from the electron channel are still preliminary. The integrated luminosities corresponding to these data are shown in Table 1

Table 1:

Integrated Luminosities (nb^{-1})

Data sample	$\sqrt{s} = 546$ GeV		$\sqrt{s} = 630$ GeV	
	UA1	UA2	UA1	UA2
$W \to e\nu$	136	142	570	738
$W \to \mu\nu$	108	-	551	-
$W \to \tau\nu$	118	-	597	-
$Z \to e^+e^-$	136	142	568	768
$Z \to \mu^+\mu^-$	108	-	555	-
$W/Z \to \bar{q}q$	-	-	-	730

2. LEPTON IDENTIFICATION IN THE UA1 AND UA2 DETECTORS

The identification of IVB and the quantitative measurements of their properties are done studying their leptonic decays. The design of the UA1 and UA2 detectors is well known and has been described elsewhere. [5].

Final states containing electrons are the simplest to be studied experimentally and have so far provided the best tests of the Standard Model. The identification of muons and taus is possible only in the UA1 detector.

In this section a brief description of the lepton identification criteria used by UA1 and UA2 is given.

2.1 Electron identification

Electron candidates are selected by a series of cuts requiring consistency between calorimeter, tracking and (in UA2 only) preshower information. In addition the electron candidate is required to be "isolated" in the sense that only a small amount of energy should be observed nearby. These cuts reduce the large background from QCD jet fragmentation.

Both experiments start with high transverse energy showers in the electromagnetic calorimeters ($E_T > 15$ GeV in UA1, > 11 GeV in UA2). Cuts are then made on the shower profile exploiting the four longitudinal samplings available in UA1 and the small lateral cell size of UA2. Small leakage into the hadronic calorimeters is also required, compatible with an electron of the appropriate energy. Next the presence of a charged track is required, whose momentum is compatible with the shower energy. In UA2, track momentum measurement is only possible in the forward regions ($20° < \theta < 40°$, $140° < \theta < 160°$) since no magnetic field is present in the central detector region. However the detector is equipped with preshower counters over the full solid angle of the calorimeters, which are required to give a hit compatible with both the track and calorimeter shower profile. The detailed isolation cuts used can be found in reference [6]. The detection efficiency found by the two experiments is $\approx 75\%$.

2.2 Neutrino identification

The presence of a non-interacting particle can be detected from an apparent lack of momentum conservation. However, since in a typical $\bar{p}p$ collision a large fraction of the energy is carried out by particles that do not leave the vacuum pipe and therefore remain undetected, only the component of the missing momentum transverse to the beam direction can be reliably measured.

For events containing a lepton candidate of transverse momentum $\vec{p}_T^{\,\ell}$, one defines $\vec{p}_T^{\,\nu}$ as

$$\vec{p}_T^{\,\nu} = -\vec{p}_T^{\,\ell} - \Sigma_i \vec{p}_T^{\,i}$$

where $\vec{p}_T^{\,i}$ is a vector with magnitude equal to the transverse energy deposited in the i^{th} cell of the calorimeter and directed from the event vertex to the estimated impact point on the cell. The sum is extended over all calorimeter cells (excluding the charged lepton). In UA1 the $|p_T^{\nu}|$ distribution is found to have an almost gaussian resolution, whilst in UA2 this resolution shows non-gaussian tails due to the incomplete angular coverage of the calorimeters.

2.3 Muon identification

The UA1 detector is equipped to detect muons. The signature for a muon is the existence of a charged track aligned spatially with signals from muon chambers after more than 9 interaction lenghts of material, and a characteristic minimum ionizing energy deposition in the calorimeter cells crossed by this track. A strong isolation of the muon candidate is required in order to reduce the background from jets.

2.4 Tau identification

The UA1 collaboration exploits its central detector performance to extract a sample of events consistent with the decay $W \to \tau\nu_\tau$, $\tau \to \nu_\tau$ + hadrons ($\approx 65\%$ of all τ decays).

Since the τ mass is small, these events are characterized by a highly collimated single jet with low charged-particle multiplicity. These events are selected by defining a "τ likelihood" combining three variables:

F : the fraction of jet energy in a cone $\sqrt{(\Delta\phi^2 + \Delta\eta^2)} < 0.4$
r : the angular separation of the leading track from the jet axis
n : the charged multiplicity.

The expected probability distributions of these variables f(F), f(r), f(n), are constructed by Monte Carlo. The τ likelihood is then defined as

$$L_\tau = \ln[f(F) \times f(r) \times f(n)]$$

The final τ sample is defined as those events having $L_\tau > 0$.

3. IVB LEPTONIC DECAYS

The final data samples for each experiment are listed in Table 2, together with associated background estimates.

Table 2:

Summary of W and Z event sample

$\sqrt{s}$ (GeV)	546	630	546	630
Process	UA1		UA2	
$W \to e\nu$ sample signal background	59 52.2±7.9 6.8±1.8	240 219.6±15.6 20.4±1.7	42 37.9±6.5 4.1±0.4	206 184.6±14.5 21.4±2.2
$W \to \mu\nu$ sample signal background	10 9.4±3.2 0.6±0.1	57 54±7.8 3±2	- - -	- - -
$W \to \tau\nu$ sample signal background	32 29.7±5.7 2.3±0.3		- - -	- - -
$Z \to e^+e^-$ sample signal background	4 < 0.1	28 < 0.7	9 8.8±3.0 0.2	30 28.9±5.5 1.1
$Z \to \mu^+\mu^-$ sample signal background	4 < 0.1	15 < 1.0		

3.1 The W sample

$W \to e\nu_e$: Figure 1 shows the inclusive transverse momentum distributions of the electron candidates in the two experiments. In both cases a clear signal is seen at $p_T^e \approx 40$ GeV/c as expected from W decay. Figure 2 shows the missing transverse energy distributions of these events. In the case of UA1 a clear signal is also seen at $p_T^{miss} \approx 40$ GeV. Accordingly the final $W \to e\nu$ sample is defined by selecting those events with $p_T^{miss} > 15$ GeV/c. However when measuring the W mass, those events whose missing p_T vectors point within $\pm 15°$ from the vertical plane (near the edges of the calorimeter modules) are removed.

In UA2 the partial coverage of the calorimeters gives a non-Gaussian resolution function in p_T^{miss} and the W signal is less clearly seen. The situation is improved by increasing the p_T^e cut to 20 GeV (shaded area on Figure 2b). In addition UA2 makes a cut on the transverse mass m_T of the $e\nu$ candidate requiring $m_T > 50$ GeV/c², where

$$m_T^2 = 2\, p_T^e p_T^{miss}(1-\cos\Delta\phi)$$

and $\Delta\phi$ is the angle between the vectors in the plane perpendicular to the beam direction. The electron p_T distributions of the selected events are shown in Figure 3.

The final sample selected by UA1 contains 299 events with an estimated background of 27.2, while UA2 has 251 events with a background of 26.4 . Due to a known track reconstruction inefficiency, the UA2 sample used for the cross sections and mass measurements is reduced to 248 events. From these numbers, together with the known efficiencies, acceptance and integrated luminosities, one can calculate

$$\sigma_W^e = \sigma(\bar{p}p \to W + X) \times BR(W \to e\nu)$$

The results obtained are given in Table 3 together with the ratios of the cross sections at the two $\sqrt{s}$ values available, and the theoretical predictions of [7]. The quoted errors are the statistic and the systematic one, respectively. The agreement is good, although the measurements are systematically above the predictions.

Table 3:

W Production Cross Sections (Electron Channel)

$\sqrt{s}$	546 GeV σ_W^e(nb)	630 GeV σ_W^e(nb)	$\sigma_W^e(630)/\sigma_W^e(546)$
UA1	0.55±0.08±0.09	0.63±0.05±0.10	1.15±0.19
UA2	0.60±0.10±0.07	0.57±0.05±0.07	0.95±0.18
Theory	$0.43^{+0.13}_{-0.06}$	$0.53^{+0.17}_{-0.09}$	1.23

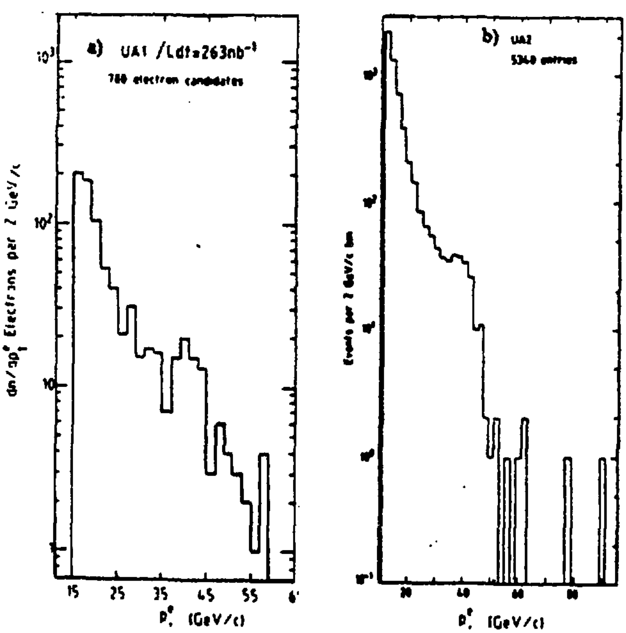

Fig. 1: Transverse momentum distributions of inclusive electron candidates:
a) UA1 data sample with $p_T^e > 15$ GeV/c (1984 data only).
b) UA2 data sample with $p_T^e > 11$ GeV/c (full statistics)

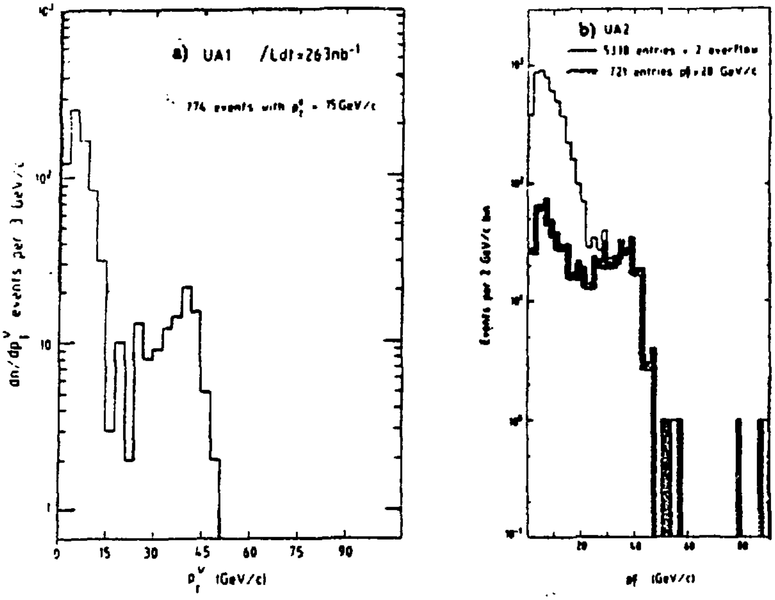

Fig. 2: Missing transverse energy distributions of the inclusive electron candidates:
a) UA1 data (1984 data only)
b) UA2 data (full statistics) The shaded area corresponds to events with $p_T^e > 20$ GeV/c.

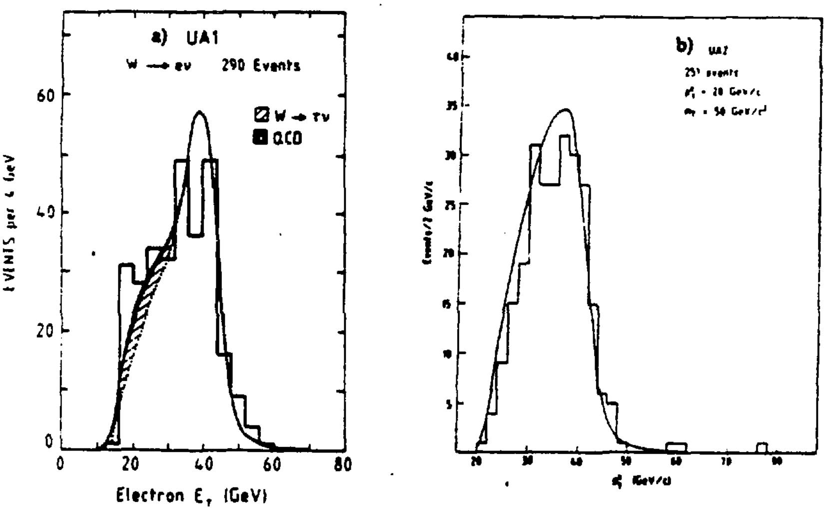

Fig. 3: Transverse energy distributions of electrons in $W \to e\nu$ events:
a) UA1 data. The curve shows the prediction for $m_W = 83.5$ GeV/c². The shaded region shows the main background contributions.
b) UA2 data. The curve shows the prediction for $m_W = 80.2$ GeV/c² including all background contributions.

The transverse mass distributions are used by both experiments to measure the mass and width of the W. This variable is less sensitive to the effect of the p_T of the W than the electron p_T spectrum which has been used in the past. UA1 obtains a background free sample of 149 events for this measurement by cutting both p_T^e and p_T^{miss} at 30 GeV/c. The results of this analysis are not yet final. Figure 4a shows the m_T distribution for the complete sample together with a prediction for m_W = 83.5 GeV. A re-evaluation of the UA1 final sample of data using identical selection criteria changes sligtly the number of events at $\sqrt{s}$ = 546 GeV. Figures 3a and 4a show the distributions of a preliminary sample of 290 events selected with identical cuts. The latest fit value is given in Table 4. The UA2 experiment, on the other hand, uses the full m_T spectrum for p_T^e > 20 GeV/c and includes the estimated background in the fit. The experimental distribution is shown in Figure 4b, and the fit results are summarized in Table 4. The main systematic error comes from the absolute calibration of the calorimeters, being ±3% for UA1 and ±1.6% for UA2. These errors cancel in the ratio m_Z/m_W. Both experiments agree well with each other and with the theoretical expectation (calculated using the measured values of the coupling constants [16], the value of $\sin\theta_W$ from neutrino data [18] and the radiative corrections of reference [17]). For UA2 the first error is statistical, the second systematic and the third is the energy scale error.

Table 4:

Mass and Width of the W (Electron Channel)

	m_W (GeV/c^2)	Γ_W (GeV/c^2)	Γ_W (upper limit)
UA1	82.7±1.0±2.7	$2.8^{+1.4}_{-1.5}$±1.3	<5.4 (90% CL)
UA2	80.2±0.6±0.5±1.3		<7.0 (90% CL)
Theory	80.3±0.9	2.48	

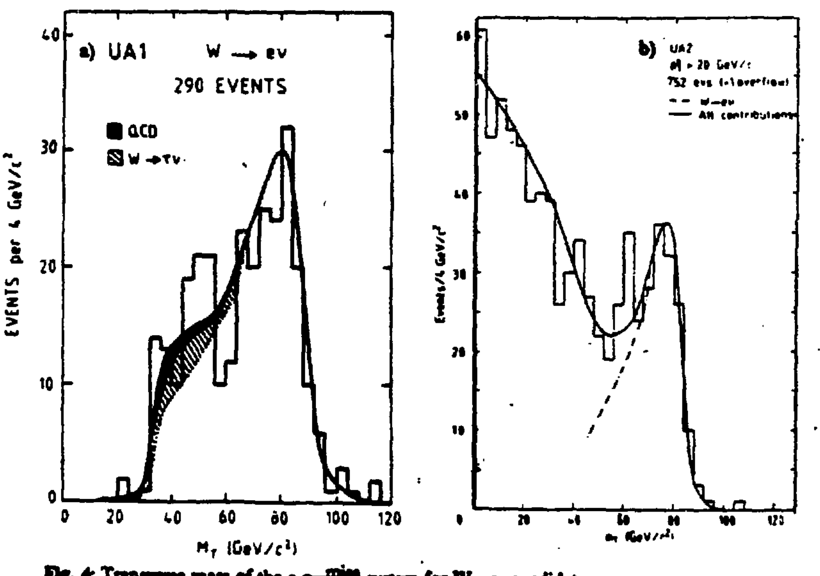

Fig. 4: Transverse mass of the e-p_T^{miss} system for W→eν candidates:
a) UA1 data. The full line shows the expectation from all sources including background (shaded area) using m_W = 83.5 GeV/c^2.
b) UA2 sample of 753 events with p_T^e > 20 GeV/c. The solid line shows the total of all contributions expected, including background, the dashed line shows the contribution from W decays for m_W = 80.2 GeV/c^2.

$W \to \mu\nu_\mu$: In order to select W decays into muons, a muon candidate with a $p_T > 15$ GeV/c and the presence of a $p_T^{miss} > 15$ GeV/c are required. The final sample consists of 10 W events at $\sqrt{s}$= 546 GeV and 57 W's at $\sqrt{s}$= 630 GeV, with a negligible background.

The transverse mass distribution of the μ-p_T^{miss} system is shown in Figure 5 for the W events at 630 GeV. The values of cross sections and masses extracted from these data are given in Table 5 These values are consistent with those found for the electron channel. However the mass resolution is limited by the precision with which high muon momenta can be measured, and does not compete with the precision obtained in the electron channels.

Table 5:

Measurements from UA1 Muon Events

$\sqrt{s}$	σ_W^μ (nb)	σ_Z^μ (pb)
546 GeV	$0.56 \pm 0.18 \pm 0.12$	$98^{+79}_{-48} \pm 20$
630 GeV	$0.63 \pm 0.08 \pm 0.11$	$66 \pm 17 \pm 11$
m_W(GeV/c^2)	$81.8^{+6.0}_{-5.3} \pm 2.6$	
m_Z(GeV/c^2)	$90.7^{+5.2}_{-4.8} \pm 3.2$	

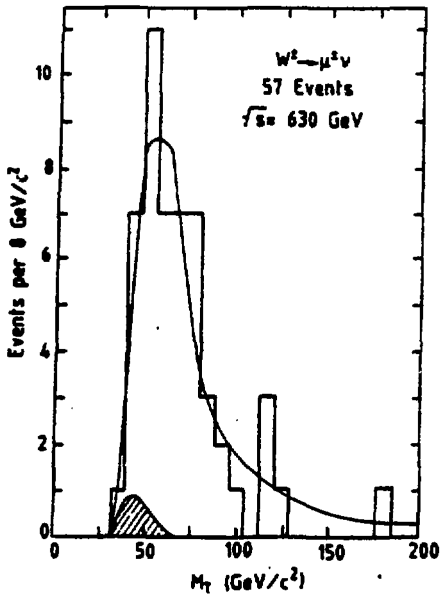

Fig. 5: Transverse mass of the μ-p_T^{miss} system for the UA1 sample of $W \to \mu\nu$ events at $\sqrt{s}$ = 630GeV. The shaded region shows the expected background contribution while the full curve shows the prediction for a W mass of 83.5 GeV/c^2.

$W \rightarrow \tau\nu_\tau$: The sample of W decays into taus is selected by requiring (see section 2.4) a $L_\tau > 0$ and a $p_T^{miss} > 15$ GeV. The transverse mass of the τ-p_T^{miss} system is shown in Figure 6, together with the expectation for a W mass of 83.5 GeV/c^2, and the calculated background. Using this data, UA1 extracts the cross section

$$\sigma_W^\tau = 0.63 \pm 0.13 \pm 0.12 \text{ nb}$$

and a best fit to the W mass of

$$m_W = 89 \pm 3 \pm 6 \text{ GeV}$$

in good agreement with other determinations.

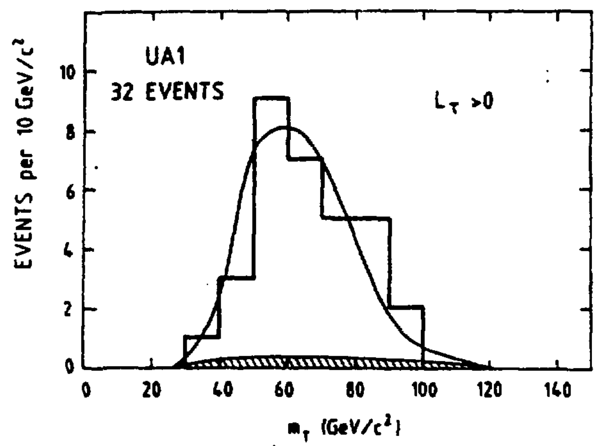

Fig. 6: Transverse mass of the τ-p_T^{miss} system for the UA1 sample of $W \rightarrow \tau\nu$ events. The shaded area shows the expected background while the curve shows the prediction for m_W = 83.5 GeV/c^2.

3.2 The Z sample

$Z^0 \rightarrow e^+e^-$: An increased rejection against hadronic background is achievable by requiring two electron candidates. Therefore less stringent cuts are used for the selection of these events in order to increase the statistics. The data samples are defined by requiring only one electron candidate to survive all the cuts. The resulting mass distributions of the electron pairs are shown in Figure 7. The Z signal is clearly seen at ≈ 90 GeV, well separated from the QCD background and the Drell-Yan pair production at lower masses. The final samples are defined by a cut on the electron pair mass at 70 GeV/c^2 (UA1) and 76 GeV/c^2 (UA2) giving samples of 32 and 39 events, with estimated backgrounds of < 0.2 and 1.3 events respectively. The production cross sections obtained are given in Table 8 and show a good agreement with the predictions of [7].

The Z mass and width are extracted from the sub-samples of well measured events, 24 from UA1 and 25 from UA2. The results are given in Table 7 and compared with the theoretical value. The agreement with expectation for the Z mass is good.

Table 7:

Mass and Width of the Z (Electron Channel)

	m_Z (GeV/c²)	Γ_Z (GeV/c²)	Γ_Z (upper limit)
UA1	93.1±1.0±3.1	$2.7^{+1.2}_{-1.0}\pm1.3$	<5.2 (90% CL)
UA2	91.5±1.2±1.7	2.7±2.0±1.0	<5.6 (90% CL)
Theory	91.6±0.7	2.54	–

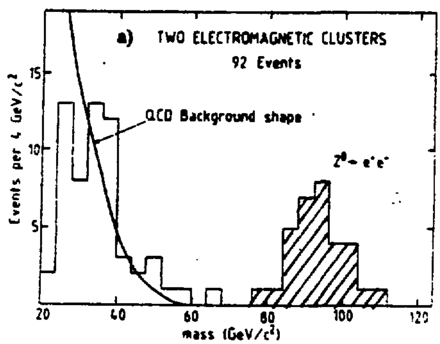

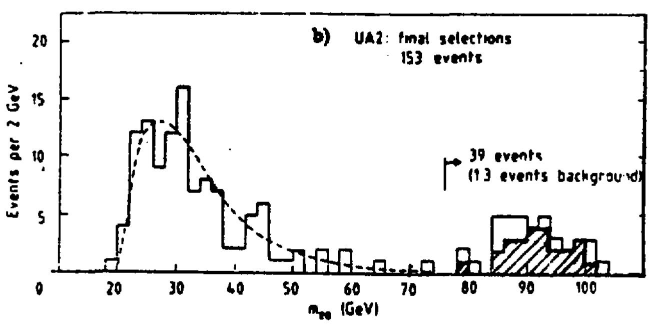

Fig. 7: Electron pairs mass distributions:

a) UA1 events with two electromagnetic clusters of $E_T > 15$ GeV. The expectation from QCD is shown as a solid curve. The shaded region indicates the $Z \to e^+e^-$ candidates.

b) UA2 events passing all the Z selections except the mass cut at 76 Gev/c². The shaded region shows the sample used for the evaluation of the Z mass. The dashed curve shows the expected QCD background.

Table 8:

Z Production Cross Sections (Electron Channel)

$\sqrt{s}$	546 GeV	630 Gev	
	σ_Z^e(pb)	σ_Z^e(pb)	$\sigma_Z^e(630)/\sigma_Z^e(546)$
UA1	$42^{+33}_{-20}\pm 6$	74±14±11	1.8±0.9
UA2	116±39±11	73±14±7	0.6±0.3
Theory	44^{+13}_{-7}	55^{+17}_{-10}	1.25

$Z^0 \to \mu^+\mu^-$: These events are selected requiring two muon candidates of p_T > 15 GeV/c. The final sample consist of 4 Z's at a center-of-mass energy of $\sqrt{s}$ = 546 GeV and 15 Z's at $\sqrt{s}$ = 630 GeV, with negligible background.
The μ-μ mass distribution of these events is shown in Figure 8. The values of cross sections and masses extracted from these data are given in Table 5.

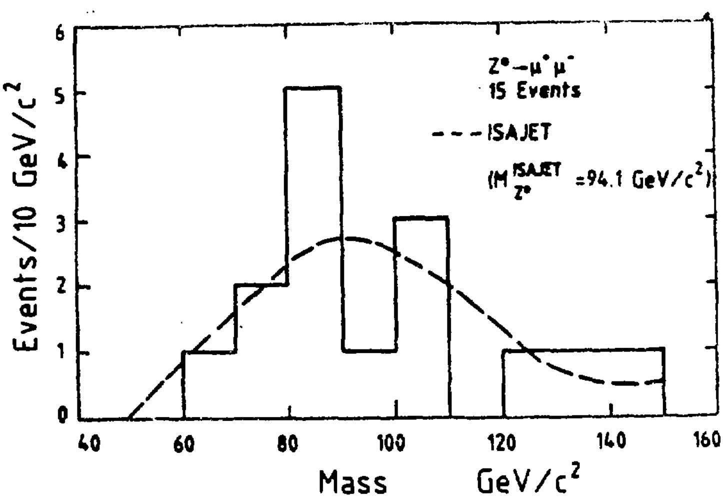

Fig. 8: Dimuon mass distribution for the UA1 sample of $Z \to \mu\mu$ events at $\sqrt{s}$ = 630 GeV. The dotted line shows a prediction for m_Z = 94.1 GeV from the ISAJET Monte Carlo program.

3.3 Number of light neutrinos

The expected value of the Z width depends crucially on the theoretical model used, and in particular on the number of "light neutrinos" ($m_\nu < m_Z/2$). The full width is given by

$$\Gamma_Z = \Sigma\, \Gamma_Z(l\bar{l}) + \Sigma\, \Gamma_Z(q\bar{q}) + N_\nu \Gamma_Z(\nu\bar{\nu})$$

where the first sum is over all charged leptons with masses $< m_Z/2$, the second term over all quark flavours, and the third term over all "light neutrinos". It is assumed that the charged members of any new families are too heavy to contribute. UA1 has set a 90% confidence limit [8] excluding new charged leptons with masses less than 41 GeV/c². Unfortunately, given the present statistics and mass resolution, a direct measurement of Γ_Z (see Table 7) does not yield much information.

A model-dependent method consists of measuring the ratio $R_{exp} = \sigma_W{}^e/\sigma_Z{}^e$, which is related to the ratio of the total widths by the equation:

$$\sigma_W{}^e/\sigma_Z{}^e = [\sigma(\bar{p}p \to W+X)/\sigma(\bar{p}p \to Z+X)]\,[\Gamma_W(e\nu)/\Gamma_Z(ee)]\,\Gamma_Z/\Gamma_W$$

This quantity is well measured, since the errors on luminosity cancel completely and those on efficiencies almost completely. The extraction of Γ_Z/Γ_W from this measurement requires the assumption of the couplings of the Standard Model. Then the total cross section ratio can be calculated, with an error due to the uncertainty on the structure functions. This error does not cancel since the u and d quark structure functions enter differently for Z and W production. Both the cross section ratio and the ratio of the leptonic widths depend on $\sin^2\theta_W$, but the product of the two is insensitive to the value chosen.

The two experiments obtain the values given in Table 9 (where the UA1 value includes measurements from both the electron and muon channel). UA2 quotes the error due to the uncertainty on the structure functions separately in the upper limit.

Table 9:

The ratio of W and Z widths

	R_{exp}	Γ_Z/Γ_W	Γ_Z/Γ_W (upper limit)
UA1	$9.1^{+1.7}_{-1.2}$	$0.98^{+0.18}_{-0.14}$	<1.30 (90% CL)
UA2	$7.2^{+1.7}_{-1.2}$	$0.82^{+0.19}_{-0.14}\pm0.6$	<1.19±0.8 (95% CL)

Even after the assumptions given above, this ratio is still affected by the existence of the top quark, since no contribution from $Z \to t\bar{t}$ occurs for $m_t > m_Z/2$, while the process $W \to \bar{b}t$ can occur until $m_t > m_W - m_b$. The expected variation of Γ_Z/Γ_W as a function of the top quark mass is shown in Figure 9 for various assumed numbers of light neutrino species. The errors on the predictions come from the error on $\sin^2\theta_W$. Also shown are the two experimental measurements, and the lower limit on the top mass from experiments at PETRA. Comparing the data points with expectation the confidence limits of Table 10 are obtained.

These limits are now approaching those from e^+e^- machines ($N_\nu < 5$ [9]) and from cosmology (N_ν < 4-6, m_ν < 1 MeV/c² [10]). Their reliability would be greatly improved if the statistics on the Z were increased and the top mass known. Progress on both directions may be expected from future $\bar{p}p$ Collider runs at ACOL.

UA1 has recently presented a 95% confidence limit [11] on the top quark mass of > 56 GeV. This has not been used in the above confidence limits since it depends crucially on a difficult theoretical calculation of the cross section for $\bar{p}p \to t\bar{t}+X$. For example, changing this cross section by a factor 2 (within the uncertainties) would move the limit to 44 GeV.

Table 10:

Upper limits on the Number of Light Neutrino Species

	Independent of m_t	High top mass
UA1	≤ 8 (90% CL)	≤ 4 (90% CL, $m_t \geq m_W$)
UA2	≤ 7 (95% CL)	≤ 3 (95% CL, $m_t > 74$ GeV/c^2)

3.4 Lepton universality

The UA1 cross section data allow a test [4] of the universality of the weak couplings to e, μ, and τ at $Q^2 = m_W^2$. The ratio of the measured cross sections, that is not affected by the systematics uncertainties on the luminosity, is equal to the ratio of the decay rates Γ. Neglecting the very small phase-space differences among the different leptonic decay, this ratio is just equal to the square of the ratio of the weak coupling constants.

For the charged current couplings UA1 obtains:

$$g^\mu/g^e = 1.01 \pm 0.07 \pm 0.04$$
$$g^\tau/g^e = 1.01 \pm 0.11 \pm 0.06$$

while for the neutral current couplings they obtain

$$g^\mu/g^e = 1.03 \pm 0.15 \pm 0.03$$

consistent with unity as expected in the Standard Model.

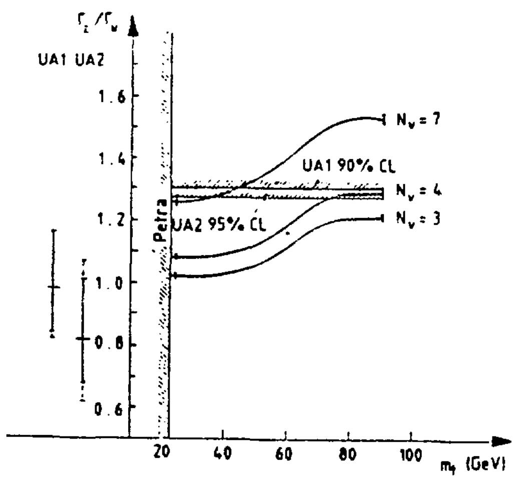

Fig. 9: The ratio Γ_Z/Γ_W predicted in the Standard Model as a function of the top quark mass for various numbers of light neutrino species. The errors on the predictions are due to the uncertainties in $\sin^2\theta_W$. Also shown are the regions excluded by PETRA and the UA1 and UA2 measurements.

4. IVB HADRONIC DECAYS

The IVB are expected to decay into quark-antiquark pairs with well defined [12] branching fractions:

$\Gamma(W \to q\bar{q}')/\Gamma(W \to e\nu) \approx 6$
$\Gamma(Z \to q\bar{q})/\Gamma(Z \to e^+e^-) \approx 20$

excluding decays with a top quark in the final state.

The observation of such decays is an important check of the Standard Model, and provides the first test-case of the ability of future Collider experiments [13] to perform spectroscopy with hadron jets identified with their parent partons.

The experimental requirements are the selection of well measured jets with optimized mass resolution and a good control of the overwhelming background from QCD two jet background. To define the jet energy, a cone is constructed around the jet axis, taken from the center of the interaction region to the centroid of the calorimeter energy cluster identified [14] as a jet. The energies deposited in the calorimeter cells within the cone are added together. The cone opening angle ($\approx 50°$) is chosen in order to optimize the jet energy resolution. Following this definition, a sample of two-jet events well contained inside the UA2 central calorimeter ($|\cos\theta_{jet}| < 0.6$, θ_{jet} = jet polar angle) is selected. A set of cuts is then applied [15] to ensure a good mass resolution for the final sample. Only jets well contained both transversely and longitudinally in the calorimeter are considered. Additional cuts are made on the transverse momentum unbalance of the two-jet system and on the quality of the jet reconstruction. The overall efficiency of the selection procedure is $\approx 66\%$.

The mass resolution of the two-jet system, determined both by direct measurements and by Monte Carlo, is found to be of the order of 8 GeV/c^2 for two-jet masses of 80 GeV/c^2, and 9 GeV/c^2 for masses of 90 Gev/c^2. Figure 10 shows the two-jet mass spectrum for the events taken at $\sqrt{s} = 630$ GeV corresponding to an integrated luminosity of 730 nb^{-1}. The data are multiplied by a factor $(M/100\ GeV)^3$ to reduce the effect of using wide mass bins in the steeply falling QCD distribution. Given the quoted mass resolutions, the W and Z peaks are not resolved. However, a broad bump is visible in the expected region of the spectrum.

A maximum likelihood fit to these data is made by using the function:

$$F(m) = A[m^{-\alpha}\exp(-\beta m) + \xi S(m)]$$

The first term in the square bracket parametrizes the QCD background. The second term is the sum of two gaussian distributions representing the W and Z signals respectively. The W distribution is taken to have a mean value m_0 and r.m.s. 8 GeV/c^2, the Z distribution has mean value $1.14m_0$ and r.m.s. 9 GeV/c^2. The relative normalization between the two gaussians is assumed equal to the expected ratio (≈ 3) between the numbers of observed W and Z decays. The parameters α, β and ξ are adjusted to maximize the likelihood function, the constant A being calculated each time to provide the appropriate normalization. The mass parameter m_0 is either set to the expected value, m_0 = 78.5 Gev/c^2, or treated as an additional free parameter. In the latter case m_0 is found to be 82 ± 3 GeV, in agreement with the value obtained from the W leptonic decays (see section 3).

The significance of the signal is 3.3 standard deviations, and its magnitude corresponds to 632 ± 190 events (with m_0 fixed) and 686 ± 210 events (releasing m_0 in the fit). This number is consistent with the number of events expected from the Standard Model after correcting for the acceptance and the efficiency of the selection criteria. The result of the fit is shown as curve (b) in the Figure 10. A poor fit to the data is obtained suppressing the signal term S(m) in the fit function ($\chi^2 = 21.1$ for 12 d.o.f); the fit is good, instead, if the data points contained in the range $65 < m < 105$ GeV/c^2 are excluded ($\chi^2 = 4.7$ for 7 d.o.f) as shown in curve (a) in Figure 10.

Other fits using either a different parametrization of the QCD background or different data samples obtained by small changes of the selection criteria, always give a signal with a statistical significance consistent with the number of events in the sample. A fit to any data sample which does not satisfy at least two selection criteria gives no evidence for a signal. No known systematic effect seems capable to create the observed signal.

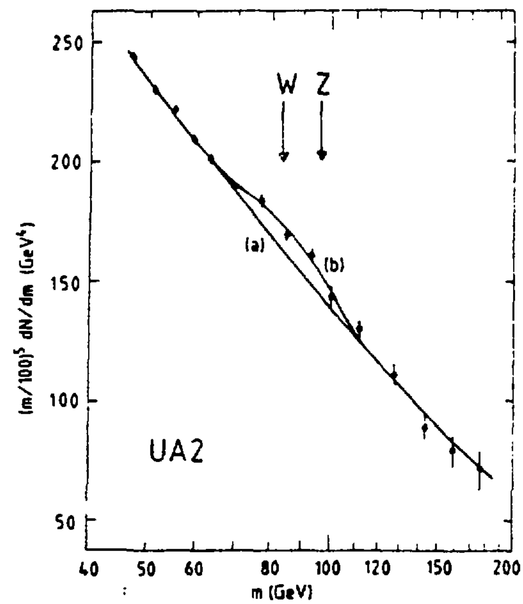

Fig. 10: Two-jet invariant mass distribution. Curve (a): best fit to the QCD background. Curve (b): best fit to the whole sample.

5. STANDARD MODEL PARAMETERS

The minimal standard model relates the masses of the weak bosons, m_W, m_Z, to the fine structure constant α_{em}, the Fermi constant G_F and and the weak mixing angle θ_W according to

$$m_W^2 = A^2/[(1-\Delta r)\sin^2\theta_W]$$
$$m_Z^2 = A^2/[(1-\Delta r)\sin^2\theta_W\cos^2\theta_W]$$

where $A = (\pi\alpha_{em}/\sqrt{2}G_F)^{1/2} = (37.2810 \pm 0.0003)$ GeV/c^2 using the measured values [16] of α_{em} and G_F, and Δr accounts for 1 loop corrections to the IVB masses.
Combining these equations one can extract $\sin^2\theta_W$ from the measured IVB masses:

$$\sin^2\theta_W = 1 - (m_W/m_Z)^2$$

This method has the advantage of eliminating errors due to absolute energy calibration, as well as radiative corrections, but is limited by the statistical error on the Z mass.

A more precise result is obtained by using the measured value of G_F and α_{em} and the calculated value of Δr. At present, Collider data do not constrain the value of Δr (see later) and so we take the value from a recent calculation [17]:

$$\Delta r = 0.0711 \pm 0.0013 .$$

assuming $m_t = 36\ \mathrm{GeV}/c^2$ and the mass of the Higgs boson equal to m_Z.
The final unknown is the value of $\sin^2\theta_W$, which must be taken experimentally at $Q^2 = m_W{}^2$ according to

$$\sin^2\theta_W = A^2/(1-\Delta r)m_W{}^2 .$$

The results are given in Table 1. All the values are in good agreement with each other and with previous determinations [18] from the deep inelastic neutrino scattering experiments. Averaging their values and assuming a charmed quark mass of 1.5 GeV/c^2 (with no error) one obtains

$$\sin^2\theta_W = 0.232 \pm 0.004 \pm 0.003$$

where the first error is experimental and the second theoretical.

The only parameter sensitive to the Higgs mechanism used in the Standard Model is

$$\rho = m_W{}^2/m_Z{}^2\cos^2\theta_W$$

which in the minimal model with a single Higgs doublet has a value of 1, neglecting small radiative corrections. The values obtained experimentally (see Table 1) are consistent with this expectation.

Finally $\sin^2\theta_W$ can be eliminated from the two definitions given above to yield a measurement of Δr. The values obtained (see Table 1 and Figure 11) are not precise enough to test the model, even using the most precise value of $\sin^2\theta_W$. With increased statistics, this measurement could be sensitive to the Higgs mass as well as the existence of new exotic particles. In the table the first value of Δr is extracted using only collider data, while the second uses the best value of $\sin\theta_W$ as input. Figure 11 summarizes the measurements of the Standard Model parameters given by UA1 and UA2.

Table II:

Measurements of the Standard Model parameters

Parameter	UA1		UA2
	e channel	μ channel	
$\sin^2\theta_w = 1 - m_W^2/m_Z^2$	0.211 ± 0.025	0.19 ± 0.15	$0.232 \pm 0.025 \pm 0.010$
$\sin^2\theta_w = A^2/(1-\Delta r)m_W^2$	$0.218 \pm 0.005 \pm 0.014$	$0.223^{+0.033}_{-0.029}$	$0.232 \pm 0.003 \pm 0.008$
ρ	$1.009 \pm 0.028 \pm 0.020$	1.05 ± 0.16	$1.001 \pm 0.028 \pm 0.006$
Δr (I)	$0.038 \pm 0.100 \pm 0.067$	-	$0.068 \pm 0.087 \pm 0.030$
Δr (II)	$0.125 \pm 0.021 \pm 0.057$	-	$0.068 \pm 0.022 \pm 0.032$

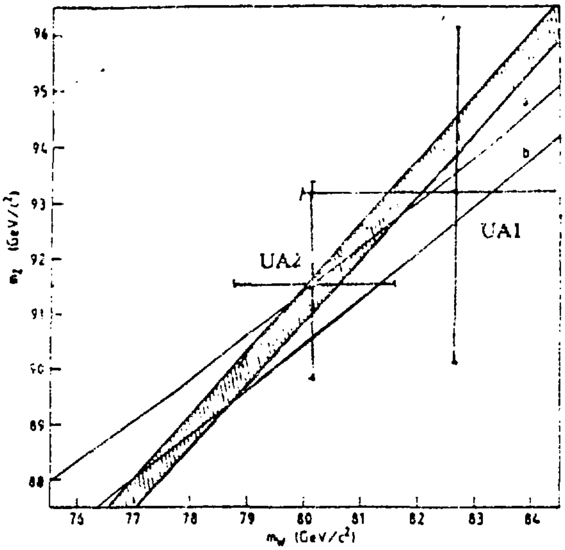

Fig. 11: Measurements of the IVB masses in the m_Z vs m_W plane from the UA1 and UA2 experiments. Only the systematic uncertainties are represented. Curve (a): Standard Model prediction with radiative corrections. Curve (b): Standard Model prediction without radiative corrections. Shaded band: region allowed by the uncertainty on $\sin^2\theta_W$ as measured by low-energy ν experiments.

CONCLUSIONS

The successful runs of the UA1 and UA2 detectors at the SppS Collider have provided a good confirmation of the Standard Model of electroweak interactions. From the study of the IVB leptonic decays, the masses, production cross sections, and couplings of the IVB's have been measured to be in good agreement with theoretical calculations. A signal compatible with the hadronic decays of the IVB is observed in the two-jet mass spectrum in the UA2 data.
Both detectors are now being upgraded to take advantage of the ten-fold increase in luminosity offered by ACOL. This high statistics data will allow much more stringent tests of the electroweak theory, and perhaps provide a first glimpse at the physics beyond the Standard Model.

ACKNOWLEDGEMENTS

I would like to thanks my colleagues on UA2, especially Paolo Bagnaia, Luigi Di Lella, Peter Jenni and Andy Parker for their help in preparing this talk and these proceedings. Thanks are also due to Steven Haywood for making available to me the latest UA1 results.

References

[1] C.Rubbia, D.Cline, P.McIntyre, Proc. Int. Neutrino Conf., Aachen, 1976 (Vieweg, Braunshweig, 1977), p. 683.

[2] S.L.Glashow, Nucl. Phys. 22 (1961), p. 579;
S.Weinberg, Phys. Rev. Lett. 19 (1967), p. 1264;
A.Salam, Proc. 8th Nobel Symposium, Aspen-Asgärden (1968), (Almqvist and Wiksell, Stockholm), p. 367.

[3] R. Ansari et al. Phys Lett 186B (1987) p. 440;
R. Ansari et al. CERN-EP/87 – 48 To be published in Physics Letters.

[4] E. Locci (UA1 Coll.), W/Z & Standard Model, International Europhysics Conference on High Energy Physics, Uppsala, Sweden, June 25-July 1, 1987;
Th. Muller (UA1 Coll.), Rencontre de Moriond on Electroweak Interactions and Unified Theories, 1987.

[5] K. Eggert et al. (UA1 Coll.), Nucl. Inst. and Methods 176 (1980) p. 217;
J. Timmer. (UA1 Coll.), Proc of the 3rd Moriond Workshop on $\bar{p}p$ Physics (1983) p. 609, Editions Frontieres 1983;
G. Arnison et al. (UA1 Coll), Phys Lett B122 (1983) 103, B129 (1983) p. 273;
P. Bagnaia et al. (UA2 Coll), Z. Phys C 24 (1984) p. 1;
B. Mansoulie (UA2 Coll.), Proc of the 3rd Moriond Workshop on $\bar{p}p$ Physics (1983) p. 609, Editions Frontieres 1983.

[6] G. Arnison et al. (UA1 Coll.), Lett. Nuovo Cimento 44 (1985) p. 1;
P. Bagnaia et al. (UA2 Coll.), Z. Phys. C 24 (1984) p. 1.

[7] G. Altarelli et al., Nucl. Phys. B246 (1984) and Z. Phys. C27 (1985) p. 617.

[8] C. Albajar et al, Phys Lett B 185 (1986) p. 241.

[9] J.F. Grivas, Rencontre de Moriond on Electroweak Interactions and Unified Theories, 1987.

[10] D. Schramm, Rencontre de Moriond on Electroweak Interactions and Unified Theories, 1987.

[11] M. Della Negra, 2nd Topical Seminar on Heavy Flavours, San Miniato, Italy (1987).

[12] J. Ellis et al., Ann. Rev. Nucl. Part. Sc. 32 (1982) p. 443.

[13] T.Akesson et al., Detection of jets with calorimeters at future accelerators, Proceedings of the CERN-ECFA Workshop on Physics at Future Accelerators, La Thuile, January 1987.

[14] P. Bagnaia et al. (UA2 Coll.), Z. Phys. C20 (1983) p. 117;
P. Bagnaia et al., Phys. Lett. 138B (1984) p. 430;
P. Bagnaia et al., Phys. Lett. 144B (1984) p. 291;
J.A.Appel et al. (UA1 Coll.), Phys. Lett. 160B (1985) p. 349.

[15] R. Ansari et al. (UA2 Coll.), Phys. Lett. 186B (1987) p. 452.

[16] Review of Particle Properties. Phys. Lett. 170B (1986) p. 1.

[17] W. Marciano XXIII International Conference on High Energy Physics, Berkeley, California, July 1986, quoting F. Jegerlehner, BERN preprint 1985.

[18] CDHSW Collaboration. H. Abramowicz et al., Phys. Rev. Lett. 57 (1986) p. 298;
CHARM Collaboration. J.V. Allaby et al. Phys. Lett. 177B (1986) p. 446;
CCFR Collaboration, presented by F. Merrit. Proc of the 12th Intl. Conf. on Neutrino Physics and Astrophysics, Sendai, Japan, June 1986;
FMMF Collaboration, presented by R. Brock, as above.

STATUS OF NEUTRINO COUNTING AND NEW QUARKS

N.G. Deshpande
Institute of Theoretical Science
University of Oregon
Eugene, OR 97403

ABSTRACT

We review the recent limits on the number of neutrino species N_ν obtained from e^+e^- colliders and from $\bar{p}p$ colliders. If majorons exist, they contribute two units to N_ν in e^+e^- colliders and conflict with the 90% CL of $N_\nu < 4.8$. We study the consequence of a fourth family of quarks and leptons on neutrino counting at $\bar{p}p$ colliders. Useful conclusions are drawn at 90% and 95% CL. Effect of majorons on neutrino counting at $\bar{p}p$ colliders is also reviewed.

I. INTRODUCTION

Three methods have been useful in setting useful limits on N_ν, the number of neutrino species. These methods are complimentary to each other and do not measure the same quantity except in the standard model. The methods are

A. Nucleosynthesis and Cosmology

This method relates primordial Helium abundance to the number of neutrino species. It is sensitive to light neutrinos of mass less than a MeV, and the sensitivity to right-handed neutrinos depends on their coupling strength. The traditional bound from this method is $N_\nu < 4$.

B. Electron-Positron Colliders

The data comes from $e^+ + e^- \rightarrow \gamma + \bar{\nu} + \nu$ reaction at $\sqrt{s} = 29$ GeV and 42 GeV. It is sensitive in principle to $m_\nu < \sqrt{s}/2$ although there is a cut on photon energy which reduces the mass limit somewhat. It is sensitive to all species of neutrinos that occur in $e^+ + e^- \rightarrow \bar{\nu} + \nu$ reaction.

C. Proton-Antiproton Collider

This is an indirect method of determining Γ_Z/Γ_W. It is sensitive to $m_\nu < m_Z/2$ and to only those neutrinos that occur in $Z \rightarrow \nu\nu$ decay. This includes right handed neutrinos, for example.

In this talk we shall focus only on the latter two methods.

II. N_ν FROM ELECTRON-POSITRON COLLIDERS

The method depends on the process $e^+ + e^- \rightarrow \gamma + \bar{\nu} + \nu$ first suggested by Ma and Okada.(1) The background for the process comes from $e^+ + e^- \rightarrow e^+ + e^- + \gamma$ with $e^+ + e^-$ along the beam direction. This can be eliminated by cuts on θ_γ^{min} and $p_{T\gamma}^{min}$. The cross-section can be written in the form

$$d\sigma/dx = f(E_\gamma, p_{T\gamma}^{min}, \theta_\gamma^{min})\sigma^{e+e-\rightarrow\nu\nu}(s) \tag{1}$$

where $x = 2E_\gamma/\sqrt{s}$ and $s = s(1 - x)$. If there are extra gauge bosons Z_i coupled to the usual neutrinos or to extra neutrinos that occur for example in models based on E_6 group, then these can be incorporated in the $e^+ + e^- \rightarrow \bar{\nu} + \nu$ cross-section following Barger, Deshpande and Whisnant.(2) When the limits on extra Z boson mass from neutral current data are incorporated the extra neutrino count ΔN_ν is always less than 0.6 for the most favorable case with three families of light right-handed neutrinos. This is too small to obtain any useful bounds at present.

The present experimental limits from different experiments as well as combined limit is presented from Levine.[3]

Search	$\sqrt{s}$ GeV	Acceptance Cuts	$L\varepsilon$ pb^{-1}	Expected Yield	Observed Yield	N_ν 90% CL
MAC	29.0	$E_{\perp\gamma} > 4.5, 2.0$ 2.6 GeV $\theta_\gamma > 40$	27,50,42	1.1	1	17
ASP	29.0	$E > 1$ GeV $\theta_\gamma > 20$	66	2.2	1	7.5
CELLO	42.6	$E_\gamma > 2.1$ GeV $\theta_\gamma > 34$	13	.7	0	15
Combined				4	2	4.8

We thus have a combined limit of

$$N_\nu < 4.8 \quad (90\%CL) \tag{2}$$

This limit is already useful to put bounds on majorons however. The model by Gelmini and Roncadelli[4] has a Higgs triplet with surviving particles χ^{++}, χ^{+}, χ^{0} and M^0 where M^0 is a pseudo-scalar Goldstone particle associated with lepton number violation and χ^0 is a scalar particle whose mass is less than 100 keV from astrophysical considerations. $Z_0 \rightarrow M^0\chi^0$ decay yields.[5]

$$\Gamma(Z \rightarrow M^0\chi^0) = 2\Gamma(Z \rightarrow \bar{\nu}\nu) \tag{3}$$

Since M^0 and X^0 will escape from the detector like neutrinos, the existence of majorons increases N_ν by two units. We then see that $N_\nu = 5$ is not compatible with the data at 90% CL.

III. LIMITS FROM SppS

Neutrino counting at SppS depends on an estimate of Γ_Z/Γ_W using theoretical information on production of $W^\pm$ versus Z^0. The original method[6] suggested by Halzen and Mursula; and Cline and Rholf has been used to limit new physics by Deshpande, Eilam, Barger and Halzen.[7] The method follows from the equation:

$$R_{expt} = \text{(number of e}\nu\text{ from } W^\pm) / (\text{number of } e^+e^- \text{ from } Z^0) \tag{4}$$

$$= [\sigma(W^+ + W^-)/\sigma(Z)][\Gamma(W \rightarrow e\nu)/\Gamma(Z \rightarrow e^+e^-)][\Gamma_Z/\Gamma_W]$$

The first two ratios in the right hand side of the equation are determined using proton structure functions and standard model with $x_W = 0.23$. These are respectively 3.3 ± 0.2 and 2.685· For R_{expt} we use the most recent limits[8] obtained by UA2 with combined data of $142 nb^{-1}$ at 546 GeV and $768\ nb^{-1}$ at 630 GeV. The limits are

$$R^{expt} = 7.2^{+1.7}_{-1.2} \tag{5}$$

< 9.52 (90%CL)

< 10.42 (95%CL)

When combined with theoretical uncertainities we have

$$\Gamma_Z / \Gamma_W < 1.16 \quad \text{at } 90\%\text{CL}$$

$$< 1.27 \quad \text{at } 95\%\text{CL} \tag{6}$$

We shall discuss various consequences of these limits in the next three sections. The discussion is largely based on a recent paper by the author with Barger, Han and Phillips.[9]

A· N_ν and mass of t quark

Because Γ_W is a function of t mass, the ratio Γ_Z/Γ_W is a function of m_t and N_ν. We calculate Γ_Z using standard model fermion couplings with $x_W = \sin^2\theta_W = 0.23$, and $M_Z = 91.9$ GeV. The contribution of each neutrino, charged lepton and quark are

$$\Gamma(Z \to \nu\nu) = \Gamma_Z{}^0 = (G_F M_Z{}^3)/(12\pi\sqrt{2}) = 0.17 \text{ GeV} \tag{7a}$$

$$\Gamma(Z \to \bar{L}L) = \Gamma_z{}^0 F(m_L{}^2/M_z{}^2) \tag{7b}$$

$$\Gamma(Z \to \bar{Q}Q) = 3\Gamma_z{}^0 F(m_Q{}^2/M_z{}^2)(1 + \alpha_s/\pi) \tag{7c}$$

where

$$F(r) = 8\beta\left[g_v{}^2(1 + 2r) + g_A{}^2(1 - 4r)\right] \tag{8}$$

Here

$$\beta = (1 - 4r)^{1/2}, \quad g_v = T_3/2 - x_W Q, \quad g_A = -T_3/2.$$

We then find

$$\Gamma_Z = 2.04 + 0.17\, N_\nu + .51\, F_t \tag{9}$$

where $F_t = [0.59 - 1.93r_t][1 - 4r_t]^{1/2}$ and $r_t = (m_t/m_Z)^2$.

We calculate Γ_W using $m_W = 80.6$ GeV and the standard formulas

$$\Gamma(W \rightarrow e\bar{\nu}) = G_F M_W^3 / 6\pi\sqrt{2} = \Gamma_W{}^0 = 0.23 \text{ GeV} \qquad (10a)$$

$$\Gamma(W \rightarrow L\bar{\nu}) = \Gamma_w{}^0 H(m_L{}^2/m_w{}^2) \qquad (10b)$$

$$\Gamma(W \rightarrow tb) = 3\Gamma_W{}^0(1 + \alpha_s/\pi)\, H\,(m_t{}^2/m_W{}^2) \qquad (10c)$$

where $H(r) = 1 - 3r/2 + r^3/2$ for $r \leq 1$ and $H(r) = 0$ for $r > 1$. The formula can be summarized as

$$\Gamma_W = 2.12 + 0.72\, H_t \qquad (11)$$

In figure 1 we plot Γ_Z/Γ_W as a function of m_t for different values of N_ν. The bounds on Γ_Z/Γ_W from the data are also plotted. We note that there is no limit on m_t at 95% CL while at 90% CL there is a limit $m_t < 68$ GeV. Our conclusions are more conservative than those reached by Halzen[10] who used bounds which are more stringent. The limit on N_ν assuming that there are no additional quarks or leptons and assuming $m_t = 45$ GeV is:

$$N_\nu < 5 \quad 90\%\ \text{CL} \qquad (12)$$

$$N_\nu < 7 \quad 95\%\ \text{CL}$$

B. Mass limits on fourth generation quarks and leptons

We now assume there is an additional family with a lepton of mass m_L accompanied by a light neutrino and an addition quark v of charge - 1/3 and mass m_v. We assume that the additional 2/3 charge quark is heavier than m_w. The widths for Z and W are now given by

$$\Gamma_Z = 2.04 + 0.17\, N_\nu + 0.51\, F_t + 0.51\, F_v + 0.17\, F_L \ (\text{GeV}) \qquad (13)$$

$$\Gamma_W = 2.12 + 0.72\, H_t + 0.23\, H_L \ (\text{GeV}) \qquad (14)$$

where F(r) and H(r) are defined as before and $N_\nu = 4$. In Fig. 2 we plot Γ_Z/Γ_W as a function of m_t for three cases: (a) when $m_L \geq m_W$, $m_v = 24$ GeV, (b) $m_L = 41$ GeV and $m_v = M_Z/2$ and (c) $m_L = 41$ GeV and $m_v = 24$ GeV. We arrive at the interesting conclusion that if $m_v = 24$ GeV then $m_t < 45$ GeV (60 GeV) regardless of m_L at 90% CL (95% CL).

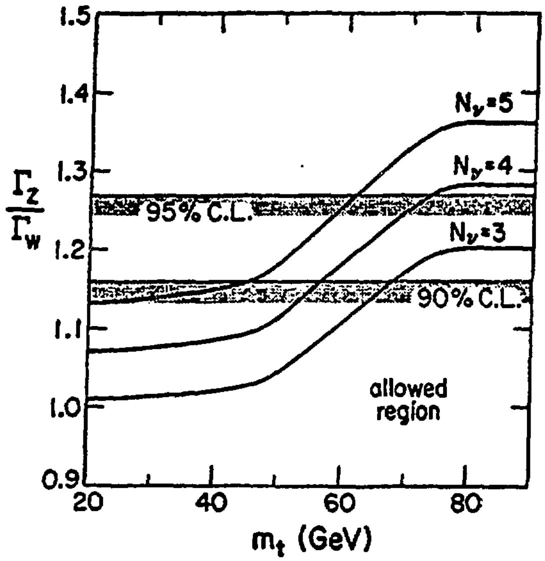

Fig. 1. Γ_Z/Γ_W predictions assuming no fourth generation charged fermions compared with the 90% and 95% experimental upper limits; results are shown versus the t quark mass, for $N_\nu = 3,4$ and 5 light neutrino species.

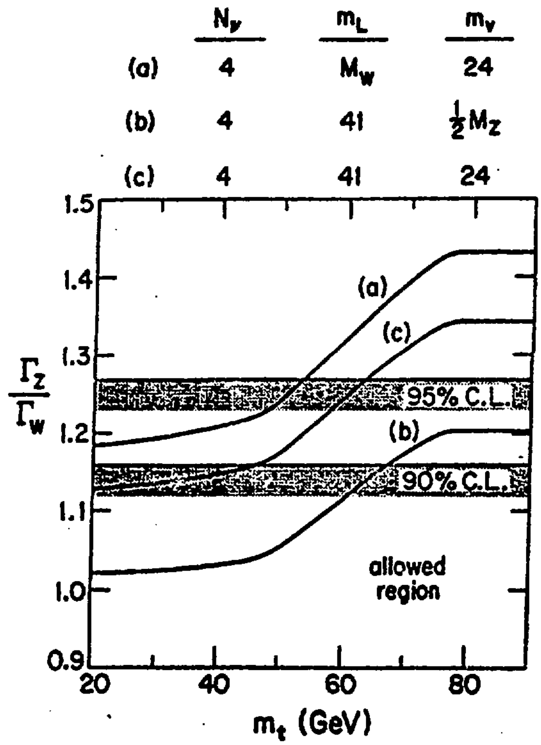

Fig. 2 Γ_Z/Γ_W predictions for three illustrative cases of fourth generation fermions: (a) $m_\nu = 24$ GeV, $m_L > M_W$; (b) $m_L = 41$ GeV, $m_\nu > M_Z/2$; (c) $m_\nu = 24$ GeV, $m_L = 41$ GeV. 90% and 95% limits are shown for comparison.

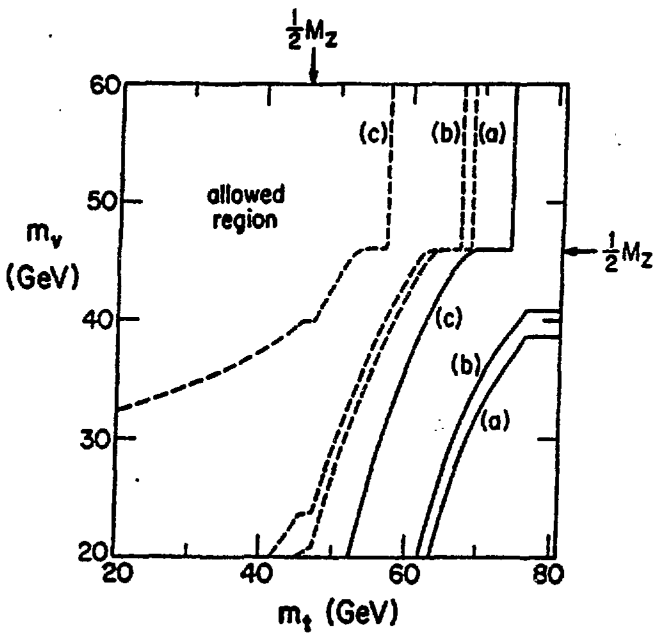

Fig. 3 90% limits (dashed curves) and 95% limits (solid curves) in the (m_t, m_ν) plane for three illustrative cases:

(a) $m_L = 24$ GeV $m(\nu_L) = 5$ GeV,

(b) $m_L = 41$ GeV, $m(\nu_L) = 0$ GeV,

(c) $m_L > M_W$. The allowed regions are to the left of the curves.

In Figure 3 we plot the allowed regions in m_ν vs m_t plane for different values of m_L at 90% CL and 95% CL.

C. Majorons and Neutrino counting.

If majorons exist in triplet Higgs representation, the widths of W and Z are altered. We have to include

$$W^+ \rightarrow \chi^{++} + \chi^- \tag{15}$$

$$W^+ \rightarrow \chi^+ + \chi^0$$

$$W^+ \rightarrow \chi^+ + M^0$$

as well as

$$Z \rightarrow \chi^0 + M^0$$

$$\rightarrow \chi^+ + \chi^- \tag{16}$$

$$\rightarrow \chi^{++} + \chi^{--}$$

Assuming three generation, the widths for W and Z are affected as

$$\Gamma_Z = \Gamma_Z^{standard} + \delta\Gamma_Z \tag{17}$$

$$\Gamma_W = \Gamma_W^{standard} + \delta\Gamma_W \tag{18}$$

We define the effective neutrino count due to these additional channels as

$$\delta N_{eff} = (\delta\Gamma_Z/\Gamma_Z^0) - (\delta\Gamma_W/\Gamma_Z^0)(\Gamma_Z^{standard}/\Gamma_W^{standard}) \tag{19}$$

This quantity depends on $m_\chi+$, $m_\chi++$ and weakly on m_t, but can be shown to lie within the range

$$1/2 < \delta N_{eff} < 2 \tag{20}$$

with value approaching 2 as $m_\chi + > m_W$, and 1/2 as $m_\chi+$ and $m_\chi++$ 0. If $m_t < 45$ GeV (60 GeV) there is no constraint on the model at 90% CL (95% CL). If $m_t > m_W$ however $m_\chi+ < 30$ GeV at 95% CL. We show results in figures 4 and 5.

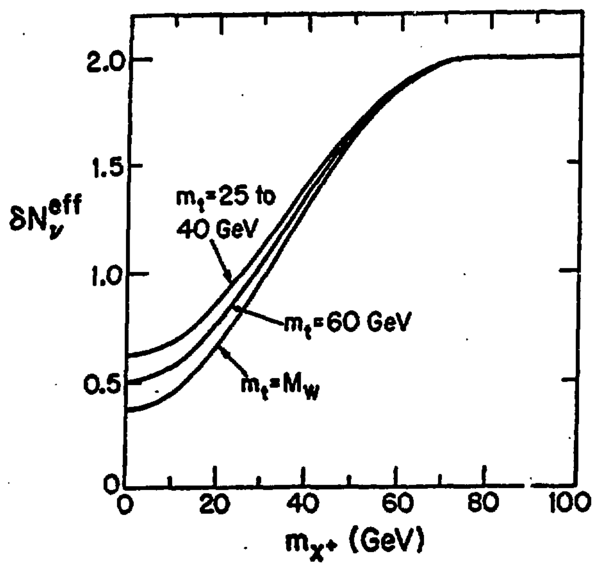

Fig. 4 The majoron-related contributions expressed as an effective number of additional neutrinos δN_ν^{eff}

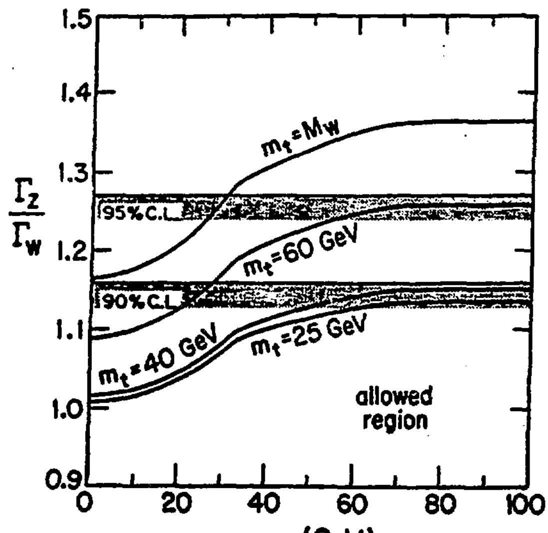

Fig. 5 The ratio Γ_Z/Γ_W for $N_\nu = 3$ as a function of $m(\chi^+)$ for a set of m_t values.

IV. CONCLUSIONS

1. From $e^+ + e^-$ data $N_\nu < 4.8$ at 90% CL. Majoron excluded at 90% CL.

2. From pp data, if $m_t = 45$ GeV and no other light particles, $N_\nu < 5$ (7) at 90% CL (95% CL)

3. If $N_\nu = 3$, $m_t < 68$ GeV at 90% CL and no limit 95% CL.

4. If $N_\nu = 4$ and no other light particles, $m_t < 55$ GeV (75 GeV) at 90% CL (95% CL).

5. If $N_\nu = 4$ and $m_\nu = 24$ GeV and m_L arbitrary, $m_t < 45$ GeV (60 GeV) at 90% CL (95% CL).

6. If $m_{\chi^+} > M_W$ then $m_t < 45$ GeV (60 GeV) at 90% CL (95% CL)

7. If $m_t > m_W$ then $m_{\chi^+} < 30$ GeV at 95% CL.

REFERENCES

1. E. Ma and J. Okada, Phys. Rev. Lett. 41, 287 (1978); K.J.F. Gaemers, R. Gastmans and F.M. Renerd, Phys. Rev. D19, 1605 (1979).
2. V. Barger, N.G. Deshpande and K. Whisnant, Phys. Rev. Lett 57, 2109 (1986).
3. T.L. Lavine, University of Wisconsin Ph.D. Thesis, December 1986, WISC - EX - 86/275.
4. G.B. Gelmini and M. Roncadelli, Phys. Lett. 99B, 411 (1981). H.M. Georgi, S.L. Glashow and S. Nussinov, Nucl. Phys. B193, 297 (1981).
5. V. Barger, H. Baer, W.-Y. Keung and R.J.N. Phillips, Phys. Rev. D26, 218 (1982).
6. F. Halzen and K. Mursula, Phys. Rev. Lett. 51, 857 (1983) D. Cline and J. Rohlf, unpublished.
7. N.G. Deshpande, G. Eilam, V. Barger and F. Halzen, Phys. Rev. Lett. 54, 1757 (1985).
8. UA2 collaboration: CERN-EP/87-05.
9. V. Barger, T. Han, N.G. Deshpande and R.J.N. Phillips, University of Wisconsin preprint, MAD/PH/335, (1987), to be published in Phys. Letts. (1987).

TESTING THE ELECTROWEAK STANDARD MODEL AT HERA

J.BLUMLEIN

Institute for High Energy Physics
Academy of Sciences of the GDR
Platanenallee 6, Berlin-Zeuthen, 1615
GDR

Abstract

The results are presented of a systematic study /1/ of HERA's potential to test the electroweak standard model. The measurement of $\sin^2\theta$ and M_W appear to be possible with statistical precisions of .002 and 100 MeV. The theoretical errors are dominated by the quark distribution uncertainties and are estimated to be less than the statistical errors. Limits can be set for the top-quark mass and the Higgs-boson mass. Extensions of the minimum model can be tested with high precision.

1. Introduction

The investigation of deep inelastic neutral and charged current $e^{\pm}p$-reactions at HERA /2/ provides the possibility to study the electroweak standard theory at high Q^2. A test of the minimum $SU(2)_L \times U(1)$-model has to take into account the existence of the various parameters of the theory and their mutual dependence. Among the quantities defining the electroweak sector (the Fermi-constant G_F, the weak mixing angle θ, the fine structure constant α and the weak boson masses M_W and M_Z) only three are independent. Conceptually, measuring one of these quantities one has to fix two others, which are precisely known, and to express the remaining parameters in terms of the basic set choosen, e.g. one can fix α and G_F and measure $\sin^2\theta$ or M_W. With M_Z determined at LEP /3/ with better than 1% one can as well replace G_F by M_Z.

As the sensitivity of the measurement to a parameter depends on the choice of the fixed parameters due to the different functional dependences implied a systematic search for the best statistical precisions has to be performed.

The theoretical errors of the analysis are implied by the experimental errors of the input parameters, the ratio $R=\sigma_L/\sigma_T$, quark mass effects, the experimental errors of the Kobayashi-Maskawa matrix elements and the uncertainty of the quark distribution parametrizations.

The kinematic area has been limited to a region where calorimeter resolution effect are tolerably small /4/. Still, a valid estimate of the potential systematic error is beyond the aim of this study as it would require detailed detector orientated Monte Carlo calculations. We have also disregarded the effect of radiative corrections /5/. Currently, these topics are under investigation in different working groups in prepearing the workshop "Physics at HERA", Oct. this year.

The outline of this talk is as follows: Section 2 summarizes basic relations used. In section 3 the statistical errors of different electroweak quantities are derived assuming an integrated luminosity of 200pb^{-1}. Section 4 deals with the theoretical errors of the analysis. In section 5 the strict parameter relations of the standard model are given up and the sensitivity of modifications of the minimum theory is studied to a varying ρ-parameter, for nonvanishing right handed weak isospin components, additional W- and Z-bosons and an eventual compositeness scale of the weak bosons.

2. Basic relations

The inclusive deep inelastic scattering cross section for neutral and charged current $e^{\pm}p$-reactions may be written using the notation /6/

$$\sigma_{nc}^{\pm} = \frac{d^2\sigma(e^{\pm}p \to e^{\pm}X)}{dx\,dQ^2} = \frac{2\pi\alpha^2}{Q^4 x}\Big\{ Y_+\left[F_2 + K_Z(-v \mp \lambda a)G_2 + K_Z^2(v^2+a^2 \pm 2va\lambda)H_2\right] + K_Z Y_-\left[(\pm a + \lambda v)xG_3 + K_Z(\mp 2va - \lambda(a^2+v^2))xH_3\right]\Big\} \qquad (1)$$

$$\sigma_{cc}^{\pm} = \frac{d^2\sigma(e^{\pm}p \to \overset{(-)}{\nu}X)}{dx\,dQ^2} = \frac{2\pi\alpha^2}{Q^4 x} K_W^2 \frac{1 \pm \lambda}{2}\left(Y_+ W_2^{\pm} \mp Y_- x W_3^{\pm}\right) \qquad (2)$$

with $v=-1/2+2\sin^2\theta$, $a=-1/2$, $Y_{\pm} = 2-2y+y^2/(1+R)$, $Y_- = 1-(1-y)^2$, $R = \sigma_L/\sigma_T$, $y = Q^2/Sx$, $S=4E_eE_p = 98400\ \mathrm{GeV}^2$ and the structure functions

$$(F_2, G_2, H_2) = x \sum_q (Q_q^2, 2Q_q v_q, v_q^2 + a_q^2)\ (q+\bar{q}) \qquad (3)$$

$$(xG_3, xH_3) = 2x \sum_q (Q_q a_q, v_q a_q)\ (q-\bar{q}) \qquad (4)$$

$$W_2^{\pm} = 2x \sum_q (q_{d(u)} + \bar{q}_{u(d)}) \qquad (5)$$

$$xW_3^{\pm} = 2x \sum_q (q_{d(u)} - \bar{q}_{d(u)}). \qquad (6)$$

λ denotes the electron polarization and $K_{Z,W}(Q^2)$ are pro - pagator functions given by

$$K_Z(Q^2) = \frac{Q^2}{(Q^2+M_Z^2)4\sin^2\theta\cos^2\theta} = \frac{Q^2}{4(A^2+Q^2\cos^2\theta\ \sin^2\theta\ )} \tag{7}$$

$$K_W(Q^2) = \frac{Q^2}{(Q^2+M_W^2)\ 4\ \sin^2\theta} = \frac{Q^2}{4(\ A^2\ \ +\ Q^2\sin^2\theta\ \ )} \tag{8}$$

expressed by the weak mixing angle and either the Z-boson mass or the Fermi constant. Here $A=A_0/(1-\Delta r)^{1/2}$, $A_0=(\pi\alpha/G_F\sqrt{2}\ )^{1/2}$ and $\Delta r\ =\ (\alpha\ /4\pi)X(M_Z,M_W,M_H,m_t)\ \approx\ .07$ for M_H=100 GeV and m_t=40 GeV /7/. M_W and M_Z are related by $\cos\theta\ =\ M_W/M_Z$.

The derivation of electroweak parameters is most conveniently performed through cross section asymmetries and ratios which are less sensitive to systematical and theoretical uncertainties. Studying a variety of different possibilities we found that best sensitivity to the electroweak parameters is provided by

$$A^{\pm}(\lambda) = [\sigma_{nc}^{\pm}(\lambda) - \sigma_{nc}^{\pm}(-\lambda)]/[\sigma_{nc}^{\pm}(\lambda)+\sigma_{nc}^{\pm}(-\lambda)] \tag{9}$$

and

$$R^{\pm}(\lambda) = \ \ \sigma_{nc}^{\pm}(\lambda)\ /\sigma_{cc}^{\pm}(\lambda) \tag{10}$$

$A^{\pm}(\lambda)$ requires to have polarized beams.

3. Statistical errors

In this section the standard electroweak theory will be assumed to be valid. The asymmetries $A^{\pm}$ and the ratios $R^{\pm}$ are calculated using the quark distribution functions as parametrized by Duke and Owens for Λ=200 MeV/8/ at maximum HERA beam energies (E_e=30 GeV, E_p=820 GeV and an integrated luminosity of 200pb^{-1}, which means 100pb^{-1} for each beam for $A^{\pm}(\lambda)$, cf. fig.1. In the Q^2-range of a few thousand GeV^2 the propagator effect of the Z-bosons is clearly visible (fig.1a) and neutral and charged current event rates become of comparable size (fig.1b).

Since the kinematic range at $S\approx10^5$ GeV^2 is rather wide one has to carefully study the kinematic dependences and cuts. Fig.2 displays the statistical precision of $\sin^2\theta$ derived from A^- (dashed line) and R^- (full line) as functions of minimum x,y, and Q^2 included. Although it appears advantageous to include very small x data, we limit $x>0.1$ to reduce the uncertainties due to sea quarks (cf. sect. 4), The minimum y-values are dictated by the detector's resolution and are y_{min}=.01 (.1) for jet-(electron) measurement /4/. Furthermore, to ensure $A^->5\%$ and $R^-<50$ we somewhat arbitrarily demand $Q^2>500$ GeV^2 . Thus, a "working area " is defined by $x > .1$, $y > .01$ and $Q^2 > 500$ GeV^2. If not stated differently both A^- and R^- are calculated for $|\lambda| = .8$ /9/. Searching for the maximum sensitivity of A^- and R^- fixing besides α a second electroweak parameter and measuring $\sin^2\theta$, M_z or M_w we find the statistical precisions summarized in table 1.

fixed / fitted		$\sin^2\theta$	M_z	M_w	G_F
$\sin^2\theta$	A^-	-	.005	.005	.007
	R^-	-	.002	.002	.005
M_z/GeV	A^-	3.02	-	.25	1.09
	R^-	.51	-	.10	.76
M_w/GeV	A^-	2.53	.27	-	1.38
	R^-	.45	.10	-	.95

Table 1

A^- gives a 2.5 times worse result than R^- if M_z is fixed and a 1.4 times worse result if G_F is fixed. Thus best sensitivity to both $\sin^2\theta$ and M_w is provided by R^- fixing α and M_z(LEP).

The availibility of two sensitive observalbles A^- and R^- suggests to simultaneously to determine two electroweak quantities, e.g. fixing α and measuring both M_w and M_z. The two-parameter χ^2-analysis yields 1σ-error contours roughly extending from $M_{w,z}$=-6GeV to $M_{w,z}$=10 GeV with parabolic errors of about 200 MeV for R^-. The error-contour for A^- is almost parallel to the former and does not allow any reduction of the errors. This is due to the dominating influence of the functions $K_{w,z}(Q^2)$ which are still of comparable size in average in the kinematical range of HERA. Therefore, with A^- and R^- two parameter fits of electroweak parameters are not possible.

It is of importance to quantify the influence of the beam-polarization in these considerations. As shown in fig. 3$^{+)}$ ΔM_w if measured via R^+ or R^- is only weakly dependend on λ. Otherwise a strong dependence is implied if $A^\pm$ are used. Since R^- is the most sensitive observable for measuring $\sin^2\theta$ and M_w the polarization of the electron beams is not needed for this purpose. If $|\lambda|$=.8 is replaced by λ=0 for R^- $\Delta\sin^2\theta$ increases from .0020 to .0023 and ΔM_w from .100 GeV to .250 GeV.

The W-exchange form factor $\Delta r = F_w - 1$ entering the functions (7,8) may be used to derive limits on the top quark- and Higgs-boson mass /7/. Fixing α, G_F and M_z the statistical error for Δr

+) The weak dependence of $\Delta\sin^2\theta$ on λ if measured with R+/- was also noticed in /10/.

are .022 for A^- and .006 for R^-. Fig. 4 illustrates the Δr-measurement for R^-. The $\pm$ statistical error is shown as the dashed area assuming M_H= 100 GeV for the central value. For $m_t > 100$ GeV /11/ a precision of $\Delta m_t = \pm$ 20 GeV is found. Furthermore, $\Delta r(M_H$=1TeV)-$\Delta r(M_H$=10 GeV) is larger than 2σ in this range.

4. Uncertainties of the analysis

The above derivation of statistical precisions of various quantities were carried out assuming a series of parameters which may introduce nonnegligible errors. Their effect will be discussed in this section.

4.1. Experimental error of electroweak parameters fixed

α and G_F are known to a precision which does not significantly influence the precision of the measured quantities. This can be different for M_Z and $\sin^2\theta$ if used as input parameters which are fixed. Taking both values from LEP /3/ $\Delta\sin^2\theta$ = .001, M_Z=50 MeV the error for measuring $M_{W,Z}$ with $A^-(R^-)$ fixing $\sin^2\theta$ implies an error of .58GeV(.28GeV) which is larger than the statistical precisions. Otherwise, fixing M_Z the corresponding errors for $\sin^2\theta$ and M_W are .0001 and .05 GeV for A^- and .0002 and .05 GeV for R^-.

4.2. $R = \sigma_L/\sigma_T$

Replacing R = 0 by the rather large value R=.1 (still allowed by experiment) an error of $\sin^2\theta$ of .0003(.0008) is introduced for $A^-(R^-)$. The corresponding errors ΔM_W are 15MeV(40 MeV).

4.3. Quark masses and mixing

Replacing the description of cross sections (1,2) by the expressions with explicit quark mass dependence /12/ and using the quark distributions /13/ a shift in $\sin^2\theta$ of .0001 and in M_W of 4 MeV is estimated. The inclusion of the errors of the Kobayashi-Maskawa matrix /14/ yields corrections at the per cent level of the statistical precisions (cf. also /10/).

4.4 Uncertainty of quark distribution parametrizations

The dominant uncertainty is implied by the uncertainty of the quark distribution parametrizations. Performing 10% changes of the sea, u_v and d_v distributions introduces the following deviations in $\sin^2\theta$

	sea	u_v	d_v
A^-	$\mp$ .0003	$\mp$ .0014	$\pm$ .0011
R^-	$\pm$ .0017	$\mp$ .0031	$\pm$ .0015

Table 2

are found.

This uncertainty thus remains only smaller than the statistical precision if the parton distributions can be controlled at the 5% level. As cutlined in /1/ (cf. also /15/) this seems to be possible using $F_2(Q^2 < 1000\ GeV^2)$ and $\sigma^+_{cc}/\sigma^-_{cc}$, which can be determined without reference to electroweak parameters, as constraints. Furthermore, one will calculate the electroweak quantities under differnt cuts and from different quantities ($A^{\pm}$, R^+, R^-) which further minimizes this uncertainty.

5. Extensions of the model

In this section we will give up the strict parameter relations of the minimum theory and allow for different type extensions.

5.1. $\rho \neq 1$

Giving up the relation $\rho = (M_W/M_Z\cos\theta)^2 = 1$ and fitting (ρ, $\sin^2\theta$) one finds parabolic errors $\Delta\rho = .01$ and $\Delta\sin^2\theta = .006$ (CCF=-.96). Fixing $\sin^2\theta$ yields $\delta\rho = .003$ /16/.

5.2. M_W and M_Z fitted from the propagators

Ignoring the relation between M_W, M_Z and $\sin^2\theta$ one can fit the gauge boson masses from the propagator terms only fixing $\sin^2\theta$ in the couplings. One obtains ΔM_Z = 3GeV(5.6 GeV) for $A^-(R^-)$ and the interesting number ΔM_W =450MeV for R^-.

5.3. Right handed isospin components

Modifying the vector- and axialvector couplings v and a to $v = I_3^L + I_3^R - 2Q\sin^2\theta$, $a = I_3^L - I_3^R$ the sensitivity to $I_3^R(e,u,d)$ is determined. Best precisions are obtained from $A^{+/-}$ with $\Delta I_3^R(e,u,d)$ = (.056,.034,.016) for A^-; for A^+ $\Delta I_3^R(e)$ improves to .03 which is comparable to the present world average/17/.

5.4. New W- and Z-bosons and the scale of weak boson compositeness

Assuming one extra W- or Z-boson resp. and fixing the masses and couplings thus that the standard model low energy limit is conserved R^- allows to detect an additional W-boson for $M_{W'} < 190$GeV(390GeV) at the $3\sigma(1\sigma)$ level. Similarly, A^- can be used to detect an additional Z-boson if $M_{Z'} < 230$GeV(400GeV), assuming in both cases the same coupling for the standard and additional gauge boson. (The explicit coupling dependence is calculated in /1/). According results for an addition W'-boson have been obtained also in /18/. In a first approximation the compositeness scale of the weak bosons should show up as an additional factor $\times\ 1/(1+Q^2/\Lambda^2)$ in the functions $K_{W,Z}$. Whereas A^- can not be used to set significant limits for Λ (cf./1/), R^- is sensitive to $\Lambda <$ 500 GeV at the 2σ level.

6.Conclusions

Referring to the standard theory best sensitivity to the electroweak parameters was found for R^-. Assuming a luminosity of 200 pb^{-1} $\sin^2\theta$ and M_W can be determined with a statistical precision of .002 and 100 MeV resp. in a kinematic range where the systematics can be controlled adequately. The corresponding precisions for A^- are 2 to 3 times worse. The theoretical error is dominated by the uncertainty of the quark distribution functions and is estimated to be less than the statistical precisions. While the measurement of A^- requires highly polarized electron beams the measurement of the electroweak parameters via R^- is only weakly dependend on the electron polarization. Extensions of the minimum theory can be tested with high precision. HERA should allow for meaningful tests of the electroweak theory complementary to e^+e^--colliders and more accurately than the presently existing $p\bar{p}$-experiments.

Acknowledgement. For discussions I would like to thank W.Hollik and J.Kühn.

References

/1/ J.Blümlein, M.Klein,T.Riemann, PHE 87-03
/2/ DESY HERA 81/10 (1981)
/3/ "Physics at LEP", CERN 86-02 Vol.I,II,ed.: J.Ellis and R.Peccei
/4/ J.Feltesse, H1-Notes 4/85-04(1985);5/85-17(1985),H1 Technical proposal, March 1986
/5/ M.Böhm, H. Spiesberger, Würzburg preprints April and December 1986
D.Y. Bardin et al. Dubna preprint July 1987;J.Phys. G7(1981)1331
J.Feltesse, DESY HERA 83/20, Oct.1983,371
/6/ M.Klein,T.Riemann, Z.Phys. C24(1984)151
/7/ W.Hollik, DESY 86-049 and references therein;D.Y.Bardin et al., Z.Phys. C32(1986)121
/8/ D.W. Duke, J.F.Owens, Phys. Rev. D30(1984) 49
/9/ DESY HERA 81/10
/10/ J.F. Wheater, Nucl.Phys. B233(1984) 365
/11/ A value for the top quark mass of O(100 GeV) is not unprobable from the recent results on B^0-$\bar{B}^0$ mixing(cf. G.Altarelli, Summary talk, EPS HEP'87, Uppsala,SWEDEN, July 1987).Furthermore,it is lower than the currently obtained upper limit of 200 GeV (cf. U. Amaldi et al., CERN EP-87/93).
/12/ H.Georgi,H.D.Politzer, Phys.Rev. D14,1829(1976);R.Barnett,Phys. Rev. D14(1976)70;R.Brock,Phys.Rev.Lett.44(1980)1027
/13/ E.Eichten et al. Rev.Mod.Phys. 56(1984)247;58(1986)1065
/14/ K.Kleinknecht,B.Renk,Proc.Int.Symp.Prod.Decay of Heavy Hadrons, Heidelberg 1986, DESY 1986, 150

/15/ J. Blümlein et al., in preparation

/16/ A measurement of ϱ to this precision could also allow to set precise limits for m_t (cf. G.Altarelli in ref./11/)

/17/ M.Klein, S.Schlenstedt, Z.Phys. C29(1985)235

/18/ R.Cashmore et al., Phys. Rep. C122(1985)275

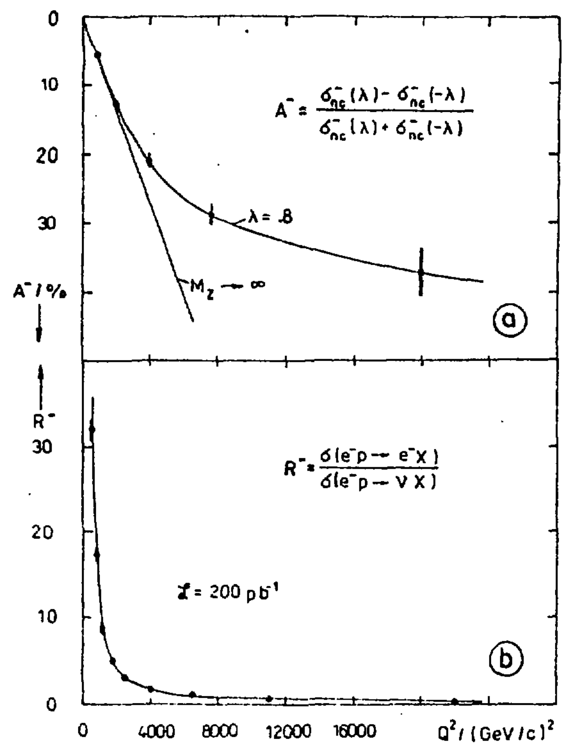

Figure 1:
Statistical precisions of A^- and R^- in dependence of Q^2

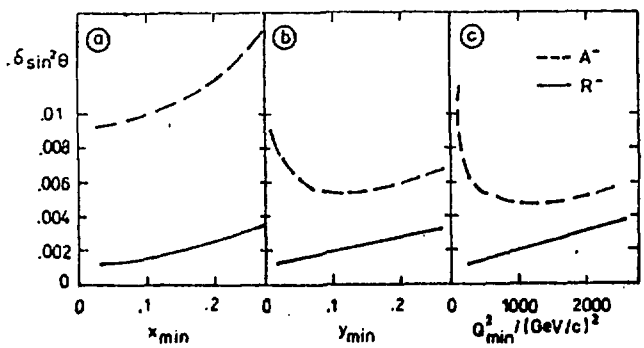

Figure 2:
Statistical precisions of $\sin^2\theta$ as a function of the minimum x,y and Q^2

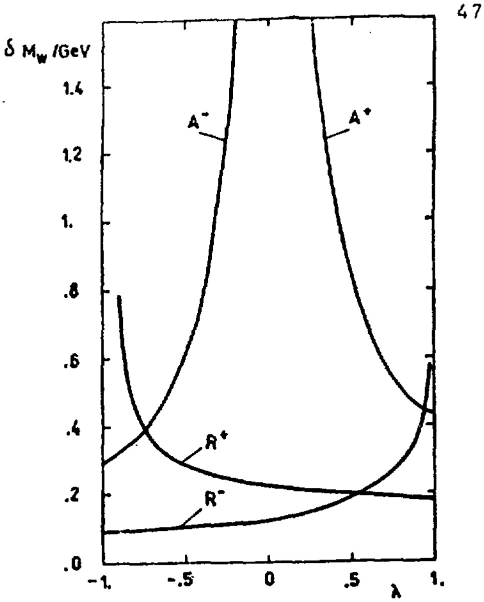

Figure 3:
Statistical precision of M_W as a function of the beam polarization and polarization difference resp. measuring $R^{+/-}$, $A^{+/-}$

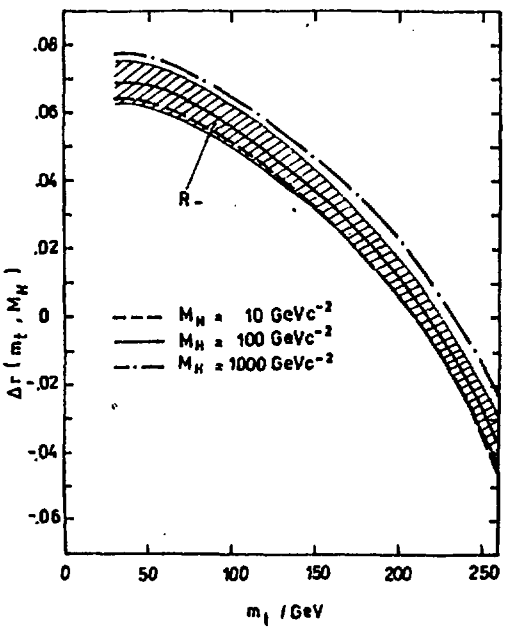

Figure 4:
Δr in dependence of m_t and M_H (ref./7/).
The shaded area corresponds to the error induced for Δr by the $\pm$ statistical error of $\overline{R}^-$ ($/\lambda/=.8$) taking M_H= 100 GeV

ZZ PRODUCTION IN A COMPOSITE MODEL

Maria Krawczyk*

Institute of Theoretical Physics
Warsaw University, Warsaw, Poland

Abstract: The effective electroweak theory with composite Z in the version proposed by Boudjema and Dombey [1] leads to the predicton that the electromagnetic couplings of the Z are substantially larger than they are in the standard electroweak theory.

-- We found that this anomalous $ZZ\gamma$ coupling may be observed in the process $e^+e^- \to ZZ$ at energy $\sqrt{s}$ bigger than 270 GeV.

-- This coupling may as well be seen in the inclusive ZZ production in $p\bar{p}$ collision for σ_{TOT} at energy $\sqrt{s}$ >900 GeV. In the p_T distribution the large contribution due to composite Z may be observed in $p\bar{p} \to ZZ\,X$ already at $\sqrt{s}$ = 630 GeV for p_T larger than 70 GeV/c.

---

* Supported in part by Ministry of Science and Higher Education, Research Problem CPBP 01.03.

Introduction

The standard electroweak theory works perfectly in full agreement with experimental data. Nevertheless there are attempts to investigate other models which would share the success of the standard theory having at the same time less parameters and avoiding the introduction of Higgs particles , not seen so far experimentally.

Here we consider the composite model by Boudjema and Dombey [1], where massive vector bosons W and Z are assumed to be bound states of elementary constituents, called haplons . The γ and other basic objects of the electroweak theory -leptons and quarks- are elementary particles and are described in a conventional manner. Similar ideas were discussed some times ago by Greenberg and Sucher [2], Chen and Sakurai [3], Fritzsch and Mandelbaum [4], Abbott and Fahri [5].

Haplons are assumed to have spin 1/2 , they carry color (N_c=3) and flavour (N_f=2) quantum numbers. To reproduce known results for low energy electroweak processes (say for $\sqrt{s}$ up to M_W) they have to carry new quantum number, called hypercolour (N_H=3). According to the prescription done by Boudjema and Dombey [1], which we adopt here, all parameters for these hypothetical particles are estimated using the old vector dominance idea .

The non-elementary structure of vector bosons W, Z leads to the effective three boson couplings due to the haplon loop. These couplings happen to be quite large in contrast to the corresponding couplings due to lepton and quark loops in the standard theory. In the work [1] the possible observation of the effective $ZZ\gamma$ coupling with one virtual Z ($ZZ^{*}\gamma$) in the process $e^{+}e^{-} \to Z\gamma$ has been discussed .

Here we propose to consider the $ZZ\gamma$ effective vertex with virtual γ ($ZZ\gamma^{*}$) in the high energy process $e^{+}e^{-} \to ZZ$ and the related hadronic process $p\,\bar{p} \to ZZ\,X$.*

We start with the description of general features of standard and composite contributions to the ZZ production in fermion -antifermion annihilation processes. Then we will present the comparison of the composite and standard approaches to the process $e^{+}e^{-} \to ZZ$. Next we discuss the inclusive ZZ production in the high energy $p\,\bar{p}$ scattering.

General remarks

We would like to test the effective $ZZ\gamma^{*}$ coupling by comparing the lowest order predictions for the process $f\bar{f} \to ZZ$ in the composite model [1] and in the standard electroweak theory (f stands for an electron or a quark) .Our aim is to answer the question whether and where this anomalous coupling may be observed. Therefore,we will simplify the computation of composite and standard contribution as much as possible .The more detailed analysis will be given elsewhere .

In the composite model this effective coupling is due to the haplon loop diagram (fig.1)

---

*Similar method of testing the compositness of gauge boson Z was dicussed in ref.[7].

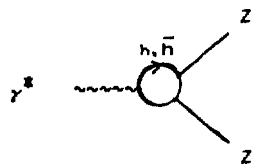

fig.1

For the process $f\bar{f}\rightarrow ZZ$ this leads to the "s-channel" contribution with the effective $ZZ\gamma^*$ coupling constant (fig.2)

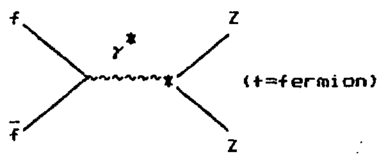

fig.2

In the standard model a similar diagram exists , with haplon loop replaced by quark and lepton loops. However, according to the anomaly cancelation the size of this effective vertex is negligible . Therefore, for the reaction $f\bar{f}\rightarrow ZZ$ in the standard theory we will consider only the "t- or u- channel" diagrams (fig.3).

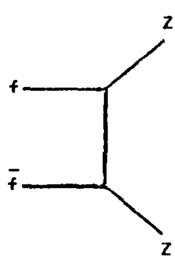

fig.3

Since we are interested in high energy processes we neglect in the following analysis masses for all standard fermions . For the boson Z we take M_Z = 92 GeV . The other standard parameters are taken in a simple way :

$$\alpha_{el} = 1/128 \ , \ \sin^2\theta_W = 1/4 \ . \qquad (1)$$

To describe the composite Z contribution we follow the approach of ref.[1] where the couplings of haplons to boson Z , α_H ,are determined (as well as their mass M_H , charge Q_H and other attributes) from the experimental low energy data using the γ-W^0 mixing and the idea of vector dominance. We refer for details to the original work [1].

For the composite model we consider in detail only the "optimistic parameters" (giving the largest chance for the observation in the near future) from [1]:

$$\alpha_H=3 \quad (g_V^H=g_A^H=g_H \ , \ g_H^2/4\pi = \alpha_H) \quad M_H=200 \text{ GeV} \quad \bar{Q}_H=1/6 \quad N_H=3 \ , (2)$$

where $\bar{Q}_H$ is the average electric charge for haplon doublet. $\bar{Q}_H=1/6$ corresponds to the charge assignment for haplons similar to that for u and d quarks.

We will consider also this set of parameters with different values for mass of haplon : M_H=400 and 600 GeV.

<u>e^+e^-===>ZZ</u>

The differential cross section is equal (in the CM system)

$$\frac{d\sigma}{d\cos\theta} = \frac{p_Z}{16\,\pi\, s\sqrt{s}} \, |\bar{M}|^2 \ , \qquad (3)$$

where p_Z is the momentum of the boson Z , $p_Z= 1/2\sqrt{s-4M^2}$. The matrix element $|\bar{M}|^2$ is averaged over the initial and summed over the final spins .

1) In the composite model we found (see also [1])

$$\overline{|M|}^2 = \frac{1}{4} N s \frac{(s-4M_Z^2)^2}{M_Z^2} (1 + \cos^2\theta) \; |I_f(s)|^2 \; ; \qquad (4)$$

here θ means the scattering angle in the e^+e^- CM system ,

$$N = [16 \; \alpha_{el} \; \alpha_H \; N_H \; N_c (2 \; \tilde{\Omega}_H)]^2 \qquad (5)$$

and the integral

$I_f(s)=$

$$= \int_0^1 dx_1 \int_0^{1-x_1} dx_2 \; \frac{x_1 \; x_2}{M_H^2 + (x_1+x_2) \; (x_1+x_2-1) \; M_Z^2 - x_1 x_2 s} \qquad (6)$$

To evaluate this integral we used the following approximation, justified for $M_H >> M_Z$,

$$I_f(s) ==> \int_0^1 dx_1 \int_0^{1-x_1} dx_2 \frac{x_1 x_2}{M_H^2 - x_1 x_2 s} . \qquad (7)$$

2) In the standard model the elementary coupling $Z <--> f\bar{f}$ is equal to

$$-i \; \frac{g}{\cos \theta_W} \gamma^\mu \frac{1}{2}(c_V^f - c_A^f \; \gamma^5) , \quad \text{where } g= \frac{e}{\sin \theta_W} \quad , \quad \alpha_{el} = \frac{e^2}{4\pi} \qquad (8)$$

with

$$\left. \begin{array}{l} c_A^e=-1/2 \\ c_V^e=-1/2+2\sin^2\theta_W \end{array} \right\} \text{for electron}$$

In the standard theory we have for $e^+e^- ---> ZZ$ (see also [6]):

$$|\bar{M}|^2 = \frac{1}{2}\ \frac{1}{4}\ \frac{\pi^2\alpha_{el}^2}{\sin^4\theta_W\ \cos^4\theta_W}\ ((c_V^e)^4 + (c_A^e)^4 + 6(c_V^e)^2(c_A^e)^2).$$

$$.[\ \frac{t}{u} + \frac{u}{t} + \frac{4\ M_Z^2\ s}{u\ t} - M_Z^4\ (\frac{1}{t^2} + \frac{1}{u^2})\ ]\ . \tag{9}$$

Results obtained for $e^+e^- \to ZZ$, for the total cross section and for the angular distribution , are presented in fig.4 .a and 4.b.*

Comparing the σ_{TOT} in the standard theory (with parameters (1)) and in the composite model (with optimistic parameters (2)), presented in fig.4a , we see that the latter contribution dominates at energy > 270 GeV. For $\sqrt{s}$ >400 GeV the composite model with M_H=200 GeV gives more than two orders of magnitude bigger predictions than the standard model .We present also the predictions for haplon masses equal 400 and 600 GeV, where the domination of the composite model occurs at higher energy.

The angular distributions are very different in both approaches, as can be see in fig.4b .For standard contribution the forward and backward scatterings dominate, whereas in the composite model we observe the $1+\cos^2\theta$ dependence. In fig.4b we ilustrate these behaviours for M_H=200 GeV and for energy 275 GeV, where the cross sections are approximately equal.

---

* Note that the sharp turning of the total cross sections is due to the different behaviour of the integral (7) for $\sqrt{s}$ bigger and less than $2M_H$.

$p\bar{p}$ ===> ZZ X

To calculate the total or the differential cross section for the inclusive ZZ production in the $p\bar{p}$ collision we used the above formulae for $q\bar{q}$ -->ZZ subprocesses with obvious modifications - for couplings:

$$\left.\begin{array}{l} c_A^u = 1/2 \\ c_V^u = 1/2 - 4/3 \sin^2\theta_W \end{array}\right\} \text{for } u\text{- quark}$$

$$\left.\begin{array}{l} c_A^{d,s} = -1/2 \\ c_V^{d,s} = -1/2 + 2/3 \sin^2\theta_W \end{array}\right\} \text{for } d,s \text{ -quark}$$

for charges:

$q_u = 2/3$

$q_{d,s} = -1/3$

and for the probability the factor $=1/N_c$.

Note ,that the charm quark contribution is neglected in the whole analysis.

The total cross section for ZZ production in $p\bar{p}$ collision is equal to

$$\sigma(s) = \int_0^1 dx_1 F(x_1, Q^2) \int_0^1 dx_2 F(x_2, Q^2) \int_{-1}^{1} d\cos\theta \frac{d\sigma^{q\bar{q}\text{---->}ZZ}}{d\cos\theta}(\hat{s}) \quad ;(10)$$

here θ means the scattering angle in the $q\bar{q}$ CM system and $\hat{s} = x_1 x_2 s$ is square of the total energy in this system. Functions $F(x, Q^2)$ are structure functions of proton or antiproton.

Numerical calculation for p $\bar{p}$ were done using Monte Carlo program on PC IBM-type computer. We have considered total cross sections and p_T- distributions for Z bosons. We used the Duke and Owens parametrization of structure functions [9] (set 2, denoted by DO2 with the energy scale $Q=M_Z$ .We have checked that the other choices of Q (equal to p_T or invariant mass $M = \sqrt{\hat{s}}$) would not change the results in a visible way. This same is true if one changes the parametrization to the parametrization by Eichten et al.[10] (set 2, Ei2) with the energy scale $Q = M_Z$, p_T or M.

The results obtained for the composite model with the optimistic parameters and for the standard model with parameters (1) are presented in figs.5. The total cross section in the composite model starts to be greater than in the standard case already at 900 GeV , at higher energy there is one order of magnitude difference between these two approaches (fig.5.a).

In the p_T- distribution (fig.5 b,c) the composite model dominates the large p_T tail. For the scattering energy $\sqrt{s}$ = 630 GeV the cross over of the predictions of the composite and standard model occurs at $p_T \sim$ 100 GeV/c for the $1/p_T d\sigma/dp_T$ (fig. 5.b) and for $p_T \sim$ 70 GeV/c for the integrated p_{T_0} - distribution (fig.5.c).

We see that the possible signature of the composite Z production in the high energy $p\bar{p}$ scattering for the energy $\sqrt{s} \leq 1$ TeV would be the higher than standard production rate for the events with large p_T Z .One may expect a similar effect for the W production in the same process.

Conclusion

We consider the anomalous effective coupling $ZZ\gamma$, reflecting the composite structure of gauge boson Z, in the high energy e^+e^- annihilation and in the inclusive $p\bar{p}$ scattering.

For these processes the predictions of the composite model in version proposed by Boudjema and Dombey [1] (with the optimistic parameters) and the standard theory are compared.

For $e^+e^- \to ZZ$ these two approaches give similar predictions for the total cross section at $\sqrt{s}=270$ GeV ; there are two orders of magnitude difference for the energy $\sqrt{s} > 400$ GeV . Unfortunately , even the energy 270 GeV will not be reach in near future for this process..

The situation in $p\bar{p} \to ZZ$ looks more promising .Here the composite contribution may dominate in the p_T - distribution even at the energy accessible now. At energy $\sqrt{s}=630$ GeV this may happen in $1/p_T d\sigma/dp_T$ for p_T >100 GeV/c and in the integrated p_{T_0} -distribution already for p_T>70 GeV/c. The composite Z may show up rather soon also in the total cross section - for $\sqrt{s} > 900$ GeV. For higher energy the standard contribution is approximately an order of magnitude smaller than the one with composite Z.

Probably the signature of the anomalous coupling $ZZ\gamma$ may be registered in the e^+e^- or $p\bar{p}$ data before the cross over of these two competitive model predictions takes place ,that means at lower energy or transverse momentum p_T quoted above.

Is there any relation of the results for the p_T distribution in $p\bar{p} \to ZZ$ with unusual events with large p_T Z and W production from UA1 collaboration [8] ? To obtain any reliable estimation in this case the more detailed analysis has to be done for ZZ as well as for the WW and WZ production and for the possible backgrou (now under preparation).

Acknowledgements

This work is based on the collaboration with dr. N.Dombey and dr. F.Boudjema. I would like to thank them for useful discussions and comments.

I have enjoyed conversation with prof. Królikowski ,prof. Pokorski and dr. Mańka and dr.Kołodziej .

I would like to thank dr. M.Markytan for sending me preprints on UA1 results and dr. Jan Kalinowski for very useful comments and reading the manuscript.

References

1.F.Boudjema and N.Dombey, An effective theory of a composite Z, preprint ,January 1987

2.O.W.Greenberg and J. Sucher, Phys.Lett. 99B 339 (1981)

3.P.Chen and J.J.Sakurai, Phys.Lett. 110B 481 (1982)

4 H.Fritzsch and G.Mandelbaum , Phys.Lett. 102B 319 (1981) ,Phys. Lett. 109B 224 (1982)

5.L.Abbott and E.Farhi ,Phys.Lett. 101B 69 (1981)

6.R.W.Brown and K.O.Mikaelian, Phys. Rev.D19 922 (1979)

7.P.Mery ,M.Perrottet and F.M.Renard Anomalous effects in e^+e^- annihilation into boson pairs: (II) $e^+e^- \to ZZ, \gamma Z, \gamma\gamma$, CERN-TH.4741/87

8.C.Albajar et al.(UA1 Collaboration) ,Production of W's with large Transverse momentum at the CERN Proton-Antiproton Collider, CERN-EP/87-82, April 24th, 1987

9.D.W.Duke and J.F.Owens, Phys.Rev.D30 49 (1984)

10.E.J.Eichten,I.Hinchcliffe, K.D.Lane and C. Quigg, Rev.Mod.Phys. 56 579 (1984)

Figure captions

1.The induced $ZZ\gamma$ coupling via haplon loop

2.$f\bar{f} \to ZZ$ in the composite model

3.$f\bar{f} \to ZZ$ in the standard electroweak theory

4. Results for $e^+e^- \to ZZ$ in the composite model (- - -) and in the standard theory (——)

a. total cross section

b. angular distribution

5. Results for $p\bar{p} \to ZZ$ in the composite model (- - - -) and in the standard theory (——)

a. total cross section

b. p_T- distribution $1/p_T d\sigma/dp_T$

c. p_{T_0}-distribution $1/\sigma_{TOT} \int_{p_T > p_{T_0}} 1/p_T d\sigma/dp_T$

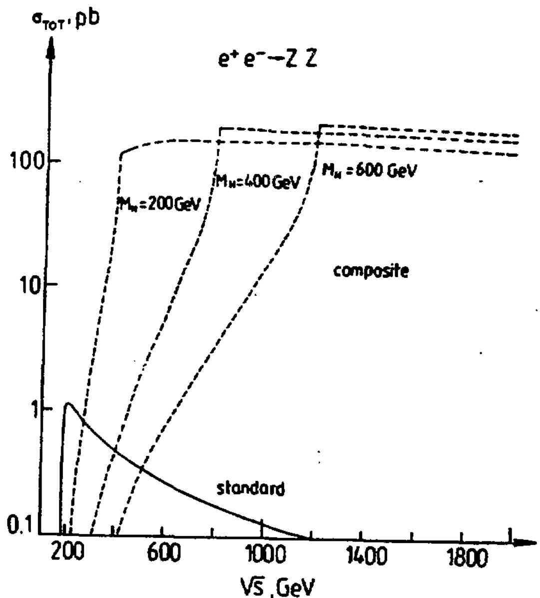
σ_{TOT}, pb
$e^+e^- \to ZZ$
100
10
1
0.1
$M_H = 200$ GeV
$M_H = 400$ GeV
$M_H = 600$ GeV
composite
standard
200
600
1000
1400
1800
$\sqrt{s}$, GeV

Rys. 4a

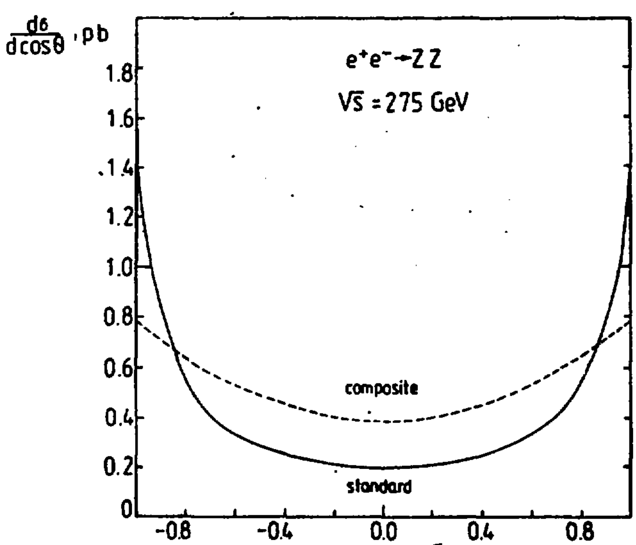
$\frac{d\sigma}{d\cos\theta}$, pb
$e^+e^- \to ZZ$
$\sqrt{s} = 275$ GeV
1.8
1.6
1.4
1.2
1.0
0.8
0.6
0.4
0.2
0
composite
standard
-0.8
-0.4
0.0
0.4
0.8
$\cos\theta$

Rys. 4b

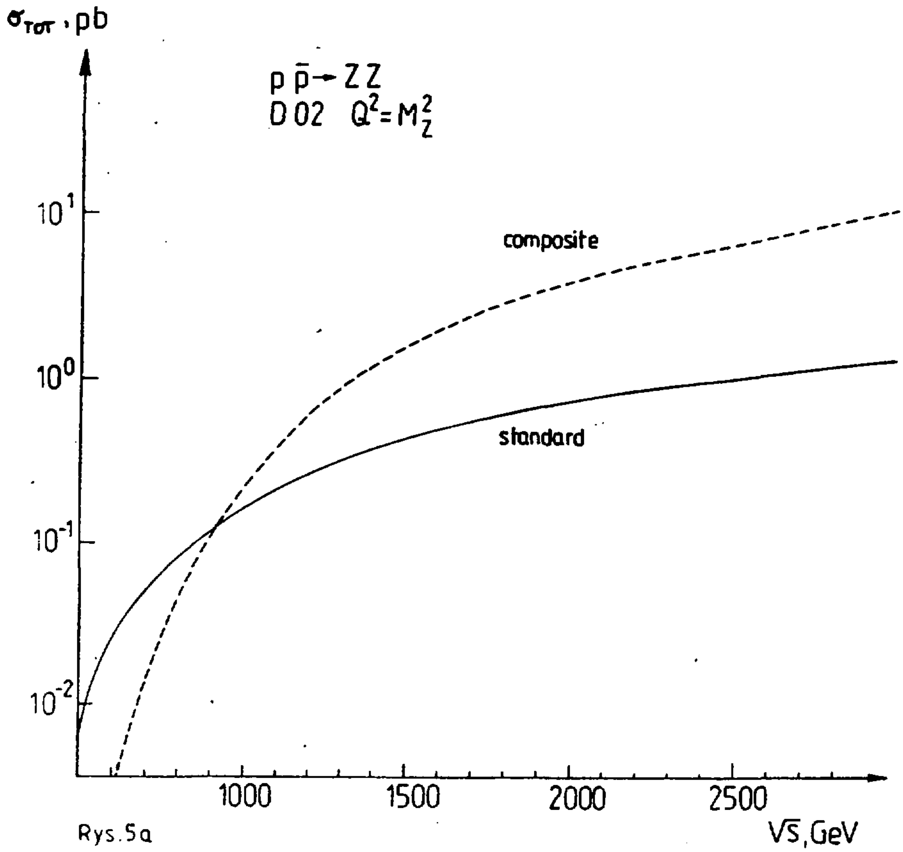

σ_{TOT}, pb
$p\bar{p} \to ZZ$
D02 $Q^2 = M_Z^2$
10^1
10^0
10^{-1}
10^{-2}
composite
standard
1000
1500
2000
2500
$\sqrt{s}$, GeV

Rys.5a

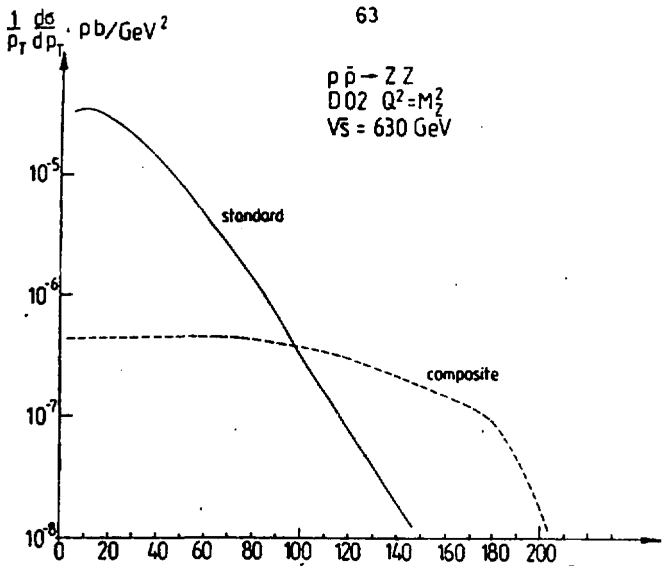

$\frac{1}{p_T}\frac{d\sigma}{dp_T}$, pb/GeV^2
$p\bar{p} \to ZZ$
DO2 $Q^2 = M_Z^2$
$\sqrt{s}$ = 630 GeV
standard
composite
10^{-5}
10^{-6}
10^{-7}
10^{-8}
0 20 40 60 80 100 120 140 160 180 200
P_T, GeV/c

Rys. 5b

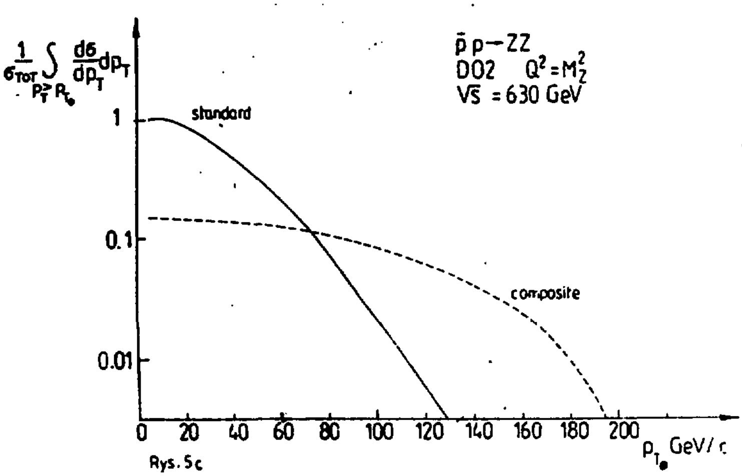

$\frac{1}{\sigma_{TOT}}\int_{p_T \geq p_{T_e}} \frac{d\sigma}{dp_T} dp_T$
$\bar{p}p \to ZZ$
DO2 $Q^2 = M_Z^2$
$\sqrt{s}$ = 630 GeV
standard
composite
1
0.1
0.01
0 20 40 60 80 100 120 140 160 180 200
p_{T_e} GeV/c

Rys. 5c

Standard-Model Higgs Searches at the SSC.

Jan Kalinowski [1]

Institute for Theoretical Physics, Warsaw University

Hoża 69, 00681 Warsaw, Poland

Abstract: The procedures for exploring the Higgs sector of the standard model at the SSC are shortly reviewed. The comparison of the effective-W approximation with the exact calculation for the process $ff \to ffWW$ shows that it reproduces the Higgs signal, while the continuum background can only reliably be computed in the exact calculation. The ability to isolate longitudinal W decay modes is discussed.

Introduction. With the discovery of the W and Z gauge bosons the model of Glashow, Salam and Weinberg has been accepted as a standard model (SM) of the electroweak interactions. Certain aspects of the model, however, have not been tested so far experimentally, for example the structure of the triple-gauge-boson coupling, the properties of the Higgs sector and the origin of mass. In the model the symmetry breaking is achieved by the Higgs mechanism and a single neutral Higgs particle emerges. Unfortunately, the present theory does not constrain its mass m_H. In the minimal three-generation SM the Higgs boson mass should be greater than about 10 GeV [1]. If a top quark mass $m_t \geq 50$ GeV or if a fourth generation of fermions exists, this lower limit disappears [2]. There is no upper limit to m_H. Nevertheless, it is generally assumed that m_H is somewhat below 1.5–2 TeV. Otherwise

---

[1] Supported in part by the Ministry of Science & Higher Education, Research Problem 01.03.

the Higgs self-energy coupling becomes strong and the perturbation theory breaks down. Even in such a case, however, use of ordinary perturbation theory may be justified by the fact that the deviations from the perturbative calculations will signal new physics.

For $m_H \leq 40$ GeV, the Higgs boson can be found at SLC or LEP if these machines reach their designed luminosity. With LEP II the range can be extended to about 80 GeV. The process considered there is the associated production $e^+e^- \rightarrow H + Z$ followed by $Z \rightarrow l^+l^-$. For a review of these topics see for example ref. 3.

In high energy hadron collisions the Higgs boson will be copiously produced. At the SSC, a pp collider with energy of 40 TeV and luminosity of $10^{33}cm^{-2}s^{-1}$, a large number of SM Higgs bosons is expected, of order 10^5/yr for $m_H \approx 300$ GeV [4]. However, it turns out that it will be more difficult to detect it because of strong SM and QCD background. Thus hadron colliders will primarily be of interest if m_H is above the reach of e^+e^- machines. If $2m_t < m_H < 2m_W$, no way has been found to overcome the QCD/SM background [5]. In this paper we will discuss the case of a heavy Higgs boson, $m_H > 2m_W$. The heavy Higgs boson decays almost exclusively into WW and ZZ pairs. Only purely leptonic decays of the Z boson are background free. However, they suffer from low event rate. Assuming that both μ's and e's can be identified, $H \rightarrow ZZ \rightarrow (l^+l^-)(l^+l^-)$ has a branching ratio $\cong 1.2 \times 10^{-3}$ which leads to 12 events in a standard SSC year. The mixed hadronic/leptonic Higgs decays have a higher rate. Although the separation of the signal from the background appears to be a serious problem, we will see that it may be possible to study the Higgs sector at the SSC for $m_H \leq 1$ TeV. Purely hadronic decay modes are overwhelmed by the QCD background events.

There are two significant production mechanisms for a heavy Higgs boson in the SSC energy range. The first is the gluon-gluon fusion [6] in which two gluons couple to a fermion loop and the Higgs boson is emitted from the loop.The second is the WW fusion mechanism [7] in which W's or Z's emitted by incident quarks collide and form the Higgs boson. It has been pointed out [4] that the latter mechanism dominates for $m_H \geq 300$ GeV, because the coupling of the Higgs boson to longitudinal W's or Z's is proportional to m_H. Duncan, Kane and Repko [8] have studied the properties of the on-shell WW scatering and the Higgs boson signal using the effective-W approximation [9] in which distribution functions for W's inside colliding protons are folded together with the on-shell WW amplitudes. The validity of this approximation has been found to be of order 20% for total cross section calculations for $W^+W^- \to H$ [10] and $qq \to q'UD$ [11] (where U and D are the quarks of a new generation). It has not been tested for the WW scattering. Moreover, in the context of Higgs boson searches the effective-W approximation cannot be reliably used to assess the impact of possible triggers on spectator quarks present in the final state. Such triggers may prove to be critical to isolate certain aspects of the WW scattering at the SSC, as advocated in ref.12. In addition, the W's in the final state will be identified by its decay products and it is important to assess the impact of kinematical cuts imposed to ensure that W's are reconstructed and their polarization measured.

To address the above issues the complete gauge invariant set of amplitudes for an arbitrary process $ff \to ffWW$ has been computed [13] without the effective-W approximation. Below I will present main results of this work. (For another exact calculations see ref.14.)

The calculations have been done using the massless spinor techniques of ref. 15 in which the final state W's are automatically decayed to massless fermions, so that the results include the full spin density matrix correlations for all final state particles. We have tested the gauge invariance by examining the scaling behaviour of our results. In refs. 13 we have focused exclusively on the charged current reactions to which $WW \to WW$ scattering diagrams contribute. The charged current sector has more singular structure in the effective-W approximation (a Coulomb pole from the photon exchange in the t channel) than e.g. $ZZ \to WW$ and therefore should yield the most sensitive comparison with the exact calculation. For simplicity explicit numerical results have been presented for the quark scattering subprocess

$$us \to dcW^+W^-. \qquad (*)$$

Comparison of the exact and the effective-W calculations. The comparison between the effective-W approximation and the exact calculations has been done both at the subprocess (*) level and after folding with the proton's quark distribution functions and we focused on a single center of mass energy for each reaction: $E_{cm}=\sqrt{s_{us}} = 1$ TeV and $\sqrt{s_{pp}} = 40$ TeV, respectively. We considered only $m_H = 0.5$ TeV or ∞. Our results are illustrative of those for other energies and Higgs masses. In order to make a comparison, it is necessary to impose a cut in the effective-W calculations to avoid the t-channel singularity from the photon exchange. We have chosen to restrict the WW center-of-mass scattering angle $\theta^*_{WW} > \theta_{min}$. Although the exact calculation is free of this singularity for comparison the same cut has been used.

The m_{WW} W-pair mass spectrum at the subprocess level is presented in fig.1 and for pp collisions in fig. 2. In the case of pp collisions only the single subprocess (*) is incorporated, the

EHLQ, $N_{set} = 2$, structure functions with the scale $Q = m_{VV}$ are used and no rapidity cut on the W's is imposed. The angular cuts, at $\theta_{min} = 10^{o}$, 30^{o} and 60^{o}, are imposed on the effective-W calculations at subprocess level and after folding and on the exact computations only at the subprocess level. Both figures show that the effective-W spectra normalization is very sensitive to this cut, while that of the exact calculation is much less so. The continuum level for $m_H = \infty$ varies by a factor of 10-20, as θ_{min} changes from 10^{o} to 60^{o}, whereas for the exact calculations it varies by a factor 1.5-2, depending on m_{VV} value. Note, however, that at any given θ_{min} the excess of the m_H=0.5 TeV peak over the $m_H = \infty$ continuum is nearly the same in both methods and mildly dependent on the θ_{min} cut. This confirms the results of ref. 10. Similar results to the above apply in the case of rapidity cuts. We anticipate that there will be a better level of agreement between the effective-W and exact calculations in sectors ZZ -> WW and ZZ -> ZZ, due to the absence of the singular photon exchange diagram. Therefore one can hope to identify those channels and cuts for which the effective-W approximation can reliably be used to evaluate not only the Higgs signal, but also the magnitude of the vector-boson scattering amplitudes.

Properties of the exact calculations. The Higgs boson decays almost exclusively to longitudinally polarized gauge bosons. Therefore in searches for Higgs it may prove very useful to measure polarization of W's. The polarization of the final state W can be detected by the decay distribution of the $f\bar{f}$ pair in the rest frame of the W, which should be of $\sin^2\theta^*$ form for longitudinal W and $1+\cos^2\theta^*$ for transverse. Fig.3 shows that at m_{VV} = 0.5 TeV the decay is predominantly longitudinal if m_H = 0.5 TeV, while is predominantly transverse for $m_H = \infty$, as expected.

In the hadronic decay mode, $W \to$ jet + jet, the above angular distribution cannot be used due to strong QCD/electroweak background from events containing W + two jets that simulate a second W. It was shown in ref. 16 that in such a case the longitudinal W's can be revealed by a careful study of correlations between transverse momenta of the two jets, p_{T1} and p_{T2}. The longitudinal W's populate the region of constant $r_{min} + r_{max}$, while transverse and other backgrounds contribute mainly to the $r_{min} = 0$ region, where $r_{min} = p_{T1}/m_{VV}$, $r_{max} = p_{T2}/m_{VV}$, $p_{T1} < p_{T2}$. Taking $m_{VV} = 0.5$ TeV, $r_{max} = 0.225$, we observe in fig.4 a peaking in the r_{min} distribution at large r_{min} for $m_H = 0.5$ TeV (so that longitudinal W's are copiously produced), whereas it falls rapidly at high r_{min} for $m_H = \infty$

The totally new feature of the exact calculation is the ability to discuss the p_T distribution of the spectator quarks present in the process (*). In the effective-W approximation spectator quarks and W's are necessarily emitted in the forward direction. It has been suggested in ref.12 that triggering on the p_T of the spectator quarks can significantly reduce the background to the Higgs signal, because the background processes tend to have spectator jets at low p_T. In fig.5 the p_T^{low} spectrum is presented, where p_T^{low} is the smallest p_T of the spectator jets. We find that a p_T cut on spectator quarks, while improving quality of the selected Higgs sample (stronger r_{min}-r_{max} correlations), tends to increase the background/signal ratio, as seen in fig.5.

Finally, I would like to mention that potentially dangerous gluon exchange diagrams with W's emitted from quarks do not, in fact, present a problem, if rapidity cuts on the W's are imposed .

Conclusions. Detection of a standard model Higgs at an e^+e^- collider is relatively straightforward, but limited to $m_H \leq 80$ GeV by planned accelerators. In pp collisions detection of Higgs is far from easy. Only purely leptonic decays are background free. The mixed hadronic/leptonic modes may be accesible for $2\, m_W < m_H \leq 1$ TeV, if sufficiently strong cuts and resolutions can be imposed. The effective W approximation reliably reproduces the Higgs signal. Production of the longitudinal W's in the hadronic decay mode can be revealed by examining correlations between the transverse momenta of the two decay product jets. The imposition of cuts on the spectator jets must be done with care to avoid the backgrounds in the Higgs signal.

Acknowledgements

I would like to thank J.F. Gunion and A. Tofighi-Niaki for the important contribution to the effords summarized herein. I thank also G. Kane, S Willenbrock, F. Olness and W. Repko for helpful conversations.

References

1. A.D. Linde, JETP Lett. 23 (1976) 64; S. Weinberg, Phys.Rev.Lett. 36 (1976) 294.
2. R.A. Flores and M. Sher, Ann.Phys. 148 (1983) 95.
3. "Physics at LEP", CERN 86-02, ed. J. Ellis and R. Peccei.
4. E. Eichten et al., Rev.Mod.Phys. 56 (1984) 579.
5. J.F. Gunion et al., Phys.Rev.D34 (1986) 101.
6. H. Georgi et al., Phys.Rev.Lett. 40 (1978) 692.
7. D.R.T. Jones and S.T. Petcov, Phys.Lett. 84B (1979) 440; R.N. Cahn and S. Dawson, Phys.Lett. 136B (1984) 196; 138B (1984) 464E.
8. M.J. Duncan, G.L. Kane and W.W. Repko, Nucl.Phys.B272 (1986) 517.
9. M.S. Chanowitz and M.K. Gaillard, Phys.Lett.142B (1984) 85; S. Dawson, Nucl.Phys.B249 (1985) 42; G.L. Kane, W.W. Repko and W.B. Rolnick, Phys.Lett.148B (1984) 367.
10. R. Cahn, Nucl.Phys.B255 (1985) 341; B262 (1985) 744E.
11. S. Dawson and S. Willenbrock, preprint LBL-21914 (1986).
12. R.N. Cahn, S.D. Ellis, R. Kleiss and W.J. Stirling, Phys.Rev.D35 (1987) 1626.
13. J.F. Gunion, J. Kalinowski and A. Tofighi-Niaki, Phys.Rev.Lett.57 (1986) 2351; J.F. Gunion, J. Kalinowski, A. Tofighi-Niaki, A. Abbasabadi and W.W. Repko, Proc. 1986 Summer Study on the design and Utilization of the SSC, Snowmass, Co.
14. D.A. Dicus and R. Vega, Phys.Rev.Lett.57 (1986) 1110.
15. J.F. Gunion and Z. Kunst, Phys.Lett.161B (1985) 333; R. Kleiss and W.J. Stirling, Nucl.Phys.B262 (1985) 235.
16. J.F. Gunion and M. Soldate, Phys.Rev.D34 (1986) 826.

Figure captions

1. Results for $d\sigma/dm_{vv}$ for the subprocess (*) at $\sqrt{s_{us}}$ = 1 TeV. In all three comparisons the exact results are represented by solid (m_H=0.5 TeV) and dashed ($m_H=\infty$) lines and the effective-W results - by dotdashed (m_H=0.5 TeV) and dotted ($m_H=\infty$) lines. The angular cuts are dersribed in the text.
2. Results for $d\sigma/dm_{vv}$ for pp collisions at $\sqrt{s_{pp}}$ = 40 TeV in cases: a) m_H=0.5 TeV; and b) $m_H=\infty$. The exact result is represented by the solid line and the effective-W results are given by dashed, dotdashed and dotted lines for θ_{min} = 60°, 30° and 10°, respectively.
3. The $|\cos\theta^*|$ distribution of the $f\bar{f}$ decay products of one W at m_{vv}=0.5 for m_H=0.5 TeV (solid) and $m_H=\infty$ (dashes) in the subprocess (*) at $\sqrt{s_{us}}$ = 1 TeV and with the cut $|y_v|$<1.5.
4. The r_{min}-r_{max} correlations for r_{max}=.225 plotted as a function of r_{min}. All parameters are the same as in fig.3.
5. $d\sigma/dm_{vv}/dp_T^{low}$ as a function of dp_T^{low} at m_{vv}=0.5 for m_H=0.5 TeV (solid) and $m_H=\infty$ (dashes) in the subprocess (*) at $\sqrt{s_{us}}$ = 1 TeV.

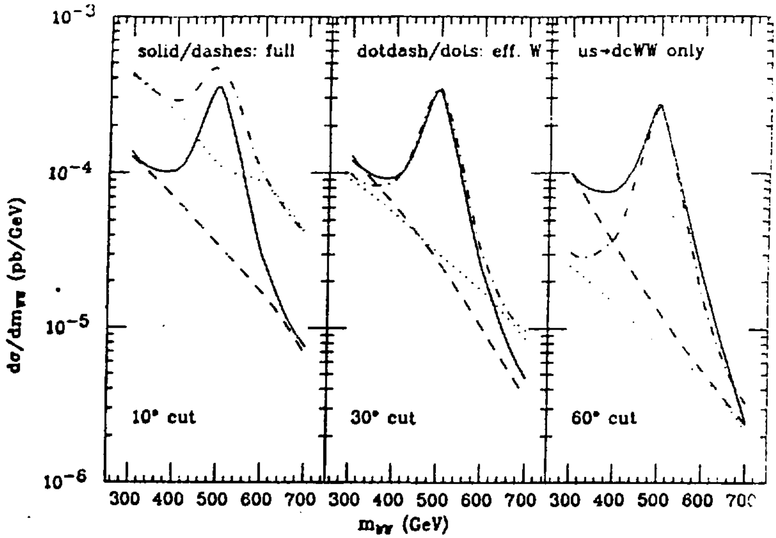

Figure 1

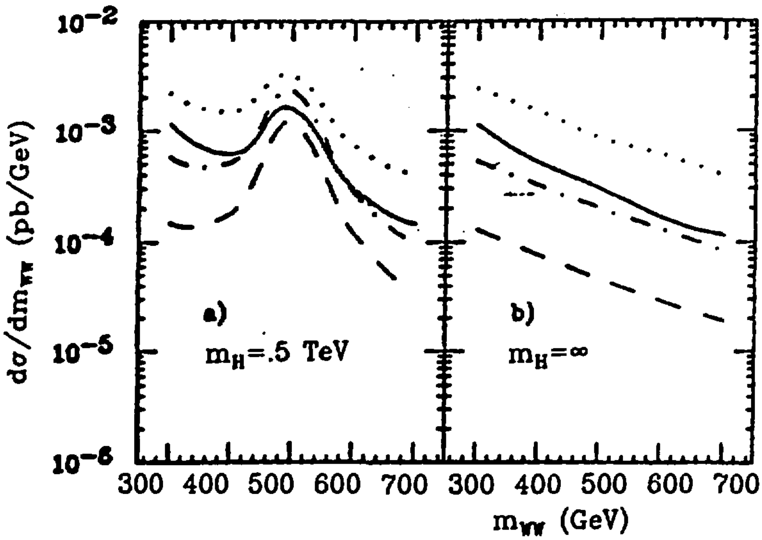

Figure 2

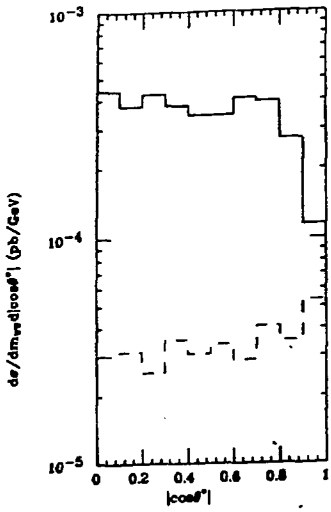

Figure 3

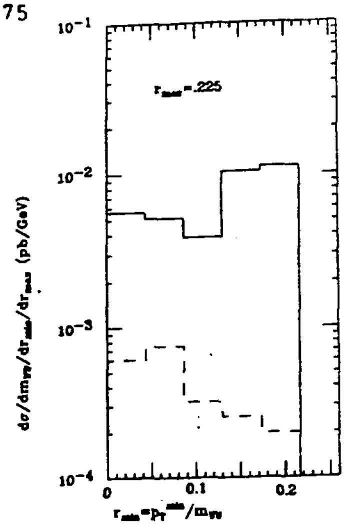

Figure 4

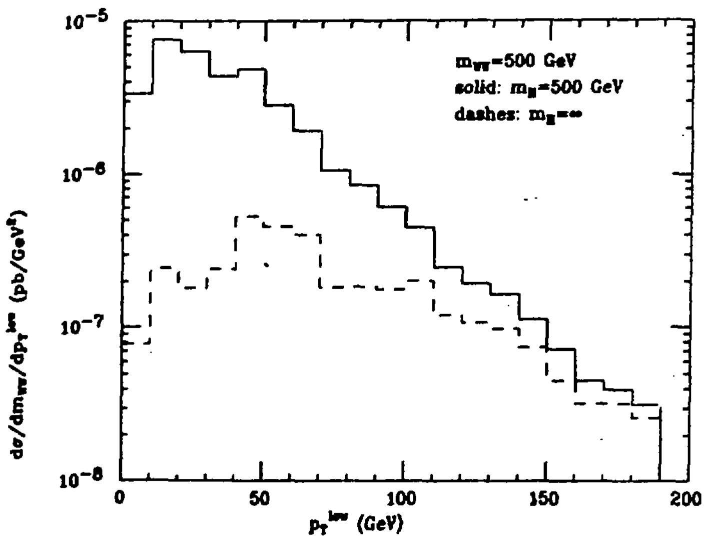

Figure 5

IS THE ANAPOLE MOMENT A PHYSICAL OBSERVABLE ?

H. Czyż, K. Kołodziej+, M. Zrałek

Dept. of Theoretical Physics, Silesian University, ul. Uniwersytecka 4
PL-40-007 Katowice , Poland

and P. Christova

Dept. of Physics, High Pedagogical Institute, Shoumen, Bulgaria

Abstract
Gauge dependence of the charged lepton anapole moment is investigated. It is shown that the anapole moment is a gauge dependent quantity.

Thirty years ago Zeldovich [1] repoted that a spin- $\frac{1}{2}$ particle in a parity-violating but CP-conserving theory, apart from well known static electromagnetic characteristics such as charge or magnetic moment, has another characteristic, that is coupling with an external electromagnetic field which he called the anapole moment of the particle. This has prompted certain researchers [2] to investigate the electron anapole moment within the standard theory of electroweak interactions. As weak interactions violate parity, electroweak radiative corrections to the basic electromagnetic interaction would give rise to an anapole moment, as in fact occurs.

Theoretical predictions both for electron and muon magnetic moments provide an excellent tool for testing a theory (QED) against experiment hence it was tempting to essay a simple test of weak radiative corrections by numerical evaluation of the electron anapole moment and then to compare this with an experimental findings.

+ Talk presented by K. Kołodziej.

However the question arises of whether or not the anapole moment can be regarded as a physical observable. While there exists a simple proof that an electric charge and a magnetic moment have to be gauge invariant it cannot be extended to an anapole moment [3]. We have investigated [4] the charged lepton anapole moment within the Glashow-Weinberg-Salam theory in the one loop approximation and in three different gauges, i.e. the linear 't Hooft-Feynman, the non-linear 't Hooft-Feynman and the unitary gauge. We found that the anapole moment is gauge dependent.

To find the electromagnetic structure of a spin- $\frac{1}{2}$ particle we consider an interaction term of the following form

$$H_I = j_\mu A^\mu_{ext} , \tag{1}$$

where A^μ_{ext} - an external electromagnetic field and j^μ - an electromagnetic current.

The electromagnetic current for a spin- $\frac{1}{2}$ particle, in momentum representation, has the following form

$$j^\mu(p_1,p_2) = -ie\bar{u}(p_2)\Gamma^\mu(p_1,p_2)u(p_1), \tag{2}$$

where p_1 and p_2 denote the 4-momenta of an incoming and outgoing particle, respectively, spinors $u(p_1)$, $u(p_2)$ satisfy the Dirac equation and 4-vector $\Gamma^\mu(p_1,p_2)$ is a 4 x 4-matrix in Dirac space.

To construct the matrix Γ^μ in a general form we can use the 16 Dirac matrices I, γ^μ, γ_5, $\gamma_5\gamma^\mu$, $\sigma^{\mu\nu} = \frac{i}{2}[\gamma^\mu,\gamma^\nu]$ and two independent 4-momenta: p_1 and p_2.

For our purposes it is more convenient to introduce new momenta P and q which are related to the previous ones as follows:

$$P = p_1 + p_2 \quad , \qquad q = p_2 - p_1 .$$

Imposing the conditions of hermiticity of current and of current conservation, the matrix Γ^μ is obtained in the following form:

$$\Gamma^\mu(P,q) = F_1\gamma^\mu + F_2 P^\mu + F_4\gamma_5(q^2\gamma^\mu + 2mq^\mu) + iF_5\gamma_5 P^\mu, \tag{3}$$

where the formfactors F_1, F_2, F_4 and F_5 are real functions of q^2

$$F_i \equiv F_i(q^2) \quad , \quad i = 1,2,4,5$$

and m is the mass of the particle.

By means of the formfactors we may define the static characteristics of a spin-$\frac{1}{2}$ particle (cf. [5]): an electric charge $Q = 2mF_2(0)+F_1(0)$, a dipol magnetic moment $M = F_3(0)/2m$, a dipol electric moment $D = -F_5(0)/2m$ and a dipol anapole moment $A = F_4(0)$. The dipol anapole moment is the one currently of interest. It is relatively simple to show that nonrelativistic coupling for the anapole has the form

$$H_I = -\frac{1}{2} A \vec{\sigma} \cdot (\vec{\nabla} \times \vec{B}),$$

where $\vec{\sigma}$ - Pauli matrices and $\vec{B}$ - external magnetic field.

Let us consider the discrete symmetries of Γ^μ given in formula (3). If any theory is P invariant then it leads to the following relationship for the matrix Γ^μ

$$\gamma_0 \Gamma^\mu(P_\alpha, q_\alpha)\gamma_0 = \Gamma^\mu(P^\alpha, q^\alpha),$$

(P_α, q_α and P^α, q^α denote the covariant and contravariant components of 4-momenta P and q, respectively) which is the cause of the disappearance of formfactors F_4 and F_5.

C invariance of any theory leads to the relationship

$$C\Gamma_\mu^T(P,q)C^{-1} = -\Gamma^\mu(P,q) \;, \qquad (C = -i\gamma_2\gamma_0),$$

giving as a result $F_4 = 0$.

Finally T (or CP) invariance gives

$$T\Gamma_\mu^T(P_\alpha, q_\alpha)T^{-1} = \Gamma^\mu(P^\alpha, -q^\alpha) \;, \quad (T = i\gamma_2\gamma_5),$$

and hence $F_5 = 0$.

Thus, if any theory violates C, but conserves CP, then, for $q^2 = 0$, the matrix Γ^μ is obtained in the form

$$\Gamma^\mu(P,q)\Big|_{q^2=0} = 2mM\gamma^\mu + \left(\frac{Q}{2m} - M\right)P^\mu + 2mA\gamma_5 q^\mu, \qquad (4)$$

where Q is an electric charge, M - a magnetic moment and A - an anapole moment of the particle.

We calculate the lepton-lepton-photon ($ll\gamma$) vertex in the frame of Glashow-Weinberg-Salam theory (GWS), in the one loop approximation and in the three different gauges:

i) the linear 't Hooft-Feynman gauge (all values of gauge parameters are equal to 1) with the gauge fixing term in the form

$$\mathcal{L}_{GF}^{LIN} = -|\partial_\mu W^{\mu+} - iM_W\varphi^+|^2 - \frac{1}{2}(\partial_\mu Z^\mu - M_Z\varphi_3')^2 - \frac{1}{2}(\partial_\mu A^\mu)^2,$$

where A_μ, Z_μ and $W_\mu^\pm$ denote photon, Z and W gauge fields, $\varphi^\pm$ and φ_3' - charged and neutral Nambu-Goldstone bosons, M_W and M_Z - gauge boson masses (We use gauge boson masses, Higgs mass and an electric charge as initial parameters);

ii) the background field gauge (with the values of gauge parameters as in the previous case) with the gauge fixing Lagrangian in the form

$$\mathcal{L}_{GF}^{BF} = -\left|(\partial_\mu - ie\frac{M_Z}{\sqrt{M_Z^2-M_W^2}}A_\mu^3)W^{\mu+} - iM_W\varphi^+\right|^2 - \frac{1}{2}(\partial_\mu Z^\mu - M_Z\varphi_3')^2 - \frac{1}{2}(\partial_\mu A^\mu)^2,$$

where A_μ^3 denotes the third component of the SU(2) gauge field before mixing

$$A_\mu^3 = \frac{1}{M_Z}\left(\sqrt{M_Z^2-M_W^2}\,A_\mu - M_W Z_\mu\right);$$

iii) the unitary gauge (cf. [6]).

The diagrams which contribute to the anapole moment in the three gauges under consideration are drawn in Fig.1. The diagrams with AA, $A\chi'$ and $A\varphi_3'$ vacuum transitions, do not contribute to the anapole moment because of, respectively, pure vector, pure scalar and pure axial couplings of photon, Higgs and φ_3' with fermions. These couplings either do not violate C or violate it in some trivial way (as in the case of φ_3').

After performing the on mass shell renormalization [7] we obtain a renormalized vertex function, for $q^2 = 0$, in the form

$$\Gamma_l^\mu\Big|_{q^2=0} = 2m_l M_l\gamma^\mu - a_l P^\mu + 2m_l A_l\gamma_5 q^\mu, \qquad (5)$$

where $M_l = -e/2m + a_l$ is the l-lepton magnetic moment, a_l stands for an anomalous magnetic moment of l-lepton; A_l is the l-lepton anapole moment. Thus formula (5) has the form predicted in (4).

We obtain the following results for the charged lepton anapole moment in the three gauges considered

i) the linear gauge

$$A_l^{LIN} = -\frac{\alpha}{16\pi}\frac{M_Z^2}{M_W^2(M_Z^2-M_W^2)}\Big\{(2M_W^2 - \frac{3}{2}M_Z^2)\int_0^1\frac{dy\,y(2-y-\frac{1}{3}y^2)}{D(M_Z,m_l,m_l)}$$

$$+\int_0^1\frac{dy\,y^2}{D(m_{\nu_l},M_W,m_l)}\left[\frac{1}{6}(m_{\nu_l}^2-m_l^2)y - (2-\frac{1}{3}y)M_W^2\right] + \sum_f \eta_f\Big[-\frac{4}{3}\ln m_f^2$$

$$+\,8\,\mathrm{Re}\int_0^1 dy\,(y-y^2)\ln D(m_f,m_f,M_Z) + \frac{1}{9} - \frac{2}{3}\frac{M_W^2}{M_Z^2}\Big]$$

$$+\left(\frac{13}{3} - \frac{M_W^2}{M_Z^2} + \frac{1}{6} + 4\frac{M_W^4}{M_Z^4}\right)\left(\ln M_W^2 - \int_0^1 dy\,\ln D(M_W,M_W,M_Z)\right)\Big\}; \qquad (6)$$

ii) the background field gauge

$$A_l^{BF} = A_l^{LIN} + \frac{\alpha}{16\pi}\,\frac{1}{M_Z^2-M_W^2}\Big[\frac{8}{9} + \left(-\frac{2}{3} - \frac{16}{3}\frac{M_W^2}{M_Z^2}\right)\Big(\ln M_W^2 - \int_0^1 dy\,\ln D(M_W,M_W,M_Z)\Big)\Big]; \qquad (7)$$

iii) the unitary gauge

$$A_l^{u} = -\frac{\alpha}{16\pi}\,\frac{M_Z^2}{M_W^2(M_Z^2-M_W^2)}\left(\frac{2}{3} - \frac{1}{3}\frac{M_Z^2}{M_W^2} + \frac{m_l^2-m_{\nu_l}^2}{M_W^2}\right)\frac{1}{2\varepsilon} + \text{finite part}; \qquad (8)$$

where m_l and m_{ν_l} denote l-lepton mass and mass of appropriate neutrino, the sum in (7) runs over all fermion flavours and colours, $\eta_f =$ $Q_f(\frac{1}{2}T_{3f} - (1-M_W^2/M_Z^2)Q_f)$, Q_f - an electric charge, T_{3f} - the third component of a weak isospin; the function D is defined as $D(m_1,m_2,m_3) =$ $(1-y)m_1^2+ym_2^2-y(1-y)m_3^2-i\varepsilon'$, ε' - a positive infinitesimal; the ε in formula (8) is a dimensional regularization parameter, $\varepsilon = 4-n$, n-space dimension.

Considering formulae (6), (7) and (8) it may be seen that the anapole in the background field gauge differs slightly from that in the linear gauge while the anapole in the unitary gauge is infinite in the limit $\varepsilon \to 0$, $(n \to 4)$ which can happen because this gauge is nonrenormalizable.

Therefore, the conclusion can be drawn that the lepton anapole moment, as defined in formula (3) is a gauge dependent quantity and hence cannot be regarded as a physical observable.

References

[1] Ya. B. Zeldovich, Zh. Eksp. Teor. Fiz. 33,1531(1957);

[2] N. Dombey, A. D. Kennedy, Phys. Lett. 91B,428(1980);

[3] N. M. Monyonko, J. H. Reid, Prog. of Theor. Phys. 73,734(1985);

[4] H. Czyż, K. Kołodziej, M. Zrałek and P. Christova, "Is the Anapole Moment a Physical Observable", submitted to Canadian Journal of Physics;

[5] H. Czyż, K. Kołodziej and M. Zrałek, Acta Phys. Polonica B18, 127(1987);

[6] D. Yu. Bardin, P. Ch. Christova and O. M. Fedorenko, Nucl. Phys. B197,1(1982);

[7] K. I. Aoki, Z. Hioki, R. Kawabe, M. Konuma and T. Muta, Suppl. Prog. Theor. Phys. 73,1(1982).

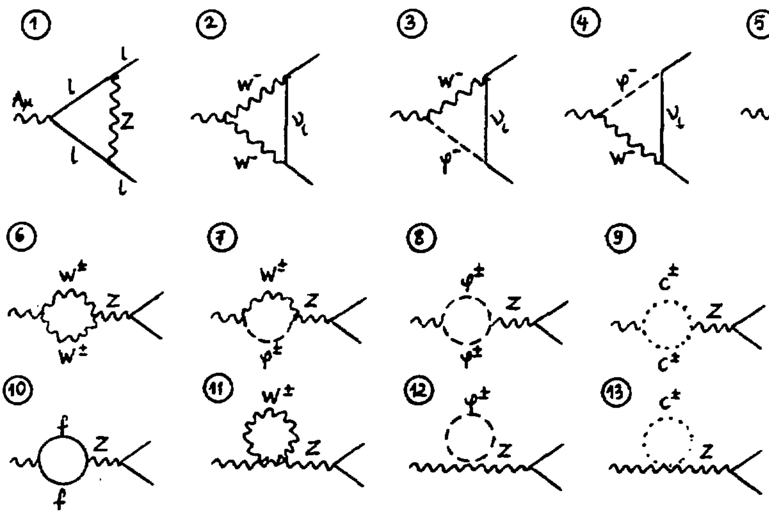

Fig.1. The diagrams which contribute to the lepton anapole moment in the three gauges considered in this paper: 1,2,3,4,5,6,7,8,9,10, 11 and 12 - the linear gauge;1,2,5,6,8,9,10,11,12 and 13 - the background gauge; 1,2,6,10 and 11 - the unitary gauge.

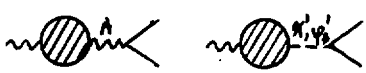

Fig. 2. The diagrams which do not contribute to the lepton anapole moment.

DOUBLE BETA DECAYS

Presented by L.-D. Fluri
Institut de Physique de
l'Université de Neuchâtel
Rue A.-L. Breguet 1
CH - 2000 NEUCHATEL
(Switzerland)

INTRODUCTION

Neutrinos being very light, neutral and weakly interacting, they are still poorly known objects: we don't know yet if they are massive or massless, if they are Dirac or Majorana spinors and we have little information about the flavour mixings of their mass eigenstates. Trying to investigate those problems is not merely curiosity but addresses fundamental questions in both paticle physics and cosmology.

Experimentally the neutrino properties are tested in direct mass measurements, in oscillation experiments, in searches for neutrino decays, in cosmic underground detectors and in double beta decay experiments. We will deal here only with the last item. The interested reader is refered to VU86 for a general and detailed survey of the properties of neutrinos.

This report is intended for people not familiar with the subject. In the first chapter, we introduce notions of Dirac and Majorana spinors and of flavour mixing. In chapter 2, we present the basic background specific to double beta decays. Chapter 3 reviews the experimental methods of double beta decays and chapter 4 overviews the present experimental results. The report ends with a short summary.

1. THEORETICAL FRAMEWORK

Our present knowledge of the neutrino charged currents (CC) is compatible with a Lagrangian interaction term

$$L^{CC} \sim \overline{l}\,\gamma^{\mu}\,(\nu_L + \eta\cdot\nu_R)\,W + \text{h.c.}$$

which changes a left- and a right-handed neutrino ν into its flavour associated charged lepton l in coupling to a W boson. The so far unobserved interactions of right handed neutrinos is summarised in the factor η which is measured to be smaller than 0.1.

For a single neutrino flavour, the Lagrangian mass term may be of the usual Dirac form

$$L^D = m_D \left(\overline{\nu_R} \cdot \nu_L + \overline{(\nu^c)}_R \cdot (\nu^c)_L \right) + \text{h.c.}$$

This term splits the four degrees of freedom of ν into left- and right-handed neutrinos and antineutrinos. The symbol ν^c stands for the charge conjugate of ν and represents the antineutrino. In case of neutral fermions however one may also introduce a Majorana mass term

$$L^M = m_L \, \overline{(\nu^c)}_R \cdot \nu_L + m_R \, \overline{\nu_L} \cdot (\nu^c)_R + \text{h.c.}$$

which somehow "couples" ν to ν^c and thus violates the lepton number by two units. The mass m_L being small, the mass term may be conveniently seen as a perturbation corresponding to the graph

$$(\nu^c)_R \longrightarrow\!\bullet\!\longrightarrow \nu_L$$

We also observe that the left- and right-handed fermions may have different masses.

Introducing now N flavours, we should expect that the weak interaction flavour eigenstates do not coincide with the mass eigenstates. For Dirac neutrinos, we thus write

$$\nu = U \cdot \nu_D$$

where ν is the column N-vector of the flavour eigenstates, U is the NxN mixing matrix and ν_D is the column N-vector of the Dirac mass eigenstates. In case of Majorana mass terms, this changes to

$$\nu_L = U_L \cdot \nu_{ML} \quad \text{and} \quad \nu_R = U_R \cdot \nu_{MR}$$

with now two distinct matrices U for the left- and right-handed parts. The symbols ν_{ML} and ν_{MR} represent the left- and right-handed N-vectors of the Majorana mass eigenstates.

More generally the mass term in the Lagrangian may be the sum of a Dirac- and of a Majorana-term. There may also exists a massless Goldstone boson, called majoron, coupling to the $(\nu^c)\nu$ current and which could be emitted in neutrinoless double beta decay. We will however not consider these cases here.

2. DOUBLE BETA DECAYS

Between the two nuclei (A,Z) and (A,Z+2) we expect the sequence of two usual β decays. This is a first order process in the weak interaction coupling constant. It would thus be largely dominant and, for that reason, one should limit oneself to those nuclei where it is forbidden,, i.e., to those cascades whose intermediate ground level of (A,Z+1) is more energetic than the initial ground level of (A,Z). We are then left with the allowed double beta decay $\beta\beta_2$, with the emission of two electrons and two anti-neutrinos. But, remembering a possible Majorana mass term, we ought to expect also the the neutrinoless double beta decay $\beta\beta_0$, the two emitted $(\nu^c)_e$ annihilating each other via the "mass term graph". Both these processes are second order in the weak interaction coupling constant. The decay rates are

$$\Gamma(\beta\beta_2) \sim f_2 \cdot |M_2|^2 \quad \text{and} \quad \Gamma(\beta\beta_0) \sim g_m \cdot f_0 \cdot |M_0|^2 \ .$$

The mass term g_m, the quantity to be measured, reads

$$g_m = \langle m\rangle_{LL}^{\ 2} \cdot a + \eta^2 \langle 1\rangle_{LR}^{\ 2} \cdot b + |\eta\langle m\rangle_{LL}\langle 1\rangle_{LR}| \cdot c \ ,$$

where we use the abbreviated notation $\langle x\rangle_{ij} = \sum U_{ie} U_{je} x_i$ and where the m_i are the mass eigenvalues. The phase space factors f_2 and f_0 are precisely known. However, the nuclear matrix elements M_2 and M_0 are hardly calculable to within one order of magnitude. But, as soon as an experiment provides a measure of both $\Gamma(\beta\beta_2)$ and $\Gamma(\beta\beta_0)$, since the matrix elements are believed to be of the same order for both decay types, it becomes possible to estimate the mass term through the nuclear model almost independant ratio $\Gamma(\beta\beta_0)/\Gamma(\beta\beta_2)$. The coefficients a, b and c, finally, are known quantities.

In the present state of experimental results, it is sufficient and illustrative to interpret the mass term in the simplest cases. Assuming no right-handed currents (η=0) and only one flavour, $\langle m\rangle_{LL} = m_1$, the electron-neutrino mass. With a second flavour, we obtain

$$\langle m\rangle_{LL} = m_1 \cdot \cos^2\theta + m_2 \cdot e^{-2i\rho} \cdot \sin^2\theta$$

Furthermore CP invariance requires ρ=0 or $\pi/2$, so that

$$\langle m\rangle_{LL} = m_1 \cdot \cos^2\theta + m_2 \cdot \sin^2\theta \quad \text{or} \qquad m_1 \cdot \cos^2\theta - m_2 \cdot \sin^2\theta$$

Cancellation may be important in the second solution.

Worth noticing, finally, is the fact that the possible candidates for double beta decay are transitions from an initial 0^+ state into either a 0^+ or a 2^+ final state. Whereas the 0^+ transitions are possible with Majorana mass terms only, the 2^+ transitions may have contributions from right-handed currents also.

3. EXPERIMENTAL METHODS

A. Geochemical methods

The geochemical method consists in comparing the isotopic abundancies in old ore with the atmospheric abundancies. Results are available so far on ^{130}Te into ^{130}Xe, on ^{128}Te into ^{128}Xe and on ^{82}Se into ^{82}Kr. One of the Te experiment (KI83) finds a large excess of ^{130}Xe and no excess of ^{128}Xe, leading to the ratio of half-life times T(128)/T(130) > 3040. The nuclear matrix elements are believed to be roughly the same for those two nuclei so that they cancel in this ratio. The theoretical calculations indicate that such a large value can only be reproduced by $\beta\beta_2$ transitions. The other experiment (HE78) on Te finds T(128)/T(130)=1580, a lower value which could accomodate $\beta\beta_0$ transitions also. The two experiments on ^{82}Se also find an evidence for $\beta\beta$ decays corresponding to the half-life times $T=(2.76\pm0.88)\cdot10^{20}$ y (SR73) and $T=(1.45\pm0.15)\cdot10^{20}$ y (KI84). In that case however no nuclear independant ratio is available and the mass term is thus more difficult to extract.

The rather large spread of these results should give an idea of their credibility.

B. Ionisation detectors

A group at Irvine is presently running a time projection chamber whose central cathode plane contains ^{82}Se. The $\beta\beta$ candidates should have the rather clean signature of two tracks spiralising in the magnetic field and flying in opposite directions from the central plane toward the anode wire planes. Measuring the energy of the transition, this experiment should be able to separate, in the energy distribution, the $\beta\beta_0$ peak from the broad $\beta\beta_2$ spectrum. The experiment however may not be able to distinguish 0^+ from 2^+ transitions.

Other time projection chambers or multiwire cells are developed by groups from Caltech, Neuchâtel and SIN and from Milano.

C. Ge crystals

Up to 200 cm^3 single crystals of Ge have been used as both high resolution intrinsic semi-conductor detectors and as sources of $\beta\beta$ decay of ^{76}Ge, whose natural abundance is about 7.7%. The advantage of this method is its very good energy resolution, typically 3 KeV at the $\beta\beta$

transition energy of 2 MeV. The $\beta\beta_2$ can be separated from the $\beta\beta_c$ as well as the 0^+ from the 2^+ transition. In order to reduce the cosmic background these detectors are operated underground and/or surrounded by vetos. To fight against natural radioactivity they are heavily shielded and only very clean material may sit in their immediate neighbour. So far no evidence for $\beta\beta$ decays have been reported and the corresponding lower limit on the half-life time is about $1.0\cdot10^{23}$ y (BE86). The experiments presently run or built with natural or enriched Ge, by groups from Pacific North West and South Carolina Universities, from Santa Barbara and Berkeley, from Bordeaux and Zaragossa and from Caltech, Neuchâtel and SIN are expected to improve that limit by one order of magnitude.

4. RESULTS

The table below summarises the experimental results on $\beta\beta$ decays as of today. It is only meant to give the reader an idea of the sensitivities already reached and is by no mean complete.

Nucleus	Measured half-life times in years (90% CL)		Theoretical estimate of $\langle m\rangle_{LL}$ in eV
^{76}Ge	$> 1.0\cdot10^{23}$	(BE86)	< 10
^{82}Se	$> 1.4\cdot10^{21}$	(MO84)	< 47
^{128}Te	$> 8\cdot10^{24}$	(KI83)	< 9
^{128}Te/^{130}Te	>3040	(KI83)	<5.7

The theoretical estimation of $\langle m\rangle_{LL}$ obviously assumes that there are no right-handed currents and, as already mentionned above, should be taken with much care when not extracted from a nuclear independant ratio. The limits quoted for $\langle m\rangle_{LL}$ are the most conservative from different nuclear calculations (HA84 and GR85), scaled (VU86) to reproduce the absolute rates observed in ^{82}Se, for ^{76}Ge, or in ^{130}Te, for ^{128}Te. Remember also that in its most naive interpretation, $\langle m\rangle_{LL}$ is the electron neutrino mass.

Observe that those figures are around the presently best limits on the electron neutrino mass from direct mass measurements.

CONCLUSION

Double beta decays has been observed in ^{130}Te by geochemical experiments. These events are suspected to be allowed $\beta\beta_2$ events.

The experiments presently running or in preparation are hoped to reach the level of other $\beta\beta_2$ decay rates: this would settle the problem of nuclear matrix elements calculation and lead to much more credible estimates of the mass term. But the real breakthrough would be the observation of $\beta\beta_0$ events which would incontestably establish the existence of Majorana mass terms in the Lagrangian.

While preparing this seminar, I have greatly benefited from the patient and very competent help of Prof. J.-L. Vuilleumier. I rest however solely responsible for any mistake or awkwardness left in spite of his collaboration. I would also not miss to thank the organisers of the 1987 Kazimierz Symposium for their warm, generous and stimulating hospitality.

References

BE86 Bellotti et al, 1986, Nuov. Cim. A95, 1
GR85 Grotz and Klapdor, 1985, Phys. Lett. 157B, 242
HA84 Haxton and Stephenson, 1984, Prog. Part. Nucl. Phys. 12,409
HE78 Hennecke, 1978, Phys. Rev. C17, 1168
KI83 Kirsten et al, 1983, Phys. Rev. Lett. 50,474
KI84 Kirsten, 1984, Proc. Conf. Neutrino 84 in Dortmund, 145
MO84 Moe et al, 1984, UC-Irvine Neutrino report 133
SR73 Srinivasan et al, 1973, Econ. Geol. 68, 252
VU86 Vuilleumier, 1986, Rep. Prog. Phys. 49, 1293

Misunderstandings and Difficulties in using Negative Binomial Distribution

Grzegorz Wrochna
Institute of Experimental Physics, University of Warsaw
Warsaw, Poland

ABSTRACT

A new way of describing the multiplicity distributions by using the Negative Binomial Distribution is critically discussed. Some misunderstandings often encountered in literature are pointed out.

1. Introduction

During the last two years, the Negative Binomial Distribution made a rapid career as a parametrization of multiplicity distributions and a candidate for the new empirical law of physics [1].

I would like to point out some misunderstandings and difficulties in this approach. Presented work has been done in collaboration with R. Szwed and A. Wroblewski. More details on this subject can be found in Ref. [2].

The paper is organized as follows:
In Section 2 the problem of using the so-called "Fake Negative Binomial Distribution" instead of the true Negative Binomial Distribution is discussed. Section 3 contains the discussion of the question: "Is KNO-scaling really accidental?" Section 4 is devoted to the comment on a "new method" to subtract diffractive component from multiplicity distributions. The last section contains a short discussion on the energy dependence of the k-parameter and its interpretation.

All remarks will be illustrated by the pp non-diffractive data [5] and the $p\bar{p}$ SPS Collider non-diffractive data [6,7].

2. "Fake Negative Binomial Distribution"

The Negative Binomial Distribution (NBD) is described by the following formula:

$$P^{NBD}(n) = \binom{n+k-1}{n} \frac{(\bar{n}/k)^n}{(1+\bar{n}/k)^{n+k}} \tag{1}$$

It has two parameters. The $\bar{n}$ parameter has the interpretation of the average. The k-parameter is connected with the dispersion $D=\sqrt{\overline{n^2}-\bar{n}^2}$ and the second central moment $C_{n,2}=\overline{n^2}/\bar{n}^2$ by formulae:

$$D_{NBD}^2 = \bar{n} + \bar{n}^2/k \tag{2}$$

$$C_{n,2} = 1 + 1/\bar{n} + 1/k \tag{3}$$

where n takes values of 0, 1, 2, 3, ...

The NBD can be used to describe distributions of charged particle multiplicities $P(n_{ch})$, but for the pp data n_{ch} is always even, so $n_{ch}=2,4,6...$ The theoretical probability distribution function is defined for all non-negative integers. Thus, instead of n_{ch}, the genuine multiplicity measure n should be used, according to the formula $n_{ch} = 2n + 2$. Note, that genuine multiplicity measure n (n=0, 1, 2, 3, ...) coincides in case of pp data with the number of negative prongs in an event $n=n_-$

Unfortunately, another procedure of calculation of the probabilities based on the NBD is very often encountered in the literature [6, 7]. The authors take from the NBD only probabilities P(n) for even integers and renormalize the whole distribution. This procedure, strictly speaking, leads to the fitting of the different theoretical distribution, which we call "Fake Negative Binomial Distribution" (FNBD). Let me stress that for the FNBD formulae (2) and (3) for the dispersion and the C_2 moment are no longer valid. Nevertheless, the name "NBD" is used by many authors also when they fit FNBD, which leads to misunderstandings.

The argument that the FNBD approximates the NBD for large $\bar{n}$ is not useful, because it is valid only in the SPS Collider energy range. Figure 1 illustrate how different are those two distributions. It shows the ratio of the k-parameters obtained by fitting the FNBD and the NBD to the pp and p$\bar{p}$ data. It is seen that Collider points are close to the unity, but deviations are dramatically increasing at smaller energies.

Thus, in fact there are two different distributions: the NBD and the FNBD.

3. Is KNO-scaling really accidental?

The statement that the *KNO-scaling* was accidental has appeared firstly in the UA5 Collaboration paper [6]. The way of arguing by the authors of Ref. [6] is schematically shown in Fig. 2. As seen in Fig. 3a the dependence $1/\bar{n}+1/K$ vs $\sqrt{s}$ has a flat minimum in the energy range between 10 and 60 GeV. Hence (based on the formula (3)) the authors conclude that the $C_{n,2}$ moment (Fig. 3b) has a similar flat minimum. Then, using the statement that the KNO-scaling requires $C_{n_{ch},2}$ to be constant, they argue that KNO-scaling is accidental.

The above argumentation contains inconsistencies:

Firstly: formula (3) is valid only for the NBD, and for the $C_{n,2}$ moment defined for the genuine multiplicity n. But in the UA5 Collaboration paper the FNBD and the $C_{n_{ch},2}$ moment are used. It should be stressed, that the sum $1+1/\bar{n}+1/K$ is not the same as the $C_{n_{ch},2}$ (compare Fig. 3a and 3b).

Secondly: Fig. 3b shows that $C_{n_{ch},2}$ has no minimum! This can be proven by the three lowest energy points, omitted in original UA5 publication [6]. Moreover, simple arithmetic shows that at the energy threshold $C_{n_{ch},2}$ goes to unity in contradiction with hypothesis about the minimum.

Thirdly: In the original formulation [9] KNO-scaling requires $C_{n_{ch},2}$ to be constant only for asymptotic energies. Properly formulated KNO-scaling [10] correctly describes the rise of the $C_{n_{ch},2}$ moments from the energy threshold up to ISR energies [11].

In conclusion: The statement that KNO-scaling is accidental seems to be a triple misunderstanding.

4. A "new method" to obtain the non-diffractive event samples

Separation of the diffractive and non-diffractive component is usually difficult. Recently a new method has been proposed [7], based on a supposition, that the NBD describes very well just the non-diffractive data. This method is illustrated in Fig. 4, showing the multiplicity distributions for 800 GeV/c pp collisions. The open points corresponds to the inelastic sample. The diffractive component is limited to the events with few lowest multiplicities. Hence, one can take inelastic data, omit 3 or 4 lowest multiplicities, fit the NBD and take the result as the non-diffractive data (full points).

We have tested such procedure for the world pp data [4] and we have compared the results with those obtained by the standard methods [5] (missing mass plots etc.). The comparison is illustrated in Fig. 5 which shows the total diffractive cross section. Open circles represent standard methods and full circles - NBD method. It is seen that the points corresponding to the standard methods are self-consistent within errors, whereas fluctuations of the NBD method are gigantic (up to 15 standard deviations).

There is a more direct way to prove this in tability. One can compare the NBD fit to the full non-diffractive distribution and to the same distribution without few lowest multiplicities. An example of the result of omitting 5 from 20 points of the distribution at energy 62 GeV is illustrated in the Fig. 6. The χ^2 contours presented as a function of the $\bar{n}$ and K show the goodness of the fit. The full distribution (Fig. 6a) has a quite well localized minimum, with $\bar{n}$ and K not strongly correlated. After omitting 5 points (Fig. 6b) the correlation rapidly rises and the minimum radically shifts (note the change of the scale) in spite of fitting to the same non-diffractive distribution. Conclusion: the mentioned NBD-method is completely unusable.

5. Energy dependence of the K-parameter and its interpretation

Figure 7 shows 1/K dependence on energy for the NBD (open circles) and for the FNBD (full circles).

In existing models [1] the K-parameter is treated as the number of clusters or as a probability. So, it should be positive. But as seen from Fig. 7 this is not the case. It is difficult to understand in terms of models why at certain energy the K-parameter changes sign although other experimental observables do not show any such violent change in the mechanism of multiparticle production.

Moreover, the NBD does not have any predictive power since it involves two free parameters for each multiplicity distribution and has no build-in scaling. There is no model to predict the dependence of the K on the energy, particle type or a phase-space region in agreement with experiment.

For the full phase-space pp data the only proposition of a parametrization for K was given by the UA5 Collaboration [6, 8]. The authors propose the linear dependence of the 1/K vs ln s. They fitted data for energies higher than 10 GeV. However the proposition has weak points because, firstly, as illustrated in Fig. 7 the 3 lowest energy data points are in contradiction with this dependence, and secondly, the FNBD was used instead of the NBD. For the NBD the linear dependence is even less convincing.

At the end of this section I would like to underline one more difficulty of the NBD approach. The NBD does not describe the pp data as good as it is often claimed. Figure 8 shows the ratio of the experimental probabilities and the probabilities calculated with the NBD, at the ISR energy range. The points should be randomly scattered around the unity which is not the case. The explicit systematic deviations are seen.

6. Conclusion

Concluding this paper, I would like to point once again a list of misunderstandings and difficulties of the NBD approach:

Many authors use the FNBD instead of the NBD without clear distinction.

The minimum of the $1/\bar{n}+1/k$ has nothing to do with the KNO-scaling, so the conclusion that the KNO-scaling is accidental is just a misunderstanding.

The NBD-fit method to obtain non-diffractive multiplicities is unusable.

There is no model to predict the dependence of the k-parameter on the energy, particle type or a phase space region and its reasonable interpretation.

Lastly, the NBD does not describe the pp data so good.

Thus, in my opinion, the NBD can be treated as one of possible parametrizations of data, but by no means the best.

REFERENCES

[1] A. Giovannini and L. Van Hove, Z. Phys. C30, 391 (1986)
L. Van Hove and A. Giovannini, "Negative Binomial Multiplicity Distributions, a New Empirical Law for High Energy Collisions" Proceedings of the XVII International Symposium on Multiparticle Dynamics, Seewinkel, Austria, 16-20 June 1986, p. 561.
A. Giovannini, "Multiparticle Phenomenology", Invited talk at the Sixth International Conference on Physics in Collision, Chicago, 3-5 September. 1986.
Torino University preprint DFTT 86/31

[2] R. Szwed, G. Wrochna, A. Wróblewski, "Mystery of the Negative Binomial Distribution", Warsaw Univ. preprint IFD/3/87, submitted to Z. Phys. C

[4] pp inelastic data:

4 GeV/c	L. Bodini et al., Nuovo Cim. 58A, 475 (1968)
5.5 GeV/c	G. Alexander et al., Phys. Rev. 154, 1284 (1967)
6.6 GeV/c	E. R. Gellert, LBL-749 (1972)
12 GeV/c	V. Blobel et al., Nucl. Phys. B69, 454 (1974)
19 GeV/c	H. Boggild et al., Nucl. Phys. B41, 285 (1972)
24 GeV/c	V. Blobel et al., Nucl. Phys. B52, 221 (1975)
35.7 GeV/c	I. V. Boguslawski et al., JINR1-10134 (1976)
50 GeV/c	V. V. Ammosov et al., Phys. Lett. 42B, 519 (1972)
60 GeV/c	C. Bromberg et al., Phys. Rev. D15, 64 (1977)
69 GeV/c	V. V. Babintsev et al., IHEP M-25 (1976)
100 GeV/c	J. Erwin et al., Phys. Rev. Lett. 32, 254 (1974)
100 GeV/c	W. M. Morse et al., Phys. Rev. D15, 66 (1977)
102 GeV/c	C. Bromberg et al., Phys. Rev. Lett. 31, 1563 (1973)
205 GeV/c	S. Barish et al., Phys. Rev. D9, 2689 (1974)
250 GeV/c	M. Adamus et al., Z. Phys. C32, 475 (1986)
303 GeV/c	A. Firestone et al., Phys. Rev. D10, 2080 (1974)
303 GeV/c	F. T. Dao et al., Phys. Rev. Lett. 29, 1627 (1972)
360 GeV/c	J. L. Bailly et al., Z. Phys. C23, 205 (1984)
400 GeV/c	R. D. Kass et al., Phys. Rev. D20, 6050 (1979)
400 GeV/c	W. S. Toothacker, UMBC77-77
405 GeV/c	C. Bromberg et al., Phys. Rev. Lett. 31, 1563 (1973)
405 GeV/c	T. Ferbel (private communication)

800 GeV/c R. Ammar et al., Phys. Lett. **B178**, 124 (1986)

493, 1032, 1471, 2062 GeV/c

A. Breakstone et al., Phys. ReV. **D30**, 528 (1984)

[5] pp non-diffractive data:

12 GeV/c J. Benecke et al., Nucl. Phys. **B76**, 29 (1974)

19 GeV/c H. Boggild et al., Nucl. Phys. **B27**, 285 (1971)

24 GeV/c J. Benecke et al., Nucl. Phys. **B76**, 29 (1974)

69 GeV/c V. V. Babintsev et al., IHEP M25 (1976)

J. Whitmore et al., Phys. Rep. **10C**, 273 (1974) and

100 GeV/c W. M. Morse et al., Phys. Rev. **D15**, 66 (1977)

102 GeV/c C. Bromberg et al., Phys. Rev. Lett. **31**, 1563 (1973)

205 GeV/c S. Barish et al., Phys. Rev. **D9**, 2689 (1974)

303 GeV/c A. Firestone et al., Phys. Rev. **D10**, 2080 (1974)

405 GeV/c C. Bromberg et al., Phys. Rev. Lett. **31**, 1563 (1973)

493, 1032, 1471, 2062 GeV/c

A. Breakstone et al., Phys. ReV. **D30**, 528 (1984)

[6] 540 GeV UA5 non-diffractive data:

G. J. Alner et al., Phys. Lett. **160B**, 199 (1985)

[7] R. Ammar et al., Phys. Lett. **B178**, 124 (1986)

[8] 200 and 900 GeV UA5 non-diffractive data:

G. J. Alner et al., Phys. Lett. **16[illegible]B**, 476 (1986)

[9] Z. Koba, H. B. Nielsen, P. Olesen, Nucl Phys. **B4[illegible]**, 317 (1972)

[10] A. I. Golokhvastov, Sov. Jour. Nucl. Phys. **27**, 430 (1978)

Sov. Jour. Nucl. Phys. **30**, 128 (1979)

[11] R. Szwed and G. Wrochna, Z. Phys. **C29**, 255 (1985)

FIGURE CAPTIONS

Fig. 1

The ratio of k_{NBD}/k_{FNBD} vs $\sqrt{s}$.

Fig. 2

Scheme of the way of arguing in Ref. [6] (left part of diagram) and conrtrarguments (the right part).

Fig. 3

a) The values of $1 + 1/\bar{n} + 1/k$ from the FNBD fits to non-diffractive sample. The curve shows the UA5 Collaboration interpolation [11].

b) The values of $C_{n_{ch},2}$ moment for the same sample.

Fig. 4

The LEBC-MPS Collaboration pp inelastic data (800 GeV/c) and the "nondiffractive data" obtained by using the FNBD fit.

Fig. 5

Comparison of the experimental diffractive cross section with the "diffractive component" obtained by subtracting the NBD fitted cross sections from inelastic topologic cross sections for $n_{ch} \geq 10$;

Fig. 6

The contours of constant χ^2 values in the FNBD fit to the non-diffractive pp multiplicity distribution at $\sqrt{s} = 62$ GeV as a function of parameters $\bar{n}$ and k;

a) all data points used;

b) data for $n_{ch} \leq 10$ omitted. Notice the shift in the best value of k between a) and b).

Fig. 7

The $1/k$ parameter of the NBD (open circles) and FNBD (full circles) fits for the non-diffractive sample. The straight line illustrates fit to the data with $\sqrt{s} < 10$ GeV, done by the UA5 Collaboration [11].

Fig. 8

The ratio of $P^{EXP}(n_{ch})/P^{NBD}(n_{ch})$ plotted as a function of reduced multiplicity $n_{ch}/\langle n_{ch}\rangle$ for the pp data at $30.4 < \sqrt{s} < 62.2$ GeV

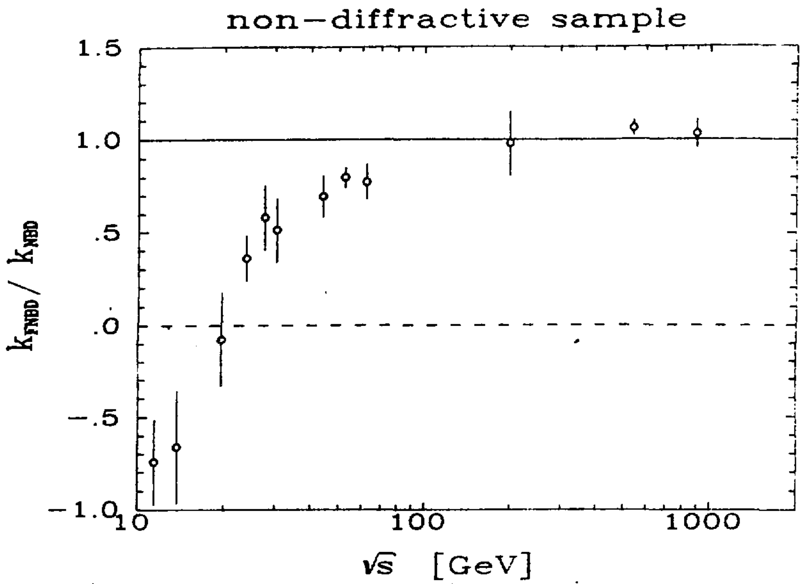
non-diffractive sample
1.5
1.0
.5
.0
−.5
−1.0
10
100
1000
k_{FNBD} / k_{NBD}
$\sqrt{s}$ [GeV]

Fig.1

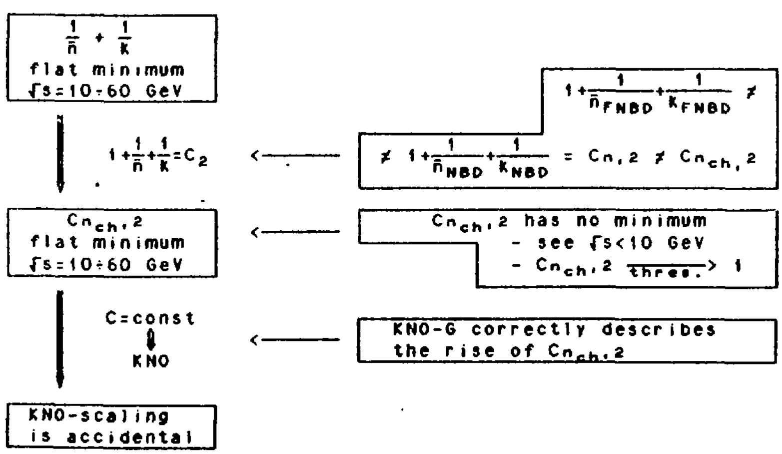
$\frac{1}{\bar{n}} + \frac{1}{k}$
flat minimum
$\sqrt{s}$=10÷60 GeV
$1+\frac{1}{\bar{n}}+\frac{1}{k}=C_2$
$1+\frac{1}{\bar{n}_{FNBD}}+\frac{1}{k_{FNBD}} \neq$
$\neq 1+\frac{1}{\bar{n}_{NBD}}+\frac{1}{k_{NBD}} = Cn,2 \neq Cn_{ch},2$
$Cn_{ch},2$
flat minimum
$\sqrt{s}$=10÷60 GeV
$Cn_{ch},2$ has no minimum
- see $\sqrt{s}$<10 GeV
- $Cn_{ch},2 \xrightarrow{thres.} 1$
C=const
KNO
KNO-G correctly describes
the rise of $Cn_{ch},2$
KNO-scaling
is accidental

Fig.2

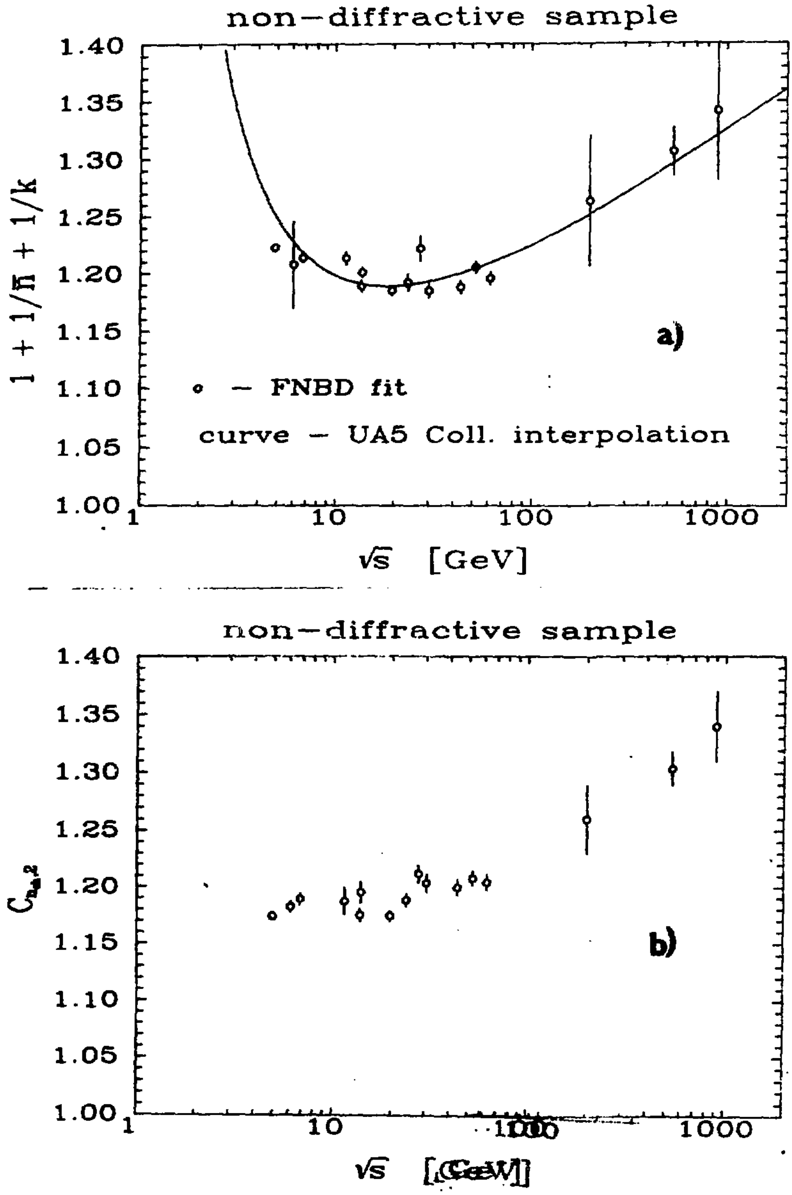
non-diffractive sample
1 + 1/n̄ + 1/k
a)
o – FNBD fit
curve – UA5 Coll. interpolation
√s [GeV]
non-diffractive sample
b)
√s [GeV]

Fig.3

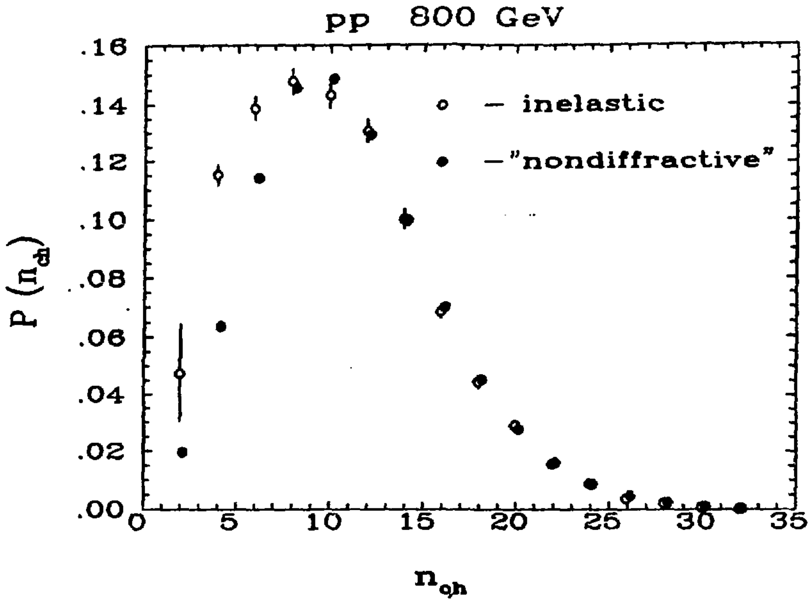
pp 800 GeV
○ – inelastic
● – "nondiffractive"
P (n_ch)
n_ch
.00
.02
.04
.06
.08
.10
.12
.14
.16
0
5
10
15
20
25
30
35

Fig.4

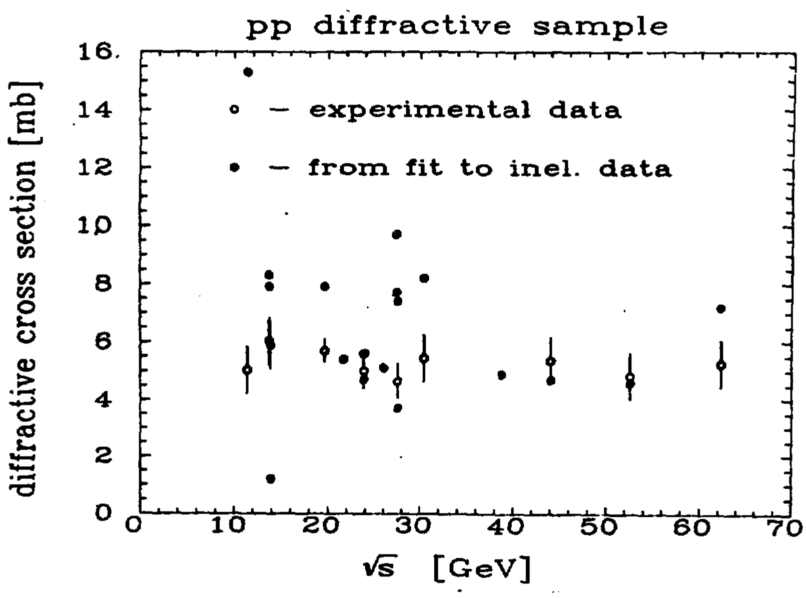
pp diffractive sample
○ – experimental data
● – from fit to inel. data
diffractive cross section [mb]
√s [GeV]
0
2
4
6
8
10
12
14
16
0
10
20
30
40
50
60
70

Fig.5

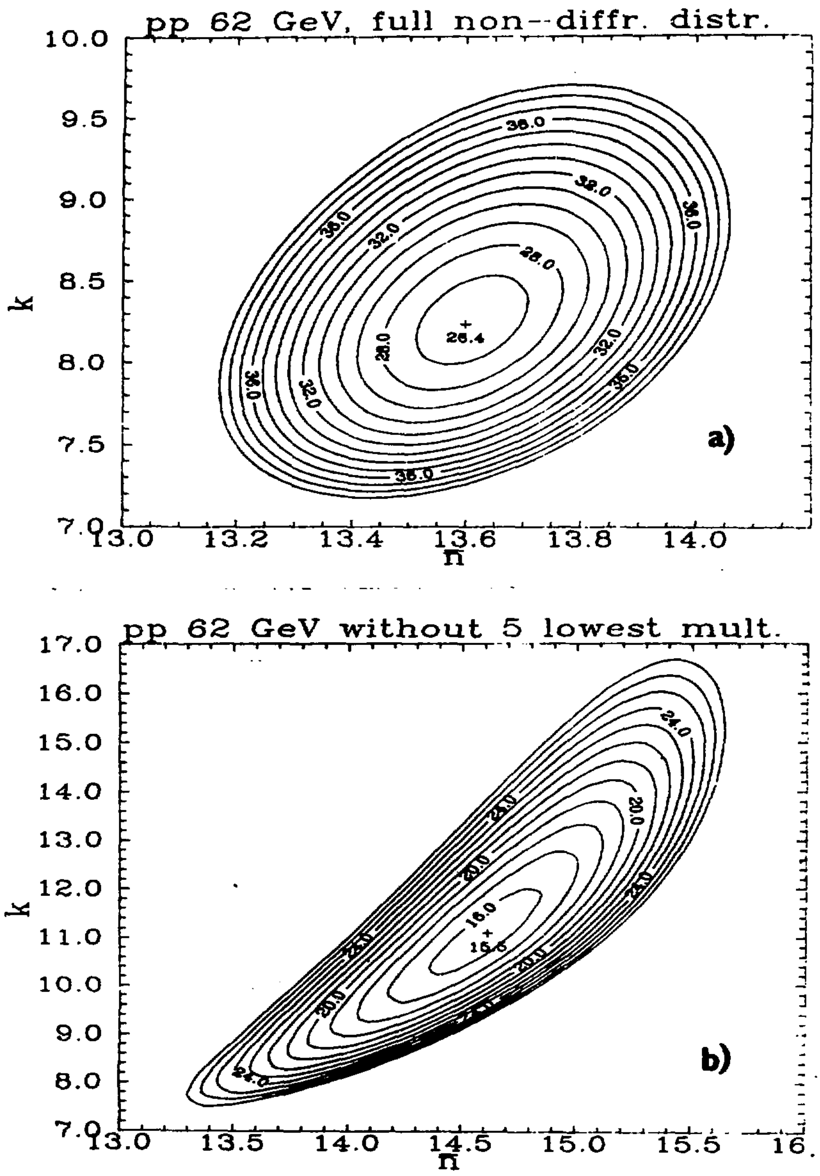
pp 62 GeV, full non--diffr. distr.
10.0
9.5
9.0
8.5
8.0
7.5
7.0
k
36.0
32.0
28.0
26.4
a)
13.0
13.2
13.4
13.6
13.8
14.0
n̄
pp 62 GeV without 5 lowest mult.
17.0
16.0
15.0
14.0
13.0
12.0
11.0
10.0
9.0
8.0
7.0
k
24.0
20.0
16.0
15.6
b)
13.0
13.5
14.0
14.5
15.0
15.5
16
n̄

Fig.6

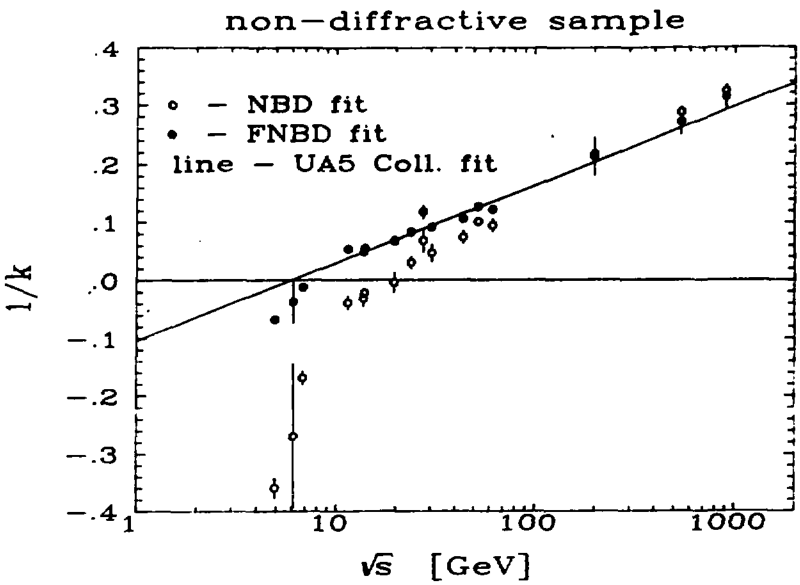
non-diffractive sample
○ – NBD fit
• – FNBD fit
line – UA5 Coll. fit
1/k
√s [GeV]

Fig.7

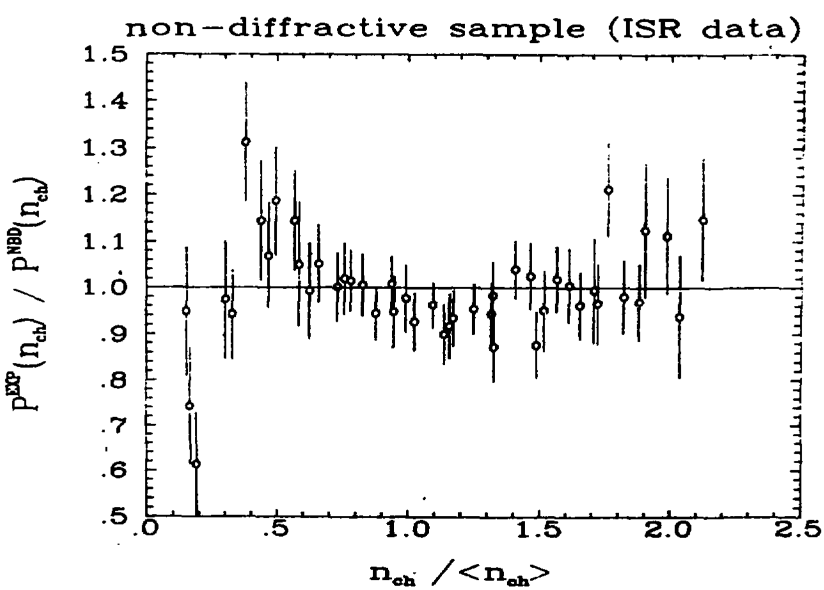
non-diffractive sample (ISR data)
P^EXP(n_ch) / P^NBD(n_ch)
n_ch /<n_ch>

Fig.8

Transverse Energy and Multiplicity Distributions in High Energy Reactions

by

M. Plümer*) and R.M. Weiner
Physics Dept.
University of Marburg
Mainzer Gasse 33
D-3550 Marburg
Federal Republic of Germany

Under rather weak assumptions a set of analytical relations between the moments of the transverse energy distribution and the moments of the underlying multiplicity distribution is established for high energy collisions. Where applicable, the relations are in good agreement with data.

In the last years, the study of transverse energy distributions in high energy collisions has attracted considerable interest, among other things because at high energies and/or with heavy ions calorimetric measurements gain more and more importance and thus transverse energy distributions become one of the main sources of information about multiparticle dynamics. Therefore it is of high theoretical and practical interest to relate the transverse energy distribution with other physical observables.

As far as we can gather correlations between multiplicities and transverse energies have been obtained so far only via Monte-Carlo calculations[1,2]. The present contribution represents an attempt to derive an analytical relation between the transverse energy and multiplicity distributions.

---

*) Postdoctoral Fellow of the Deutsche Forschungsgemeinschaft

In a given rapidity interval, the transverse energy distribution, $w(E_T) \equiv \frac{1}{\sigma}\frac{d\sigma}{dE_T}$, is related to the corresponding multiplicity distribution, $P(n) \equiv \frac{\sigma_n}{\sigma}$, as follows ($\sigma = \sum_m \sigma_m$ is the inelastic cross section)

$$w(E_T) = \sum_{n=0}^{\infty} P(n)\; f(E_T|n) \tag{1}$$

where

$$f(E_T|0) = \delta(E_T); \tag{2}$$

$$f(E_T|n) = \int d\varepsilon_{T1} \ldots \int d\varepsilon_{Tn} \; \Big(\delta\Big(\sum_{i=1}^{n} \varepsilon_{Ti} - E_T\Big) \cdot$$

$$\cdot \frac{1}{\sigma_n} \frac{d\sigma_n}{d\varepsilon_{T1} \ldots d\varepsilon_{Tn}}\Big) \quad (n \geq 1)$$

is the conditional probability to observe a transverse energy E_T at a given multiplicity n and ε_T is the single particle transverse energy. Since experimental data on $\frac{1}{\sigma}\frac{d\sigma}{dE_T}$ in general do not contain the zero multiplicity contribution, from here on only the modified distribution

$$\begin{aligned} \tilde{w}(E_T) &= \sum_{n=1}^{\infty} \tilde{P}(n)\; f(E_T|n), \\ \tilde{P}(n) &\equiv P(n)/(1-P(0)) \end{aligned} \tag{3}$$

will be considered; moments like $\langle E_T^m \rangle$ or $\langle n^m \rangle$ will always refer to $\tilde{w}(E_T)$ and $\tilde{P}(n)$, respectively.

If the single particle transverse momentum is weakly or not at all correlated with multiplicity as it is the case at Fermilab and ISR energies[3], one finds for the first moments

$$\langle E_T \rangle = \sum_n \tilde{P}(n) \cdot n \cdot \langle \varepsilon_T \rangle_n \sim \langle n \rangle \langle \varepsilon_T \rangle \tag{4}$$

In order to obtain corresponding relations for the higher moments, one has to make assumptions about the n-particle inclusive transverse energy distribution. We shall assume here that it factorizes into a product of n single particle transverse energy distributions $g(\varepsilon_T)$, i.e. that the transverse energies ε_T of individual particles are uncorrelated:

$$\frac{1}{\sigma_n}\frac{d\sigma_n}{d\varepsilon_{T1}\ldots d\varepsilon_{Tn}} = \prod_{i=1}^{n} g(\varepsilon_{Ti}) \tag{5}$$

The validity of this assumption has been tested[1,2] up to energies of $\sqrt{s}$ = 30 GeV in Monte Carlo calculations of correlations between E_T, $\langle n\rangle$ and $\langle p_T\rangle$.

Together with (5), (1) and (2) yield

$$\langle E_T^m\rangle = \sum_{j=1}^{m} a_{mj} \langle n \cdot (n-1) \cdot \ldots \cdot (m-j+1)\rangle \tag{6}$$

with

$$\begin{aligned} a_{11} &= \langle\varepsilon_T\rangle \\ a_{22} &= \langle\varepsilon_T\rangle^2,\ a_{21} = \langle\varepsilon_T^2\rangle \quad \text{etc.} \end{aligned} \tag{7}$$

With an exponential ansatz,

$$g(\varepsilon_T) = \mu^2\ \varepsilon_T \cdot e^{-\mu\varepsilon_T} \tag{8}$$

the results further simplify to

$$\tilde{w}(E_T) = \sum_n \tilde{P}(n) \cdot \mu \cdot \frac{(\mu E_T)^{2n-1}}{(2n-1)!} \cdot e^{-\mu E_T} \tag{9}$$

and

$$\langle E_T^m\rangle = \left(\frac{2}{\mu}\right)^m \cdot \langle n \cdot (n+\tfrac{1}{2}) \cdot \ldots \cdot (n+\tfrac{m-1}{2})\rangle \tag{10}$$

In the following, this formalism will be applied to the discussion of experimental data.

For pp-collisions at $\sqrt{s}$ = 31 GeV, the charged[2], neutral[4] and total[5] transverse energy distributions in the central rapidity region have all been measured in separate experiments. A customary parametrization is

$$\tilde{w}(E_T) = \frac{\alpha}{\Gamma(\alpha)}\ (\alpha E_T)^{p-1}\ e^{-\alpha E_T} \tag{11}$$

The value of $\langle E_T\rangle$, α and p as well as the respective rapidity interval for the 31 GeV data are given in table 1, where we have also included data obtained at 27.4 GeV[6]. In ref. 2, the charged E_T-distribution has been observed for $|\eta|<0.8$. Integration over that distribution yields

$$\langle E_T^{ch}\rangle = 1.38,\ \langle (E_T^{ch})^2\rangle = 3.12 \tag{12}$$

With an average p_T in this region of 0.40 GeV[7], one obtains from eq. (10) $\langle n_{ch}\rangle = 3.25$, $\gamma_2 = 0.48$, where

$$\gamma_2 = (\langle n^2\rangle - \langle n\rangle^2)/\langle n\rangle^2.$$

This is to be compared with the values found in the same rapidity interval in ref. 8, $\langle n_{ch}\rangle = 3.27$ (3.13) and $\gamma_2 = 0.46$ (0.49); here the values given in brackets were obtained by the authors of ref. 8 by correcting the data on P(n) in order to fit KNO-functions measured at higher energies.

Thus, in the case of charged particles, the first two moments of $\tilde{P}(n)$ as calculated from $\tilde{W}(E_T)$ through eq. (10) are in good agreement with the corresponding experimental data on $\tilde{P}(n)$.

If one corrects for the slight differences in rapidity intervals (cf. table 1), comparison of the charged, neutral and total E_T-data for a fixed interval in the central rapidity region indicates

$$\frac{\langle E_T^{ch}\rangle}{\langle E_T^{tot}\rangle} \approx \frac{\langle E_T^{0}\rangle}{\langle E_T^{tot}\rangle} \approx \frac{1}{2} \tag{13}$$

Since the E_T^0-measurements did not distinguish[7] between pions and η-particles, this result does not necessarily imply, as suggested in ref. 9, that isospin symmetry is violated. On the other hand, if isospin is indeed violated (which is conceivable for a narrow rapidity interval), the great similarity of the charged and neutral E_T-distributions[2,4] (at least in the region where both distributions have been measured, i.e. for 1.5 GeV$\leq E_T \leq$12 GeV) indicates a corresponding similarity of the underlying multiplicity distributions, i.e. $P_{ch}(n) \sim P_0(n)$.

However, to obtain an unambiguous interpretation of the data one will first have to clarify how much the η-particles contribute as compared with the neutral pions.

For an analysis of E_T-distributions obtained at collider energies, the present model will have to be generalized to include correlations between multiplicity and transverse momentum. Also, to get a better approximation the ε_T-correlations can be taken into account in the derivation of eq. (6). Work in this direction is in progress.

Instructive discussions with G.N. Fowler and E.M. Friedlander are gratefully acknowledged.

This work has been funded in part by the German Federal Minister for Research and Technology (BMFT) under the contract number 06 MR 777 and Gesellschaft für Schwerionenforschung, Darmstadt.

Table 1 : Parameters of experimentally observed E_T - distributions

	$\sqrt{s}$ (GeV)	pseudo rapidity interval	$\langle E_T \rangle$ (GeV)	α	p
$\langle E_T^{ch} \rangle$	31	$\|\eta\| < 0.8$	1.38	-	-
$\langle E_T^{0} \rangle$	31	$\|\eta\| < 0.9$	1.54	1.62 ± 0.01	2.50 ± 0.0
$\langle E_T^{tot} \rangle$	31	$\|\eta\| < 1.0$ *)	3.07	1.16 ± 0.04	3.56 ± 0.2
$\langle E_T^{tot} \rangle$	27	$-0.65 < \eta < 1.32$	3.06	0.98	3.0

*) Particles were grouped in clusters, and only those with cluster pseudorapidity $|\eta_c| < 0.7$ were kept.

R e f e r e n c e s

1. C. De Marzo et al., Nucl.Phys. B211, 375 (1983).
2. H. Gordon et al., Phys.Rev. D28, 2736 (1983).
3. A. Breakstone et al., Phys.Lett. 132B, 463 (1983).
4. A.L.S. Angelis et al., Phys.Lett. 141B, 140 (1984); A.L.S. Angelis et al., Phys.Lett. 168B, 158 (1986).
5. B. Callen, in Quark Matter 84, ed. K. Kajantie, Springer 1985, p. 133.
6. H.E. Miettinen, Nucl.Phys. A418, 315c (1984).
7. M. Tannenbaum et al., Preprint BNL-38470 (1986).
8. T. Akesson et al., Phys.Lett. 119B, 464 (1982).
9. S.Y. Shmakov and V.V. Uzhinskii, JINR-Dubna-Preprint E2-87-5.

Minijets *

Meng Ta-chung
Fachbereich Physik der FU Berlin, Berlin

Recently there has been much interest[1-3] in "minijets" or "low-transverse energy jets" in hadron-hadron collisions. Why do they attract so much attention? What are they?

Perhaps I should begin this discussion by reminding you: Multiparticle production processes take place in approximately 80% of the high-energy hadron-hadron collision events. An event of this kind can be characterized by the multiplicity (n) of the produced charged hadrons and/or the energy flow (E_T) in the transverse direction of the beam. Distributions of n and E_T have been measured for various processes (pp, $\bar{p}p$, πp etc.) at various (total cms) energies ($\sqrt{s}$) in different kinematical regions (defined by the pseudorapidity η and the azimuth angle Φ of the final state hadrons).

It has been observed by UA1 collaboration[1] that a considerable fraction (approximately 6% at $\sqrt{s}$=200 GeV, 17% at 900 GeV) of minijet-events exist in the data sample of minimum-bias events. Minijets were found[1] when the n- and the E_T-distributions were measured in the kinematical region $|\eta|<2.5$ under the condition that at least 5 GeV enters the trigger cone of radius $R=[(\Delta\eta)^2+(\Delta\Phi)^2]^{1/2}=1$ in the η-Φ space. The characteristics of the minijet data sample are indeed very striking: It is seen in particular that the average multiplicity of minijet-events is approximately twice as high as that in non-minijet-events; and that the multiplicity distribution of the minijet-events, when plotted in the KNO form, is much narrower than the corresponding

*Supported in part by Deutsche Forschungsgemeinschaft (DFG: Me 470/5-1)

curve for minimum-bias events. Perhaps this is the reason why it is expected[2] that minijets should have very much in common with the jets (high-E_T-jets) in hard collisions.

Chao, Pan and myself took a closer look[3] at the data[1]. The result of our analysis[3] strongly suggests that the minijet-events and the ordinary minimum-bias events are closely related to one another, and that their relationship can be described by standard statistical methods.

The attempt of applying standard statistical methods to the minijet problem is motivated by the observation[4] that such methods can be used to describe the rapidity-dependence of multiplicity distributions in hadron-hadron[5] as well as in other[6] collision processes. Having learned[4] that the multiplicity distribution data in limited rapidity intervals ("rapidity window") can be described simply by the binomial distribution law, provided that the multiplicity- and the rapidity-distributions of the particle-producing system(s) are known, it is rather natural for us to ask[3] whether the minijet phenomenon[1] can be understood in a similar way.

There are several reasons which make us expect that statistical fluctuation should play an important role in this phenomenon.
(a) It is known empirically that transverse energy E_T and charge multiplicity n are approximately proportional to each other.
(b) High-energy hadron-hadron as well as the collision experiment[5,6] show that multiplicity fluctuations in small rapidity windows are larger than those in larger windows. (c) The procedure used by UA1 collaboration[1] is in fact a measurement of n- and E_T-distributions in a given rapidity window under the condition that a minimum amount (E_{T0}=5 GeV) of E_T enters the trigger cone where the trigger cone itself is a window in the η-Φ space.

Consider an inelastic nondiffractive hadron-hadron collision at cms energy $\sqrt{s}$. Let $P(E_T;s)$ be the E_T-distribution of the emitting system that dominates the rapidity region under consideration.

The probability density of observing an amount of transverse energy E_{TW} in the rapidity window w inside the rapidity region is

$$P_w(E_{Tw}; s) = \int dE_T P(E_T;s) B(E_T, E_{Tw}; q_w; \epsilon). \qquad (1)$$

Here, $q_w(s) = \langle E_{TW}\rangle / \langle E_T \rangle$ is the average probability, at total cms-energy $\sqrt{s}$, for a unit of transverse energy to be inside the given rapidity window. (The energy scale is fixed by the parameter ϵ). $\langle E_T\rangle$ and $\langle E_{TW}\rangle$ are the average values of E_T and E_{TW} respectively. $B(E_T; E_{TW}; q_W; \epsilon)$ is the generalized binomial distribution for the continuous radom variables E_T/ϵ and E_{TW}/ϵ:

$$B(E_T, E_{Tw}; q_w; \epsilon) = \frac{\Gamma(E_T/\epsilon+1)}{\Gamma(E_{Tw}/\epsilon+1)\Gamma(E_T/\epsilon - E_{Tw}/\epsilon+1)} q_w^{E_{Tw}/\epsilon} (1-q_w)^{E_T/\epsilon - E_{Tw}/\epsilon} \qquad (2)$$

Since the *minijet-trigger* can be viewed as a moving window with an energy cut, the probability density for a given amount of transverse energy E^j_{TW} (j for jet) to be inside w <u>and</u> for a part of it (E^c_{TW}) to enter the trigger cone c with threshold energy E_{T0}(=5 GeV) can be written as:

$$P^j_w (E^j_{Tw}; E_{To}) = \int_0^{E^j_{Tw}/2} dE^c_{Tw} P_w(E^j_{Tw}; s) \; B(E^j_{Tw}/2, E^c_{Tw}; q_c; \epsilon) \; \theta(E^c_{Tw} - E_{To}) \qquad (3)$$

Note that the trigger cone receives contributions from the "jet side" only, while those on the "away side" which compensate the momentum of the jet are not included. We calculated the transverse energy distribution for minijet events from Eq.(3) where we used the empirical value for $q_c=2<E^c_{TW}>/<E^j_{TW}>$ and an empirical fit for $P_W(E_{TW};s)$. The result for $<E^j_{TW}>P^j_W$, when plotted as a function of $z_W=E^j_{TW}/<E^j_{TW}>$ is shown in Fig.1, where the data/1/ for the corresponding multiplicity distribution $<n^j_W>P^j_W$ as a function of $n^j_W/<n^j_W>$ are given.

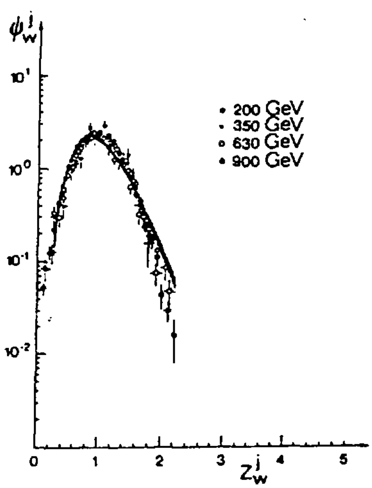

Fig.1 KNO-plot for minijet events (see text)

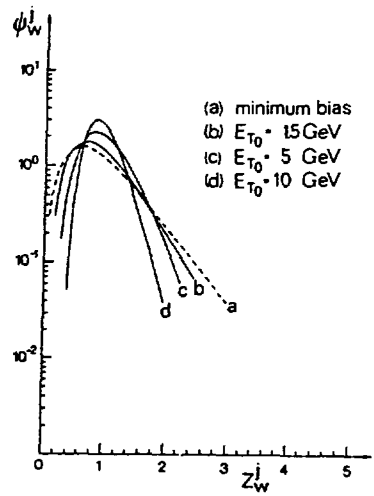

Fig.2 Threshold-dependence of KNO-plots for minijet events (see text)

The calculated result, as well as qualitative arguments (given in Ref. 3) show that the narrowness of the distribution for the minijet sample is attributable to the method of event selection. We also calculated other quantities measured by UA1 collaboration in this connection: the multiplicity distribution for non-minijet events, the average multiplicities and the average transverse energy per particle both for minijet- and for non-minijet-events, and the relative occurrence of minijet for different s-values. The obtained results are in agreement with the data[1]. It should be pointed out that all these quantities depend significantly on the threshold energy E_{T0} of the trigger cone. This dependence is illustrated in Fig.2.

The fact that minijets/low-E_T-jets phenomena can be understood in such a manner has led us to ask the following questions: "Is it useful to differentiate between events which have low-, medium- or high-transverse-energy in a given η- and/or Φ-window? "What is the relationship, if any, between such events?" We think these questions should be of considerable interest. It is because: Experimentally, minimum-bias events, minijet-events and jet-events are collision events which have different values of transverse energy in given η-Φ windows. Theoretically, according to the popular parton and/or QCD based dynamical models[2], such events are due to "soft processes" "semi-hard processes" and "hard processes" respectively. Hence, it is generally expected that experimental data for different categories of events will yield useful information on different kinds of reactions.

A systematic data analysis[7] has been carried out in Berlin, the aim of which is to answer the above-mentioned questions. The time is too short for a detailed discussion. Let me just tell you the general conclusion and show you some examples.

The result of this analysis can be summarized as follows: The transverse energy spectra in pseudorapidity and/or azimuthal angle windows are related to one another in a simple way. In fact, the relationship is nothing else but that given in Eq.(1), where q_W can in general be calculated by the geometry of the experimental apparatus. Exceptional behaviours appear only in events associated with very large transverse energies $E_T \gtrsim 40$ GeV.

As examples let me show you some of the test we made:

Test 1: We consider the experiment of B. Brown et el.[8], in which high-transverse-energy events produced in proton-proton collisions at 400 GeV/c were studied using a large-acceptance multiparticle spectrometer. We use the cross section obtained for $\Delta\Phi = 2\pi$ as input and calculate that for $\Delta\Phi = 4\pi/5$ and that for $\Delta\Phi = \pi/5$ (See Fig.2 of Ref. 8). Here, the corresponding values for q_W are respectively 2/5 and 1/10, which is simply a consequence of azimuthal symmetry.

First, we calculate the slopes of the curves. This is of some interest because empirically[8] all three sets of data are well fitted by simple exponential functions $d\sigma/dE \sim \exp(-\alpha E_T)$ in the large-E_T region. In fact, the following values for α have been given by Brown et al.[8]: $\alpha = 0.84 \pm 0.02$, 1.25 ± 0.05 and 2.5 ± 0.1 for $\Delta\Phi = 2\pi$, $4\pi/5$ and $\pi/5$ triggers, respectively. By using $\alpha = 0.84$ for $\Delta\Phi = 2\pi$ as input, we calculate the α-values for $\Delta\Phi = 4\pi/5$ and $\Delta\Phi = \pi/5$. The values are: 1.3 and 2.4 respectively.

Second, we calculate the cross-sections $d\sigma/dE_T$ for $\Delta\Phi = 4\pi/5$ and $\Delta\Phi = \pi/5$ by inserting that for $\Delta\Phi = 2\pi$ into Eq.(1). We use the value for $E_T = 0$ to determine the proportionality constant between $d\sigma/dE_T$ and $P(E_T;S)$ and thus obtain the absolute $d\sigma/dE_T$-values for $\Delta\Phi = 4\pi/5$ and for $\Delta\Phi = \pi/5$. These are shown as solid curves in Fig. 3.

Test 2: We consider the total transverse energy distribution in the UA1-experiment of G. Arnison et al.[9] at the CERN proton-antiproton collider. The data[9] are for $\sqrt{s} = 540$ GeV, and pseudo-rapidity region $|\eta| < 1.5$. Here we use exactly the same input as that in Ref.3, which is an empirical E_T-distribution for $|\eta| < 2.5$ at $\sqrt{s} = 540$ GeV. Because of the Φ-symmetry and the flatness of the η-distribution in the central rapidity region, q_W can be obtained also in this case from the geometry: $q_W = 3/5$. The calculated result is shown, together with the data[9], in Fig.4.

Test 3: We consider the transverse-energy distribution over the pseudorapidity interval $|\eta|<1$ and an azimuthal range $\Delta\Phi = 300°$ in the UA2 experiment by M. Banner et al.[10]. In this proton-antiproton collision experiment at $\sqrt{s} = 540$ GeV, a segmented calorimeter is used to study large E_T-jets. Here, we use as input the UA1 data[9] for $|\eta|< 1.5$ and $\Delta\Phi = 360°$ for the same reaction at the same energy. The values for q_W are determined from the geometry, where the symmetry in Φ and the flatness in the η-distribution are taken into account. They are: $\frac{2}{3} \times \frac{300°}{360°} = \frac{5}{9}$ and $\frac{2}{3} \times \frac{60°}{360°} = \frac{1}{9}$ respectively. The calculated result for $\Delta\Phi = 300°$ and that for $\Delta\Phi = 60°$ are shown in Fig.5 together with the UA2 data[10].

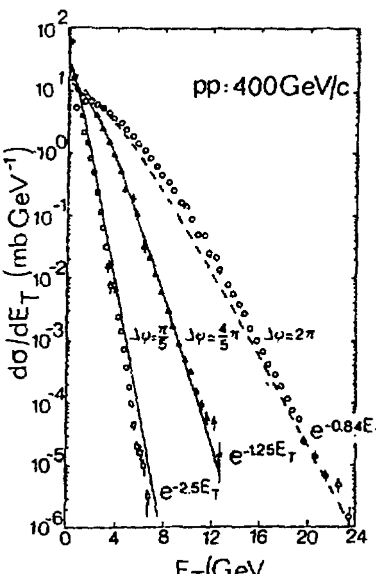

Fig.3 Cross section obtained with three different azimuthal acceptances as a function of transverse-energy contained with the trigger modules. Data are taken from Ref.8. The solid lines for the $\Delta\Phi = 4\pi/5$ and the $\Delta\Phi = \pi/5$ data set are the calculated result of Test 1. The dashed line is explained in Ref. 7.

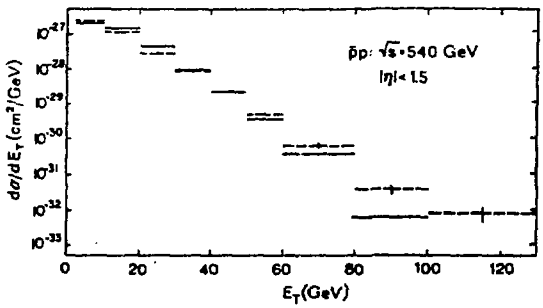

Fig.4 Total transverse--energy distribution in the rapidity region $|\eta|<1.5$ GeV. Data, shown as dashed lines, are taken from Ref. 9. The calculated result of Test 2 is shown as solid lines.

Fig.5 Transverse--energy distributions over the whole azimuthal region. Data are taken from Ref.10. The solid curves are the calculated result of Test 3.

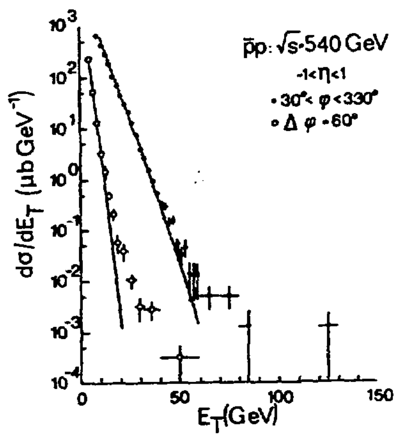

References

1) Ceradini et al. (UA1 Coll.) CERN Report EP-85-196

2) G. Pancheri and C. Rubbia, Nucl. Phys. A418, 117 (1984); G. Pancheri and Y. Srivastava, Phys. Lett. 159B, 69 (1985); F.W. Bopp, P. Aurenche and J. Ranft, Phys. Rev. D33, 1867 (1986); Cai Xu, Wu Yuan-fang and Liu Lian-sou, High-Energy Physics and Nuclear Physics, (to be published). R. Hwa, Talk given at Aspen Workshop on Multiparticle Strong Interaction Dynamics (1986). G. Pancheri, Talk given at the same

Workshop (1986). M. Jacob and P.V. Landshoff, Mod. Phys. Lett. A1, 657 (1986). L. Durand and Pi Hong, Phys. Rev. Lett. 56, 303 (1987). A. Capella, J. Tran Thanh Van and J. Kwiecinsky, Phys.Rev. Lett. 58, 2015 (1987).

3) Chao Wei-qin, Meng Ta-chung and Pan Ji-cai, Phys. Rev. Lett. 58, 1399 (1987).

4) Chao Wei-qin, Meng Ta-chung and Pan Ji-cai, Phys. Rev. D35 152 (1987); Phys. Lett. 176, 211 (1986).

5) G.J. Alner et al. (UA5 Coll.) Phys. Lett. 160B 193; 199 (1985) M. Adamus et al. (NA22 Coll.) Phys. Lett. 177B 239 (1986).

6) M. Derrick et al. (HRS/PEP Collaboration), Phys. Lett. 168B, 299 (1986). I. Derado, Talk given at the Aspen Workshop on Multiparticle Strong Interaction Dynamics, 1986 (unpublished).

7) Meng Ta-chung and Pan Ji-cai, Berlin preprint FUB-HEP/87-4.

8) R. Brown et al., Phys. Rev. Let. 49, 711 (1982).

9) G. Arnison et al. (UA1-Collaboration), Phys. Lett. 123B, 115 (1983). More recent references on UA1 jet experiments can e.g. be found in: F. Ceradini, in Proceedings of the 23rd International Conference on High-Energy Physics, Berkeley, CA (1986) p. 1051.

10) M. Banner et al. (UA2-Collaboration), Phys. Lett. 118B, 203 (1982). More recent references can e.g. be found in A. Roussric, in Proceedings of this Symposium.

PION AND BARYON PRODUCTION IN HIGH p_T PROTON-PROTON INTERACTIONS AND DIQUARK SCATTERING *

M. Szczekowski
Institute of Nuclear Studies, Warsaw, Poland
Ames-Bologna-CERN-Dortmund-Heidelberg-Warsaw Collaboration

Abstract:

Few examples of recent data on high p_T pion and proton production from Split Field Magnet detector at ISR are presented. The features of inclusive particle production and correlations observed between particles in trigger and spectator jets support the conjecture of hard diquark scattering as a source of high p_T baryons.

---

* Submitted to the Symposium

1. INTRODUCTION

Hard scattering of elementary particles with production of high transverse momentum jets is one of the most important tests for parton models and Quantum Chromodynamics (QCD) [1]. Studies of leading particles in jets showed that knowledge of the particle identity directly gives information about the underlying parton scattering [2]. Identification of leading mesons in large p_T jets allowed the separation of gluon scattering from other high p_T processes [3]. The behaviour of leading baryons produced at high p_T showed new features unexplained within a standard parton model: the relative proton yields $\sigma(p)/\sigma(\pi)$ depend on p_T at fixed scattering angle θ, on θ at fixed p_T, and on c.m.s energy $\sqrt{s}$ at fixed $x_T = 2p_T/\sqrt{s}$ and θ; in contrast, relative K^+ and $\bar{p}$ yields are nearly independent of kinematic variable [4]. In this short report I will present the recent results of the analysis of high p_T processes at ISR energies obtained in the Split Field Magnet detector by ABCDHW Collaboration [5]. The experiment is briefly described in section 2. In section 3 the ratios of inclusive cross sections for negative and positive pions separately are disscussed. In phase space regions limited by geometric acceptance of Cherenkov counters the ratios are studied as functions of transverse momentum p_T, reduced longitudinal momentum $x = 2p_L / \sqrt{s}$ and scattering angle θ and compared with parton model calculations. The data on correlations between theidentified trigger particle and the properties of spectator jets are presented in sect. 4.

2. EXPERIMENT

The experiment was performed with the Split Field Magnet (SFM) Detector at the CERN Intersecting Storage Rings (ISR). The detector consists of a system of multiwire proportional chambers and an array of scintillation counters for time-of-flight measurements [6b].

A three step trigger logic selects events with a high p_T track at a c.m.s. scattering angle $\theta \approx 10^0$, 20^0 or 45^0. These tracks can be identified with threshold Cherenkov counters [5,6b]. The present statistics for reconstructed high p_T events is of the order of 10^6.

3. <u>RATIOS OF INCLUSIVE CROSS-SECTIONS</u>

Pion ratios of inclusive cross-sections $R^+ = \sigma(\pi^+)/\sigma(\pi^+ + K^+ + p)$ and $R^- = \sigma(\pi^-)/\sigma(\pi^- + K^- + \bar{p})$ for proton-proton interactions at $\theta \approx 10^0$, 20^0 and 45^0 were measured at two c.m.s. energies: $\sqrt{s} = 31$ GeV and 63 GeV as functions of x and p_T.

The x dependence of the data is illustrated in figs 1,2 and 3 for different fixed values of p_T. Independent of a chosen p_T value, the fraction of negative pions R^- is a steeply rising function of x. At x = 0.5 only a few percent of the cross section is left for heavier particles (K^-, $\bar{p}$) for all values of p_T. The fraction of positive pions shows the opposite behaviour. Starting from $R^+ \approx 0.6$ at $x \approx 0$ it decreases with increasing x.

The dependence of R^+ and R^- on x, observed here at medium and high values of p_T, resembles closely the behaviour of positive and negative pion fractions at low transverse momenta. In the soft hadronic interaction this behaviour is generally understood as a reflection of the leading proton effect [7]. In the quark models of soft hadron scattering this effect is explained by the diquark content of the forward-backward jets in proton-proton collisions. Similar properties of pion production at low and high p_T suggest a common origin of this behaviour: the fragmentation of diquarks with a substantial contribution of fast protons which suppresses the relative positive pion contribution at higher x. For negative particles this process is absent and pions dominate.

To describe the p_T dependence of R^+ and R^- shown in figs 4 and 5 for different fixed values of the hard scattering of quarks and gluons was simulated by the Monte Carlo program described in detail in ref.[8]. The process of diquark scattering was not included in this version of the simulation program. The model describes reasonably well the negative pion ratios at both energies but the positive pion ratios are not described properly by the model. The discrepancy between the model and the data is increasing for smaller angles ($\theta \approx 20^\circ$). A similar discrepancy was observed previously for the complementary data on high p_T baryon production in proton-proton collisions [4a]. Although the production of antiprotons was well described by the standard quark model, in the case of proton production this model failed to describe the magnitude and θ and p_T dependence of the proton relative yields. The contribution from diquark scattering [9] was proposed to explain the features of high p_T proton production [10]. The model applies to particles with $p_T > 2.5$ GeV/c. The predictions of this model for R^+ shown in figs 4 and 5 are in good agreement with the high p_T end of the data. About 90% of the high p_T protons originate from diquark scattering in this phase space region.

We conclude that the qualitative and quantitative predictions of the diquark model are in good agreement with the data at higher values of p_T. This indicates the presence of diquark fragmentation also in high p_T jets. The confirmation of this hypothesis should come from the correlation data.

4. CORRELATIONS BETWEEN TRIGGER AND SPECTATOR JETS

For the events with high p_T baryon production a typical hard scattering four jet structure is observed: scattered partons fragment into high p_T "trigger" and "away" jets and noninteracting partons form two low p_T spectator jets. The hypothesis that high p_T baryons are produced by hard diquark scattering leads to the prediction of well defined correlations between these jets as shown in fig. 6. The spectator jets, at $\theta \approx 0^\circ$, should be due to a system of two valence quarks in the case of positive meson triggers and to single valence quarks for proton triggers from diquarks fragmentation.

A study of the ratios $R^+(p/\pi^+) = \varrho^+(p)/\varrho^+(\pi^+)$ of densities of positive particles associated with proton and π^+ meson triggers respectively allows to discriminate between fragmentation of diquarks and quarks in spectator jet region ($x > 0.3$). If high p_T protons are diquark fragments R^+ (p/π^+) should decrease with x since for large x positive fragments are dominantly protons which are easily produced in diquark fragmentation and are suppressed in quarks fragmentation [11]. This kind of behaviour is indeed observed in fig.7,8 and 9 for triggers at $\theta \approx 10^\circ$, 20° and 45° respectively. These data are in qualitative agreement with hard diquark scattering giving rise to high p_T protons. Similar correlations have been observed recently for events with high p_T trigger particles detected at $\theta \approx 90^\circ$[12].

If high p_T protons indeed originate from diquark scattering the corresponding spectator fragments should be compared to charge densities from single quark (current) jets in deep inelastic lepton scattering (DIS). For pion triggers on the other hand the spectator particles should behave like target jets in DIS. The correlation between the fragmentation variable z and the reduced longitudinal momentum x as measured in this experiment can be obtained from straightforward parton model calculations [13]. The ratio $R_\rho = \rho^-/\rho^+$ turns out to be a very sensitive indicator of the nature of the parent partons. In fig.10 acceptance corrected values of R_ρ are shown as a function of x for different trigger (π^+, π^-, p) particles and compared with predictions from deep inelastic neutrino scattering [14]. The agreement for (uu) and (ud) jets in νp, $\bar{\nu} p$ and $\pi^-$and π^+triggers is indeed striking. On the other hand R_ρ for proton triggers shows an increase of negative charge density ρ^-at large x. By comparison of these data with models the nature of corresponding scattered diquarks can be investigated: if only (ud) systems are involved in high p_T diquark scattering then R_ρ should correspond to single u - quark scattering. As can be seen in fig. 11 the data fall well above this prediction and indicate a substantial contribution from scattered (uu) diquarks. Further evidence for the scattering of (uu) diquarks comes from the appearance of Δ^{++}resonances in the trigger jet as shown in fig.12.

5. CONCLUSIONS

The conjecture of hard diquark scattering leading to substantial production of high p_T baryons in high energy proton-proton collisions gains further support from the recent data from Split Field Magnet detector. Both the peculiar properties of the inclusive high p_T proton production and the charge correlations between trigger and spectator jets can be explained by the scattering of tightly bound two quark objects. Further confirmation of the existence of such objects should come from studies of baryon production in deep inelastic lepton scattering and e^+e^- annihilations.

REFERENCES

[1] M.Jacob, Proceedings of 22nd int. Conf. on High Energy Physics, Leipzig (1984), 150.

[2] ABCDHW Collaboration,
A.Breakstone et al., Zeitschr. fur Phys.C27(1985)205.

[3] A.Breakstone et al., Phys. Lett. 135B(1984)510.

[4] A.Breakstone et al., Phys.Lett. 147B(1984)237.
D.Antreasyan et al., Phys.Rev. Lett. 38(1977) 112, 115.

[5] A.Breakstone et al., CERN preprint CERN/EP 87-23 to be published in Zeitschr. fur Phys.C
A.Breakstone et al., CERN preprint CERN/EP 87-8 to be published in Zeitschr. fur Phys. C.

[6] a) M.Della Negra et al., Phys.Lett. 59B(1975)481.
b) D.Drijard et al., Nucl.Phys. B208(1982)1.

[7] A.Breakstone et al., Phys.Lett.132B(1983)458.
J.L.Bailly et al., Zeitschr. fur Phys.C31(1986)367.

[8] T.Lohse, Diploma Thesis, University of Dortmund (1982).

[9] S.Ekelin and S.Fredriksson, Phys.Lett.148B(1984)509.

[10] A.Breakstone et al., Zeitschr. fur Phys.C25(1985)335.

[11] S.J.Brodsky and G.R.Farrar, Phys.Rev.Lett. 31(1973)1153.
S.J.Brodsky and J.F.Gunion, Phys.Rev.D17(1978)848.

[12] A.M.Smith et al., Phys.Lett. 184B(1987)293.

[13] M.Della Negra et al., Nucl.Phys. B127(1977)1.

[14] P.Allen et al., Nucl.Phys. B214(1983)369.
J.Bell et al., Phys.Rev. D19(1979)1.
M.Derrick et al., Phys.Rev. D24(1981)1071.

FIGURE CAPTIONS

Fig. 1 Pion ratios $R^+ = \sigma(\pi^+)/\sigma(\pi^+ + K^+ + p)$ and $R^- = \sigma(\pi^-)/\sigma(\pi^- + K^- + \bar{p})$ at fixed $p_T = 2.1$ GeV/c and two c.m.s. energies $\sqrt{s} = 31$ GeV and $\sqrt{s} = 62$ GeV as functions of a reduced longitudinal momentum x.

Fig.2 Pion ratios $R^+ = \sigma(\pi^+)/\sigma(\pi^+ + K^+ + p)$ and $R^- = \sigma(\pi^-)/\sigma(\pi^- + K^- + \bar{p})$ at fixed $p_T = 2.5$ GeV/c (R^-) and $p_T = 2.9$ GeV/c (R^+) and two c.m.s. energies $\sqrt{s} = 31$ GeV and $\sqrt{s} = 62$ GeV as functions of a reduced longitudinal momentum x.

Fig. 3 Pion ratios $R^+ = \sigma(\pi^+)/\sigma(\pi^+ + K^+ + p)$ and $R^- = \sigma(\pi^-)/\sigma(\pi^- + K^- + \bar{p})$ at fixed $p_T = 1.3$ GeV/c (R^-) and $p_T = 1.5$ GeV/c (R^+) and two c.m.s. energies $\sqrt{s} = 31$ GeV and $\sqrt{s} = 62$ GeV as functions of a reduced longitudinal momentum x. The R^- data from the experiment [6a] at $\sqrt{s} = 53$ GeV are shown for comparison.

Fig. 4 Positive and negative pion fractions at $\sqrt{s} = 62$ GeV and fixed scattering angle $\theta = 26^\circ$ for R^+ and $\theta = 18^\circ$ for R^- shown as functions of transverse momentum. The predictions of the parton models described in the text are also presented.

Fig. 5 Positive and negative pion fractions at $\sqrt{s} = 31$ GeV and a fixed scattering angle $\theta = 20^\circ$ for R^+ and $\theta = 14^\circ$ for R^- shown as functions of transverse momentum. The predictions of the parton models described in the text are also presented.

Fig. 6 Expected flavour composition of spectator jets for pion and proton triggers.

Fig. 7 Ratios of positive spectator secondaries associated with proton and π^+ triggers at $\theta \approx 10^\circ$ with $p_{lab} >$ 13 GeV/c. The error bands indicated at large x are predictions from deep inelastic neutrino scattering.

Fig. 8 Ratios of positive spectator secondaries associated with proton and π^+ triggers at $\theta \approx 20^\circ$ and $p_{lab} >$ 13GeV/c.

Fig. 9 See fig. 8, but for proton and π^+ meson triggers at $\theta \approx 45^\circ$ and $p_T > 3.5$ GeV/c ($\langle p_T \rangle = 3.9$ GeV/c).

Fig. 10 Charge density ratio ρ^-/ρ^+ as a function of x for pion and proton triggers. The shaded strips are predictions from deep inelastic neutrino and antineutrino scattering experiments for (ud) and (uu) target jet systems.

Fig. 11 Charge density ratio ρ^-/ρ^+ for proton triggers compared to predictions from deep inelastic neutrino scattering for pure u - quark fragmentation and for a mixture of 33% d - quark and 67% u - quark.

Fig. 12 Uncorrected invariant $p\pi^+$ - mass distributions for proton trigger particles at (a) $\theta \approx 10^\circ$ and 13 GeV/c $< p_{lab} <$ 18.1 GeV/c, (b) $\theta \approx 20^\circ$ and 13 GeV/c $< p_{lab} <$ 18.1 GeV/c, (c) $\theta \approx 45^\circ$ and $p_T > 4$ GeV/c.

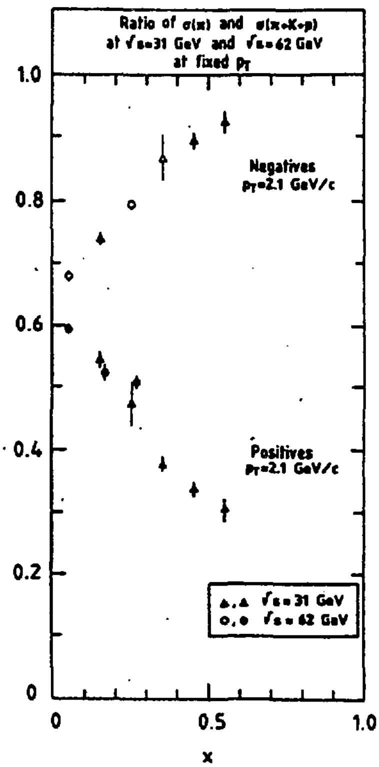

Ratio of σ(π) and σ(π+K+p)
at √s=31 GeV and √s=62 GeV
at fixed p_T
Negatives
p_T=2.1 GeV/c
Positives
p_T=2.1 GeV/c
▲,△ √s = 31 GeV
○,● √s = 62 GeV
1.0
0.8
0.6
0.4
0.2
0
0
0.5
1.0
x

Fig. [illegible]

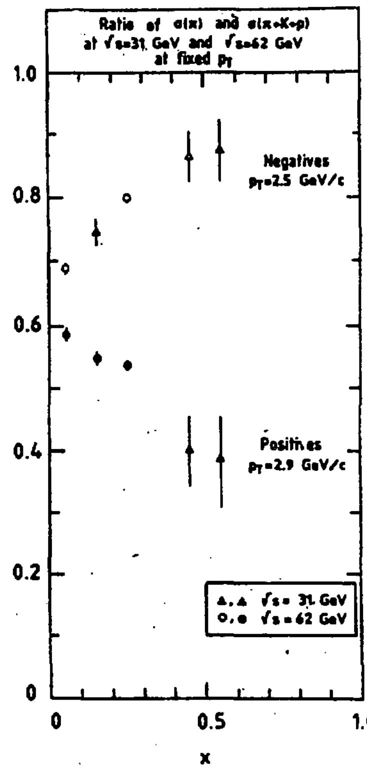

Ratio of σ(π) and σ(π+K+p)
at √s=31 GeV and √s=62 GeV
at fixed p_T
Negatives
p_T=2.5 GeV/c
Positives
p_T=2.9 GeV/c
▲,△ √s = 31 GeV
○,● √s = 62 GeV
1.0
0.8
0.6
0.4
0.2
0
0
0.5
1.0
x

Fig. [illegible]

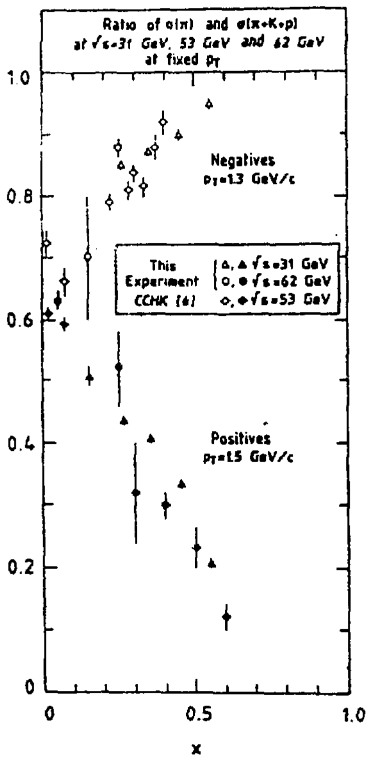
Ratio of σ(π) and σ(π+K+p)
at √s=31 GeV, 53 GeV and 62 GeV
at fixed pT
Negatives
pT=1.3 GeV/c
This Experiment
CCHK (6)
Δ, ▲ √s=31 GeV
o, ● √s=62 GeV
◇, ◆ √s=53 GeV
Positives
pT=1.5 GeV/c
1.0
0.8
0.6
0.4
0.2
0
0
0.5
1.0
x

Fig. 3

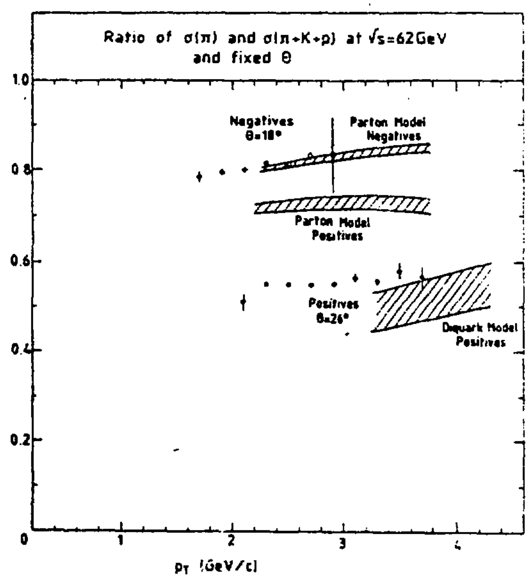
Ratio of σ(π) and σ(π+K+p) at √s=62GeV
and fixed θ
Negatives
θ=18°
Parton Model
Negatives
Parton Model
Positives
Positives
θ=26°
Diquark Model
Positives
1.0
0.8
0.6
0.4
0.2
0
1
2
3
4
pT (GeV/c)

Fig. 4

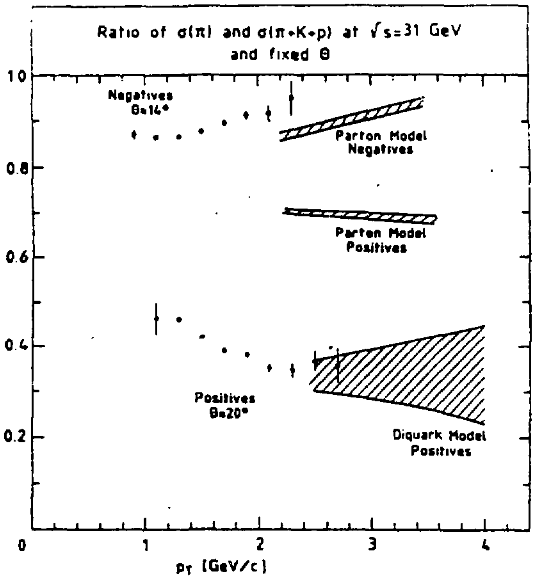
Ratio of σ(π) and σ(π+K+p) at √s=31 GeV
and fixed θ
Negatives
θ=14°
Parton Model
Negatives
Parton Model
Positives
Positives
θ=20°
Diquark Model
Positives
1.0
0.8
0.6
0.4
0.2
0
1
2
3
4
pT (GeV/c)

Fig. 5

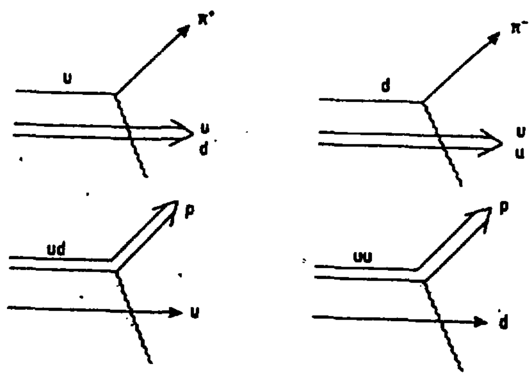
π⁺
u
u
d
π⁻
d
u
u
p
ud
u
p
uu
d

Fig. 6

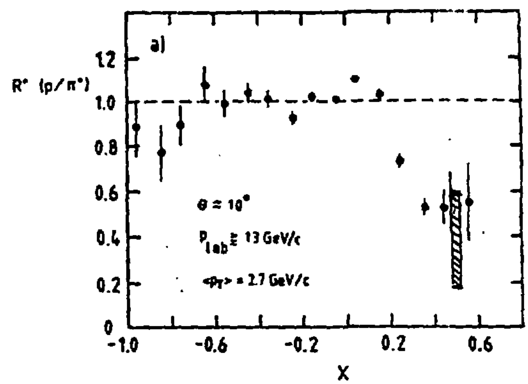
a)
R* (p/π°)
1.2
1.0
0.8
0.6
0.4
0.2
0
-1.0
-0.6
-0.2
0.2
0.6
X
θ = 10°
P_{lab} ≅ 13 GeV/c
<p_T> = 2.7 GeV/c

Fig. 7

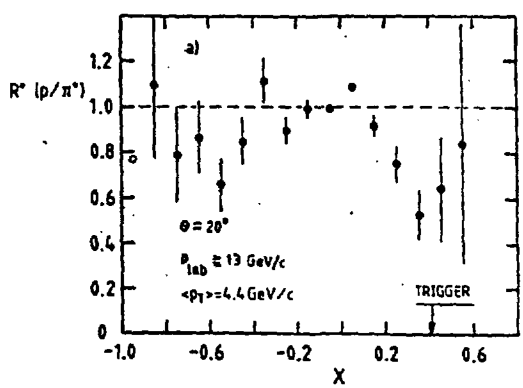
a)
R* (p/π°)
1.2
1.0
0.8
0.6
0.4
0.2
0
-1.0
-0.6
-0.2
0.2
0.6
X
θ = 20°
P_{lab} ≅ 13 GeV/c
<p_T> = 4.4 GeV/c
TRIGGER

Fig. 8

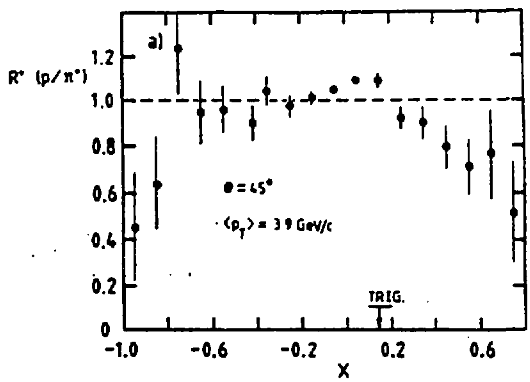

a)
R* (p/π*)
1.2
1.0
0.8
0.6
0.4
0.2
0
θ = 45°
⟨p_T⟩ = 3.9 GeV/c
TRIG.
-1.0
-0.6
-0.2
0.2
0.6
X

Fig. 9

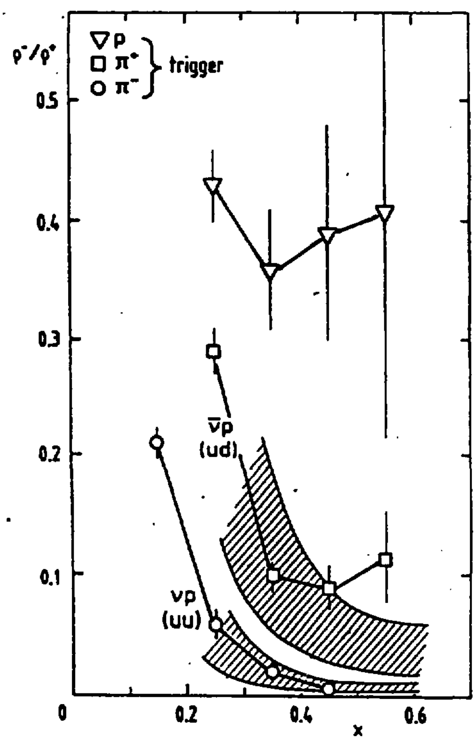

ρ⁻/ρ⁺
▽ p
□ π⁺
○ π⁻
trigger
0.5
0.4
0.3
0.2
0.1
0
ν̄p
(ud)
νp
(uu)
0.2
0.4
0.6
x

Fig. 10

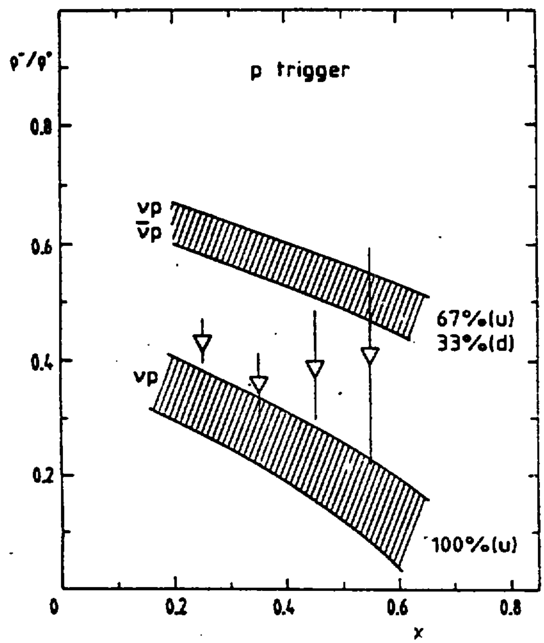
p trigger
ρ^-/ρ^+
0.8
0.6
0.4
0.2
0
0.2
0.4
0.6
0.8
x
νp
$\bar{\nu}$p
67%(u)
33%(d)
νp
100%(u)

Fig. 11

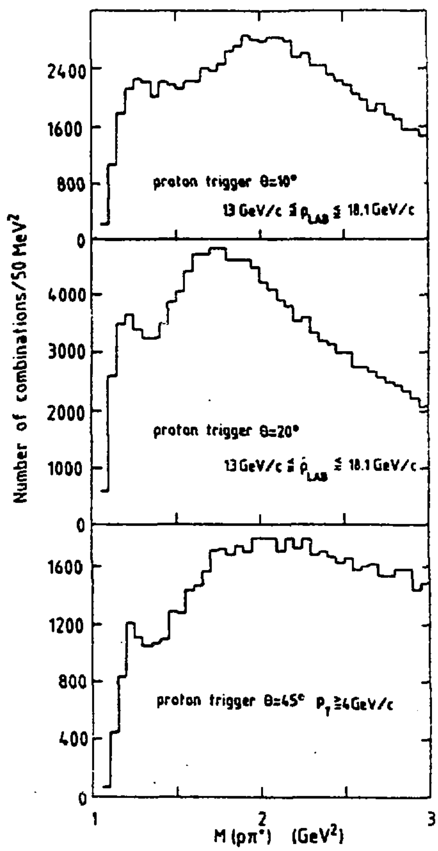

Number of combinations/50 MeV^2
2400
1600
800
0
proton trigger θ=10°
13 GeV/c ≦ p_{LAB} ≦ 18.1 GeV/c
4000
3000
2000
1000
0
proton trigger θ=20°
13 GeV/c ≦ p_{LAB} ≦ 18.1 GeV/c
1600
1200
800
400
0
proton trigger θ=45° p_T ≧ 4 GeV/c
1
2
3
M (pπ°) (GeV^2)

Fig. 18

ASYMPTOTIC KNO SCALING FOR QCD JETS

by

Antonio Bassetto

Dipartimento di Fisica 'G.Galilei'
Via Marzolo 8, 35131 Padova (Italy)

Istituto Nazionale di Fisica Nucleare
Sezione di Padova

Abstract

We exhibit the asymptotic KNO profile function for QCD jets in e^+e^- annihilation.

Perturbative QCD provides us with a definite prediction for the multiplicity distribution of partons occurring in a jet evolution [1].

In the leading logarithmic approximation (LLA), related to the asymptotic regime in which the transverse momentum Q of the parent parton is much larger than other hadronic scales, this prediction takes the simple form of a non-linear differential equation for the generating function of the multiplicity moments $n_K(s) = \langle n(n-1)\cdots(n-K+1)\rangle$

$$F(s,u) = \sum_{K=0}^{\infty} \frac{(u-1)^K}{K!} n_K = \sum_{n=0}^{\infty} u^n P_n(s), \quad (1)$$

$P_n(s)$ being the probability of producing n gluons out from an initial gluon jet (*) [1,2]

$$\frac{d^2}{ds^2} \log F(s,u) = u F(s,u) - 1 ,$$

$$F(0,u) = 1 , \quad F'_s(0,u) = 0 , \quad (2)$$

where $s \simeq \log \langle n(Q)\rangle$.

(*) In DLA the radiation is dominated by its soft gluon content.

The physics leading to the equation (2) is carefully explained for instance in ref. [1] and will not be repeated here.

If we set $u = \exp\left[-\beta/\langle n\rangle\right]$ and consider the limit $s\to\infty$, the solution of eq. (2) exhibits a KNO scaling behaviour [3], i.e.

$$F\left(s, \exp(-\beta/\langle n\rangle)\right) \underset{s\to\infty}{\longrightarrow} \Phi(\beta) , \qquad (3)$$

$\Phi(\beta)$ being the solution of the differential equation

$$\frac{d^2}{d(\log\beta)^2} \log\Phi = \Phi - 1 \qquad (4)$$

with boundary conditions

$$\Phi(0) = -\Phi'(0) = 1 . \qquad (5)$$

$\Phi(\beta)$ is in turn related to the asymptotic limits of the normalized multiplicity moments

$$\gamma_K = \lim_{s\to\infty} n_K(s)\left[n_1(s)\right]^{-K} \qquad (6)$$

and to the KNO profile function f(x), according to the equations

$$\Phi(\beta) = \sum_{k=0}^{\infty} \frac{(-\beta)^k}{k!} f_k = \int_0^{\infty} e^{-\beta x} f(x)\, dx \,. \tag{7}$$

Eq. (4) with the conditions (5) can be solved for $\Phi(\beta)$ in an implicit form, which is insuitable for performing an inverse Laplace transform. Alternatively it can be converted into the following recursive relation for f_k [3]

$$f_0 = f_1 = 1 \,,$$

$$f_k = \frac{k^2 k!}{2(k^2-1)} \sum_{m=1}^{k-1} \frac{f_m}{m\, m!} \frac{f_{k-m}}{(k-m)(k-m)!} \,, \quad k \geq 2 \,, \tag{8}$$

which can be solved by simple iteration giving rise to a unique sequence $\{f_m\}$.

We are lead in this way to a problem of moments (i.e. to reconstruct f(x) from the sequence $\{f_k\}$).

One can show [3] that $\Phi(\beta)$ is analytic in the disc $|\beta| < |\beta_0|$ with

$$\beta_0 = -\exp \int_1^{\infty} \frac{dx}{x} \left[\frac{1}{\sqrt{2(x-1-\log x)}} - \frac{1}{x-1} \right] \simeq -2.55 \,. \tag{9}$$

As a consequence an analytic continuation is necessary before taking its inverse Laplace transform.

We have solved this problem of moments in the Hilbert space $L_2(0,\infty)$ [4]

$$\hat{f}(x) = s\text{-}\lim_{N \to \infty} e^{-|\beta_0| x} \sum_{K=0}^{N} \hat{f}_K L_K(|\beta_0| x) \qquad (10)$$

L_k being the complete set of the Laguerre polynomials and the sequence $\{\hat{f}_k\}$ being uniquely determined by the sequence $\{f_k\}$ according to the equations

$$\hat{f}_K = - \sum_{q=0}^{K} \binom{K}{q} \frac{(-|\beta_0|)^{q+1}}{q!} \hat{f}_q \, . \qquad (11)$$

Few polynomials are sufficient to obtain a good approximation, once the expansion variable has been suitably chosen ($\xi = |\beta_0| x$). In the e^+e^- case, assuming that the two $q,\bar{q}$ jets evolve independently, we have [3]

$$\Phi^{(\rho)}(\beta) = \left[\Phi\left(\frac{\beta}{\rho} \right) \right]^{\rho} \; , \quad \rho = \frac{X}{\xi} \; . \qquad (12)$$

The KNO profile function $f^{(\rho)}(x)$ can again be obtained as an expansion over Laguerre polynomials starting from the recursive relation [3]

$$f_0^{(\rho)} = f_1^{(\rho)} = 1 \quad ,$$

$$f_k^{(\rho)} = \rho^{1-k}\frac{f_k}{k^2} + \sum_{m=1}^{k-1}\frac{(k-1)!\,\rho^{1-m}}{m!\,(k-m)!}\,\frac{f_m}{m}\,f_{k-m}^{(\rho)} \quad , \qquad k \geq 2 \quad , \tag{13}$$

analogous to eq. (8). We report in fig. 1 for 90 values of x between 0 and 4.5 the results with N=10 and N=30. (dotted and continuous line respectively).

Finally we compare in fig. 2 $f^{(\rho)}(x)$ with the negative binomial distribution

$$f_{NB}(x) = \frac{K^K}{\Gamma(K)}\,x^{K-1}\,e^{-Kx} \quad , \qquad K = \frac{8}{9}|\beta_0| . \tag{14}$$

(continuous and dotted lines respectively).

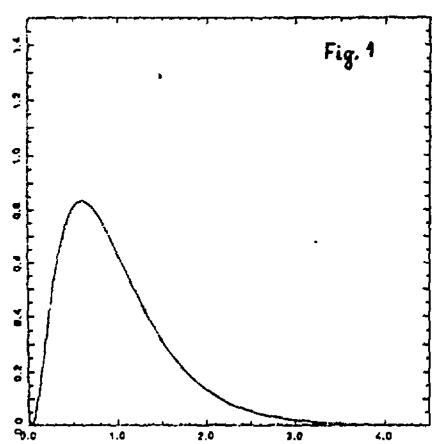

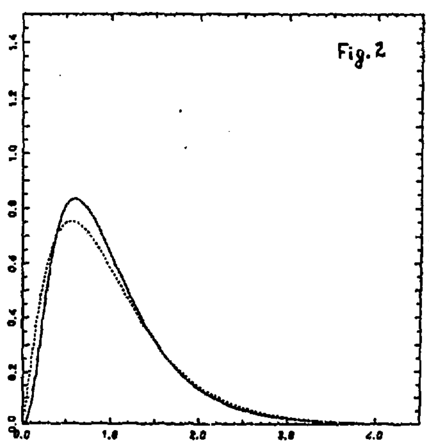

The similarity between the two curves is not surprising as they share the first two moments and the exponential fall-off at ∞. It might explain the behaviour of the first few moments noticed in ref. [5]:

$$\left(\frac{f_{\ell+1}}{f_\ell} - 1\right)\frac{1}{\ell} \sim \frac{1}{k} \quad , \quad \ell = 0, 1, 2 \ldots \tag{15}$$

The value of k in eq. (15) is lower than the ones found in present e^+e^- data [6], whose energy is certainly still far from the region where our asymptotic expansion might apply. As however the observed value of k is seen to decrease with increasing energy [7], it is not inconceivable that our result might start being relevant already at LEP energies, at least as "zeroth order" approximation.

References

[1] A. Bassetto, M. Ciafaloni, G. Marchesini, Phys. Reports 100 (1983) 201.

[2] Yu.L. Dokshitzer, V.S. Fadin, V.A. Khoze, Z. Phys. C15 (1983) 325.

[3] Yu. L. Dokshitzer, V.S. Fadin, V.A. Khoze, Z. Phys. C18 (1983) 37.

[4] A. Bassetto, Proceedings of the XXII Rencontres de Moriond, Les Arcs 1987 (France).

[5] R.D.Malaza and B,R. Webber, Nucl. Phys. B267 (1986) 702.

[6] M. Derrik et al., Preprint ANL-HEP-PR 86-03 (1986).

[7] TASSO collab.- M. Althoff et al.- Z. Phys. C22 (1984) 307.

RECENT RESULTS FROM THE EUROPEAN MUON COLLABORATION

R. Windmolders

Université de l'Etat, Mons, Belgium

INTRODUCTION

The results presented in this report have been obtained in recent phases of the experimental program developed at CERN by the European Muon Collaboration (EMC). In the first two sections we will discuss spin asymmetries measured in interactions on a polarised target. The spin dependent structure function g_1 is derived from the muon asymmetry and its integral compared with sum rule predictions. The asymmetries observed for positive and negative hadrons give further information on the contributions of the constituent quarks to the nucleon spin. In the third section we analyse the profile of the hadron jet resulting from the fragmentation of the struck quark and ~~derive~~ a value of the QCD coupling constant α_s in the context of the Lund string model. Properties of baryon and antibaryon production in the fragmentation process are derived ~~in the last section~~.

1. SPIN DEPENDENT STRUCTURE FUNCTIONS IN DEEP INELASTIC SCATTERING

a) Formalism

In the leading order of the electromagnetic coupling the double differential cross section for the reaction $\mu N \rightarrow \mu X$ is given by

$$\frac{d^2\sigma}{d\Omega dE'} = \frac{4\alpha^2 E'^2}{Q^4} \cos^2\frac{\theta}{2}\left(W_2(\nu,Q^2) + 2\, W_1(\nu,Q^2)\, \mathrm{tg}\, \frac{\theta}{2}\right) \qquad (1)$$

where θ is the muon scattering angle, $\nu = E - E'$ the energy of the exchanged virtual photon and $(-Q^2)$ its four-momentum squared (fig. 1). The scaling hypothesis implies that at large (ν, Q^2) the two structure functions W_1 and W_2 depend only on the reduced variable $x = Q^2/2M\nu$:

$$\begin{aligned} \nu\, W_2\,(\nu,Q^2) &\rightarrow F_2(x) \\ M\, W_1\,(\nu,Q^2) &\rightarrow F_1(x) \end{aligned} \qquad (2)$$

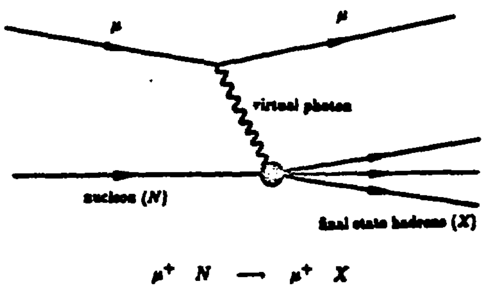

Figure 1
Lowest order Feynman diagram for muon-nucleon scattering

When spins are taken into account the right-hand side of formula (1) defines the average $\frac{1}{2}\left(\frac{d^2\sigma}{d\Omega dE'}\uparrow\uparrow + \frac{d^2\sigma}{d\Omega dE'}\uparrow\downarrow\right)$ for beam and target spins parallel ($\uparrow\uparrow$) or antiparallel ($\uparrow\downarrow$).

In a similar way, the difference $\left(\frac{d^2\sigma}{d\Omega dE'}\uparrow\downarrow - \frac{d^2\sigma}{d\Omega dE'}\uparrow\uparrow\right)$ can also be written as a function of two structure functions G_1 and G_2 [1]:

$$\frac{d^2\sigma\uparrow\downarrow}{d\Omega dE'} - \frac{d^2\sigma\uparrow\uparrow}{d\Omega dE'} = \frac{4\alpha^2}{Q^2}\ \frac{E'}{E}\left(M\ G_1(\nu,Q^2)\ (E+E'\cos\theta) - Q^2G_2(\nu,Q^2)\right) \qquad (3)$$

with scaling properties given under the same conditions by:

$$\begin{aligned} M^2\ \nu\ G_1\ (\nu,Q^2) &\rightarrow g_1(x) \\ M\ \nu^2\ G_2\ (\nu,Q^2) &\rightarrow g_2(x) \end{aligned} \qquad (4)$$

In this experiment we measure the asymmetry, defined as the ratio of (3) to (1), for projectile and target spins along the beam direction:

$$A = \frac{d\sigma\uparrow\downarrow - d\sigma\uparrow\uparrow}{d\sigma\uparrow\downarrow + d\sigma\uparrow\uparrow} \quad . \qquad (5)$$

In the quark-parton model the structure functions $F_2(x)$ and $G_2(x)$ are given by the probability of finding a quark of flavour i carrying a fraction x of the nucleon momentum and having its spin projection along (q_i^+) or opposite (q_i^-) to the nucleon spin:

$$F_2(x) = x \sum_i e_i^2\ (q_i^+(x) + q_i^-(x)) \qquad (6)$$

$$2\ g_1(x) = \sum_i e_i^2\ (q_i^+(x) - q_i^-(x)) \qquad (7)$$

By measuring the asymmetry A(x) we thus investigate the spin structure of the constituent quarks.

The Bjorken sum rule [2], derived from light cone algebra, predicts that the difference of the integrals of $g_1(x)$ for protons and neutrons is proportional to the ratio of the axial and vector coupling constants G_A and G_V measured in β decay. Including a correction for QCD radiative effects, the relation becomes [1]:

$$\int_0^1 (g_1^p(x) - g_1^n(x))\, dx = \frac{1}{6} \left|\frac{G_A}{G_V}\right| (1 - \alpha_s(Q^2)/\pi) \; . \tag{8}$$

Separate predictions also exist for the integrals of g_1^p and g_1^n. The Ellis-Jaffe sum rule [3], based on SU(3) current algebra and assuming an unpolarised strange quark sea, predicts the values:

$$\begin{aligned} \int_0^1 g_1^p\,(x)\, dx &= 0.200 \pm 0.005 \\ \int_0^1 g_1^n\,(x)\, dx &= -0.010 \pm 0.005 \end{aligned} \tag{9}$$

b) Experimental Data

The EMC has evaluated the spin asymmetry (5) by collecting large samples of interactions of polarised muons on nucleons polarised in the direction of the beam or in the opposite direction.

The positive muon beam, obtained from pion decay, was polarised to ~80%. The target consisted of two 38 cm long sections of irradiated ammonia cooled to 0.3°K and located in a 2.5T magnetic field produced by a superconducting coil [4]. The two sections were polarised in opposite directions and separated by a gap of about 20 cm, in such a way that the sign of the polarisation could be unambiguously determined from the position of the interaction point. Scattered muons were detected by the EMC forward spectrometer which had been upgraded in order to allow data taking at intensities as high as 4.10^7 muons per accelerator pulse (fig. 2). Large data samples were collected at 3 different beam energies with at least one reversal of the target polarisation during each data taking period. The numbers of accepted events and the imposed limits on the kinematic variables are listed in Table 1.

Table 1

E	100 GeV	120 GeV	200 GeV
Q^2min	1.5 GeV^2	2.0 GeV^2	3.0 GeV^2
ν min	10 GeV	10 GeV	20 GeV
$(y=\nu/E)_{max}$	0.85	0.85	0.85
θ min	1°	1°	1°
Nr. accepted events	182000	417000	605000

Kinematic cuts and statistics for different beam energies

The systematic reversal of the target polarisation cancels in first order the apparent asymmetry due to the different acceptances of the upstream and downstream parts of the target. The remaining effect due to the change of the ratio of the acceptances of the 2 parts before and after the reversal is small, when averaged over all data taking periods, and has been included in the systematic errors.

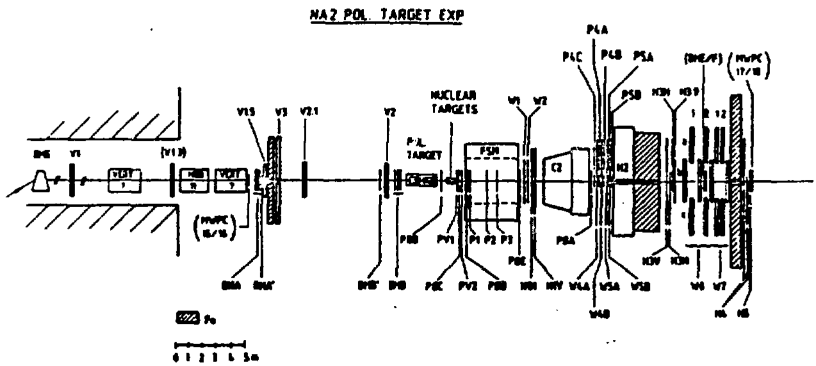

Figure 2

The EMC apparatus for the polarised target runs

The measured asymmetry Δ, defined as the average of the asymmetries before and after polarisation reversal, is related to the physical asymmetry A, defined in (5) by:

$$\Delta = p_T \, p_B \, f \, A \qquad (10)$$

when p_T and p_B are the target and beam polarisations and f is the fraction of events due to interactions on polarised protons in the ammonia target. This fraction is of the order of 3/17 since only the 3 free protons in the ammonia (NH_3) are polarised but also contains an x dependence due to the variation of the ratio $F_2^n(x)/F_2^p(x)$.

Since two independent structure functions G_1 and G_2 contribute to the cross section (3), the asymmetry A(x) also contains 2 terms:

$$A = D\,(A_1 + \eta\, A_2) \tag{11}$$

weighted by the kinematic factors

$$D = y(2-y)/(y^2+2(1-y)(1+R))$$

and (12)

$$\eta = (1-y)\sqrt{Q^2}/(Ey(1-y)/2)$$

where $R = \sigma_L/\sigma_T$.

The first term (A_1) represents the virtual photon-nucleon asymmetry

$$A_1 \doteq \frac{\sigma_{1/2} - \sigma_{3/2}}{\sigma_{1/2} + \sigma_{3/2}} = \frac{2x(1+R)}{F_2(x)} g_1(x) \tag{13}$$

where $\sigma_{1/2}$ ($\sigma_{3/2}$) is the photon-nucleon cross section for total spin 1/2(3/2). The second term (A_2) arises from the interference of transverse and longitudinal amplitudes and cannot be measured with the target configuration used in this experiment. It can however, be shown that $A_2 \leq \sqrt{R}$ [5] and, since η is small in the covered kinematic range, the second term of eqn. 11 can be neglected and included in the systematic errors.

Summing up the contributions due to the change of the ratio of acceptances with time, to the uncertainty in beam and target polarisation, to the uncertainty on the fraction f, to the effects of A_2 and of the use of different value of R, the uncertainty on the radiative corrections and the effects of electro-weak interference, we estimate the systematic errors to be less than 0.017 at low x and less than 0.065 at high x.

c) Results

The values of the asymmetry $A_1(x)$ measured in this experiment are shown in fig. 3 with those obtained previously in two SLAC-YALE experiments [6,7]. The results are consistent in the medium x region where the datasets overlap. The predictions of the Carlitz-Kaur model [8] agree with the data for $x \gtrsim 0.25$ but strongly overestimate the asymmetry at low x.

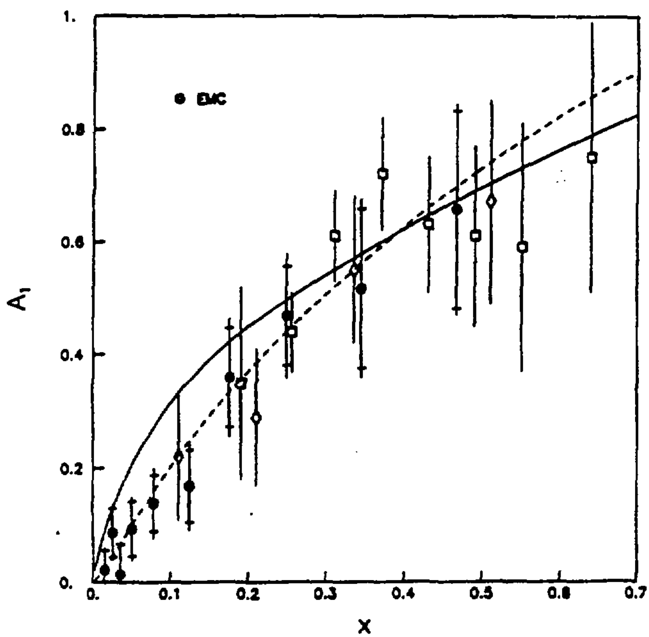

Figure 3

Spin asymmetries measured by EMC and by the experiments of ref. [6,7]. The dotted curve represents the prediction of ref. [8] and the dashed curve the parameterisation described in section 2.

The presentation of A_1 as a function of Q^2 for different intervals of x (fig. 4) shows that the present experiment considerably extends the kinematic range of the data. Within the errors we do not observe any evidence for scaling violations.

The values of $x\,g_1(x)$ corresponding to the asymmetries of fig. 3 are shown in fig. 5. For comparison with the sum rules we also show the values of the integral $\int_x^1 g_1(x')dx'$ as a function of the lower limit. Extrapolating to x = 0 with the parameterisation *represented by the dotted line* we obtain

$$\int_0^1 g_1(x)\,dx = 0.122 \pm 0.013 \text{ (stat.)} \pm 0.027 \text{ (syst.)} \quad (14)$$

for a mean Q^2 of 10.7 GeV^2. This value is compatible with a previous evaluation based on the data of ref. [6,7] with a much larger extrapolation to x = 0 (0.155 ± 0.050) but is significantly lower than the Ellis-Jaffe sum rule prediction [3] (0.185 ± 0.005 after the QCD correction).

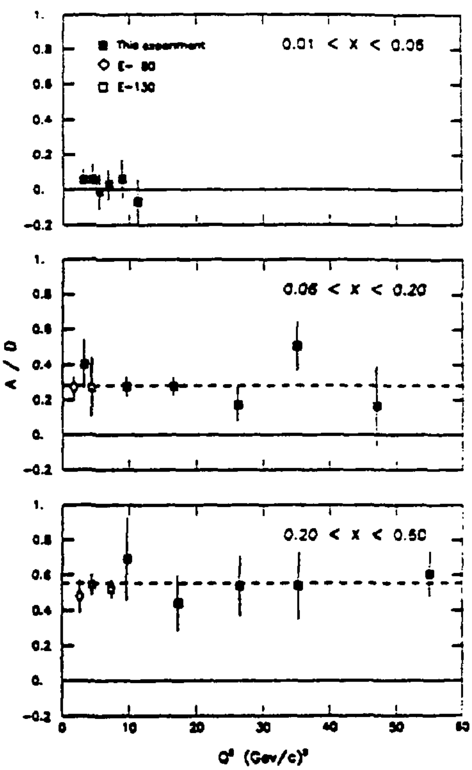

Figure 4

The spin asymmetry A_1 as a function of Q^2 for 3 different x intervals, for EMC data (■) and for those of ref. [6,7] (◇,□)

This discrepancy suggests that some assumptions used in the derivation of the sum rule predictions are not fulfilled. An interpretation in terms of a polarisation of the strange sea seems rather unlikely, taking into account the size and the sign of the effect. Another explanation recently presented by Jaffe [9] is based on the non-conservation of the U(1) axial current in QCD. It suggests that QCD could drastically modify the sum rule predictions and reduce the integral of $g_1^p(x)$ to values close to the present experimental result.

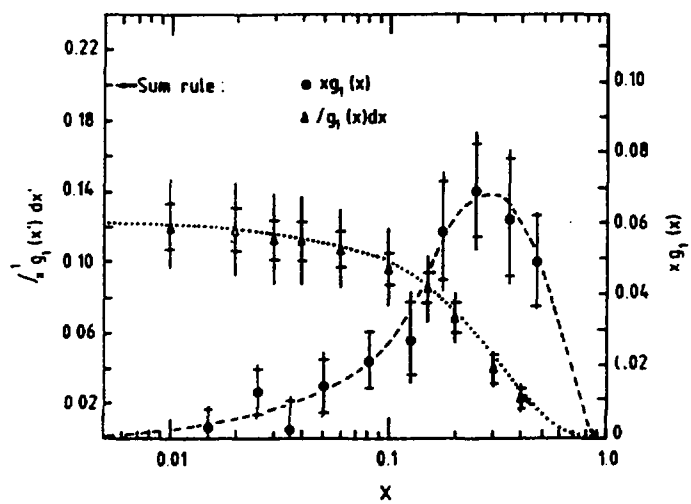

Figure 5

The values of $xg_1(x)$ and of $\int_x^1 g_1(x')dx'$ derived from the asymmetries of fig. 3.

In order to satisfy the Bjorken sum rule [2] with the measured value of $\int_0^1 g_1^p(x)dx$, the contribution from the neutron structure function ($\int_0^1 g_1^n(x)dx$) has to be negative and much larger in absolute value than previously expected (~ -0.08). Assuming this to be true we may calculate the net spin carried by a quark of flavour i

$$S_i = \frac{1}{2} \int_0^1 (q_i^+(x) - q_i^-(x))\, dx \tag{15}$$

by combining the results of (7) for the proton and the neutron if strange quarks do not contribute

$$\begin{aligned} S_u &= 0.334 \pm 0.024 \text{ (stat.)} \pm 0.049 \text{ (syst.)} \\ S_d &= -0.239 \pm 0.024 \text{ (stat.)} \pm 0.049 \text{ (syst.)} \quad . \end{aligned} \tag{16}$$

These results show that the total spin of the quarks (S_u+S_d) represents only a small fraction (~ 20%) of the nucleon spin and imply that the rest must be carried by gluons or be due to orbital angular momentum.

2. SPIN ASYMMETRIES IN HADRON PRODUCTION

Additional information on the u and d quark contributions to the inclusive asymmetry A_1 can be obtained from the asymmetries for positive and negative hadrons $A^{\pm}(x)$. If we define the asymmetry for a quark of flavour i by

$$A_i(x) = \frac{q_i^+(x) - q_i^-(x)}{q_i^+(x) + q_i^-(x)} \tag{17}$$

and consider all charged hadrons as pions, the hadron asymmetries can be written:

$$\begin{aligned} A^+(x) &= \frac{4A_u(x)u(x)+A_d(x)\zeta}{4u(x)+d(x)\zeta+5\bar{q}(x)(1+\zeta)} \\ A^-(x) &= \frac{4A_u(x)u(x)\zeta+A_d(x)d(x)}{4u(x)\zeta+d(x)+5\bar{q}(x)(1+\zeta)} \quad . \end{aligned} \tag{18}$$

In these formulas, ζ represents the ratio of the unfavoured to the favoured fragmentation functions for a fractional energy z above some threshold $z_\circ$:

$$\zeta(z_\circ) = \int_{z_\circ}^{1} D_u(z)dz / \int_{z_\circ}^{1} D_f(z)dz \quad . \tag{19}$$

For a large enough $z_\circ$, $A^+(A^-)$ will thus approach A_u (A_d).

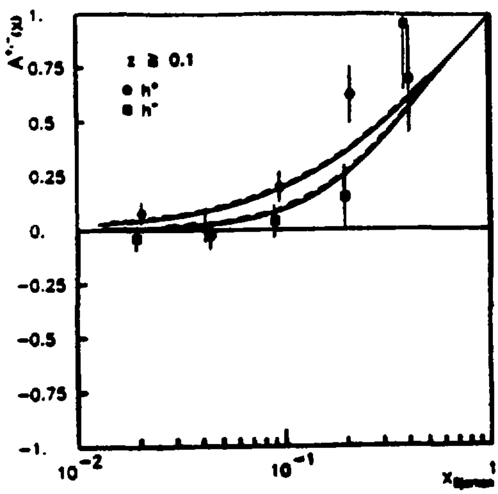

Figure 6

Spin asymmetries for positive (A^+) and negative (A^-) hadrons as a function of x. The curves are obtained with the parameterisation of A_u and A_d described in the text.

The values of A^+ and A^- obtained for z>0.1 are shown in fig. 6 for different intervals of x. Although the errors are rather large and do not allow a determination of A_u and A_d separately for each interval, it can be seen that the asymmetries for negative hadrons are smaller than those for positive hadrons. Using the full x range we obtain the averages

$$\langle A^{+} \rangle = 0.150 \pm 0.034 \text{ (stat.)}$$
$$\langle A^{-} \rangle = 0.037 \pm 0.037 \text{ (stat.)} \qquad (20)$$

for $\langle x \rangle = 0.1$.

It may be noted that the existing data on the muon and on the hadron asymmetries can be well reproduced by a simple phenomenological model in which the u and d quark asymmetries are parameterised as

$$A_u(x) = x^{\alpha}$$
$$A_d(x) = \frac{x-x_0}{1-x_0}\, x^{\beta} \quad . \qquad (21)$$

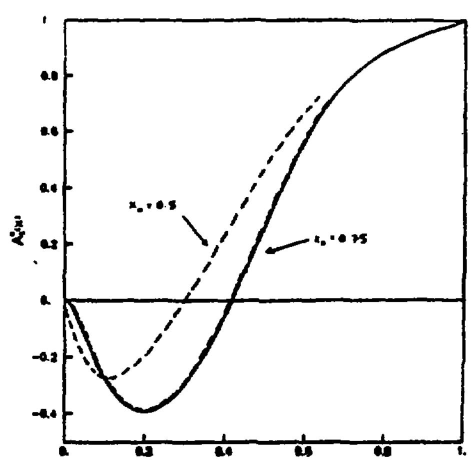

Figure 7

Values of $A_1^n(x)$ obtained from the parameterisation of A_u and A_d described in the text.

With the exponents α and β adjusted to fit the measured value of $\int_0^1 g_1^p(x)dx$ and to satisfy the Bjorken sum rule (α = 0.49, β = 0.14) and x_o arbitrarily set to 0.5, we obtain the curves shown in figs. 3 and 6. The spin asymmetry on neutrons A_1^n derived from this parameterisation has large negative values at low x and becomes positive around x=0.3. A different choice of x_o changes the shape of A_1^n but does not change its sign at low x (fig. 7). Our results thus imply that the spin asymmetry on neutrons must be significantly different from zero at least over a part of the x range. This feature should be investigated by future polarised target experiments.

3. DETERMINATION OF THE QCD COUPLING CONSTANT α_s FROM THE HADRON ENERGY FLOW

In this section we analyse the energy flow of the hadrons in the forward jet within the formalism proposed by Ochs and Stodosky [10]. The aim of this analysis is to evaluate the relative contributions of the various processes involving gluons in QCD (fig. 8b) with respect to the fundamental QPM diagram (fig. 8a).

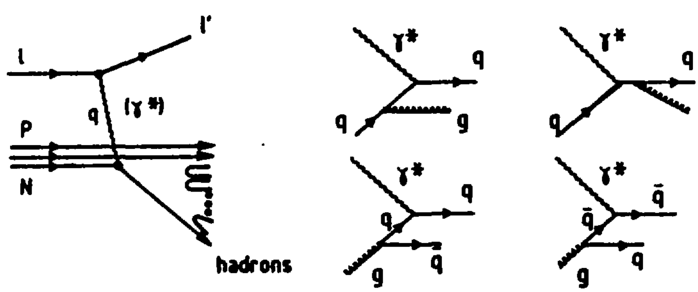

(a) (b)

Figure 8

The mechanism of deep inelastic μ-N scattering in the quark-parton model (a) and in first order QCD (b)

The energy flow will be presented as a function of

$$\lambda = x_F/p_T = P_{/\!/}/(\tfrac{W}{2}\,p_T) = (2\,\mathrm{cotg}\,\theta)/W \qquad (22)$$

where W is the total energy in the (γ^*N) rest frame, $P_{/\!/}$ and p_T are the momentum components of a given hadron parallel and perpendicular to the γ^* direction and θ the angle between the hadron and the virtual photon.

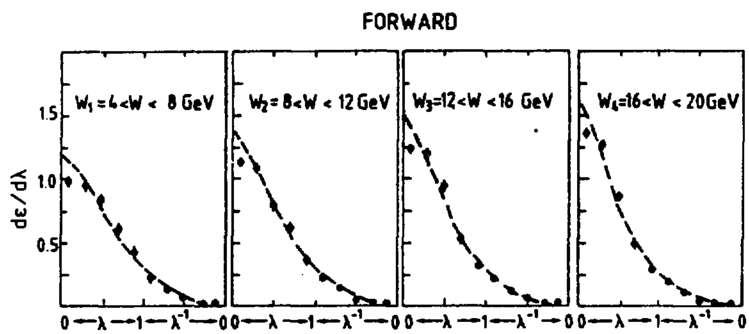

Figure 9

Differential energy flow in the forward hemisphere as a function of $\lambda = x_F/p_T$ for 4 intervals of the hadronic cms energy W. The curves are the fitted profile functions $\rho(\lambda) = M/(1+M^2\lambda^2)^{3/2}$.

Figure 9 shows the distribution of the reduced energy $\varepsilon = E_i/E_{jet}$, where E_{jet} is assumed to be the sum of the energies of all charged hadrons in the forward hemisphere, as a function of λ for 4 intervals of W. It has been noticed previously [11] that these distributions are consistent with scaling in the backward hemisphere. In the forward hemisphere they show a characteristic energy dependence which may be used to discriminate between various fragmentation models. The comparison of the $d\varepsilon/d\lambda$ distributions for the different W intervals clearly shows a shift to lower values of λ when W increases. To evaluate this effect we have fitted the profile function proposed in ref. [10]:

$$\frac{d\varepsilon}{d\lambda} = \frac{M}{(1+\lambda^2 M^2)^{3/2}} \tag{23}$$

excluding the low values of $\lambda(\lambda<0.2)$ where the distributions may be affected by overspill from the backward hemisphere.

The resulting values of the parameter M are shown in fig. 10 with the predictions of the Lund string model [12] and the independent jet model [13]. The latter fails to reproduce the W dependence of M, even with values of Λ as large as 1 GeV. On the other hand the Lund model fits the data quite well and the optimal value of Λ can be expressed in terms of α_s using the leading order QCD formula:

$$\alpha_s(Q^2) = \frac{12\pi}{(33-2n_f)\log(Q^2/\Lambda^2)} \tag{24}$$

For an average Q^2 of 20 GeV^2 and 4 quark flavours ($n_f=4$) we obtain:

$$\alpha_s = 0.29 \pm 0.01\ (\text{stat.}) \pm 0.02\ (\text{syst.}) \quad . \tag{25}$$

In this result, the quoted systematic error reflects only the uncertainty in the definition of the hadron sample. The result is derived in the frame of the Lund string model and no attempt was made to evaluate the uncertainty resulting from the choice of this particular fragmentation scheme.

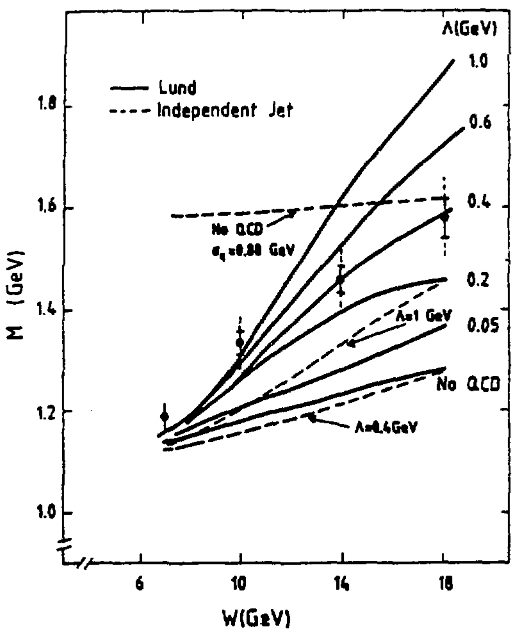

Figure 10

Fitted values of the parameter M in the energy profile distributions, with predictions from the Lund model and the independent jet model

4. BARYONS AND ANTIBARYONS IN QUARK FRAGMENTATION

Deep inelastic scattering can be further investigated by measuring the distribution of conserved quantum numbers among the final state hadrons. These distributions are expected to vary with the dominant flavour of the interacting constituent and provide more detailed tests of the fragmentation models. It has been shown previously that the total charge in the forward hemisphere is directly related to the charge of the struck quark [14]. A similar property has recently been observed for the strangeness, with an excess of (S = +1) over (S = -1) particles in the forward hemisphere for the kinematic regions where the interaction occurs preferentially on a u quark (x>0.05) [15]. A similar effect is also expected in relation with the baryon number conservation and has been observed in the NA9 experiment where charged particles could be identified by time-of-flight or by Cerenkov counters over a large momentum range [16].

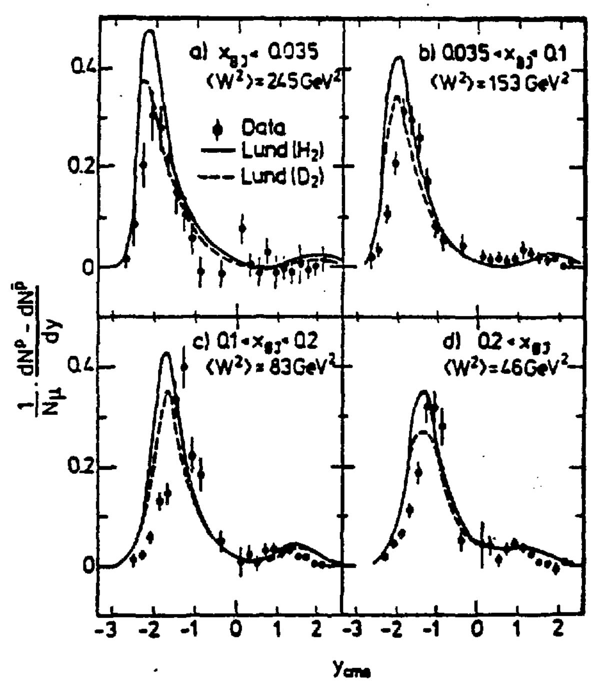

Figure 11

Rapidity distribution of the excess of protons on antiprotons in 4 intervals of x (μ-p and μ-D data at 280 GeV).

In fig. 11 we present the rapidity distribution dN/dy of the excess of protons over antiprotons in 4 intervals of x. Target remnants produce in all cases a large peak in the backward hemisphere. In the forward direction a small excess of protons is observed around y=1 for x>0.035. This effect can be explained by a preferential emission of the proton (i.e. the particle containing the interacting quark) in the forward direction when a (p-$\bar{p}$) pair is produced. The relation between forward protons and (p-$\bar{p}$) events is further illustrated by the peak in fig. 12 which presents the ratio of the proton rapidity distributions for events containing an antiproton and for all events.

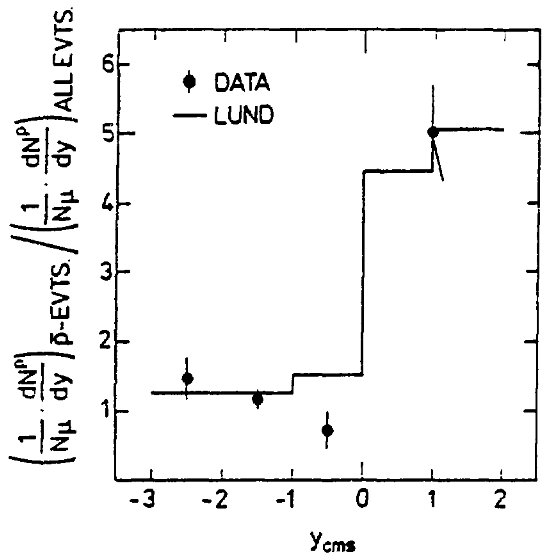

Figure 12

Ratio of the proton rapidity distribution obtained in events containing an antiproton to the proton rapidity distribution in all events

CONCLUSIONS

Spin asymmetries have been measured for the first time in high energy muon nucleon scattering. The obtained values of A_1^p are consistent in the overlap region at medium x with those measured previously in e-p experiments at much lower energy. At low x, the asymmetry is close to zero. This leads to a value of $\int_0^1 g_1^p(x)dx$ much lower than the one predicted by the Ellis-Jaffe sum rule (0.0122±0.013 ±0.027 vs. 0.185±0.005). If the Bjorken sum rule holds, this result implies that A_1^n must be negative at least over a part of the x range and larger (in absolute value) than expected.

The spin asymmetry is larger for positive than for negative hadrons suggesting that the d quark has a negative asymmetry in the low x region.

The hadron energy flow in the forward hemisphere is consistent with the Lund string model expectations with α_s=0.29±0.01±0.02 for an average Q^2 of 20 GeV^2 and 4 flavours.

The proton and antiproton rapidity distributions show that in $p\text{-}\bar{p}$ production the nature of the struck quark favours the production of leading protons.

ACKNOWLEDGEMENTS

I would like to thank the organisers of the symposium and my Polish colleagues for their hospitality. I am indebted to all my colleagues in the EMC and especially to V. Papavassiliou and L. Ropelewski for their help during the preparation of this talk.

REFERENCES

[1] V.W. Hughes and J. Kuti, Ann. Rev. Nucl. Part. Sci., 33 (1983) 611.
[2] J.D. Bjorken, Phys. Rev. 148 (1966) 1467.
[3] J. Ellis and R.L. Jaffe, Phys. Rev. D9 (1974) 1444.
[4] S.C. Brown et al., Proc. 4th Int. Workshop on Polarised Target Materials and Techniques, Bonn, p.103 ed. W. Meyer (1984).
[5] M.G. Doncel and E.de Rafael, Nuovo Cim. 4A (1971) 363.
[6] M.J. Alguard et al., Phys. Rev. Lett. 37 (1976) 1261; M.J. Alguard et al., Phys. Rev. Lett. 41 (1978) 80.
[7] G. Baum et al., Phys. Rev. Lett. 51 (1983) 1135.
[8] R. Carlitz and J. Kaur, Phys. Rev. Lett. 38 (1977) 673.
[9] R.L. Jaffe, Phys. Lett. 193B (1987) 101.
[10] W. Ochs and L. Stodolsky, Phys. Lett. 69B (1977) 225; H. Fesefeldt, W. Ochs. L. Stodolsky, Phys. Lett. 74B (1978) 389.
[11] P.B. Renton, Review of Hadron Production in Lepton Nucleon Scattering, Proc. of the IX Warsaw Symposium on Elementary Particle Physics.
[12] B. Andersson et al., Phys. Rep. 97 (1983) 31; G. Ingelman, The Lund Monte Carlo for Deep Inelastic Lepton Nucleon Scattering, LEPTO Version 4.2
[13] P. Hoyer et al., Nucl. Phys. B161 (1979) 349; A. Ali et al., Phys. Lett. 93B (1980) 155.
[14] J.P. Albanese et al., Phys. Lett. 144B (1984) 302.
[15] M. Arneodo et al., Zeits. Phys. C34 (1987) 283.
[16] J.P. Albanese et al., Nucl. Instr. and Meths. 212 (1983) 111.

THE NEW MUON EXPERIMENT AT CERN

Eva-Maria Kabuß

Max-Planck-Institut für Kernphysik, P.O. Box 103980, D-6900 Heidelberg 1, F.R. Germany

New Muon Collaboration

ABSTRACT

The extension of the muon programme at CERN by the NA37 collaboration will mainly study two aspects of deep inelastic muon-nucleus scattering. Firstly, a simultaneous high luminosity measurement of the hydrogen and deuterium structure functions will allow to determine the neutron structure function F_2^n, $F_2^p-F_2^n$ and F_2^n/F_2^p with high precision over a large Q^2 and x range. Secondly, detailed studies of the nuclear dependence of the structure function ratios F_2^A/F_2^D, of $R=\sigma_L/\sigma_T$ and the cross section for J/ψ production will provide a basis for understanding the EMC effect.

MOTIVATION

The proton structure function F_2^p has been measured with great precision by several experiments and QCD analysis performed for the combined data [1,2]. Unfortunately the existing deuterium data are much more limited in the Q^2 range [2,3] so that no unique determination of the neutron structure functions F_2^n is possible. In addition F_2^n is distorted by the systematic errors of both the hydrogen and the deuterium data and the relative normalisation uncertainties. It is necessary to clarify this situation by a simultaneous measurement on hydrogen and deuterium over a large range in x ($0.005<x<0.75$) and Q^2($1<Q^2<200$ GeV^2/c^2) to extract the Q^2 dependence of F_2^n, $F_2^p-F_2^n$ and F_2^n/F_2^p [4].

This will allow us study a lot of problems:

1. $F_2^p-F_2^n$ is a pure non-singlet structure function, if the seaquark distribution of neutrons and protons are identical. A QCD analysis over a large Q^2 and x range will therefore result in a determination of the QCD scale parameter Λ independent of the shape of the gluon distribution and heavy quark thresholds.

2. The Gottfried summ rule

$$J = \int_0^1 \frac{1}{x}(F_2^p-F_2^n)dx = \frac{1}{3}$$

essentially tests the flavour symmetry of the sea distribution. The large error on the present value of $0.235^{+0.110}_{-0.099}$ is mainly due to the necessary extrapolation to low x.

3. At x>0.35 the ratio F_2^n/F_2^p allows to determine the ratios of the down to up quark distributions. The values at very low x can provide a test of the assumption of a flavour symmetric sea in proton and neutron.

In addition a possible difference between J/ψ production on hydrogen and deuterium can be investigated.

Another result of deep inelastic muon nucleus scattering was the discovery of the EMC effect, that the structure functions obtained from free and bound nucleons are different [5]. It was shown for the first time that the nuclear medium perturbs the quark and gluon structure of the nucleon. This has given rise to a lot of experimental and theoretical activity but the current experimental information is insufficient to understand the origin of the EMC effect [6]. A high statistic experiment with small systematic errors covering a large x range can help to solve the following problems.

1. The A dependence at medium $x(x\sim0.6)$ is well established to be proportional to log A [7] but the Q^2 dependence is not known yet. A measurement can help to decide whether the EMC effect at medium x is governed by perturbative QCD which would predict $d(F_2^A/F_2^D)/d\ln Q^2\sim5*10^{-3}$.

2. The A dependence at low x $(x\sim0.15)$ seems to be weak. But discrepancies exist between different experiments so that it is not clear yet whether there is a Q^2 dependence in this region [8]. The A and Q^2 dependence has not yet been established especially in the shadowing region at very low x and Q^2 .

3. There have been some speculations about an A dependence of $R=\sigma_L/\sigma_T$ which is needed to extract F_2 from the measured cross sections. However, a recent measurement at low Q^2 finds no evidence [9] for a difference between iron and deuterium larger than 2-3%.

4. For x>1 only low Q^2 results on $F_2^{A_1}/F_2^{A_2}$ exist [10].

5. The study of J/ψ production allows to investigate a possible A dependence of the gluon distribution.

In addition the measurement of hadron distributions from nuclear targets can give further information on the possible source of the EMC effect.

THE EXPERIMENT

The NA37 collaboration (Amsterdam-Bielefeld-Freiburg-Heidelberg-Indiana-Mainz-Mons-Neuchâtel-Santa Cruz-Sin-Torino-Uppsala-Warsaw-Wuppertal) uses the EMC spectrometer at the CERN M2 muon beam [11]. Several changes and upgrades have been made especially to decrease the systematic errors.

The spectrometer (fig. 1) consists of a beam spectrometer (BMS, BHA, BHB), the target platform and the forward spectrometer magnet (FSM) surrounded by wire chambers to measure the tracks leaving the target. Some wire planes have been added to improve the track measurement at low angles.

The trigger is split into two parts, a low and a high angle trigger. The efficiency of the large angle trigger (H_1, H_3, H_4), which was previously used by the EMC, was improved considerably. The small angle trigger using the hodoscopes H_1', H_3', H_4' has been added to cover a large Q^2 and x range in a single experiment.

To achieve low systematic errors on ratios it is crucial to measure pairs of nuclei simultaneously. A special target platform was designed which houses complementary target setups of 2 or 3 different nuclei. It allows frequent changes of the target position so that an equal acceptance is ensured for all targets.

To reduce the error on the beam momentum from ~0.3% to <0.1% a second beam spectrometer of about 35m length using a high precision magnet (MNP26) has been added.

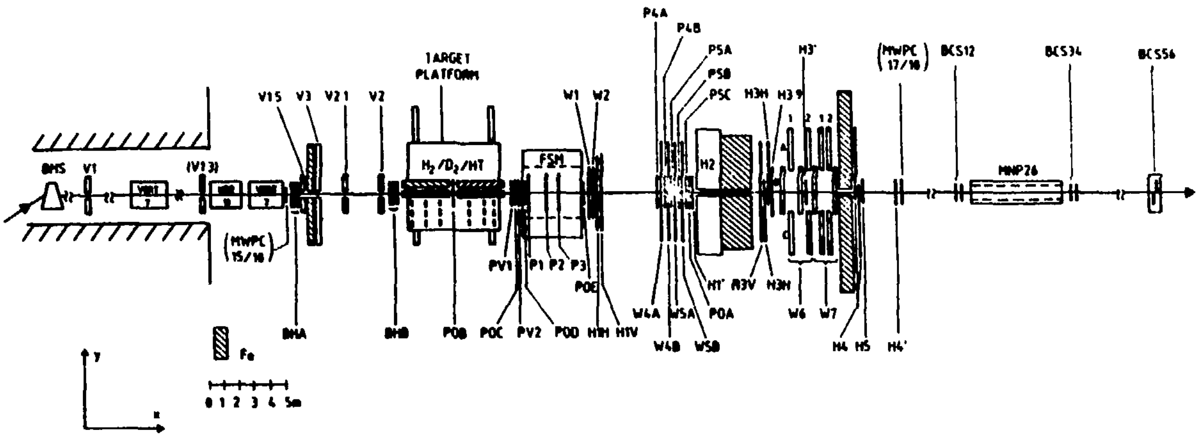

V : Vetocounter
BH : Beam hodoscope
H : Hodoscope
H2 : Calorimeter
P : Proportional chamber
W : Drift chamber
BCS : Beam calibration proportional chamber
BMS : Beam momentum station
FSM : Forward spectrometer magnet

FIG. 1 The NA37 Spectrometer

The experimental programme splits into three parts:

1. The hydrogen-deuterium measurement uses liquid targets of 3m length. With 10^{13} incoming muons and three beam energies (90, 200, 280 GeV) it should be possible to achieve an error on the neutron structure function of 1% at small x and about 10% at the largest x.

2. The 'thin target' measurement uses pairs or triples of targets of about 100 gr/cm^2. It is planned to measure with D_2, He, Li, C, Si, Ca, Nb, Ho to study ratios at small x and hadron distributions.

3. To study the A and Q^2 dependence at large x, $R=\sigma_L/\sigma_T$ and the J/ψ production it is necessary to use a 'thick active target' (C, Pb) of about 600 gr/cm^2.

Data taking started in 1986 covering the first two items and is continuing this year. The thick target measurement is scheduled for 1988.

REFERENCES

1) EMC, J.J. Aubert et al., Nucl. Phys. B259, 189 (1985).
2) For example, A. Bodek et al., Phys. Rev. D20, 1471 (1979), M.D. Mestayer et al., Phys. Rev. D27, 285 (1983).
3) EMC, J.J. Aubert et al., CERN preprint, CERN-EP/87-66.
4) NMC, Proposal to the SPSC, CERN/SPSC 85/18.
5) EMC, J.J. Aubert et al., Phys. Lett. 123B, 275 (1983).
6) D.v. Harrach, Invited talk at XI Int. Conf. on Particles and Nuclei, Kyoto (1987).
7) R.G. Arnold et al., Phys. Rev. Lett. 52, 727 (1984).
8) BCDMS, A.C. Benvenuti et al., CERN preprint, CERN-EP/87-13.
9) A. Bodek, Talk at XXII Recontres des Moriond, Les Arcs (1987).
10) D. Day, Talk at XI Int. Conf. on Particles and Nuclei, Kyoto (1987).
11) EMC, O.C. Allkofer et al., Nucl. Instr. Meth. 179, 445 (1981).

Average Hadron Multiplicity in Deep Inelastic Scattering

Wojciech Dębski
Institute for Theoretical Physics
Polish Academy of Sciences, Warsaw, Poland

Abstract

The problem of the x dependence of the average charged hadron multiplicity in the deep inelastic lepton-hadron scattering is investigated in the first order of perturbative QCD.

The hadron multiplicity is known to be one of the simplest characteristic of the final hadron state. However even such a simple quantity can give us useful information about the final hadron state formation especially when a few mass scales are involved in a process under consideration.

In this paper we consider the total charged hadron multiplicity $\langle N_{DIS}\rangle$ in the deep inelastic μ-p scattering (DIS). The kinematics of the process is shown in fig.1 and the following standard variables are introduced :

$Q^2 = -q^2 = -(l-l')^2$ virtuality of the exchanged photon

$x = \frac{-q^2}{2pq}$

$W^2 = (p + q)^2 = \frac{1-x}{x} \cdot Q^2$ center-of-mass hadron energy.

The problem of the multiplicity of hadrons produced in DIS has already been investigated by Bassetto [1] and independently by Kisielev and Petrov [2,3]. They were able to sum up infinite series of Feynman diagrams in the leading log approximation (LLA) and using the soft hadronisation hypothesis* [4,5] have obtained asymptotical prediction for very large Q^2 and x far from kinematical boundaries. They claim that the growth of the hadron multiplicity with Q^2 in DIS is asymptotically the same as in $e^+- e^-$ annihilation. Recently the EMC collaboration has published [6] a new data on the average multiplicity of the charged hadrons produced in the deep inelastic μ-p scattering. As can be seen from fig.2 the multiplicity depends not only on W^2 but also on x (or Q^2) at fixed W^2. Unfortunately, the LLA results cannot be simply compared with experimental data because in the LLA :

* According to this hypothesis an average hadron multiplicity is proportional to the parton one.

1. Q^2 is assumed to be very large but experimental data has been obtained for Q^2 less than 200 GeV^2, what certainly is not an asymptotical value.
2. x dependence in the relation between W^2 and Q^2 is dropped away as a non-leading effect so that $W^2 \underset{LLA}{\approx} Q^2$.

Therefore, a more careful analysis of the Q^2 and W^2 dependence of the multiplicity is needed. In this paper we would like to present the results obtained in the first order of perturbative QCD. We feel that this approximation is justified, because the EMC data are certainly in the nonasymptotical region. The full analysis is in progress and will be presented elsewhere.

On very simple physical grounds one can expect the Q^2 and W^2 dependence of the multiplicity. Since total available phase space for the hadron production is determined by the hadron energy W^2 involved in the process, therefore it is natural to expect an increase of the multiplicity together with increasing W^2. An increase of N_{DIS} with Q^2 for fixed W^2 is also expected in the framework of the QCD improved parton model since the virtual photon with virtuality q^2 forces the incoming quark to have virtuality up to q^2 which can be attained only by emission of other partons.

In the first order of the perturbation theory the total gluon multiplicity is simply connected with the emission of one gluon from the struck quark and can be described by the following formula:

$$N_{QCD} = \frac{\sigma^1(x,\ Q^2,\ Q_0^2)}{\sigma^0(x,Q_0^2)} \tag{1}$$

where :

$$\sigma^0 = \frac{1}{x} F_2(x,Q_0^2) \tag{2}$$

is the scaling part of the nucleon structure function taken from the experimental data [7], and

$$\sigma^1 = \int_{xd}^{1} \frac{dz}{z} \frac{1}{z} F_2(z, Q_0^2) \frac{z}{x} H_{QCD}\left(\frac{x}{z}, Q^2, Q_0^2\right) \tag{3}$$

is the cross section for the production of the gluon with the off-shell mass Q_0^2. The scale Q_0^2 has to be introduced because of the infr-red (IR) sensitivity of the gluon multiplicity and provides an IR cut-off: $d = 1 + Q_0^2/Q^2$.

The perturbative part of σ^1 namely H_{QCD}, is given by the amplitude for one gluon production :

$H_{QCD} \propto$

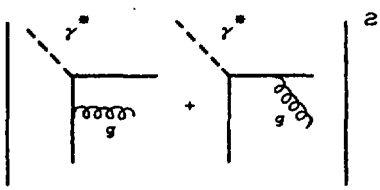

and reads

$$\frac{1}{x} H_{QCD} = \frac{\alpha \cdot C_F}{2\pi}\left[\frac{1+x}{1-x} \log\left(\frac{k_+}{k_-}\right) - \frac{2x}{1-x} \frac{k_+ - k_-}{q^2} - 6x^2 \frac{k_- - k_+}{q^2} \right.$$
$$\left. + \frac{1}{2(1-x)} \cdot \left[1 + \frac{x}{1-x} \frac{Q_0^2}{q^2} \right]^2 + xQ_0^2\left(\frac{1}{k_-} - \frac{1}{k_+} \right) + 3x^3 \frac{k_-^2 - k_+^2}{q^4} \right] \tag{4}$$

where

$$k_- = \frac{-1}{1-x} Q_0^2$$

$$k_+ = Q_0^2 + \frac{1}{x} q^2$$

For the nucleon structure function F_2 we have taken the parametrisation given by the EMC collaboration [7] :

$$\frac{1}{x} F_2 = 4.52\, x^{-0.41}(1-x)^{3.24} + 0.85\, x^{-1}(1-x)^{7.31} . \qquad (5)$$

The QCD formula (1) cannot be directly compared with the experimental data. One has to specify a phenomenological model for nonperturbative fragmentation of gluons and quarks into hadrons. Below we assume that each gluon (treated as a massive cluster) produces on average a number of hadrons, say A. Therefore for the measured multiplicity we adopt the following formula :

$$N_{DIS} = A * N_{QCD} + \tilde{N}, \qquad (6)$$

where $\tilde{N}$ represents the contribution from remaining partons (diquark, struck quark, etc.). The $\tilde{N}$ is parametrised in the following form :

$$\tilde{N} = C + B \cdot \log \frac{W^2}{1 \mathrm{GeV}^2} \qquad (7)$$

assuming that nonperturbative effects give rise to $\log(W^2)$ dependence. Such a parametrisation should not be surprising since $\tilde{N}$ contains the contribution from the struck quark which certainly may introduce the W^2 dependence. It is also well known that for very low energy, where perturbative effects are expected to be negligible, the multiplicity grows like log of the available energy W^2 [8]. On the other hand the above functional dependence of $\tilde{N}$ is nonleading because in the first order of the strong coupling constant the leading term of N_{QCD} behaves like $\log^2(W^2)$.

The parameters A, B and C have been set by fitting N_{DIS} to the data and read (for $Q_0^2 = 1\ \mathrm{GeV}^2$)

A = 1.11

B = 0.93 for $\chi^2/\mathrm{dof} = 43/23$

C = 1.14

The result of the fit is shown in fig.2. The visible variation of the multiplicity with x for fixed W^2 comes in this model only from the perturbative effects and shows the same tendency as is seen in data. Also quite good agreement with the data has been obtained. For comparison the dashed lines represent the results of the Lund model [6]. The results presented in fig.2 have been obtained for $Q_o^2 = 1\ GeV^2$. In fact the parameters A, B and C are Q_o^2 dependent and their dependence is depicted in fig.3. The strong Q_o^2 dependence of A is easily understood : the heavier off-shell gluon can on average produce more hadrons. In the model Q_o^2 is introduced by hand to separate perturbative and nonpertubative part of the gluon cascade, so that the cancellation of Q_o^2 dependence between A and N_{QCD} is expected (physical quantities should be Q_o^2 independent). The stability of B and C as functions of Q_o^2 indicates that such a cancellation really takes place.

Concluding, we have shown that the first order QCD calculation with the proposed phenomenological model of the hadronisation can explain the observed x dependence of the charged hadron multiplicity

Acknowledgement

I would like to express my appreciation and gratitude to prof. S. Pokorski and to dr. J. Kalinowski for many stimulating discussions and help in preparation of this paper and also to prof. A. Bassetto for illuminating discussions during the conference.

References

1. A. Bassetto, Nucl. Phys. B202, 493 (1982)
2. A. V. Kiselev, V. A. Petrov, Sov. J. Nucl. Phys. 38, 1304 (1983)
3. G. Sh. Dzhaparidze, A. V. Kiselev, A. Petrov Sov. J. Nucl. Phys. 35, 927 (1982)

   A. V. Kiselev, V. A. Petrov, O. P. Yushchenko, CERN preprint CERN-TH-4684/87
4. A. Bassetto, M. Ciafaloni, G. Marchesini, Phys. Rep. 100, 201 (1983)
5. Ya. I. Azimov, Yu. L. Dokshitzer, V. A. Khoze, S. I. Troyan, Z. Phys. C27, 65 (1985)
6. EMC, M. Arneodo at al. Phys. Lett. 165B, 22 (1985)
7. EMC, J. J. Aubert et al. Nucl. Phys. B272, 158 (1986)
8. S. Berlag at al, Z. Phys. C11, 283 (1982).

Figure Captions

1. $e\mu$ scattering in the one-photon approximation.
2. Average charged hadron multiplicity as a function of x for fixed W^2. Data are taken from the EMC collaboration [6]. The solid lines represent the predictions of the proposed model. Dashed lines – the predictions of the Lund model (taken from [6]).
3. Q_0^2 dependence of the parameters of the model.

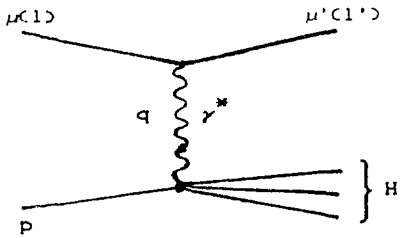

Fig. 1

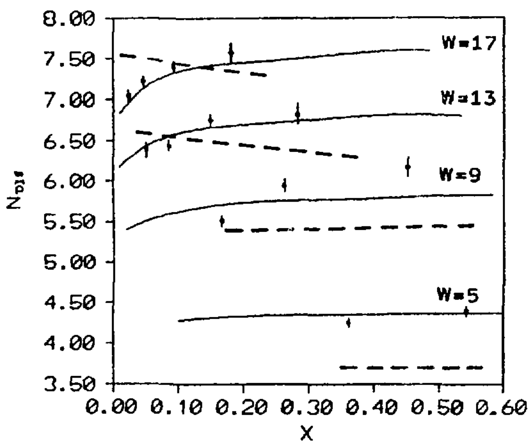

Fig. 2

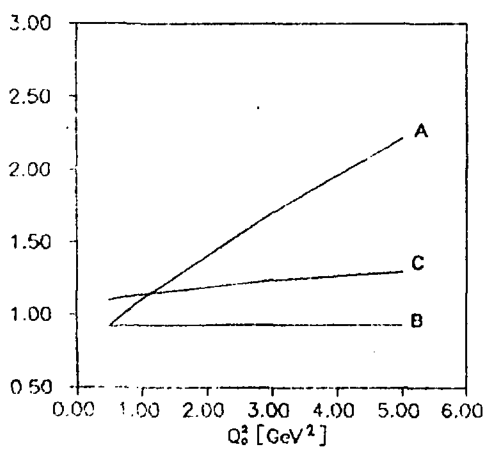

Fig. 3

PION CORRELATOR AS CHRONOMETER, SPEEDOMETER AND THERMOMETER FOR HADRON MATTER

Yu.M.Sinyukov
Institute for Theoretical Physics, Kiev, USSR

A method which make it possible to find out the hydrodynamical motion of hadron matter is proposed. The method is based on the analysis of Bose-Einstein pion correlations. It makes it possible to measure the time, the expansion rate and the freeze-out temperature for the matter produced in high-energy hadronic and nuclear collisions.

1. In 1960, the connection between the Bose-Einstein correlations of pions and the size and shape of a pion-emitting region was established [1]. The probability of a joint registration of two identical pions with momenta $\vec{p}_1$ and $\vec{p}_2$ which were localized initially at the points $\vec{x}_1$ and $\vec{x}_2$ looks like

$$W_{x_1 x_2}(p_1, p_2) \sim |\Psi_{x_1 x_2}(p_1, p_2)|^2 \sim 1 + \cos[(\vec{p}_1 - \vec{p}_2)\cdot(\vec{x}_1 - \vec{x}_2)] \tag{1}$$

Due to the wave function symmetrization the expression (1) contains the interference term (correlator) depending on the distance between the pion sources. The first zero (width) of the correlator which is considered as a function of the momentum difference $\Delta\vec{p} = \vec{p}_1 - \vec{p}_2$ is inversely proportional to the emission region demension a along a direction parallel to $\Delta\vec{p}$. The similar effect for photons has been first used in the interferometric stellar telescope by Hanbury Brown and Twiss [2]. The method interferometric telescope has been later transformed into the interferometric microscope method of measuring excited nuclei and clusters size [3].

If noncoherent radiation sources of bosons are independently distributed in the region D with the density $\rho(\vec{x})$, the probability of joint registration of two identical particles with momenta $\vec{p}_1$ and $\vec{p}_2$ takes the following form

$$W_D(p_1, p_2) \sim \int_D d^3x_1 d^3x_2\, \rho(x_1)\rho(x_2)\left[1 + \cos[(\vec{p}_1 - \vec{p}_2)\cdot(\vec{x}_1 - \vec{x}_2)]\right] \tag{2}$$

The density $\rho(x)$ is determined by the type of an emitting system.

If the rest spherical claster of the radius r decays, the correlation term in (2) looks like [1]

$$W(P_1,P_2) \sim 1+\left[\frac{3j_1(|\vec{P}_1-\vec{P}_2|r)}{|\vec{P}_1-\vec{P}_2|r}\right]^2 \qquad (3)$$

where $j_1(x)$ is spherical Bessel function. The first zero of $R(|\vec{p}_1-\vec{p}_2|)$ determines the claster's size $r = 4{,}49/|\Delta\vec{p}|_0$.

If the prolate-shape rest system radiates, the correlator is approximated by the 3-dementional Gaussian form [4] . Its widths determine the longitudinal a and the transversal r effective sizes of emitting object [4] :

$$R(\vec{\Delta p}) = exp[-r_\perp^2(\Delta p_\perp)^2]\,exp[-a(\Delta p_\parallel)^2] \qquad (4)$$

At the present time the interferometric analysis of a dimention and shape of an emission region is based on models of this type. The common property of the models (3), (4) is that the R(Q,P)-correlator in momentum space depends only on the momentum difference $p_1^{\parallel}-p_2^{\parallel}= 2Q$ along the direction of interest, but not on the momentum sum $p_1^{\parallel}+p_2^{\parallel}= 2P$:

$$R_{rest}(Q,\ P) \neq f(P), \quad Q_0(P) = \text{constant} \qquad (5)$$

In this paper we analyse the interference picture that would be found out under the pion interferometric"microscope" in the systems with an internal relative motion of radiation sources. In other words,has one get any possibilities to reveal the hydrodynamical motion of a hadron matter that is predicted for high-energy hadronic and nuclear collisions [5] ?

2. In our paper [6,7] have been demonstrated in what manner the pion interferometry theory can be generalize for the hydrodynamical theory of multiparticle production.

First at all the description based on the two-particle quantum mechanical wave function must be replace by the quantum- field description taken into account the multipionic final states. So the probabilities such as (1),(2) is replaced by the differential inclusive cross-section

$$\pi^- : W(p_1) \longrightarrow \sigma_T^{-1}\left(d\sigma^3_{inc}/d^3p_1\right) \equiv n(\vec{p}_1) \tag{6}$$

$$\pi^-\pi^- : W(p_1,p_2) \longrightarrow \sigma_T^{-1}\left(d\sigma^6_{inc}/d^3p_1 d^3p_2\right) \equiv n(\vec{p}_1)n(\vec{p}_2)\left[1+R(p_1,p_2)\right]$$

where $R(p_1,p_2)$ is the correlator generated by an interference of identity pions. Secondary, we must take into account that in the hydrodynamical approach the pion emission occurs from the spacelike hypersurface Σ_c , where a hadronic fluid achieves the freeze-out temperature T_c and decays into secondary particles. In this picture the fluid elements can be considered as radiation sources. The sources generally have not identical spectra in its own rest system [10], moreover they move with different velocities $u^\mu(x)$ and radiate in different times $t = t_0(x)$. The radiation duration time Δt (the decay time of a fluid element) is negligible [8] .The radiation of a pion field from a hypersurface Σ_c have been considered on the base of the relativistically-invariant statistical method developed in [9] . As a result, the two-particle correlator of identical pions have the form [6]

$$4p_1^0p_2^0 n(\vec{p}_1)n(\vec{p}_2)R(p_1,p_2) = \iint_{\Sigma_c} d\sigma_\mu(x_1)d\sigma_\nu(x_2)(p_1^\mu+p_2^\mu)(p_1^\nu+p_2^\nu)\times$$
$$f\left(\frac{p_1u(x_1)}{T_c}\right)f\left(\frac{p_2u(x_2)}{T_c}\right)\cos(p_1-p_2)(x_1-x_2) \tag{7}$$

The expression (6) now differs from (2) by substitutions: $d^3x \to d\sigma_\mu$, $\rho(x) \to f(pu(x))$, and by the presence of the relativistic kinematic factor before cosine. The thermal factor $f=(2\pi)^3(\exp(pu/T_c)-1)^{-1}$ in (7) have the maximum value at the point x_0 where the hydrodynamical velocity coincides with the velocity of the pion registrated:

$$\mathrm{Max}\, f(pu(x_0)) \text{ at } \vec{v}_{hydr}(x_0) \equiv \frac{\vec{u}(x_0)}{u^0(x_0)} = \vec{v}_\pi = \frac{\vec{p}}{p^0}$$

The presence of a 4-velocity gradient in (7) leads to an effective cut off the integration region because of the heat factor and cosine. So the saddle-point method can be use.

We go over to rapidity variables of secondary pions

$$p_i^{0} = m_{i\perp}\, ch\,\theta_i\,,\; p_i^{\parallel} = m_\perp\, ch\,\theta_i\,,\; m_\perp^2 = m_\pi^2 + \vec{p}_\perp^{\,2}\,;\; Q = \frac{p_1^{\parallel} - p_2^{\parallel}}{2}$$

$$p = \frac{p_1^{\parallel} + p_2^{\parallel}}{2}\,;\; \alpha = \frac{\theta_1 - \theta_2}{2} \approx \frac{Q}{\sqrt{p^2 + m_\perp^2}}\,,\; \theta = \frac{\theta_1 + \theta_2}{2} \approx arch\frac{p}{m_\perp}\,,\; (\alpha \ll 1) \qquad (8)$$

Here $p_i^{\parallel}$ is the momentum projection on the collision axis, $\vec{p}_{i\perp}$ are the transversal components. One-particle rapidity distribution in hydrodynamical theory has the form in central rapidity region

$$\frac{dN}{d\theta} = H(\theta) = \tau(\theta) S_\perp N_0\left(\frac{T_c}{m_\pi}\right);\; S_\perp = \pi r_\perp^2,\; \tau(\theta) = \left(\frac{du^{\parallel}}{dx}\right)^{-1} \qquad (9)$$

where $N_0 = (gT_c^3/2\pi^2)F(m/T_c)$ [8] is the number pion density at the final stage, $g=3$ for the pion triplet, $s_\perp$ is transversal area of a hydrodynamical tube at the final stage, $\frac{du^{\parallel}}{dx}$ is the gradient of 4-velocity longitudinal component of the fluid element, which moves with rapidity θ.

If we limit ourselves to the correlation measurements in the region $th^2\alpha \ll 1$ and neglect the terms $\sim th^4\alpha$ in the pion correlator, the hydrodynamical correlator in a central rapidity region for pions with equal transversal masses $m_{1\perp} = m_{2\perp}$ ($|\vec{p}_{1\perp}| = |\vec{p}_{2\perp}|$) has the form:

$$R(\alpha,\theta) = \lambda\, exp\left[-4m_\perp T_c\, \tau^2(\theta)\, th^2\alpha\right] cos\left[(4m_\perp + 6T_c)\,\tau(\theta)\, th^2\alpha\right] \qquad (10)$$

The factor $\lambda = 1$ at $\vec{p}_{1\perp} = \vec{p}_{2\perp}$. The factor $\lambda < 1$ in the general case when the directions of the momenta $\vec{p}_{1\perp}$ and $\vec{p}_{2\perp}$ are not fixed to be exactly parallel, and when we take into account that the interference is not complete for various reason. As distinct from the standard model [1 - 4], where the relative motion of sources is absent, dimension of a system is not present in expression (10). If one determines it formally according to the usual interferometric method via the correlator width Q_o (connected with rapidity width α_o according to (?): $a_{eff} \sim 1/Q_o$, there are then two effective lengths depending by the hydrodynamical regime. If we deal with the moderate velocity gradients of a hadronic fluid, $\frac{\partial u''}{\partial x} = \frac{1}{\tau} \ll T_c$, the effective length $a_{eff} = a_T = \tau\sqrt{\frac{T_c}{m_\perp}}$ is the longitudinal size of a fluid element forming the one-particle spectrum density at the points $p_1, p_2 \approx P/2$ [7]. In this case, the correlator behaviour is oscillatory, the velocity gradient is large, $\frac{\partial u''}{\partial x} > T_c$, and the effective length $a_{eff} = a_H = \sqrt{\frac{\tau}{m_\perp}}$ is the distance between the fluid elements which contribute to the one-particle spectrum densities at the points p_1 and p_2. The distance a_H exceedes the size a_T of the elements themselves: $a_H > a_T$. The typical regimes of the correlator $R(Q,P)$ behavior for the Landau-model [8] and the scaling-model [5,11,12] in $\bar{p}p$-collisions ($T_c \approx m_\pi$, $r_\perp \approx 1/m_\pi$) are plotted in Fig.1 for $P=0$. The factor $\lambda = 1$. The effective demensions depending upon hydrodynamical velocity gradient and the heat broadening of the hydrodynamical spectrum are of the order $a_{eff} = 1 \div 5$ fm, while the whole lengths of decaying system are within $15 \div 20$ fm. So the energy density $\mathcal{E}$ culculated by the formula $\mathcal{E} = E/s_\perp a_{eff}$ would be overestimation if the system possessing a developed hydrodynamical motion is mistaken for a system without internal motion.

3. We perform the qualitative experimental test enabling us to find out what variant of matter evolution takes place in high energy hadronic or nuclear collisions.

a). The formation of an intermediate massive cluster (fireball): the absence of a developed hydrodynamical motion.

At the present time the interferometric analysis of the demensions and shape of an emission region is based on models just this type (see Eqs. (3);(4)). The common property of the models expressed by Eq. (5), i.e. the $R(Q,P)$-correlator in momentum space depends only on the momentum difference 2Q along the direction of interest, but not on the sum 2P . The width of the same correlator $R(\alpha, \theta)$ expressed in the rapidity variables decreases according to Eq. (8) when the rapidity sum 2θ increases (see Fig.2).

b). The emergence of a global hydrodynamical regime for the matter evolution in the events with high multiplicity fluctuations of $p\bar{p}$- collisions and ultra-relativistic heavy ion collisions.

In accordance with the basic results of the hydrodynamical approach [5,8,11,12] , the function $\mathcal{T}(\theta)$ connected with one-particle rapidity spectrum via Eq.(7) is a constant in the scaling-model or slowly decreases as in the Landau- model when the $|\theta|$ increases (in c.m.s.). If the plateau in the central region of the rapidity destribution is observed, the width α_0 of the hydrodynamical correlator $R(\alpha, \theta)$ in the rapidity variables does not change when the detected-particles rapidity sum 2θ increases in c.m.s. (see Fig.2). The same correlator $R(Q,P)$ in momentum variables undergoes a broadening with increasing momentum sum 2P, due to (8) (see Fig.3)

$$Q_0(P \neq 0) = Q_0(P=0)\sqrt{1 + P^2/m_\perp^2} \tag{11}$$

This gives rise to the initation of decreasing inthe sources size $r_{eff} \sim 1/Q_0(P)$ according to (11), when the momentum sum increases. Thus the rapidity difference is a natural variable for hydrodynamical correlators, and the momentum difference is natural variable for the interference the radiation from a rest media. If the rapidity plateau is absent (the Landau-model leads to a Gaussian-type falling of a rapidity distribution), the hydrodynamical correlator gains a broadening additional to (11) (see Fig.2,3). We also note that the effective hydrodynamical length has specific dependence on the transversal mass of detecting particles, $a_{eff} \sim 1/\sqrt{m_\perp}$, for all hydrodynamical models.

c). The break-up of the hot quark-gluon matter into drops because of large density fluctuations at the stage of phase qg $\rightarrow$ h transition [11].

If the global hydrodynamical regime break down and a fluid decays into drops, the typical rapidity distance between drops is unity [11]. As a result, the contribution into the correlator comes from the radiation of a single drop only (the typical rapidity width α_o of the correlator $\alpha_o \ll 1$). Owing to homogeneity in the rapidity distribution of drops [11], the correlator does not depend on the rapidity sum 2θ in a longitudinal direction, as does the scaling-hydrodynamics correlator: $R_{drop}(\alpha_{\parallel}, \theta_{\parallel}) = R_{drop}(\alpha_{\parallel}, 0)$. In virtue of spherical symmetry of the drop decay the characteristic relations must be valid at any decay mechanism:

$$R_{drop}(\vec{p}_1 - \vec{p}_2, \vec{p}_1 + \vec{p}_2 = 0) = R(|\vec{p}_1 - \vec{p}_2|) \tag{12}$$

4. If the tests indicate the existence of a global hydrodynamical regime, one can perform detailed analyses of the regime using the correlator (10). We shall demonstrate the analyses for the scaling regime of matter evolution forming in nucleus-nucleus collisions [5,12]. For the scaling model the decay isoterm has the form $\tau^2 = t^2 - x^2$, and $\tau = \left(\frac{d\,y''}{dx}\right)^{-1}$ means the proper time of the system expansion. The longitudinal velocity destribution has the form $v_{hyd} = x/t$.

In hadronic and nuclear collisions the initial condition and, therefore, the parameters of hydrodynamical flow change from one collision event to another. So it is necessary to express the parameters in terms of observable quantities and to select the events with the same parameters. The plateau height in the central region $H = H(0)$ in c.m.s. will be taken as one of the main observable quantities identifying the physical picture. The height of plateau H and the total pion multiplicity in the central region N are connected with the hydrodynamical parameters of the scaling-model [7,12] (for Landau-model see [7])

$$\tau = \frac{H}{S_{\perp} N_o(T_c)}, \quad X''_{max} - X''_{min} \equiv a_s = 2\tau\, sh\left(\frac{N}{2H}\right), \quad S_o = \frac{3.7 N_c(T_c)}{\tau_o}\tau \tag{13}$$

where s_0 is the initial entropy density, $\tau_0 = (0.5 \div 1)$ fm is the initial time of the hydrodynamical stage formation. We note that the measurement of only the plateau height H in ultrarelativistic nuclear collisions does not make it possible to reliably determine τ, since only 40% variations of the transverse radius r and the temperature T_c at the final stage of matter evolution lead to a change in τ by an order of magnitude due to the presence of the factor $s_\perp N_0(T_c)$ in (9). The proper time of the expansion τ and the freeze-out temperature T_c can be determined directly from the correlation date.

The correlator behaviour at chosen $m_\perp \gg T_c$ (or $m_\perp > \bar{m}$) depends on the two parameters τ and T_c (and on the common normalising multiplier λ). It can be determined by the fitting of correlation data by formula (10) when the plateau height H(0) is fixed. We would remind if the plateau is absent in events with a fixed value of H(0), the $\tau(\theta)$ is the inversal gradient of the longitudinal component of the hydrodynamical 4-velocity $u^\mu(x)$ at the final stage. If the value τ and T_c are determined at fixed H(0) one can find the transversal area $s_\perp$ according to formula (13): $s_\perp = H/\tau N_0(T_c)$.

The described method of determining the freeze-out temperature and transversalarea from the correlation data on longitudinal momenta enables us to separate the contributions to the transversal momentum from heat radiation and transversal hydrodynamical motion.

REFERENCES

1. G.Goldhaber, S.Goldhaber, W.Lee, A.Pais. Phys.Rev.,1960,120,325
2. R.Hanbury-Brown and R.Q.Twiss. Phil. Mag., 1954, 45, 663.
3. G.I.Kopylov, M.I.Podgoretski, Sov.J.Nucl.Phys.,1972, 15, 219.
4. T.Acesson et al. Phys Lett., 1987, 187B, 420.
5. J.D.Bjorken. Phys.Rev., 1983, D27, 140.
6. A.N.Makhlin, Yu.M.Sinyukov. Yad. Fiz. (USSR), 1987, 46, No 8,637 (Preprint ITP-86-27E, 1986, Kiev, USSR).

7. V.A.Averchenkov, A.N.Makhlin, Yu.M.Sinyukov. Yad.Fiz. (USSR), 1987, 46, No 10. (Preprint ITP-86-118E, 1986, Kiev, USSR).

8. L.D.Landau. Isvestija Ac.Nauk USSR, Serija Fiz., 1953, 17, 51.

9. Yu.M.Sinyukov. Phys.Lett., 1983, 127B, 443.

10. M.I.Gorenstein, Yu.M.Sinyukov. Phys.Lett., 1985, 142B, 425.

11. M.I.Gorenstein, Yu.M.Sinyukov, V.I.Zhdanov. Phys.Lett., 1977, 71B, 199.

12. H.Von Gersdorff, L.McLerran, M.Kataja, P.V.Ruuskanen. Phys.Rev., 1986, D34, 794.

FIGURES

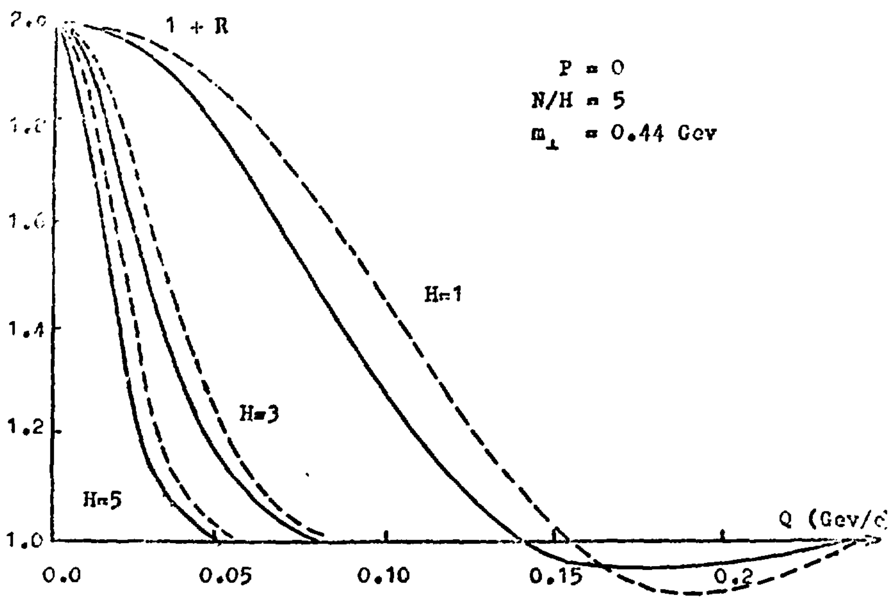

Fig.1. The Q-dependence of the correlator $R(Q,P)$ at $P=0$ for the scaling-model (S), plotted by a continuous line and the Landau model (L) plotted by dashes at different plateau heights $H(0)$ in pp-collisions. When $H=1$, $a_S=17$fm, $a_L=14$fm, $a_{eff}=1$fm; when $H=3$, $a_S=50$fm, $a_L=42$fm, $a_{eff}=2.5$fm; when $H=5$, $a_S=80$fm, $a_L=70$fm, $a_{eff}=5$fm.

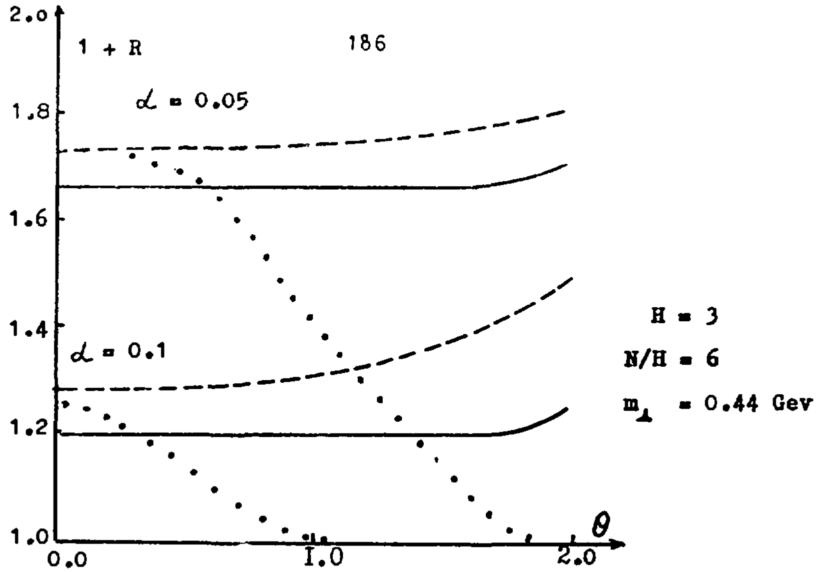

Fig.2. The θ -dependence of the correlator $R(\alpha, \theta)$ at different for S-, L- models and the rest cluster (C) model (dots).

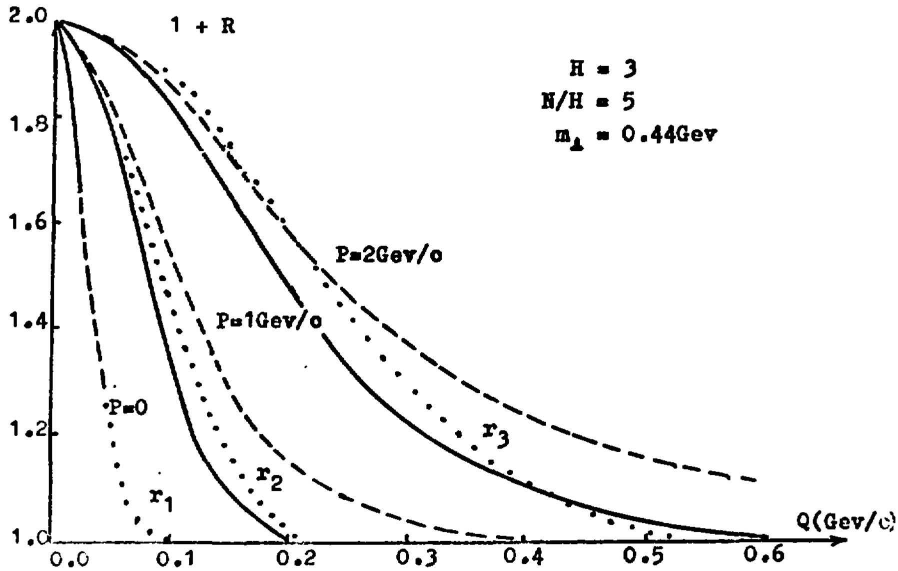

Fig.3. The correlator $R(Q,P)$ at different valuis P for S-,L-, and C-models. The hydrodynamical S-,L- correlators at different values P are approximated by the claster model with different claster radii: r_1=4,3fm, r_2=1.[illegible]fm, r_3=0.8fm. At P=0 the curves of S-,L-, C-models are indistinguishable in the figure scale.

THE η-η' MIXING IN INCLUSIVE PRODUCTION AND GLUEBALL COMPONENT CONTRIBUTION

Batunin A.V., Likhoded A.K., Petrov V.A.
Institute for High Energy Physics
Serpukhov, Moscow region, 142284, USSR

1. The unusual properties of the G-meson found in the $\pi^- p$ experiment/1/ manifest themselves, in particular, in the enhanced $\eta\eta'$ decay mode. In ref./2/ the given property is related with anomalously large gluon component of the η'-meson/3/. Recently, the inclusive cross section of the π^0 and η-meson production and preliminary estimates of the η'-meson yield were obtained in $\pi^- p$ interaction at 360 GeV/c /4/. The unusually large η'-meson production observed in this experiment requires a detailed analysis in the frame of reliable model. For this case we choose the model for inclusive hadron production/5/ which is recently offered by us and based on the dual topological unitarization (DTU) scheme with a quark-gluon picture of the hadron interactions. The main results of the model are the following: 1) the valence quark contribution is dominant in the fragmentation region of the initial hadron; 2) in the same region ($x_F \gtrsim 0.5$) the directly produced particles are dominant, so the contributions from the higher resonances decay products can be neglected. The latter, at the same time, explains the essential difference in the ratios of the η and π^0-meson production in the central region (where $\sigma^{\eta}/\sigma^{\pi^0} = 0.07 \pm 0.055$, see ref./6/) and in the fragmentation one (where the same ratio is equal to 0.45 ± 0.05, see ref./4/).

2. Thus according to the model/5/ the inclusive cross section of the π^0 and η-meson production is of the form:

$$z^* \frac{d\sigma}{dz} = \sum_n \sigma_n(s) \sum_{i,j} \int_{z_+}^{1} \int_{z_-}^{1} f^i_{a,n}(x) f^j_{b,n}(y) \, z^* \frac{dP^{ij \to c}}{dz}(x,y,z) \, dx\, dy \,, \quad (1)$$

where parameters $\sigma_n(s)$ and n-particle distribution function $f^i_{a,n}(x)$ of the quark $\underline{i}$ in the hadron $\underline{a}$ were defined earlier/5/. The probability of the particle $\underline{c}$ emission from the sheet (ij) was defined in the form:

$$z^*\frac{dP^{ij\to c}}{dz}(x,y,z) = \beta^i_c\, B^{-1}(g^2, 1-\alpha_i)\left(\frac{z_\pm}{x}\right)^{1-\alpha_i}\left(1-\frac{z_\pm}{x}\right)^{g^2-1}\left(1-\frac{z_-}{y}\right)^{g^2-\alpha_j} + \beta^j_c \cdot \begin{Bmatrix} z_+ \leftrightarrow z_- \\ x \leftrightarrow y \\ \alpha_i \leftrightarrow \alpha_j \end{Bmatrix}$$
$$+\, g_c^2\left(1-\frac{z_\pm}{x}\right)^{g^2-\alpha_i}\left(1-\frac{z_-}{y}\right)^{g^2-\alpha_j};\ \sum_c g_c^2 = g^2,\ \sum_c \beta^i_c = \sum_c \beta^j_c = 1. \qquad (2)$$

$$(z_\pm = 1/2(\sqrt{z^2 + 4m^2_{\perp c}/s} \pm z),\ z = 2p^*_c/\sqrt{s}\,.)$$

The coefficients β^i_c define the relative fragmentation probability of the quark $\underline{i}$ to the particle $\underline{c}$. In our case:

$$\beta^i_\eta = \sin^2(\varphi-\varphi_0)\beta^i_{\pi^0},\ \beta^i_{\eta'} = \cos^2(\varphi-\varphi_0)\beta^i_{\pi^0},\ \beta^{u,d}_{\pi^0} \cong 1/4(V/PS+1)^{-1} \qquad (3)$$

where φ is the singlet-octet mixing angle, $\varphi_0 = 35{,}26°$ and the ratio of the vector meson production to pseudoscalar one V/PS is 1.3 /5/. Latter follows from the quark combinatorics rules. The parameter g^2 was defined by us earlier ($g^2 = 1.1 \pm 0.2$) when describing the vector meson spectra in Kp interaction /5/. We obtain the best description of the x-dependence and absolute value of π^0-meson production (at $x \gtrsim 0.4$ at 360 GeV/C) at $g^2 = 1.3$, which coincides within the error with those found earlier.

As may easily be seen, at high energy in the fragmentation region of the initial hadron probability (2) admits a simple interpretation of the form of the fragmentation functions:

$$z^*\frac{dP^{ij\to c}}{dz} = \begin{cases} \beta^i_c \cdot D^{i\to c}(z), & z \gtrsim 0.5 \\ \beta^j_c \cdot D^{j\to c}(z), & z \lesssim -0.5 \end{cases} \qquad (4)$$

Theoretical curve (dashed line on Fig.1) for the directly produced π^0-mesons (using formula (3)) goes through experimental points at $x \gtrsim 0.8$ - just in the region where prompt π^0 mesons are dominant. The total π^0 meson production in the forward hemisphere is calculated by adding the contribution from the decay of $\rho^{\pm}$ (curve 1) and ω, η and η' mesons (the hatched area on fig.1) : $\sigma^{\pi^0}_{x\geqslant 0} = 45.6$ mb in comparison with the experimental value $49.7 \pm 1.0 \pm 1.1$ /4/. When fitting the experimental meson production points at $x \gtrsim 0.4$ (curve 2 on fig.1) using (3) we obtain $\sin^2(\varphi - \varphi_0) = 0.62 \pm 0.05$, which corresponds to $\varphi = (-17 \pm 3)^\circ$. This value coincides practically with the established one -18° (see, for example, ref./7/).

Thus there is an agreement between π^0 and η-meson production rate. In the case of comparison of η' and η-meson one we have to expect in the frame of usual η-η' mixing at $\varphi = -17^\circ$:

$$R = \sigma^{\eta'}/\sigma^{\eta} = \mathrm{ctg}^2(\varphi - \varphi_0) = 0.60 \qquad (5)$$

Almost this value was obtained in the charge exchange reaction $\pi^- p \to \eta(\eta')n$ at $p_{lab} \leqslant 40$ GeV/c : $R = 0.55 \pm 0.06$ /7/. But measured in inclusive experiment at $p_{lab} = 360$ GeV/c this ratio is:

$$R = 3.6 \pm 1.8 \quad \text{at } x \geqslant 0.3 \, , \qquad (6)$$

i.e. essentialy larger.

3. Let us try to remove the disagreement between the theory and the experimental result (6) by the consideration of the three dimensional picture of the η-η'-G mixing/8/ , where one introduces an additional glueball component G orthogonal to the planar η-η' basis. Then instead of the only singlet-octet mixing angle there appear three different angles (like the Euler's angles). Lately, one carried out the analysis/9/ in the three dimensional mixing picture of the quark composition of the η and η'-mesons, indicating almost twice less contents of the light u,d-quarks in the η'-meson wave function squared $|\psi_{\eta'}|^2$ in comparison with the η-meson. This fact is in a good agreement with result (5) if one considers the η, η'-meson production as a result only of the u,d-quark fragmentation from the initial hadrons; but it is obviously in contradiction with result (6). On

the other hand just that analysis/9/ reveals a considerable glueball admixture in the η'-meson ($\sim 1/3\,|\Psi_{\eta'}|^2$) and almost complete absence of the glueball states in the η-meson ($\lesssim 0.05\,|\Psi_{\eta}|^2$). Then it follows that we have a possibility to understand both (5) and (6) by taking into account the glueball component contribution into η'-meson production, which becomes visible only with increasing energy.

4. The glueball states arise naturally in the DTU scheme cutting off the diagrams with handles in the 1/N expansion/10/ in the t-channel (see Fig.2). Such diagrams join to the action on the two-cylinder level and that is why they have a strong energy-threshold dependence. How does one take explicitly into account the glueball production in the frame of our "DTU-standart" model/5/ (in the sense of cutting off only cylinder diagrams)[**]? For this purpose we used the analogy with QCD. The two-gluon annihilation is known to give the main contribution to the η_c, η'_c, χ_J-meson production, which decay then into the J/Ψ-meson plus photon. From experiments we know the energy dependence $x^* d\sigma/dx|_{x=0}^{pN\to J/\psi X}$ at $\sqrt{s}=$ 10-63 GeV, and thus one can derive the dressed gluon distribution functions in the initial hadrons and also their fragmentation functions into the two-gluon states (like glueballs) /10/. The only remaining task is to find the normalization parameter λ_g, corresponding to the probability of the revealing cylinder with handle instead of two cylinders at cutting off in the third order of the 1/N expansion. The unexplained anomalously large photon production rate effect in the Sp̄pS collider/12/ may help us[*]. We attribute the additional photons to the γ-decay production of the glueball produced mesons. The lightest candidate for this role is the above mentioned η'-meson, and thus there is a possibility to

---

[*] The number of photons is expected to be approximately equal to the sum of charged π-mesons from the naive isotopic invariance. This statement is right for the low energy, but in the Sp̄pS collider 30%-exceeding of the photons have been found.

present the "SppS-effect"/12/ as a result of reaching full capacity glueball action, whose trace has hardly been perceptible at 360 GeV/c. Then we obtain by the fit to the photon inclusive spectrum at $\sqrt{s}$ = 540 GeV /12/ (see Fig.3) in accordance with prescription/10/ $\lambda_G = 0.03 \pm 0.01$. The dashed curve corresponds to the total photon production at the UNK energy $\sqrt{s}$ = 6 TeV (Serpukhov,USSR), where the glueball mechanism $gg \to \eta' \to \gamma + \ldots$ yields more than half of the observed photons in the pseudorapidity interval $|\eta| < 5$.

If one comes back to p_{lab}= 360 GeV/c with the obtained value λ_G= 0.03 one is able to calculate the glueball mechanism contribution in the reaction $\pi^- p \to \eta' X$: $\sigma^{gg \to \eta'}_{theor}(x_F > 0.3)$ = 0.12 mb. This value diminishes lightly the discrepancy between theory and experiment/4/ (0.52 mb and 2.9 $\pm$ 1.5 mb,respectively), but it can not remove it completely because of concentration of the glueball contribution in the central region of the η'-meson spectrum.

Thus if further processing of the data on η'-meson production does not decrease preliminary result (6) then the new phenomenon occurs in $\pi^- p \to \eta' X$, which can not be explained even by attracting the glueball mechanism of the η'-meson production.

5. Acknowledgements.

We are pleased to acknowledge E.P.Kistenev, M.L.Nekrasov, V.A. Stopchenko and V.R.Zoller for interesting discussions.

References

1. Binon F. et al.-Sov.J.Yad.Fiz.39(1984)831
2. Gershtein S.S.,Likhoded A.K.,Prokoshkin Yu.D.-Sov.J.Yad.Fiz. 39(1984)251
3. Novikov V. et al.-Nucl.Phys.B165(1980)55
4. Aguilar-Benitez M. et al.-Preprint CERN/EP 86-165,Geneva,1986
5. Batunin A.V.,Likhoded A.K.,Tolstenkov A.N.-Sov.J.Yad.Fiz. 42(1985)424
6. Akesson T. et al.-Preprint CERN/EP 86-84,Geneva,1986
7. Apel W.D. et al.-Phys.Lett.83B(1979)131
8. Ei-ichiro Kawai-Phys.Lett.124B(1983)262
9. Rosner J.-Phys.Rev.D27(1983)1101
Baltrusaitis R.M. et al.-Phys.Rev.D32(1985)2833
10. Batunin A.V.,Likhoded A.K.,Petrov V.A.-Preprint IHEP 86-233, Serpukhov,1986
11. Capella A.,Tran Thanh Van J.-Z.Phys.C10(1981)249
Kaidalov A.B.,Ter-Martirosyan K.A.-Phys.Lett.117B(1982)247
12. UA5 Collaboration.Alpgard K. et al.-Phys.Lett.115B(1982)71

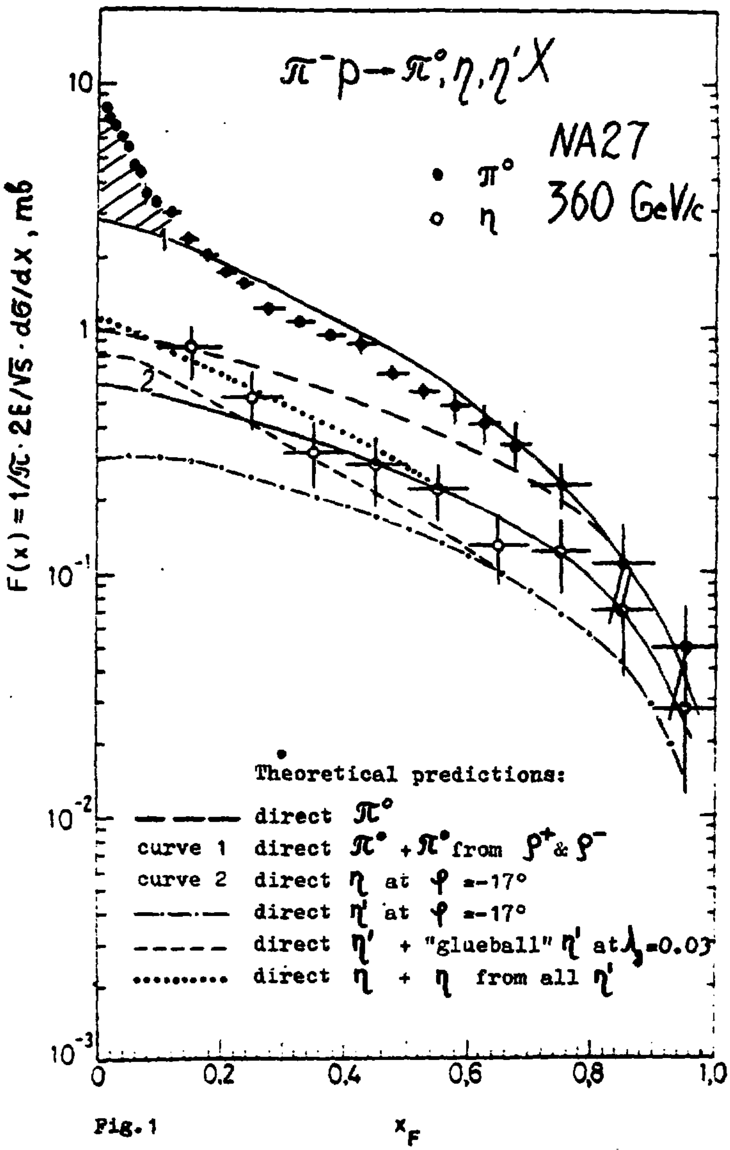

$\pi^- p \to \pi^\circ, \eta, \eta' X$
NA27
• π°
∘ η
360 GeV/c
$F(x) = 1/\pi \cdot 2E/\sqrt{s} \cdot d\sigma/dx$, mb
Theoretical predictions:
direct π°
curve 1 direct $\pi^\circ + \pi^\circ$ from ρ^+ & ρ^-
curve 2 direct η at φ =-17°
direct η' at φ =-17°
direct η' + "glueball" η' at λ_g=0.03
direct η + η from all η'
x_F

Fig. 1

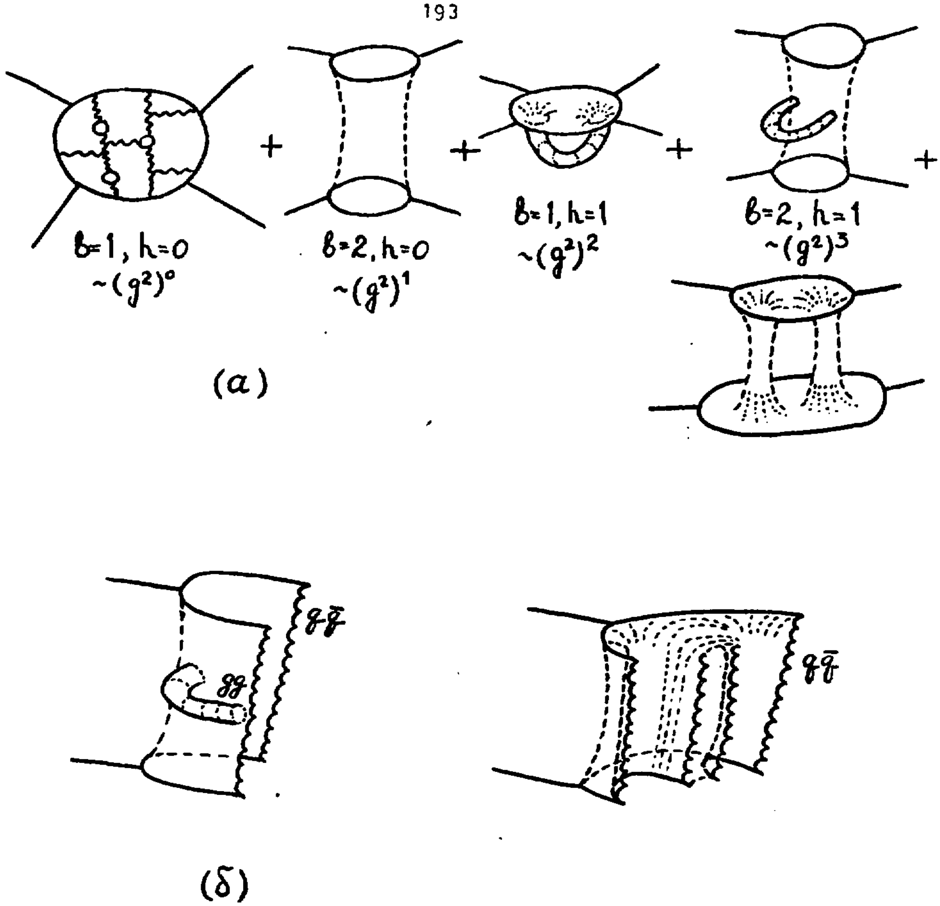

Fig.2 The first terms in 1/N expansion - a). Absence of the valence quark-antiquark pairs in the initial hadrons causes planar diagram absence.
The glueball production at cut off of handles and usual hadron production at cut off of cylinders - b).

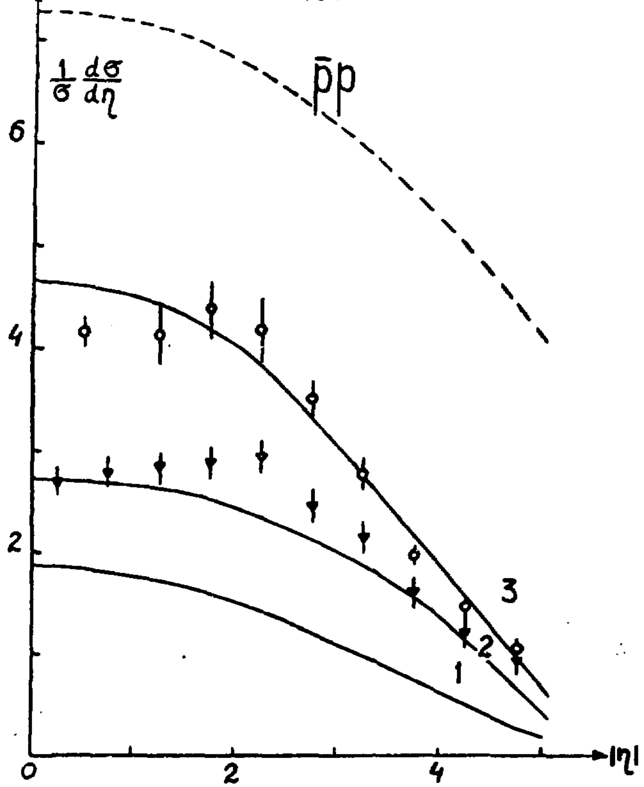

Fig.3 The inclusive spectrum of photons (circles) and charged π mesons (triangles) in $\bar{p}p$ interaction in S$\bar{p}$pS collider/12/.
Curve 1 - photons from "glueball" η',
2 - photons from direct $\pi^0, \rho^{\pm}, \omega, \eta, \eta'$;
3 is 1 & 2. Dashed curve is the same as 3 but at $\sqrt{s}$ = 6 TeV.

NARROW DIBARYONS

Bekhzad S. Yuldashev

High Energy Division
Physical Technical Institute
Tashkent, 700084, U.S.S.R.

Abstract

A short review of recent experimental data on search of the narrow dibaryon resonances is presented.

1. INTRODUCTION

It is well known that the problem of the possible existence of dibaryon resonances is not a new one and is discussing from time to time for a long period [1-5] . In last decade this question has been raised again and mainly due to observation [6] of structures in cross-section differences between parallel and antiparallel longitudinal ($\Delta\sigma_L$) and transverse ($\Delta\sigma_T$) total cross sections in pp interactions as well as from polarization measurements. These results and data from other experiments [7-9] (see also references in [10]) can be interpreted as a reflection of the possible existence of $^1D_2$, $^3F_3$ and $^1G_4$ proton - -proton resonances with masses about 2.14, 2.26 and 2.43 GeV and with rather high ($\Gamma \gtrsim$ 100-200 Mev) widths.

The indirect evidence for dibaryons also comes from an analysis of data on the production of so-called cumulative secondaries [11,12] ,i.e. hadrons produced into kinematical region forbidden by kinematics of scattering on a single nucleon bound into a nucleus. In addition, the EMC-effect [13] does not contradict an assumption of the existence of dibaryons or 6- -quark bound states. The similar conclusion can be drawn from an analysis of high four-momentum transfered scattering of nucleons on the light nuclei [14] .

From the theoretical point of view there are no serious objections against dibaryons. Indeed, several models like, for example, the quark bag model [15] , the model of nonadiabatic rotational bands [16] , the string model [17] and some others predict the existence of multibaryon resonant states.

In this report I will present a short summary of recent experimental results [18-41] on search of narrow ($\Gamma \lesssim 50$ Mev) non--strange dibaryon resonances in hadron-nucleus and nucleon-nucleon interactions in the primary momentum range p_o= (1.0-300) GeV/c. The evidence for direct observation of narrow dibaryons came out now from many experiments performed with primary pion, proton and heavy ion beams at different energies and many types of targets.

Due to space -limit in this review I have restricted myself by consideration of low-mass ($M \lesssim 2\ m_N + m_\pi$) dibaryon candidates. More information about dibaryons with masses $M > 2.1$ Gev can be found in [3-5] .

2. DI-PROTON MASS SPECTRA

The routine way to look for dibaryons is a study of effective mass distribution of nucleon pairs produced in nucleon scattering or in interactions of primary particles with nuclei. From this point of view the bubble chamber experiments have some advantage. Indeed, in this case selecting protons stopped in the visual volume one can reach a good accuracy ($\lesssim$ 1-2 %) in the momentum determination of protons what means one will have a relatively high effective mass resolution.

2.1 INTERACTIONS WITH NUCLEI

Apparently, the first indication on the possible observation of narrow dibaryon signal came out from early bubble chamber experiments [18,19] in which the two-proton correlations had been studied in hadron-nucleus interactions. There have been seen narrow peaks in the distributions of two-proton effective mass spectra at $M(pp) \simeq 1.92 - 1.93$ GeV. However, due to limited statistics an interpretation of these peaks as possible signals of diproton resonances was doubtful.

Recently, the new high statistics data were reported [21–41]. Our group has looked [19,25,26,36,40,41] for diproton resonant states in $\pi^{-12}C$, $p^{20}Ne$, $p^{12}C$, $d^{12}C$, $\alpha^{12}C$ and $C^{12}C$ - interactions in the primary momentum range from 4 to 300 GeV/c. It turns out that independently of the type of projectile, its energy and a sort of target in the M(pp) distribution there are narrow peaks exceeding a background for more than 4 standard deviations. As an example Figs 1 a,b show the M(pp) distributions in $\pi^{-12}C$ at 4 and 40 GeV (data at both energies are combined) and in $p^{20}Ne$ interactions at 300 GeV. The dashed lines represent corresponding background distributions obtained by random mixing of protons from different events of the given type ($\pi^- C$ or pNe) but at fixed proton topology in final state. It should be stressed that in this analysis no cuts have been applied to emission angles of protons and their momenta have been restricted to interval $0.22 \leq p_{1,2} \leq 0.40$ GeV/c. In this range the momenta of about 92 % of secondary protons were determined by range in a bubble chamber. That leads to the resolution in determination of M(pp) to be less than 2.7 MeV.

As one can see in both types of interactions at $M(pp) \simeq 2m_p$, 1922, 1939 and, possibly, at 1950 MeV there are narrow peaks which become statistically more significant if one combines together the $\pi^- C$ and pNe data (Fig.1c). The first peak at $M(2p) \simeq 2m_p$, as it is well known [42–44], is due to the final state interaction between secondary protons. The other peaks can be interpreted as a manifestation of narrow dibaryons.

The smooth line represents the approximation of the combined M (pp) distribution with the sum of two Breit-Wigner functions and the background spectrum. In result of approximation (χ^2/NDF =0.81) for the masses and widths of possible dibaryons was obtained

$M_1(pp) = 1922 \pm 1.3$ MeV, $\Gamma_1 = 11 \pm 3.6$ MeV;

$M_2(pp) = 1940 \pm 0.4$ MeV $\Gamma_2 = 10 \pm 4.5$ MeV

It should be underlined that the probability to describe the experimental M(pp) distribution by the smooth curves (shown in Fig.1c) like $f(M)= KZ^{\alpha} \exp[-(\beta Z + \gamma Z^2)]$, where $Z = M(2p) - 2m_p$, is too low (χ^2/NDF = 2.6 when K is fixed by normalization condition to the experimental number of combinations, and χ^2/N.D.F. = 1.7 when K is free). The peaks are standing over background for 4.1 and 4.5 standard deviations at M_1= 1922 MeV and M_2=1940 MeV respectively.

The similar results were obtained by our group [36] in the analysis of semi-inclusive reactions : $(p, d, \alpha, {}^{12}C) + {}^{12}C \rightarrow pp + X$ at 4.2 GeV/c. These data come from the 2m propane bubble chamber exposed at Dubna accelerator to heavy ion beams. Fig.2 shows the M(pp) spectra obtained for different combinations of proton pairs. The following notations have been used : p_s – slow protons, having momenta of $0.2 \leq p \leq 0.3$ GeV/c; p_f – fast protons with momenta $0.3 \leq p \leq 0.7$ GeV/c; in addition, $p_s^f (p_s^b)$ means slow protons emitted into forward (backward) hemisphere and p_f^f (p_f^b) – fast protons emitted at $\theta_{lab} < 90°$ $(\theta_{lab} \geq 90°)$ in the laboratory system. Only events containing at least one proton emitted into backward hemisphere were considered. As one can see from Fig.2 there are peaks at masses

M(pp) $\simeq$ 1904, 1920, 1935 and 1970 MeV which are standing over background for more than 3 standard deviations.

It should be noted that the peaks in M(pp) distribution at approximately the same masses have been seen by us also in π^-C and pNe interactions from 4 to 300 GeV/c (Fig.3). The recent analysis of $\pi^{\pm}$Ne interactions at 30 GeV/c [45] obtained in BEBC by the Seattle-Strasbourg-Warsaw collaboration reveals peaks in M(pp) spectrum (Fig.4) approximately at the same masses as it has been observed in the abovementioned experiments.

Fig.5 shows the M(pp) distributions in π^{-12}C, p^{20}Ne and (p, d, α ,C)^{12}C interactions from 4 to 300GeV/c. The following cuts have been applied : 1) both protons have momenta of $0.3 \leq p_{1,2} \leq 0.75$ GeV/c; 2) both protons should be emitted at laboratory angles $\Theta_{1,2} > 30°$ - this cut allows to reduce significantly a background from so-called recoil protons emitted out of target nucleus due to rescattering of primary or/and secondary hadrons; 3) the angle between two protons, Θ_{12}, should be greater than 110°. The last cut makes it possible to look in detail especially the region of high values of M(pp). It is seen, that independently of the type of projectile, its primary energy and a sort of target there is a clear narrow peak at M(pp) $\simeq$ 2020 MeV. The fit of combined distribution by a sum of Breit-Wigner function and background distribution for the mass and width of possible dibaryon gives :

$M_3(pp) = 2017 \pm 1.3$ MeV, $\qquad \Gamma_3 = 5 \pm 2$ MeV.

Several groups have reported on the observation of statistically significant structures approximately at same mas -

...es in M(pp) distributions for proton pairs produced in hadron-nucleus interactions [20-24, 27, 30-34] . Some of these experimental data are shown in Figs. 6-11. The narrow peaks at $M(np) \simeq M(pp) \simeq$ 1940 MeV and $M(pn) \simeq M(pp) \simeq$ 2025 MeV have also been seen (Fig.12) in low energy pd interactions [37].

2.2. NUCLEON-NUCLEON INTERACTIONS

To my knowledge only one group has searched for narrow dibaryons in inelastic nucleon-nucleon interactions [24,30,35]. The authors have seen (Fig.13) narrow peak at $M(pp) \simeq 1936$ MeV in reaction $np \to pp\pi^-$ at primary momentum $p_o = 1.25$ GeV/c. It is interesting to note that this peak appears only in events where the 4-momentum transfered from primary neutron to secondary π^- meson exceeds $t_{n\to\pi^-} = 0.3$ GeV^2/c^2 (Fig.13a), while at $t_{n\to\pi^-} < 0.3$ GeV^2/c^2 (Fig.13b) there is no signal in M(pp) distribution. Roughly speaking this means that dibaryons can be produced in NN interactions going through baryon exchange. The same group have reported on the observation of peaks at higher masses ($M(pp) \simeq 1965$ and $M(pp) \simeq 2025$ MeV) in np interactions at 2.23 and 5.1 GeV/c (Fig.14).

The masses and widths of possible dibaryons determined in these experiments are the following :

$$M_1(pp) = 1936 \pm 3 \text{ MeV}, \qquad \Gamma_1 = (0.7 \pm {}^{1.6}_{0.7}) \text{ MeV}$$

$$M_2(pp) = 1965 \pm 2 \text{ MeV}, \qquad \Gamma_2 = (1.0 \pm {}^{2.0}_{1.0}) \text{ MeV}$$

3. "MASS LEVELS" OF DIBARYONS

A compilation of masses and widths of possible dibaryon candidates is given in Table 1. It should be noted that the numbers given in the parentheses mean the values of M(pp) or M(pn) determined from the peak positions in corresponding effective mass distribution, i.e. data from experiments in which authors did not give dibaryon masses obtained from a fit of experimental spectra.

Fig.15 shows the "mass levels" of possible dibaryon candidates and there is a clear indication that the data from different experiments are populating the corresponding narrow "bands" disposed one after another at distance from $\simeq 15$ MeV to $\simeq 60$ MeV. The mean values of masses of the possible dibaryon candidates averaged in each "band" are given in Table 2.

As it follows from Fig.15 one can conclude that in many independent experiments performed with a wide variety of projectiles and targets in the primary momentum range $p_0 = (1 - 300)$ GeV/c there are observed statistically significant narrow peaks at approximately the same masses of dinucleon system. A probability that the observed peaks in mentioned data are due to statistical fluctuations in accordance to estimates is less than 10^{-7}.

Thus we can conclude that the abovementioned results can be interpreted in favour of the existence of the family of narrow dinucleon resonances.

4. DIBARYON MESSAGE FROM MOMENTUM AND ANGULAR SPECTRA OF SECONDARY NUCLEONS

It turns out that in the momentum and angular spectra of secondary nucleons produced in hadron-nucleus interactions there are some features which, in principle, can be caused by production and decay of dibaryon resonances.

Fig.16 shows the angular distributions of secondary protons with momenta of $0.2 \leq p \leq 1.0$ GeV/c in $p^{20}Ne$ interactions at 300 GeV/c for events with the fixed number of protons in final state [17] .It is seen that the cos θ_{Lab}-distributions for events with $n_p = 2$ and 3 do not obey to a simple exponential form $dN/\cos\theta_{Lab} \sim \exp(-B\cos\theta_{Lab})$ which describes well data at $n_p = 1$ and $n_p \geq 4$.

In events with $n_p=2$ and 3 we observe some "extra"-protons at $\cos\theta_{Lab} \leq -0.4$ compared to what would be expected from the exponential fall-off. Moreover, these "extra"-protons contribute mainly into region of momenta $0.2 \leq p \leq 0.5$ GeV/c leading to an appearance of a "plateu" [48] in the momentum distribution of protons emitted into backward hemisphere in the laboratory frame (Fig.17). In addition , in accordance to our experimental data [46] the possible dibaryons are in the laboratory system relatively slow (Fig.18) i.e. $\beta_{pp} \simeq 0$.

Now if one suggests, that some part of the abovementioned "extra"-protons comes from decays of dibaryons with masses $1900 \leq M(pp) \leq 2100$ MeV and $\beta \simeq 0$, then the momenta of decay protons (emitted in opposite direction) will depend on M(pp) as $p = 1/2\,[M^2(pp) - 4\,m_p^2]^{1/2}$. Substituting the corresponding values of M(pp) we will obtain that the dominant number of protons from decays of possible dibaryons should be in the range $0.2 \lesssim p \lesssim 0.5$ GeV/c, i.e. in the region where we have observed the "extra"-protons.

Another evidence for the existence of narrow structures in the momentum spectra of secondary nucleons also comes from the precise measurements performed with use of low-energy pion beam at TRIUMF [49] . In this experiment the momentum spectra of protons and neutrons emitted out of the Carbon nucleus after absorbtion of slow π^- mesons have been measured. The narrow structures in the kinetic energy distributions of protons and neutrons have been seen (Fig.19). The authors claim that the evident structures observed at 50,60 and 70MeV "...can not be exhaustively understood only in terms of the two-nucleon absorption model".

By arrows in Fig.19 I have shown the expected positions of structures appearance of which one would see if there is a contribution from decays of slow ($\beta \simeq 0$) dibaryons with masses mentioned in Table 2. As it is seen, the expected values of nucleon kinetic energy almost correspond to the positions of the observed structures.

The authors of this experiment [47] claimed that structures below the threshold of reaction $\pi^-(2N) \to NN$ (like $\pi^+ d \to pp$, $\pi^- d \to nn$) can be ascribed, for example, to neutrons coming from pion captures by α-clusters with the deuteron and one of the neutrons acting as "spectator" respectively. In my opinion this hypothesis contradicts data on the observation of narrow peaks around $M(pp) \simeq M(pn) \simeq$ $\simeq 1940$ and 1965 MeV in np and pd interactions [24,30,35,37] and the discussed structures rather could be a reflection of a production of dibaryons.

5. ON THE SPIN OF DIBARYONS

There are no conclusive results on spin (J) and parity (P) of possible dibaryon candidates and the main reason for this is relatively low statistics. An attempt to determine J^P for dibaryons with masses M(PP) = 1922 MeV and M(PP) =1939 MeV has been made by our group [46] . Fig.20 shows the cos θ_p^* - distributions of decay protons after substraction of background in the rest system of dibaryon with a given mass. The angle θ_p^* was determined as an angle between the vectors of the total dibaryon momentum and the momentum of one of decay protons. There is possible indication of non-zero spin for both resonant states. The curves in Fig.20 represent best fits of data by functions corresponding to the J^P-states : 1^- and 2^+. As one can see for dibaryon candidate at M(PP) = 1922 MeV neither 1^- nor 2^+ can be ruled out, while for the second candidate at M(PP) = = 1940 MeV the $J^P = 2^+$ state looks preferable.

The similar analysis have been carried out for dibaryon candidate with the mass M(PP) = 1966 MeV in Ref. [32] . The authors conclude that this possible resonance can be considered as the two-proton system in P-wave state with the total spin J = 2.

6. THE WIDTH OF DIBARYONS

As it follows from data in Table 1 no unambiguous conclusion can be done on the width , Γ, of possible dibaryon candidates because of large errors. However, it seems that for all discussed candidates the value of Γ is not greater than several tens of MeV.

7. CONCLUSION

In many independent experiments there were observed the similar narrow resonant-like structures in the effective mass distributions of nucleon-nucleon system. Since the positions of these peaks and their widths do not depend upon either the type of interaction (NN, hA) or the primary energy these results can be considered as a strong evidence in favour of the existence of narrow dibaryon resonances.

I would like to thank S.A.Azimov, V.M.Chudakov, E.L.Feinberg, A.B.Kaydalov, L.A.Kodratyuk, G.A.Leksin, E.M.Levin, V.A.Matveev, T.Siemiarczuk, S.Tkaczyk, A.A.Yuldashev and P. Zielinski for helpful discussions.

Special mention must be made of the truly excellent organization of conference at Kazimierz by A.Wróblewski and his colleagues from Warsaw.

REFERENCES

1. G.A.Leksin, Preprint ITEP N 854, Moscow, 1971.

2. M.M.Makarov, Uspekhi Fiz. Nayk (UFN), 136 (1982) 185; Sov. Phys. Usp. 25 (1982) 83.

3. A.Yokosawa , Phys.Reports, 64 (1980) 47.

4. K.K.Seth, Talk given at 1984 Workshop on Electron and Photon Interactions at Medium Energies, Bonn.

5. B.Tatischeff, Report IPNO-DRE 85-19, Orsay, 1985, presented at the XI th Europhysics Conf.,July 1-5, 1985, Paris.

6. I.P.Auer et al., Phys.Rev.Lett. 41 (1978) 1436; ibid 41 (1978) 358;

I.P.Auer et al.,Phys.Lett.,70B (1977) 475;ibid 67B (1977) 113.

I.P.Auer et al., Phys. Rev., D24(1981) 2008

7. K.Hidaka et al., Phys.Lett. 70B (1977) 479.

8. T.Kamae et al., Phys.Rev.Lett. 38 (1977) 468.

9. T.S.Bhatia et al., Phys.Rev.Lett. 49 (1982) 1135.

10. B.Tatischeffet al., Report IPNO-DRE 85.14., Orsay, 1985

11. A.M.Baldin et al., Sov.J.Nucl.Phys.13 (1973) 79.

12. A.M.Baldin, Proc.of the XX-th Int.Conf.on High Energy Physics, Tokyo, 1980.

G.A.Leksin, Preprint ITEP, N 147, Moscow, 1978.

V.V.Stavinski, Elem.Part. and Atomic Nucl.,8 (1977) 429.

13. J.J.Aubert et al., Phys.Lett., 123B (1983) 275.

A.Bodek et al., Phys.Rev.Lett. 50 (1983) 1431; ibid 51 (1983) 534.

R.G.Arnold et al., SLAC-Pub-3257 (1983).

14. L.A.Kondratyuk, in the book "Nucleon-Nucleon and Hadron-

-Nucleus Interactions at Intermediate Energies", ed.A.A. Vorobijev et al., Leningrad, 1984, p.402.

15. R.L.Jaffe, Phys.Rev.Lett., 38 (1977) 195.
P.Mulders et al., Phys.Rev.Lett. 40 (1978) 1543.
V.A.Matveev, P.Sorba, Nuovo Cim., 115A (1978) 217.

16. M.H.Mac Gregor, Phys.Rev. D20 (1979) 1616.

17. M.Imachi et al., Prog.Theor.Phys. 55(1976) 551; ibid. 57(1977) 517.

18. V.S.Verebryusov et. al., Preprint ITEP-273, Moscow, 1964.

19. S.A.Azimov et al., Sov.J.Nucl.Phys. 19 (1974) 317.

20. B.S.Aladashvili et al., Nucl.Phys. A274 (1976) 486.

21. A.A.Bairamov et al., JINR Preprint PI-83-207, Dubna, 1983.

22. T.Siemiarczuk et al., Phys.Lett. 128B (1983) 367; ibid. 137B (1984) 434.

23. V.V.Glagolev et al., JINR Preprint EI-83-59; I-83-556; PI-83-565, Dubna, 1983. Sov.J.Nucl.Phys.40 (1984) 482.

24. K.Beshliu et al., JINR Preprint DI-83-815, Dubna, 1983.

25. S.A.Azimov et al., Preprint PTI 27-84-FVE, Tashkent,1984; Sov. J.Nucl.Phys.42 (1985) 913.

26. S.A.Azimov et al., JETP Letters, 40 (1984) 316.

27. V.B.Agakishiev et al., JINR Preprint, I-84-103, Dubna,1984.

28. B.Tatischeff et al., Phys.Rev.Lett. 52 (1984) 2022.

29. V.V.Glagolev et al.,Zeit. f.Phys. 317A (1984) 335.

30. K.Beshliu et al., JINR Preprint, DI-85-433, Dubna, 1985.

31. K.N.Ermakov et al.,Preprint N 1089, Leningrad Inst.Nucl. Phys., Leningrad, 1985.

32. O.B.Abdinov et al., JINR Rapid Co N 15-86, 34, Dubna, 1986.

33. A.I.[illegible]in et al., JETP Letters, 43 (1986) 455.

34. V.V. [illegible]v et al., Zeit. f. Phys., [illegible] (1986) 391.

35. Yu.A.Trojan, JINR Preprint, P2-86-35, Dubna, 1986.

36. [illegible].Alimov et al., Preprint FTI 52-87-FVE, Tashkent, 1987.

37. V.[illegible]drecv et al., in the book: "NN and Hadron-Nucleus Interactions at Intermediate Energies", ed.A.A.Vorobijev et al., Leningrad, 1986, p.80.

38. A.[illegible]Prokof[illegible], I.I.Strakovsky, in the book "NN and hA Interactions at Intermediate Energies", ed. A.A.Vorobijev et al., Leningrad, 1984, p.7.

39. [illegible].Prokofjev, I.I.Strakovsky, in the book "NN and hA Interactions at Intermediate Energies", ed.A.A.Vorobijev et al., Leningrad, 1986, p.5.

40. [illegible].S.[illegible]ldashev, Proc.of the XVII Int.Sym.on Multiparticle Dynamics, Seewinkel, Austria, 16-20 June 1986, Ed.M.Markytan et al., World Scient.Pub., Singapore, 1987, p.789.

41. [illegible].S.Yuld[illegible]v, Talk given at the II Workshop "Quarks and N[illegible]lei", Leningrad, 20-24 April 1987, unpublished.

42. [illegible].[illegible]oonin., Phys. Lett. 70B (1977) 43.

43. [illegible].Lednicky, V.L.Ljuboshitz, Sov.J.Nucl.Phys. 35 (1981) 1316.

44. S.A.Azimov et al, Phys.Rev.D29 (1984) 1304.

45. [illegible].Tracz[illegible], [illegible].Wroblewski, private communication.

46. S.A.Azimov et al., Preprint FTI 44-87-[illegible], [illegible]

47. [illegible].L.Allaberdin et al., Sov.J.Nucl.Phys.39 (1984) 662,

48. [illegible].Allaberdin et al., Sov.J.Nucl.Phys. 39 (1984) 840.

49. C.Ce[illegible]i et al., Preprint INFN/AE-82/9, Sezione di Trieste, 1982.

Table 1. THE POSSIBLE DIBARYON CANDIDATES OBSERVED IN HADRON-NUCLEUS AND NUCLEON-NUCLEON INTERACTIONS

Reaction	Primary momentum, GeV/c	Mass of Dibaryons Candidate, *) MeV	Width, *) MeV	Ref.
1. $\pi^{-12}C \rightarrow pp + X$	4 - 40	(~ 1909)	($\leq$ 15)	[25,26,40,41]
2. $p^{20}Ne \rightarrow pp + X$	300	1922 ± 1.3 1940 ± 0.4 1954 ± 5.0 2017 ± 1.3	11 ± 3.6 10 ± 4.5 21 ± 20 5 ± 2	
3. $(p,d,\alpha,{}^{12}C) + {}^{12}C \rightarrow pp + X$	4.2 per nucleon	(~ 1904) (~ 1918) (~ 1935) (~ 1958) (~ 1970) (~ 2020)	($\leq$ 10) ($\leq$ 10) ($\leq$ 15) ($\leq$ 15) ($\leq$ 15) ($\leq$ 10)	[36]
4. $\pi^{\pm}\ {}^{20}Ne \rightarrow pp + X$	30	(~ 1905) (~ 1925) (~ 1940) (~ 1960)	($\leq$ 10) ($\leq$ 10) ($\leq$ 10) ($\leq$ 15)	[45]
5. $(\pi^{-}, A) + {}^{12}C \rightarrow pp + X$	4.2; 4.0	1926 ± 1.4 1964 ± 3.6 2026 ± 6.6	11.0 ± 1.9 32.4 ± 3.2 31.9 ± 5.2	[27]

Table 1. (continued)

6. $\pi^{-}\,{}^{12}C \to pp + X$	5.0	1981 ± 1 1965 ± 2 2016 ± 3 1989 ± 1	≤ 3 11 ± 4 30 ± 14 ≤ 9	[21,32]
7. $p + {}^{20}Ar \to pp + X$	1.0	(~ 1930) (~ 1960)	(≤ 10) (≤ 10)	[31]
8. $\pi^{-} +$ Freon $\to pp + X$ $\pi^{-} + {}^{20}Ne \to pp + X$	4.0 6.2	(~ 1910) (~ 1925)	(≤ 20) (≤ 30)	[33]
9. ${}^{4}He + p \to pp + X$	8.6	2035 ± 15	30 ± 23	[25]
10. $d + p \to pp + X$ $d + p \to nn + X$	3.3 3.3	2020 ± 10 2030 ± 20	45 ± 20 75 ± 20	[22]
11. $pd \to pp + X$ $pd \to pn + X$	0.8 - 1.0	1948 ± 9 2033 ± 9 1953 ± 3 2024 ± 5	39 ± 30 35 ± 9 34 ± 7 32 ± 11	[37]
12. $np \to pp + X$	1.25 - 5.1	1936 ± 3 1965 ± 2 (~ 2025)	$0.7 \pm {}^{1.0}_{0.7}$ $1.0 \pm {}^{2.0}_{1.0}$ 30	[24, 30,35]

*) The numbers in parentheses correspond to the position of peak in mass distribution

Table 2. THE AVERAGE MASSES OF POSSIBLE DIBARYONS

N	Mean Mass, MeV	Number of Experiments
1.	1907 ± 2	4
2.	1922 ± 5	7
3.	1936 ± 2	5
4.	1961 ± 2	10
5.	2025 ± 6	10

FIGURE CAPTIONS

Fig.1 The M(pp) distributions for protons with momenta of $0.22 \le p \le 0.40$ GeV/c in π^-C interactions from 4 to 40 GeV(a) and in pNe collisions at 300 GeV/c(b). The combined data are shown in Fig.1c. The dashed lines represent corresponding background spectra. The solid curve is the result of fit of combined spectrum by a sum of two Breit-Wigner functions and background distribution. A prediction of the intranuclear cascade model is shown by the dotted line. The dash-double-dotted curves correspond to fits of experimental data by smooth function $f(z) = Kz^{\alpha} \exp[-(\beta z + \gamma z^2)]$, where $z = M(pp) - 2m_p$.

Fig.2 The M(pp) distributions of different combinations of protons in $(p,d,\alpha,C)C$ interactions at 4.2 GeV/c per nucleon (for details see the text). The dashed curves represent background spectra.

Fig.3 The M(pp) spectra for protons with momenta $0.22 \le p \le 0.75$ GeV/c in π^-C interactions at 4(a) and 40 GeV/c(b) and in pNe collisions at 300 GeV/c(c). The combined data are shown in Fig.3d. The curve represents background.

Fig.4 The M(pp) distribution for protons with momenta of $0.22 \le p \le 0.40$ GeV/c in π^-Ne interactions at 30 GeV/c (from Ref.[45]).

Fig.5 The M(pp) distributions for protons with momenta of $0.30 \le p \le 0.75$ GeV/c in (π^-,p,d,α,C)+(C,Ne) interactions from 4 to 300 GeV/c(for details see in the text).

Fig.6 The M(pp) distributions in π^-C interactions at 5 GeV/c (from Refs[21,32]). The dashed lines correspond to a contribution of background.

Fig.7 The M(pp) spectrum in $(\pi^-,A)C$ interactions at 4.2 GeV/c (from Ref.[27]). A contribution of background is shown by the dashed line.

Fig.8 The M(pp) distribution of secondary protons produced in pAr interactions at 1.0 GeV/c(from Ref.[31]).

Fig.9 The M(pp) spectra in π^-Freon and π^-Ne interactions at 4.6 and 6.2 GeV/c(from Ref.[33]).

Fig.10 The M(pp) spectrum in dp interactions at 3.3 GeV/c (from Ref.[22]).

Fig.11 The two-nucleon effective mass distribution in Hep interactions at 8.6 GeV/c (from Ref.[23]).

Fig.12 The M(pn) (a) and M(pp) (b) spectra in pd interactions from 0.97 to 1.37 GeV/c (from Ref.[37]).

Fig.13 The two-proton effective mass distributions in reaction $np \to pp\pi^-$ at 1.25 GeV/c for events where $t_{n\to\pi^-} > 0.3$ GeV^2/c^2 (a) and $t_{n\to\pi^-} < 0.3$ GeV^2/c^2 (b) (from Refs [24,30,35]). The crosses show background spectrum.

Fig.14 The M(pp) distribution in np interactions at 5.1 GeV/c (from Ref.[30]). The crosses show background spectrum.

Fig.15 The "mass levels" of the possible dinucleon resonances.

Fig.16 The angular spectra of protons with momenta of $0.2 \le p \le 1.0$ GeV/c in semi-inclusive pNe interactions at [illegible] GeV/c. The solid lines represent results of fit to the simple exponential form : $f(\cos\theta) \sim \exp(B \cos\theta)$.

Fig.17 The ratio of inclusive cross sections of protons produced at $\vartheta_{lab} > 90°$ and at $0° \le \vartheta_{lab} \le 180°$ in π^-C and pNe interactions from 4 to 300 GeV/c.

Fig.18 The momentum (a-c) and the angular(a'-c') distributions of protons from "resonance" and "non-resonance" regions of M(pp) spectra in π^-C and pNe interactions from 4 to 300 GeV/c. The corresponding ratios "resonance to background" are shown in Figs.18d,d'.

Fig.19 The kinetic energy spectra of neutrons and protons produced in π^-C interactions at 113 MeV/c (from Ref.[49]).

Fig.20 The angular distributions of decay protons in the rest system of dibaryon candidates at masses M(pp)= 1922 MeV (a) and M(pp)= 1940 MeV (b). The curves represent best fits of data by functions corresponding to $J^P = 1^-$ and $J^P = 2^+$ states.

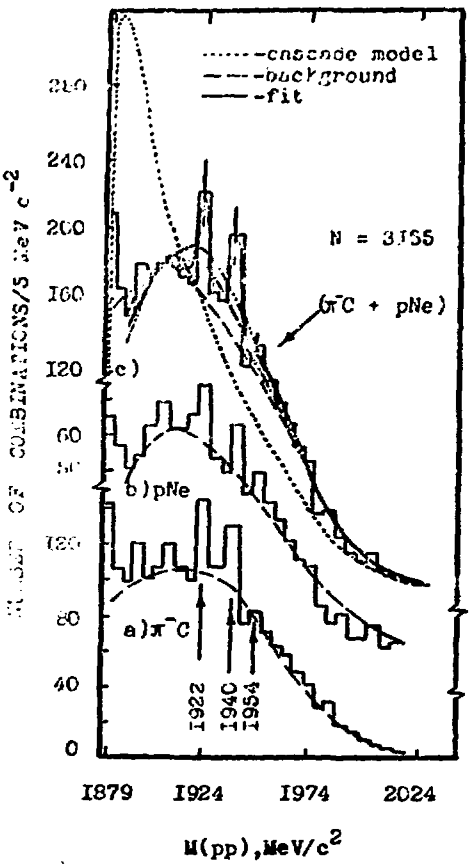
-cascade model
-background
-fit
240
200
160
120
60
80
40
0
c)
b)pNe
a)π^-C
(π^-C + pNe)
1922
1940
1954
1879
1924
1974
2024
M(pp),MeV/c^2

Fig.I.

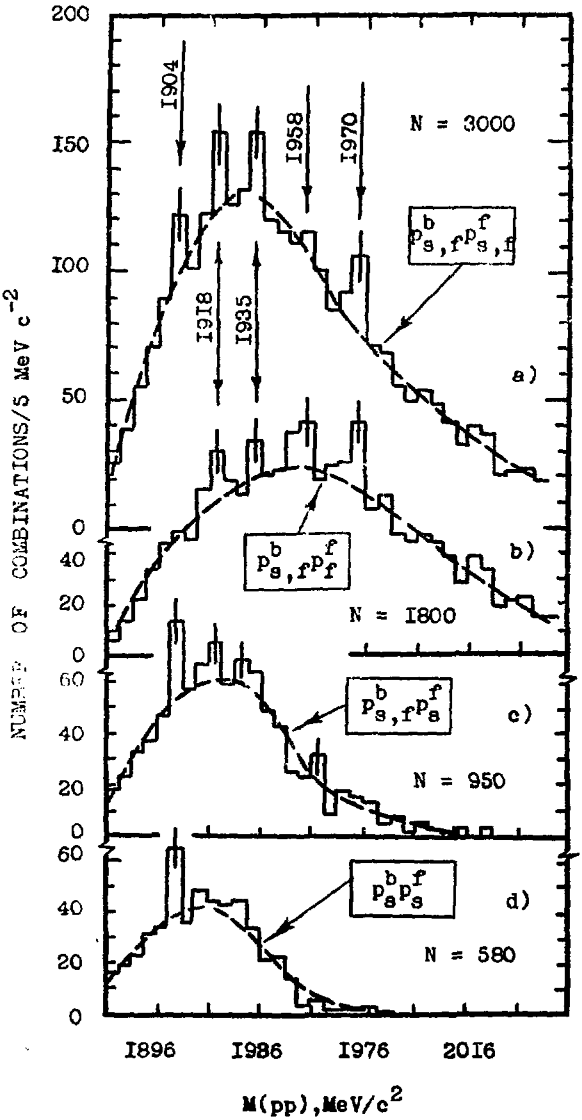

NUMBER OF COMBINATIONS/5 MeV c^{-2}
1904
1918
1935
1958
1970
N = 3000
$p^b_{s,f}p^f_{s,f}$
a)
$p^b_{s,f}p^f_f$
b)
N = 1800
$p^b_{s,f}p^f_s$
c)
N = 950
$p^b_s p^f_s$
d)
N = 580
1896
1986
1976
2016
M(pp),MeV/c^2

Fig.2.

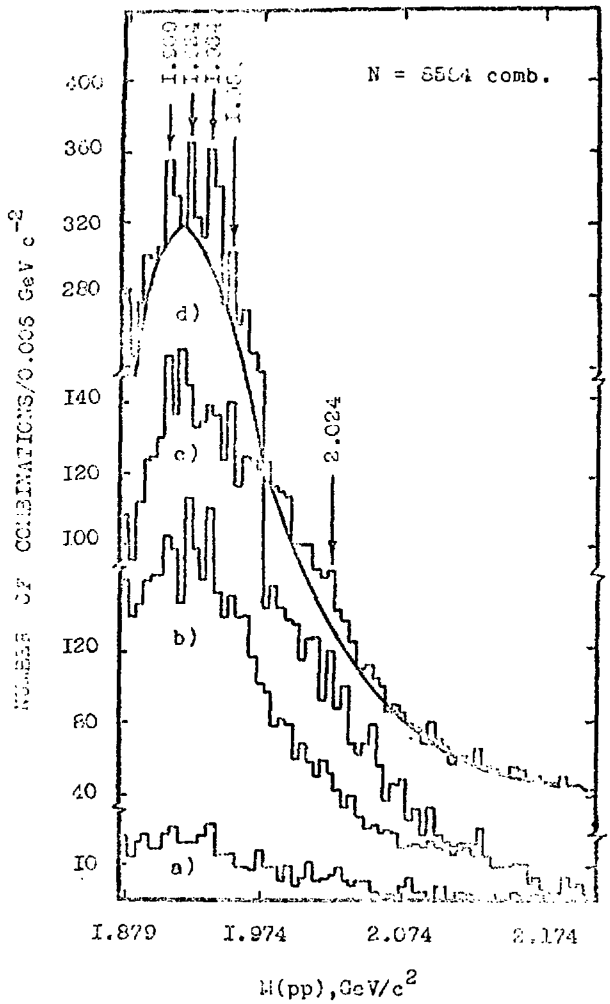
N = 8564 comb.
2.024
d)
c)
b)
a)
NUMBER OF COMBINATIONS/0.005 GeV c^{-2}
M(pp),GeV/c^2
I.879
I.974
2.074
2.174

Fig.3.

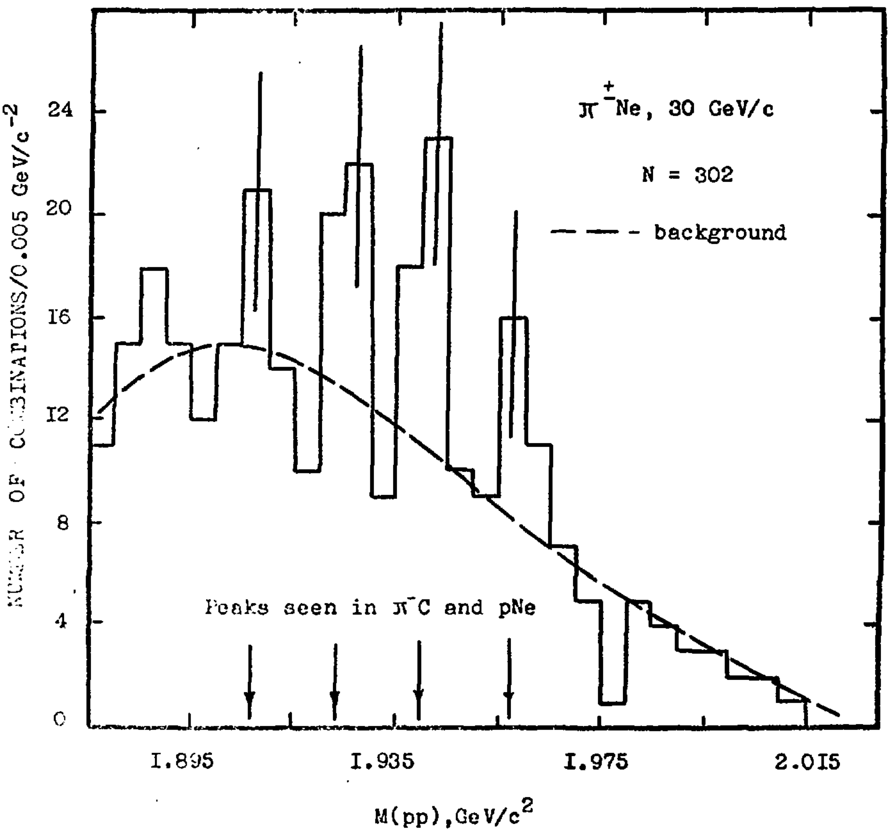

$\pi^{\pm}$Ne, 30 GeV/c
N = 302
background
Peaks seen in π^{-}C and pNe
NUMBER OF COMBINATIONS/0.005 GeV/c^{-2}
0
4
8
12
16
20
24
1.895
1.935
1.975
2.015
M(pp),GeV/c^2

Fig.4.

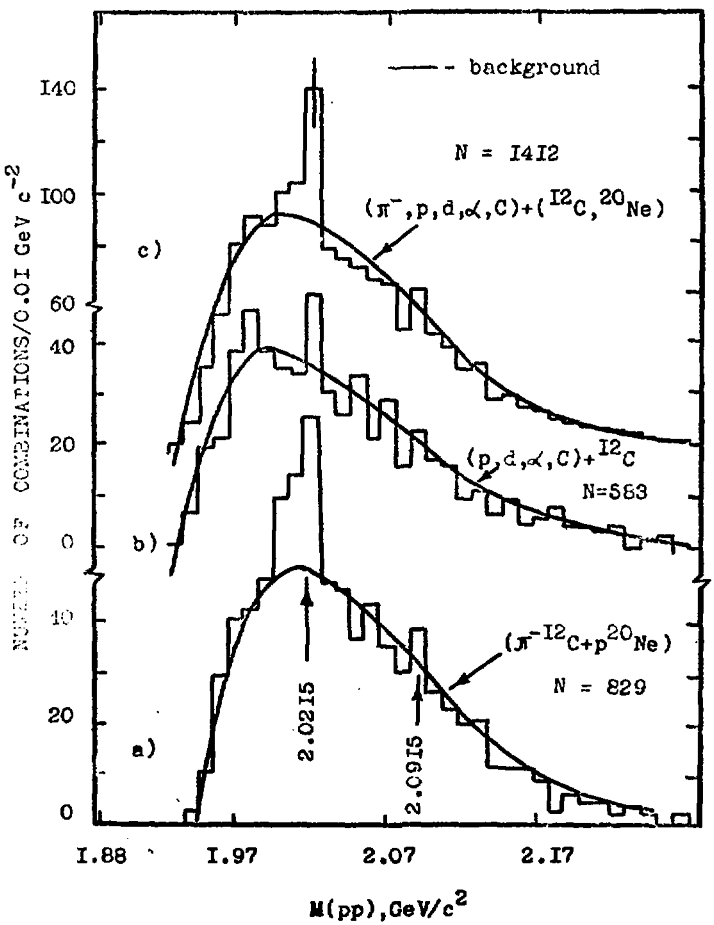

background
N = I4I2
(π⁻, p, d, α, C)+(I2C, 20Ne)
(p, d, α, C)+I2C
N=583
(π⁻I2C+p20Ne)
N = 829
2.02I5
2.09I5
c)
b)
a)
NUMBER OF COMBINATIONS/0.0I GeV c⁻²
M(pp), GeV/c²

Fig.5.

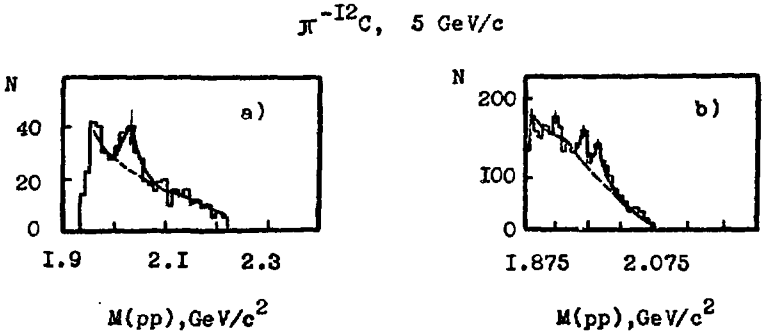

Fig.6.

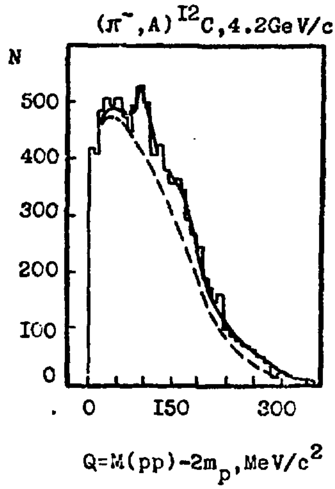

Fig.7.

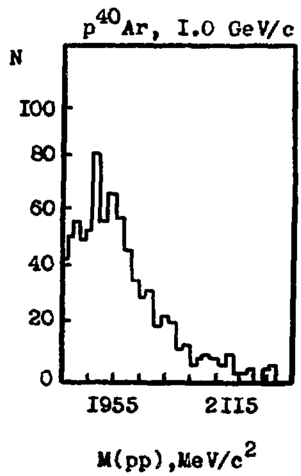

Fig.8.

π^-Freon, 4.6GeV/c

π^-Ne, 6.2 GeV/c

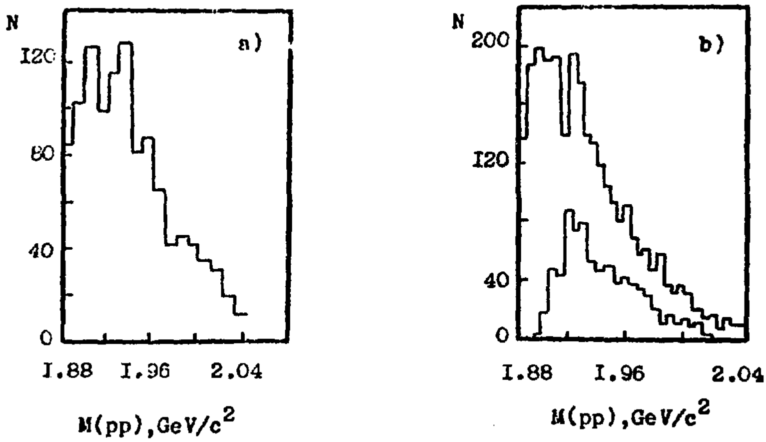

Fig. 9.

dp→ppn, 3.3GeV/c

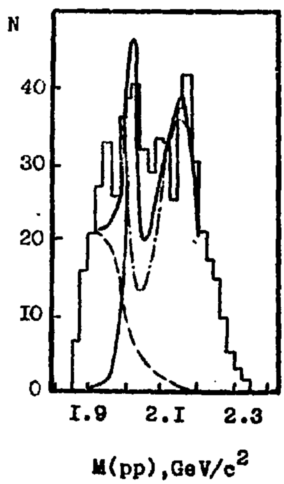

Fig. 10.

^{4}Hep→dppn, 8.6GeV/c

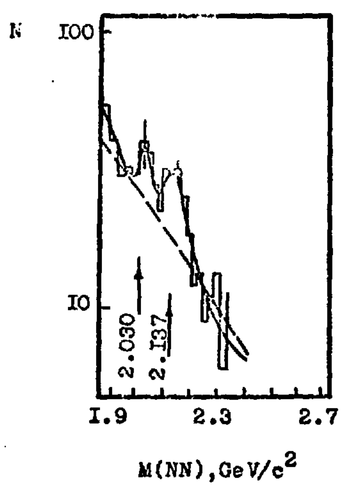

Fig. 11.

pd → ppn, (0.97 - I.37) GeV

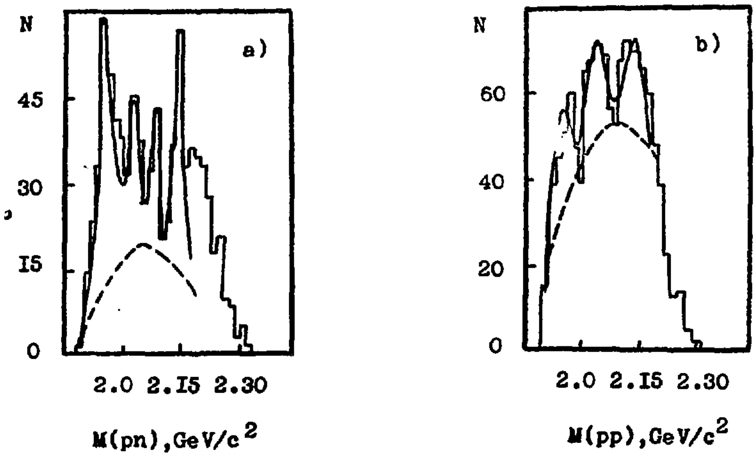

Fig.I2.

np,I.25 GeV/c

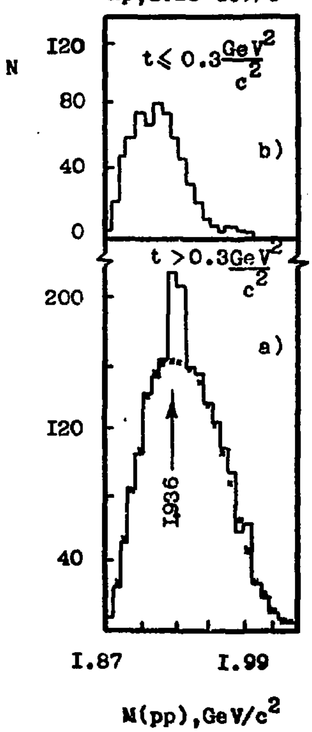

Fig.I3.

np, 5GeV/c

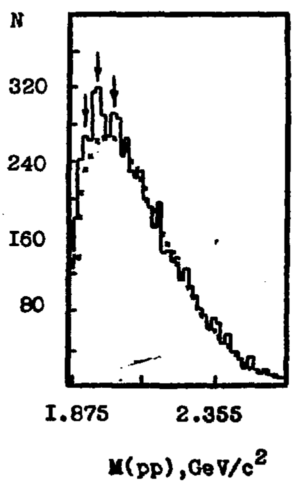

Fig.I4.

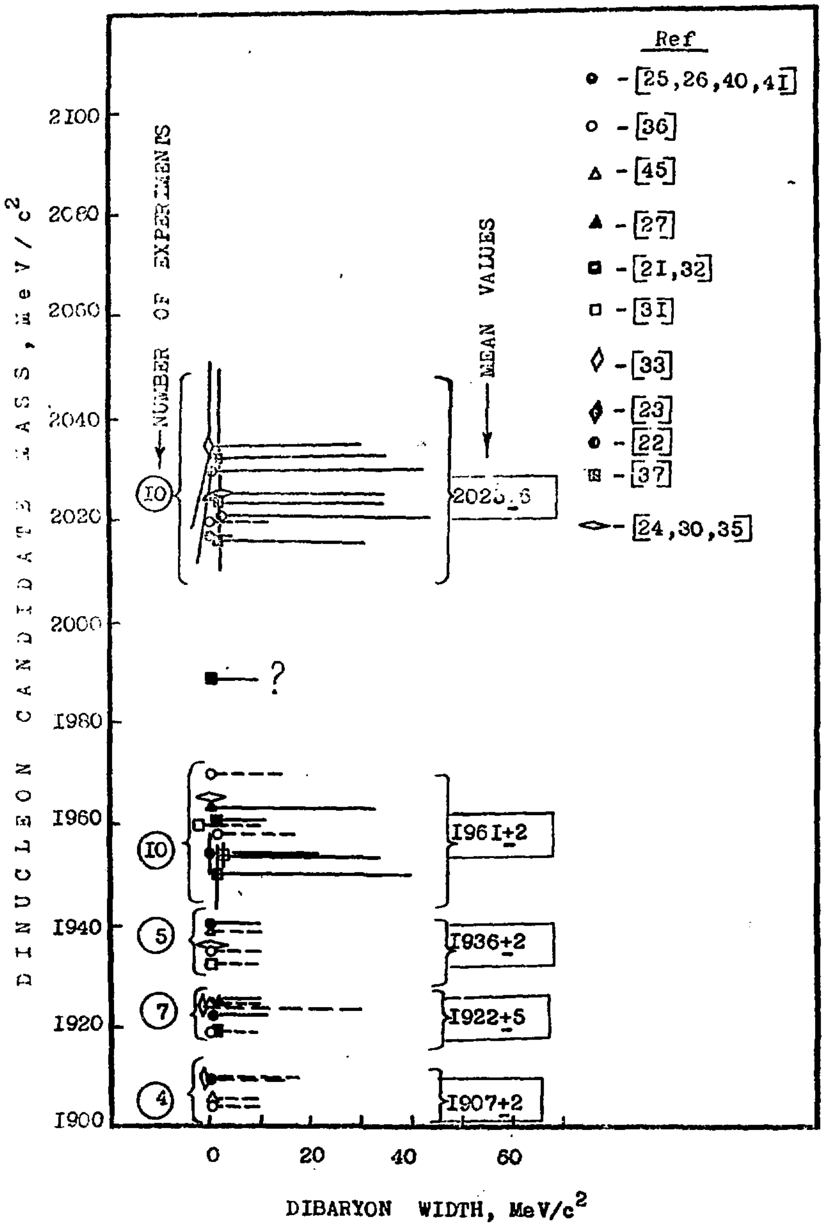

Ref
- [25,26,40,4I]
- [36]
- [45]
- [27]
- [2I,32]
- [3I]
- [33]
- [23]
- [22]
- [37]
- [24,30,35]
DINUCLEON CANDIDATE MASS, MeV/c²
NUMBER OF EXPERIMENTS
MEAN VALUES
2I00
2080
2060
2040
2020
2000
I980
I960
I940
I920
I900
IO
IO
5
7
4
?
I96I+2
I936+2
I922+5
I907+2
0
20
40
60
DIBARYON WIDTH, MeV/c²

Fig.I5.

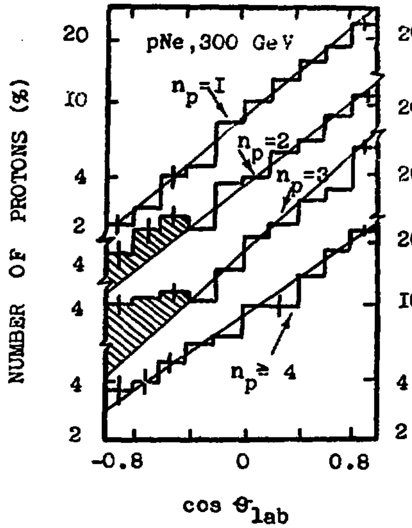
pNe,300 GeV
n_p=I
n_p=2
n_p=3
n_p≥ 4
NUMBER OF PROTONS (%)
cos θ_lab

Fig.I6.

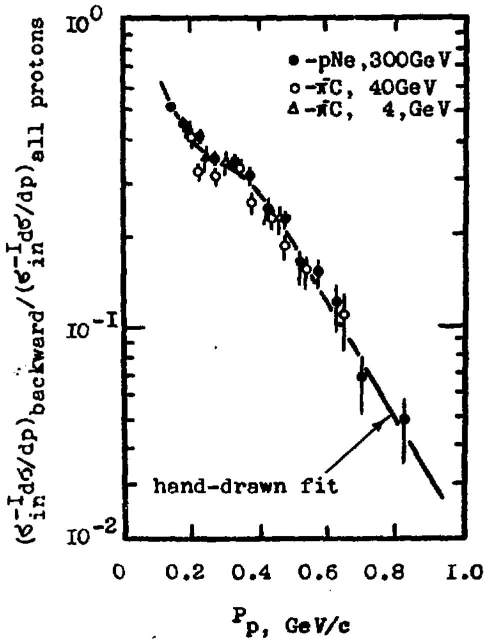
● -pNe,300GeV
o -π̄C, 40GeV
Δ -π̄C, 4,GeV
hand-drawn fit
P_p, GeV/c

Fig.I7.

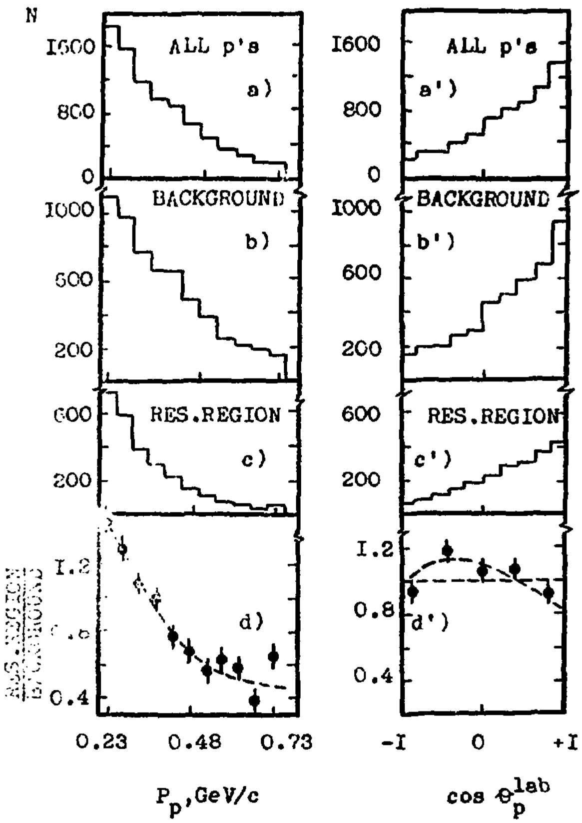
N
1600
800
0
1000
600
200
600
200
1.2
0.8
0.4
ALL p's
a)
BACKGROUND
b)
RES.REGION
c)
d)
RES.REGION/BACKGROUND
0.23
0.48
0.73
P_p,GeV/c
1600
800
0
1000
600
200
600
200
1.2
0.8
0.4
ALL p's
a')
BACKGROUND
b')
RES.REGION
c')
d')
-1
0
+1
$\cos \theta_p^{lab}$

Fig.18.

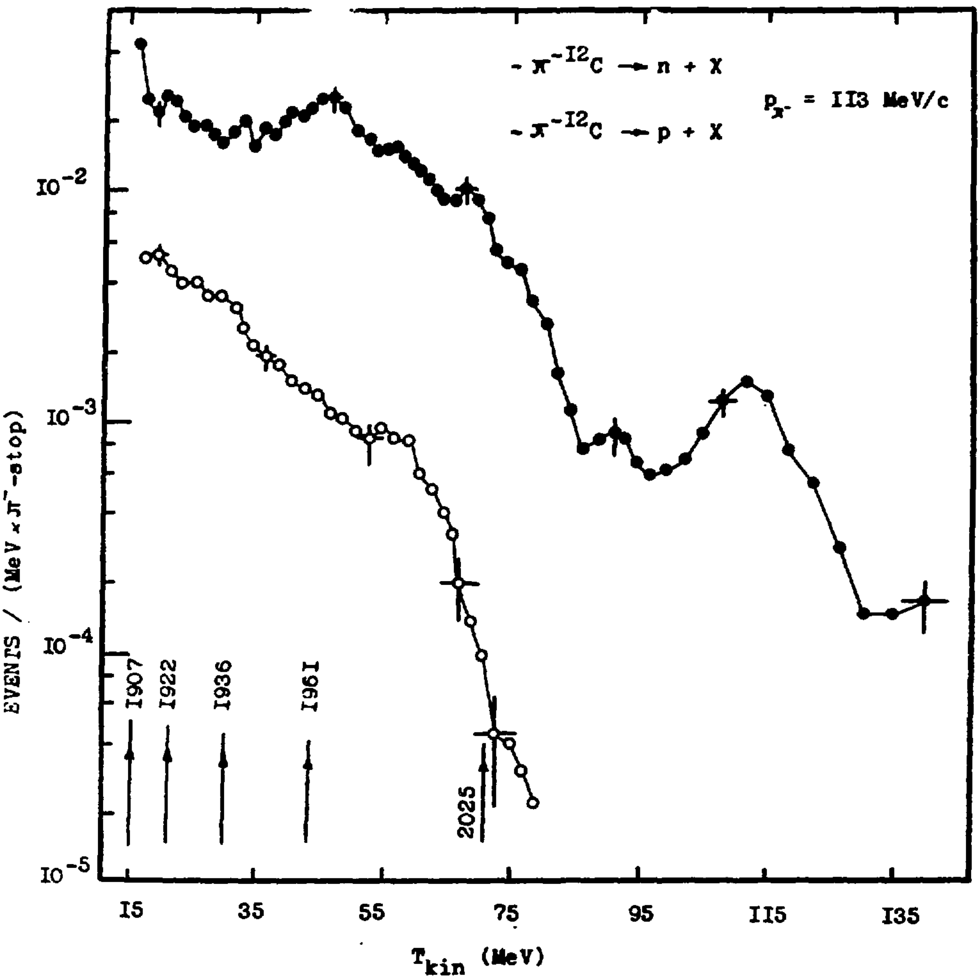

π^{-} ^{12}C → n + X
π^{-} ^{12}C → p + X
p_{π^-} = 113 MeV/c
EVENTS / (MeV × π^--stop)
10^{-2}
10^{-3}
10^{-4}
10^{-5}
1907
1922
1936
1961
2025
15
35
55
75
95
115
135
T_{kin} (MeV)

Fig.19.

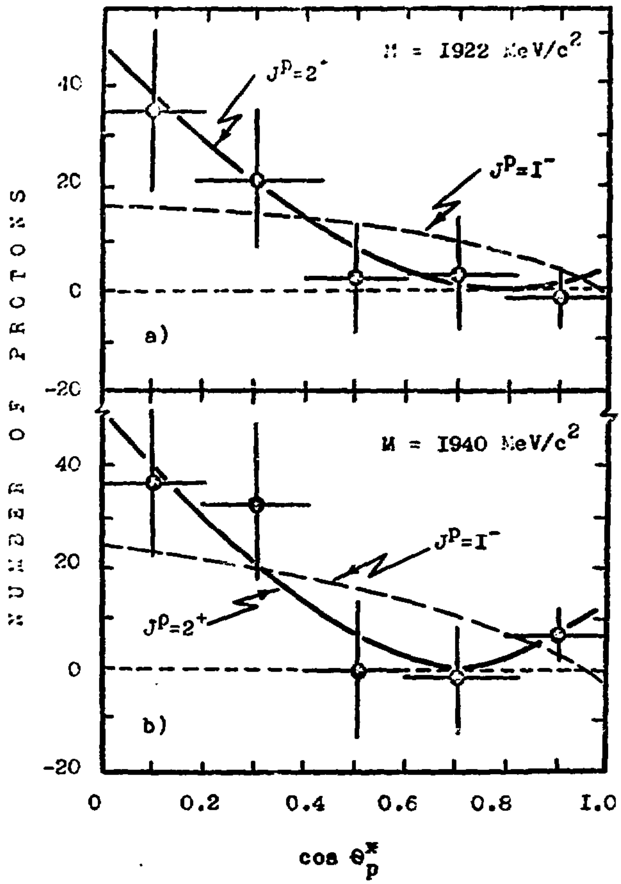
M = 1922 MeV/c^2
$J^P=2^+$
$J^P=1^-$
a)
M = 1940 MeV/c^2
$J^P=1^-$
$J^P=2^+$
b)
NUMBER OF PROTONS
40
20
0
-20
0
0.2
0.4
0.6
0.8
1.0
cos Θ_p^*

Fig.20.

RELATIVISTIC MODEL OF BARYON VALENCE-QUARK STRUCTURE: MAGNETIC MOMENTS AND AXIAL-VECTOR COUPLINGS

Zbigniew Dziembowski, Tomasz Dzurak, and Adam Szczepaniak
Institute of Theoretical Physics, Warsaw University
Hoza 69, PL-00-681 Warszawa, Poland

Lech Mankiewicz
Nicolaus Copernicus Astronomical Centre of Polish Academy of Sciences, Bartycka 18, PL-00-716 Warszawa, Poland

Presented by A.Szczepaniak

ABSTRACT

The magnetic moments of the baryon octet are calculated in a relativistic constituent quark model formulated in the light-cone Fock approach. Invoking a natural idea of strangeness dependent hadron size we find very good agreement (to an accuracy of 1σ) for the recent precision hyperon magnetic-moment data and reveal (10-15)% discrepancy for the Σ^- and nucleon. It suggests pions as a missing ingredient in the baryon magnetic moment calculations. In addition, the axial-vector couplings, the axial-vector form factor of the nucleon and pion-nucleon coupling are calculated.

Recently a positive progress has occurred in our understanding of the composition of hadrons in terms of their quark quanta. Several powerful nonperturbative methods have been developed which allow detailed predictions for the hadronic wave functions directly from QCD. Sum rule analysis of Chernyak and Zhitnitsky [1] and lattice gauge theory calculations [2] have demonstrated that the nucleon and pion valence-quark distribution amplitudes are highly structured and significantly broader than the nonrelativistic δ-function form. In a recent work [3-4] we have attempted to bridge the results of nonperturbative QCD methods and the quark model approach. Three ideas turn out to be vital for a successful derivation of the basic features of the CZ distribution amplitude, i.e., (a) the use of the light-cone Fock approach, (b) a nonstatic relativistic spin wave function, and (c) small transverse size of the valence-quark configuration. The presented model, together with the concept of scale dependent effective quark mass provides a consistent description of the measured high momentum transfer form factors, the CZ distribution amplitudes, and some basic low energy nucleon and pion properties [5].

The purpose of this paper is to investigate some other predictions of the new relativistic approach. Thus, we present an extension of the nucleon wave function to the case of strange particles and discuss magnetic moments of the nucleon octet. The motivation for the work is provided by new, accurate data [6] on the magnetic moments of the charged Σ and Ξ hyperons, along with substantial discrepancies between the data and the static quark-model predictions. Let us quote as a typical example of the static model results the prediction by Rosner [7]. Table 1 shows a comparison with the recent experimental data. There are already model-independent analyses of the observed disagreement, due to Franklin [8] and Lipkin [9]. They come to the conclusion that a good understanding of baryon magnetic moments will require a model with quark-moment contributions which are nonstatic and/or baryon dependent. A role of relativistic effects in the context have also been emphasized by several authors [10-11].

Table 1. Baryon magnetic moments (in nuclear magnetons) in the static constituent quark model (CQM).

Baryon moments	Experiment	Static CQM
$\mu(p)$	2.793+0.000	2.79
$\mu(n)$	-1.913+0.000	-1.86
$\mu(\Lambda)$	-0.613+0.004	-0.58
$\mu(\Sigma^+)$	2.379+0.020	2.68
$\mu(\Sigma^-)$	-1.14+0.05	-1.05
$\mu(\Xi^o)$	-1.250+0.014	-1.40
$\mu(\Xi^-)$	-0.69+0.04	-0.47

We use the light-cone formalism [12] which provides a consistent relativistic framework in momentum space in terms of Fock-state basis defined at equal-$x^+ = t + z$, rather then the conventional equal-t wave functions. With the valence-quark-dominance assumption baryon wave functions is taken to be simple generalization of the nonrelativistic constituent quark model one. In view of the relativistic motion of quarks, the momentum distribution is taken to be as a relativistic Gaussian [12]

$$\phi(x_i, \vec{k}_{\perp i}) = A \exp[- \frac{1}{6\alpha_D^2}\sum \frac{\vec{k}_{\perp i}^2 + m_i^2}{x_i}] \qquad (1)$$

The baryon states of interest have two identical quarks (except those of the Λ) which we shall label with i = 1 and 2. The overall symmetry of the wave function in momentum, spin, and flavor spaces then implies that the spin-flavor wave functions for B = p, n, Σ^+, Σ^-, Ξ^o, and Ξ^- are symmetric under exchange of 1 and 2, but for the Λ it is antisymmetric. Thay have the form

$$\chi_{\uparrow}^{B}(x_i,\vec{k}_{\perp i},\lambda_i) = J_{\uparrow}(\hat{1},\hat{3},\hat{2}) + J_{\uparrow}(\hat{2},\hat{3},\hat{1}), \tag{2a}$$

with

$$J_{\uparrow}(\hat{1},\hat{2},\hat{3}) = \bar{u}_{\lambda_1}(M_B + P_\mu\gamma^\mu)\,\gamma_5\, v_{\lambda_2}\,\bar{u}_{\lambda_3}\,u_{\uparrow},$$

and for the Λ

$$\chi_{\uparrow}^{\Lambda}(x_i,\vec{k}_{\perp i},\lambda_i) = \bar{u}_{\lambda_1}(M_\Lambda + P_\mu\gamma^\mu)\,\gamma_5\, v_{\lambda_2}\,\bar{u}_{\lambda_3}\,u_{\uparrow}, \tag{2b}$$

$\hat{1}$, $\hat{2}$, and $\hat{3}$ are collective momentum-helicity indices $(x_i,\vec{k}_{\perp i},\lambda_i)$, $i = 1,2,3$. u_λ and v_λ are the light-cone spinors of ref. [13]. We keep flavor and color implicit. The nonstatic spin wave functions (2) are obtained from conventional wave functions with $J^P = \frac{1}{2}^+$ transformed to the light-cone using a Melosh-type rotation of the quark spinors [4].

The resultant Lorentz-invariant light-cone wave functions are

$$\psi_{\uparrow}^{B}(\hat{1},\hat{2},\hat{3}) = \phi(x_i,\vec{k}_{\perp i})\ \chi_{\uparrow}^{B}(x_i,\vec{k}_{\perp i},\lambda_i)/(\prod_i x_i)^{1/2} \tag{3}$$

Their normalizations are given by

$$2\int [dx\ d^2k_\perp]\ \sum \left|\psi_{\uparrow}^{B}(\hat{1},\hat{2},\hat{3})\right|^2 = 1$$

The $[dx\ d^2k_\perp]$ is the volume element in momentum space. We emphasize the point made earlier that the nucleon wave function of the form (3), together with the small transverse size hypothesis provides the essential features of the CZ distribution amplitudes.

We start by discussing the magnetic moments. The anomalous magnetic moment of any spin-1/2 system can be identified [14] from the spin-flip matrix element of the electromagnetic current j^μ

$$\Gamma^{+}_{\uparrow\downarrow} = \langle B(P+q,\uparrow)\,|\frac{j^+(0)}{P^+}|\,B(P,\downarrow)\rangle$$

$$= \sum\int [dx\ d^2k_\perp]\ \psi_{\uparrow}^{+B}(\hat{1}',\hat{2}',\hat{3}')\,\frac{\bar{u}_m}{\sqrt{k_m^+}}\,\gamma^+ Q_m\,\frac{u_m}{\sqrt{k_m^+}}\,\psi_{\downarrow}^{B}(\hat{1},\hat{2},\hat{3}) \tag{4}$$

where Q_m is the charge of the struck quark with the final momentum $\vec{k}'_{\perp m} = \vec{k}_{\perp m} + (1 - x_m)\vec{q}_\perp$ while the spectator quark have final momentum $\vec{k}'_{\perp i} = \vec{k}_{\perp i} - x_i\,\vec{q}_\perp$ for $i \neq m$. Note, that we neglect the quark anomalous magnetic moments. If the light-cone coordinates are chosen [15] as $P^\mu = (P^+, M_B^2/P^+, 0_\perp)$ for the baryon moving along the z-axis and $q^\mu = (0, 2P\cdot q/P^+, \vec{q}_\perp)$ for the photon, the helicity-flip matrix element of the current $j^+ = j^0 + j^3$ have the simple form

$$\Gamma^{+}_{\uparrow\downarrow} = -\,q_L\,F_2(q^2)/M_B$$

where $q_L = q^1 - iq^2$ is used for the transverse momentum transfer. Hence, the anomalous magnetic moment $a = F_2(0)$ becomes

$$a = -M_B\,\frac{\partial}{\partial q_L}\,\Gamma^{+}_{\uparrow\downarrow}\Big|_{q=0} \tag{5}$$

It was pointed out by several authors [16] that the spinor rotation of constituent quarks, arising from a Lorentz transformation associated with the boost P^μ to $P^\mu + q^\mu$, gives rise to sizable corrections to baryon magnetic moments. Note that the Drell-Yan formula (4) is especially suited to study the effects. It is related to the following advantages obtained by using the light-cone formalism: (i) There is no Wigner-like rotation in (4). (ii) The wave function (3) is invariant under all kinematical Lorentz transformations, that contain the Lorentz boost along the 3-directions. Thus the simple and exact boost treatment, together with the proper relativistic kinematics of the internal relative motion present in (4), apparently invalidate the ordinary independent-quark-model additivity assumption. To illustrate numerical importance of the effects we use the basic wave functions (3) and formula (5) to calculate the baryon magnetic moments.

The parameters entering our expressions for the magnetic moments are the quark masses and the momentum scale α_B which determines the size of baryon valence wave function. We assume that quarks in baryons have typical constituent masses. To be specific we use the values $m_u = m_d = 363$ MeV and $m_s = 538$ MeV given by Rosner's fit to baryon masses. For the momentum scale we have decided to vary it freely in the range 300 - 500 MeV, in order to show explicitly the dependence on this parameter. The results for the seven measured magnetic moments are given in table 2. Before being compared with experiment, the Λ moment have to be corrected for $\Lambda-\Sigma^0$mixing [17], which changes $\mu(\Lambda)$ by about -0.04 n.m.

Table 2. Baryon magnetic moments (in nuclear magnetons) in the relativistic CQM as functions of the baryon momentum scale α_B (in MeV)

α_B	$\mu(p)$	$\mu(n)$	$\mu(\Lambda)^{a)}$	$\mu(\Sigma^+)$	$\mu(\Sigma^-)$	$\mu(\Xi^0)$	$\mu(\Xi^-)$
300	2.737	-1.686	-0.638	2.481	-1.00	-1.330	-0.60
320	2.718	-1.663	-0.635	2.464	-1.00	-1.320	-0.61
340	2.697	-1.640	-0.631	2.446	-1.00	-1.309	-0.61
360	2.676	-1.615	-0.627	2.428	-1.00	-1.297	-0.62
380	2.653	-1.590	-0.623	2.408	-0.99	-1.284	-0.62
400	2.629	-1.564	-0.619	2.389	-0.99	-1.272	-0.63
420	2.605	-1.538	-0.614	2.368	-0.99	-1.258	-0.64
440	2.580	-1.511	-0.609	2.347	-0.98	-1.245	-0.65
460	2.554	-1.484	-0.604	2.325	-0.98	-1.231	-0.65
480	2.528	-1.457	-0.598	2.303	-0.98	-1.217	-0.65
500	2.502	-1.429	-0.592	2.281	-0.98	-1.202	-0.66

a) Value corrected for the effect of $\Lambda-\Sigma^0$mixing of ref. [17].

General characteristic exhibited by these results are briefly discussed below:

(a) In the nucleon sector, the theoretical predictions are, for any scale α_N, too small compared to the experimental values. If we take the nucleon momentum scale be equal to, say $\approx$ 320-360 MeV, as in ref.[5], then we must consider other effects to account for the missing 10-15% in the observed proton and neutron magnetic moments.

(b) In the strange baryon sector a remarkable regularity can be observed. We note that the measured magnetic moments of all hyperons but the Σ^- can be reproduce (to an accuracy of 1σ) if one allow α_B to increase with strangeness. This fit yields the hyperon momentum scale of $\alpha_\Sigma \approx \alpha_\Lambda \simeq 420$ MeV and $\alpha_\Xi \approx 440$ MeV. For the Σ^- our relativistic calculation gives value discrepant by $\simeq 0.1$ n.m. which is several times the standard deviations of the recent data both from fine-structure splitting in Σ^- exotic atoms [18] and beam-polarization-precession technique [19]. Thus one again has another case which suggests the importance of some other contributions.

Let us mention that a similar features are observed in the relativistic model calculation of the hyperon axial-vector couplings. The calculation of axial-vector form factors, is essentially identical to that of the EM form factor in eq. (4) except of the replacement $\gamma^+ \rightarrow \gamma_5 \gamma^+$. The prediction on G_A/G_V for measured transitions [20] are given in table 3. Again the relativistic calculation with a dependence of the hadron size on the number of strange quarks provides very good (to an accuracy of 2σ) description of the data. In addition, in figs. 1 and 2 we present the axial-vector form factor of the nucleon and pion-nucleon coupling versus q^2.

Table 3. Baryon axial-vector couplings in the relativistic COM.

α	Transition	$\Xi^- \rightarrow \Lambda$	$\Sigma^- \rightarrow \Lambda$	$\Lambda \rightarrow p$	$\Sigma^- \rightarrow n$
	Experiment a)	0.25+0.05	0.03+0.08	0.70+0.03	-0.34+0.05
300		0.33	0	0.83	-0.28
400		0.32	0	0.71	-0.24
500		0.30	0	0.58	-0.20

a) Ref. [20]

To understand intuitively the observed hierarchy of the baryon spatial sizes (which decrease with strangeness) we note that for a Coulomb-like potential the bound state size is proportional to m^{-1}, where m is the reduced mass. Thus, in potential models one can anticipate a decrease of the hadron size when adding strange quark. In ref. [10] Isgur and Karl quote a decrease by 4% and 13% per additional strange quark in a harmonic and Coulomb potential, respectively.

Our main conclusion therefore is that the relativistic COM, together with the concept of strangeness dependent baryon size, offers a large quantative improvement over the nonstatic description of the hyperon magnetic moments. With the large baryon-dependent non-additive magnetic moment contributions the model fulfills the requirements of general quark-model analyses of refs. [8] and [9]. The residual disagreement just for the Σ^- and nucleon suggests the nature of the dominant missing ingredient in the baryon wave functions. It is known from work of several authors [21] that for those three baryons magnetic moment contributions from a nonvalence $q\bar{q}$ component with pion quantum numbers are of numerical importance.

REFERENCES
[1] V.L.Chernyak and A.R.Zhitnitsky, Phys. Rep. 112 (1979) 173; Nucl. Phys. B201 (1982) 492; V.L.Chernyak and I.R.Zhitnitsky, Nucl.Phys. B246 (1984) 52.
[2] I.D.King and C.T.Sachrajda, Nucl. Phys. B279 (1987) 785; G.Martinelli and C.T.Sachrajda, Phys.Lett. B190 (1987) 151.
[3] Z.Dziembowski and L.Mankiewicz, Phys. Rev. Lett. 58 (1987) 2175.
[4] Z.Dziembowski, Warsaw University Preprints IFT/24/87 and IFT/25/87.
[5] Z.Dziembowski,Warsaw University Preprint IFT/26/87; Z.Dziembowski and L.Mankiewicz, in Proceedings of the Second International Conference on Hadron Spectroscopy, Hadron'87, edited by K.Takamatsu (KEK, Tsukuba, Japan, 1987), p.222; J.Bienkowska, Z.Dziembowski, and H.J.Weber, Phys. Rev. Lett. 59 (1987) 624.
[6] M.Aguilar-Benitez et al.(Particle Data Group), Phys. Lett. 170B (1976) 1.
[7] J.Rosner,In High Energy Physics-1980, edited by L.Durand and L.G.Pondrom, AIP Conference Proceedings No 68 (American Institute of Physics, New York, 1981).
[8] J.Franklin, Phys.Rev. D20 (1979) 1742, and D29 (1984) 2648.
[9] H.Lipkin, Phys. Rev. D24 (1981) 1437, and Nucl. Phys. B214 (1983) 136.
[10] N. Isgur and G.Karl, Phys. Rev. D21 (1980) 3175.
[11] J.Franklin, Phys. Rev. Lett. 45 (1980) 1607; H.Georgi and A.Manohar, Phys. Lett. 132B (1983) 183; Z.Dziembowski and L.Mankiewicz, Phys. Rev. Lett. 55 (1985) 1839.
[12] S.J.Brodsky, T.Huang, and G.P.Lepage, in Quarks and Nuclear Forces, edited by D.Fries and B.Zeitnitz, Springer Tracks in Modern Physics, Vol. 100 (Springer-Verlag, Berlin, 1982); J.M.Namysłowski, Prog. Part. Nucl. Phys. 14 (1984) 49.
[13] G.P.Lepage. and S.J.Brodsky, Phys. Rev. D22 (1980) 2175.
[14] S.J.Brodsky, and S.D.Drell, Phys. Rev.D22 (1980) 2236.
[15] S.D.Drell and T.N.Yan, Phys. Rev. Lett. 24 (1970) 181.
[16] W-Y.P.Hwang, Z. Phys. C16 (1983) 327; I.Picek and D.Tadic, Phys. Rev. D27 (1983) 665.
[17] R.H.Dalitz and F.von Hippel, Phys. Lett. 10 (1964) 153; A.J.Macfarlane and E.C.G.Sudarshan, Nuovo Cimento 31 (1964) 1176; J.Franklin, D.Lichtenberg, W.Namgung, and D.Carydas, Phys. Rev. D24 (1981) 2910.
[18] D.W.Hertzog et al., Phys. Rev. Lett.51 (1983) 1131.
[19] G.Zapalec et al., Phys. Rev. Lett. 57 (1986) 1526.
[20] M.Bourquin et al., Z. Phys. C21 (1983) 27.
[21] J.O.Eeg and H.Pilkuhn, Z. Phys. A287 (1978) 407; G.E.Brown, M.Rho, and V.Vento, Phys. Lett. 97B (1980) 434; F.Myhrer,

ibid. 125B (1983) 359; G.E.Brown and F.Myhrer, ibid. 128B (1983) 229; S.Theberge and A.W.Thomas, Nucl. Phys. A393 (1983) 252; Z.Dziembowski and L.Mankiewicz. Phys. Rev. D36 (1987) .

[22] A.Del Guerra et al., Nucl. Phys. B107 (1976) 365; W.A.Mann et al., Phys. Rev. Lett. 31 (1973) 844; S.Barish et al., Phys. Rev. D16 (1979) 3103; N.J. Baker et al., Phys. Rev. D23 (1981) 2499.

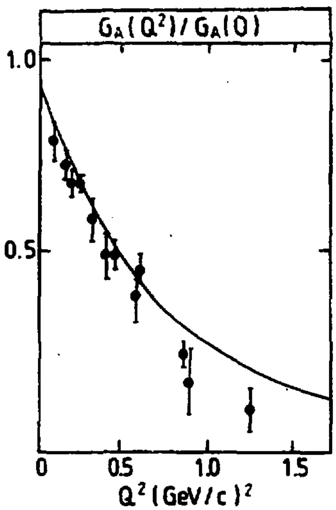

Fig.1 Axial-vector form factor versus q^2. The data are from ref. 22,

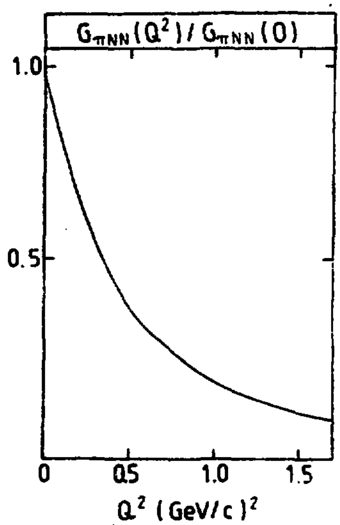

Fig.2 Pion-nucleon form factor.

LEADING HEAVY FLAVOURED BARYON PRODUCTION AT THE ISR

(BCFL Collaboration)
G.Anzivino, G.Bari, M.Basile, G.Cara Romeo, L.Casaccia, L.Cifarelli,
F.Cindolo, A.Contin, G.D'Ali, C.Del Papa, S.De Pasquale, P.Giusti,
G.Iacobucci, I.Laakso, G.Maccarrone, T.Massam, R.Nania, F.Palmonari,
E.Perotto, G.Prisco, P.Rotelli, G.Sartorelli, G.Susinno, L.Votano,
M.Willutzky and A.Zichichi

Dipartimento di Fisica dell'Università, Bologna, Italy
Istituto Nazionale di Fisica Nucleare, Bologna, Italy
CERN, Geneva, Switzerland
Dipartimento di Fisica dell'Università, Cosenza, Italy
Istituto Nazionale di Fisica Nucleare, LNF, Frascati, Italy
Dipartimento di Fisica dell'Università, Lecce, Italy
Istituto di Fisica dell'Università, Palermo, Italy

(presented by R. Nania)

The production of heavy flavoured baryons, Λ_c^+ and Λ_b^0, has been studied in pp interactions at the ISR. Both baryons are observed in the forward region, for $x_F \geq 0.35$. The results confirm the heavy baryon production to be governed by the "leading hadron" effect. The cross-section for $(\bar{D}\Lambda_c^+)$ associated production has been estimated with various hypotheses concerning the possible charm production mechanisms. A preliminary cross-section value is also given for $(\bar{B}\Lambda_b^0)$ production.

1. INTRODUCTION

In this report are presented new results on charmed and beautyful baryon production in pp interactions at $\sqrt{s} = 62$ GeV. Data were collected in experiment R422 that, with increased statistic and solid angle, represented a continuation of our past R415 experiment, also performed at the ISR in similar conditions and at the same energy[1-6]. The characteristic of both experiments was their capability to trigger on high p_t single leptons (electrons or positrons), likely originated from the semileptonic decay of heavy flavoured states (antistates), and to search for the associated antistates (states) via an invariant mass analysis of their hadronic decay into charged particles. The reactions studied were the following.
For charm:

$$p + p \rightarrow \bar{D} + \Lambda_c^+ + X \qquad (1a)$$

$$\hookrightarrow e^- + X$$

where the Λ_c^+, the lightest charmed baryon with quark composition "udc", is detected via the 3-body hadronic decay into strange

$$\Lambda_c^+ \rightarrow pK^-\pi^+ \qquad (1b)$$

For beauty:

$$p + p \rightarrow \bar{B} + \Lambda_b^0 + X \qquad (2a)$$

$$\hookrightarrow e^+ + X$$

where the Λ_b^0, the lightest beauty baryon with quark composition 'udb', is detected by means of its hadronic decay into charm either via the 4-body channel

$$\Lambda_b^0 \rightarrow pD^0\pi^- \qquad \text{(2b)}$$
$$\rightarrow K^-\pi^+$$

or the 6-body channel

$$\Lambda_b^0 \rightarrow \Lambda_c^+\pi^+\pi^-\pi^- \qquad \text{(2c)}$$
$$\rightarrow pK^-\pi^+$$

The results presented here refer to the observation of charm and beauty baryon signals, to the study of their production mechanisms and to the estimate of their cross-sections.

2. DATA TAKING AND FILTER

The set-up used in R422 experiment has already been described elsewhere[7-8]. It consisted of the well known Split Field Magnet (SFM) spectrometer, equipped in the 90° regions with respect to the beam axis by two powerful electron detectors: a Lead Scintillator sandwich calorimeter[9] and, symmetric with respect to the first one, a Lead Limited Streamer Tube sandwich calorimeter [10], the latter being the only difference with respect to the old R415 set-up.

The total number of collected events by means of the 90° single electron trigger was 3.3×10^7, corresponding to an integrated luminosity $L = 1.27\times 10^{37}\ cm^{-2}$. The data were submitted to a refined electron filter analysis whose reduction power was of the order of 10^{-2}. For details about the analysis procedure, we refer the reader to References 7-8. The events surviving the off-line filter were fully reconstructed and the electron track was required to originate from the common event vertex. In more than 99% of the events, only one electron track was present and satisfied all conditions imposed.

The background level in the remaining sample of $\simeq 4.5\times 10^5$ electron and positron triggers with $p_t > 0.5$ GeV/c was estimated from calibration runs and Monte Carlo studies[7]. About 50% of the final leptons were due to lepton pair contamination (external γ conversions and π^0, η Dalitz decays) and to known sources such as Compton effect or $K_{\ell 3}$ decay, while the residual contribution from charged hadrons was at the few percent level. This implied that the ratio $e_{genuine}/e_{background}$ was approximately 1:1. The overall lepton detection efficiency was 0.28 ± 0.05 (for $p_t \geq 1$ GeV/c), taking into account both the on-line trigger and the off-line analysis. For charged hadrons, this was 1.5×10^{-5}.

About 20% of the final event sample contained a 'leading' proton which, in pp interactions, can be easily identified[11] as the fastest positively charged particle with $x_F > 0.3$ (where $x_F = 2|p_L|/\sqrt{s}$ is the Feynman variable). This 'leading' proton was used in the invariant mass analysis of heavy baryon decays.

3. Λ_c^+ ANALYSIS

3.1 Invariant mass study

Only particles associated to the event vertex (within ± 5 cm), with $\Delta p/p < 30\%$, were retained. The $(pK^-\pi^+)$ triplets of decay (1b) consisted of a 'leading' proton (see Section 2) plus any two particles of the appropriate charge, belonging to the same x_F hemisphere as the proton and having rapidity $|Y| > 1.2$. These particles were respectively assigned the proton, kaon and pion masses unless contrarily identified by the TOF system (which, due to its small solid angle coverage and limited momentum range for identification, acted as a veto only at the few percent level). Due to the above specified conditions for $(pK^-\pi^+)$ selection, the search for Λ_c^+ only applied to the forward region, i.e. for $|x_F(\Lambda_c^+)| \geq 0.35$. This region, as suggested by previous findings[1,4], is particularly efficient for heavy baryon detection due to the well-known "leading" baryon [illegible]ect in pp interactions[12], which holds true not only for the proton itself but also for other bar[illegible] [illegible]aining valence quarks of the incident proton ("ud" in the Λ_c^+ case). For what concerns the le[illegible] [illegible]ger it was required a ($\Delta p/p < 15\%$) in order to avoid any charge ambiguity.

Figure 1a shows the ($pK^-\pi^+$) invariant mass plot obtained in the presence of an e^-. The same plot, for e^+, is shown in Fig.1b.

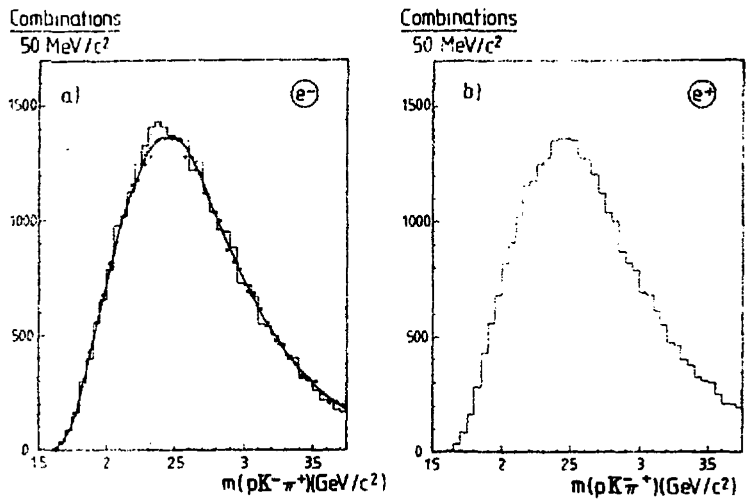

FIGURE 1

The ($pK^-\pi^+$) invariant mass spectrum: a) e^- trigger, b) e^+ trigger. The full-line curve and the points superimposed in a) represent the estimated background (i.e. the e^+ trigger spectrum) normalized to the total area outside the Λ_c^+ region, $2.10 < m(pK^-\pi^+) < 2.50$ GeV/c^2.

An excess of 330 ± 100 mass combinations is visible in Fig.1a, in the interval ($2.25 \div 2.45$) GeV/c^2. The central value of this interval, 2.35 GeV/c^2, is shifted by $\simeq 70$ MeV/c^2 with respect to the nominal Λ_c^+ mass (2.28 GeV/c^2). This shift is attributed to local systematic effects, both on momenta and angles, caused by field mapping (of the highly inhomogeneous SFM) and alignment (of the many individual wire chambers) problems, which had already been observed in the past R415 experiment[1]. The background curve superimposed in Fig.1a is derived from the spectrum of Fig.1b normalized to the mass region where no signal is expected. It has been checked that this spectrum is indeed well reproduced by the "event-mixing" technique. It should be pointed out that the interpretation of the effect in Fig.1a as a Λ_c^+ signal strongly relies on the fact that this signal disappears in the "wrong" charge, e^+ triggered spectrum of Fig.1b.

In order to improve the signal/background ratio, more stringent $\Delta p/p$ cuts were applied to the three p, K, π particles and a limit was set on the maximum allowed number of ($pK^-\pi^+$) combinations/event. Moreover, a higher transverse momentum ($p_t > 0.65$ GeV/c) for the e^- and the presence of a "leading" system in the hemisphere opposite to the ($pK^-\pi^+$) triplet (following the hint of a possible "long range" correlation in the Λ_c^+ forward production[1]) were required. The result is shown in Fig.2 where a clear peak of 81 ± 24 combinations is obtained, corresponding to a signal/background ratio of $\simeq 1/3$. The width of this signal is compatible with the expected mass resolution.

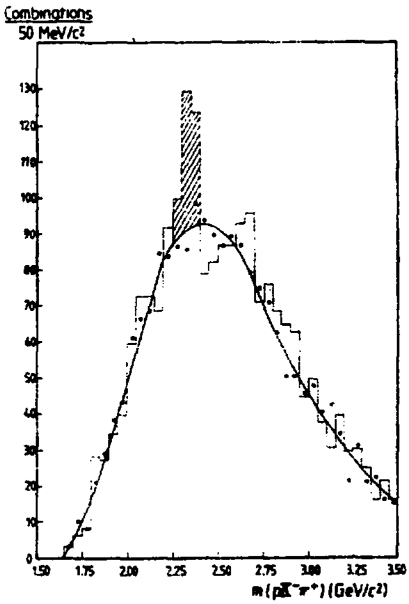

FIGURE 2
The Λ_c^+ invariant mass spectrum obtained with more stringent conditions, as described in the text. The background (curve and points superimposed) is derived as for Fig.1a, by means of the e^+ triggered spectrum.

3.2 Production distributions

From the signal of Fig.1a, the p_t and x_F distributions of the Λ_c^+ were derived using the in−out technique [2,3,8]. The transverse momentum distribution was fitted as $dN/dp_t^2 \propto e^{-bp_t}$, with $b = 2.6 \pm 0.5$ (GeV/c)$^{-1}$, in excellent agreement with our previous result[2].

The longitudinal momentum distribution could be parametrized as $dN/dx_F \propto (1-x_F)^a$, with $a = 2.3 \pm 1.3$. This value indicates a rather flat x_F production distribution for the Λ_c^+, as expected from R415 results[3,6]. The above value of b has been recently confirmed by another experiment at the ISR[13], where $b = 2.0 \pm 0.5$ was measured.

3.3 Cross-section estimates

Table 1 gives the model dependent ($\bar{D}\Lambda_c^+$) cross-section estimates obtained by assuming $(Ed\sigma/dx_F dp_t^2) \propto (1-x_F)^3\, e^{-2.5p_t}$ for the $\bar{D}$ and $(d\sigma/dx_F dp_t^2) \propto f(x_F)\, e^{-2.5p_t}$ for the Λ_c^+, with various hypotheses concerning the $f(x_F)$ parametrization. The branching ratios $B(\Lambda_c^+ \to pK^-\pi^+) = (2.2 \pm 1.1)\%$[14] and $B(\bar{D} \to e^- X) = (12.25 \pm 1.1 \pm 0.6)\%$[15] have been used. For the baryon, a Lorentz-invariant phase-space decay was assumed, while for the antimeson a 3-body (V−A) decay matrix was used in the calculation[16]. The hypothesis of no correlation between the $\bar{D}$ and the Λ_c^+ was made[17].

Λ_c^+ model	$\sigma_{partial}$ (μb) $[x_F > 0.35]$	σ (μb)
i) $d\sigma/dx_F$ = const.	36±22	56±34
ii) $d\sigma/dx_F \propto (1-x_F)^1$	59±35	128±77
iii) $d\sigma/dx_F \propto (1-x_F)^2$	84±50	285±171
iv) $d\sigma/dx_F \propto (1-x_F)^5$	166±100	1450±870

TABLE 1

Cross-section estimates for $pp \to (\bar{D}\Lambda_c^+) + X$, derived with different hypotheses on the Λ_c^+ longitudinal production distribution.

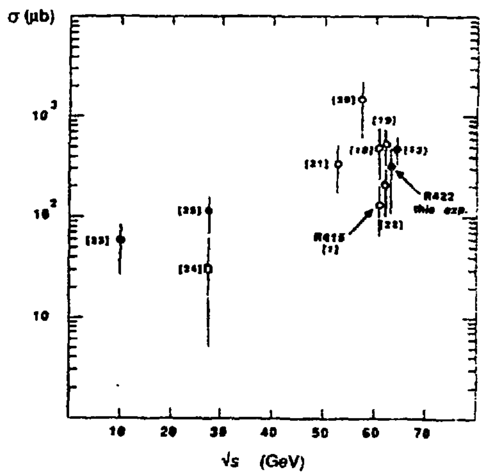

FIGURE 3
Compilation of Λ_c^+ cross-section estimates in pp interactions as a function of $\sqrt{s}$ [o: $d\sigma/dx_F(\Lambda_c^+)$ = constant; •: $d\sigma/dx_F(\Lambda_c^+) \approx d\sigma/dx_F(\Lambda^0)$; □: model independent].

From Table 1 one sees that a central meson-like behaviour for $f(x_F)$ causes a prohibitive increase of the cross-section (model "iv"). When $f(x_F)$ has a rather flat behaviour (models "i", "ii" or "iii"), the cross-section is of the order of ≈ 100 μb. Figure 3 shows a compilation of existing Λ_c^+ cross-section measurements in pp interactions[1,13,18–25], as a function of $\sqrt{s}$. The σ values of R422 (model "iii") and of R415[1] (model "i") are in good agreement within the errors. All measurements in Fig.3 (except one[24] which is model independent) are obtained assuming a rather flat x_F behaviour for the Λ_c^+, i.e.

a 'leading' baryon production mechanism. Also notice that they all refer to ($pK\pi$) or ($\Lambda\pi\pi\pi$) decays, for which a common branching ratio value of $\approx 2\%$ was assumed. If this value, based on a unique measurement[14], is underestimated*, all cross-section values would consequently be overestimated.

Figure 4 shows the $d\sigma/dx_F$ distribution of the Λ_c^+ (model 'iii'). The corresponding Λ^0 and $\bar{\Lambda}^0$ distributions, as measured at the ISR in another experiment[26], are also shown. The $\bar{\Lambda}^0$ distribution clearly differs from both the Λ^0 and Λ_c^+ distributions (as expected since the antibaryon does not contain any valence quark of the incident proton, while both the Λ_c^+ and Λ^0 contain two valence quarks). The strange and charmed baryon distributions have similar shapes. The ratio $(d\sigma/dx_F)_{\Lambda_c^+}/(d\sigma/dx_F)_{\Lambda^0}$ turns out to be about 1/40 in the high x_F region.

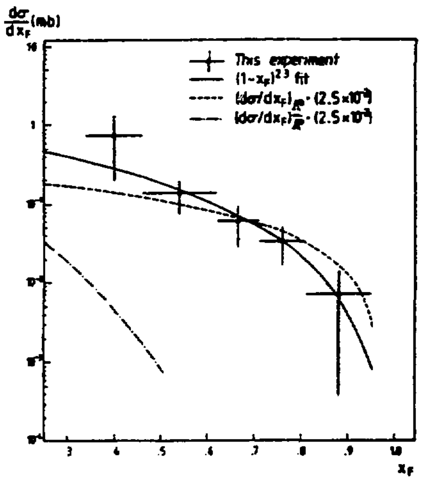

FIGURE 4
The estimated $d\sigma/dx_F$ behaviour for the Λ_c^+ (full line) in this experiment, compared to Λ^0 (dashed line) and $\bar{\Lambda}^0$ (dashed-dotted line) production, as given by a fit of the data of Reference 26.

4. Λ_b^0 *ANALYSIS*

4.1 [$p(K^-\pi^+)\pi^-$] invariant mass study

The 4-body system [$p(K^-\pi^+)\pi^-$] of decay (2b) was required to belong to events where an e^+ was present with a high transverse momentum, $p_t > 0.8$ GeV/c, and a momentum uncertainty $\Delta p/p < 15\%$. For the 'leading' proton, defined in Section 2, $\Delta p/p < 8\%$ was required. The K^-, π^+, π^- were any three particles with $\Delta p/p < 30\%$ and the appropriate charges. The proton, kaon and pion masses were assigned, unless a TOF veto was found (see Section 3.1). Here again all four particles, plus the positron, had to originate from the reconstructed event vertex within ± 5 cm. The 4-body combinations selected in this way were then submitted to the following conditions:

– to have a rapidity $Y_{4-body} > 1.4$ (this condition, coupled to the 'leading' proton identification method, was used to enhance the expected forward baryon yield);

* This has been recently suggested by LEBC-EHS experiment[24].

– to contain at least one particle belonging to the hemisphere opposite to that of the proton (this requirement, corresponding to the involvement of large angles in the 4-body invariant mass, was intended to increase the acceptance in the higher mass region);
– to be correlated to a resonant ($K^-\pi^+$) charm contribution from the D^0 meson. This was achieved by operating a scan of the ($K^-\pi^+$) invariant mass spectrum by intervals 150 MeV/c^2 wide in the neighbourood of the D^0 nominal mass (1.86 GeV/c^2).
Figure 5a shows the $m[p(K^-\pi^+)\pi^-]$ spectrum corresponding to $m(K^-\pi^+)$ in the (1.90 ÷ 2.05) GeV/c^2 interval (this will be referred to as the "IN" interval from now on). The same spectrum, obtained instead for "wrong" e^- triggers, is superimposed in Fig.5a after normalization to the mass regions well below and above the enhancement. No signal shows up in this case* and the spectrum provides the background shape. As a cross-check, Fig.5b shows the normalized $m[p(K^-\pi^+)\pi^-]$ spectra, corresponding to e^+ and e^- respectively, but with $m(K^-\pi^+)$ falling in any of the two intervals, (1.75 ÷ 1.90) and (2.05 ÷ 2.20) GeV/c^2, below and above the IN interval. After background subtraction, the signal of Fig.5a corresponds to 52± 16 combinations, with a ratio combinations/events of ≃ 1.3. Its width, ≃200 MeV/c^2, agrees with the expected 4-body mass resolution.

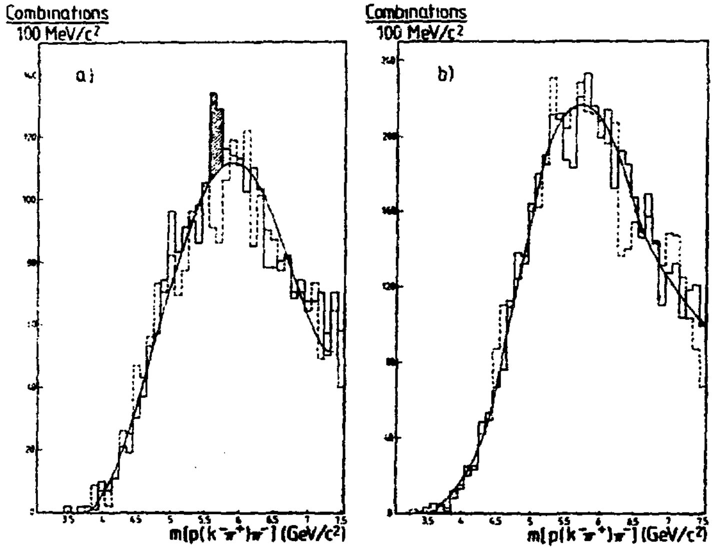

FIGURE 5
The $[p(K^-\pi^+)\pi^-]$ invariant mass. The full-line histogram corresponds to e^+ triggers, the dashed-line histogram to e^- triggers: a) $1.90 \leq m(K^-\pi^+) < 2.05$ GeV/c^2 (IN interval); b) $1.75 \leq m(K^-\pi^+) < 1.90$ GeV/c^2 and $2.05 \leq m(K^-\pi^+) < 2.20$ GeV/c^2. The curves superimposed are fits to the e^- triggered spectra.

---

* In principle a Λ_b^0 signal could also be present in association with an e^- coming from $\bar{B} \to \bar{D} \to e^- X$ decay. However, Monte Carlo studies predict that, with $p_t(e) > 0.8$ GeV/c, a factor of ≃8 less events should be expected in the e^- case, with respect to e^+ (from the direct $\bar{B} \to e^+ X$ decay).

Notice that, as already observed for the Λ_c^+, the central value of the IN interval, 1.975 GeV/c², is shifted upwards by ≈100 MeV/c² with respect to the nominal D^0 mass. Such a shift can again be attributed to systematic effects, as explained in Section 3.1. Therefore, the signal of Fig.5a can indeed be interpreted as due to the $\Lambda_b{}^0$ baryon, detected through decay (2b), at the mass (5.65 +0.10 −0.21) GeV/c². The above D^0 mass shift has been included in the quoted errors. This value agrees within few percents with the one previously measured in similar conditions and through the identical decay channel in R415 experiment[4].

4.2 $[(pK^-\pi^+)\pi^+\pi^-\pi^-]$ invariant mass study

For decay (2c) the single particles were selected as in Section 4.1. Further conditions were imposed on the 6-body system:

– to have a rapidity $Y_{6-body} > 1.7$ (here again "leading" conditions were required);

– to belong to very high multiplicity events, i.e. with $n_{charged} > 12$ (this was motivated by the non negligible multiplicity of the decay system itself);

– to be related to a visible energy in the opposite x_F hemisphere with the condition $.25 < |\Sigma x_F| < .65$;

– to correspond to a resonant $(pK^-\pi^+)$ charm system. All these three particles were required to belong to the same hemisphere and here again a scan was made of the $m(pK^-\pi^+)$ spectrum, by intervals 200 MeV/c² wide, this time around the Λ_c^+ nominal mass value.

The resulting 6-body invariant mass spectra are shown in Fig.s 6a and 6b, which are analogous to Fig.s 5a and 5b.

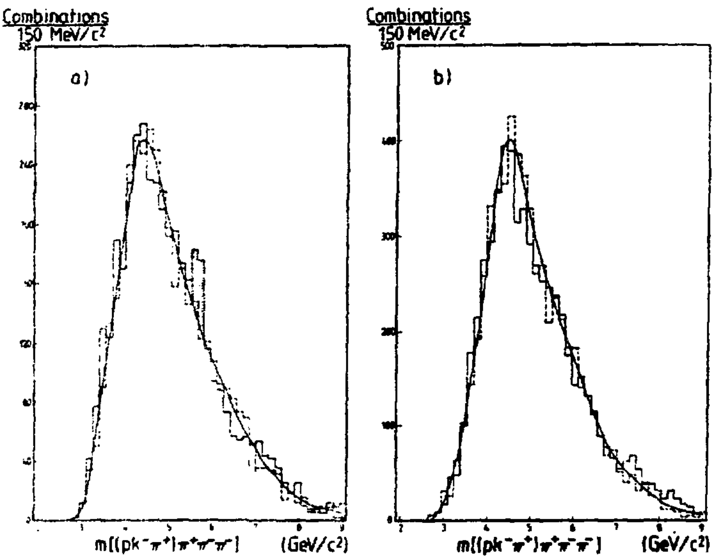

FIGURE 6

The $[(pK^-\pi^+)\pi^+\pi^-\pi^-]$ invariant mass. The full-line histogram corresponds to e^+ triggers, the dashed-line histogram to e^- triggers: a) $2.23 \le m(pK^-\pi^+) < 2.43$ GeV/c² (IN interval); b) $2.03 \le m(pK^-\pi^+) < 2.23$ GeV/c² and $2.43 \le m(pK^-\pi^+) < 2.63$ GeV/c². The curves superimposed are fits to the e^- triggered spectra.

An enhancement is visible in the $m[(pK^-\pi^+)\pi^+\pi^-\pi^-]$ spectrum of Fig.6a, in the region $(5.5 \div 5.8)$ GeV/c^2, only for e^+ triggered events when $2.23 \leq m(pK^-\pi^+) < 2.43$ GeV/c^2 (IN interval). It corresponds to (90 ± 19) combinations, with a combinations/events ratio of $\simeq 2.5$ (a value higher than in Section 4.1 due to the increased decay multiplicity). The peak width is now $\simeq 300$ MeV/c^2. The central value of the IN interval (which contains the Λ_c^+ nominal mass value) is 2.33 GeV/c^2. It should be noticed that, in this case also, this value is shifted upwards by $\simeq 50$ MeV/c^2 with respect to the nominal Λ_c^+ mass. The mass of the signal in Fig.6a, once the Λ_c^+ mass shift is taken into account, can be quoted as $(5.65\ +0.15\ -0.20)$ GeV/c^2, in excellent agreement with the mass value derived by means of the D^0 decay channel (2b) of Section 4.1. Due to its characteristics, the 6-body signal of Fig.6a can again be interpreted as an evidence for the observation of the Λ_b^0 in a different decay channel.

4.3 Λ_b^0 mass

A summary of the theoretical situation concerning the Λ_b^0 mass estimates is given in Reference 27. Five theoretical predictions obtained in the framework of potential models are reported, together with their corresponding lower and upper bounds. The corresponding average Λ_b^0 mass value is $(5.59\ +0.07\ -0.21)$ GeV/c^2. The weighted average relative to the three experimental (R415 and R422) measurements is $(5.57\ +0.23\ -0.22)$ GeV/c^2. Despite the errors involved, from these numbers we can easily conclude that there is a very significant agreement between experiment and theory. An additional theoretical value, obtained instead using "scalar lattice QCD"[28], strongly disagrees both with the previously quoted theoretical estimates and with the experimental measurements.

4.4 Cross-section estimates

A preliminary attempt has been made to estimate the $(\bar{B}\Lambda_b^0)$ cross-section for reaction (2a). Only the data of the D^0 decay channel (2b) have been used. The hypotheses assumed for the $\bar{B}$ and the Λ_b^0 are identical to those relative to the $\bar{D}$ and the Λ_c^+ in Section 3.3: for the antimeson, a "central" production, and, for the baryon, a "leading" production (model "1", see Table 1). In first approximation, the transverse momentum distribution of charm ($d\sigma/dp_t \propto e^{-2.5p_t}$) has been applied to the beauty case*. For the branching ratios, the following values have been taken: $B(\bar{B} \to e^+X) = (12.3 \pm 0.8)\%$[30] and $B(D^0 \to K^-\pi^+) = (5.4 \pm 0.4)\%$[30]. Only a partial cross-section will be given here, working out the acceptance of the apparatus under the same conditions (see Section 4.1) which allowed the Λ_b^0 to be observed, i.e. $Y[p(K^-\pi^+)\pi^-] > 1.4$ and $x_F(p) > 0.3$. The result is $B(\Lambda_b^0 \to pD^0\pi^-) \cdot \sigma_{partial} = (0.15 \div 0.5)\ \mu b$. The same value, in the past R415 experiment[5], once the corrections for the updated $D^0 \to K^-\pi^+$ branching ratio and for slight analysis differences are applied, is $(0.45 \div 1.25)\ \mu b$. The present $B \cdot \sigma_{partial}$ value is lower due to the fact that the number of observed Λ_b^0 events is a factor of $\simeq 3$ smaller than what expected from R415 extrapolation.

5. CONCLUSIONS

The results of experiment R422 are a confirmation of R415 results. The Λ_c^+ baryon is again observed with increased statistics. Its p_t and x_F production distributions compare well with previous findings. Also the open beauty state Λ_b^0 is newly observed, by means of two different decay channels. Its mass (averaged over R422 and R415 measurements) is found to be $\simeq 5.6$ GeV/c^2, in very good agreement with theoretical predictions. The "leading" effect dominates charm and beauty baryon production in pp interactions. Finally, the cross-section estimates indicate, once more, that heavy flavours are copiously produced in the ISR energy range.

---

* A different parametrization, like $e^{-0.85p_t}$, could be used[29]. This would lead to a lower cross-section value due to the presence of the $p_t > 0.8$ GeV/c cut for the e^+.

REFERENCES

1) M.Basile et al., Nuovo Cimento 63A (1981) 230.
2) M.Basile et al., Nuovo Cimento Lett. 30 (1981) 481.
3) M.Basile et al., Nuovo Cimento Lett. 30 (1981) 487.
4) M.Basile et al., Nuovo Cimento Lett. 31 (1981) 97.
5) M.Basile et al., Nuovo Cimento 65A (1981) 391.
6) M.Basile et al., Nuovo Cimento 65A (1981) 408.
7) M.Basile et al., Nuovo Cimento 65A (1981) 421.
8) G.Anzivino et al., "A new measurement of Λ_c^+ baryon production in proton-proton interactions at $\sqrt{s} = 62$ GeV", preprint CERN-EP (1987), in preparation.
9) M.Basile et al., Nucl. Instr. and Meth. 169 (1979) 93.
10) M.Basile et al., Nucl. Instr. and Meth. 235A (1985) 74.
11) P.Capiluppi et al., Nucl. Phys. B70 (1974) 1.
12) M.Basile et al., Nuovo Cimento 66A (1981) 129.
13) A.Medinnis, private communication.
14) MARK II, G.S.Abrams et al., Phys. Rev. Lett. 44 (1980) 10.
15) MARK III, R.M.Baltrusaitis et al., Phys. Rev. Lett. 54 (1985) 1976.
16) A.Ali and E.Pietarinen, Nucl. Phys. B154 (1979) 519.
17) LEBC-EHS, M.Aguilar-Benitez et al., Phys. Lett. 164B (1985) 404.
18) K.L.Giboni et al., Phys. Lett. 85B (1979) 437.
19) J.Irion et al., Phys. Lett. 99B (1981) 495.
20) W.Lockman et al., Phys. Lett. 85B (1979) 443.
21) D.Drijard et al., Phys. Lett. 85B (1979) 452.
22) M.Heiden, Thesis, University of Heidelberg, FRG (1981).
23) BIS-2, A.N.Aleev et al., Zeit. Phys. C23 (1984) 333.
24) LEBC-EHS, M.Begalli et al., submitted to Phys. Lett. (1987), and A.Goshaw, private communication.
25) T.Aziz et al., Nucl. Phys. B199 (1982) 424.
26) S.Erhan et al., Phys. Lett. 85B (1979) 447.
27) A.Martin and J.M.Richard, preprint CERN-TH 4584/86.
28) S.Samuel and K.J.M.Moriarty, Phys. Lett. 175B (1986) 197.
29) Y.Afek, C.Leroy and B.Margolis, Phys. Rev. D22 (1980) 86.
30) M.Aguilar-Benitez et al., "Review of particle properties", Phys. Lett. 170B (1986) 1.

CHARM PHOTOPRODUCTION IN THE NA14-II EXPERIMENT

NA14-II Collaboration: Athens Technical University, Universidad Autonoma Barcelona, CERN, Imperial College London, Orsay LAL, Paris Collège de France, Saclay, Southampton University, Strasbourg CRN et Université Louis Pasteur, Warsaw University.

presented by D. BLOCH, CRN Strasbourg, France.

Abstract:

The aim of the CERN-NA14-II experiment is the study of charm photoproduction mechanisms and the lifetime measurement of charmed mesons. The peculiarity of this experiment is the combined use of a microvertex silicon detector where primary and secondary vertices are measured with a high precision, and a large acceptance spectrometer where charged tracks and photons are fully analysed and identified. We present preliminary results based on a part of the total statistics acquired in 1985-1986.

Experimental details:

The experiment was performed in the E12 e-γ beam at the CERN SPS. The NA14 spectrometer, whose complete description can be found elsewhere(1), was previously operated for the study of the deep inelastic Compton scattering(2). Now it is associated with a silicon active target and a stack of microstrip hodoscopes (Fig. 1).

The bremsstrahlung photon beam is provided in 3 steps $p \to \gamma\ (\pi^0) \to e^- \to \gamma$ which allow a large reduction of the hadronic contamination ($h/\gamma \sim 10^{-5}$) and the energy measurement for photons above 50 GeV. The high flux photon beam (1.2×10^7 γ/cycle > 50 GeV, mean energy≈80 GeV) is incident on a silicon active target of 10 % X_0, installed in a 1 T·m magnet which sweeps the electromagnetic background.

Primary interaction and charm decays occur in this target composed of 32 silicon planes of 300 μm thickness and 200 μm interspace, each segmented in 24 vertical strips of 2.1 mm wide (Fig. 2)(3). The particle multiplicity is measured in each strip allowing: to reject electromagnetic events and those with a secondary interaction, to reconstruct independently the main vertex when "grey tracks" from the target nucleus are emitted, to flag secondary vertices by a jump in multiplicity (Fig. 5a).

Immediately 1 cm downstream of the target is a stack of 10 microstrip planes comprising 4 Y-Z and 1 U-U' (± 30°) doublets, 1000 strips of 50 μm pitch per plane (Fig 2). Thus the track projections can be matched in space, improving the reconstruction very close to the primary interaction and revealing a charm decay by the measurement of an offset (Fig. 5b-c)[4]. In order to reduce the cost of the electronics, 2 strips from different regions are read on the same channel.

The spectrometer itself has an angular acceptance up to 275 mrad in the laboratory both to charged particles and to photons. 70 MWPC planes in between and downstream of the two magnets allow to analyse charged tracks from ~ 2 up to 100 GeV/c. Three electromagnetic calorimeters measure photons and electrons in the same acceptance. For the purpose of this present charm search, only the threshold Cerenkov counter # 2 is used to disentangle π from K/P in the range $6.3 < P < 21.6$ GeV/c, and π/K from P above 21.6 GeV/c.

The trigger requires a hadronic interaction, asking for some minimal multiplicity in the active target and for the detection of at least 1 upward and 1 downward charged track through scintillator hodoscopes. We have recorded 5 M events in 1985 and 12 M events in 1986. The electromagnetic contamination is 10 %. The trigger efficiency is 35 % for hadronic interactions, increasing with the beam energy and thus leading to a factor 2 enrichment for charm. But as charm photoproduction represents only about 1 % of the total cross section, a large effort was devoted to the filtering procedure.

Charm signals:

First we process all raw data events through a fast pattern program which reconstructs charged tracks using only a part of the MWPC planes. Then two filtering philosophies are considered:

1) A specific filter requiring a very clean active target selects 3 % from 5 M events recorded in 1985. The corresponding $K^-\pi^+\pi^+$ invariant mass distribution is presented in figure 3 for different cuts in L/σ, where the decay length L is measured with an error σ typically $\approx 500\ \mu m$ (throughout the paper, the charge-conjugate states are implicitly included). The D^+ signal is clearly visible with a low background, but the statistics is poor[5].

2) The second method is used on our 1986 data. Combining the charged tracks with the active target and the microstrips informations, criteria are defined to select events with an offset track or with a secondary vertex[6]. We retain thus 20 % of the events which are processed through the full pattern recognition program, taking about 1.5 s/event on an IBM 3090.

According to our Monte-Carlo simulation the filtering efficiency is 70 % for D mesons, independently of the decay length and of the transverse momentum P_T. The $K^-\pi^+\pi^+$ mass spectrum is shown on figure 4, for 4.5 M envents from 1986. The S/B ratio is 3 and 60 D^+ are measured in the mass range (1.815, 1.905) GeV. We have imposed a flight $L > 10\ \sigma$.

Figure 5 is the illustration of a charmed event candidate with a decay $D^- \rightarrow K^+\pi^-\pi^-$ observed in the microvertex silicon detector. A grey track is emitted at large angle in the active target and an other π^+ is reconstructed.

Based on all 12 M events from 1986, figure 6 represents the $K^-\pi^+$ mass distribution from those $D°$ mesons which are produced by a D^{*+} decay. Asking for a $K\pi\pi$-$K\pi$ mass difference between 143 and 149 MeV and a flight $> 2\ \sigma$, we get 88 $D°$ and a ratio $S/B \approx 4.4$.

Figure 7 shows the cumulated available invariant mass distribution of charged and neutral D mesons, including all $D° \rightarrow K^-\pi^+$ from 1986 data with a 4 σ flight cut. We observe a signal of 510 D mesons in the mass range (1.815, 1.905) GeV with a ratio $S/B \approx 1$.

$D°$ meson lifetime:

The $D°$ meson signal produced by a D^{*+} decay (Fig. 6) presents a low background and allows a limited cut on the time of flight. Figure 8 shows the time of flight distribution for ~ 80 $D°$ mesons. An exponential fit gives a lifetime $\tau_{D°} = (4.45 {}^{+.75}_{-.67}) \cdot 10^{-13}$ s (errors are statistical only) [6] quite in agreement with the 1986 world average $(4.3 {}^{+.5}_{-.4}) \cdot 10^{-13}$ s [7], but with larger errors than a recent FNAL-E691 result: $(4.35 \pm .15 \pm .10) \cdot 10^{-13}$ s [8].

P_T^2 distribution of D mesons:

The cumulated statistics of 510 D meson signals is compared in figure 9 with the normalized background, taken in the same mass range but with no cut on flight (dashed line). Charmed mesons are produced at higher P_T than ordinary hadronic states whose distribution is compatible with an $\exp(-6m_T)$ dependance.

Comparison is also made on the same figure with the Lund Monte-Carlo simulation of the lowest order QCD prediction: the fusion $\gamma g \rightarrow c\bar{c}$ [9]. For two choices of the charmed quark mass (m_c = 1.2 or 1.5 GeV, full curves), this model is in good agreement with our data. However in order to get a detailed comparison with the theory, second order QCD predictions should have to be taken into account.

Conclusion:

We have observed a clear signal of charmed D°, D^+ mesons which will be completed this year by exploiting our full statistics, and by using the calorimeter informations in order to analyse decay channels with a π°. Lifetime measurements will be pursued and P_T, X_F, Y distributions for D mesons will allow a more detailed comparison with QCD predictions.

Acknowledgements:

I gratefully acknowledge the organizing committee, and especially T. HOFMOKL, for their invitation and hospitality. I thank P. ROUDEAU for providing me our last results and J.P. ENGEL for revising the manuscript which was typed by Mrs. L. SEIFERT.

References

1. E.Augé, Thèse de 3e cycle, Orsay, LAL 83-09 (1983)
   D.Bloch, Thèse de doctorat d'Etat, Strasbourg, CRN-HE 85-06 (1985)
   C.Seez, Ph. D. Thesis, Imperial College, London, HEP T 118 (1983)
   G.Wormser, Thèse de doctorat d'Etat, Orsay, LAL 84-45 (1984)

2. P.Astbury et al., Phys. Lett. 152B (1985) 419

3. R.Barate et al., Nucl. Instr. and Methods, A235 (1985) 235

4. S.Petrera, G.Romano, Nucl. Instr. and Methods, A174 (1980) 61

5. M.Primout, NA14-II internal note (1987)

6. C.Krafft, Thèse, Orsay, LAL 87-28 (1987)

7. Review of Particle Properties, Particle Data Group, Phys. Lett. 170B (1986)

8. J.C.Anjos et al., Phys. Rev. Lett. 58 (1987) 311

9. L.Jones, W.Wyld, Phys. Rev. D17 (1978) 759
   H.Fritzsch, K.H.Streng, Phys. Lett. 72B (1978) 385

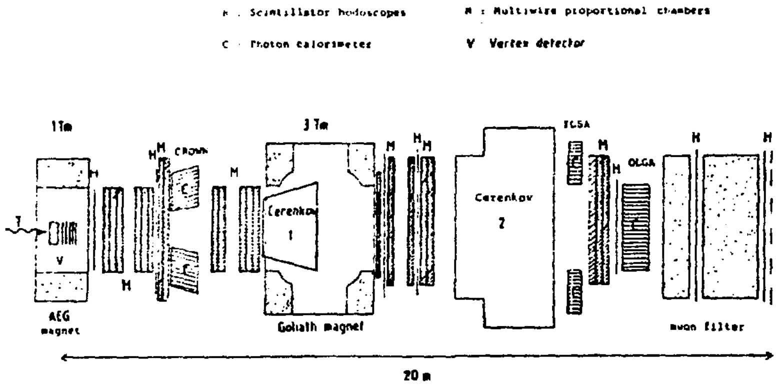

Figure 1: the NA14-II spectrometer

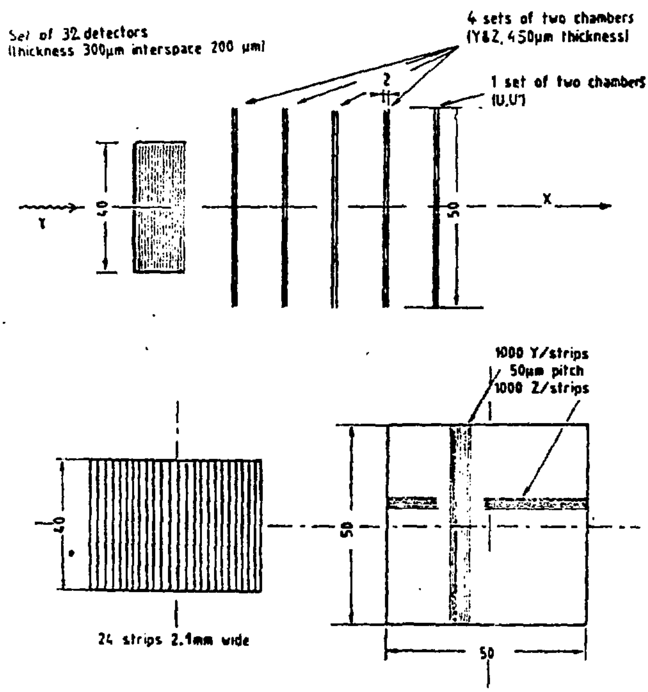

Figure 2: the microvertex silicon detector

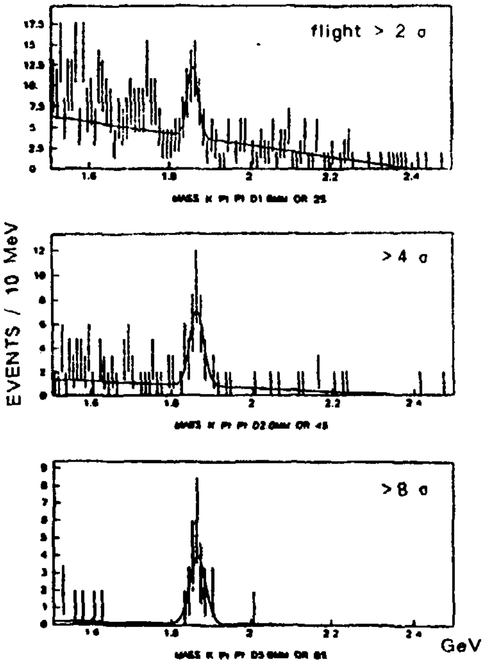

Figure 3: clean active target filter

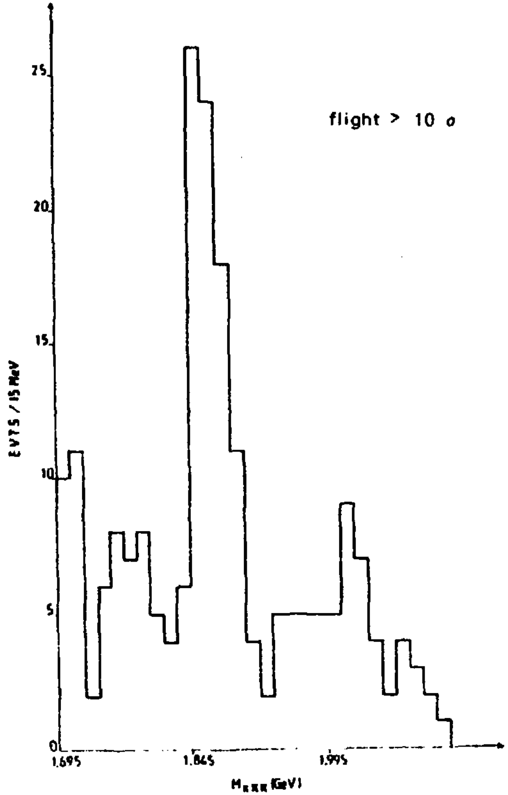

Figure 4: microstrip filter

$K^-\pi^+\pi^+$ invariant mass distribution

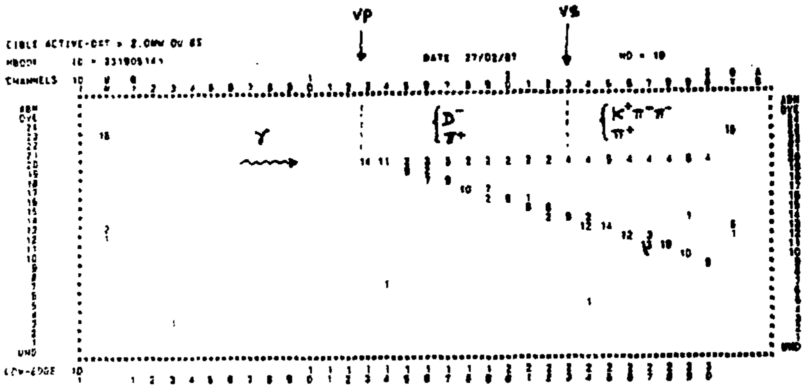

a) silicon active target response

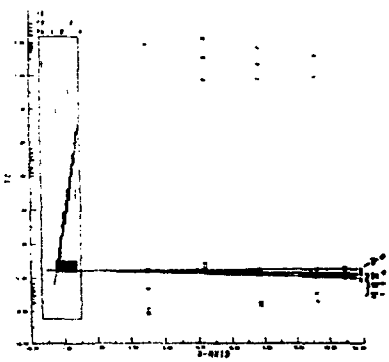

b) active target and microstrip hodoscopes response

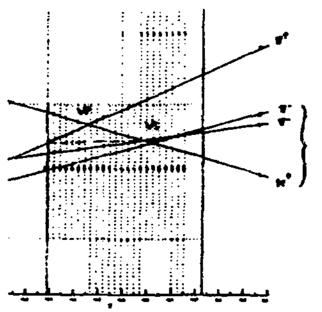

c) reconstructed tracks with the microstrips

Figure 5: display of a candidate event with a charmed decay $D \rightarrow K\pi\pi$

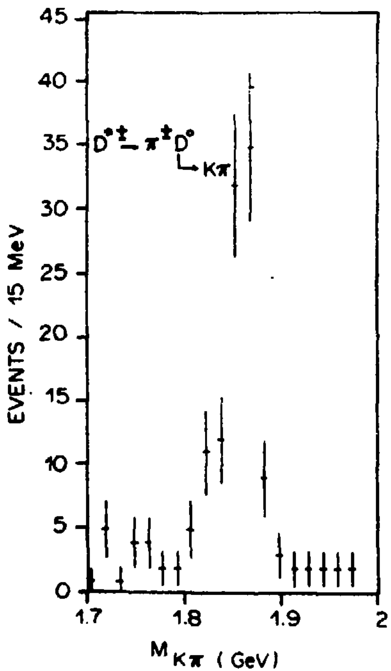

Figure 6:

D^0 mass spectrum from D^{*+} decay (flight > 2 σ)

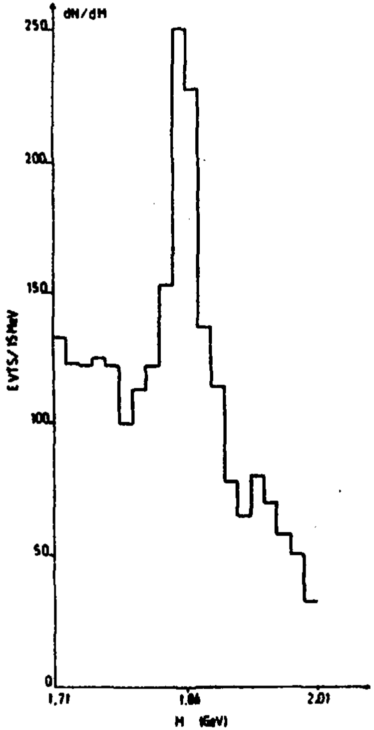

Figure 7:

cumulated D meson invariant mass distribution

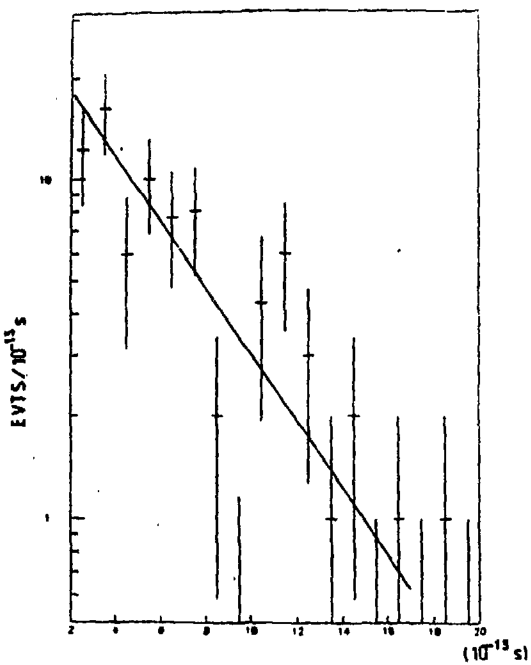

Figure 8: lifetime distribution for $D^{\circ} \rightarrow K^{-}\pi^{+}$ from D^{*+} decay

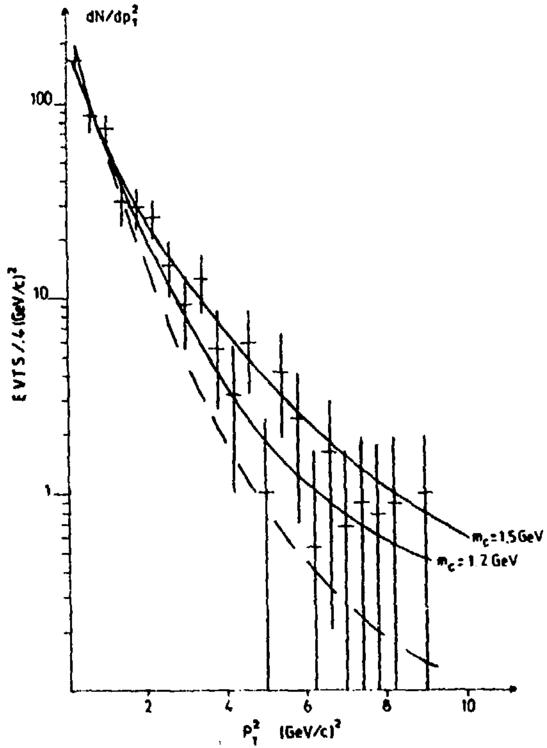

Figure 9: P_T^2 distribution of D mesons
dashed curve: normalized background
full curves: QCD γg fusion model

Production of μe pairs in neutrino interactions at 3 - 20 GeV neutrino energy

SKAT - Collaboration

(IHEP Berlin-Zeuthen - IHEP Serpukhov)

presented by H.E. Roloff

1. Introduction

The production of opposite sign dileptons in neutrino interactions at high energies is well understood as being due to charm production with succeeding semileptonic decay. Most other experiments study the dilepton production in an energy range starting at about 30 GeV. Our data allow the study of charm production near the charm threshold.

For the production of like-sign dileptons there is up to now no theoretical explanation for the measured rates. The associated charm production e.g. gives a rate less by a factor of about 10. Other sources as B- production can be excluded at our energies. So our results will be critically since especially the associated charm production is expected to be strongly suppressed at our low energies.

2. Selection of μe-events

We used the neutrino wide band-beam of the Serpukhov accelerator with an averaged neutrino energy $\langle E_\nu \rangle \approx 7$ GeV. As detector we used the heavy liquid bubble chamber SKAT /1/.

We started from about 10060 charged current events which were selected as described in /2/. To increase the efficiency of muon-selection we applied the momentum cut $p_\mu > 1$ GeV/c. A track is accepted as e^+/e^--candidate if two of the following criteria are satisfied: characteristic spiralization or strong multiple scattering, high energetic δ-electrons, Brems- γ's pointing to the track, annihilation (only e^+). To reduce the background from photons converting near the primary vertex we required that the e-track has to be clearly visible at a distance of 1.5 cm from the primary vertex and that there is no other e-track at the vertex.

To reduce the background from missclassified leaving π's for the μ^-e^- events we required in addition that $p_\mu > p_e$, and for δ-electron background reduction we introduced an angle cut for the angle between the muon- and electron direction. After correcting for losses and efficiencies we got

from $\nu_\mu N \longrightarrow \mu^- X$: 10060 events

for $\nu_\mu N \longrightarrow \mu^- e^+ X$: 18 events + 15.1 %

and for $\nu_\mu N \longrightarrow \mu^- e^- X$: 6 events + 8.6 %

The background sources are estimated as given in the following table (the numbers given are number of events).

backgr.	asymm. γ's Dalitz pairs	$\overset{(-)}{\nu_e}$ N cc-inter.	compton-electrons	δ-electr.	total
μe^+	0.8 ± 0.3	0.06 ± 0.02	-	-	0.9±0.3
μe^-	0.8 ± 0.3	1.1 ± 0.4	1.6 ± 0.5	0.24±0.02	3.7±0.7

3. Results for $\nu_\mu N \longrightarrow \mu^- e^+ X$

The ratio of opposite sign dilepton production normalized to our charged current data sample comes out to be

$$\frac{\sigma(\nu_\mu N \longrightarrow \mu^- e^+ X)}{\sigma(\nu_\mu N \longrightarrow \mu^- X\ )} = (2.0 \pm 0.5) \cdot 10^{-3}$$

with the experimental cuts $E_\nu > 3$ GeV, $p_\mu > 1$ GeV/c, $p_e > 0.4$ GeV/c. Requiring that the mass of the hadronic system has to be greater than m_{Λ_c}, $W > 2.3$ GeV, we obtain with the same other cuts the ratio above the charm threshold

$$\frac{\sigma(\nu_\mu N \longrightarrow \mu^- e^+ X)}{\sigma(\nu_\mu N \longrightarrow \mu^- X\ )} = (4.6 \pm 1.2) \cdot 10^{-3}$$

In several experiments /3/ there are indications for the production of charmed baryons. We compared our data with a Monte Carlo sample for the two processes

$$\nu_\mu N \longrightarrow \mu^- \Lambda_c^+ \quad \text{quasielastic}$$
$$\qquad\qquad\qquad \hookrightarrow e^+ X$$

and

$$\nu_\mu N \longrightarrow \mu^- D X$$
$$\qquad\qquad\qquad\qquad \hookrightarrow e^+ X'$$

In figure 1 the contributions of Λ_c^+ (dashed line) and D-production (dashed dotted line) are shown. It can be seen that a cut at $W > 2.6$ GeV separates the two processes to a high degree.

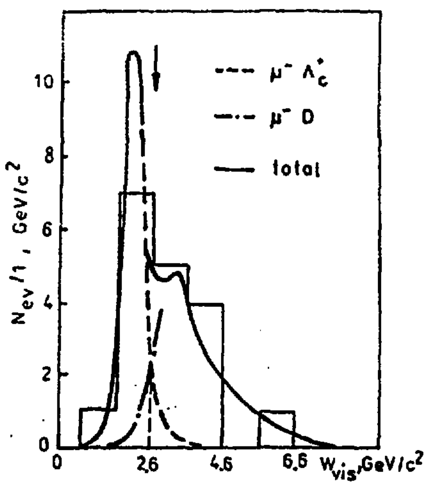

Applying this cut to our data we got

from $\nu_\mu N \longrightarrow \mu^- e X$: 18 events

for $\nu_\mu N \longrightarrow \mu^- \Lambda_c^+$: 8 events

and for $\nu_\mu N \longrightarrow \mu^- DX$: 10 events,

Taking into account the branching ratios for a decay of Λ_c^+ and D into $e^+ + X$, we calculate the cross section ratios

$$R_{\Lambda_c^+} = \frac{\sigma(\nu_\mu N \longrightarrow \mu^- \Lambda_c^+)}{\sigma(\nu_\mu N \longrightarrow \mu^- X)} = (6.7 + 3.5) \cdot 10^{-2}$$

$$R_D = \frac{\sigma(\nu_\mu N \longrightarrow \mu^- D X)}{\sigma(\nu_\mu N \longrightarrow \mu^- X)} = (2.5 + 0.9) \cdot 10^{-2}$$

and for the total charm production rate:

$$R_c = \frac{\sigma(\nu_\mu N \rightarrow \mu^- c X)}{\sigma(\nu_\mu N \rightarrow \mu^- X)} = (9.2 \pm 3.6) \cdot 10^{-2}$$

with the cuts $E_\nu > 3$ GeV, $W > 2.3$ GeV, $p_\mu > 1$ GeV/c.
This is in a good agreement with the results of other experiments /4/ and our own results on strange particle production /5/.

4. Results for $\nu_\mu N \rightarrow \mu^- e^- X$

The ratios of like sign dilepton production normalized to the charged current data and to the opposite sign dilepton production come out to be

$$\frac{\sigma(\nu_\mu N \rightarrow \mu^- e^- X)}{\sigma(\nu_\mu N \rightarrow \mu^- X)} = (2.5^{+4.3}_{-1.4}) \cdot 10^{-4}$$

and

$$\frac{\sigma(\nu_\mu N \rightarrow \mu^- e^- X)}{\sigma(\nu_\mu N \rightarrow \mu^- e^+ X)} = 0.12^{+0.22}_{-0.08}$$

with the cuts $p_\mu > 1$ GeV/c, $p_e > 0.04$ GeV/c, $p_\mu > p_e$, $E_\nu > 3$ GeV.

Figure 2 shows that our data near the charm threshold are not explained by the mechanism of associated charm production.

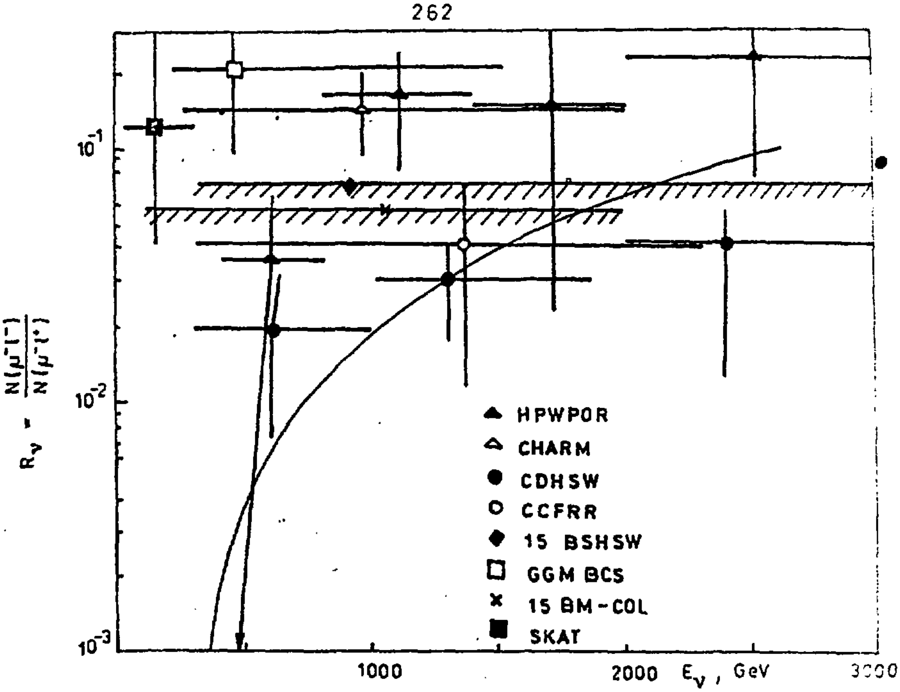

5. Summary

Our results on opposite sign dilepton production confirm the interpretation being due to charm production. We measured first time the Λ_c^+ - quasielastic cross section in neutrino interactions.

Our results on like sign dilepton production are not consistent with associated charm production, but need more data to increase the measuring accuracy.

References

/1/ Kuznetsov,E.P. et al., Preprint IHEP 71-75, Serpukhov (1971)

/2/ Baranov, D.S. et al., Z.f.Phys., C21 (1984), 189
Baranov, D.S. et al., Z.f.Phys., C21 (1984), 197

/3/ Baker et al., Phys.Rev. D Vol. 32, No.3, Particle and Fields, 1985

/4/ Ballagh, M.C. et al., Phys.Rev. D24, No.1 (1981)

/5/ Ammossov, V.V. et al., Z.f.Physik, C30 (1986), 183

TOPONIUM AT LEP

S.Zylberajch
CEN Saclay, France

Abstract. We present a brief survey of Toponium studies done at the CERN LEP I and LEP II Physics workshops[6,8]. If produced at the LEP energy, the first toponium S-states could be detected in less than one year in the present LEP experiments. Detailed studies on spectroscopy and polarization will be far more difficult.Toponium could be a very good tool to look at non standard physics.

INTRODUCTION Quark-antiquark systems are good tools to study quark interactions : quarkonium spectroscopy provides information about the quark-antiquark potential, and the decay branching ratios and asymetries reflect the strong and electroweak couplings.

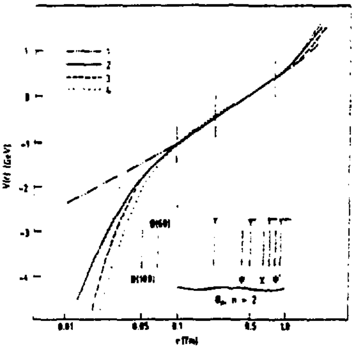

Fig. 1

Because of asymptotic freedom heavy quark-antiquark systems are non relativistic and can be described by a Schrödinger equation with a potential having a Coulomb singularity at the origin and a long range linear confinement term .In figure 1 four such potentials[1,2,3,4] are shown and it is seen that in the region probed by the Ψ and Υ spectroscopies, that is between 1. and 0.1 fm, all published potentials agree within the experimental errors . Heavier masses are needed to explore the coulombian behavior at short distance, between 0.1 and 0.01 fm. This is a strong motivation to look at the Toponium (Θ).

TOPONIUM SPECTROSCOPY From the Ψ and the Υ families we have learned that the potential is independant of the mass and the flavor of the quarks. In figure 2 are plotted the binding energies for the S- and P-states . The first bound state is expected to lie about 2 GeV below the open top threshold and the number of sub-threshold bound Θ s-states has been estimated to be [5]:

$$n_0 \sim 2(m_t/m_c)^{1/2}$$

The total number of narrow bound states is expected to be twice the square of this number :

$$n_t = 2\, n_0^2$$

This gives a total number of about 200 bound states including at least 10 bound S-states, with a splitting of a few hundreds of MeV between the two first S-states and only a few tens of MeV between the last ones . This is about twice the expected beam spread δW at LEP I as seen in figure 3. Thus except for the first S-states, beam spread will smear out all the rich spectroscopy . A precise measure of the ^1S-^2S mass difference will provide a relevant measurement of the QCD scale parameter Λ_{MS} (fig. 4), and the measurement of higher radial excitations , in the Ψ and Υ region could provide a good ' a posteriori ' check of the hypothesis of mass and flavour independence.

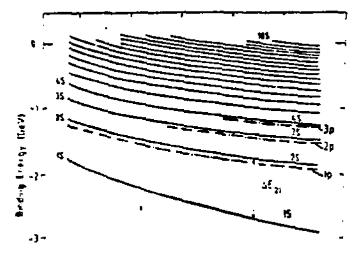

Fig. 2

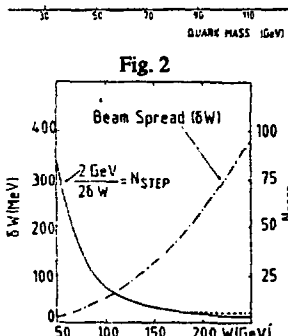

Fig. 3

The fine structure splitting of the P-states is a relativistic effect and scales from the Ψ to the Υ like the square of the quark velocity inside the quarkonium :

$$(\delta m_b/\delta m_c) = (\beta_b/\beta_c)^2$$

Since the top quark is much heavier than the bottom and charm quarks we expect a mass difference of a few MeV . Because of this small mass difference it will not be possible to resolve the $^3P_0$ $^3P_1$ $^3P_2$ splitting. In figure 2 one sees that the radiative transitions from the ^2S-state to the ^1S-state via the ^1P will proceed with the emission of two monochromatic photons , one of about 100 MeV and the second of a few hundreds of MeV . These will probably be very hard to detect in all present LEP experiments with the possible exception of L3. At any rate these radiative decays will have much smaller branching ratios than the modes discussed in the next section.

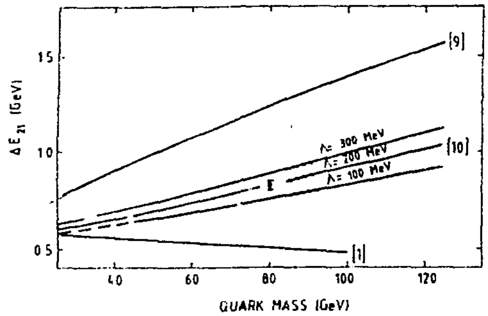

Fig. 4

TOPONIUM DECAY Θ decays are expected to be dominated by the week interactions. This is unlike the cases of Ψ and Υ where decays to 3 gluons (fig.5 d) and charged lepton pairs via γ exchange (fig.5 a) dominate. In the LEP I region,(m $_\Theta$ < 100 MeV) annihilation via Z^0 and W exchanges dominates (fig.5 b,c). The width is less than 1MeV unless m $_\Theta$ ~ m_Z in wich case the width may be near 10 MeV.These values are model dependent and may be wrong by a factor of 2. At higher Θ masses (LEP II), single quark decay (SQD) will play a leading role in toponium (fig.5e): this is an independent internal decay of the top quark or antiquark into bottom and W. If the toponium mass is much higher than the Z^0 mass, the SQD decay becomes more and more dominant and the decay width becomes comparable to the beam energy spread. If the width is of the order of the transition width between the ^1S- and the ^2S-state, the individual structures disappear.

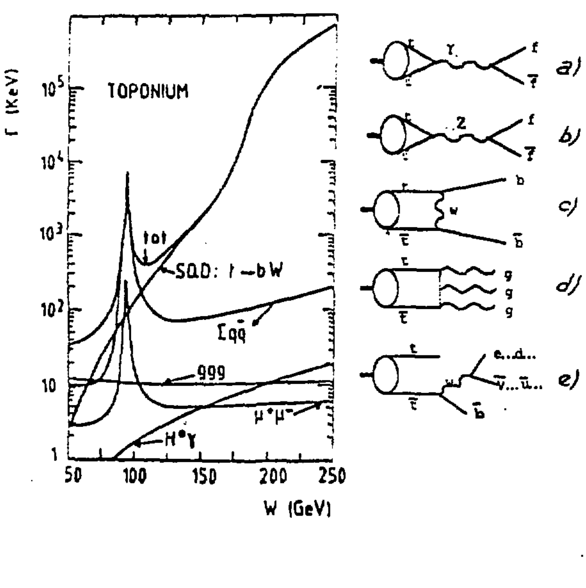

Fig. 5

EXPERIMENTAL PROCEDURE A search for Θ is greatly facilitated by a knowledge of the open top threshold since the Θ mass should be about 2 GeV below this threshold. To find the Θ we will then scan the suspected interval by steps of twice the beam spread.

Determination of open top threshold:

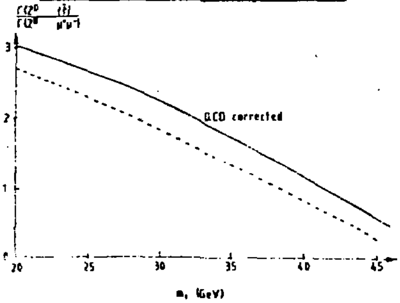

Fig.6

- If the Θ is lighter than the Z^0, the top mass can be determined either by the ratio of the Z^0 t - $\bar{t}$ decays to the $\mu^+\mu^-$ QED production [7] (fig. 6), or by the shape of the lepton spectrum from top semileptonic decays [6,7]. Figures 7 a,b show how the end point of the spectrum of P_t varies with m_Θ, and figure 7 c shows the background from secondary decays from t quark.

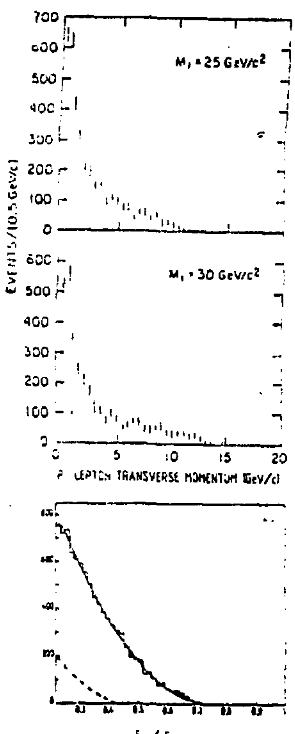

Fig. 7

- If the toponium is above the Z^0 the open top threshold can be found by a binary scan of the SQD events sample. These decays have a more spherical topology than the q - $\bar{q}$, l - $\bar{l}$ events that can be eliminated with geometrical cuts [6,8](fig. 8). Accordingly we will look for spherical events at the the highest energy available. If there are some we will then go to half the energy and proceed further by adding or substracting each time an energy equal to half the preceding increment. Below the $W^+ W^-$ threshold the Z^0 radiative tail background ($e^+e^- \to Z^0\gamma$) can be removed by a cut on the missing longitudinal momentum to remove the hard photon going through the beam pipe. Above this threshold we can remove the direct W^+W^-, which are produced back to back, with a cut on the colinearity of the two W's. We expect to get the top mass with an error of about 1 GeV, within a few weeks.

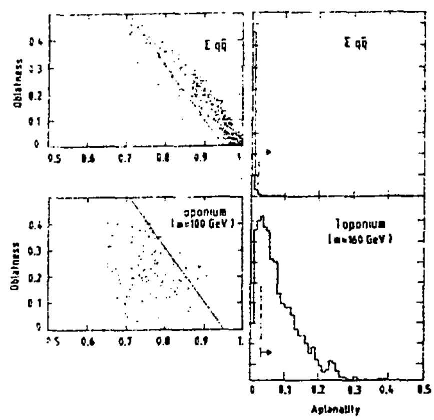

Fig. 8

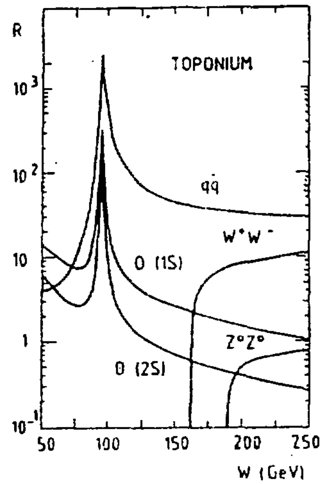

Fig. 9

Scan for toponium : Figure 9 shows the predicted cross sections for q - $\bar{q}$ production and on-resonance Θ production nor malized to σ_0, the electromagnetic leptons cross section as a function of center-of-mass energy, s :

$$\sigma_0(e^+e^- \xrightarrow{\gamma^*} \mu^+\mu^-) \sim \frac{86.8}{s} \text{nb}$$

We see that at low energy, signal and background are of the same order of magnitude , but above the Z^0 , the background is about 20 times larger . Thus we will need to use the SQD sample to reduce it. Scanning an interval of 2 GeV , and requiring a 3 standard deviation signal, the necessary integrated luminosity can be computed:

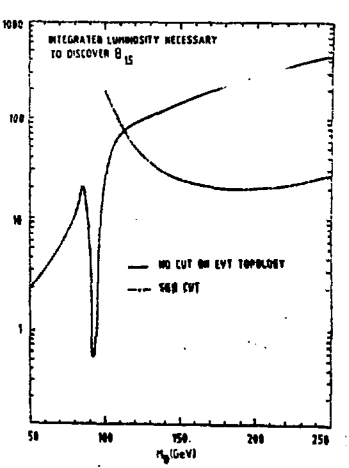

Fig. 10

$$L = 9 \; \frac{R_\theta\, \varepsilon_\theta + R_B\, \varepsilon_B}{R_\theta^2\, \varepsilon_\theta^2 \sigma_0} \; \frac{2 \text{ GeV}}{2\delta W}$$

where R_θ and R_B are the toponium and background cross section normalised to σ_0, and ε_θ and ε_B the detection efficiency. Figure 10 shows the necessary integrated luminosity as a function of m_Θ .
The above formula is correct if the Θ is far away from the Z^0 where the background amplitude via photon exchange and the Θ amplitude will add uncoherently (fig. 11 a). On the other hand if the Θ is in the Z^0 peak,both amplitudes interfere and we will get dips in the cross section (fig. 11 b).

The expected cross section is [13]:

$$R_\theta \Rightarrow \frac{R_{peak}}{2}\left\{1 - \mathrm{Re}\left[\Pi_j\left(\frac{E-m_{\theta j}-i\Gamma_{\theta j}}{E-m_{\theta j}+i\Gamma_{\theta j}}\right)\left(\frac{E-m_Z-i\Gamma_Z}{E-m_Z+i\Gamma_Z}\right)\right]\right\}$$

This should give a serie of very narrow dips in the Z^0 peak (fig. 12 a) but convoluted with the finite beam spread,this structure will be partially smeared out (fig. 12 b).

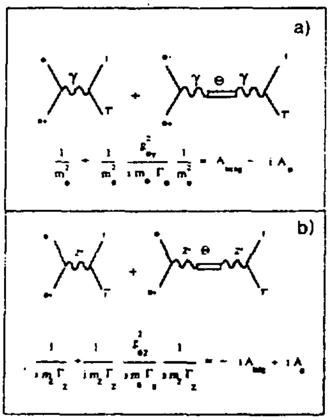

Fig. 11

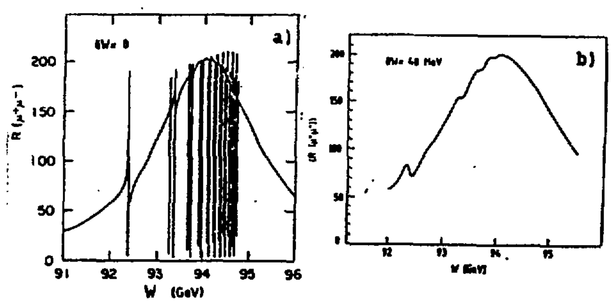

Fig. 12

The interference effect depends strongly on the Θ width, which decreases rapidly as the mass difference between the Z^0 and the Θ increases .That is why near the Z^0 peak the interference could be detected within a few days but will require more and more luminosity if the toponium mass goes away from the top of the Z^0 peak : fig. 13 a shows the number of events produced in a scan between 90 and 94 GeV for a run of 10 days, and fig. 13 b shows what we expect in a scan between 94 and 97 GeV for a run of 2 to 3 months.

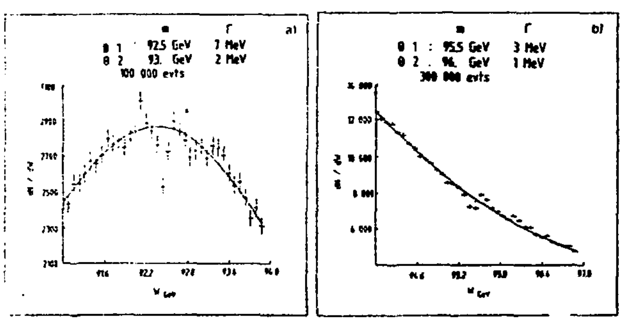

Fig. 13

<u>CONCLUSION</u> Toponium could be detected within a few days to a few weeks if lighter than the Z^0 , within a few days if it has the Z^0 mass. If the present trend (ARGUS, UA1 ...) [11] is

confirmed, the toponium will be out of reach at LEP I but could be found within a few weeks to a few months at LEP II .

Once the Θ^1S found what should be the next step ? $\Theta\,^2S$ will require between 200 and 300 inverse picobarns (fig. 14). It will take even more time to measure the toponium polarization : figure 15 shows the predicted asymetry as defined in [12], using a clean sample by selecting semileptonic SQD events with an isolated hard lepton : the error bars shown correspond to a run of 200 inverse picobarns with unpolarized beams. With partially polarized beams ($P \sim .5$), the needed luminosity will still be of the same order of magnitude. With fully polarized beams , we could gain a factor of 3 on the luminosity wich will represent less than one year of data taking...

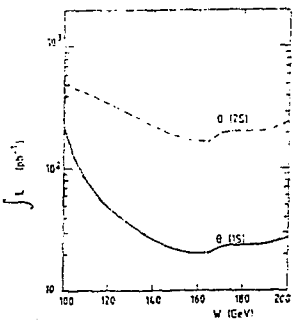

Fig. 14

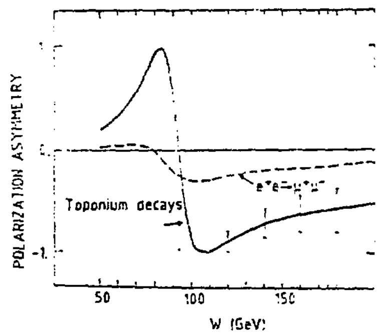

Fig. 15

Our best chance will be if the world is non-standard . Then the toponium aspect will change spectacularly : the width will increase dramatically so that it will be impossible to miss such a strong effect :

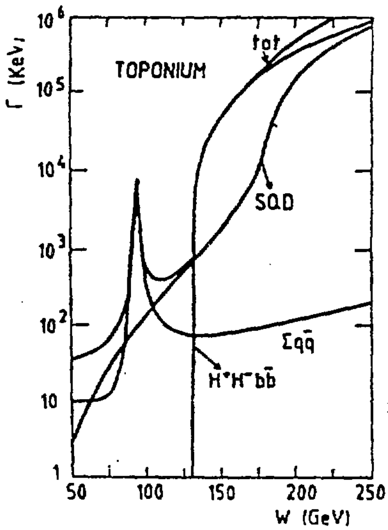

Fig. 16

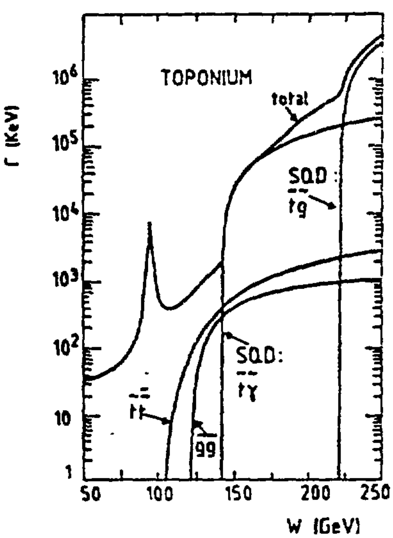

Fig. 17

Figure 16 shows what will happen if the toponium can decay into two charged higgs The decay width will rise sharply and erase the resonance structure. and figure 17 shows what will happen with SUSY particles . We will find extremly large decay rates, missing energy and momentum, carried away by the lightest susy particle. and no individual resonance. Such a big effect will be a clear indication of new physics.

TOPONIUM Physics will be difficult.

The minimum we can expect will be a better understanding of electroweak and strong interactions within the Standard Model. With luck we could also open a window on a new physics domain within a few months. Discrimination between the different theories will require much more time and effort.

Acknoledgements

I am grateful to P.Igo-Kemenes, J.Mallet, J.Rander and J.Rich for their help in preparing this report. I would like to thank all organizers of the Symposium for their hospitality in Poland.

References

[1] A.Martin, Phys. Lett. 100B (1981) 511.
[2] W.Buchmüller.G. Grunberg and S.-H.H.Tye, Phys. Rev. Lett. 45 (1980) 103.
[3] G.Bhanot and S. Rudaz, Phys. Lett. 78B (1978) 119.
[4] E.Eichten et al., Phys. Rev. D17 (1979) 3090. and D21 (1980) 203.
[5] C.Quigg and L.Rosner, Phys.Lett. 72B (1978) 462.
[6] W.Buchmüller et al. , CERN-EP/86-02 , 21 february 1986 .
[7] T.Himel , SLAC-PUB-3510 , november 1984.
[8] P.Igo-Kemenes et al., CERN-EP/87-49 , 2 march 1987 .
[9] J.L.Richardson , Phys.Lett. 82B (1979).
[10] K.Igi and S.Ono , Phys.Rev. D33 (1986).
[11] J.Ellis and J.S.Hagelin , CERN-TH.4679/87
[12] S.Güsken et al., Nucl.Phys. B262 (1985) 393.
[13] A.Martin, Phys. Lett. 156B (1985) 411.

An extensive bibliography can be found in [6] and [8].

TIME PROJECTION CHAMBERS AT LEP

A. Minten

CERN, European Organization for Nuclear Research, Geneva, Switzerland

1. INTRODUCTION

In 1989 the e^+e^- storage ring LEP at CERN will start operation. Four LEP experiments are under construction. Two of them, ALEPH and DELPHI, use a Time Projection Chamber (TPC) as a central tracking detector.

In the following we will first recall the principles of TPC, and then describe the technical solutions applied in the case of the two LEP detectors.

2. THE TIME PROJECTION CHAMBER, GENERAL PROPERTIES [1]

2.1 Principle of operation (fig. 1)

The TPC consists basically of a cylindrical barrel, closed by a negative high voltage electrode at one end and a set of wire chambers at the other. The axial electric field $\vec{E}$ is degraded linearly along the axis of the cylinder by means of a resistor chain, and a solenoidal magnetic field $\vec{B}$ parallel to $\vec{E}$ is superimposed. Tolerances for homogeneity and parallelism of the field $\vec{E}$ and $\vec{B}$ is of the order of 10^{-4}.

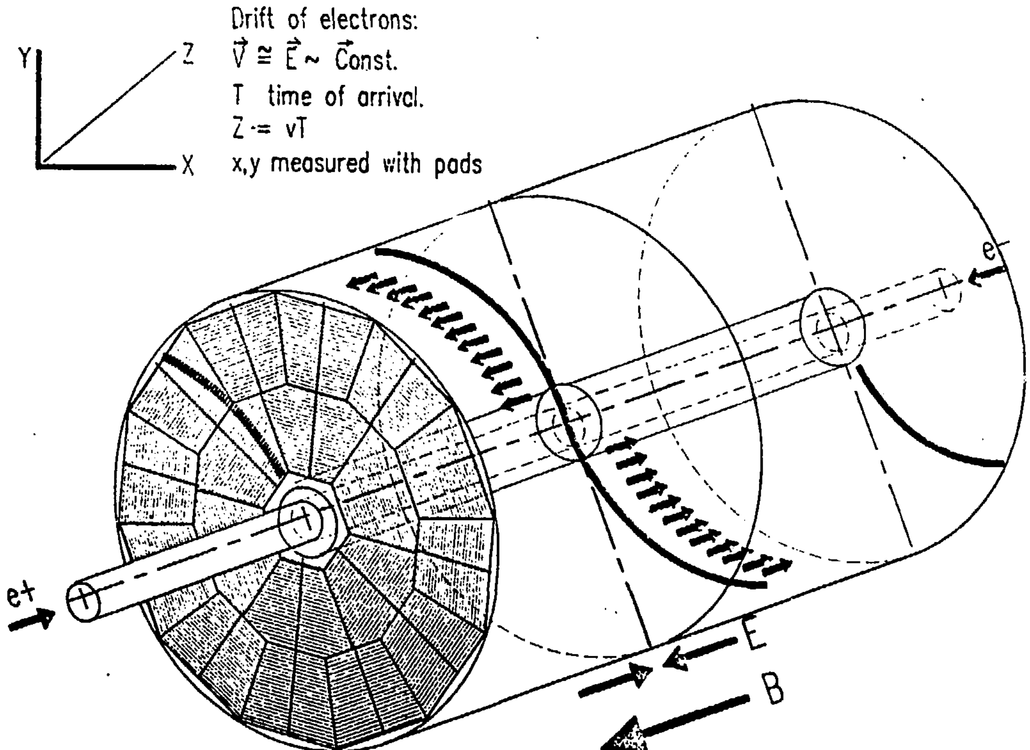
Drift of electrons:
$\vec{V} \cong \vec{E} \sim \vec{C}onst.$
T time of arrival.
Z = vT
x,y measured with pads
Y
Z
X
e+
e-
E
B

Fig.1

The passage of a charged particle generates a track of electron-ion pairs. Electrons drift parallel to the electric field to the detector end plate and are registered. The track coordinates are determined through

$$(x, y)_{track} = (x, y)_{endplate}$$
$$z_{track} = v_{drift} \cdot t_{drift}$$

from the measurement of the electrons arrival location $(x, y)_{endplate}$ and arrival time t_{drift}, for known drift velocity.

2.2 Detectors [2]

The detection device(s) on the detector endplate(s) consist of proportional wire chambers (MWPC). They are usually subdivided into "sectors" (fig. 1). The sector carries azimuthal wires for gas amplification and readout, and radially oriented pads which register the induced signal from the avalanche on the wires. The pads give an unambiguous (x, y) or, in a *cylindrical geometry*, (r, ϕ) *point* in the detector plane. The additional readout of the drift (arrival) time adds the z coordinate and complements a space point.

The precision of the (r, ϕ) measurement and thereby of the track reconstruction stems from an interpolation of the charge induced on adjacent pads (fig. 2). It is therefore that the readout must contain pulseheight information. Pulseheight and time are obtained, in the *current technique*, by means of Flash Analog-to-Digital Converters (FADC).

The resolution in $(r\phi)$ along a padrow is described by a so-called Gaussian "pad response function" [3]

$$P_i(\phi) = \text{const. exp} \frac{(\phi - \phi_i)^2}{2\,\sigma^2_{PRF}}$$

where ϕ_i is the centre of the ith pad, and σ_{PRF} describes the lateral extension of the induced pulses. The interpolation is performed between two (or three) adjacent pads with pitch Δ

$$\phi = \frac{\sigma^2_{PRF}}{\Delta} \ln^{Pi}/Pi + 1 + (i + \tfrac{1}{2})\Delta$$

The radial coordinate r is taken from the geometrical position of the pad concerned.

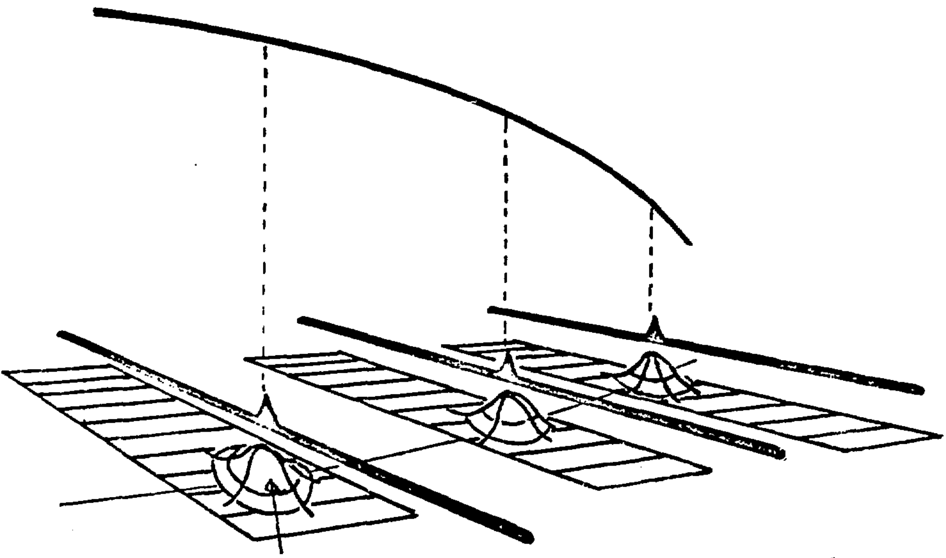

Fig. 2 Principle of the readout [3]

2.3 Distortions [4]

Three types of distortions limit the resolution of the TPC:

(a) The $\vec{E} \times \vec{B}$ effect. This effect is due to the transverse force on the drifting electron when $\vec{E}$ and $\vec{B}$ are not exactly parallel. This can be avoided in the drift volume by imposing sufficiently strict tolerances. It cannot be avoided close to the sense wires where the electric field lines necessarily converge on the wire. The $\vec{E} \times \vec{B}$ force causes a smearing of incoming electrons along the wire and across the pads. In a practical case the maximum smearing can be 3 mm, and the corresponding uncertainty in the track positioning is

$$\sigma_{EB} \approx \frac{\Delta}{\sqrt{12}\, n} \approx 50\ \mu m$$

where $n \approx 300$ is the number of primary electrons drifting to a 3 cm long pad.

(b) Diffusion. Transverse diffusion due to electron gas collisions result an approximately gaussian smearing with [2]

$$\sigma_T \approx \sqrt{2Dt_D} \approx 6 \text{ mm}$$

for 1 m of drift (D is the gas dependent diffusion coefficient).

The track centre can be determined to

$$\sigma_T^1 \approx \frac{\sigma_T}{\sqrt{n}} \approx 350 \text{ µm} .$$

A further improvement comes from the trapping of transversely drifting electrons by the magnetic field. This causes a spiraling with the cyclotron frequency $\omega = e/m\ B$ around the electric field lines. The diffusion is thereby reduced to

$$\sigma_D \approx \frac{\sigma_T^1}{\omega t} \approx 50 \text{ µm}$$

where t is the mean time between collisions.

(c) Positive ions. Primary ionization in the TPC, and, much more important, gas amplification at the sense wires produce positive ions. These ions drift in the direction opposite to the electrons to the high voltage electrode. The drift velocity is, depending on gas composition, of the order of 1 m/s. Positive ions generate a static space charge and thereby an electric field, which by superposition distorts the external field and thereby the drift trajectories. Microscopic distortions of the order of several centimetres, apparent track displacement have been observed [5]. In order to avoid space charge and the distortions connected to it the concept of "gating" has been devised. The "gate" consists of an additional wire grid in front of the MWPC (fig. 3). The gating grid is usually closed to drifting ions and electrons, and no gas amplification takes place. The gating grid is opened at the occurrence of a trigger indicating a good event (calorimetric trigger, beam crossing trigger) and stays open for a time ℓ_D/v_D, where ℓ_D is the active length of the chamber.

OPEN AND CLOSED GRID CONFIGURATIONS

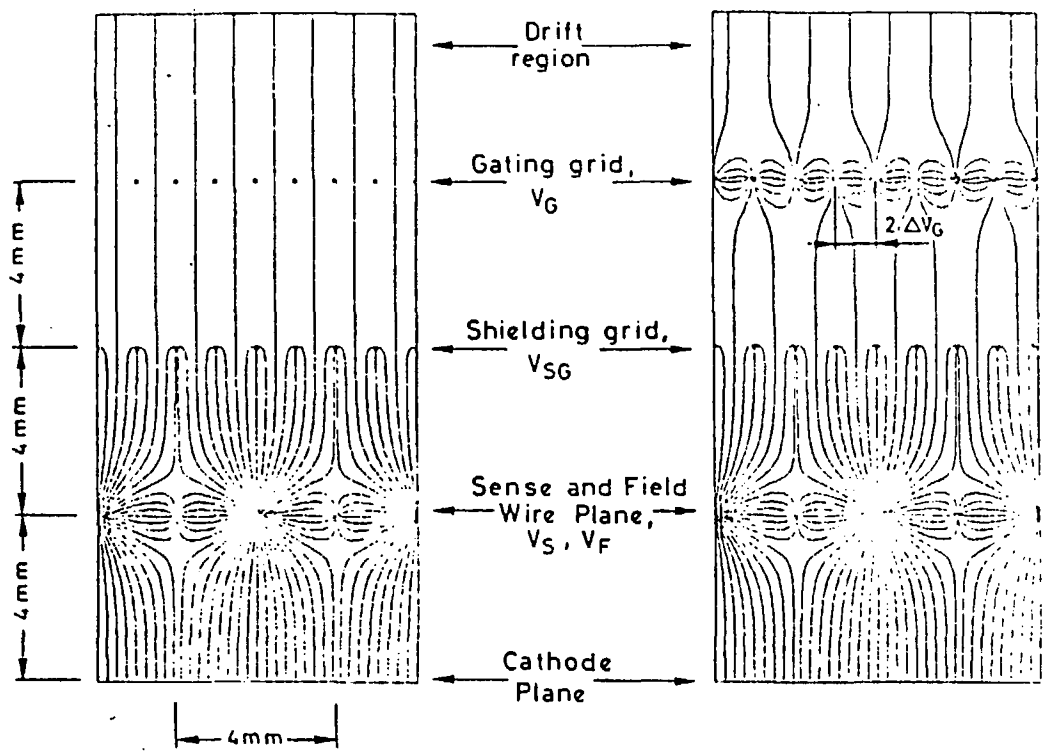

OPEN GATE

Fig. 3

CLOSED GATE

2.4 TPC performance

The performance of the TPC to a large extent described by its:

- Resolution. The overall ($r\phi$) resolution is given by

$$\sigma_{r\phi} = \sqrt{\sigma_o^2 + \sigma_{EB}^2 + \sigma_D^2} \simeq 150\ \mu m.$$

Here the σ_o term contains variations and fluctuations due to track angles, track curvature, and readout sensitivity. The longitudinal resolution is determined by longitudinal diffusion, provided that the FADC clock runs sufficiently fast empirically

$$\sigma_z \simeq 1\ mm\ [4]$$

Other positive performance criteria are:

- Almost full solid angle coverage.
- 3 dimensional readout with space point reconstruction and no ambiguities in track recognition.
- Many samples of dE/dx readout along a track.

On the other hand, certain properties limit the TPC performance. These are:

- A long lifetime of about 20 μs/m of an event drifting through the chamber.
- Field distortions by positive ions.

This makes altogether the TPC a powerful detector, but adapted mainly to low rate experiments, and perfectly matched to a e^+e^- collider.

3. APPLICATIONS OF TIME PROJECTION CHAMBERS

3.1 Overview

The main application of the time projection method is in the frame of e^+e^- experiments. The method was introduced for the PEP4 experiment at SLAC by D. Nygren and coll. from LBL Berkeley. Another device was built for the TOPAZ experiment at TRISTAN (KEK). We will describe here in some detail the two chambers used in the ALEPH [6] and DELPHI [7] experiments at LEP (CERN). We will discuss TPC designs, parameters, components, readout, calibration, and terminate with an indication of the status of construction and planning.

The TPC detectors are built by consortium which are a subset of the collaborations preparing the experiments.

- ALEPH: CERN, Glasgow, Mainz, MPI München, Pisa, Trieste, Wisconsin (Project Leader: J. May).
- DELPHI: CERN, Collège de France, Orsay, Saclay (Project Leader: J.E. Augustin).

3.2 Design and parameters

Both ALEPH and DELPHI TPC's are of cylindrical shape, with an inner bore to contain vacuum tube and inner detectors, and with a central high voltage electrode and two detector endplates.

The parameters of the two detectors are listed below:

	ALEPH	DELPHI
- Total length [m]	4.40	2.68
- External diameter [m]	3.60	2.32
- Bore diameter [m]	0.60	0.65
- Magnetic field [T]	1.5	1.2
- Gas	A + 9% CH_4	A + 20% CH_4
- Drift field [V/cm]	135	220
- Number of detector scalars	36	12
- Number of electronic channels	48000	22000

3.3 TPC components

The mechanical and electrical components of the TPC are:

(a) The field cages, i.e. the inner and outer field cage. The purpose of the field cage is threefold:

- To provide a uniform (10^{-4}) axial electric field in the cylindrical volume between the central HV electrode and the endplates on ground potential. This is achieved by excellent mechanical tolerances and a highly linear voltage dividing resistor chain.

- To provide a tight gas containment with less than 10 ppm O_2 contamination. The two LEP TPC's are layed out for atmospheric pressure operation, but the DELPHI field cage can stand evacuation.
- To insulate the high voltage on the inner side of the cage from the ground potential on the outer side, without punch through between the electrodes. This insulation (and the gas tightness) is to be achieved with a minimum amount of matter in the cage walls. The construction methods applied make use of Cn electrodes on G10 foils, of honeycomb structures for stability, and of mylar and aluminium foils for gas scaling. The thickness of 20 (35)mm and 0.017 (0.027)X_o are reached for ALEPH (DELPHI).

(b) The detector endplates. The two endplates are subdivided into 18 (6) sectors for ALEPH (DELPHI). Each sector carries on the inside a proportional chamber with azimuthal sense wires, field wires parallel to them and with radially oriented cathode pads. The pads yield the rϕ coordinates, the wires serve essentially for dE/dx measurements. The sense/field wire grid is preceded by a decoupling shielding grid and a (pulsed) gating grid (figs 4, 5).

(c) The magnet. It has to be of solenoidal type, with highly homogeneous field (10^{-4}), and to the same tolerance parallel to the electric field. Both the ALEPH and DELPHI magnets are equipped with superconducting coils which provide 1.5 and 1.2 T, respectively.

3.4 Readout

The detector signal is sensed by a preamplifier which is adapted to the negative wire pulse or to the positive (and smaller) pad pulse. The signal is then transported via twisted pair cables to a shaper and to the digitization unit. There a FADC scans the signal advanced by a 12.5 (15.0) MHz clock. The dynamic range is 256 (512) channels, as given by a 8 (9) bit ADC. This range is appropriate to accommodate the variations in pad response and from ionisation (logarithmic rise, Landau fluctuation and angular effects).

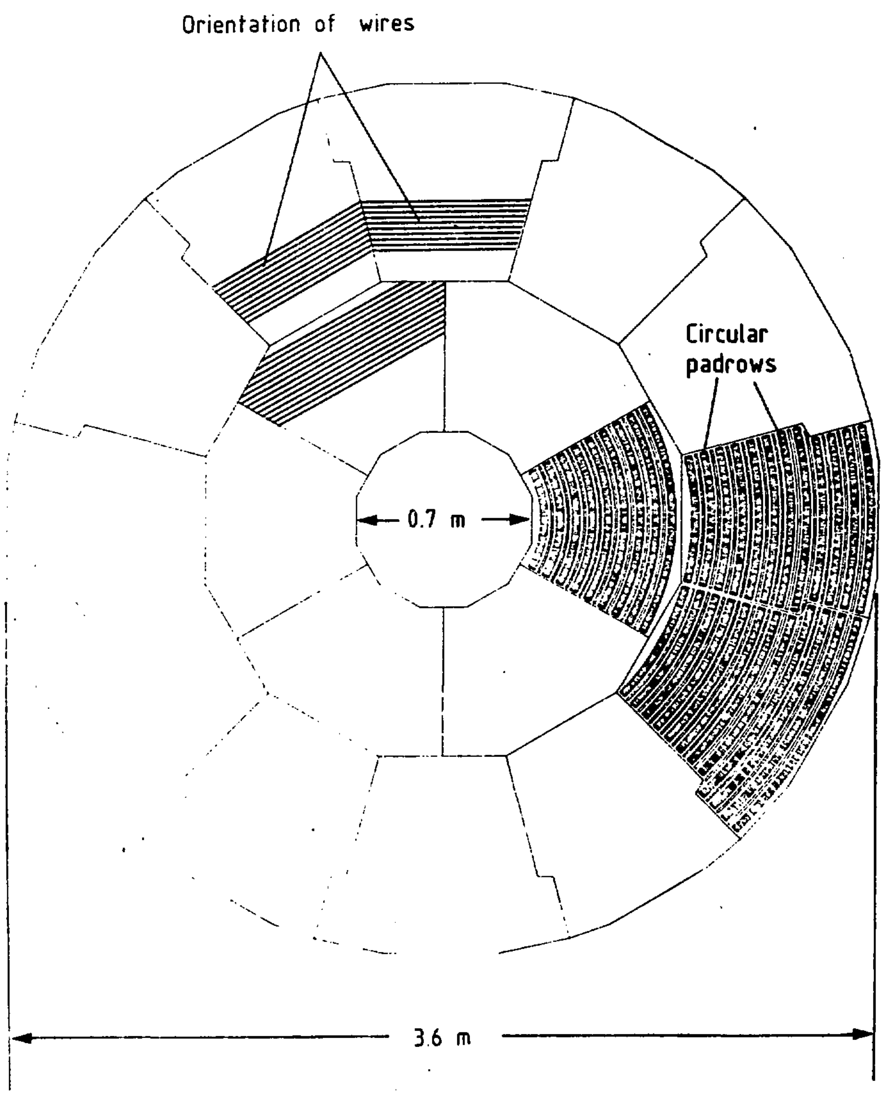

Fig. 4 Detector plane of the ALEPH TPC

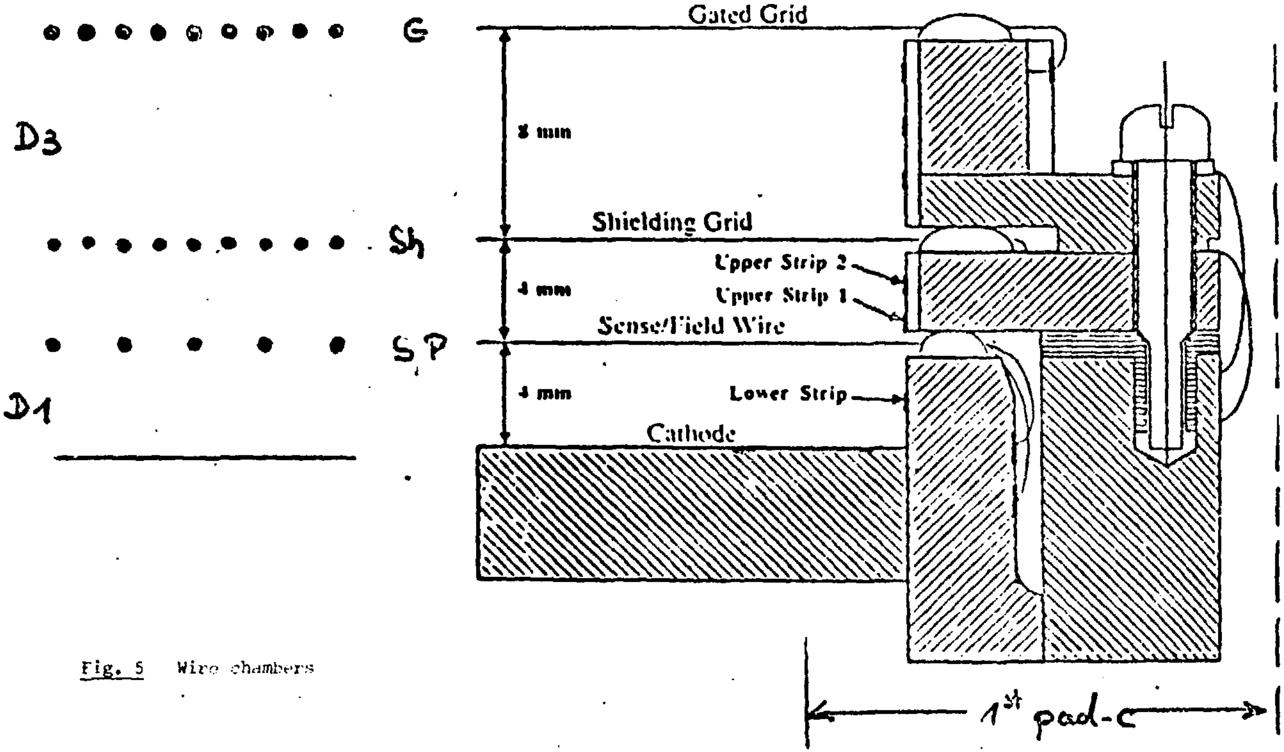

Fig. 5 Wire chambers

Digitized data are further processed by local MC 68020 processors. This "local intelligence" assumes the tasks of system check, data acquisition and calibration.

3.5 Calibration

The calibration aspect enters at two distinct and independent levels:

(a) Electronic calibration is required in order to make the sensitivity of the readout channels equal and known. This is necessary since spatial resolution is obtained by interpolation between adjacent pads. The measurement of energy loss is another reason. Electronic calibration is achieved by applying a standard signal at the input (e.g. pulsing the field wires) and adjusting the slope of the ADC such that equal digitizations are obtained. The change of slope is achieved by adjustments through 4 Digital-to-Analog Converters (DAC).

(b) Geometrical calibration is needed in order to recognize and correct for geometrical distortions due to mechanical, electrical or magnetic imperfections. The calibration method consists of introducing a laser beam into the sensitive volume of the chamber and to detect the necessarily straight ionised tracks. The ALEPH TPC is equipped with two Nd-YAG lasers, the beam of which is each split into 15 subbeams in one half chamber (fig. 6).

4. STATUS AND PLANNING

Both DELPHI and ALEPH TPC are in an advanced stage of construction. The field cages are complete, the detector sectors are in part built, readout electronics is industrially produced and delivered.

The ALEPH TPC is operating as a system with cosmic rays and laser beams, but only partially equipped with detector sectors and readout.

Completion is expected for early 1988, underground installation is foreseen toward the end of 1988.

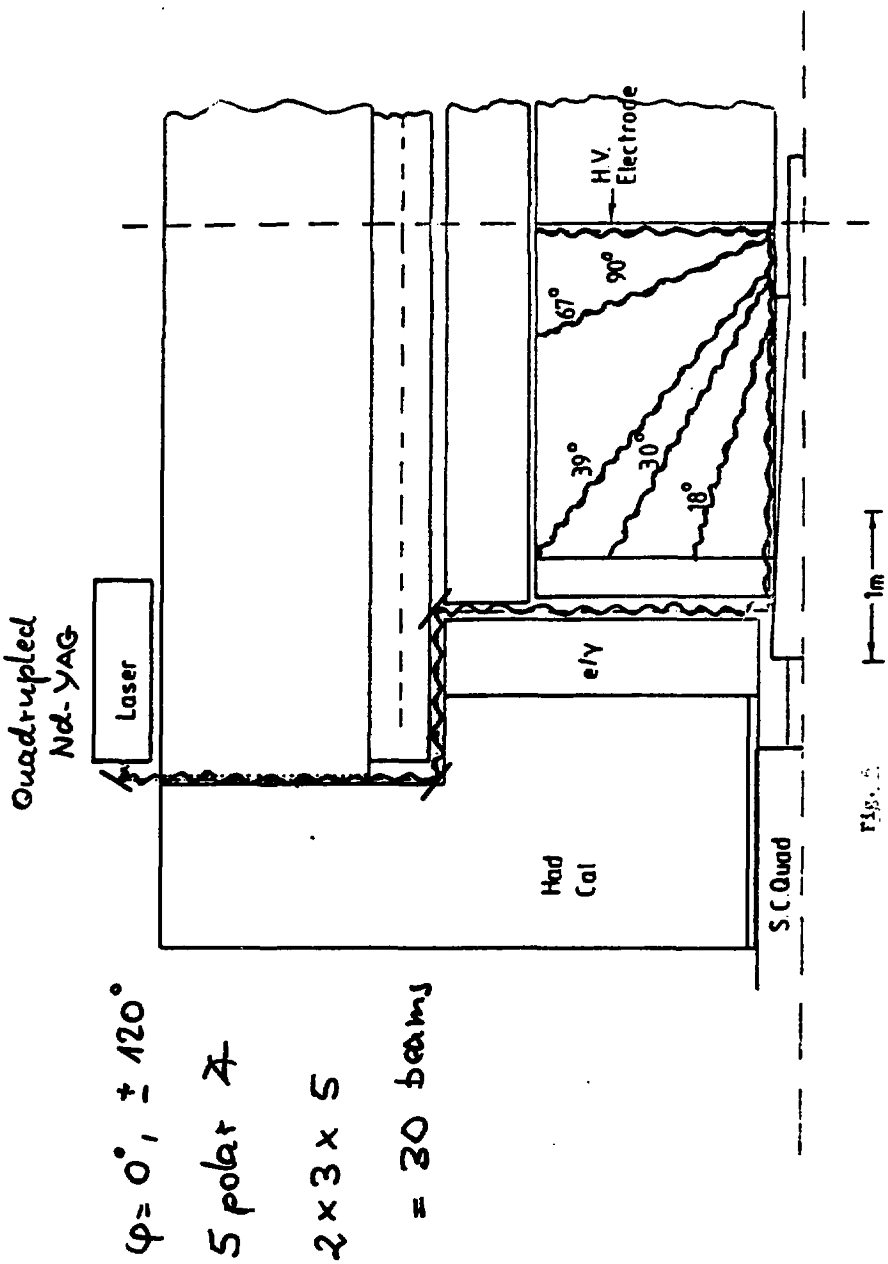
Quadrupled
Nd-YAG
Laser
H.V.
Electrode
90°
67°
39°
30°
18°
e/γ
Had
Cal
S.C.Quad
1m
φ = 0°, ± 120°
5 polar ∡
2 × 3 × 5
= 30 beams

Fig. 6

REFERENCES

[1] Vancouver Workshop 1983, AIP Conference Proceedings 108 (1984).

[2] F. Sauli, CERN Yellow report, CERN 77-09 (1977).

[3] J. Richstein, Thesis, Universität Dortmund (1986).

[4] J. May, Stanford Workshop on Collider Detectors (1987) unpublished.

[5] ALEPH TPC, private communication.

[6] ALEPH Technical report, CERN/LEPC 83-2 (1983).

[7] DELPHI Technical proposal, CERN/LEPC 83-3 (1983).

Project of a Tagged Neutrino Facility at Serpukhov

G. Bohm, IHEP Berlin - Zeuthen, GDR

The tagged neutrino facility at the IHEP Serpukhov is being built by a Serpukhov-Dubna-Pisa-Berlin/Zeuthen - collaboration. It should start physics in 1 to 2 years from now with the U-70 accelerator. In the more distant future it could possibly be used at the UNK, being one of the main experimental roads to ν-physics there. In the first section of this talk, I shall introduce the principle of this new kind of ν-beams. The second section is a short review of the experimental technics, the third will concern the possibilities for ν-physics, the fourth a proposal to study charged kaon decays in a first stage of the experiment.

1. Working principle

At present two ways are well known to produce energetic ν-beams in the laboratory. Starting from a collimated, but not monoenergetic charged or neutral hadron beam, after a decay tube and a muon shield, wide-band ($\overset{(-)}{\nu}_\mu$, $\overset{(-)}{\nu}_e$) beams are formed; narrow-band beams use a monoenergetic charged hadron beam instead. The neutrinos (ν_μ, resp. $\bar{\nu}_\mu$ from the charge conjugated beam) are produced by $\pi \to \mu\nu$ and $K \to \mu\nu$ decays. The radial distance of the vertex in the ν-detector is then used to constrain the ν-momentum. The uncertainty of the parent particle (π or K) and its decay kinematics - the decay point and therefore the angle of the ν against the beam direction is only known to be in a certain interval - determine the errors of primary ν-energy and direction.

The tagging principle, which will be used here, rests on simultaneous measurement of the decay partners of the ν for charged $K_{\mu 2}$ resp. Ke_3 decays in an intense momentum selected unseparated beam of about 35 GeV/c. In the former case, the muon angle against the beam direction, in the latter, angles and energies of the electron and the two photons from π^0 decay will be determined. Using a long beam spill, the ν-events will be related to their parent decays by time and geometrical information. The tagging station is required to keep the information from all candidate decays preceding a trigger signal from the ν-detector.

An event is accepted, if the geometrical information from the tagging station and the ν-detector is matching as well as the timing (within 10 nsec). Defined in this way, the tagged ν-beams will have the characteristics given in table I and fig. 1. /1/, /2/

Table I: Characteristics of tagged ν-beams:

		$\overset{(-)}{\nu_e}$	$\overset{(-)}{\nu_\mu}$
Mean energy E		12.5 GeV	23.4 GeV
Tagged ν-events*/ $3 \cdot 10^{13}$ protons	ν:	0.003	0,14
	$\bar{\nu}$:	$1.6 \cdot 10^{-4}$	0.007
Energy resolution (RMS) $\sigma(E)$		0.75 GeV	1.15 GeV
Angular " " $\sigma(\vartheta)$		0.4 mrad	0.6 mrad
Background contamination		$1,2 \cdot 10^{-3}$	$1,4 \cdot 10^{-3}$

2. Experimental set-up

The experimental set-up is shown schematically in fig. 2.
It consists of a beam line with deflecting magnets M1, M2 and quadrupols Q1 ... 7, hodoscops H1 ... H4 for momentum analysis and Čerenkov counters Č1 ... Č5 for monitoring the beam intensity and composition, a 60 m long evacuated decay pipe with thin windows in the beam region, 3 doubletts of 4 x 4 m^2 hodoscop planes H5 ... H10 with mutually perpendicular strips of 14 mm width, a fine grained electromagnetic calorimeter (TAS) based on lead-scintillator sandwich blocks of size 7,6 x 7,6 x 32 cm^3 (22 radiation length), a muon identifier (MID), a 30 m long muon shield, and the ν-detector, consisting of a big liquid Argon calorimeter (BARS) and a muon spectrometer (MS).
The BARS consists of two vessels, with an overall weight of 600 t, the MS is made of iron-toroids and coordinate planes, consisting of crossed layers of drift tubes. All parts of equipment have been successfully prototyped and are now being constructed or installed.

3. Physics goals

The ν-physics, which may be contemplated for this experiment, can reasonably be based on a statistics of $2\cdot10^5$ ν_μ-events; ν_e-events are down by a factor ~40 and $\bar{\nu}_{e,\mu}$ again by factors ~20 resp.
This disadvantage of a rather limited statistics is compensated by the fact, that systematic errors are much lower than in other ν-beams, because all parameters of the incoming ν will be determined at the level of an individual event.
More quantitatively, the following advantages apply:

- pure ν_e, ν_μ, $\bar{\nu}_e$, $\bar{\nu}_\mu$ -beams with 2 - 3 orders of magnitude less flavour contamination than in conventional beams. High energy ν_e, $\bar{\nu}_e$ -beams are practically not existing.
- better (by factor 3 ÷ 4) estimation of primary energy
- better (by factor 5÷10) estimation of ν-angles
- absolute normalisation better by an order of magnitude
- known ν-production vertex

The most obvious goals will be

- Detailed investigation of ν_e - ν_μ universality by (differential) cross-section ratios for CC and NC
- Measurement of absolute cross sections as functions of energy (this is not at all obsolete in the lower energy range considered here. Moreover it will improve conventional experiments by checking their Monte-Carlo-corrections).
- search for ν-oszillations ($\nu_e \rightarrow \nu_\tau$) and lepton mixing.
  For other items - measurement of structure functions, study of rare processes (dilepton-channels, large missing energy)- the statistics may be low, but nevertheless the above mentioned advantages apply as well.

4. Study of K^+ -decays

An obvious way to use the tagging station before the completition of the large ν-detector is to study charged K-decays.
After all, the U-70 with booster intensity is a good kaon factory - and kaon decay studies, esp. with high statistics - have always been and continue to be of high value for the development - and restriction -

of elementary particle theories.

On the experimental side, with hadron beam intensity 10^8/s, we can have up to 10^6 K-decays/s in the vacuum pipe. With the hodoscops, TAS and a μ-identifier alone we have already very fast and efficient possibilities for angular measurements and γ-spectroscopy.

Most important for useful physics will be a fast and sophisticated multilevel trigger and efficient data reduction - this is also under development.

As a further upscale, there are designs for a large gas Cerenkov counter for electron detection at the end of the decay pipe, an ironfree toroidal magnet in between the first two hodoscop planes and a hadron calorimeter instead of the passive μ-shield for μ-identification. Among the proposed items are the following:

CP-violation: measurement of differences in partial nonleptonic decay rates resp. Dalitz-plot densities between K^+ and K^-. Because such differences in $\Delta S = 1$ channels can only exist, if $\varepsilon' \neq 0$, this would be the most direct test of the Wolfenstein model.

Lepton-nb violation: search for $K \to \pi e \mu$, $K^\pm \to \pi^\mp e^\pm e^\pm$, $K^\pm \to \pi^\mp \mu^\pm \mu^\pm$

Radiative K-decays: search for $K^\pm \to \pi^\pm \gamma\gamma$ and $K^\pm \to \pi^\pm \mu^+ \mu^-$ study of $K^\pm \to \pi^\pm e^+ e^-$ and $K^\pm \to \pi^\pm \pi^0 \gamma$

The latter studies are of importance for theoretical models in the framework of chiral effective Lagrangians.

Other more or less automatically accumulated data on the life times of $K^\pm$ can be used to test CPT, and on the branching ratio for Ke_3 decays to improve the Kobayashi-Maskava matrix element Vus.

The start of this decay programme is - in minimal stage - proposed for the next year.

References:

/1/ A.A. Boikov et al., preprint IHEP 80 - 156, Serpukhov, 1980
A.A. Boikov et al., preprint IHEP 80 - 158, Serpukhov, 1980

/2/ S.P. Denisov et al., preprint IHEP 81 - 98, Serpukhov, 1981

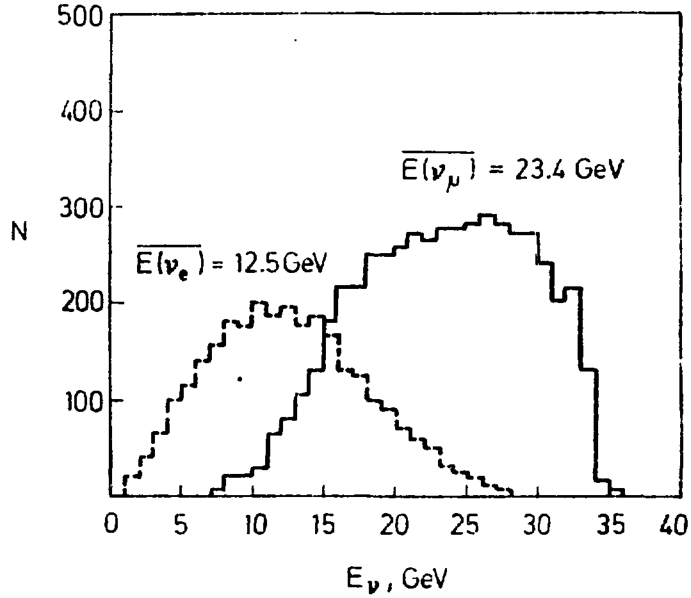

Fig.1 Energy distribution of ν_e and ν_μ for equal numbers of Ke_3 and $K\mu_2$ decays

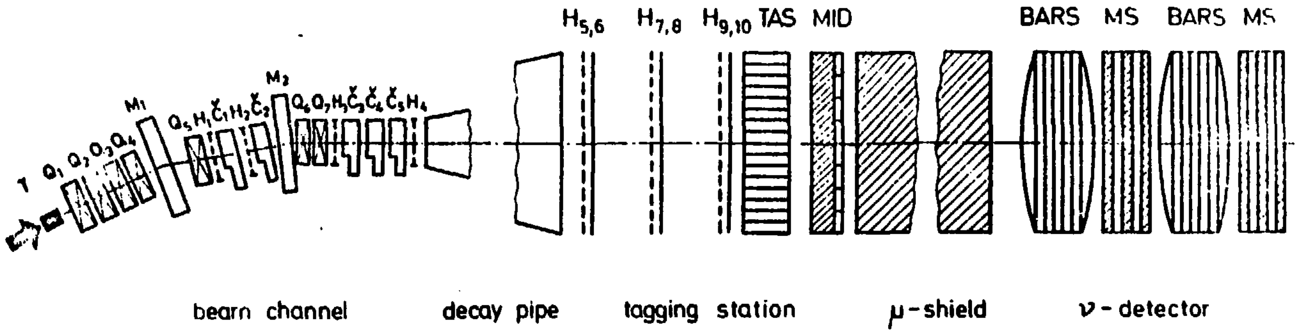

Fig. 2 Schema of tagged neutrino facility at the Serpukhov accelerator

On Superstrings and the Unification of Particle Interactions

Jean-Pierre Derendinger

Institut für Theoretische Physik
ETH - Hönggerberg
CH - 8093 Zürich, Switzerland

1. Introduction

Anomaly-free superstring theories [1,2] could bring a solution to the long-standing problem of quantum gravity. This is the main motivation to consider the possibility of unifying all interactions in a fundamental superstring theory, at a scale close to the scale of quantum gravity, $M_P \sim 10^{19}\,GeV$. However, the choice of the fundamental superstring theory is far from unique. There is first the choice of the space-time dimension. The most symmetric anomaly-free superstrings are characterized by a ten-dimensional Minkowski space. But many other theories can be constructed in lower dimensions, and they could as well lead to attractive unified theories. Many of the lower dimensional theories are related to ten-dimensional strings by compactification, but many of them are new, independent theories. There are two extreme options. Insisting on the unicity of the fundamental superstring leads to consider ten-dimensional theories, with a necessary dynamical compactification of the extra dimensions. But one can also require staying with four-dimensional space-time, avoiding compactification.

In the framework of ten-dimensional superstrings, only two theories satisfy both the requirements of supersymmetry and absence of anomaly, which is related to the absence of divergences. They are characterized by the gauge groups $SO(32)$ and $E_8 \otimes E_8'$. In fact, $SO(32)$ can be realized either with open superstrings [3] or with heterotic strings [4], while only heterotic strings can accomodate $E_8 \otimes E_8'$. These two string theories possess the same massless sector. Their effective low-energy theories will differ only when higher order effects induced by the massive string modes are computed. For phenomenological reasons, $E_8 \otimes E_8'$ has proven to be much more attractive than $SO(32)$. At the level of the ten-dimensional theory, the choice is then essentially unique. However, the process of compactification from ten to four dimensions does not preserve this uniqueness. The geometry of the six compactified dimensions is not fully determined by the equations of motion of the string theory. Many possibilities exist, including Calabi-Yau spaces [5] and orbifolds [6]. Starting from a unique theory, one then gets several possible particle contents and gauge groups at energies much lower than the Planck scale where compactification occurs. This scale is also the scale of the massive string modes, which should then have some implications for the discussion of compactification and of the low-energy effective theory.

In the case of four dimensions, there is no compactification, but many anomaly-free string theories exist and there is no prescription for selecting a model out of the several possibilities. The construction of four-dimensional string theories essentially proceeds by imposing suitable boundary conditions on the string coordinates [7]. This method has been shown to provide many new one-loop finite string models, with various gauge groups and various spectra of massless states [7–9].

These notes are divided in two parts. First, some of the characteristic features of the effective Lagrangian of superstrings will be discussed, essentially focussing on the case of compactified ten-dimensional heterotic strings, under the assumption that the effective theory is supersymmetric. At energies much smaller than the Planck scale M_P, the superstring unified theory corresponds to an effective field theory describing the interactions of the massless modes of the strings. To be realistic, the spectrum of massless states must contain quarks, leptons, gauge bosons and the Weinberg-Salam Higgs scalars, and the parameters of the effective Lagrangian should also 'predict' the correct values of masses, coupling constants and scales of symmetry breaking. Supersymmetry is a basic ingredient in understanding the scales of a unified theory of strong and electroweak interactions [10]. It is also present in the fundamental superstring, and could then survive the processes of low-energy field theory limit and/or compactification. Also, imposing supersymmetry at energies lower than the Planck scale restricts very much the arbitrariness of the effective Lagrangian, making much easier the discussion of its relation to the fundamental superstring theory. At present stage, no firm predictions exist for a non supersymmetric effective theory.

In the second part, some aspects of the construction of four-dimensional superstrings will be presented. In particular, the procedure used ~~in Ref. [9] to~~ obtain gauge groups with low ranks will be summarized.

2. The effective theory

Up to now, most of the investigations of the effective field theory of superstrings assume that the fundamental theory is the heterotic string with gauge group $E_8 \otimes E_8$. The reason is that there are compactifications of the heterotic string which lead to gauge groups and massless states very close to a realistic extension of the Standard Model. This is the case of some Calabi-Yau spaces [11] studied in Ref. [12], and also of some orbifolds [6,13]. These different possibilities are in fact the only realistic candidates for a unified superstring theory known at present.

2.1. Gauge groups and spectra

The ten-dimensional heterotic string possesses many different compactification vacua which preserve one supersymmetry in four dimensions. These vacua are probably all degenerate because of supersymmetry. Most of them would lead to disastrous phenomenology. Realistic cases are indeed only a small minority of all vacua, but they show common features which offer the opportunity of a global discussion of the phenomenological implications of heterotic superstrings.

String dynamics requires the six compactified dimensions to live on a Ricci flat compact space [5]. Supersymmetry in four dimensions implies that the holonomy group of the compact space is $SU(3)$. It also requires the space to be kählerian. Two classes of such spaces are known. Manifolds satisfying the above requirements are called Calabi-Yau spaces. Even though there exists a large number of Calabi-Yau spaces, there is probably a unique manifold producing three massless generations of quarks and leptons and their supersymmetric partners, and compatible with a realistic symmetry breaking pattern [11]. Several cases are known with four generations [5]. The gauge group of Calabi-Yau compactifications is always a subgroup of $E_8 \otimes E_8'$. This is related to the necessary embedding of the connection with $SU(3)$ holonomy into one of the E_8 factors of the heterotic gauge group. The choice of the subgroup is suggested by phenomenology requirements and not, at present, by dynamical arguments. One must require that a convenient symmetry breaking pattern into $SU(3) \otimes SU(2) \otimes U(1)$ exists with the scalar fields contained in the spectrum of massless states. As a consequence, E_6 has to be broken, but many choices of subgroup exist [14]. The smallest gauge group containing $SU(3) \otimes SU(2) \otimes U(1)$ compatible with phenomenology is in fact $SU(3) \otimes SU(2) \otimes U(1) \otimes U(1)'$, with a new $U(1)$ factor with specific quantum numbers for quarks and leptons. Notice that E_8' is a hidden sector in the sense that the spectrum of massless states does not contain states with $SU(3) \otimes SU(2) \otimes U(1)$ as well as E_8' interactions.

The second class of compact spaces leading to supersymmetric compactifications of the heterotic strings corresponds to orbifolds [6]. These spaces are obtained by dividing by a discrete group a manifold which, in the case of strings, is in general a six-torus. Orbifolds are not manifolds. They have singularities. It is however possible to define properly the propagation of strings on such spaces. Their predictions for the low-energy effective theory are quite similar to those of Calabi-Yau spaces. The gauge group is a subgroup of $E_6 \otimes SU(3) \otimes E_8'$. The $SU(3)$ factor is not broken as it was the case with Calabi-Yau spaces. As in the case of Calabi-Yau compactifications, the effective, low-energy gauge group is always larger than $SU(3) \otimes SU(2) \otimes U(1)$. The same new $U(1)$ group is always present below the Planck scale, but much larger symmetries can also arise. A potential problem with orbifolds is that they produce in general a too large number of quark-lepton generations. More realistic orbifolds require more sophisticated constructions [13].

The spectra of massless states of heterotic strings compactified on Calabi-Yau manifolds and on orbifolds are essentially similar. The states are naturally classified in supersymmetry multiplets, since by assumption compactification leaves one supersymmetry in four dimensions. The gauge multiplet of local supersymmetry is the *supergravity multiplet*, with the spin 2 graviton and its spin 3/2 partner, the gravitino. A *Yang-Mills multiplet* (gauge bosons and spin one-half gauginos) is associated to the effective gauge group, which is always larger that $SU(3)\otimes SU(2)\otimes U(1)$. The *chiral matter multiplets* (left-handed spin one-half states and scalars), which should contain quarks, leptons and Higgs scalars, are classified in replications of generations of 27 states. This is the consequence of the embedding of $SU(3)\otimes SU(2)\otimes U(1)$ in E_6. Each quark-lepton generation is enlarged to a **27** multiplet of E_6, even though E_6 is broken. The $SU(3)\otimes SU(2)\otimes U(1)$ quantum numbers of the 27 states are the following: we first have the 15 quarks and leptons:

$$(3,2,1/6)+(\overline{3},1,1/3)+(\overline{3},1,-2/3)$$
$$+(1,2,-1/2)+(1,1,1).$$

In addition, we have twelve new states transforming according to

$$(3,1,-1/3)+(\overline{3},1,1/3)$$
$$+(1,2,1/2)+(1,2,-1/2)+2(1,1,0).$$

An important result is that the new $U(1)$ gauge group which is always present in both Calabi-Yau and orbifold compactifications imposes that all the 27 states remain massless as long as this new symmetry is not broken. The scale of the new neutral gauge boson is then also the scale of the new (spin 0 and 1/2) states enlarging each quark-lepton generation. The number of generation is related to the geometry of the compact space used to compactify heterotic strings. The spectrum of massless states can also contain some chiral multiplets in real representations of the gauge group. Their number and their classification depend very much on the choice of the compact space. These multiplets are essential for spontaneous symmetry breakings at intermediate scales ($M_W \ll E \ll M_P$), which must also preserve supersymmmetry. Calabi-Yau compactifications always produce such states, while orbifolds forbid them in general. As a consequence the scale of the new $U(1)$ gauge boson (and of the new states enlarging each fermion generation) should be close to the weak interaction scale in orbifold compactifications. This scale can however be very large (even close to the Planck scale) in Calabi-Yau compactifications. A firm prediction of this scale relies upon a precise knowledge of the effective Lagrangian.

String compactification also produces some *gauge singlet chiral multiplets*. Their number depends on the geometry of the compact space, but two of these singlets play a particular role, and are associated with *classical symmetries* of the underlying string theory [5,15]. The *scale invariance* of the string theory generates a *dilaton* massless mode with specific couplings directed by scale invariance. Also, compactified superstrings have a *rescaling property* related to the fact that string equations of motion do not fix (classically) any scale. The radius of the compact space can then be freely rescaled. This symmetry generates a 'breathing' massless mode. Once redefined in a way appropriate to the supergravity formalism, these two gauge singlets correspond to two chiral multiplets S and T with very specific couplings. These two multiplets play a crucial role when the explicit form of the effective supergravity Lagrangian is investigated.

2.2. The effective supergravity Lagrangian

At energies much smaller than the Planck scale, the interactions of the massless modes of compactified superstrings are described by an effective supergravity Lagrangian. Again, compactification is assumed to preserve one supersymmetry in four dimensions. This Lagrangian contains different components. It can be split (somewhat arbitrarily) into two parts:

$$\mathcal{L}_{eff} = \mathcal{L}_0 + \mathcal{L}_1. \tag{1}$$

$\mathcal{L}_0$ contains all terms with at most two space-time derivatives. In particular, it includes all terms of dimensions up to four, but some terms of higher dimensions, without derivatives are also present. $\mathcal{L}_0$ has the familiar form of four dimensional supergravity theories [16]. It is fully described by two functions of the chiral multiplets, the Kähler function $\mathcal{G}(z, z^*)$ and the function defining the gauge field kinetic terms, $f_{\alpha\beta}(z)$. These two functions introduce in general interactions of arbitrary high dimensions, but without derivatives. $\mathcal{L}_1$ contains all higher derivative terms (like Lorentz Chern-Simons forms) and their supersymmetrization. The presence of these contributions requires an extension of the formalism of four-dimensional supergravity [17]. On the other hand, these new terms are a crucial feature of superstring theories, since the mechanism of anomaly cancellation appears essentially in this sector of the effective theory.

At the classical level, the form of $\mathcal{L}_0$ is essentially determined by the classical symmetries of the string theory, $N = 1$ supersymmetry and the origin (in terms of ten-dimensional states) of the massless fields [15,18]. At this order, $\mathcal{L}_1$ also receives contributions, which are only partly known. Determining $\mathcal{L}_0$ means obtaining the two functions

$$\begin{gathered} \mathcal{G}\left(S,S^*,T,T^*,C^i,C_i^*\right), \\ f_{\alpha\beta}\left(S,T,C^i\right), \end{gathered} \tag{2}$$

where C^i represents all matter multiplets with gauge quantum numbers (mainly the states of 27 and 27*). The only gauge singlet multiplets which we keep in this discussion are the two 'geometrical' singlets S and T. The complex fields S and T have imaginary, pseudoscalar components originating from the antisymmetric tensor of the ten-dimensional massless supergravity multiplet. They have then *axion-like symmetries* of the form:

$$Im\,S,T \rightarrow Im\,S,T + constants. \tag{3}$$

As a consequence

$$\begin{gathered} \mathcal{G} = \mathcal{G}\left(S+S^*,T+T^*,C^i,C_i^*\right) \\ f_{\alpha\beta} = (aS+bT)\,\delta_{\alpha\beta} + F_{\alpha\beta}\left(C^i\right) \end{gathered} \tag{4}$$

where a and b are constants, and F is an arbitrary function. The two classical symmetries, scale invariance and the rescaling property, mean that

$$\begin{aligned} \mathcal{G} = &- ln\,(S+S^*) - 3ln\,(T+T^*) \\ &+ ln\,(WW^*) + g\left(\frac{C^i}{\sqrt{T+T^*}},\frac{C_i^*}{\sqrt{T+T^*}}\right). \end{aligned} \tag{5}$$

The superpotential W takes the form

$$W = \lambda_{ijk}C^iC^jC^k + \omega, \tag{6}$$

up to higher dimension terms, suppressed by $M_P{}^{-n}, n \geq 1$. This form is due to the E_6 and E_8 gauge symmetry. The only arbitrary function is g. The function $f_{\alpha\beta}$ is fully determined:

$$f_{\alpha\beta} = cS\delta_{\alpha\beta}, \tag{7}$$

where c is a constant. In simple truncations [15], which are related to orbifold compactifications but probably not to Calabi-Yau compactifications, the function g reads

$$g = -3ln\left(1 - \frac{2C^iC_i^*}{T+T^*}\right) \tag{8}$$

so that finally [15,19]:

$$
\begin{aligned}
\mathcal{G} &= -ln\,(S+S^*) - 3ln\left(T+T^* - 2C^iC_i^*\right) + in\,(WW^*)\,, \\
W &= \lambda_{ijk}C^iC^jC^k + \omega \\
f_{\alpha\beta} &= cS\delta_{\alpha\beta}.
\end{aligned}
\tag{9}
$$

The coupling constants λ_{ijk} contain the Yukawa couplings of quarks and leptons, which are in principle calculable from the superstring theory. The corresponding supergravity Lagrangian is the starting point for the so-called *superstring inspired models.*

The scalar potential, including terms bilinear in the gaugino fields, is a sum of positive terms:

$$
\begin{aligned}
V_{eff} =& \left|\frac{1}{4t_c}\frac{1}{\sqrt{st_c}}W + \frac{1}{2}s\left(\overline{\lambda}^\alpha\lambda^\alpha\right)\right|^2 \\
& \frac{1}{48st_c^2}W_iW^{i*} + \frac{9}{2st_c^2}\left(gC_i^*T^{\alpha i}{}_jC^j\right)^2,
\end{aligned}
\tag{10}
$$

where

$$
\begin{aligned}
s &= Re\,S = \frac{1}{2}(S+S^*)\,, \\
t_c &= \frac{1}{2}\left(T+T^* - 2C^iC_i^*\right),
\end{aligned}
\tag{11}
$$

and W_i is the derivative of W with respect to C^i. The positivity of the scalar kinetic terms removes the apparent singularity in s and t_c, and ensures the positivity of the potential. This potential has remarkable properties: the necessary breaking of supersymmetry is induced only by *gaugino condensation* [20,21]:

$$
<\overline{\lambda}^\alpha\lambda^\alpha>=\Lambda_c{}^3 \neq 0. \tag{12}
$$

The minima of the potential have zero cosmological constant, $< V_{eff} >= 0$. Possible vacuum expectation values of the scalar fields C^i will in general induce intermediate symmetry breakings of the gauge group to finally obtain $SU(3)\otimes SU(2)\otimes U(1)$. It is remarkable that all directions in C^i which can be used for a realistic symmetry breaking satisfy

$$
\begin{aligned}
&< \lambda_{ijk}C^jC^k > \sim < W^i >= 0 \\
&< \lambda_{ijk}C^iC^jC^k >= 0
\end{aligned}
\tag{13}
$$

Then, for relevant directions, $< W >= \omega$, and the vacuum expectation values $< C^i >$ are not determined by minimizing the potential. The potential has *flat directions* and the scales of intermediate breakings are free (at the classical level at least). The minimization of the potential in supersymmetry breaking directions will cause ω, Λ_c^3 and $< st_c >$ to adjust themselves in order to have $< V >= 0$. The potential has also flat directions in the singlet sector, leaving all breaking scales undetermined at the classical level. This is a remnant of the scale invariance of the superstring theory.

As already mentioned, supersymmetry is broken only when gauginos condensate, and, from the structure of the potential, when the superpotential W contains a constant term ω [20]. Gaugino condensation will occur in general in the hidden sector. The hidden gauge group is an asymptotically-free force. The gauginos of the hidden sector will then form condensates at a scale Λ_c close to the scale where this force becomes confining.

At this point, there is an important difficulty. The scale of supersymmetry breaking is fully determined by the hidden sector. It will then induce supersymmetry breaking corrections to the visible sector of the theory. However, the classical Lagrangian does not contain any *soft breaking term*, even when gaugino condensation is included [21]. Then, only higher order loop corrections can transmit the effect of supersymmetry breaking to the visible sector. Ultimately, the soft breaking terms generated by higher order corrections should induce the breaking of $SU(2)\otimes U(1)$ at the right scale, ~ 100 GeV. This will be feasible only with a large scale Λ_c of gaugino condensation, which is fixed by the hidden sector. Thus, finding the right scales involves a subtle interplay of the visible and hidden sectors, controlled by quantum corrections. This situation corresponds essentially to *no-scale supergravity models* [22], except that all parameters are now in principle calculable in terms of the fundamental superstring theory. Numerical predictions rely heavily upon higher order quantum corrections. These corrections fall in different classes. Supergravity loop corrections have a physical cut-off at the Planck scale M_P, where the full superstring theory turns on. They are in principle easily calculable. For instance the one-loop effective potential has been computed [23], and shows a tendency to curve the flat directions and to push the vacuum expectation values towards the Planck scale, where the calculation loses its validity. In this region, we face real superstring corrections and a complete analysis is missing. Notice that one-loop superstring corrections are in principle calculable since the string theory is finite at this order at least.

More precise, numerical predictions, like for instance values of Yukawa couplings, require a deeper understanding of the compactification process. The unique known model which can be made realistic as far as gauge groups, massless states and symmetry breaking are concerned, is the Calabi-Yau compactification of heterotic strings found in Ref. [11]. Its structure and predictions have been analyzed [12] under several assumptions concerning the compactification vacuum. Even for a well defined Calabi-Yau space, this vacuum is far from unique. There is an infinite number of vacua leading to the same symmetry breaking pattern, but with several different discrete symmetries applying in the effective theory. These discrete symmetries are in general important to avoid unwanted Yukawa couplings, or to forbid disastrous processes like, for instance, fast nucleon decay. Details of the effective theory will then strongly depend on the choice of the real vacuum, which results from string dynamics and can hardly be investigated with present technology.

3. On four-dimensional superstrings

String theories are constructed from two basic building blocks: the bosonic string containing 24 real, light-cone string coordinates X^I, and the superstring made of 8 real light-cone bosonic coordinates and 8 two-dimensional (world-sheet) spinorial coordinates S^a. Notice that the crucial number is twenty-four, since a spinor corresponds to two real degrees of freedom. The superstring brings naturally supersymmetry, whose interest for low-energy phenomenology has been already mentioned. It is also an essential ingredient in understanding the vanishing of the cosmological constant. For each of these two cases, the string Lagrangian is a two-dimensional field theory, and the right- and left-movers form independent sectors. Then, for instance, heterotic strings [4] are obtained by associating the left-movers of the bosonic string and the right-movers of the superstring. The number of components of the string theory is a consequence of two-dimensional conformal invariance, which is the remnant of the reparametrization invariance of the world-sheet, necessary for a physically satisfactory model. The conformal anomaly will only cancel for this critical number of string coordinates, and this cancellation has to occur separately for left- and right-movers.

This critical number of string fields can be translated into a critical space-time dimension once boundary conditions are imposed. We will only consider here closed strings: open strings are a particular subcase with identical left-and right-movers. Imposing that all string coordinates are periodic functions of $\tau \pm \sigma$ leads to the most symmetric situation, with the largest space-time symmetry. In this case, one can construct a full Lorentz algebra in space-time dimension 26 for the purely bosonic string or 10 for the purely superstring case. There are however many other possible boundary conditions which will lead to different space-time properties. These more general boundary conditions sometimes correspond to compactifications of the most symmetric model, with the largest space-time dimension. This is the case if left- and right-mover coordinates are treated symmetrically, with the same boundary conditions. However, a string theory with different boundary conditions for left- and right-movers is not in general equivalent to a compactified, larger dimensional theory.

For closed strings, the admissible boundary conditions are of the form

$$Z^I(\tau \pm \sigma - \pi) = e^{-2i\pi\theta_I} Z^I(\tau \pm \sigma) + v^I \tag{14}$$

for bosonic coordinates, and

$$S^\alpha(\tau \pm \sigma - \pi) = e^{-2i\pi\theta_\alpha} S^\alpha(\tau \pm \sigma) \tag{15}$$

for fermions. They contain two different quantities, the *shifts* v^I and the *twists* θ. The shifts v^I are characteristic of compactification, when space-time has the geometry of a generalized torus. The simplest example arises when one space direction X^A is a circle of radius R. Then the boundary condition for a closed string coordinate in this spatial direction is naturally written

$$X^A(\sigma = 0, \tau) = X^A(\sigma = \pi, \tau) + 2\pi R n. \tag{16}$$

The integer n counts how many times the string coordinate loops around the circle. The shifts v^I are the generalization of this simple situation to the case of an arbitrary number of string coordinates, which can be either left- or right-movers. They span a lattice and introduce new string states corresponding to winding sectors which often contain massless states leading to large, non abelian gauge groups. The twists θ are present for instance in orbifold models [6]. In these cases, they correspond to the discrete symmetries used in defining the orbifold. The role of twists is crucial to reduce the rank of the gauge group. In general, in a string theory without twisted bosons, the rank of the gauge group is the same as the number of 'internal' coordinates. To be complete, one should consider a matrix of twists. Here, we will only consider abelian twists θ_I associated to the coordinate Z^I, or to a given spinor. Notice also that twists require working with complex bosonic string fields. Twists generate twisted sectors, with new string states which are in general massive. They do not generate new gauge symmetries, but can produce new massless matter (i. e. spin 0 or 1/2) states.

However, choosing boundary conditions is not enough to provide a physically satisfactory model. The string theory must satisfy additional conditions. The consistency of the quantum theory (i. e. the finiteness property) corresponds to the invariance of loop amplitudes under modular transformations of the world-sheet of loop diagrams. At one-loop, the world-sheet is a torus. Modular invariance leads then to constraints on the boundary conditions along to the two non contractible loops on the torus. There is a further condition arising at two loops. The corresponding world-sheet is obtained by 'gluing' two tori. There is then a new non contractible loop connecting the two handles, leading in general to a new constraint on boundary conditions. Higher loop diagrams are obtained by gluing further tori, but only repeating the same conditions of modular invariance. There is then no new constraint beyond two loops. The one-loop path integral is essentially the partition function for the string states. Modular transformations act on the partition function and mix in general different boundary conditions. The problem is then to find a set of twists and shifts such that modular transformations close on this set. The sum of the partition functions for all boundary conditions in the set is then modular invariant at one loop. The last step is then to impose two-loop modular invariance, which may introduce further constraints.

Many four-dimensional string theories can be constructed along this line, by choosing boundary conditions such that the space-time symmetry contains only four-dimensional Lorentz transformations, all other string coordinates corresponding to internal degrees of freedom [7-9]. They possess various gauge groups and massless spectra. The rank of the gauge group is in general very large, and in most cases [7,8] it is twenty-two. This is certainly far too large for a realistic unified model, containing the standard $SU(3) \otimes SU(2) \otimes U(1)$ model. Reducing the rank is then an important issue, and can be obtained with twisted bosons, generalizing orbifold compactifications. The most interesting theories use the same set of string coordinates as the heterotic string. The bosonic sector is used to produce the gauge group, which can be physically attractive in many cases, and the fermionic sector allows space-time supersymmetry in four dimensions, an important feature of many unified models of strong and electroweak interactions. We will now summarize the construction of twisted four-dimensional superstrings [9], leading to many string theories with lower rank gauge groups. In particular, rank eight or sixteen are favoured by the solution of the constraints of modular invariance.

The strategy to construct twisted four-dimensional superstrings is then as follows. We start with the following set of string coordinates: the left-movers are purely bosonic:

$$\begin{aligned} &X^a(\tau+\sigma) \qquad a=1,2 \\ &Z^I(\tau+\sigma) \qquad I=1,\ldots,11, \end{aligned} \tag{17}$$

while the right-movers are those of the superstring:

$$\begin{aligned} &X^a(\tau-\sigma) \qquad a=1,2 \\ &S^\alpha(\tau-\sigma) \qquad \alpha=1,2 \\ &Z^k(\tau-\sigma) \qquad k=1,2,3 \\ &S^{\alpha k}(\tau-\sigma) \qquad k=1,2,3 \end{aligned} \tag{18}$$

Real and complex bosons are respectively denoted by X and Z. The four-dimensional space-time light-cone coordinates are X^a, $a=1,2$, and should then be fully periodic. We then assign a twist θ and a shift v to the other complexified boson coordinates. We also assign a twist to each right-moving fermion. The requirement of $N=1$ space-time supersymmetry implies that the four right-moving spinors should have the same twists as the right-moving bosons. The space-time spinorial coordinate S^α is then periodic. The other right-mover states will however be twisted in order to avoid a larger ($N=2$ or 4) supersymmetry. The full set of boundary condition is then specified by

$$W=(0,\theta_k,(\theta_k,v_k)|(\theta_I,v_I)), \qquad k=1,2,3, \quad I=1,\ldots,11, \tag{19}$$

where the entries coreespond respectively to S^α, $S^{\alpha k}$, Z^k and Z^I. This vector W can be splitted into a rotation vector R containing the twists, and a shift vector V.

We omit the transverse, periodic bosons X^a. In addition the closure of Lorentz and supersymmetry algebras imposes that

$$\theta_1 + \theta_2 + \theta_3 = 0 \qquad \text{mod } 1 \tag{20}$$

for the fermion twists. At this point, requiring $N = 1$ supersymmetry is not essential for the rest of the formalism. It is only an assumption, due to 'phenomenological' motivations. One could as well twist the spinor S^α and break all supersymmetries, or obtain $N = 2$ by choosing, say, $\theta_2 = 0$. This would not lead to any fundamental change of the following discussion.

The next and most important problem is to solve the constraints of modular invariance. The procedure is to combine partition functions of string fields with given boundary conditions in a modular invariant way. The method we follow is analogous to the discussion of Ref. [24], generalized to allow for twisted bosons. There is however an important complication: the partition function of a zero twist boson (which can however have a shift) is not the $\theta = 0$ case of the partition function of a twisted boson. This is essentially due to winding states, which are anyway absent for non trivial twists. This is apparent in the mode expansion of a boson with boundary condition (14), which reads

$$Z^I(\tau \pm \sigma) = z^I + \frac{i}{2} \sum_n \frac{1}{n - \theta_I} \alpha^I_{n-\theta_I} e^{-2i(n-\theta_I)(\tau \pm \sigma)}, \tag{21}$$

with

$$z^I = v^I \left(1 - e^{-2i\pi\theta_I}\right)^{-1}. \tag{22}$$

This last expression cannot be used for $\theta = 0$. Twisted bosons have no zero modes, corresponding to the quantized momenta of shifted bosons. This difficulty can be circumvented with the help of a projector

$$\begin{aligned} \mathcal{P}_{\theta\phi} = \delta_{\theta 0}\delta_{\phi 0} &= 1 \qquad \text{for zero twists} \\ &= 0 \qquad \text{otherwise} \end{aligned} \tag{23}$$

which allows to treat all cases simultaneously. The full partition function for a particular pair of boundary conditions W and W' is

$$\begin{aligned} Z^W_{W'} = Z^0_0 \prod_{k=1}^{3} Z^{\theta_k}_{\phi_k} \left[(1 - \mathcal{P}_{\theta_k\phi_k}) Z^{-1}{}^{\theta_k}_{\phi_k} + \mathcal{P}_{\theta_k\phi_k} Z^{v_k}_{u_k}\right] \cdot \\ \cdot \prod_{I=1}^{11} \left[(1 - \mathcal{P}_{\theta_I\phi_I}) Z^{-1}{}^{\theta_I}_{\phi_I} + \mathcal{P}_{\theta_I\phi_I} Z^{v_I}_{u_I}\right]^*, \end{aligned} \tag{24}$$

in terms of the partition functions for a twisted fermion (Ξ^{θ}_{ϕ}) and a shifted boson (Z^{v}_{u}). We then impose modular invariance on combinations

$$Z = \sum_{A,B} C^{W_A}_{W_B} Z^{W_A}_{W_B}, \tag{25}$$

and solve for the coefficients $C^{W_A}_{W_B}$. One-loop modular invariance is in general not sufficient to ensure having a physically satisfactory string theory. Anyway, it does not fully determine the coefficients. A further condition arises from two-loop diagrams. We use a generalized GSO projection (in analogy with [24]) to take this last constraint into account. As already mentioned, a modular invariant combination (25) involves in general many different boundary conditions. The corresponding string theory always contains an untwisted sector and several twisted sectors, with different projectors $\mathcal{P}$.

The equations of modular invariance applied on combinations (25) are very complicated to solve in general. They are however much simpler in the case where all relevant projectors $\mathcal{P}$ satisfy the condition

$$\frac{1}{4}\left(\sum_{I=1}^{11} \mathcal{P}_{Iab} - \sum_{k=1}^{3} \mathcal{P}_{kab}\right) = 0 \qquad \mathrm{mod}\ 1, \tag{26}$$

where the indices a and b refer to all possible vectors W_a and W_b. This particular condition restricts the possible values of the rank of the gauge group to 16 or 8 (or even 0). There are probably more general solutions leading to other values of the rank, but a more sophisticated treatment of the conditions of modular invariance is necessary.

The solution of the equations of modular invariance assuming Eq. (26), associated with the mass formula allow us to construct explicitely the massless states as well as the massive levels, and then to obtain the gauge group and the massless chiral multiplets for each set of shifts and twists. As an example, the construction of the Z_3 orbifold string theory, with gauge group $E_6 \otimes SU(3) \otimes E_8$ [6] begins with the four shift vectors

$$\begin{aligned} v_0 &= ((1/2)^6 | (1/2)^{22}) \\ v_1 &= (0^6 | 0^{14}, (1/2)^8) \\ v_2 &= (0^6 | 0^6, (1/2)^8, 0^8) \\ v_3 &= (0^6 | 0^{19}, 1/3, 1/3, 2/3), \end{aligned} \tag{27}$$

and with the twist vector

$$R = (0,(1/3)^3,(1/3)^3|(1/3)^3,0^6)\,, \tag{28}$$

where the superscripts indicate the multiplicity of the entries. Modular transformations then generate all possible combinations, with entries defined modulo 1, of these basic vectors. The vector v_0 alone corresponds to the $SO(44)$ model with $N = 4$ supersymmetry. The effect of v_1 and v_2 is to break $SO(44)$ into $SO(12) \otimes SO(16) \otimes SO(16)$, but also to generate new massless states enlarging each $SO(16)$ factor to E_8. At this point, the gauge group is then $SO(12) \otimes E_8 \otimes E_8$. Adding v_3 then breaks the second E_8 group into $E_6 \otimes SU(3)$. The twists are then used to break completely the $SO(12)$ part, reducing the rank to sixteen. At every step of the construction, some new massless states are created, but some others are projected out by modular invariance. Notice that the rotation vector R carries the Z_3 discrete symmetry used to define the orbifold. This discrete symmetry is relevant when the full states are constructed as products of left-movers and right-movers. The orbifold case corresponds to the subset of states which are Z_3 invariant. The set of vectors (27) and (28) can indeed lead to different string theories depending on the prescription of discrete symmetries used to define the product states. With the help of this Z_3 symmetry, one can check that the spectrum of massless states obtained by our construction is identical to the spectrum described in Ref. [6]. This theory is however not very attractive since the number of quark-lepton generations is 36.

Using this example as a starting point, one can now construct a theory with a rank eight gauge group by completing the set of basic shift and twist vectors. We then add the vector

$$W_2 = R_2 + V_4, \tag{29}$$

where

$$\begin{aligned} R_2 &= \left(0,\frac{1}{5},\frac{2}{5},\frac{2}{5},\frac{1}{5},\frac{2}{5},\frac{2}{5}|0^3,(\frac{1}{4})^4,0^6\right) \\ V_4 &= \left(0^6|0^{14},(\frac{1}{5})^4,\frac{4}{5}\right) \end{aligned} \tag{30}$$

The shift vector V_4 is used to break the E_6 part of the gauge group of the Z_3 orbifold into $SO(10) \otimes U(1)$. However, the introduction of the new rotation vector R_2 means that the E_6 part will completely disappear. We then obtain the rank eight gauge group $SO(10) \otimes SU(3) \otimes U(1)$, which is already much closer to familiar Grand Unified Theories. This new theory has however the same fatal problem as our previous example: the number of quark-lepton generations is far too large. Notice that the twist vector R_2 treats asymmetrically left- and right-movers. The corresponding string theory cannot be obtained by compactification of a larger dimensional string.

In general, our analysis shows that gauge groups with rank eight or sixteen are easily obtained. These gauge groups are also quite often attractive unifying symmetries, and the massless matter multiplets fall also quite naturally into quark-lepton generations, at most enlarged to the 27-dimensional E_6 multiplet. It is however more difficult to obtain a small enough number of generations. This is a general problem in the framework of superstring theories. Compactifications of the heterotic strings have the same tendency, even though a few examples with three generations are known. Finding a realistic four-dimensional superstring theory with a small rank gauge group is still an open issue.

There are many phenomenological reasons to insist in reducing the size of the gauge group of superstring unified models. For instance, a large gauge group is much harder to break into $SU(3) \otimes SU(2) \otimes U(1)$ by the Higgs mechanism. As we have seen in Section 2, a hidden sector can be very useful when generating supersymmetry breaking. However, a satisfactory scale for this breaking can be obtained only if the hidden sector does not contain large non abelian (simple) components [19]. There is no necessity, and certainly no evidence of a very large gauge group. Four-dimensional superstrings with twisted bosons may ultimately provide a minimal superstring extension of the Standard Model. Such a theory would be very hard to distinguish from the minimal supersymmetric extension of the Standard Model, at energies much smaller than the Planck scale.

References

[1] M. B. Green and J. H. Schwarz, *Phys. Lett* **149 B** (1984) 117; **151 B** (1985) 21; *Nucl. Phys.* **B 255** (1985) 93.

[2] For reviews see: J. H. Schwarz, *Phys. Rep.* **89** (1982) 223.
M. B. Green, *Surveys in High Energy Physics* **3** (1983) 127.

M. B. Green, J. H. Schwarz and E. Witten, *Superstring Theory* (Cambridge University Press, 1987).

[3] M. B. Green and J. H. Schwarz, *Nucl. Phys.* **B 181** (1981) 502; **B 198** (1982) 252; **B 198** (1982) 441.

[4] D. J. Gross, J. A. Harvey, E. Martinec and R. Rohm, *Phys. Rev. Lett.* **54** (1985) 502; *Nucl. Phys.* **B 256** (1985) 253; **B 267** (1986) 75.

[5] P. Candelas, G. T. Horowitz, A. Strominger and E. Witten, *Nucl. Phys.* **B 258** (1985) 46.

[6] L. Dixon, J. A. Harvey, C. Vafa and E. Witten, *Nucl. Phys.* **B 261** (1985) 651; **B 274** (1986) 285.

[7] K. S. Narain, *Phys. Lett.* **169 B** (1986) 41.

[8] K. S. Narain, M. H. Sarmadi and E. Witten, *Nucl. Phys.* **B 279** (1987) 369.
H. Kawai, D. C. Lewellen and S. H. Tye, *Phys. Rev. Lett.* **57** (1986) 1832; *Nucl. Phys.* **B 288** (1987) 1.
M. Meuller and E. Witten, *Princeton preprint*, (1986).
Da-Xi-Li, *Phys. Rev.* **D 34** (1986) 3780.
W. Lerche, D. Lüst and A. N. Schellekens, *Nucl. Phys.* **B 287** (1987) 477.
I. Antoniadis, C. P. Bachas and C. Kounnas, *Nucl. Phys.* **B 289** (1987) 87.
K. S. Narain, M. H. Sarmadi and C. Vafa, *Harvard preprint HUTP-86/A089* (1986).

[9] A. H. Chamseddine and J.-P. Derendinger, *preprint ETH-PT/87-2* (1987).

[10] For a review see: H. P. Nilles, *Phys. Rep.* **110** (1984) 1.

[11] S.-T. Yau, *in Proceedings of the Argonne Symposium on Anomalies, Geometry and Topology* (World Scientific, Singapore, 1985).

[12] B. R. Greene, K. H. Kirklin, P. J. Miron and G. G. Ross, *Phys. Lett.* **180 B** (1986) 69; *Nucl. Phys.* **B 278** (1986) 667; **B 292** (1987) 606.

[13] L. E. Ibáñez, H. P. Nilles and F. Quevedo, *Phys. Lett.* **187 B** (1987) 25.
L. E. Ibáñez, J. E. Kim, H. P. Nilles and F. Quevedo, *Phys. Lett.* **191 B** (1987)

282.

L. E. Ibáñez, H. P. Nilles and F. Quevedo, *Phys. Lett.* **192 B** (1987) 332.

[14] E. Witten, *Nucl. Phys.* **B 258** (1985) 75.

S. Cecotti, J.-P. Derendinger, S. Ferrara, L. Girardello and M. Roncadelli, *Phys. Lett.* **156 B** (1985) 318.

M. Dine, V. Kaplunowsky, M. Mangano, C. Nappi and N. Seiberg, *Nucl. Phys.* **B 259** (1985) 519.

J. D. Breit, B. A. Ovrut and G. Segrè, *Phys. Lett.* **158 B** (1985) 33.

[15] E. Witten, *Phys. Lett.* **155 B** (1985) 151.

[16] E. Cremmer, S. Ferrara, L. Girardello and A. Van Proeyen, *Nucl. Phys.* **B 212** (1983) 413.

[17] S. Cecotti, S. Ferrara, L. Girardello and M. Porrati, *Phys. Lett.* **164 B** (1985) 46.

S. Cecotti, S. Ferrara, L. Girardello, A. Pasquinucci and M. Porrati, *Phys. Rev.* **D 33** (1986) 2504.

[18] C. P. Burgess, A. Font and F. Quevedo, *Nucl. Phys.* **B 272** (1986) 661.

[19] J.-P. Derendinger, L. E. Ibáñez and H. P. Nilles, *Nucl. Phys.* **B 267** (1986) 365.

[20] J.-P. Derendinger, L. E. Ibáñez and H. P. Nilles, *Phys. Lett.* **155 B** (1985) 65.

[21] M. Dine, R. Rohm, N. Seiberg and E. Witten, *Phys. Lett.* **156 B** (1985) 55.

[22] J. Ellis, C. Kounnas and D. V. Nanopoulos, *Nucl. Phys* **B 241** (1984) 406; **B 247** (1984) 773; *Phys. Lett.* **143 B** (1984) 410.

A. B. Lahanas and D. V. Nanopoulos, *Phys. Rep.* **145** (1987) 1.

[23] J. D. Breit, B. A. Ovrut and G. Segrè, *Phys. Lett.* **162 B** (1985) 303.

P. Binétruy and M. K. Gaillard, *Phys. Lett.* **168 B** (1986) 347.

M. Quiros, *Phys. Lett.* **173 B** (1986) 265.

Y. J. Ahn and J. D. Breit, *Nucl. Phys.* **B 273** (1986) 75.

P. Binétruy, S. Dawson, I. Hinchliffe and M. K. Gaillard, *Berkeley preprint LBL-22339 / UCB-PTH-86/31* (1986).

A. Font, F. Quevedo and M. Quiros, *Phys. Lett.* **188 B** (1987) [illegible]

[24] H. Kawai, D. C. Lewellen and S. H. Tye, *in* [8].

EFFECTIVE ACTION FOR STRINGS *

K.Meissner, J.Pawełczyk and S.Pokorski

Institute of Theoretical Physics
Warsaw University
Hoża 69, 00-681 Warsaw, P o l a n d

(presented by J.Pawełczyk)

Abstract: The construction of the effective action for SST II is discussed. The one-loop corrections are calculated.

* Supported in part by Polish Ministry of Science and High Education, Research Problem CPBP 01.03

Let us consider a theory described by a classical action $S = S(\phi_o, \phi_H)$ which depends on a certain number of light states ϕ_o and heavy states ϕ_H. The states ϕ_o are light in a sence that their typical mass is much smaller then the typical mass (let call it M) of the heavy states ϕ_H . We define an effective action S_{eff} (ϕ_o) for the light states ϕ_o by

$$e^{-S_{eff}} = \int D\phi_H \, e^{-S(\phi_o, \phi_H)}$$

In string theory we do not know the form of $S(\phi_o, \phi_H)$ so we can not construct S_{eff} explicity. What we can do is to study S matrix elements of the theory and construct such an effective action that reproduces them. In practice this corresponds to calculation of the appropriate set of Feynman diagrams which have heavy states on the internal lines only. The results for the light states exchange are reproduced by quantization of S_{eff}.

The exact effective action S_{eff} is, (even in ordinary field theory) very complicated, non-local functional of ϕ_o. In the case when we are interested in the low energy physics (compare to the scale M) we can expand S_{eff} in powers of E/M where E is the energy of the typical process with the light states only. This corresponds to the expansion of S_{eff} in derivatives. Such S_{eff} turns out to be local and its components can be calculated term by term useing symmetries of the theory. For such an effective action we define the effective lagrangian by $S_{eff} = \int dx \, \mathcal{L}_{eff}(x)$, where dx is an invariant measure over space-time.

The Fermi interaction is an example of such a construction. In the GSW model four lepton interaction with energies much smaller then the masses of W, Z bosons can be approximated by $\frac{1}{M_H^2}(\bar{\psi}\psi)(\bar{\psi}\psi)$.

This is the first step in expansion in powers of derivatives. The next term in $\mathcal{L}_{eff}$ is proportional to $\frac{1}{M_N^4}(\bar{\Psi}\Psi)(\partial_\mu\bar{\Psi})(\partial^\mu\Psi)$.

Now we turn our attention to the SST II case. For this case M is the Planck mass. $M_p \sim \frac{1}{\sqrt{\alpha'}} \sim 10^{19}$GeV. The light states are massless and they form N = 2 supermultiplet of 10 D supergravity [1] . The expansion parameter is $\alpha' k^2$ where k represents typical momentum of external particles. In the lagrangian this expansion will correspond to increasing number of derivatives of the fields. From now on we restrict our considerations only to that part of $\mathcal{L}_{eff}$ which describes self-interactions of gravitons.

The lowest order process (in $\alpha' k^2$) is three graviton interaction. The result is proportional to $\alpha' k^2$. In order to reproduce this result from an effective lagrangian $\mathcal{L}_{eff}$ we need three graviton vertex with two derivatives. In addition S_{eff} has to be invariant under general coordinate transformation because the string theory is. This uniquely determines the effective action to be the standard Einstein action [2] .

$$S_{eff} = -\frac{1}{2\kappa^2}\int dx\, R \tag{1}$$

where $\kappa^2 = 8\pi G = 4g^2(\alpha')^4$, G is the gravitational constant g - the string coupling. This result is not renormalized by the string loops because three particle Green's functions vanish at loop level [3] . There can not appear square and cube of curvature tensor terms, because they would give $(\alpha' k^2)^2$, $(\alpha' k^2)^3$ contributions to the g three graviton vertex. (The above argument is not appropriate to the special "Gauss-Bonnet combination" for R tensor, but it has been shown [4] that such term do not appears also). It is easy to see now that up to terms of the order $(\alpha' k^2)^3$

SST II theory has the effective lagrangian of N=2 supergravity.

$$\mathcal{L}_{eff} = (\text{ N=2 10D SUGRA }) \tag{2}$$

Now we consider four graviton process. The tree level result for SST II theory is [1] :

$$A^{tree} = -\frac{(\alpha')^3}{4} \kappa^2 \frac{\Gamma(-\alpha' s/4)\,\Gamma(-\alpha' t/4)\,\Gamma(-\alpha' u/4)}{\Gamma(1+\alpha' s/4)\,\Gamma(1+\alpha' t/4)\,\Gamma(1+\alpha' u/4)} \tag{3}$$
$$\xi^1_{\mu_1\nu_1}\,\xi^2_{\mu_2\nu_2}\,\xi^3_{\mu_3\nu_3}\,\xi_{\mu_4\nu_4} \cdot K^{\mu_1\mu_2\mu_3\mu_4}\,K^{\nu_1\nu_2\nu_3\nu_4}$$

where ξ's are polarization tensors for gravitons, K is standard kinematic factor $K^{\mu_1 \dots \mu_4} = k_{1\rho_1} \cdot \dots \cdot k_{4\rho_4}\, t^{\mu_1\rho_1\mu_2\rho_2\mu_3\rho_3\mu_4\rho_4}$ [1,5]. In the above amplitude we have to separate massless from massive contributions. Only the latter may contribute the correction to $\mathcal{L}_{eff}$. It has been shown [6] that the lowest order correction is

$$\Delta_1 \mathcal{L} = \frac{(\alpha')^3}{16\,\kappa^2} \cdot \zeta(3) \cdot Y \tag{4}$$

where $Y = t^{\mu_1\mu_2 \dots \mu_8}\, t^{\nu_1\nu_2 \dots \nu_8}\, R_{\mu_1\mu_2\nu_1\nu_2} \cdot \dots \cdot R_{\mu_7\mu_8\nu_7\nu_8}$
This correction is of order $(\alpha' k^2)^4$. The lower order terms from A^{tree}(including the massless states exchange) are obtained from the uncorrected effective action given by eq.(1).

Now we descuss one-loop SST II scattering amplitude for four--gravitons. The result for the amplitude is the following [1],[9]

$$A^{one-loop} = \frac{\kappa^4}{128\pi^6} \frac{1}{\alpha'}\, \xi^1_{\mu_1\nu_1} \cdots \xi^4_{\mu_4\nu_4} \cdot K^{\mu_1 \dots \mu_4}\, K^{\nu_1 \dots \nu_4}$$
$$\int_F \frac{d^2\tau}{\tau_2^2} \left(\prod_{i=1}^{4} \frac{d^2 z_i}{\tau_2} \right) \exp\left\{ -2\pi\alpha' \sum_{i<j} k_i k_j G_{ij} \right\} \tag{5}$$

where F is the fundamental domain, $z_i = \sigma_i\tau + \eta_i$, $\tau = \tau_1 + i\tau_2$,
$0 \leq \sigma_i, \eta_i \leq 1$; G is the Green's function.

As in the previous case we have to separate massless from massive contributions to $A^{\text{one-loop}}$. Massive part will give correction to the effective lagrangian. We expect that massless contribution to the scattering amplitude will be reproduced by quantization of string field analog of the $\mathcal{L}_{eff}$ given by eq.(2). Of course one can try to quantize this effective lagrangian directly considering it as a quantum field theory. In this case one has to cut the momentum in the massless loop at the scale $\frac{1}{\alpha'}$ in order to have the finite result. Even if one could do it preserving all symmetries of this supergravity it is hardly to expect that one may get the same result as from string field theory [7].

How one can destinguish massive from massless intermediate states in the string loop ? One way is to use the operator formalism of Green and Schwarz [1] for which one can directly recognize massless modes [7]. Here we utilize less apparent but much simpler method. The scattering amplitude (5) contains the following factor

$$e^{-2\pi\alpha'\sum_{i<j} k_i k_j G_{ij}} = \tag{6}$$
$$= e^{-2\pi\tau_2\alpha'\sum_{i<j} k_i k_j (\sigma_i-\sigma_j)^2} \cdot \exp\left\{\alpha'\sum_{i<j} k_i k_j \ln\left|\frac{\theta_1(z_i-z_j|\tau)}{\theta_1'(0|\tau)}\right|\right\}$$

One can easely see that due to the τ_2 interaction the first exponential on the r.h.s. of eq.(6) can not be expanded in powers of momenta. We shall call it "zero modes" term and we shall show that this factor produces non-analytical behaviour of the scattering amplitude. It is commonly know that such behaviour signals the appearance of massless intermediate states. Thus we identify this exponential with the massless modes in the loop.

Explicit calculations [8] shows that the "zero mode" term integrated over F gives the following result.

$$2\int_0^{1/2} d\tau_1\,(1-\tau_1)^{-1/2}\left(e^{-b} - b\,E_1(b)\right)$$

where $b = -(1-\tau_1)^{1/2}\,\pi\alpha'\{\,s[(\sigma_1-\sigma_2)^2 + (\sigma_3-\sigma_4)^2] +$

$$+\ t[(2\leftrightarrow 4)] + u[(2\leftrightarrow 3)]\ ; \qquad (7)$$

$$E_1(b) = \mp i\pi\Theta(-b) - \gamma - \ln|b| - \sum_{n=1}^{\infty}\frac{(-b)^n}{n\cdot n!}$$

The logarythmic part of the above represents the non-analyticity. The question now arise about the interpretation of the terms in eq.(7) (plus the kinematical factors K from (5)). The part independent on the Mandelstam variables in eq.(7) is proportional to $\frac{1}{\alpha'}$. It corresponds to the quadratic divergency of the appropriate N=2 supergravity one-loop amplitude [1,7] . The imaginary part is connected to the existance of the non-analyticity.
The infinite series in (7) appears due to the modular cut-off which in fact works like a momentum cut-off. When $\alpha' \longrightarrow 0$ the contribution from this series vanishes.

The massive states contribution come from the second exponential on the r.h.s. of eq.(6). They give the following corrections to $\mathcal{L}_{eff}$ [8]

$$\Delta_2\mathcal{L} = \frac{1}{2\kappa^2}\frac{(\alpha')^5 g^2}{2^{10}\pi^7}\,\zeta(3)\left(1-\frac{3}{4}\ln 3\right)\cdot t^{\mu_1\cdots\mu_8}\,t^{\nu_1\cdots\nu_8}$$

$$(D_8 R_{\mu_1\mu_2\nu_1\nu_2})(D^8 R_{\mu_3\mu_4\nu_3\nu_4})(D_6 R_{\mu_5\mu_6\nu_5\nu_6})(D^6 R_{\mu_7\mu_8\nu_7\nu_8}).$$

It is worth noticing that the above correction has the same tensor structure as the $(\alpha' k^2)^{10}$ correction from the tree process.

Note added. We also want to mention that recently Sakai and Tanii [9] have considered this subject from different point of view.

References

[1] J.H.Schwarz, Phys.Rep. 89C (1982)223

[2] J.Scherk and J.H.Schwarz, Nucl.Phys. B81 (1974) 118

[3] E.Martinec, Phys.Lett. 171B (1987) 189,

[4] Tetsaver and Tseythin, PL 185B (1987) 52

[5] J.Atick and Sen , SLAC preprint, SLAC-PUB-4815, Jan.1987

[6] D.Gross and E.Witten, Nucl.Phys. B277(1986) 1

[7] K.Meissner and J.Pawełczyk, in preparation

[8] K.Meissner, J.Pawełczyk and S.Pokorski, in preparation

[9] N.Sakai and Y.Tanii, Nucl.Phys. B287 (1987) 457

SPECIFICS OF THE PARTICLE MOTION AND SPREADING OF PERTURBATIONS IN THE FRONT FORM TWO-DIMENSIONAL RELATIVISTIC DYNAMICS

A.A. Mayorov, S.N. Sokolov
Institute for High Energy Physics, Serpukhov, USSR
V.I. Tretyak
Institute of Applied Problems of Mechanics and Mathematics, L'vov, USSR

Abstract

Motion of classical particles connected by a direct relativistic interaction is analysed. The front form of relativistic Lagrangian dynamics and its Hamiltonian analogue are used. For the two-particle system with interaction depending only on the invariant relative coordinate, the emergence of pathologies (i.e. sudden stops of trajectories, formation of nonphysical and tachionic regions, superlight velocities) at large coupling constants is investigated. For the interactions having field interpretation, the dependence of dynamics on the rank of field is studied. The Lagrangian and Hamiltonian phase portrait of the system are compared and the Hamiltonian description is shown to embrace a larger class of nonpathological systems. For the many-particle systems, the spreading out of acoustic perturbations is studied and it is shown that only the longwave components of the perturbation can pass large distance and their speed is smaller than the velocity of light. Along the string (obtained by the limiting procedure), the speed of sound is limited by the velocity of light. The results are illustrated by the numerical calculations of the one-dimensional crystals of finite length.

INTRODUCTION

The relativistic theory of direct interactions (RTDI) is complicated, and little is known about the dynamics of systems described by RTDI though this subject is touched in many papers (see, e.g., papers in [1]). In ref. [2], the Lagrangian RTDI in the two-dimensional space-time in the front form of dynamics was constructed and its relations with the predictive and Hamiltonian mechanics were established. The Lagrangian in this theory depends only on the first derivatives of the particle coordinates. So this theory is technically relatively simple. This offers a possibility to reveal specific features of the relativistic dynamics and to start studyng some of the principal problems of RTDI.

One of the most important problems of RTDI is the validity of the causality principle. RTDI respects this principle in the sense that in this theory the Cauchy problem can be solved : the present state of the dynamical system determines all future ones so nothing like an influence of the future on the past may happen. However, it is not clear how the causality in the Gauchy sense is related with the "macro" causality formulated in terms of events and signals registrated with the help of thermodynamically irreversible processes.

Let us suppose the existence of a short-range direct instantanious interaction between nucleons at the distances of the order of one Fm. To what speed of the shock-wave a direct internucleon interaction can lead ? If this speed is limited, then how and why ? If it may exceed the velocity of light, how can it be reconciled with the reasonigs of Einstein concerning signal transmission ?

Another problem is the space-time description of the motion of an electron near the Coulomb centre at the distances smaller than the classical electron radius. Can RTDI give such a description ? If not, are the difficulties technical or fundamental ones ?

There also exist many problems related to bound states with zero, negative, or even imaginary rest masses.

Besides, a number of more theoretical questions have to be answered before the formalism of RTDI can be used with some confidence. What are qualitative differences between the relativistic and nonrelativistic equations of motion ? What pathologies may be encountered in the solutions of these equations ? What happends to pathologies, if one passes from the Lagrangian description to the Hamiltonian one ?

In this paper, these questions will be considered with the help of a number of examples, calculated analytically or numerically.

1. LEAST ACTION PRINCIPLE

In the single-time relativistic mechanics, the action has form

$$S(\Gamma) \doteq \int_{\Gamma} L\, d\tau,$$

where the Lagrangian L satisfies the set of the Poincare-invariance conditions /3/, τ is an evolution parameter, and integration is made from τ^{a} to τ^{b} along the path Γ which is followed by the configuration of the system (as a function of τ). If the particles interact, the invariance conditions require, generally speaking, the dependence of L on the derivatives of coordinates of all orders with respect to τ /3/. This hampers the formulation of the equations of motion and the invastigation of the dynamical properties of systems. The only important exception /2/ is a front form of dynamics in the two-dimensional space-time (with coordinates t,x), for which the Poincare-invariance conditions permit interaction Lagrangians depending on x_i and $v_i=dx_i/d\tau$ only. The class of such Lagrangians is sufficiently large (as large as in the nonrelativistic mechanics), and we will consider below only such Lagrangians. For them, the Poincare-invariance conditions (if c=1 and τ =t-x) read

$$\frac{\partial L}{\partial \tau}=0, \quad \sum_i \frac{\partial L}{\partial x_i}=0, \quad \sum_i \left\{ x_i \frac{\partial L}{\partial x_i} + \left(1+2v_i\right)\frac{\partial L}{\partial v_i} \right\} = L. \qquad (1.1)$$

The general solution of (1.1) for the two-particle system may be written as:

$$L = -hY(\rho, \eta), \qquad (1.2)$$

where $h=m_1k_1+m_2k_2$, m_i are particle masses, $k_i=(1+2v_i)^{1/2}$ are the Lorentz-factors of particles, ρ =rm/h is an invariant relative distance (passing into $r=x_1-x_2$ in the nonrelativistic limit), $m=m_1+m_2$, $\eta=(k_1-k_2)/(k_1+k_2)$ is an invariant relative velocity (passing into $(v_1-v_2)/2$ in the nonrelativistic limit), Y is an arbitrary function. In the many-particle case, L may also be written as (1.2), where $h=\sum m_i k_i$ and Y depends on all the independent combinations like ρ and η that can be made from x_i, k_i. For the free particle system, Y=1, L=-h.

We assume that the evolution of the physical system is defined by the least action principle

$$\Gamma : S(\Gamma) = \min_{\Gamma'} S(\Gamma'), \tag{1.3}$$

where all the paths Γ, Γ' have ends at the same points. If the minimum of the action exists and is reached inside the domain of L, (1.3) can be replaced by the stationarity condition $\delta S = 0$, that leads to the Euler-Lagrange equations

$$\frac{d}{d\tau}\frac{\partial L}{\partial v_i} = \frac{\partial L}{\partial x_i} .$$

Eqs. (1.4) are equivalent to (1.3) in the region, where the Gess matrix $G=(\partial^2 L/\partial v_i \partial v_j)$ is positive definite. In other regions, where G is invertible, eqs. (1.4) describe other extrema or saddle points of the functional S, which corresponds to negative effective masses of some particles. Eqs. (1,4) and their solutions in such regions will be considered as formal (unphysical).

2. SOLUTION OF THE EQUATIONS OF MOTION FOR TWO PARTICLES

The Poincare-invariance conditions lead to the conservation of three quantities

$$E = \sum v_i L_{v_i} - L, \quad P = \sum L_{v_i} + E, \quad K = -\tau P - \sum x_i L_{v_i} \tag{2.1}$$

inside each region of the phase space of variables x_1, v_1, x_2, v_2 where the Gess matrix is invertible. This gives a possibility to express x_1, x_2 through ρ, v_1, v_2, τ :

$$x_{\substack{1\\2}} = \left[K + \tau P \mp \rho h L_{v_{\substack{2\\1}}}/m\right]/P_{\mp}, \tag{2.2}$$

where $P_{\pm} = E \pm P$, and to reduce the solution of (1.4) to one quadrature. For the Lagrangian (1.2)

$$P_+ = hY_+(\rho,\eta), \qquad P_- = Z(\rho,\eta)/h, \tag{2.3}$$

where

$$Y_\pm = Y \pm \rho Y'_\rho, \quad m_\pm = m \pm \eta\mu, \quad \mu = m_1 - m_2,$$
$$Z = m_+ m_- (1-\eta^2)^{-1} \left(Y_- - 2(m_+/m_-)\eta Y'_\eta \right). \tag{2.4}$$

Multiplying both sides of eqs. (2.3), we get an equation

$$P_+ P_- = Y_+ Z \equiv T(\rho,\eta) \tag{2.5}$$

relating ρ and η and defining (on the phase plane of relative variables ρ, η) the family of trajectories $\rho(\eta)$ parametrically depending on the value of $P_+ P_-$. The family fills (without gaps) the strip $-1 < \eta < 1$ whose edges, $\eta = \pm 1$, correspond to the case, when the velocity of one of the particles reaches the velocity of light. To turn the set of trajectories $\rho(\eta)$ into a true phase portrait, one has to include in the picture the directions of motion along the trajectories using

$$\dot{\rho} = \eta 2 m m_+^{-2} T'_\eta / \Delta, \tag{2.6}$$

where

$$\Delta = \frac{\partial(A_+, A_-)}{\partial(h,\eta)} = \frac{Y_+}{P_+}\left(T'_\eta - \rho \frac{\partial(Y_+, Z)}{\partial(\rho,\eta)}\right) = \frac{Y_+}{P_+}\left(Y'_{+\eta} Z_+ + Z'_\eta Y_0\right),$$
$$Z_+ = Z + \rho Z'_\rho, \quad Y_0 = Y_\pm \mp \rho Y_{\pm\rho} = Y - \rho Y'_\rho - \rho^2 Y''_{\rho\rho}. \tag{2.7}$$

The singular points $\Delta = 0$ (at $\eta \neq 0$) coincide with the points, where the Gessian

$$|G| = \frac{\partial(L_{v_1}, L_{v_2})}{\partial(v_1, v_2)} = \frac{m_+^6}{\eta(1-\eta^2)8h^5}\Delta = \frac{Y_+^5 m_+^6}{\eta(1-\eta^2)8P_+^5}\Delta. \tag{2.8}$$

vanishes and the equations of motion lose sense.

In the general case, the lines $|G|=0$ divide the phase portrait of the relative motion into regions, among which there is usually a physical region (where the Gess matrix is positive - definite and the action has a minimum), and a number of unphysical regions including possibly tachionic regions with $P_+P_-<0$. Figs. 2-8 show that the trajectories $\rho(\tau)$, $\eta(\tau)$ may either go along the boundaries $|G|=\Delta=0$, or tend to some points on the boundaries (these points do not belong to the trajectories).

3. DEPENDENCE ON THE COUPLING CONSTANT

The phase portrait of a two-particle system with the potential λB in the nonrelativistic case does not depend (up to scaling transformations) on the magnitude of the coupling constant λ (if it does not change sign). In the relativistic case the shift of λ alters qualitatively the character of motion. Let us conside these changes for the case, when the invariant interaction $\lambda B=Y-1$ depends on the relative coordinate ρ only. This corresponds to velocity-independent interactions in the nonrelativistic limit.

The basic quantities in case $Y=Y(\rho)$ are found explicitly:

$$\begin{aligned} &\eta(\rho)=\pm\left[(P_+P_- - m^2Y_+Y_-)/(P_+P_- - \mu^2Y_+Y_-)\right]^{1/2}, \\ &\dot\rho/P_+ = \eta 2mm_+^{-2}/Y_0, \qquad T=m_+m_-Y_+Y_-/(1-\eta^2), \\ &P_+\Delta = \eta 8m_1m_2Y_0Y_-Y_+(1-\eta^2)^{-2}, \\ &|G| = m_1m_2m_+^6P_+^{-6}Y_0Y_-Y_+^6(1-\eta^2)^{-3}. \end{aligned} \tag{3.1}$$

Looking at them, one can see that the boundaries $\Delta=|G|=0$ on the phase portrait are vertical lines $\rho=$const defined by any of eqs.

$$Y_0=0, \text{ or } Y_-=0, \text{ or } Y_+=0. \tag{3.2}$$

The boundaries $Y_{+-}=0$ separate tachionic regions, where $P_+P_-<0$ and the velocity of the center-of-mass corrdinate $X=(K+\tau P)/P_-$ exceeds the velocity of light (the velocities of particles remain smaller than that of light). The values $\eta=\pm1$ at $P_+P_-\neq0$ may be approached only at the ends of the tachionic boundaries where families of the phase trajectories converge. The physical region (where min S exists) corresponds to the simultaneous fulfilment of inequalities $Y_{0,+,-} > 0$. It always includes the region, where the interaction λB and the functions $(Y_{0,+,-}-1)$ are small.

Denote $B_{\pm}=B\pm\rho B'$, $B_0=B_{\mp}\mp\rho B'_{\pm}=B-\rho B'-\rho^2 B''$ and rewrite (3.2) as

$$B_0=-1/\lambda, \quad B_-=-1/\lambda, \quad B_+=-1/\lambda. \tag{3.3}$$

In the (ρ, B)-plane, where B is the value of function $B_{0,+,-}$, the roots of equ. (3.3) (or (3.2)) correspond to the intersections of the line $B=-1/\lambda$ with the curves $B_{0,-,+}(\rho)$. Let us take, as an example of $B(\rho)$, a smooth bell-like potential: $B(\rho)=\exp(-\rho^2)$. The curves $B_{0+,-}$ are drawn in fig. 1. The tachionic region is $B_+ < B < B_-$. The curve B_0 intersects the curves B_-, B_+ always at the points, where they have extrema. Hence, the tachionic region at every $1/\lambda$ is divided by the boundary $Y_0=0$. The phase portraits on figs. 2-8 correspond to the values of λ marked by fat points on fig. 1. If the potential $B(\rho)$ has a more complicated shape, the curves $B_{0,+,-}$ make more oscillations and the number of regions grows us, but no new elements appear on phase portraits.

The world-lines corresponding to the trajectory A in figs. 2,5 and to the pieces a,...,e of the trajectory A in fig. 3 are plotted on figs. 9, 10, 11, respectively. On all the figures, $|P_+| = |P_-|$, i.e. , P=0 for tardions, and E=0 for tachions.

The motion of relativistic particles has a pecularity that can be noted on figs. 9 and 10. The left particle at $\lambda>0$ (fig.9) during its approach to the right one before slowing down is somewhat accelerating. At the same time, at $\lambda < 0$ (fig.10) it is slowing down before accelerating. An inversion of acceleration takes place during some time both at the entry into the region of intensive interaction and at the exit from this region. This effect at $\lambda > 0.85$ becomes so strong (fig.11), that the left particle accelerates almost up to the velocity of light, the physical region ends, and the trajectory terminates. The effect of acceleration inversion is an indication of the closeness to the boundary of the physical region.

4. INTERACTION WITH THE FIELD INTERPRETATION

As is shown in /2/, starting from the two-dimensional field theory with the action integral of the Fokker type and with the Green function containing $\theta(t_1-t_2)$ or $\theta((t_1-t_2)$ sign $r)$, and considering two particles interacting via the local massless field of the rank n, one can obtain the Lagrangians

$$L = -h\left[1+\alpha m|\rho|^{-1} m_+^{-2}(1+\eta^2)^n(1-\eta^2)^{1-n}\right] \qquad (4.1)$$

The Lagrangian (4.1) for n=1 was obtained by Staruszkiewicz /4,5/ for the representation of "two histories" of particles, interacting according to the electromagnetic action of Wheeler-Feynmann with the half-sum of the retarded and advanced Green functions. Some properties of such description for a number of interactions are considered in /5,6/, the corresponding quantum problem is considered in /4,7/. The equations of motion is case of repulsion are integrated for the symmetric electromagnetic (n=1) and scalar (n=0) interactions in /8/ and /9/, respectively. Though the concept of the front form of dynamics is not used in these papers explicitly, the reasonings in /6,8/ are very close to this concept and the evolution parameter τ = t-x (or τ =t+x) is actually used.

The Lagrangians (4.1) are remarkable in many ways. In particular, the solutions of the motion equations can be found for them in an analytic form for any n. Note, that (4.1), (2.6) and the relation $Y_0=Y_+ - \rho Y'_+$ give

$$Y_0 = Y_+ = 1, \qquad (4.2)$$

whence we immediately obtain $\partial(Y_+, Z)/\partial(\rho,\eta) = 0$, which according to (2.8), (2.9) gives

$$\Delta = T'_\eta/\dot{P}_+, \qquad \dot{\rho}/P_+ = \eta^2 m m_+^{-2}. \qquad (4.3)$$

Eq. (4.2) also means that $P_+ = h > 0$ and $T = Z$. Note that the free Lagrangian is a conserved quantity. Calculating explicitly

$$T = Z = \left[m_+ m_- + 2\alpha m|\rho|^{-1}(1+\eta^2)^{n-1}(1-\eta^2)^{-n}(1+(2-4n)\eta^2+\eta^4)\right]/(1-\eta^2) \qquad (4.4)$$

and solving the equation $P_+P_-=T$ with respect to ρ, we find

$$|\rho(\eta)|=2\alpha m(b-c\eta^2)^{-1}(1+\eta^2)^{n-1}(1-\eta^2)^{-n}[1+(2-4n)\eta^2+\eta^4], \qquad (4.5)$$

where $b=P_+P_--m^2$, $c=P_+P_--\mu^2$. Obviously, $d\rho/\dot\rho=A(\eta)d\eta$, where $A(\eta)=\rho(\eta)'_\eta/\dot\rho(\eta)$ is a rational expression of η, therefore the quantity

$$\tau(\eta)=\tau^\circ+\int_{\eta^\circ}^{\eta}d\eta\, A(\eta) \qquad (4.6)$$

is always expressed in elementary functions.

The phase portraits of all the Lagrangians (4.1) have some common features. It immediately follows from (4.1) that they are symmetric with respect to the sign of ρ and, up to an overall scale, do not depend on $|\alpha|$. According to (4.4) they are symmetric with respect to the sign of η as well. Since $\dot\rho>0$ at $\eta>0$, the motion along the phase trajectory in the upper half-plane is realized always in the direction of growth of ρ. In case of attraction (at $\alpha<0$), there is always a tachionic region since $T(\rho,0)=m^2+2\alpha m/|\rho|<0$ at $|\rho|<-2\alpha/m$. The lines $\rho=\rho_G(\eta)$, where the Gessian $|G|=0$, are defined by the equation $dT/\eta\, d\eta=0$ from which at $|\rho|\neq0$ we get

$$|\rho_G|=-\alpha m m_1^{-1}m_2^{-1}(1+\eta^2)^{n-2}(1-\eta^2)^{-n}\mathcal{P}_n(\eta), \qquad (4.7)$$
$$\mathcal{P}_n(\eta)=1-n+2\eta^2(1+n-2n^2)+\eta^4(1-n).$$

At $n=0,1$

$$|\rho|=2\alpha m\,[1+(1-2n)\eta^2]/(b-c\eta^2),$$
$$\Delta=8\eta\,[m_1m_2+\alpha m|\rho|^{-1}(1-n)]\,P_+^{-1}(1-\eta^2)^{-2}.$$

In case of repulsion, at $n=0,1$ and at $\eta\neq0$ Δ has no zeros and the phase portraits have no unphysical regions. The distance between particles at the turing points $|\rho|_{min}=2\alpha m/b$ is arbitrary small at sufficiently large energy.

In case of attraction, the phase portraits look essentially different at $n=0$ (fig. 12) and at $n=1$ (fig.13). At $n=0$, the factor Δ entring the Gessian becomes zero at lines $|\rho| = -\alpha m/m_1 m_2 = \rho_1$. At $|\rho| < \rho_1$ there is an unphy - sical region (including tachionic region). The trajectory $\rho(\eta)$ for any given value of P_+P_- consists of two or three disconnected pieces ending in the corners of the unphysical region.

At $n=1$, the factor Δ does not depend on ρ and at $\eta \neq 0$ may not become zero, the Gessian $|G| = m_1 m_2 (m_+/P_+)^6 (1-\eta^2)^{-3}$ is positive, and the matrix G is positive definite, which is still true in the tachionic region $(\tau<0)$ as well. From this view- point the latter can be classified as a physical subregion. Thus, the trajectories may nowhere be interrupted except at the line $\rho=0$, where neither the Lagrangian, nor the quantities derived from it are defined. For $n\geqslant 2$ see figs. 14,15.

5. DISTINCTIONS OF THE HAMILTONIAN FORMALISM

The Hamiltonian description has a number of qualitative distinctions from the Lagrangian one in the relativistic case. Here we briefly consider the distinctions related to the emergence of nonphysical regions.

The Hamiltonian description in two-dimensional space-time in the front form of dynamics can be specified by three functions P_+, P_-, K of coordinates x_i and of the canonic momenta π_i, satisfying commutation relations

$$[P_\pm, K]_\partial = \pm P_\pm, \quad [P_+, P_-]_\partial = 0, \quad [\pi_i, x_j]_\partial = \delta_{ij}, \tag{5.1}$$

where $[,]_\partial$, is the Poisson bracket. For our purposes it is convenient to choose $P_{+,-}, K$ in the form

$$P_- = -\sum \pi_i, \quad P_+ = -W\sum m_i^2/\pi_i, \quad K = -\sum x_i \pi_i, \tag{5.2}$$

where the function W is invariant in the sense $[P_-, W]_\partial = [K, W]_\partial = 0$ and may depend on invariant relative coordinates only. In case of two particles, we take K, P_- as collective coordinates and

$$R = -mr\Big/\left(\sum m_i^2/\pi_i\right) \tag{5.3}$$

and the combination

$$\zeta = -(\pi_1/m_1 - \pi_2/m_2)\Big/(\pi_1/m_1 + \pi_2/m_2) \tag{5.4}$$

of momenta, as relative ones. It is easy to check that R, ζ are canonically independent from K, P_- :

$$[K,R]_\partial = [P_-,R]_\partial = [K,\zeta]_\partial = [P_-,\zeta]_\partial = 0. \tag{5.5}$$

The Hamiltonian of the relative motion is the function

$$P_+P_- = (m^2 - \mu^2\zeta^2)\,W(R,\zeta)\Big/(1-\zeta^2) \equiv \widetilde{T}(R,\zeta). \tag{5.6 }$$

In the case $W'_\zeta = 0$,which will be considered , the phase trajectories $\zeta(R)$ and the direction of motion along them are defined by expressions

$$\zeta(R) = \pm\left\{[P_+P_- - m^2W(R)]/[P_+P_- - \mu^2W(R)]\right\}^{1/2}, \tag{5.7}$$

$$\dot{R} = [H,R]_\partial = 2\zeta P_+ m(m+\mu\zeta)^{-2}_{,} \quad \left(H \equiv (P_+ + P_-)/2\right). \tag{5.8}$$

The regions, where $P_+P_- < 0$, will be called tachionic, the rest ones, tardionic.

Let us consider the transition from the Lagrangian picture to the Hamiltonian one. This transition (the Legendre transformation) needs solving the system of equations

$$\pi_i = \partial L/\partial v_i \tag{5.9}$$

with respect to velocities v_i . These equations are solvable in the regions where the Gessian $|G| = \partial(\pi_1,\dots)/\partial(v_1,\dots)$ is different from zero. In the relativistic case, eqs. (5.9) due to a kinematical dependence of the interaction Lagrangian on velocities, are nonlinear, and, if the boundaries, where the Gessian vanishes, and nonphysical regions, separated by these boundaries, are present , the mapping $\pi \to v$ is nonunique. Let us construct this mapping formally.

The conservation laws (2.5) for the Lagrangian $L = -hY$ in the two-particle case give

$$W = -hY_+/(m_1^2/\pi_1 + m_2^2/\pi_2), \qquad (5.10)$$

and eqs. (5.10) take form

$$\pi_{\frac{1}{2}} = -m_+ h^{-1}(1 \pm \eta)^{-1}[m_{\frac{1}{2}} Y_- + m_+(\pm 1 - \eta) Y'_\eta/2]. \qquad (5.11)$$

At $Y'_\eta = 0$, the ratio π_1/π_2 depends on η only, while the combination $q = m_1^2/\pi_1 + m_2^2/\pi_2$ depends only on h (and r), , and we obtain

$$\eta = \zeta, \qquad (5.12)$$

$$h/Y_-(r/h) = -\sum m_i^2/\pi_i. \qquad (5.13)$$

Eqs. (5.11), (5.13) entail

$$W = Y_+ Y_-, \qquad (5.14)$$

and (5.14) after dividing by r turns into

$$\rho Y_-(\rho) = R. \qquad (5.15)$$

The substitution of the solution $\rho = \rho(R)$ of eq. (5.15) into (5.14) completes formally the Legendre transformation:

$$W(R) = Y_+(\rho(R)) Y_-(\rho(R)) = Y_+(\rho(R)) R/\rho(R). \qquad (5.16)$$

The solution $\rho(R)$ f rks at the points, where

$$dR/d\rho = (d/d\rho)\rho Y_-(\rho) = Y_0 = 0 \qquad (5.17)$$

and the Gessian equals zero. If the portrait in ρ, η variables contains no unphysical regions, its mapping on the (R, ζ)-plane occupies the strip $|\zeta| < 1$ and does not differ qualita - tively from the initial portrait (compare these strips on fig. 16, 17 and 2,5). However, in the Hamiltonian case there is a formal possibility to extend the region of variation of the variable ζ up to all $\zeta \in \mathbb{R}$, and, using (5.7), to construct the phase portrait outside the strip $|\zeta| < 1$, adding regions with no counterpart in the Lagrangian description (figs. 16, 17). These regions turn out to be tachionic in the given case.

If the phase portrait of the Lagrangian system contains nonphysical regions, the corresponding phase portrait turns out to be foliated. For example, the dependence of R on ρ for the Lagrangian $L = -h[1+\lambda \exp(-\rho^2)]$ at $\lambda = 1.53$ is unmonotonous and the portrait in R, ζ -variables consists of several partially overlapping regions (fig. 18). In particular, at $2.55 < |R| < 2.95$ one has three different sets of trajectories $\zeta(R)$ corresponding to different solutions of eq. (5.15) (substituted into W). It should be stressed that among the regions that partially overlap there are two regions corresponding to physical regions (where the Gess matrix is positive-definite) on the Lagrangian phase portrait. Hence, the fixation of the state of a system by the variables x_i, π_i in the given case does not permit the unambiguous calculation of the system evolution , even if only the physical regions are considered.

Let us see now how the behaviour of a dynamical system depends on the magnitude of interaction in the Hamiltonian formalism. We take W of the form $W = 1 + 2\lambda B(R)$, $B = \exp(-R^2)$. At $|\lambda| \ll 1$, the Hamiltonian with such interaction is approximately equivalent to the Lagrangian $L = -h[1 + \lambda B(\rho)]$ (the phase portraits of the Hamiltonian at $\lambda = \pm 0.6$ do not differ perceptibly from figs. 16, 17). When $|\lambda|$ is growing, no qualitative changes occur with the phase portrait in case of repulsion. In case of attraction, if $|\lambda|$ is large enough (in the given case at $\lambda < -1$) a tachionic region in the strip $|\zeta| < 1$ appears , and tardionic regions are inserted into the tachionic regions outside this strip (fig. 19, $\lambda = -2$). In a more general case, the replacement of the function $B(R)$ by a function with more extrema give rise at large $|\lambda|$ to a number of tardionic and tachionic regions forming a chess-board pattern. As it follows from (5.9), trajectories cannot have interruptions inside the regions (they have ends in the corners of techionic regions, where they converge). While the superlight velocities

v_i in the Lagrangian case are impossible, in the Hamiltonian case they are admissible and may arise even in tardionic regions. The calculation of the velocities $v_i = \partial H/\partial \pi_i$ gives

$$1 + 2v_i = W_- m_i^2/\pi_i^2, \qquad (5.18)$$

where $W_- = W - RW'_R$. Since $1 + 2v_i > 0$ corresponds to the motion with a sublight velocity, while $1 + 2v_i < 0$ corresponds to the motion with a superlight velocity, at $W_- = 0$ both particles simultaneously (in τ) reach the velocity of light, and at $W_- < 0$ both particles move faster than light. Since the sign of W_- may differ from the sign of W , the super-light velocities may happen in the tardionic region $P_+P_- > 0$, $W > 0$. For instance, we have for the chosen W at $\lambda = -0.9$ everywhere $W > 0$, but there are two sectors of R , where $W_- < 0$ and the world-lines $x_i(t)$ have superlight pieces (fig. 20). Note , that there are no irregularities at the points $W_- = 0$, where the particles reach the velocity of light.

Since k_i and ρ at $1 + 2v_i < 0$ are imaginary, there are no Lagrangians equivalent to the Hamiltonians with $W_- < 0$. In fact, the equivalence is ruined even for positive, but sufficiently small W_-. To see this fact, let us take an arbitrary $W(R)$ and perfom formally the inverse Legendre transformation. Eqs. (2.1) and (5.3) lead to

$$L = -\frac{1}{2}\left(k_1^2 \pi_1 + k_2^2 \pi_2 + Wq\right), \qquad (5.19)$$

where $q = m_1^2/\pi_1 + m_2^2/\pi_2$. Eq. (5.18) gives $k_i = -Fm_i/\pi_i$ where $F = W_-^{1/2}$, whence we got for h or ρ the equations

$$h = -qF, \qquad \rho = R/F(R). \qquad (5.20)$$

Finding the solution $R = R(\rho)$ and using the relation $\pi_i = -Fm_i/k_i$, we finally get

$$L = -h\,(F + W/F)/2, \qquad (5.21)$$

where $F = F(R(\rho))$, $W = W(R(\rho))$. The Gessian of the transformation is

$$|G| = \partial(\pi_1,\pi_2)/\partial(v_1,v_2) = [\partial(v_1,v_2)/\partial(\pi_1,\pi_2)]^{-1} =$$
$$= \pi_1^3\pi_2^3\,[m_1^2m_2^2\,W_-(W_- - RW'_{-R}/2)]^{-1} = m_1 m_2 K_1^{-3} K_2^{-3}\,Y_- Y_0 ,$$

where $Y = -(F + W/F)/2$, $Y_- = Y - \rho Y'_\rho$. At finite $W,\ W',\ W''$, the Gessian has no zeroes, and the phase portrait of the Lagrangian contains no bounderies $Y_0 = 0$ separating the unphysical regions, but it contains the lines $W_- = 0$, $W_- - RW'_-/2 = 0$, where $|G| = \infty$. Consider the case when $W > 0$, $W_- > 0$, but W_- is small in some region. In this case, the dependence of ρ on J is nonmonotonous , and the solution $R(\rho)$ at some ρ is triple-valued. At such ρ, one Hamiltonian description corresponds to three different Lagrangians and the fixation of the state in terms of x_i, v_i does not define the motion uniquely. The phase portrait of the system in variables ρ, η becomes foiled (see fig. 21).

Note that the above case $W > 0$, $W_- > 0$ is a physical one according to all main criteria : the velocities of particles are always smaller than that of light, the motion is regular everywhere, no ruptures occur, no tachionic regions are present. Therefore the absence of a (unique) Lagrangian description is, seemingly , a deficiency of the approach itself, or, to be more precise, of its inherent assumption that the state of the system is fully fixed by coordinates and velocities (and not by higher derivatives $d^n x/d\tau^n$ or by momenta). The Hamiltonian formalism is applicable to a larger class of system : an equivalent Hamiltonian description exists for any nonpathalogical (i.e., without nonphysical regions) Lagrangian description (due to $G \neq 0$), but there are Hamiltonian systems, including the ones with interactions depending only on the invariant distance, for which no equivalent Lagrangian descriptions exist.

6. PROPAGATION OF SOUND WAVES

One of the postulates of the special relativity is an assertion that signals propagate with a limited speed. Different papers on the relativistic theory of direct interactions treat this assertion differently : some of them put it in the basis of the formalism assuming that only retarded interaction propagating with the velocity of light is acting between particles /10/, other ones admit an advanced interaction but try to eliminate its open manifestation with the help of an absorber /11/, the third ones leave the question open and require only the Lorentz-invariant formulation of the theory.

The front form of dynamics, which is adopted in this paper, assumes the presence of both retarded interaction (from the left particle on the right one) and advanced interaction (from the right particle on the left one). The presence of advanced interaction is, as a rule, considered as an indication of the advanced propagation of signals. However, the question of the velocity of the signal propagation is much less obvious.

Strictly speaking, to become a signal the transferred perturbation has to influence many particles and induce the irrevercible processes that register the perturbation. In a purely mechanical system, one of the most important kinds of perturbations suitable for the signal transfer is a sound wave It can be registered and may propagate at large distances.

Consider a system of N identical particle with a paired interaction described by a Lagrangian

$$L = -m\sum k_i - \sum_{i,j}(k_i + k_j)\,B(\rho_{ij}, \eta_{ij}), \qquad B(0,0) = 0. \tag{6.1}$$

The equations of motion of such a system have form

$$\sum G_{ij}\,\ddot{x}_j = Y_i\,, \tag{6.2}$$

where G_{ij} and Y_i may be expressed through $C_{ij} = C(\rho_{ij}, \eta_{ij}) = B(\rho_{ij}, \eta_{ij}) + B(-\rho_{ij}, -\eta_{ij})$, $C_{ij\rho} = \partial C_{ij}/\partial \rho_{ij}$ and so on.

Let this system make a (one-dimensional) crystal (chain), i.e., be in the state close to the stable equilibrium. The invariant distances $a_i = |\rho_{i,i+1}|$ in equilibrium are defined by the conditions

$$Y_i = 0, \quad \eta_{ij} = 0. \tag{6.3}$$

We assume that particles interact with the nearest neighbours only ($C_{ij}=C$, if $|i-j|>1$) and function $C(\rho,\eta)$ has only two minima at $\rho=\pm a$. Then the equilibrium of the first particle gives $a_1=a$, and that of other particles gives $a_i=a$. The Gess matrix in the equilibrium position has form

$$G=\frac{a}{k^3}=\begin{pmatrix} M_1-\varepsilon & -\varepsilon/2 & 0 & 0 & \cdot \\ -\varepsilon/2 & M-\varepsilon & -\varepsilon/2 & 0 & \cdot \\ 0 & -\varepsilon/2 & M-\varepsilon & -\varepsilon/2 & \cdot \\ \cdot & \cdot & \cdot & \cdot & \cdot \end{pmatrix} \quad (6.4)$$

where $M=(m+2C-2C_{\eta\eta})/a$, $\varepsilon=(a^2C_{\rho\rho}-C_{\eta\eta})/a$, $M_1=M+(a^2C_{\rho\rho}+C_{\eta\eta})/2a$, $C=C(a,0)$ and where have taken into account that the requirement of the existence of small harmonic oscillations entails $C_\eta(a,0)=C_{\rho\eta}(a,0)=0$.

The condition of positive-definiteness of G puts a limitation on the ratio $\alpha=-\varepsilon/2(M-\varepsilon)$: at $\varepsilon>0$ and $M_1>M$ $|G|>0$ at any N, if

$$\varepsilon/2\leqslant(M-\varepsilon)/2. \quad (6.5)$$

This inequality, clearly, leads to some limitations on the velocity of sound.

Let us obtain the equations of motion for the case of small perturbations of a crystal. In contrast to the nonrelativistic case, when it is sufficient to require the smallness of only the deviations from the equilibrium positions, while the velocities may be arbitrary, in the relativistic case the smallness of the relative velocities (the velocity $v=P/P_-$ of the centre-of-mass coordinate $X=(K+\tau P)/P_-$ of the crystal, as a whole, may be large). Putting $y_i=x_i-\bar{x}_i$, $\bar{x}_i=X+a\cdot i-a(N+1)/2$ and leaving in (6.2) only the terms of the first order in $y,\dot{y}$ we get for internal particles the linearized equations of motion of the form

$$k^{-2}\left[(M-\varepsilon)\ddot{y}_i-(\ddot{y}_{i-1}+\ddot{y}_{i+1})\varepsilon/2\right]= \\ =fa^{-2}\left[y_{i-1}-2y_i+y_{i+1}-(\dot{y}_{i+1}-\dot{y}_{i-1})a/k\right], \quad (6.6)$$

where $f = 2aC_{pp}(a,0)$.

Let us pass to the limit of continuous matter $(a\to 0,\ N\to\infty)$, i.e., to the case of relativistic string. Let there exist the limits

$$M_0 = \lim_{a\to 0} M, \quad \varepsilon_0 = \lim_{a\to 0} \varepsilon, \quad f_0 = \lim_{a\to 0} f, \quad q_0 = \lim_{a\to 0} C_{qq}/a .$$

Then (6.6) at $a\to 0$ passes into eq.

$$k^{-2}(M_0^{*} - f_0)\ddot{y} = f_0\left(y_{xx}k^2 - 2\dot{y}_x\right), \tag{6.7}$$

where $M_0^{*} = M_0 - 2q_0$ is a density of medium and f_0 is the Young modulus. The equantity $y(\tau, x)$ in (6.7) is a deviation not from the immobile point x, but from the point moving with the velocity v. Passing to the deviations $z(\tau,x) = y(\tau, x(0)-v\tau)$ from immobile points and taking into account that $y_x = z_x$,

$y_\tau = z_\tau + v z_x$, $y_{\tau\tau} = z_{\tau\tau} + 2v z_{\tau x} + v^2 z_{xx}$, we get

$$(M_0^{*}-f_0)k^{-2}z_{\tau\tau} + 2\left[(M_0^{*}-f_0)k^{-2}v + f_0\right]z_{\tau x} + \left[(M_0^{*}-f_0)k^{-2}v^2 - f_0\right]z_{xx} = 0. \tag{6.8}$$

Passing from the variables of the front form of dynamics to the usual variables t, x by means of substitutuins $u(t,x) = z(t-x, x)$, $z_\tau = u_t$, $z_x = u_x + u_t$, $k = \left[(1+s)/(1-s)\right]^{1/2}$,

we finally get the equation

$$\left(\frac{M_0^{*}}{1-s^2} - \frac{f_0 s^2}{1-s^2}\right)u_{tt} + \frac{2s}{1-s^2}\left(M_0^{*} - f_0\right)u_{tx} + \left(\frac{M_0^{*}s^2}{1-s^2} - \frac{f_0}{1-s^2}\right)u_{xx} = 0, \tag{6.9}$$

which is a usual relativistic equation of the sound propagation in the medium moving with the velocity s. In particlar, at $s=0$ we have

$$M_0^{*}u_{tt} = f_0 u_{xx}, \tag{6.10}$$

whence one can see that the sound propagates in both directions with the same velocity $w = (f_0/M_0^{*})^{1/2}$. The phase and group velocities coincide. In the limit of continuous medium

(6.7) gives $f_0 \leq M_0^\circ$. Accounting for the condition of resolvability of eq. (6.7) with respect to $\ddot{y}$ (that excludes the equality $f_0 = M_0^\circ$), we obtain the limitation

$$f_0 < M_0^\circ, \quad w^2 < 1 . \qquad (6.11)$$

Hence, the velocity of sound in the continuous medium (in the relativistic string) may approach the velocity of light , but cannot reach it. Note that eq. (6.7) corresponds to small oscillations of the string with the Lagrangian $L_S = -\int K(\sigma)\left[M_0^\circ + f_0\left(1 - y_\sigma'/K(\sigma)\right)^2/2\right]d\sigma$.

Let us now return to eq. (6.6) describing the evolution of acoustic perturbations in an infinite crystal and see what happens, if the wavelength becomes comparable with the distance between particles. Let the crystal be at rest. The substitution of the solution of the form $y_e = \exp\left[i(\omega\tau - pa\ell)\right]$ into (6.6) relates with p by meand of a dispersion equation $\omega^2\left[M - \varepsilon(1 + \cos pa\right) = 2f\left[a^{-2}(1 - \cos pa) + a^{-1}\omega \sin pa\right]$,which can be solved both with respect to ω , and with respect to p:

$$\omega = \pm 2\theta a^{-1}\left[g/(1+\theta^2 M/M^\circ)\right]^{1/2} / \left\{1 \mp \left[g/(1+\theta^2 M/M^\circ)\right]^{1/2}\right\}, \qquad (6.12)$$

$$p = \frac{2}{a}\,\mathrm{arctg}\left\{\frac{wa}{2}\;\frac{-g \pm \left[g - (wa/2)^2(1-g)M/M^\circ\right]^{1/2}}{g - (wa/2)^2 M/M^\circ}\right\},$$

where $\theta = \mathrm{tg}(pa/2)$, $g = f/M^\circ$, $M^\circ = (m + 2C)/a$.

These relations, as usual, make sense (i.e., uniquely correspond to the solution of initial eq. (6.6)) only inside the first Brillouin zone /12/: $|pa| < \pi$ or $|\theta| < \infty$.

We illustrate the main features of the sound propagation in the relativistic crystal with the results of computation of motion for the system of forty identical particles described by the Lagrangian (6.1) with $B(\rho) = \lambda\left[\mathrm{arctg}\,(\rho - a - \delta) - \mathrm{arc\,tg}\,(\rho - a + \delta)\right]$. Initially, the system was at rest. Then it was perturbed by a particle coming from the right that has interacted with only the rightmost particle of the system by means of the potential

$B_1 = \lambda_1 \cos^3(\pi\rho/2\rho_1)$ at $|\rho|<|\rho_1|$ and $B_1=0$ at $|\rho|>|\rho_1|$

during a short period of time determined by the interaction radius ρ_1. The figures below correspond to $m=1$, $a=0.25$, $\delta=0.25$. Varying the parameters λ, a, δ one can obtain crystals with a desired density and the Young modulus, and varying λ_1, ρ_1 one can choose the magnitude and the frequency of the perturbation. Increasing the rigidity of the cristal almost up to the limit dictated by inequality (6.5), leads to a strong dispersion of a wave packet with an advanced propagation of the perturbation (fig. 22, $\lambda = 1.09$, $g = 0.902$, $\rho_1 = 0.5$). However, such picture is typical for the short wave-lengths only. The long-wave perturbations even in the system of maximal rigidity, as is seen from fig. 23 ($\rho_1 = 1.5$), propagate without dispersion and with sub - light velocities.

One can see from this example that if the distances between particles and the range of direct interaction are microscopic, and the crystal has macroscopic dimensions, the macroscopic distances will be passed only by a long-wave acoustic signal moving slower than light.

References

1. Relativistic Action at a Distance: Classical and Quantum Aspect. Proceedings, Barselona, Spain 1931. - Lecture Notes in Physics, 1982, v. 162.
2. Sokolov S.N., Tretyak V.I. - IHEP preprint 85-66, Serpuk - hov, 1985; TMF, 1986, v. 67, No.1, p. 102-114.
3. Gaida R.P., Klyuchkovsky Yu.B., Tretyak V.I. - TMF, 1980, v.44, No.2, p. 194-208.
4. Staruszkiewicz A. - Preprint TPJU 10/70, Cracow, 1970.
5. Staruszkiewicz A. - Ann. der Phys., 1970, v. 25, p. 362.
6. Staruszkiewicz A. - Acta Phys.Pol. B, 1971, v. 2, p. 259.
7. Staruszkiewicz A. - Ann. Inst.H. Poincare, 1976, v. 24A, p. 359.

8. Rudd R.A., Hill R.N. - J. Math.Phys., 1970, v. 11, p. 2704.
9. Stephas P. - Phys.Rev. D., 1985, v. 31, p. 319.
10. Poincare H. - Rend. Circ.Mat. Palermo, 1906, v. 21, p. 129.
11. Wheeler J.A., Feynman R.P. - Rev. Mod. Phys., 1949, v. 21, p. 425.
12. Dav,uov A.S. Theory of Solid Body (in russian) -M.: Nauka, 1976.

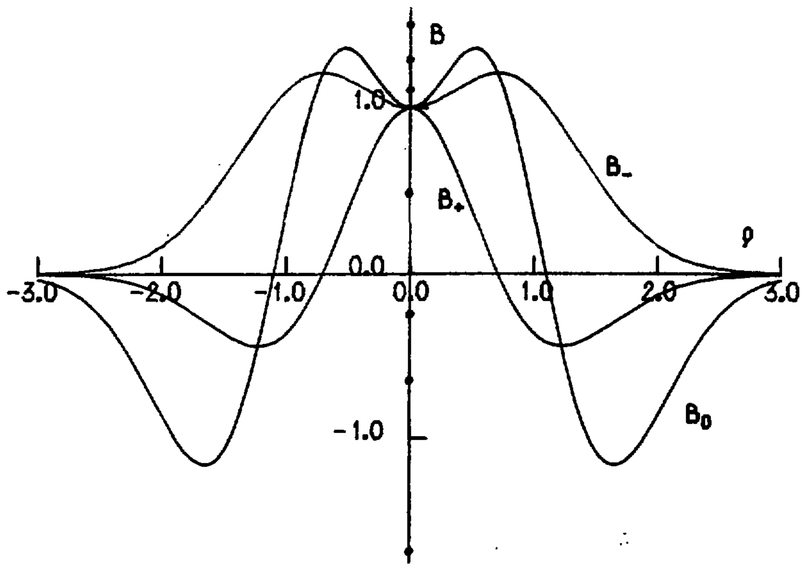

Fig. 1. Functions B_0, B_-, B_+ . Tachionic region lies between curves B_- and B_+ .

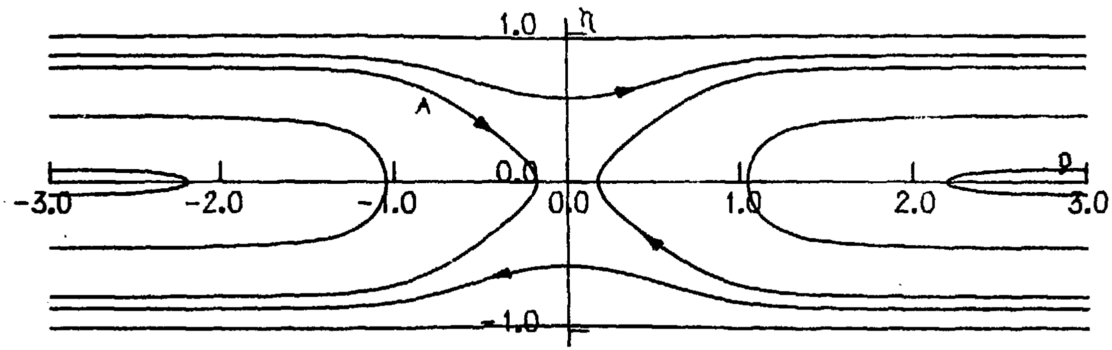

Fig. 2. Phase portrait of the Lagrangian $L(\rho) = -h[1+\lambda B(\rho)]$.
Repulsion : $\lambda = 0.6$, $B = -1.67$. Phase trajectory A corresponds to the trajectories of particles on fig. 9. Here and below arrows indicate the direction of motion along a phase trajectory.

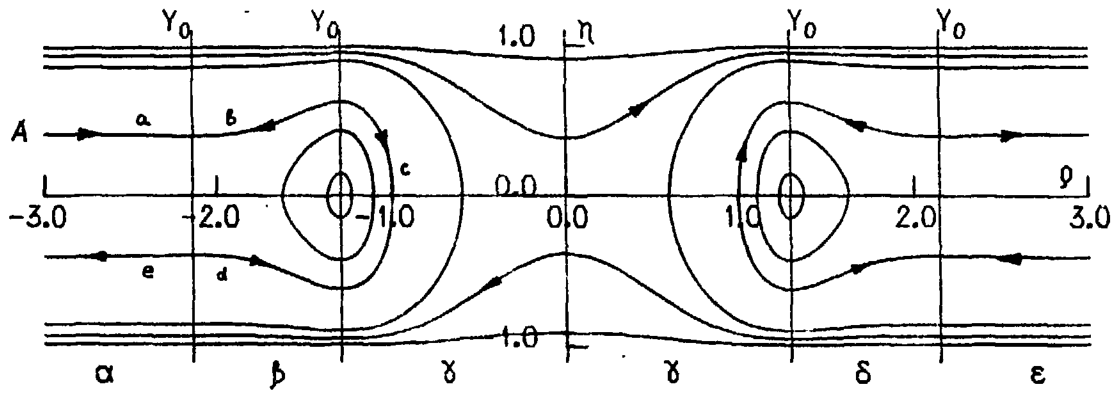

Fig. 3. Phase portraits of $L(\rho)$. Strong repulsion: $\lambda = 1.53$, $B=-0.64$, $\alpha, \gamma, \varepsilon$ are physical regions, β, δ are nonphysical regions, Y_0 is a line, where $Y_0 = 0$. Line A corresponds to the trajectories of particles on fig.11.

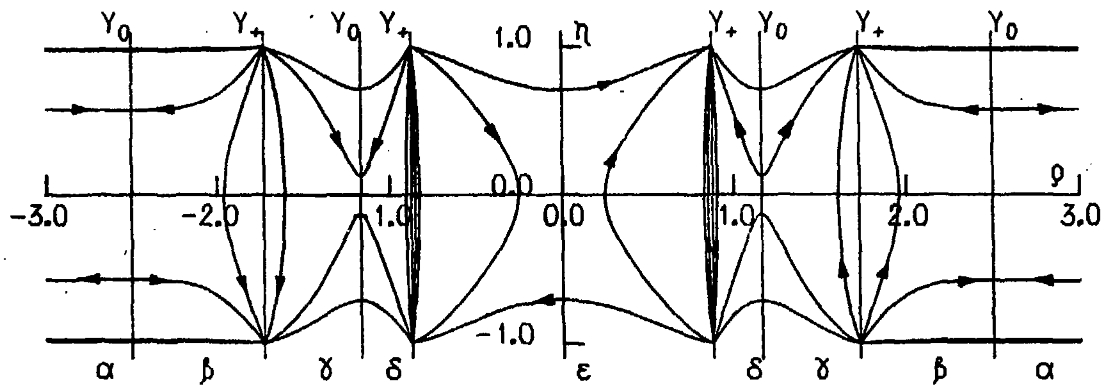

Fig. 4. Phase portrait of $L(\rho)$. Strong repulsion: $\lambda=4$, $B=-0.25$, α, ε are physical regions, β, γ, δ are nonphysical regions, γ, δ are tachionic regions, Y_0, Y_+ are the lines, where, respectively, $Y_0=0$ or $Y_+=0$.

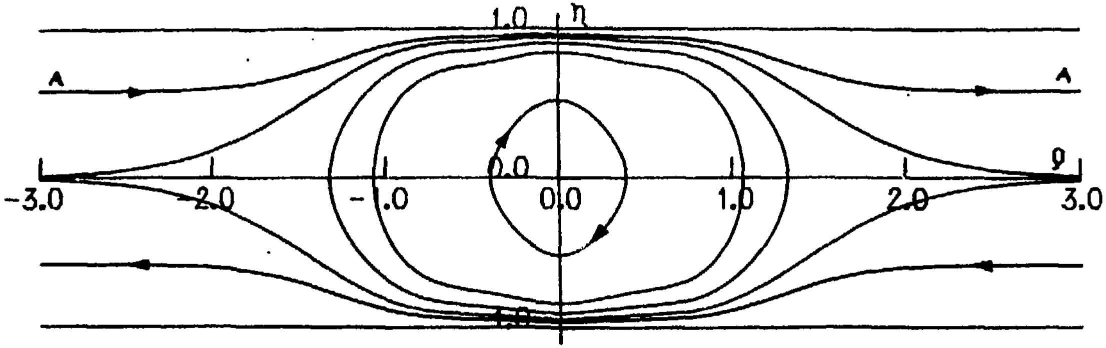

Fig. 5. Phase portrait of $L(\rho)$. Attraction: $\lambda = -0.66$, $B = 1.5$
Phase trajectory A corresponds to the trajectories of particles on fig. 10.

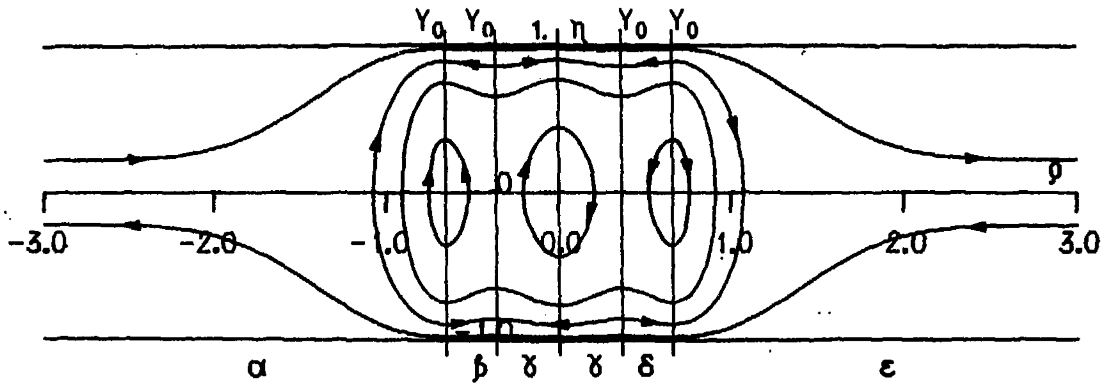

Fig. 6. Phase portrait of $L(\varphi)$. Strong attraction: $\lambda = -0.78$, $B = 1.2$, β, δ are nonphysical regions.

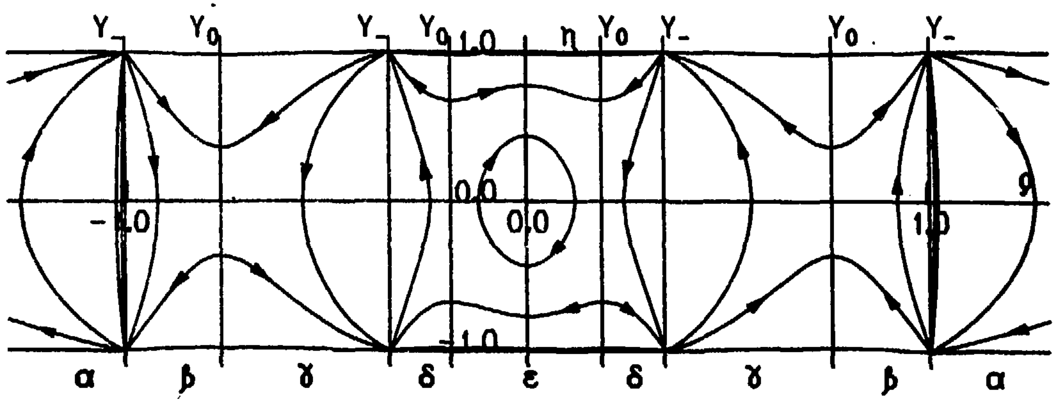

Fig. 7. Phase portrait of $L(\rho)$. Strong attraction: $\lambda = -0.91$, $\beta = 1.1$.
Regions β, γ, δ are nonphysical, γ , δ , tachionic.

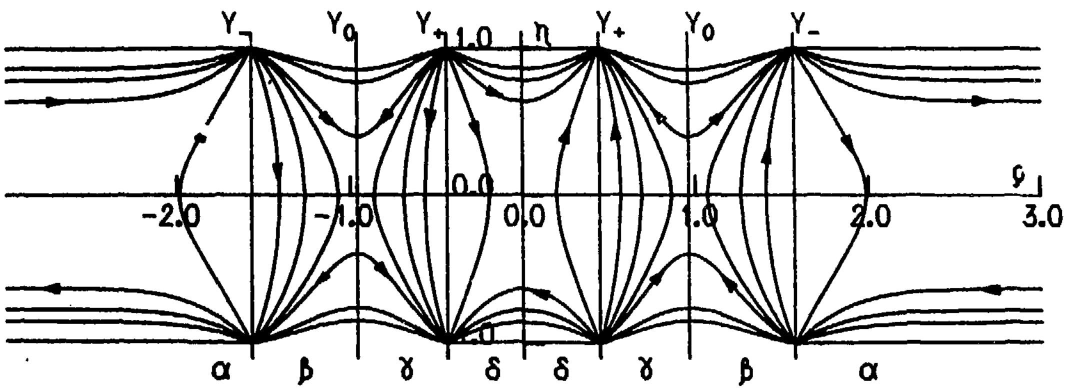

Fig. 8. Phase portrait of $L(\rho)$. Strong attraction: $\lambda=-2$, $B=0.5$. Regions β, γ, δ are nonphysical, β, γ , tachionic. In region δ, trajectories correspond to the maximum of the action, the particles behave as particles with negative masses.

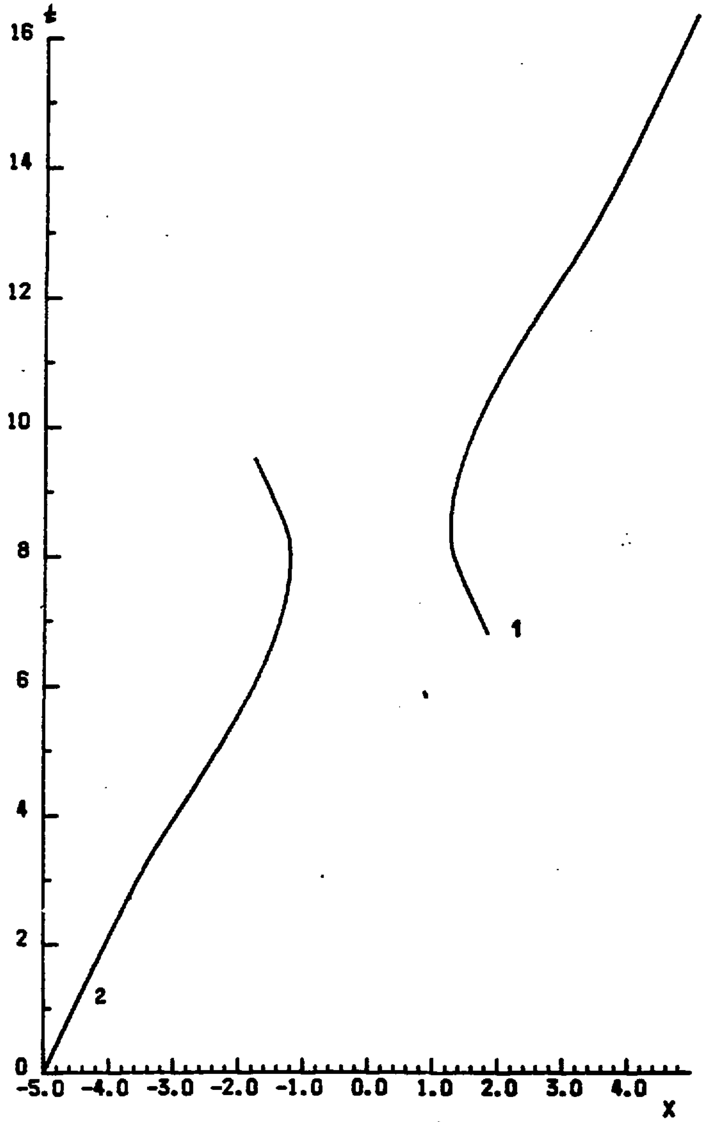

Fig. 9. The Lagrangian formalism. World lines of particles. Repulsion: $\lambda = 0.6$, $E = 4.53$.

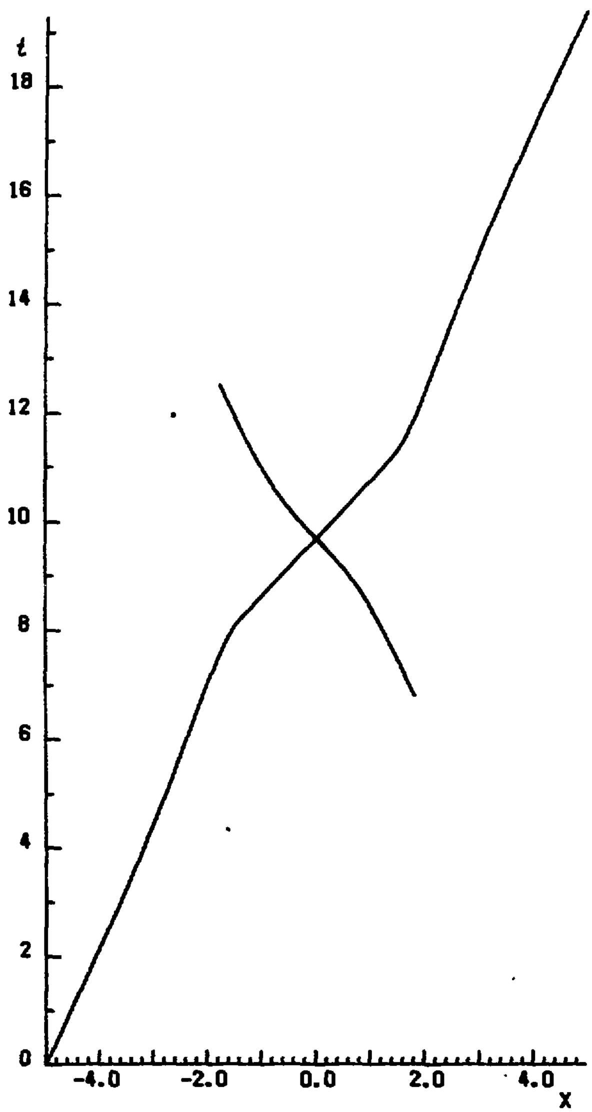

Fig. 10. The Lagrangian formalism. World lines of particles. Attraction: $\lambda = -0.66$, $E = 4.53$.

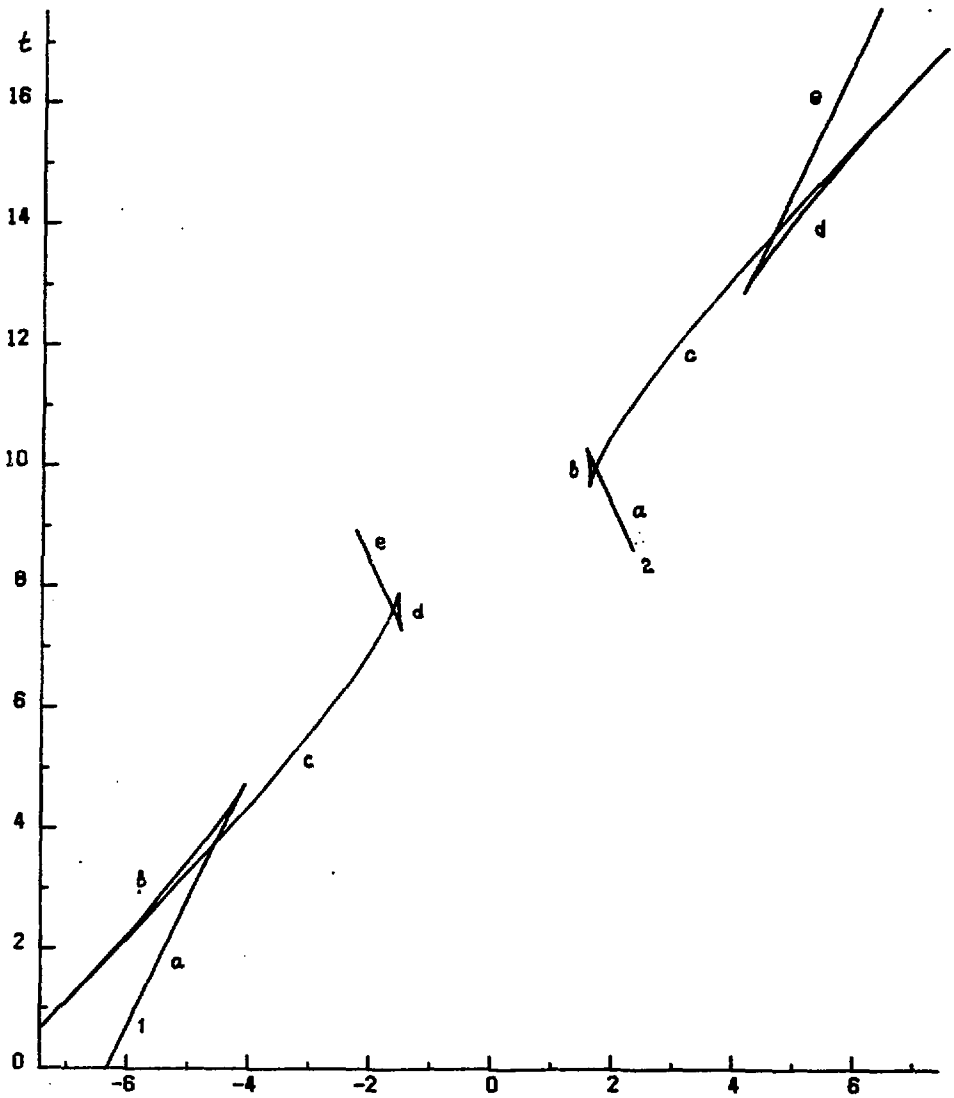

Fig. 11. The Lagrangian formalism. World lines of particles . Strong repulsion: $\lambda = 1.53$, $E = 4.53$. Segments a,...,e correspond to the segments of the trajectory on fig. 3.

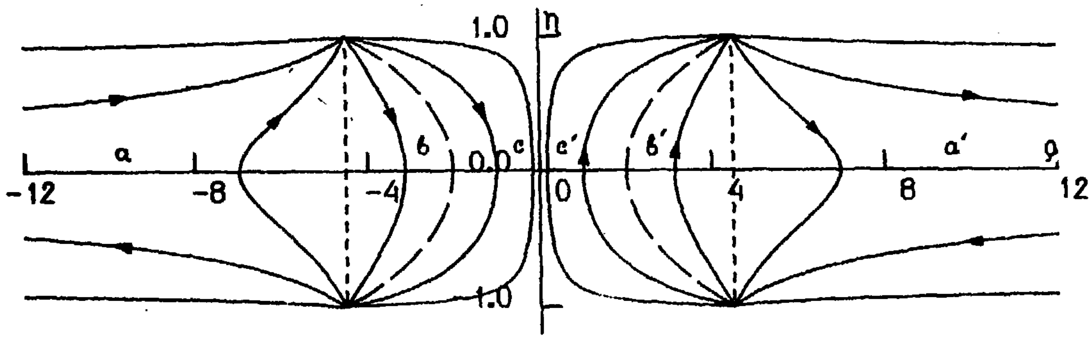

Fig. 12. Interaction with a field interpretation at $\eta=0$. Attraction: $\alpha/m=-1$. The dotted lines correspond to $|G|=0$, the dashed lines are the boundaries of tachionic regions. Region with $|\rho|<4.5$ is nonphysical, region with $|\rho|< 2(1+\eta^2)$ is tachionic.

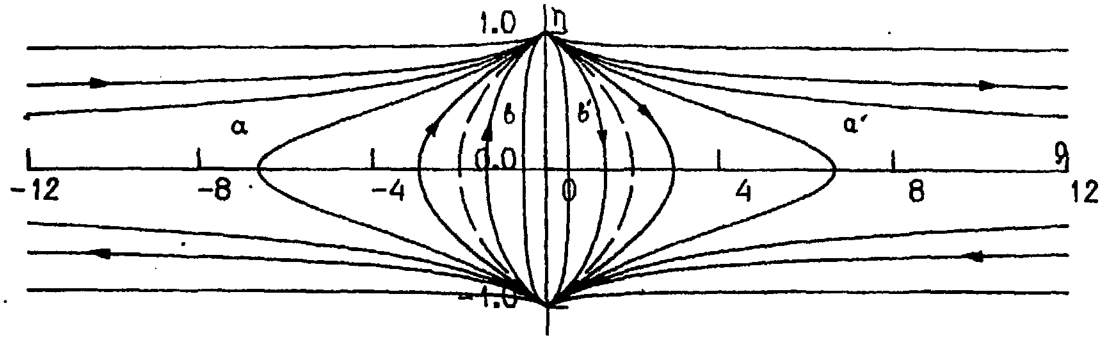

Fig. 13. Interaction with a field interpretation at $\eta = 1$. Attraction: $\alpha/m = -1$, $|\rho| < 2(1-\eta^2)$ is a tachionic region. The dashed line is its boundary.

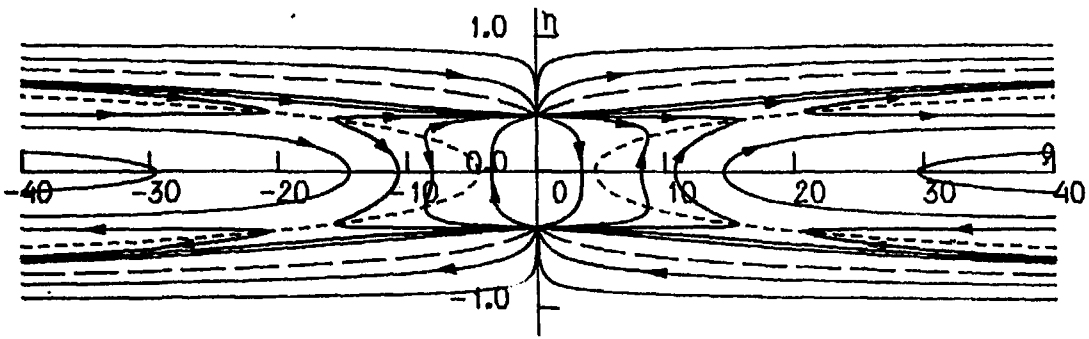

Fig. 14. Interaction with a field interpretation at $n=2$. Repulsion: $\alpha/m=1$. The dashed lines are boundaries of tachionic regions lying at $|\eta|$ close to 1. The dotted line is a boundary $|G|=0$ of physical regions.

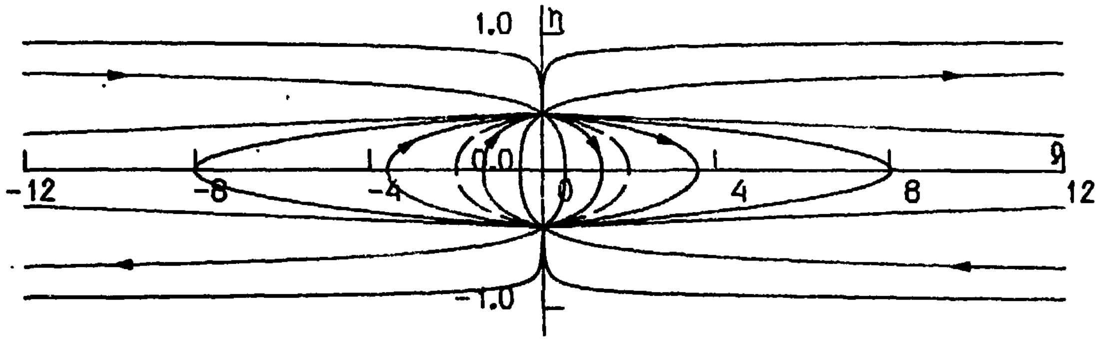

Fig. 15. Interaction with a field interpretation at $n=2$. Attraction: $\alpha/m=-1$.
The dashed line is a boundary of tachionic region.

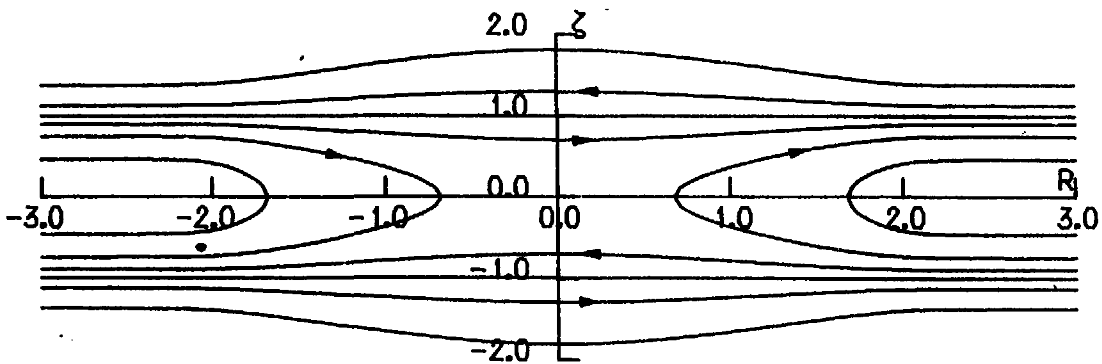

Fig. 16. Phase portrait of the Hamiltonian system corresponding to the Lagrangian $L(\rho)$. Repulsion: $\lambda = 0.6$. The direction of motion here and below is shown for the case $P_- > 0$. $|\zeta| < 1$ is a tardionic region, $|\zeta| > 1$ are tachionic "nonlagrangian" regions.

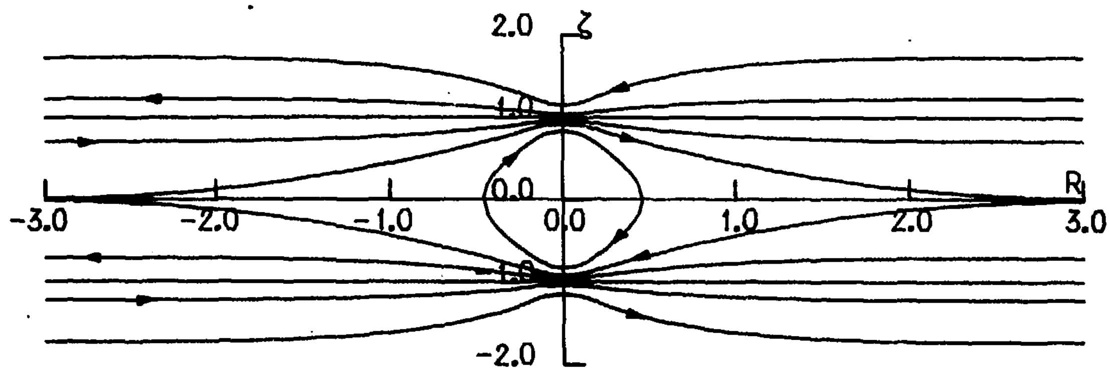

Fig. 17. Phase portrait of the Hamiltonian system corresponding to the Lagrangian $L(\rho)$. Attraction: $\lambda = -0.66$. $|\zeta| < 1$ is a tardionic region. $|\zeta| > 1$ are tachionic "nonlagrangian" regions.

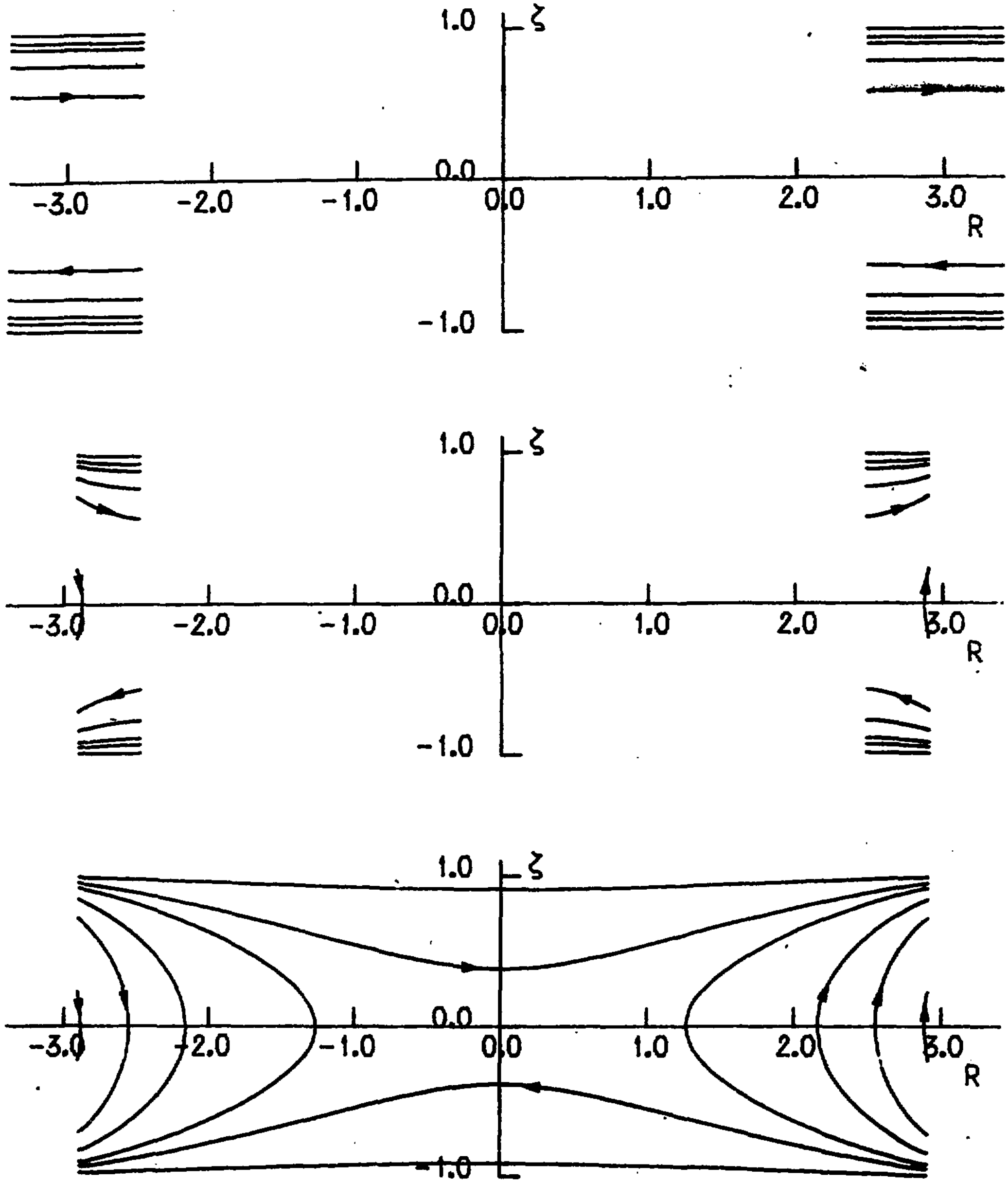

Fig. 18. Multi-layered phase portrait of the Hamiltonian system corresponding to the phase portrait of the Lagrangian system on fig. 3. Layers β, δ correspond to nonphysical regions. Nonlagrangian regions $|\zeta| > 1$ are omitted.

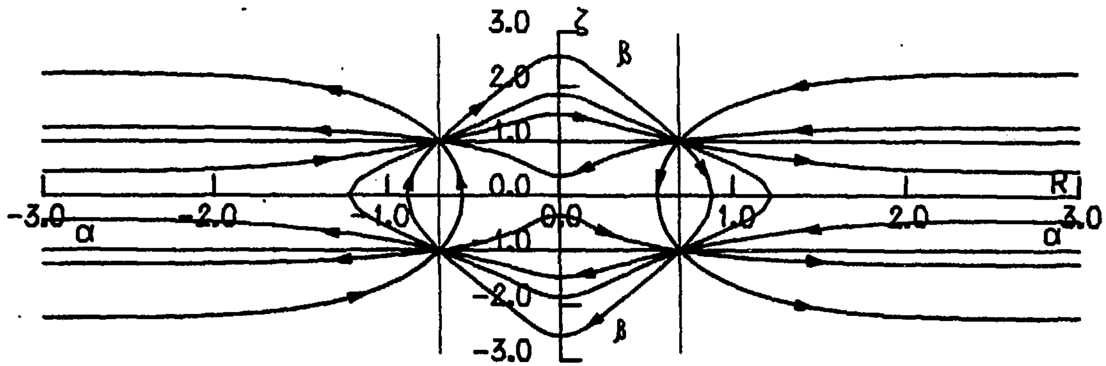

Fig. 19. Phase portrait of a Hamiltonian system. Strong attraction: $\lambda = -2$.
Regions α and β are tardionic, all the rest are tachionic.

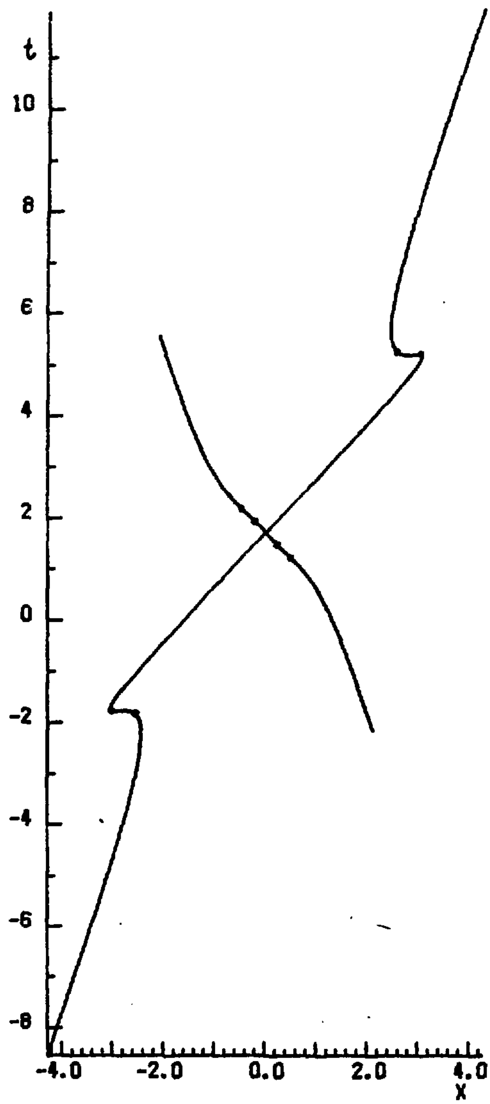

Fig. 20. World lines of particles in the Hamiltonian picture. Attraction: $\lambda=-0.9$. The ends of segments of superlight velocities are marked by dots.

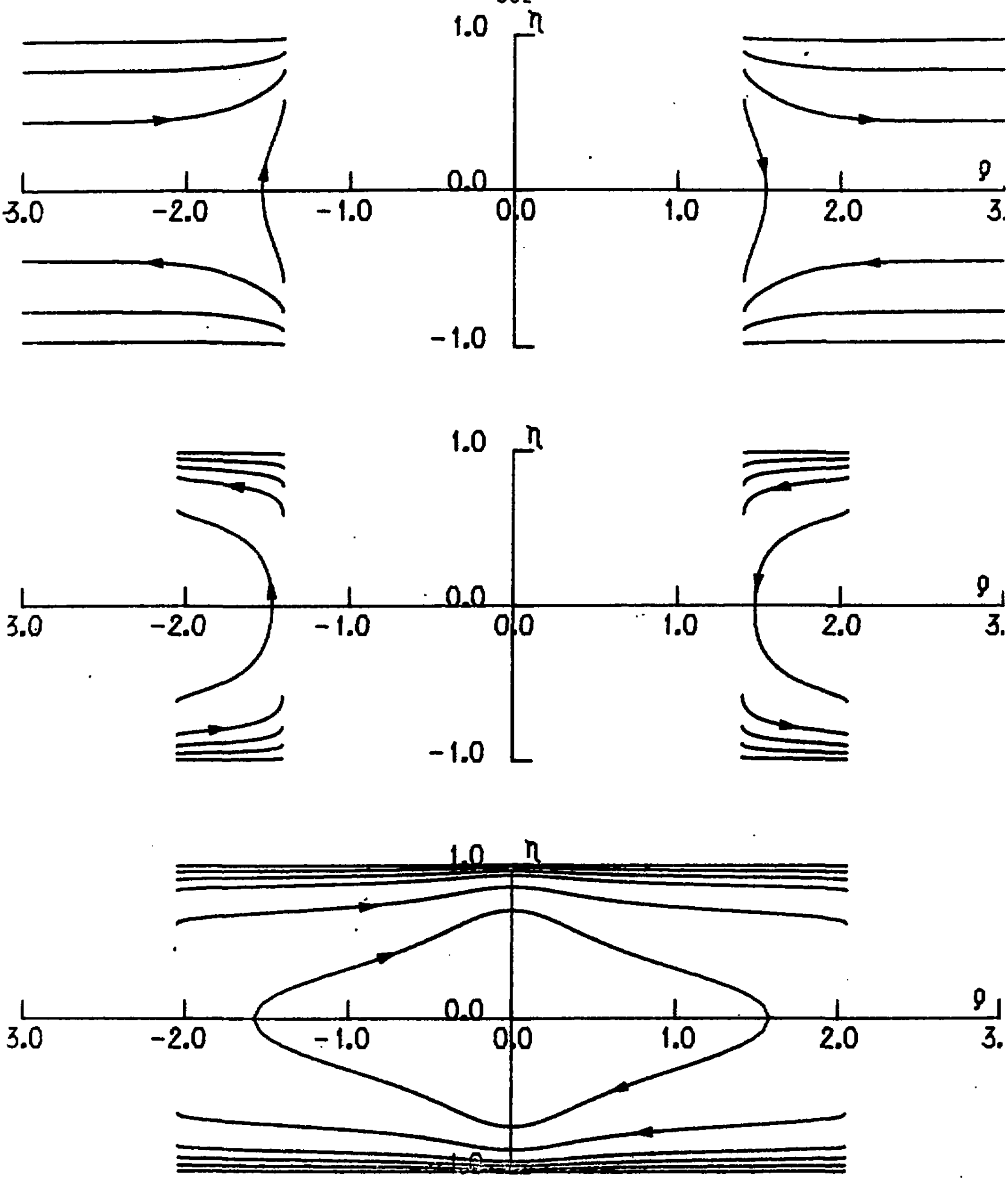

Fig.21. Multi-layered phase portrait of the Lagrangian system corresponding to the strip $|\zeta|<1$ of the Hamiltonian phase portrait with $\lambda=-0.64$.

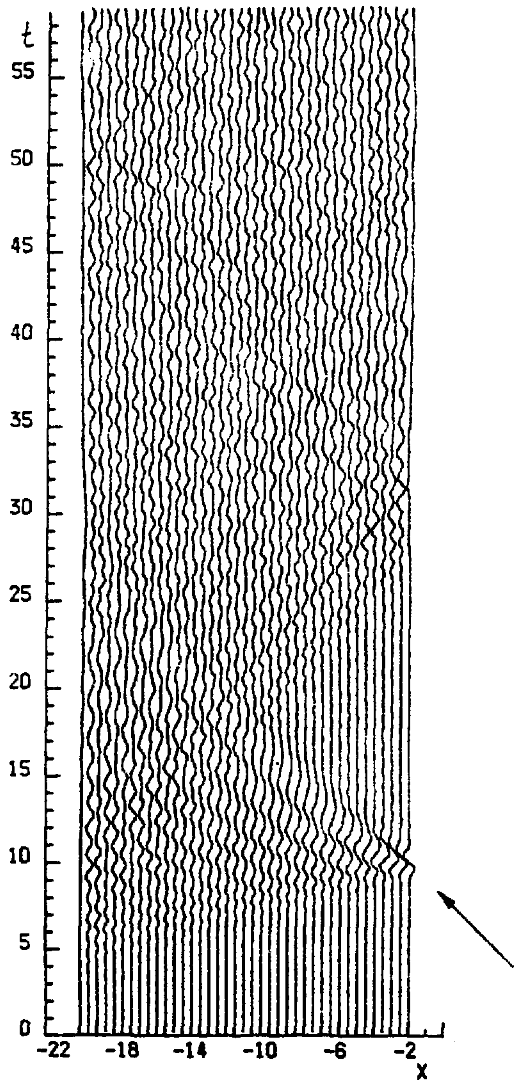

Fig.22. Propagation of perturbation in a very rigid crystal at short blow. Deviations are given in the scale 20:1.

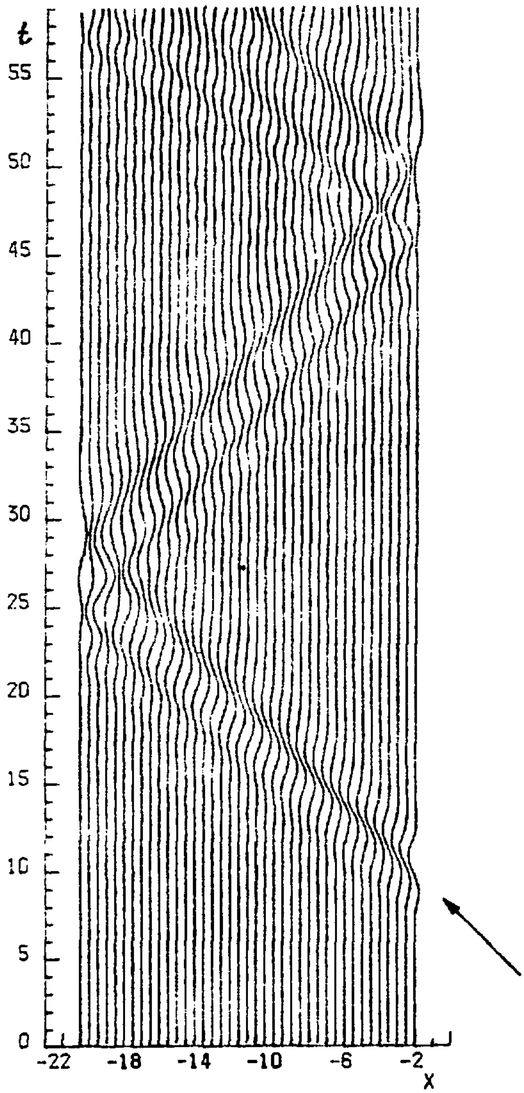

Fig. 23. Propagation of perturbation in a very rigid crystal at soft blow. Deviations are given in the scale 20:1.

THEOREM PROVING WITH FIRST-ORDER PREDICATE LOGIC: III.*

B.Humpert

IKOSS Research & Development
CH-8048 ZURICH, Switzerland
55, Albulastr.

and

CERN Theory Division
CH-1211 GENEVA, Switzerland

ABSTRACT

We give an introduction into 'Theorem Proving/Automated Reasoning' by presenting in this third paper a number of explicit examples. A variety of (simple) 'Thinking Problems' were chosen to illustrate several points: (i) how a problem is translated into the language of first-order predicate logic, (ii) how an actual deduction-chain proceeds: length, complexity,..., and (iii) how the different resolution techniques can be applied most efficiently. The selected examples, however, do not represent the spectrum of the possible applications of the Automated Theorem Proving (ATP) systems.

* Submitted to the Symposium

Overview

1. Introduction
2. Simple Job-Assignment
3. Complex Job-Assignment
4. Lion and Unicorn
5. Truth-Teller (Knights) and Liars (Knaves)
6. Schuberts Steamroller
7. School Boys
8. Salt and Mustard
9. Tiles plus Holes
10. Checkerboard
11. Missionaries and Cannibals
12. Billiard Ball Weighing
13. Some Insights
14. Conclusions

1. Introduction

There exist computer systems which allow for highly complex deductions: conjectured 'Theorems' can be proved from a set of 'Axioms'. This field of "Automated Theorem Proving (ATP)" or "Automated Reasoning (AR)" has meanwhile reached a quite high level of performance which sometimes goes substantially beyond the human abilities.

Contrary to our earlier papers [1,2] which focused on the presentation of the theoretical concepts and particular deduction schemes, we here are concerned with the application of these systems on a set of illustrative examples. This paper thus aims to give insight into the utility, power and flexibility of the ATP-systems for the solution of problems which demand for a great deal of logical reasoning, or which need repeated trials to come closer to a solution path. We here limit ourselves to a set of "Thinking Problems" whose presentation should not primarily be considered as a source of entertainment, but rather as an abstraction of real-life problems. Their closer inspection makes obvious that they do not allow for easy solutions by conventional mathematical techniques, but instead, they typify classes of problems where the solutions are found by trial-and-error. Our subsequent presentation therefore aims to discuss a set of such problems in order to illustrate their formulation in the framework of first-order predicate logic, such that they admit for logical deductions by the inference techniques. Having, in addition, excellent ATP-systems [3,4] at hand, we furthermore give insight into their use in solving unusual problems which, and this is an essential condition, allow for their formulation in the language of first-order predicate logic.

Our subsequent presentation has a second aim: whilst preparing the description of a problem for an ATP-system, the hidden and sometimes unknown assumptions in the axiom system of that problem have to be recognized. That this is not easy, leading frequently to wrong formulations, or that one or the other important information completely falsifies the original problem, should also become more clear from our presentation. There is no doubt that the translation of a problem into the language of an ATP-system is one of the more difficult tasks. The constants, functions and predicates have to be defined in a 'natual', meaning problem-appropriate way, allowing for an efficient deduction of new clauses and finally the sought contradiction. Furthermore, the axioms and constraints of the problem must be formulated such as to allow for easy insight and an optimal deduction.

Let us make a few introductory remarks on some of the examples [3-11]. In sections 2 and 3 we consider the problem of assigning a set of jobs to several persons such that a number of defining constraints are satisfied. In section 4 we show how the selection of a particular element out of the set of week days proceeds according to several intricate selection criteria. The problems concerning true and un-true statements ('Knights and Knaves', etc.), as discussed in section 5, are unusual in that they present a first-order description of a higher-order problem. We here give details of the deduction steps. Schubert's Steamroller problem of section 6 shows some of the arising ambiguities if a problem is cast in the clause form of first-order predicate logic. Until recently this problem was considered a challenge to existing ATP-systems. From the schoolboy problem of section 7 we learn that some problems allow even for a solution in propositional logic if the encoding is chosen appropriately. The problem of section 8 again asks for some object-person identification according to specified criteria. The 'Tiles plus Hole' problem in section 9 requires the shifting of tiles according to well specified rules which simply express the physical constraints of this system. The actual search of the most optimal solution is left to the ATP-system. The description and simulation of such a system by purely mathematical techniques, doubtless would pose problems even to an experienced researcher. The checkerboard problem of section 10 leads to the investigation whether an arbitrarily shaped area can be covered by a set of elementary bulding blocks, and it can be viewed as an abstraction of similar problems in circuit layout-design. Thinking problems like 'Missionaries and Cannibals' (section 11), require determining who must go where at what time and their solution indicates how problems in everyday scheduling must be approached. The 'Billiard Ball' problem of section 12 demonstrates in a nice way how far one can get with ATP-systems if the set of axioms is optimally chosen. It presents difficulties which are also encountered when planning for instance a trip in a city with visits to several people, taking traffic constraints etc. into account, whereby the trip must be completed in a specified amount of time. Section 13 summarizes some general insights from ATP-experiments, and section 14 is reserved for the summary.

After these general introductory remarks lets us go to the examples!

2. Simple Job-Assignment

We consider in this section a simple, if not trivial, reasoning problem in order to illustrate the method of submitting a problem to an ATP-system.

The problem is as follows:

Roberta (R) and Steve (S) hold, between them, two jobs. Each one has one job. The jobs are teacher (To) and nurse (No). The job of nurse is held by a male. Who holds which job?

The solution of this problem is obvious: Roberta is the teacher and Steve is the nurse.

The submission of this problem to an ATP-system demands for a set of constant (Cst) and predicate (Prd) definitions such as:

```
R ...Cst: Roberta,  F[x]    ...Prd: Person x is female,
S ...Cst: Steve,    M[x]    ...Prd: Person x is male,
No...Cst: Nurse,   HJ[x,y]...Prd: Person x holds job y.
To...Cst: Teacher,
```

We now give the clauses describing the problem and the interrelations, and subsequently discuss their meaning:

(1,2)	$HJ[x,No] \vee HJ[x,To]$	($x=R,S$)
(3,4)	$\sim HJ[x,No] \vee \sim HJ[x,To]$	($x=R,S$)
(5,6)	$HJ[R,y] \vee HJ[S,y]$	($y=No,To$)
(7,8)	$\sim HJ[R,y] \vee \sim HJ[S,y]$	($y=No,To$)
(9)	$\sim HJ[x,No] \vee M[x]$	
(10)	$F[x] \vee M[x]$	
(11)	$\sim F[x] \vee \sim M[x]$	
(12)	$F[R]$	
(13)	$M[S]$	
(14)	$\sim HJ[S,No]$	(denial of claim)

Clause (1) expresses the fact that any of the two persons $x=(R,S)$ can, in principle, hold one or the other job. The complementary clause (3) however specifies that if a person x holds one of the two jobs, it <u>can not</u> exercise the other. This becomes immediately obvious from the equivalent forms:

(3a)	$HJ[x,No] \rightarrow \sim HJ[x,To]$
(3b)	$HJ[x,To] \rightarrow \sim HJ[x,No]$

Clauses (1) and (3) together therefore state that each person can hold only one of the two possible jobs:

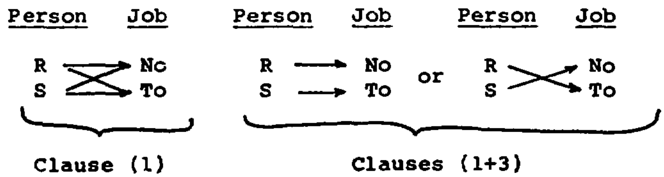

Clause (5) says that any of the two jobs y=(No,To) in the puzzle can be held by one or the other person, whereas clause (6) imposes that each job is held by only one of the two persons. The identification therefore must be in one-to-one correspondence. Clause (14) denies the claim that S holds the job of nurse; its use will lead to a proof by contradiction.

In order to derive new information we use UR-resolution which considers a set of clauses simultaneously and demands that one of them be a non-unit clause; the newly derived clause is then required to be a unit clause. The deductive reasoning steps of an ATP-system are then as follows:

```
[12;1] + [11;1]  => [15] :  ~M[R]
[15;1] + [ 9;1]  => [16] :  ~HJ[R,No]
[16;1] + [1,2;1] => [17] :   HJ[R,To]
[17;1] + [5,6;1] => [18] :   HJ[S,No]
```

The clauses (17) and (18) thus are the sought information. In this deduction we have not made any use of the clause (14) (denial of claim). If, instead, our derivation had started with the clause (14) the derivation chain would be as follows:

```
[14;1] + [ 6;2]  => [19] :   HJ[R,No]
[19;1] + [ 9;1]  => [20] :    M[R]
[20;1] + [11;2]  => [21] :  ~F[R]
[21;1] + [12,1]  => [22] :     □     (Contradiction)
```

3. Complex Job-Assignment

Having understood how to deal with a simple assignment problem, we now want to learn how an ATP-system deals with a much more complex example. The problem is as follows:

Roberta(R), Thelma(T), Steve(S) and Pete(P) hold among them eight different jobs. Each person holds exactly two jobs. The jobs are: Chef(Ch), Guard(Gu), Nurse(Nu), Telephone-Operator(Op), Police Officer(Po) (male or female), Teacher(Te), Actor(Ac), and Boxer(Bo). The job of nuse is held by a male. The husband of the chef is the telephone operator. Roberta is not a boxer. Pete has no education past the ninth grade. Roberta, the chef and the police officer went golfing together. Who holds which jobs?

We first seek the solution of this problem in the way an intelligent human being would solve it. One way is to make a coordination-table (see Table 3.1) with the names of the persons listed on the top-row and the possible jobs enumerated on the leftmost column. The idea is to fill the squares with y(es) or n(o) as the conclusions are drawn from the statement of the problem. For each of the four people in the problem one proceeds by crossing off possibilities until only two remain. At that point, the remaining two squares can immediately be filled with y(es). Note that this problem abounds implicit information, some obvious and some somewhat more subtle. For example, R and S are female while S and T are male. All eight jobs are filled, which means they are held by one of the four people. No job is held by more than one person. The problem also con-tains some rather hidden information which, if not used, will not allow for a solution of the problem.

We first focus on R (which is a female name!). From the problem's statement we deduce:

R is <u>not</u> Bo	(stated in problem)
R is <u>not</u> Nu	(R female, but male required)
R is <u>not</u> Ac	(R female, can not be actor)
R is <u>not</u> Op	(R female, can not be husband)
R is <u>not</u> Ch, Po	(since they went golfing together)

R can therefore only hold the jobs: Gu(ard) and Te(acher). The formulation of the problem says that there are four persons, eight jobs, and that each person holds exactly two jobs. Implicit in this is the fact that no job is held by two people. As a result, the jobs: Gu, Te can be crossed off the list of possible jobs for all other persons: T, S, P.
We now focus on the person T (which again is a female name!) and apply the same arguments as for R:

T is <u>not</u> Nu	(T female, but male required)
T is <u>not</u> Ac	(T female, can not be actor)
T is <u>not</u> Op	(T female, can not be husband)
T <u>is</u> Ch	(Ch has husband and T is only female left)
T is <u>not</u> Po	(Ch and Po went golfing together).

T can therefore only hold the jobs: Ch(ef) and Bo(xer). Focusing now on the persons P and S, we must make use of the deeply hidden information that in the USA in the 1980s the jobs of nurse, police officer and teacher each required more than a ninth-grade education. Thus P cannot hold the jobs: Nu, Po. As a result, P holds the jobs: Ac(tor) and Op(erator). The remaining unassigned jobs are then attributed to S: Nu(rse), Po(lice officer).

In order to submit this problem to an ATP-system we first have to define the constants, predicates and functions. For the constants we use the same definitions as given above in the description of the problem. The used predicates (Prd) and functions (Fct) are:

M[x]	...	Prd: Person x is male.
F[x]	...	Prd: Person x is female.
HJ[x,y]	...	Prd: Person x holds job y.
GT[u,v]	...	Prd: u must be greater than v.
H[x,y]	...	Prd: x is the husband of y.
j1[x]	...	Fct: Job j1 depends on person x.
jh[y]	...	Fct: Jobholder-person jh depends on job y.
gr[x]	...	Fct: Education-grade gr of person x.

These definitions allow us to give the first set of clauses with their meaning being discussed subsequently:

(1) F[R]
(2) F[T]
(3) M[S]
(4) M[P]
(5) F[x] ∨ M[x]
(6) ∼F[x] ∨ ∼M[x]
(7) ∼HJ[R,Bo]
(8) HJ[x,Nu] --> M[x]
(9) HJ[x,Ac] --> M[x]
(10) HJ[x,j1(x)]
(11) HJ[x,j2(x)]
(12) HJ[jh(y),y]
(13) H[x,jh(Ch)] -> HJ[x,Op]
(14) HJ[x,Op] -> H[x,jh(Ch)]
(15) F[jh(Ch)]
(16) H[x,y] -> M[x]
(17) H[x,y] -> F[y]
(18) ∼GT[gr(P),9]
(19) HJ[x,Nu] -> GT[gr(x),9]
(20) HJ[x,Po] -> GT[gr(x),9]
(21) HJ[x,Te] -> GT[gr(x),9]

The clauses (1-6) are simple; they define the persons R, T to be female and the persons S, P to be male. The clauses (5-6) certify that each person is either male or female, but not both. The clauses (7-9) formalize the condition that R is not a Bo(xer) and that the jobs: Nu(rse), Ac(tor), must be hold by a male. The clauses (10-12) state that for every person x there exist two different jobs j1 and j2 which, in fact depend on the particular person x; equivalently, for every job y there is a person (jobholder) which also depends on the job y. The clauses (13-16) formalize the statement: the husband of the Ch(ef) is the Op(erator), whereby the statements (15-16) say that husbands are male, and wives are female. The clauses (18-21) express the constraint that Nu(rses), Po(lice officers) and Te(achers) must have education-grades above 9, but the grade of P(ete) is lower than 9.

In order to give the second set of clauses we must define a few more equality-predicates (Eq-Prd):

EP[x1,x2]	...	Eq-Prd: for the persons(R,T,...)
EJ[y1,y2]	...	Eq-Prd: for the jobs(Ch,Po, ...)
EQ[u,v]	...	Eq-Prd: general

The second set of clauses then reads:

(22) $\sim$HJ[R,Ch]	
(23) $\sim$HJ[R,Po]	
(24) $\sim$HJ[x,Ch] $\vee$ $\sim$ HJ[x,Po]	
(25) $\sim$EP[R,T]	(32) EP[x,x]
(26) $\sim$EP[R,S]	(33) EJ[x,x]
(27) $\sim$EP[R,P]	(34) EQ[x,x]
(28) $\sim$EP[T,S]	(35) HJ[x,y] $\wedge$ $\sim$EJ[y,j2(x)] -> EJ[y,j1(x)]
(29) $\sim$EP[T,P]	(36) $\sim$EP[x,z] $\wedge$ HJ[x,y] -> $\sim$HJ[z,y]
(30) $\sim$EP[P,S]	(37) F[jh(y)] $\wedge$ $\sim$ HJ[R,y] -> HJ[T,y]
(31) $\sim$EJ[j1(x),j2(x)]	(38) M[jh(y)] $\wedge$ $\sim$ HJ[S,y] -> HJ[P,y]

Clauses (22-24) encode the information of: "R(oberta), the Ch(ef) and the Po(lice officer) went golfing". In particular clause (24) says that for any person x, x can either be the Ch(ef) or the Po(lice officer) but not both. The clauses (25-31) ascertain that the four persons T,S,P,R, as well as the two jobs held by a person, are all different. The clauses (32-34) express the reflexivity property of the equality predicates. The clause (35) says: if a person holds a job, and if that job is not equal to the second job held by the person, then it is equal to the first job held by the person. Similarly, clause (36) imposes that for any two distinct persons, if one of them has a particular job, then the other can not have this job. The clauses (37-38) allow a reasoning program to add information based on facts such as: "a particular job is held by a female other than R(oberta)".

The third set of clauses concerns the way which is used to find a solution of the problem. We here will follow the steps an intelligent human being would choose, by crossing off in a formal way the squares in a person-job table. We therefore are obliged to introduce a few new predicates and functions, as well as to explain the notation and utility of a list function. Let us focus first on the -function (denoted by curly-brackets) which has two arguments. In the first argument is an item of the list and in the second argument is the rest of the list or the '*' -item (meaning 'end'). The list-function then consists of a chosen number of   -functions, each one being positioned in the second argument of the preceding   -function such that for instance:

$$\begin{aligned} li(\alpha,*) &= \{\alpha,*\} && * \text{ end} \\ li(\alpha,\beta,*) &= \{\alpha,\{\beta,*\}\} \\ li(\alpha,\ldots,\varepsilon,*) &= \{\alpha,\{\beta,\ \ldots\{\varepsilon,*\}\}\ldots\} \end{aligned}$$

The new predicates (Prd) and functions (Fct) then are:

PJ[..] ... Prd: list of possible person-job pairings.
PP[..] ... Prd: list of possible job-person pairings.
TD[..] ... Prd: list of persons whose jobs are determined.

$\underline{(x,y)}$ ... Fct: for possible person-job pairings.
$\overline{(x,y)}$ ... Fct: for successful person-job pairings.
jf(x) ... Fct: for bookkeeping of persons whose jobs are determined.

Furthermore, we introduce the simplifying notation:

$$\begin{aligned} PJ1[\alpha,\beta,\ldots,\varepsilon,*] &\equiv PJ[\ li(\alpha,\beta,\ldots,\varepsilon,*)\ ] \\ PP1[\alpha,\beta,\ldots,\varepsilon,*] &\equiv PP[\ li(\alpha,\beta,\ldots,\varepsilon,*)\ ] \\ TD1[\alpha,\beta,\ldots,\varepsilon,*] &\equiv TD[\ li(\alpha,\beta,\ldots,\varepsilon,*)\ ] \\ EQ1[(\ldots),(\ldots)] &\equiv EQ[\ li(\ldots),\ li(\ldots)\ ] \end{aligned}$$

by simply leaving aside the li-function and putting a 1 at the end of the predicate name. We are now in the position to present the clauses of the third set:

(39-42) PJ1[(x,Ch),(x,Gu),...,*] $\quad x \equiv (R,T,S,P)$
(43-50) PP1[(R,y),(T,y),(S,y),(P,y), *] $\quad y \equiv (Ch,Gu,Nu\ldots)$
(51) $\sim$ HJ[x,y] -> EQ[(x,y),crossed]
(52) EQ[{crossed,x} , x]
(53) PJ1[(x,y),(x,z),*] $\wedge \sim$ EP[x,w] -> EQ[(w,x),crossed]
(54) PJ1[(x,y),(x,z),*] $\wedge \sim$ EP[x,w] -> EQ[(w,z),crossed]

(55) PJ1[(x,y),(x,z),*] -> HJ[x,y]
(56) PJ1[(x,y),(x,z),*] -> HJ[x,z]
(57) PJ1[(x,y),*] -> HJ[x,y]

(58) TD1[jf(R),jf(S),jf(T),jf(P),*]
(59) PJ1[(x,y),(x,z),*] -> EQ[jf(x),crossed]
(60) $\sim$ TD1[*]

(61) $HJ[x,y] \rightarrow EQ[(x,y),(\overline{x,y})]$
(62) $EQ1[(\ (x,y),(\overline{x,y}),w)\ ,\ (\ (\overline{x,y}),(x,y),w)\ ]$
(63) $EQ1[(\ (\overline{x,y}),(\overline{x,z}),v,w)\ ,\ (\ (\overline{x,y}),(\overline{x,z}),*)\ ]$
(64) $PJ1[(\overline{x,y}),(\overline{x,z}),*] \rightarrow EQ[jf(x),crossed]$
(65) $PJ1[(\overline{x,y}),(x,z),*] \rightarrow HJ[x,z]$

The clauses (39-42) enumerate all possible job-to-person pairings in the form of a recursive list; the predicates PJ[..] resp. PJ1[..] and the pairing-function (x,y) have been introduced for this purpose. Similarly the clauses (43-50) enumerate all possible person-to-job pairings in the form of a recursive list. If a particular person does not hold a particular job the corresponding pairing-function (x,y) is replaced by the expression 'crossed'; this is the essential action of the clauses (51-52) whereby (52) eliminates the pairing-function from the lists in (31-50). When a person's two jobs have been determined, those jobs are no longer possible for any other person, and consequently they must be crossed off from the list of all other persons; this is what is done by the clauses (53-54). The clauses (55-57) then serve to convert information from the PJ-predicate to the HJ-predicate. The clause (57), in particular, directly connects a person to a job when the other persons who could hold that job have been elimiated. The clauses (58-60) are introduced for bookkeeping. If a person's two jobs have been determined, that person's name is erased from the list of the TD, resp. TD1-predicate. The function jf(x) (jobsof(x)) was introduced in order to be replaced by 'crossed' once the crossoff-condition (59) is satisfied. The clause (60) is the halting condition once all jobs of all persons have been found. What happens if the ATP-system finds the two jobs of a person, but in terms of the HJ-predicate? The clauses (61-65) take care of that situation. The information is first converted from the (x,y)-function to the (x,y)-function by the demodulator in clause (61). The demodulators (62-63) eliminate all other possible pairings (x,y) once the two job-pairings of one and the same person are found. This elimination of all other possible person-job pairings, in particular then applies to the arguments of the corresponding PJ1-predicates, which allows for the replacement of the corresponding jf(x)-function by 'crossed' as done in clause (64). Clause (65) is needed to care for the situation where a person's job is determined either directly in terms of the predicate HJ or by eliminating jobs.

Some of the reasoning steps of an ATP-system are given in the following account where, in particular, it is shown how the crossing-off of anticipated person-job pairings takes place and how the elimination of a person from the TD1 control-predicate comes about, once its two jobs have been determined.

```
[ 7] + [51] => [66]  EQ[(R,Bo), crossed]
[66] + [39] => [67a] PJ1[(R,Ch),(R,Gu),...,(R,Ac),crossed *]
[52] + [67a]=> [67]  PJ1[(R,Ch),....,(R,Ac),*]

[22] + [51] => [68]  EQ[(R,Ch),crossed]
[68] + [67] => [69a] PJ1[crossed,(R,Gu),...,(R,Ac),*]
[69a]+ [52] => [69]  PJ1[(R,Gu),...,(R,Ac),*]

[23] + [51] => [70]  EQ[(R,Bo),crossed]
[70] + [69] => [71a] PJ1[(R,Gu),(R,Nu),(R,Op),crossed,(R,Te),(R,Ac),*]
[71a]+ [52] => [71]  PJ1[(R,Gu),(R,Nu),(R,Op),(R,Te),(R,Ac),*]

[ 1] + [ 6] => [72]  ~M[R]
[72] + [ 8] => [73]  ~HJ[R,Nu]
[72] + [ 9] => [74]  ~HJ[R,Ac]
[72)]+ [16] => [75]  ~H[R,y]
[75] + [14] => [76]  ~HJ[R,Op]

[73] + [51] => [77]  EQ[(R,Nu),corssed]
[74] + [51] => [78]  EQ[(R,Ac),crossed]
[76] + [51] => [79]  EQ[(R,Op),crossed]
[71]+[77-79]=> [80]  PJ1[(R,Gu),(R,Te),*]

[80]+[53]+[25]=>[81] EQ[(T,Gu),crossed]
[80]+[54]+[25]=>[82] EQ[(T,Te),crossed]
[80]+[53]+[26]=>[83] EQ[(S,Gu),crossed]
[80]+[54]+[26]=>[84] EQ[(S,Te),crossed]
[80]+[53]+[27]=>[85] EQ[(P,Gu),crossed]
[80]+[54]+[27]=>[86] EQ[(P,Te),crossed]

[80] + [59] => [82]  EQ[jf(R),crossed]
[58] + [82] => [83a] TD1[crossed,jf(S),jf(T),jf(R),*]
[83a]+ [52] => [83]  TD1[jf(S),jf(T),jf(P),*]
```

In the above text we have shown how the "Complex Job-Assignment" problem is solved as close as possible to an intelligent human being. In particular we have made heavy use of the demodulators. We now present the solution of the same problem using a straightforward approach.

The earlier clauses (1-38) which characterize the interrelations in the complex coordination problem are still valid. The subsequent clauses however which mainly set up the solution path are here changed. For this purpose we need to define a few new predicates (Prd):

```
HJ7[x;j1,..,j7] ≡ HJ[x,j1] V ... V HJ[x,j7]
HT[x,y1,y2] ... Prd: Person x holds jobs y1 and y2.
SO[problem] ... Prd: Problem has been solved.
```

We now give the new set of predicates and subsequently discuss their meaning:

(1) $HJ[R,y] \vee HJ[T,y] \vee HJ[S,y] \vee HJ[P,y]$ $(y = Ch, Gu, \ldots)$
(2) $HJ7[x;\ Gu,Nu,Op,Po,Te,Ac,Bo]$
(3) $HJ7[x;\ Ch,Nu,Op,Po,Te,Ac,Bo]$
(4) $HJ7[x;\ Ch,Gu,Op,Po,Te,Ac,Bo]$
(5) $HJ7[x;\ Ch,Gu,Nu,Po,Te,Ac,Bo]$
(6) $HJ7[x;\ Ch,Gu,Nu,Op,Te,Ac,Bo]$
(7) $HJ7[x;\ Ch,Gu,Nu,Op,Po,Ac,Bo]$
(8) $HJ7[x;\ Ch,Gu,Nu,Op,Po,Te,Bo]$
(9) $HJ7[x;\ Ch,Gu,Nu,Op,Po,Te,Ac]$

(10) $HT[R,y1,y2] \wedge HT[T,y3,y4] \wedge HT[S,y5,y6] \wedge HT[P,y7,y8] \rightarrow SO(problem)$
(11) $HT[x,y] \wedge HJ[x,z] \wedge \sim EJ[y,z] \longrightarrow HT[x,y,z]$

(12) $\sim EJ[Ch,Gu]$
(13) $\sim EJ[Ch,Nu]$
(14) $\sim EJ[Ch,Op]$
(15) $\sim EJ[Ch,Po]$
(16) $\sim EJ[Ch,Te]$
(17) $\sim EJ[Ch,Ac]$
(18) $\sim EJ[Ch,Bo]$

(19) $\sim EJ[Gu,Nu]$
(20) $\sim EJ[Gu,Op]$
(21) $\sim EJ[Gu,Po]$
(22) $\sim EJ[Gu,Te]$
(23) $\sim EJ[Gu,Ac]$
(24) $\sim EJ[Gu,Bo]$

(25) $\sim EJ[Nu,Op]$
(26) $\sim EJ[Nu,Po]$
(27) $\sim EJ[Nu,Te]$
(28) $\sim EJ[Nu,Ac]$
(29) $\sim EJ[Nu,Bo]$

(30) $\sim EJ[Op,Po]$
(31) $\sim EJ[Op,Te]$
(32) $\sim EJ[Op,Ac]$
(33) $\sim EJ[Op,Bo]$

(34) $\sim EJ[Po,Te]$
(35) $\sim EJ[Po,Ac]$
(36) $\sim EJ[Po,Bo]$
(37) $\sim EJ[Te,Ac]$
(38) $\sim EJ[Te,Bo]$

(39) $\sim EJ[Ac,Bo]$

(40) $\sim SO[problem]$

The clause (1) simply expresses the fact that for any job in the problem, any out of the eight, the job is held by one of the four people. This can be understood by the form

$$\sim HJ[R,y] \wedge \sim HJ[T,y] \wedge \sim HJ[S,y] \longrightarrow HJ[P,y]$$

meaning that if the job y is not held by three of the persons, it must be held by the fourth one. Since the particular form of this clause can be manipulated into several different forms which all make the same statement, it applies to all four persons simultaneously. The elimination of six jobs for a person implies that the person holds the remaining two; this is encoded in the clauses (2-9). If a person does not hold job y1 and does not hold job y2 and does not hold ... job y6, then the person holds job y7 and job y8. In formal form this reads:

$$\sim HJ[x,y1] \wedge \sim HJ[x,y2] \wedge \ldots \wedge \sim HJ[x,y6] \quad \text{-->} \; HJ[x,y7]$$
$$\sim HJ[x,y1] \wedge \sim JH[x,y2] \wedge \ldots \wedge \sim HJ[x,y6] \quad \text{-->} \; HJ[x,y8]$$

If the implication sign -> is eliminated we find the disjunction of literals. Conceptually, the given steps must be repeated for all subsets of jobs from the set of eight. Since there are 28 such subsets, there would be 56 clauses. However careful inspection of the 56 clauses shows that only eight distinct clauses result - each clause appears seven times. The final eight clauses (2-9) are thus generated by simply omitting each time one from the set of eight, as indicate by the empty space. Clause (11) defines the HT-predicate. If a person holds a job y <u>and</u> a job z, <u>and if</u> the jobs y <u>and</u> z are not equal, <u>then</u> the person x holds the two jobs y and z.

The clauses (12-39) ascertain that all jobs are different, and clause (40) serves as a condition for the contradiction.

4. <u>Lion and Unicorn</u> [5]

This subsection serves to present a thinking problem which was cast in the entertaining form of a fairytale. We give the relevant excerpt:

> When Alice entered the forest of forgetfulness, she did not forget everything. She often forgot her name, and the most likely thing for her to forget was the day of the week. Now, the lion and the unicorn were frequent visitors to this forest. These are two strange creatures. The lion lies on Mondays, Tuesdays and Wednesdays, and tells the truth on the other days of the week. The unicorn, on the other hand, lies on Thursdays, Fridays and Saturdays, but tells the truth on the other days of the week. One day Alice met the lion and the unicorn resting under a tree. They both made the same statement: <u>Yesterday was one of my lying days</u>! From these two statements, Alice, who was a bright girl, was able to deduce the day of the week. What was it?

The solution of this problem is immediately seen by considering the Table 4.1 where we have indicated at which days the lion and the unicorn say the truth (T) and at which days their statements are not true (N). Since there is no day at which both animals lie (N-N) we have to look for the day where both say the truth (T-T). Sunday is such a day. However, since the statement of the lion does not fit with what is known, namely that he says the truth on Saturdays, we have to discard this possibility. We thus have to look for the combinations (N-T) and (T-N). By careful inspection we note that Thursday is the only day which fits the statements of the two animals.

Before we can fomulate this problem in the language of firstorder logic we must define the predicates, functions and constants. We identify the predicates (Prd) as:

MO[x] ... Prd: the day x is a Monday
TU[x] ... Prd: the day x is a Tuesday

SA[x] ... Prd: the day x is a Saturday
SO[x] ... Prd: the day x is a Sunday

M[x] ... Prd: x is a member of the set y.
L[x,y,z]...Prd: x says at day y that he lies at day z.

Similarly the meaning of the functions (Fct) and constants (Cst) is:

ld(t) ... Fct: lying-days of the animal t.
yd(x) ... Fct: yesterday day before the day x.
td ... Cst: today.
l,u ... Cst: lion, unicorn (animals).

We first axiomatize the week days by using the "common sense reasoning" that, for instance, Wednesdays and Fridays means not Saturdays and not Sundays etc. The axioms then read:

(1) MO[x] <--> ∼TU[x] V ∼ WE[x] V ... V ∼ SU[x]
(2) TU[x] <--> ∼WE[x] V ∼ TH[x] V ... V ∼ MO[x]
(3) WE[x] <--> ∼TH[x] V ∼ FR[x] V ... V ∼ TU[x]
(4) TH[x] <--> ∼FR[x] V ∼ SA[x] V ... V ∼ WE[x]
(5) FR[x] <--> ∼SA[x] V ∼ SU[x] V ... V ∼ TH[x]
(6) SA[x] <--> ∼SU[x] V ∼ MO[x] V ... V ∼ FR[x]
(7) SU[x] <--> ∼MO[x] V ∼ TU[x] V ... V ∼ SA[x]

The axioms for the function yd(x) (yesterday) read:

(8)	$MO[yd(x)] \leftrightarrow TU[x]$	(12)	$FR[yd(x)] \leftrightarrow SA[x]$
(9)	$TU[yd(x)] \leftrightarrow WE[x]$	(13)	$SA[yd(x)] \leftrightarrow SU[x]$
(10)	$WE[yd(x)] \leftrightarrow TH[x]$	(14)	$SU[yd(x)] \leftrightarrow MO[x]$
(11)	$TH[yd(x)] \leftrightarrow FR[x]$		

The axioms for the function ld(t) are:

(15) $M[x, ld(l)] \leftrightarrow MO[x] \vee TU[x] \vee WE[x]$
(16) $M[x, ld(u)] \leftrightarrow TH[x] \vee FR[x] \vee SA[x]$

The axioms for the predicate L[x,y,z] are:

(17) $\sim M[x,ld(t)] \wedge L[t,x,y] \rightarrow M[y,ld(t)]$
(18) $\sim M[x,ld(t)] \wedge \sim L[t,x,y] \rightarrow \sim M[y,ld(t)]$
(19) $M[x,ld(t)] \wedge L[t,x,y] \rightarrow \sim M[y,ld(t)]$
(20) $M[x,ld(t)] \wedge L[t,x,y] \rightarrow M[y,ld(t)]$

The statements of the lion and the unicorn are encoded as follows:

(21) $L[l,td,yd(td)]$
(22) $L[u,td,yd(td)]$
(23) $\sim TH[(td)]$

All what remains to be done is to convert the formulas (1)-(22) in clausal-form, adding the clauses MO[x], ..., SU[x], and also putting the negated conjecture as already shown in formula (23). This problem was successfully run by an existing ATP-system. Since the list of deduction steps is rather long we refrain from an exposition of the proof.

5. Truth-Teller (Knights) and Liars (Knaves) [6]

We consider in this sub-section a identification problem which shall illustrate in another way the process of gaining information from an ATP-system.

The problem stated in everyday language is as follows:

> On a certain island the inhabitants are partitioned into those who always tell the truth and those who always lie. You land on the island and meet three inhabitants: A, B, and C. You ask A: "Are you a truth-teller or a liar?". He mumbles something that you cannot make out. You ask B what A said. B replies: "A said he is a liar". C then volunteers: "Don't believe B, he's lying!"What can you tell about A, B and C?

Before we can formulate this problem in the language of an ATP-system, we have to introduce some functions (Fct):

```
      l(x) ...    Fct: x is a liar
      t(x) ...    Fct: x is a truth-teller
   sd(x,y) ...    Fct: person x said statement y.
```

We formulate the problem using a single predicate that is used to indicate that a given statement is true. TR[..] thus means that its argument is a true statement.

The ATP-program reads:

```
(1)   TR[t(x)] ∨   TR[l(x)]
(2)  ~TR[t(x)] ∨ ~ TR[l(x)]
(3)   TR[t(x)] ∧   TR[sd(x,y)]  -->  TR[y]
(4)   TR[l(x)] ∧   TR[sd(x,y)]  -->  TR[y]
(5)   TR[y]    ∧   TR[sd(x,y)]  -->  TR[t(x)]
(6)   TR[y]    ∧   TR[sd(x,y)]  -->  TR[l(x)]
(7)   TR[sd(B,sd(A,l(A)))]
(8)   TR[sd(C,l(B))]
```

The clause (1) expresses the fact that either statement t(x) is true or statement l(x) is true or that both are true. Clause (2) pins down that everyone is either a liar or a truth-teller, but not both. The meaning of the clauses (3-6) should be clear and the clauses (7-8) simply encode the event that took place.

In order to see how an ATP-system might solve this problem we apply its basic algorithm. We therefore place the axioms (1-6) in the general axiom list, and the last two in the set-of-support list. There are no demodulators for this problem.

Hyperresolution is the most useful inference rule. The weight of each clause is calculated by the number of symbols in its argument-list, excluding commas and parenthesis. Thus, the weight of clause (7) is 7 and the weight of clause (8) is 5 ('TR' counts as a single symbol).

We now follow the deduction procedures of the ATP-system:

```
[ 8+3+1]       => [ 9]   :   TR[l(B)] ∨ TR[l(C)]
[ 8+4+1+1]     => [10]   :   TR[t(C)] ∨ TR[t(B)]
[ 7+3+1]       => [11]   :   TR[sd(A,l(A))] ∨ TR[l(B)]
[10+3+7]       => [12]   :   TR[t(C)] ∨ TR[sd(A, l(A))]
[11+3+1]       => [13]   :   TR[l(B)] ∨ TR[l(A)]
[11+4+1]       => [14]   :   TR[l(B)] ∨ TR[t(A)]
[13+2+10]      => [15]   :   TR[l(A)] ∨ TR[t(C)]
[13+4+11+13]   => [16]   :   TR[l(B)]
[16+2+10]      => [17]   :   TR[t(C)]
```

From these clauses we thus can conclude that B is a liar and that C tells the truth. Do we know anything about A? The answer is no. One, in fact, could run the same program two more times - one denying that A is a liar, and one denying that A is a truth-teller. In either case a proof could be obtained, so that *nothing* can be concluded about what A said.

The above presentation of the derivation chain is only an extraction of the actual computer-run since all the generated clauses, which were subsumed by earlier clauses, were left aside. Thus, a more complete account of the above derivation is:

```
[8+3+1]        => [ 9] : W=7
[8+4+1]        => [10] : W=7
[8+5+1]        => sub 10
[8+6]          => sub  9

[7+3+1]        => [11] : W=9
[7+6]          => sub 11

[9+2+1]        => sub  9
[9+4+1]        => sub  1
[9+4+9]        => sub  9
[9+5+8]        => sub  1
[9+2+1]        => sub  9
[9+4+8]        => sub  1
[9+4+8+9]      => sub  9

[10+2+1]       => sub 10
[10+2+9]       => sub  1
[10+3+8]       => sub  1
[10+2+1]       => sub 10
[10+2+9]       => sub  1
[10+3+7]       => [12] : W=9

[11+3+1]       => [13] : W=7
[11+4+1+1]     => [14] : W=6
[11+4+1+7]     => sub  1
[11+4+9+7]     => sub  9
[11+4+11+7]    => sub 11
[11+5+1]       => sub 14
[11+6]         => sub 13
[11+5+7]       => sub  1
[11+2+1]       => sub 11
[11+2+10]      => sub 12
[11+4+7+11]    => sub 11
[11+4+1+8]     => sub 12
[11+4+9+8]     => sub 11
[11+5+8]       => sub 12

[13+2+1]       => sub
[13+2+10]      => [15] : W=7
[13+4+7+11]    => sub 13
[13+4+1+8]     => sub 15
[13+4+9+8]     => sub 13
[13+5+8]       => sub 15
[13+2+1]       => sub 13
[13+4+11+1]    => sub 14
[13+4+11+13]   => [16] : sub(9,11,13,14)

[16+2+1]       => sub 16
[16+2+10]      => [17] : sub (10,12,15)
[16+5+8]       => sub 17

[17+2+1]       => sub 17
[17+3+8]       => sub 17
```

In this section we discuss a second, similar thinking problem which is considered "a hard nut to crack, even for advanced logic hackers"[6]. The problem is cast in the form of a little story:

> The only inhabitants of an island are either 'knights' which always tell the truth or are 'knaves' which always lie. Both are either rich or poor. A man of this island falls in love with a girl and wishes to marry her. The girl however wants to marry only a rich 'knave'. Suppose the man is indeed a rich 'knave'. How can he convince her in one statement that he fullfills her conditions. What should he say?

The solution is obvious. The man should say: *I am a poor knave*. Then the girl can deduce that he is a 'knave', because no 'knight'can say that he is a 'knave', and because he can't have said the truth, he must be a rich 'knave'.

The formulation of this problem in first-order logic is rather difficult due to a number of inherent complications which we will discuss later. Nevertheless we notice that we don't have the classical ATP-situation of proving the correctness of a theorem, but we require to construct a solution. This can be achieved by formulating the problem in such a way that we are interested in the instantiation of a variable which is existentially quantified when the axioms and the conjecture are formulated.

We first define the predicates (Prd):

SA[x,y]	...	Prd: x says y.
TR[x,u]	...	Prd: x is true (u is an open parameter)

and functions (Fct) plus constants (Cst):

k(x), h(x)	...	Fct: x is a knight, knave
p(x), r(x)	...	Fct: x is poor, rich
and(x,y)	...	Fct: logical conjunction
or(x,y)	...	Fct: logical disjunction
a	...	Cst: man who wants to marry the girl.

The axioms of the problem then read:

(1) $(\forall x,u)$ $TR[k(x),u] \longleftrightarrow \sim TR[h(x),u]$
(2) $(\forall x,u)$ $TR[r(x),u] \longleftrightarrow \sim TR[p(x),u]$
(3) $(\forall x,y,u)$ $TR[k(x),u] \longrightarrow \{ SA[x,y] \longleftrightarrow TR[y,u] \}$
(4) $(\forall x,y,u)$ $TR[h(x),u] \longrightarrow \{ SA[x,y] \longleftrightarrow \sim TR[y,u] \}$
(5) $(\forall x,y,u)$ $TR[and(x,y),u] \longleftrightarrow TR[x,u] \wedge TR[y,u]$

and the conjectu e is given the form:

(6) $(\exists x)$ SA[a,x] <--> TR[and(ka,ra),x]

Note, in the above formula we have introduced the simplifying notation: h(a) ha, which we also will use lateron.
Let us comment on the formulas (1)-(6) where the theorem (6) is the most difficult part. First-order logic has limitations which become transparent in this example: (i) it is not really constructive, usually one proves the correctness of a possible solution for a problem; (ii) quantification is allowed only over individuals, not over functions, predicates and formulas; (iii) an implication is true even if the premise is false. A remedy for (i) has been indicated earlier - we simply introduce an existentially quantified variable and let the deduction mechanism determine its value. The remedy for (ii) consists in the introduction of a predicate TR[x] (which means "it is true that ..."; and the redefinition of all predicates and logical connectives as Boolean <u>functions</u>: k(x), h(x), p(x), r(x), and(x,y), or(x,y), whereby the action of the latter two Boolean 'operators' has to be axiomatized explicitly. As a result of (iii), the formulation of the theorem (6) poses problems. Using the implication-sign instead of the equivalence-sign leads, after a few deduction steps, to the conclusion that nobody can say that he is a 'knave': SA[z, k(z)] . The equivalence-sign is still not enough, the reason being that the variable x appears only on the left-hand side of (6). Thus generalizing TR[x,u] such that it has two arguments, as it would be for instance in relevance logic, leads to the expected result. The meaning of (6) is as follows: "There exists a statement x from the man (named 'a') which shall be equivalent to the fact that he really is a rich 'knave'".

Putting the 'axioms' and the negated 'conjecture' in conjunctive normalform leads to the following set of clauses:

(1) : $\sim$TR[k(x),y] $\vee$ $\sim$ TR[h(x),y]
(2) : TR[k(x),y] $\vee$ TR[h(x),y]
(3) : $\sim$TR[r(x),y] $\vee$ $\sim$ TR[p(x),y]
(4) : TR[r(x),y] $\vee$ TR[p(x),y]
(5) : $\sim$TR[k(x),z] $\vee$ $\sim$ SA[x,y] $\vee$ TR[y,z]
(6) : $\sim$TR[k(x),z] $\vee$ SA[x,y] $\vee$ $\sim$ TR[y,z]
(7) : $\sim$TR[k(x),z] $\vee$ $\sim$ SA[x,y] $\vee$ $\sim$ TR[y,z]
(8) : $\sim$TR[k(x),z] $\vee$ SA[x,y] $\vee$ TR[y,z]
(9) : $\sim$TR[and(x,y),z] $\vee$ TR[x,z]
(10) : $\sim$TR[and(x,y),z] $\vee$ TR[y,z]
(11) : TR[and(x,y),z] $\vee$ $\sim$ TR[x,z] $\vee$ $\sim$ TR[y,z]
(12) : $\sim$ SA[a,x] $\vee$ $\sim$ TR[and(ka,ra),x]
(13) : SA[a,x] $\vee$ TR[and(ka,ra),x]

The proof steps are as follows:

```
[13;2]+[ 9;1] => [14] :  SA[a,x] v   TR[ka,x]
[13;2]+[10;2] => [15] :  SA[a,x] v   TR[ra,x]
[15;2]+[ 3;1] => [16] :  SA[a,x] v ~ TR[pa,x]
[16;2]+[10;2] => [17] :  SA[a,x] v ~ TR[and(z,pa),x]
[ 8;1]+[14;2] => [18] :  SA[a,x] v TR[y,x] v SA[a,y]
[18;2]+[17;2] => [19] :  SA[a,x] v SA[a,and(z,pa)]
[19]  + Fac   => [20] :  SA[a,and(z,pa)]             x <-- and(z,pa)
[20;1]+[ 5;2] => [21] : ~TR[ka,x] v TR[and(z,pa),x]
[21;1]+[ 2;1] => [22] :  TR[ka,x] v TR[and(z,pa),x]
[22;2]+[ 9;1] => [23] :  TR[ka,x] v TR[z,x]
[23]  + Fac   => [24] :  TR[ka,x]                          z <--  ka
[24;1]+[ 7;1] => [25] : ~SA[a,x] v ~ TR[x,y]
[25;1]+[20;1] => [26] : ~TR[and(z,pa),y]
[11;1]+[26;1] => [27] : ~TR[z,y] v ~ TR[pa,y]
[27;1]+[24;1] => [28] : ~TR[pa,y]                          z <--  ka
[ 4;2]+[28;1] => [29] :  TR[ra,y]
[11;3]+[29;1] => [30] :  TR[and(z,ra), x] v~TR[z,x]
[30;2]+[24;1] => [31] :  TR[and(ka,ra),x]
[31;1]+[12;2] => [32] : ~SA[a,x]
[32;1]+[20;1] => [33]    □                           x <-- and(z,pa)
```

6. Schubert's Steamroller [8-11]

In this section we present a problem which merits attention because it can be combinatorially very difficult. It also illustrates the danger of using natural language for a problem description, since, as is demonstrated in the following example, it can give rise to ambiguities.

In 1978, L. Schubert presented the following problem (which came to be known as Schubert's Steamroller) as a challenge to the existing ATP-systems. The problem, described in natural language, is as follows:

> Wolves, foxes, birds, caterpillars, and snails are animals, and there are some of each of them. Also there are some grains, and grains are plants. Every animal either likes to eat all plants or all animals much smaller than itself that like to eat some plants. Caterpillars and snails are much smaller than birds, which are much smaller than foxes, which in turn are much smaller thant wolves. Wolves do not like to eat foxes or grains, while birds like to eat caterpillars but not snails. Caterpillars and snails like to eat some plants. Therefore there is an animal that likes to eat a grain-eating animal.
> Is this true?

Before we can cast this problem in the formal form of first-order predicate logic we have to define the needed predicates:

A[x]	... x is an animal	G[x]	... x is a grain
B[x]	... x is a bird	P[x]	... x is a plant
C[x]	... x is a caterpillar	S[x]	... x is a snail
F[x]	... x is a fox	W[x]	... x is a wolf
E[x,y]	... x likes to eat y	M[x,y]	... x is much smaller than y.

We now give the formal form of the axiom- and the conjecture-clauses and subsequently explain how they are derived:

(1):	$\sim W[x] \vee A[x]$	(6):	$W[w]$
(2):	$\sim F[x] \vee A[x]$	(7):	$F[f]$
(3):	$\sim B[x] \vee A[x]$	(8):	$B[b]$
(4):	$\sim C[x] \vee A[x]$	(9):	$C[c]$
(5):	$\sim S[x] \vee A[x]$	(10):	$S[s]$
		(11):	$G[g]$

(12): $\sim G[x] \vee P[x]$

(13): $\sim A[x] \vee \sim P[y] \vee \sim A[z] \vee \sim P[v] \vee E[x,y] \vee \sim M[z,x] \vee \sim E[z,v] \vee$
$E[x,z]$

(14): $\sim C[x] \vee \sim B[y] \vee M[x,y]$
(15): $\sim S[x] \vee \sim B[y] \vee M[x,y]$
(16): $\sim B[x] \vee \sim F[y] \vee M[x,y]$
(17): $\sim F[x] \vee \sim W[y] \vee M[x,y]$
(18): $\sim W[x] \vee \sim F[y] \vee \sim E[x,y]$
(19): $\sim W[x] \vee \sim G[y] \vee \sim E[x,y]$
(20): $\sim B[x] \vee \sim C[y] \vee E[x,y]$
(21): $\sim B[x] \vee \sim S[y] \vee \sim E[x.$

(22): $\sim C[x] \vee P[h(x)]$
(23): $\sim C[x] \vee E[x,h(x)]$
(24): $\sim S[x] \vee P[i(x)]$
(25): $\sim S[x] \vee E[x,i(x)]$

(26): $\sim A[x] \vee \sim A[y] \vee \sim G[z] \vee \sim E[x,y] \vee \sim E[y,z]$

where (x,y,z,v) are variables, (w,f,b,c,s,g) are Skolem-constants and h(x), i(x) are Skolem-functions. The formulas (1)-(25) constitute the set of 'axioms' and the formula (26) is the 'conjecture'.

We indicate their origin by showing how the sentences of the problem are encoded by formulas in first-order predicate logic. Lateron these formulas are converted to normal clause form by using the (equivalent) calculation rules and the Skolemization trick:

Sentence-1: Clauses (6)-(11) and (1)-(5)

$$(\exists w,f,b,c,s,g) \quad W[w] \wedge P[f] \wedge B[b] \wedge C[c] \wedge S[s] \wedge G[g]$$
$$(\forall x) \quad W[x] \vee P[x] \vee B[x] \vee C[x] \vee S[x] \longrightarrow A[x]$$

Sentence-2: Clause (12)

$$(\forall x) \quad G[x] \longrightarrow P[x]$$

Sentence-3: Clause (13)

$$(\forall x) \quad A[x] \longrightarrow (\forall y) \{ P[y] \longrightarrow E[x,y] \} \vee$$
$$(\forall y) \{ (A[y] \wedge M[y,z] \wedge (\exists z)(P[z] \wedge E[y,z])) \longrightarrow E[x,y] \}$$

Sentence-4: Clause (14)-(17)

$$(\forall x,y) \quad \{C[x] \vee S[x]\} \wedge B[y] \longrightarrow M[x,y]$$
$$(\forall x,y) \quad \{B[x] \wedge P[y]\} \longrightarrow M[x,y]$$
$$(\forall x,y) \quad \{F[x] \wedge W[y]\} \longrightarrow M[x,y]$$

Sentence-5: Clause (18)-(21)

$$(\forall x,y) \quad \{P[x] \vee G[x]\} \wedge W[y] \longrightarrow E[y,x]$$
$$(\forall x,y) \quad \{B[x] \wedge C[y]\} \longrightarrow E[x,y]$$
$$(\forall x,y) \quad \{B[x] \wedge S[y]\} \longrightarrow E[x,y]$$

Sentence-6: Clause (22)-(25)

$$(\forall x) \quad \{C[x] \vee S[x]\} \longrightarrow (\exists y) \{P[y] \wedge E[x,y]\}$$

The conjecture (26) follows from the expression:

$$(\exists x,y) \left\{ A[x] \wedge A[y] \wedge \left[E[x,y] \wedge (\exists z) \left(G[z] \wedge E[y,z] \right) \right] \right\}$$

which encodes the statement: "Therefore there is an animal ... ". There is a slight interpretation ambiguity which stems from the expression: "grain-eating animal". In the above form we have used it in the sense: an animal that eats some grain. Alternatively it may be construed to mean: an animal that eats every grain, so that the conclusion is interpreted as:

$$(\exists x,y)\Big\{A[x]\wedge A[y]\wedge\Big[E[x,y]\wedge(\forall z)\ \big[G[z]\longrightarrow E[y,z]\big]\Big]\ \Big\}$$

Unfortunately matters are not so simple as they may appear since there is a third interpretation given by the expression:

$$(\exists x,y)\Big\{A[x]\wedge A[y]\wedge(\forall z)\ \Big[G[z]\longrightarrow\big[E[x,y]\wedge E[y,z]\big]\Big]\ \Big\}$$

Although all three versions have been dealt with in the literature, we will limit ourselves to the one given by the conjecture (26).

The derivation of the contradiction proof via an ATP-system is quite long. We therefore refrain from pursueing this example any further and refer the interested reader to the specialized literature.

7. School Boys [7]

We present in this section a thinking problem which can be solved within the propositional logic if the appropriate propositions are defined.

The problem is cast in the following little story:

> All the boys, in a certain school, sit together in one large room every evening. They are of no less than five nationalities - English, Scotch, Welsh, Irish and German. One of the Monitors is very observant and takes notes of everything that happens. The following are some of his notes:
>
> (1) Whenever some of the English boys are singing 'Rule, Britannia', and some not, some of the Monitors are wide awake;
>
> (2) Whenever some of the Scotch are dancing reels, and some of the Irish fighting, some of the Welsh are eating toasted cheese;
>
> (3) Whenever all the Germans are playing chess, some of the Eleven are not oiling their bats;
>
> (4) Whenever some of the Monitors are asleep, and some not, some of the Irish are fighting;
>
> (5) Whenever some of the Germans are playing chess, and none of the Scotch are dancing reels, some of the Welsh are not eating toasted Cheese;

(6) Whenever some of the Scotch are not dancing reels, and some of the Irish are not fighting, some of the Germans are playing chess;

(7) Whenever some of the Monitors are awake, and some of the Welsh are eating toasted cheese, none of the Scotch are dancing reels;

(8) Whenever some of the Germans are not playing chess, and some of the Welsh are not eating toasted cheese, some of the Irish are fighting;

(9) Whenever all the English are singing 'Rule, Britannia', and some of the Scotch are not dancing reels, none of the Germans are playing chess;

(10) Whenever some of the English are singing 'Rule, Britannia', and some of the Monitors are asleep, some of the Irish are not fighting;

(11) Whenever some of the Monitors are awake, and some of the Eleven are not oiling their bats, some of the Scotch are dancing reels;

(12) Whenever some of the English are singing 'Rule, Britannia', and some of the Scotch are not dancing reels, ...

Here, the Monitor's notes break off suddenly. The problem is to complete the sentence, if possible.

We refrain here from giving the solution of this problem in order to let the alerted reader to find it himself.
One comes closer to the computer solution by defining the following propositions:

E	... some English sing.	$\bar{E}$	... some English sing <u>not</u>.
S	... some Scotch dance.	$\bar{S}$	... some Scotch dance <u>not</u>.
I	... some Irish fight.	$\bar{I}$	... some Irish fight <u>not</u>.
W	... some Welsh eat.	$\bar{W}$	... some Welsh eat <u>not</u>.
G	... some Germans play.	$\bar{G}$	... some Germans play <u>not</u>.
M	... some Monitors are awake.	$\bar{M}$	... some Monitors are <u>not</u> awake.
O	... some of the Eleven are oiling their bats.	$\bar{O}$	... some of the Eleven are <u>not</u> oiling their bats.

With these propositions the above statements (1)-(12) are cast in the following formal form:

(1)	$E \wedge \bar{E} \dashrightarrow M$		(11)	$M \wedge \bar{O} \dashrightarrow S$
(2)	$S \wedge I \dashrightarrow W$		(12)	$E \wedge \bar{E}$
(3)	$G \dashrightarrow \bar{G} \vee \bar{O}$		(13)	$M \wedge \bar{M}$
(4)	$M \wedge \bar{M} \dashrightarrow I$		(14)	$S \wedge \bar{S}$
(5)	$G \dashrightarrow S \vee \bar{W}$		(15)	$I \wedge \bar{I}$
(6)	$\bar{S} \wedge \bar{I} \dashrightarrow G$		(16)	$W \wedge \bar{W}$
(7)	$M \wedge W \dashrightarrow \sim\bar{S}$		(17)	$G \wedge \bar{G}$
(8)	$\bar{G} \wedge \bar{W} \dashrightarrow \sim I$		(18)	E
(9)	$E \wedge \bar{S} \wedge G \dashrightarrow \bar{E}$		(19)	$\bar{S}$
(10)	$E \wedge \bar{M} \dashrightarrow \bar{I}$			

The derivation chain of an ATP-system now is as follows:

[18] + [1]	=>	[20]	:	$\bar{E} \dashrightarrow M$	
[18] + [9]	=>	[21]	:	$\bar{S} \wedge G \dashrightarrow \bar{E}$	
[18] + [10]	=>	[22]	:	$\bar{M} \dashrightarrow \bar{I}$	
[19] + [6]	=>	[23]	:	$\bar{I} \dashrightarrow G$	
[17] + [3]	=>	[24]	:	$\bar{G} \vee \bar{O}$	
[22] + [13]	=>	[27]	:	$\bar{I} \vee M$	
[27] + [23]	=>	[31]	:	$M \vee G$	
[21]+[19]+[31]	=>	[38]	:	$\bar{E} \vee M$	
[38] + [20]	=>	[43]	:	M	<--
[43]+[11]+[24]	=>	[44]	:	$S \vee \bar{G}$	
[43] + [4]	=>	[45]	:	$\bar{M} \dashrightarrow I$	
[43] + [7]	=>	[46]	:	$\sim W \vee \sim S$	
[23] + [22]	=>	[57]	:	$\bar{M} \dashrightarrow G$	
[46] + [2]	=>	[68]	:	$\sim S \vee \sim I$	
[46] + [16]	=>	[69]	:	$S \dashrightarrow \bar{W}$	
[68] + [44]	=>	[80]	:	$I \dashrightarrow \bar{G}$	
[69] + [5]	=>	[83]	:	$G \dashrightarrow \bar{W}$	
[80] + [8]	=>	[90]	:	$\sim I \vee \sim \bar{W}$	
[83] + [57]	=>	[93]	:	$M \dashrightarrow \bar{W}$	
[90] + [45]	=>	[97]	:	$\sim \bar{W} \vee \sim \bar{M}$	
[97] + [93]	=>	[106]	:	$\sim \bar{M}$	<--

Looking at proposition (43), one of the conclusions is: $M \equiv$ "<u>some</u> Monitors are awake". Looking at the proposition (106) we realize that we can make a stronger statement. Since : $\bar{M} \equiv$ "<u>some</u> Monitors are not awake", its negation $\sim \bar{M}$ says : "no Monitors are not awake", which means that <u>all</u> Monitors are asleep. Doubtless, this is a stronger statement than the earlier one. Note that the propositions (12),(14) and (15) were not needed.

8. Salt and Mustard [7]

In this section we consider the 'Salt and Mustard Problem' which comes from Lewis Carroll [13]. It is substantially harder than the preceding problem, and it has an interesting history as described in the indicated reference.

The problem is as follows:

> Five friends, Barry, Cole, Dix, Land and Mill, agreed to meet every day at a certain hotel-table. They devised the following rules, to be observed whenever beef appeared on the table:

(1) If Barry takes salt, then either Cole or Lang takes one only of the two condiments, salt and mustard: if he takes mustard, then either Dix takes neither condiment, or Mill takes both.

(2) If Cole takes salt, then either Barry takes only one condiment, or Mill takes neither: if he takes mustard, then either Dix or Lang takes both.

(3) If Dix takes salt, then either Barry takes neither condiment or Cole takes both: if he takes mustard, then either Lang or Mill takes neither.

(4) If Land takes salt, then either Barry or Dix takes only one condiment: if he takes mustard, then either Cole or Mill takes neither.

(5) If Mill takes salt, then either Barry or Lang takes both condiments: if he takes mustard, then either Cole or Dix takes only one.

The problem is to discover whether these rules are compatible; and, if so, what arrangements are possible.

In this problem several assumptions are implicit which we here would like to specify:

(i) 'If Barry takes salt' can have two meanings: (1) 'He takes salt only'; (2) 'He takes both condiments'. And so with all similar phrases.

(ii) 'Either Cole or Lang takes one only of two condiments' allows for three possible meanings: (1) 'Cole takes one only, Lang takes both or neither'; (2) 'Cole takes both or neither, Lang takes one only'; (3) 'Cole takes one only, Lang takes one only'. And so with all similar phrases.

(iii) Every rule is understood as implying the words 'and vice verse'. Thus the first rule would imply the addition: 'and, if either Cole or Lang takes only one condiment, then Barry takes salt'.

In order to formulate this problem in the first-order predicate logic, we introduce the following predicates (Prd):

B[x] ... Prd: x takes both salt and mustard.
N[x] ... Prd: x takes neither salt nor mustard.
O[x] ... Prd: x takes exactly one of salt and mustard.
S[x] ... Prd: x takes salt.
M[x] ... Prd: x takes mustard.

The constants of the problem are:

b = Barry, c = Cole, d = Dix, l = Lang, m = Mill.

The axioms of the problem are given by the following list of logical expressions:

Exactly one holds: B[x] or N[x] or O[x] :

(1) :	$B[x] \vee N[x] \vee O[x]$
(2) :	$O[x] \longrightarrow \sim B[x]$
(3) :	$O[x] \longrightarrow \sim N[x]$
(4) :	$B[x] \longrightarrow \sim N[x]$

Definition of O[x] :

(5) :	$O[x] \longrightarrow S[x] \vee M[x]$
(6) :	$O[x] \longrightarrow \sim S[x] \vee \sim M[x]$

Definition of N[x] :

(7) :	$N[x] \longrightarrow \sim S[x]$
(8) :	$N[x] \longrightarrow \sim M[x]$
(9) :	$\sim S[x] \vee \sim M[x] \longrightarrow N[x]$

Defintion of B[x] :

(10):	$B[x] \longrightarrow S[x]$
(11):	$B[x] \longrightarrow M[x]$
(12):	$\sim S[x] \vee \sim M[x] \longrightarrow B[x]$

Clauses of Rule-(1):

(13):	$S[b] \longrightarrow O[c] \vee O[1]$
(14):	$M[b] \longrightarrow N[d] \vee B[m]$
(15):	$O[c] \longrightarrow S[b]$
(16):	$O[1] \longrightarrow S[b]$
(17):	$N[d] \longrightarrow M[b]$
(18):	$B[m] \longrightarrow M[b]$

Clauses of Rule-(2):

(19):	$S[c] \longrightarrow O[b] \vee N[m]$
(20):	$M[c] \longrightarrow B[d] \vee B[1]$
(21):	$O[b] \longrightarrow S[c]$
(22):	$N[m] \longrightarrow S[c]$
(23):	$B[d] \longrightarrow M[c]$
(24):	$B[1] \longrightarrow M[c]$

Clauses of Rule-(3):

(25):	$S[d] \longrightarrow N[b] \vee B[c]$
(26):	$M[d] \longrightarrow N[1] \vee N[m]$
(27):	$N[b] \longrightarrow S[d]$
(28):	$B[c] \longrightarrow S[d]$
(29):	$N[1] \longrightarrow M[d]$
(30):	$N[m] \longrightarrow M[d]$

Clauses of Rule-(4):

```
(31):  S[l]   -->  O[b] ∨ O[d]
(32):  M[l]   -->  N[c] ∨ N[m]
(33):  O[b]   -->  S[l]
(34):  O[d]   -->  S[l]
(35):  N[c]   -->  M[l]
(36):  N[m]   -->  M[l]
```

Clauses of Rule-(5):

```
(37):  S[m]   -->  B[b] ∨ B[l]
(38):  M[m]   -->  O[c] ∨ O[d]
(39):  B[b]   -->  S[m]
(40):  B[l]   -->  M[m]
(41):  O[c]   -->  M[m]
(42):  O[d]   -->  M[m]
```

The derivation chain of the new clauses is very long. We therefore refrain from giving the complete list of derived clauses and limit ourselves to a few examples plus the complete list of the relevant ones:

```
[17] + [1] => [43]   :   M[b] ∨ B[d] ∨ O[d]
[29] + [1] => [49]   :   M[d] ∨ B[l] ∨ O[l]
```

=> [316]	: S[b]	=> [611]	: ∼O[b]
=> [319]	: ∼N[b]	=> [612]	: ∼M[c]
=> [509]	: O[l]	=> [613]	: ∼B[c]
=> [510]	: ∼B[l]	=> [615]	: ∼N[m]
=> [511]	: ∼N[l]	=> [627]	: ∼S[c]
=> [600]	: N[d]	=> [629]	: N[c]
=> [601]	: B[b]	=> [631]	: M[l]
=> [604]	: ∼O[d]	=> [632]	: ∼O[c]
=> [605]	: ∼B[d]	=> [635]	: ∼S[l]
=> [606]	: ∼S[d]	=> [640]	: ∼M[m]
=> [607]	: ∼M[d]		
=> [608]	: S[m]		

Putting the derived clauses for the five persons separately, we find:

<u>Barry:</u>	B[b],		∼N[b],	∼O[b],	S[b]
<u>Cole :</u>	∼B[c],	∼M[c],	N[c],	∼O[c],	∼S[c]
<u>Dix :</u>	∼B[d],	∼M[d],	N[d],	∼O[d],	∼S[d]
<u>Land :</u>	∼B[l],	M[l],	∼N[d],	O[l],	∼S[l]
<u>Mill :</u>		∼M[m],	∼N[m],		S[m]

These derived unit clauses allow us to conclude:

Dix and Cole take neither salt nor mustard,
Barry takes both,
Lang takes mustard but not salt,
Mill takes salt but not mustard.

This hard problem illustrates how the fact that a clause set in non-Horn makes working with it difficult. Note that the first unit clause is not derived until fairly late in the run, and then there is another long wait for the second one. In the course of the run, more than 32'000 clauses were generated and then subsumed. The formulation given here may not be the most optimal one, but it has the advantage of being a very straightforward translation of the problem.

9. Tiles plus Hole

We consider in this section the 'Tiles plus Hole' game which consists of a scrambled set of 15 numbered tiles plus one hole within a four-by-four tray:

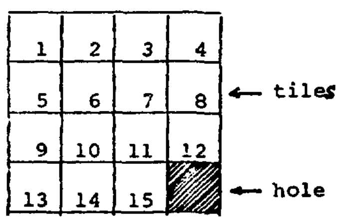

You are allowed to slide the tiles, up, down, left, or right, with the goal of putting them eventually in order.

To submit this type of problem to an ARP, the starting configuration must be represented and the possible moves of the hole must be defined, since moving a tile in effect moves the hole. Finally, a means is needed for the ATP-system to know when the problem has been solved.

Before we give the clauses of this problem we define the needed predicates (Prd) and functions (Fct) and we also make use of the earlier defined list-function:

```
  li(α, β, ..., ε,*)    ≡ { α,{ β ,    ... {ε,*} } ... }
  n(x)                  .... Fct: characterizes the tile x(number).
  h                     .... Cst: hole.
  * ≡ end               .... Cst: 'end-of-list','end-of-line'.
ST[...]                 .... Prd: state of tray with tiles-list.
EQ[...]                 .... Prd: equality-demodulator.
ST1[α ,β ,...,*]         =   ST[li( α , β ,...,*)]
EQ1[ (..),(..)]          =   EQ[li(..), li(..)]
```

Note, for simplicity of notation we again use the convention to drop the li-function in the argument list of the predicates and add a '1' at the end of the predicate name: ST -> ST1, etc.

We are now in the position to state the clauses and subsequently explain their meaning:

```
(1)    ST1[ n( 1), n( 6), n( 2), n( 4), *,
            n( 5), h,     n( 3), n( 8), *,
            n( 9), n(10), n( 7), n(11), *,
            n(13), n(14), n(15), n(12), * ]

(2)    ST1[ n( 1), n( 2), n( 3), n( 4), *,
            n( 5), n( 6), n( 7), n( 8), *,
            n( 9), n(10), n(11), n(12), *,
            n(13), n(14), n(15), h,     * ]

(3)    EQ1[ (h, n(x), y) , (n(x), h, y) ]

(4)    EQ1[ (h,x,y,z,u,n(w),v), (n(w),x,y,z,u,h,v) ]
```

*The clause (1) defines the initial state of the tray by gi*ving the position of all tiles on the tray in the form of a list whereby the end of the lines are marked by the *-symbol, meaning 'end-of-line'. The function n(x) introduces the tile number at that particular position on the tray. Thus the tray position is fixed by the position on the list whereas its content (meaning the tile number) is given by the argument of n(..) . The end of the list is again indicated by the *. The clause (2) determines the state one would like to reach. Note the negation sign which allows for a contradiction proof. The clauses (3) and (4) are demodulators which describe the sidewise displacement of the hole (clause(3)) and its up-down movement (clause(4)). This latter movement follows from an interchange of the first and (the following) fifth position in the list; remember that the * ('end-of-line') also takes a position in the list!

Sofar, the discussion has been in terms of moves that interchange the hole with a tile. However there are more complex moves, such as the diagonal move, which changes the position of the hole and that of two tiles; the hole could be moved up and to the right with the corresponding tile-movements, of course. The program can in fact develop such a clause on its own by applying paramodulation on the clauses (3-4). To see what happens, we first rename the variables in clause (3):

(3) EQ1[(h,n(x7), x8),(n(x7),h,x8)]

(4) EQ1[(h,x,y,z,u,n(v),w),(n(v),x,y,z,u,h,w)]

In clause (4) we seek the variable replacement which causes the first argument of clause (3) and the first argument of clause (4) to become identical. The unification succeeds when x is replaced by n(x7), and x8 by (y,z,u,n(v),w). Next we make this variable replacement uniformely in clauses (3-4), getting temporarily clauses (3a) and (4a). Then we substitute the second argument of clause (3a) for the first argument of (4a), and after renaming the variable x7 to x we obtain the form

(5) EQ1[(n(x),h,y,z,u,n(v),w),(n(v),n(x),y,z,u,h,w)]

If paramodulation is applied to this last clause and any ST1-clause, the attempt will either fail because there is not diagonal move possible, or it will produce a new ST1-clause.

10. Checkerboard

We consider in this section a thinking problem which has a simple, well-known solution. Nevertheless the solution of this checkerboard problem, as we present it to an ATP-system allows for the treatment of similar or related problems whereby the solution can no longer be given by a simple thinking-trick. The most simple version of the 'Checkerboard Problem' reads:

There is a squared checkerboard of: 8x8 = 64 fields whereby its upper left and lower right squares have been removed as shown by the figure below:

<u>Modified Checkerboard:</u>

with missing squares

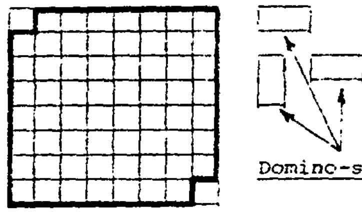

Domino-stones

There is a set of domino-stones of size: one-by-two units. Can the modified checkerboard be fully covered by these domino-stones?

This thinking problem can be considered as an abstraction and/or simplification of a problem of pratical value. We can think of the selling of land in portion of squares, or the optimal arrangement of furnitures in a room, or the optimal layout of pipes, or of laying out a circuit with the constraint of not having wires cross, and the like.

There exists a simple solution of the above thinking problem which we would like to mention before going to the formulation of a more general solution path with an ATP-system. Imagine the checkerboard consists of white and non-adjacent black squares. Before removing the top-left and bottom-right white squares there are 32 white and 32 black squares on the checkerboard. Each domino-stone placed on the checkerboard covers one white and one black square. If the top-left and bottom-right (white) squares are removed there is an imbalance between the number of white and black squares, and consequently the checkerboard can no longer be fully covered by the domino-stones.

The above thinking-trick is quite nice for the particular problem; it however is not of general value. Had we removed one black and one white square, or had we removed ten squares the argument could no longer be applied. We therefore present now a more general way of solving this problem by an ATP-system.

We define the AC-predicate, AC for "achievable", with essentially two arguments. The first one gives the number of the row under consideration, whereas the second one is a list of the status of each square in that row: the symbols r=removed, n=not_covered and c=covered indicate their status. For instance:

AC[row(1), sq(r,n,n,n,n,n,c,c)]

represents the state of the checkerboard where row 1 has its first square removed, and the last two squares are covered by a domino-stone. Note that the functions: row( ) and sq( ) were introduced for convenience. For clearness of presentation we drop the first one, but keep in mind that the first AC argument gives the row-number.

Notice that the particular arrangement of the domino-stones does not matter; they thus can be placed horizontally and vertically. If we now were to consider all possible sequences of plays, the program would be forced to examine more than six trillion sequences. By choosing an order in which to play the domino-stones, and also by ignoring dublicate paths to the same particular covering, fewer than 500 partial coverings result. In order to illustrate our notion of 'dublicate paths' we show in Fig. 10.1 two possible ways of covering rows 1 and 2 (with other coverings being possible) which are considered as equivalent. The important points for the two (and all other) different ways of placing the domino-stones are, that square 1 in row 1 has not been touched (because it was removed) and that square 1 of row 2 still needs to be covered.

In the placing of the domino-stones, we will have the ATP-program observe a few simplifying rules:

1) The program shall start placing domino-stones at the top of the checkerboard with row 1 where the left-most square has been removed.

2) A row will not be left until all of its available squares have been covered.

3) All horizontal plays that the program wishes to make must precede any vertical play.

4) When a vertical play is made, all the remaining squares (in a row) are also covered, and this simultaneously, by vertical plays.

As a result, this latter rule 4) allows domino-stones to be placed vertically, and consequently to cover squares in the next row. It, however, does not allow, for example, a domino-stone to be placed horizontally in a row unless all of the previous rows had their available squares covered. The rule 4) is obeyed by, for example, playing domino-stones horizontally in a row as far as possible, and then playing vertically into the next row. The above set of rules leads, for any newly derived AC-clause, to implications.

AC[2, sq(n,n,n,n,n,c,c,c)], for instance, implies that all squares of row 1 are covered. It also implies that no square of the rows 3-8 has yet been covered. This last implication follows from the requirement of making all vertical plays, that affect a row, simultaneously. The above AC-clause can be achieved by placing in row 1 the domino-stones first horizontally to cover the squares 2-7, and placing subsequently a domino-stone vertically to cover the eighth square of the rows 1 and 2, and finally placing in row 2 a domino-stone horizontally to cover the squares 6-7. According to the above rules 1)-4) the clause: AC[2, sq(c,c,n,n,n,n,n,n)] can not be generated. If it were, it would imply that the seven squares of row 1 are covered and that row 3 would be completely uncovered. This can not happen: first, the square 1 of row 2 must be covered by a domino-stone horizontally since square 1 of row 1 had been removed and square 1 of row 3 is uncovered. Second, the domino-stone on row 2 also covers square 2. Third, since all remaining squares of row 2 are not covered, all seven squares of row 1 must have been covered horizontally, which is not possible. The clause: AC[2, sq(n,c,c,c,c,c,c,c)] can be generated in several different ways: playing seven domino-stones vertically or placing six horizontally and one vertically. Whichever sequence of plays occured, has no effect on the next play. Therefore, only the state of the board is recorded, not the particular way it was achieved by placing the domino-stones. Thus, since only the partial covering is considered and not the particular placing of the domino-stones that achieve it, subsumption is used to discard all but one of the paths to each partial cover.

We are now in the position to formulate the program for an ATP-system, and subsequently we discuss some of its particularities:

```
( 1) : AC[1, sq(r,n,n,n,n,n,n,n)]
( 2) : AC[x, sq(n,n,y3...y8)]         --> AC[x, sq(c,c,y3...y8)]
( 3) : AC[x, sq(y1,n,n,y4...y8)]      --> AC[x, sq(y1,c,c,y4...y8)]
( 4) : AC[x, sq(y1,y2,n,n,y5...y8)]   --> AC[x, sq(y1,y2,c,c,y5...y8)]
  :
  :
  :
( 8) : AC[x, sq(y1...y6,n,n)]         --> AC[x, sq(y1...y6,c,c)]
( 9) : AC[x, sq(y1...y8)]  --> AC[x+1,sq(cpl(y1),cpl(y2),...cpl(y8))]
(10) : EQ[cpl(c),n]
(11) : EQ[cpl(n),c]
(12) : EQ[cpl(r),n]
(13) : AC[9,sq(y1...y8)]            { subsumer clause
(14) : ~AC[8,sq(c,c,c,c,c,c,c,n)]   { (in separate liste)
```

The clause (1) gives the initial condition of row 1 before any domino-stones have been placed. The clauses (2-8) permit an ATP-program to place domino-stones horizontally whereby the status of two adjacent squares is changed from n to c. Note that there is a variable in the first argument of the AC-predicate meaning that these clauses can, in principle, be applied to any row. The clause (9) serves to place domino-stones vertically. A domino-stone placed vertically covers one square in each of the two adjacent rows, and the squares have the same number between 1 and 8. If, in a row under consideration, the status of a square is c or r, then a domino-stone can not be placed vertically starting with that square. These properties suggest that an AC-clause is defined to advance the row number and to give the status of each square in the new row, based on the status of the squares on the preceding row. The employed mechanism is 'complementation'. A complement-function: cpl( ) is defined which switches the status of a square: c <-> n and r -> n. The idea is that if a square is c(overed) or r(emoved), then the one below it can not be c(overed) by placing a domino-stone vertically. This procedure thus implies that the placing of several vertical domino-stones proceeds simultaneously. The clauses (10-12) serve as demodulators to define or rewrite the AC-clauses containing a cpl-function to new ones with the constants r,n and c only.

There is one problem left. Without any additional clauses there is the possibility that some domino-stones could be placed vertically into the non-existing row 9. To prevent such an occurence, one relies on subsumption such that it immediately removes any new AC-clause which plays into row 9, meaning that it classifies that newly generated clause as less general than itself. To block clause (13) from participation it is placed on a special list that is kept separate from those clauses that are consulted by the inference rules. Clause (14) denies that the checkerboard can be fully covered by domino-stones placed horizontally and vertically, and it therefore serves as the termination condition. Note, that the status of its last square is n. This results from the form of the clauses that enable the program to make vertical and horizontal plays, and hence from the form of the clauses generated by a reasoning program.

As for choosing the appropriate inference rule, note that the object is to find AC-states which are represented by positive unit clauses. Thus, two inference mechanisms come to mind:
<u>UR-resolution</u> yields a unit clause from a set of unit clauses plus one non-unit clause (these may be positive or negative), whereas <u>Hyperresolution</u> yields a positive clause (with one or

more literals) from a set of positive clauses plus one non-positive clause. Employment of the <u>set-of-support strategy</u> with clause (1) or the clauses (1) and (14) in the set-of-support will further strengthen the search process.

The submission of the above program to an ATP-system did not lead to a contradiction proof, but instead the program exhausted all of the sequences of plays restricted by the ordering rules 1)-4) given earlier, and it therefore generated all of the possible AC-states. Since the ordering rules do not rule out any covering, the conclusion, that no covering exists, is correct. The subsumption-trick to recognize that a parial covering has been obtained by one sequence of playing, and that any other sequence of producing the same partial covering is unneeded, proved to be of valuable help to reduce drastically the combinatorics of the problem.

The above program has also be tested on a modified checkerboard which in fact <u>can</u> be covered by domino-stones, whereby the placing of the domino-stones can be reconstructed from the actual computer-run by following the generated AC-clause.

To this point we have considered checkerboards that are only slightly modified. We now would like to show how more complicated and perhaps more realistic cases can also be dealt with by an ATP-system. Suppose for example we wish to consider covering a checkerboard with one-by-two domino-stones that may have a number of its squares missing. Subsequently, we also will treat the same problem where however the domino-stones are of size: on-by-three. And finally we wil consider the problem of covering a modified checkerboard consisting of exactly 26 squares, with a possible choice of the checkerboard as shown in Fig. 10.2(a). Suppose, seven one-by-two and four one-by-three domino-stones are given. Can the above defined checkerboard be covered? In Fig. 10.2(b) we have given a particular solution. The first of the above-mentioned extensions is solved by using the {} -function (defined by curly-brackets) which has two arguments. In the first argument is the first item of the list or is the 'end'-item which, for ease of notation, is again abbreviated by the asterix: '*'. The list-function: li(..) then consists of a chosen number of {..} -functions, each one being positioned in the second argument of the preceding {..} -function such that for instance

$$
\begin{aligned}
li(\alpha, *) &= \{\alpha, *\} \qquad\qquad (* \equiv \text{end}) \\
li(\alpha, \beta, *) &= \{\alpha, \{\beta, *\}\} \\
li(\alpha, \beta, \ldots, \varepsilon, *) &= \{\alpha, \{\beta, \ldots \{\varepsilon, *\}\} \ldots\}
\end{aligned}
$$

By using this list-function we represent the status of the checkerboard as

```
li(n,n,...,c,*          (row 1)
   n,r,...,n,*          (row 2)
   ...........
   n,n,...,n,*)         (row 8)
```

In this example, the first row of the checkerboard is completely uncovered except for the last square, and the second square in row 2 has been r(emoved); all other squares are n(ot-coverd). The end of each row is marked by the constant: * end. Thus, an arbitrarily modified board can easily be represented by one of the huge lists. We now employ the convention that any leading arguments (in the list) that are 'c(overed)' or '*'-ed are removed from the list. This means that the initial argument will always be an 'n' as long as at least one uncovered square remains on the board. We shall rely on the demodulators to remove undesirable leading arguments in the deduced clauses and thus 'trim' the clauses by the appropriate EQ-clauses. With the above introduced simplified list-notation the ATP-program is rather short and simple:

```
(1) : AC[li(n,n,r,n,n,n,n,n,*,
            n,n,n,n,r,n,n,n,*,
            . . . . . . . . .
            n,n,n,n,n,n,n,n,*)]

(2) : AC[li(n,n,xrest)]          --> AC[trim(xrest)]
(3) : AC[li(n,y2...y9,n,xrest)] --> AC[trim(li(y2,...y9,c,xrest))]
(4) : EQ[trim(li(c,x)),trim(x)]
(5) : EQ[trim(li(*,x)),trim(x)]
(6) : EQ[trim(li(n,x)),li(n,x)]
(7) : EQ[trim(*),*             ]
(8) : ~ AC[*]
```

The clause (1) gives the initial state of the checkerboard, and the clauses (2-3) place domino-stones horizontally and vertically. The clauses (4-7) serve as demodulators to 'trim' the list. The clause (8) denies that the checkerboard can be completely covered with one-by-two domino-stones and it thus serves for a contradiction proof.

Suppose the domino-stones are now of size: one-by-three. This can be easily accomodated in the preceding formulation by replacing the clauses (2-3) by the following expressions:

```
(2): AC[li(n,n,n,xrest)]       --> AC[trim(xrest)]
(3): AC[li(n,y2...y9,n,y11...y18,n,xrest)]
                          --> AC[trim(li(y2...y9,c,y11...y18,c,xrest))]
```

The last extension of the checkerboard problem consists in finding the domino-stone coverage of a 26-square board whereby a limited number of one-by-two and one-by-three domino-stones is used. This problem is solved with the preceding technique. The AC-predicate is given two more arguments which give the number of the unplayed one-by-two and one-by-three domino-stones. Thus the initial state clause is replaced by

```
(1) : AC[7,4; li(n,n,...)]
```

whereby the first two arguments give the number of unplayed one-by-two and one-by-three domino-stones. The clauses for playing horizontally and vertically are almost the same.

```
(2) : AC[u,v;li(n,n,xrest)] ∧ GT[u,o] -> AC[(u-1),v;trim(xrest)]
(3) : AC[u,v;li(n,y2...y9,n,xrest)] ∧ GT[u,o]
          --> AC[(u-1),v;trim(li(y2...y9,c,xrest))]
(4) : AC[u,v;li(n,n,n,xrest)]∧ GT[v,o] -> AC[u,(v-1);trim(xrest)`
(5) : AC[u,v;li(n,y2...y9,n,y11,...y18,u,xrest)]  GT[v,o]
          --> AC[u,(v-1);li(y2...y9,c,y11...y18,c,xrest)]
```

where (2-3, place one-by-two domino-stones and the clauses (4-5) place one-by-three domino-stones. All the other clauses and demodulators can be taken over from the earlier program in unchanged form.

There are many more of this kind of problems which we will leave to the interested reader. We can think of covering the checkerboard with "domino-stones" of different shape such as for instance a right-angle, or of leaving certain areas completely uncovered, and so on.

11. Missionaries and Cannibals

We consider in this section a scheduling problem which reveals some of the characteristics one often meets, and we show its description and elegant solution. The essence of such problems is contained in the folowing "Missionaries and Cannibals" problem:

There are three missionaries and three cannibals on the west bank of a river. There is a boat on the west-bank that can hold no more than two people. The missionaries wish to cross to the east-bank. But they have a problem: If on either bank the cannibals can ever outnumber the missionaries, the outnumbered missionaries will be eaten. Is there a way for the missionaries to get their wish - to get to east-bank without loosing anyone?

This problem is somewhat similar to the scheduling difficultties one is faced if a number of meetings must be held where some of them must run in parallel. Suppose that various constraints exist on scheduling all the meetings, whereby some must proceed others while some must not be held in parallel. Certain speakers have prior travel arrangements and must give various talks consistent with their prior plans. The question is: with all of the constraints, does a schedule exist that conforms to the requirements?

The solution of the above thinking problem proceeds in three steps. We first must represent the starting situation at the beginning of the problem. Next, the clauses must be found which enable an ATP-system to move the missionaries, cannibals and the boat from one side of the river to the other and back, whereby the program must take the constraints into account that the missionaries always must outnumber the cannibals, and that the boat can not take more than two persons. Finally, the ATP-system must be able to tell when the thinking problem has been solved, or determine, if possible, that it can not be solved. If the problem is solvabel, then an arrangement is found in which the three missionaries are on the east-bank of the river. If it is not solvable, then every sequence of boat trips results at some point in the solution where the cannibals outnumber the missionaries, or it leads to a sequence of boat trips that simply result in repeating a missionaries-cannibals assignment where, for example, one cannibal goes forth and back on the river, forever.

The setup of an efficient ATP-program for this problem makes use of the so-called "successor function" s(x) which has as value: x incremented by one unit. Thus the successor of 0 is 1, of 1 is 2, and of 2 is 3. Therefore ss(0) s(s(0)) acts like the number 2. We furthermore introduce the functions: west(x,y), east(x,y) which give the number of missionaries cannibals in their first/second argument and this for the west- and the east-bank separately. As a last essential ingredient we define the predicate AC[west(..),e/w, east(..)] which stands for "achievable". Its firs argument contains the function west(..) giving the number of persons (missionaries and cannibals) on the west-bank, and its third argument, with the function east(..), gives the same information for the east-bank. The letters e and w in the second argument indicate where the boat is on the west- or the east-bank.

We are now ready to fomulate the ATP-program and subsequently discuss some of its particularities:

```
(1):AC[west(sss(o),sss(o)),w,east(0,0)]

(2):AC[west(x,s(y)),w,east(z,w)]    -> AC[west(x,y),e,east(z,s(w))]

(3):AC[west(x,y),e,east(z,s(w))]    -> AC[west(x,s(y)),w,east(z,w)]

(4):AC[west(ss(x),y),w,east(z,w)]   -> AC[west(x,y),e,east(ss(z),w)]

(5):AC[west(x,y),e,east(ss(z),w)]   -> AC[west(ss(x),y),w,east(z,w)]

(6):AC[west(s(x),s(y)),w,east(z,w)]-> AC[west(x,y),e,east(s(z),s(w)]

(7):AC[west(x,y),e,east(s(z),s(w))]-> AC[west(s(x),s(y)),w,east(z,w)]

(8):AC[west(s(x),y),w,east(z,w)]    -> AC[west(x,y),e,east(s(z),w)]

(9):AC[west(x,y),e,east(s(z),w)]    -> AC[west(s(x),y),w,east(z,w)]

(10):AC[west(x,ss(y)),w,east(z,w)]  -> AC[west(x,y),e,east(z,ss(w))]

(11):AC[west(x,y),e,east(z,ss(w))]  -> AC[west(x,ss(y)),w,east(z,w)]

(12):   AC[west(o,o),u,east(sss(o),sss(o)]

(12a):  AC[west(o,y),u,east(sss(o),w)]

(13) :   AC[west(s(x),ss(x)),u,east(z,w)]   }
(14) :   AC[west(s(x),sss(x)),u,east(z,w)]  }  subsumer clauses
(15) :   AC[west(x,y),u,east(s(w),ss(w))]   }  (on special list)
(16) :   AC[west(x,y),u,east(s(w),sss(w))]  }
```

Clause (1) encodes the initial state with three missionaries and three cannibals and the boat on the west-bank of the river. Tha clause (2),(3) and (8),(9) move one cannibal (resp. one missionary) from the east- to the west-bank and also in reverse direction. Similarly, all the other clauses up to (11) move two persons across the river. Note that the starting number of persons on either side of the river is left open via the variables x,y,z,w. The clause (12) denies that this thinking problem is solvable. Note in particular that the position of the boat is left open and that <u>all</u> missionaries and <u>all</u> cannibals are required to be on the east-bank. Had we limited ourselves to requiring that only all the missionaries should be on the east-bank with the cannibals being arbitrary, we would have described this case by clause (12a).

The clauses (13-16) serve to block certain damaging boat trips - those that place more cannibals on one side of the river than missionaries. The mechanism to prevent such clauses from being active is subsumption. Recall that subsumption discards unwanted clauses as soon as they are generated; they are discarded before they can be added to the retained information, and hence before they can be used. Thus, rather than blocking the bad trips, the clauses (13-16) are used to immediately discard those clauses which would lead to unwanted actions. For example, two missionaries and three cannibals on the west-bank must be avoided. One missionary and either two or three cannibals on the west-bank must be avoided. Similar conditions on the east-bank must be avoided. All possible arrangements can be characterized by the difference between the number of missionaries and the number of cannibals. The clauses (13-16) suffice. Now, if any bad trip is taken resulting in an excess of cannibals over missionaries on either side of the river, the results are immediately subsumed by one of the clauses (13-16), and hence discarded. None of the clauses (13-16) however are allowed to participate in the inference mechanisms, in the search for achievable arrangements. Consequentely they are placed on a list that is consulted for the purpose of discarding less general information than is present; hence subsumption comes into play. Again in (13-16) a variable occupies the position of the boat for it does not matter where the boat is when an excess occurs.

With the above discussion we have aimed to give an elegant solution of the posed problem although other solutions might have been possible. The explained method has the advantage that it allows for easy variations of the thinking problem and its solution. One might for instance wonder about the changes if four missionaries and cannibals are waiting to get across the river. The changes are as follows: clause (1) and (12) have to be modified as to account for the fact that there are four missionaires and cannibals.

```
 (1) : AC[west(ssss(o),ssss(o)),u,east(o,o)]
(12) : AC[west(o,o,u,east(ssss(o),ssss(o))]
(12a): AC[west(o,y),u,east(ssss(o),w)]
```

and two more subsumer clauses must be added:

```
(17) : AC[west(s(x),ssss(x),u,east(z,w)]
(18) : AC[west(x,y),u,east(s(w),ssss(w))]
```

Going one step further and assuming that there are five missionaries and five cannibals with a boat that will hold three people, demands for the following changes: again the clauses (1) and (12) have to be modified as to account for the increased number of missionaries and cannibals. They formally will be the same except that there will be five instead of four successive s-functions. The earlier clauses (2)-(11) describe the transfer of one or two persons, missionaries and cannibals, across the river. This set now has to be extended as to describe the transfer of three persons in the boat across the river: three missionaries, or three cannibals, or two missionaries and one cannibal, whereby the crossing of two cannibals and one missionary shall be exclude. Finally the set of subsumption clauses has again to be extended by two more clauses, additonal to the ones discussed above. The solution of this latter situation with five missionaries and five cannibals and maximally five people in a boat is as follows:

a) First three cannibals cross to the east-bank and one returns,
b) Then two more cannibals cross, and one returns,
c) Then three missionary cross, and one missionary and one cannibal return,
d) Then three missionaries cross, and one cannibal returns,
e) Finally, the three cannibals cross.

In the foregoing we have presented the solution of the thinking problem mainly based on the "successor-function" s(x). We now show a different method which takes advantage of the demodulators, and which has the advantage that it uses one single transition axiom. The AC-predicate takes the form:

AC [same(x1,x2),u, other(x3,x4)]

The first argument of this AC-predicate lists the number of missionaries and cannibals on that side of the river where the boat is. The second argument (variable u) gives the position of the boat: w = west-bank, e = east-bank. The third argument gives the number of missionaries and cannibals on that side of the river which is opposite to where the boat is. The information on the number of missionaries and cannibals is given by the first and second argument of the functions: "same(x1,x2)" and "other(x3,x4)", where the variables x1 and x3 (x2 and x4) give the number of missionaries (cannibals). Besides of the AC-predicate we also will use the predicate: LE(less or equal) and EE (equal). Furthermore, we introduce a few functions: check(x,y) will certify that there are never more cannibals than missionaries on either side of the river; rev(u) reverses the position of the boat, and finally:

$$ge(x,y) = \begin{cases} \text{true} & \text{if } x \geq y \\ \text{false} & \text{if } x < y \end{cases} \quad \text{(for x,y integers)}$$

We now are in the position to give the ATP-program, and we subsequently will discuss some of its particularities:

```
 (1)  AC[same(3,3),u,other(o,o)]

 (2)  AC[same(x1,x2),x,other(x3,x4)] ∧ P[xm] ∧ P[xc]
      LE[xm,x1] ∧ LE[xc,x2] ∧ LE[(xm+xc),2] ∧
      EE[check((x1-xm),x2-xc)),true] ∧ EE[check((x3+xm),(x4+xc)),true]
      --> AC[same((x3+xm),(x4+xc)),rev(u),other((x1-xm),(x2-xc))]

 (3)  P[0]
 (4)  P[1]
 (5)  P[2]

 (6)  EQ[check(o,x),true]
 (7)  EQ[check(x,y),ge(x,y)]
 (8)  EQ[rev(w),e]
 (9)  EQ[rev(e),w]

(10)  ~ AC[same(3,3),e,other(o,o)]
```

The "pick"-predicates P[..] give the acceptable numbers of missionaries and cannibals to be transfered over to the other side of the river. The EQ[..] serve as demodulators for the "check" -and "rev(erse)"-functions. The clause (1) gives the starting state and the clause (10) denies that the sought state can be reached. The clause (2) is the transition axiom which leads to new AC-states whereby the LE-predicates certify that the number of persons in the boat is below 3, and the EE-predicates certify that the number of cannibals is always smaller than the number of missionaries on either side of the river. Note that the number of missionaries (and also cannibals) changes side from "same" to "other", as it should be.

12. Billiard Ball Weighing

We are in this section concerned with a thinking problem of a more difficult nature than what we have considered so-far, because each move must add a maximum of possible new information in order to arrive at a solution. It therefore asks for some kind of optimization of information. The formulation of the "Billiard Ball" problem is as follows:

There are 12 billiard balls, eleven of which are identical in weight. The remaining ball - the odd one - has a different weight. You don't know whether it is heavier or lighter. You are given a balance-scale for weighing the balls. Can you find which ball is the odd ball in three weighings, and also find out whether it is lighter or heavier than the others?

This problem presents difficulties which are also encountered when planning for instance a trip in a city with visits to several people taking traffic constraints etc. into account, whereby the trip must be completed in a specified amount of time.

The billiard ball problem would be simple to solve if there were no limitations on the number of weighings. However, since we are expected to find the odd-ball, and also whether it is heavier or lighter, in at most three weighings, we must get as much as possible information form each of them. The essential point thus is to realize what information a balance can give and then imparting that knowledge in the representation of the problem.

The billiard balls need, in particular, not be numbered but instead they are characterized by the information that one can deduce from the weighing process. Assuming for the moment equal numbers of balls on the left and right pan of the scale, it may tip to the left telling us that the odd-ball might either be heavier and lying on the left pan with all the remaining balls being of standard weight, or the odd-ball might be lighter and lying on the right pan again with all other balls being of standard weight. Thus all balls on the left pan are of heavy or standard weight whereas all balls on the right pan are of light or standard weight. Analogous conclusions can be drawn if the scale tips to the right, or even if it stays in balance. We therefore are lead to define the four weight-classes:

- heavy or light or standard ≡ hls
- heavy or standard ≡ hs
- light or standard ≡ ls
- standard ≡ s

where each ball, at any time, is in one of the four classes. As we learn the results of the weighings, a ball may change from being in one class to being in another. After a weighing, the particular classes of the balls in the two pans of the scale are known. For example, if one ball is weighed against another and the scale tips to the left - the left side goes down and the right side goes up - then the ball on the left is in the hs-class and the one on the right is in the ls-class. Note however that the weighing of one ball against another does, in general, not provide sufficient information to arrive at a determination of the odd-ball in three weighings. Obviously, each weighing may change the classification of the balls that are being weighed. In the initial state, all balls are in the hls-class since nothing is known about them.

As a result of the above insight, we define a state-predicate which gives the number of balls in the above defined classes and also lists the number of remaining weighings. The initial state for instance is described by

AC[state { hls(12), hs(0), ls(0), s(0), re(3) }] ≡
AC1[12, 0, 0, 0; 3]

AC stand for "achievable". For ease of notation we drop the "state"-functions and simply list the number of balls in the four classes plus the remaining number of weighings: (hls, hs, ls, s; re), and we indicate this simplified notation with a '1' at the end of the predicate name.

In order to present the basic idea of solving the problem under investigation, we first discuss the transition axiom. Starting from an AC-state with the ball-setting: (xhls,xhs,xls,xs), it picks the setting: (yhls,yhs,yls,ys), for the right pan and the setting:(zhls,zhs,zls), for the left pan out of the starting ball-sets. Three different situations can now occur: the scale may stay in balance, it may tip to the left or it may tip to the right. For these three situations we can determine the number of balls in the four classes as shown in Table 12.1.

If the <u>scale stays in balance</u>, we know that all the balls we have just weighed are in the s-class. Consequently, those selected from amoung the starting hls-class and put in the two pans are now knowns to be in the s-class. The remaining number of balls in the hls-class thus is: xhls-(yhls+zhls). Similar arguments apply for the remaining number of balls in the hs- and ls-classes. The total number of balls in the s-class is equal to the sum of the original set xs plus those in the two pans (since the scale balances) which are not in the s-class.

If the <u>scale tips left</u>, no balls will remain in the hls-class since all balls taking part in the weighing process must be either in the hs- or ls-class, and all those not taking part in the weighing process must be in the s-class. Those in the left pan are obviously in the hs-class, and those in the right pan must be in the ls-class. As a result, no ball is left in the hls-class whereas the hs-class contains:(zhls+zls) balls (from the left pan) and there are:(yhls+yls) balls in the ls-class (from the right pan). The s-class is composed of the original set xs plus the zls balls in the left pan (which tipped) and the yhs balls in the right pan (which moved up) plus all those balls in the hls-, hs- and ls-classes which did not take part in the weighing process.

If the <u>scale tips right</u>, the above arguments apply in an analogous way. No balls remain in the hls-class since all balls taking part in the weighing process must be either in the hs- or ls-class, and all those not taking part in the weighing process are in the s-class. The number of balls in hs-class is:(yhls+yhs) (from the right pan), and the ls-class has: (zhls + zls) balls (from the left pan). The s-class is composed of the original set xs plus the yls in the right pan (which tipped) and the zhs balls in the left pan (which went up) plus all those balls in the hls-, hs- and ls-class which did not take part in the weighing process.

The actual formulation of the transition axiom takes into account several points which we now discuss:

- By convention no standard balls are ever placed in the left pan. There is not point in putting standard balls in both the left and the right pan of the balance scale, since this simply would doublicate a weighing in which the smaller number of standard balls in the two pans is removed from both.
- Assuming that the odd-ball is only slightly different in weight from the standard balls, it only makes sense to weight the <u>same</u> number of balls in each pan of the scale. Thus the number of points in the two pans are the same, between 0 and 6:

$$0 \leq (yhls+yhs+yls+ys) = (zhls+zhs+zls) \leq 6$$

- Since we are interested only in states which eventually lead to the identification of the odd-ball, some of the AC-states must be discarded, if it can be shown that they definitely will not lead to an identification of the odd-ball. There is no point in pursueing the consequences of such non-solvable states. The transition axiom therefore contains a numerical test which allows for the detection of a great many (but not all!) of such states. The test consists of comparing the number of possible solutions, meaning the number of possibilities for the odd-ball, with the number of possible outcomes that can occur for the remaining weighings. The first number is given by twice the number of balls in the hls-class plus the number of balls in the hs-and ls-classes. Since each weighing can produce three outcomes, the second number is equal to 3^n where n is the number of remaining weighings. Thus, if for a state: (2 hls+ hs+ls) $> 3^n$, then that state is definitely non-solvable, meaning that the odd-ball can not be determined within the remaining number of weighings, and it consequently is prevented by this test, from being generated via the transition axiom.

In summary, new AC-states can be generated by applying a transition axiom to the initial state. Since a transition axiom corresponds to a weighing, and since a weighing can produce three possible outcomes - the scale may tip to the left, tip to the right, or it may stay in balance - three new AC-states are obtained from the original one. In actual fact, the transition axiom first generates a record-predicate (RD) which collects together all the possible outcomes of the weighing process and which allows for the subsequent deduction of the resulting AC-states. These latter AC-states give rise to new RD-predicates which again allow for the derivation of new AC-states and so on.

Having understood the AC-state and its transition axiom, we now also need the SO- (or SO1-) predicate to characterize and find the "solvable" states which definitely will allow for the determination of the odd-ball. The generation of new AC-states is not sufficient to assure the determination of the odd-ball. Instead, the problem requires that a sequence of weighings, regardless of which of the three outcomes may occur at each weighing, finally leads to the determination of which is the odd-ball. We emphasize that it is not enough that only one or two of the three possible outcomes eventually will lead to the odd-ball. The idea is that of choosing a weighing so well that <u>each</u> of the three outcomes leads to the next weighing, where the next weighing is based on which of the three outcomes actually has occured. The next weighing must also have this same property of leading to good weighings. Finally, the last weighing must be such that the odd-ball can be identified. A state is called "solvable" if it is one of the type just described. Three states can be immediately classed as solvable:

SOl[0, 1, 0, 11; 0]
SOl[0, 0, 1, 11; 0]
SOl[0, 0, 0, 12; 0]

whereby in all of them no further weighings remain. In the first one 11 of the billiard balls are in the s-class and one is in the hs-class, which means that this last one is in fact the heavy odd-ball. Similarly, the second SO-state leads to the identification of the odd-ball as light. The third SO-state in which all 12 billiard balls are in the s-class, is <u>defined</u> as solvable, although this state indicates that the problem was incorrectly given; nevertheless this clause will turn out to be useful.

Since a state is "solvable" if a weighing starting with that state leads to three new solvable states, we take the given solvable states and work backwards, expanding the set of solvable states, with the help of the RD-predicate, until the initial state is finally included among the solvable states. The process we are about to present can therefore be described as proceeding in forward direction: generating an RD-state and subsequently the AC-states until the three weighings have been made. At that point, the program proceeds in reverse, adding new solvable states to the known ones until the initial state has been proved solvable. Actually, the forward and reverse process are not completely separated, nor need they be. Depending on the clause on which the program is currently focusing, the program may be reasoning in either direction.

We are now in the position to give the ATP-program, and we subsequently discuss some of its particularities:

(1) : P[0]
(2) : P[1]

⋮

(7) : P[6]

$$
\begin{aligned}
(8)\ :\ & \mathrm{AC1}[x1,x2,x3,x4;xr] \wedge P[y1] \wedge P[y2] \wedge P[y3] \wedge P[y4] \wedge \\
& \mathrm{LE}[y1,x1] \wedge \mathrm{LE}[y2,x2] \wedge \mathrm{LE}[y3,x3] \wedge \mathrm{LE}[y4,x4] \wedge \\
& \mathrm{GT}[(y1+y2+y3+y4),0] \wedge \mathrm{LE}[(y1+y2+y3+y4),6] \wedge \\
& P[z1] \wedge P[z2] \wedge P[z3] \wedge \\
& \mathrm{LE}[(y1+z1),x1] \wedge \mathrm{LE}[(y2+z2),x2] \wedge \mathrm{LE}[(y3+z3),x3] \wedge \\
& \mathrm{EQ}[(y1+y2+y3+y4),(z1+z2+z3)] \wedge \\
& \mathrm{LE}[(z1+Z2+y1+y3),3^{xr-1}] \wedge \mathrm{LE}[(z1+z3+y1+y2),3^{xr-1}] \wedge \\
& \mathrm{LE}[2\cdot\{x1-(y1+z1)\} + \{x2-(y2+z21)\} + \{x3-(y3+z3)\},3^{xr-1}] \\
& \qquad \longrightarrow \mathrm{RD1}[up,\ ua,\ ul,\ ur;\ ba]
\end{aligned}
$$

```
(9) : RD1[up,ua,ul,ur,ub]  -->  AC1[ul]
(10): RD1[up,ua,ul,ur,ub]  -->  AC1[ur]
(11): RD1[up,ua,ul,ur,ub]  -->  AC1[ub]

(12): SO1[0,1,0,11;0]
(13): SO1[0,0,1,11;0]
(14): SO1[0,0,0,12;0]

(15): RD1[up,ua,ul,ur,ub] ∧ SO1[ul] ∧ SO1[ur] ∧ SO1[ba] --> SO1[up]

(16): ~SO1[12,0,0,0;3]
```

We comment on the program. Note that we again have dropped the "state()"-function in the AC-predicate (whose argument consists of a list) and have introduced a '1' at the end of the predicate name, instead. The clauses P[0], ..., P[6], standing for "pick 0...6 balls", permit a reasoning program to pick balls from the various classes. The predicates LE (less or equal) and GT (greater than) introduce checks that no unreasonable choice of balls for the right and left pan in the weighing process are made. There is also a check to exclude AC-states which definitely will lead to unsolvable states. The RD1-predicate has five arguments where each of them is a list. The first one gives the parent ball setting (parent), the second one describes the taken action by listing the number of balls from the four classes for the left and right pan (action), the third, fourth and fifth arguments, each lists the number of balls in the (hls,hs,ls,s) -classes if a weighing has been carried out whereby the third one covers the case for "dip left", the fourth one for "dip right" and the fifth one for "balance". The arguments in the RD1-predicate are thus lists which are defined as follows:

```
parent... up =  {x1,x2,x3,x4; xr}
action... ua =  {y1,y2,y3,y4}, {z1,z2,z3}
left  ... ul =  {0,(z1+z2),(y1+y2),(x4+x3-y3)+(x2-z2)+x1-
                                        (y1+z1);xr-1 }
right ... ur =  {0,(y1+y2),(z1+z2),(x4+x3-z3)+(x2-y2)+x1-
                                        (y1+z1);xr-1 }
balance...ub =  {x1-(y1+z1),x2-(y2+z2),x3-(y3+z3),x4+(y1+y2+y3)
                                    +(z1+z2+z3);xr-1 }
```

Note, for simplicity of notation we have dropped the function-heading (for each list) given on the left-hand side of the above list, as well as the "state"-function in front of the lists and have added the '1' at the end of the predicate-name, instead.

The clauses following the transition axiom, derive the three AC1-states corresponding to the three possible outcomes of a weighing. The subsequent clauses define the three initial "solvable"-states whereas the next clause allows for the derivation of new solvable states which are defined in close analogy to the AC- (resp. AC1-) states. The last clause denies that the initial state is solvable. It enables a reasoning program to know that the puzzle has been solved, since it allows for a proof by contradiction.

The best approach to solve this problem with an ATP-system is to use "Hyperresolution" combined with the SS-strategy, whereby the initial state and the one that denies that the initial state is solvable are placed in the set-of-support.

Attempts to solve the above problem with an ATP-system have lead to its solution, and, in fact, have revealed more than 40 non-trivially distinct solutions within less than 22 seconds on an IBM 3033 computer.

13. Some Insights

The above examples give several insights which we would like to summarize:

1) Replacing in an ATP-system the specific with the general, is preferable. If the constants in a clause can be replaced by variables one may expect a gain in efficiency. Furthermore, a ATP-system discards all instances of existing or new information, retaining the more general fact only. This process is called subsumption, and it preserves in most (but not all) resolution refinements the completeness property.

2) If several copies of the same literal (with identical arguments) occur in a clause, the extra copies are deleted from the clause by a process called "collapsing dublicate literals".

3) The process of finding a solution might seem to an unexperienced person surprisingly long for such a trivial problem. This comes simply from the fact that an ATP-system can not leave out all the (many) intermediate steps which a human being undergoes in his thinking process, but usually is not aware of.

4) A mechanism exists, called weighting, which allows an ATP-system to consider certain facts more important than others. The program thus can be told to key on this fact, at least at the start.

5) Adding a denial clause (which was left aside in the above example) has the advantage that the ATP-system seeks a contradition which then acts as a convenient termination condition.

6) It is important to realize that a problem must be completely characterized by the set of initial clauses in order to avoid logically wrong conclusions. Furthermore a viable path to a solution can easily be overlooked.

7) It can well arise that there is redundant information among the clauses defining the problem, which means that some of the original clauses can, in fact, be derived from the other clauses. Redundancy and dependence are present in an ATP-system and they often contribute to a much more efficient reasoning of a program as compared to the case where the initial clause set is completely independent.

8) The fact that there is missing information in the description of a problem can in most cases be deduced from the fact that obvious facts are missing from the program's way of reasoning.

9) Finding extra information whilst solving a prob.em is quite common in an ATP-system's attempt. However if too much extra information is found, the problem never gets solved. Thus one important item one needs to pay attention whilst using an ATP-system is how to curtail the finding of extra information.

14. Conclusions

This paper is the third part of an introductory tutorial on "Theorem Proving/Automated Reasoning". It focuses on the use of Automated Theorem Proving (ATP)-systems by showing how thinking problems of various degrees of complexity are solved. Our presentation has several aims: to demonstrate how a problem is cast into the language of first-order predicate logic, how it then is submitted to an ATP-system, and finally how the deduction process proceeds. From the wide field of possible applications including mathematics (group-, set-, number-,.. theory), real-time systems control, robotics, automatic programming, logic circuit design/validation, program debugging/verification, expert systems, communication protocols, hardware verification, and so on, we have limited ourselves to a set of thinking problems or puzzles which do not require any specialized knowledge. A presentation of more "practical" problems and their solution will be given in a forthcoming article.

What have we learnt? The solution of a problem with an ATP-system is not straightforward! The first difficulties begin if a formulation in first-order predicate logic is sought. The problem at hand however could well be of higher-order logic, or it might ask for suggestions not only a proof. Once a problem is in the appropriate first-order form, a second difficulty arises as to the most appropriate resolution method, the right emphasis on particular clauses, the choice of the best search-strategy, and so on. If a proof is found, we have solved the problem we have submitted to the ATP-system. However we might not yet have the answer to our overall problem because the chosen axiom-system does not fully represent the actual problem situation.If no proof is found, the third difficulty becomes transparent: one doesn't know whether ones conjecture is incorrect, or whether the system simply couldn't find the right deduction-chain.

With these critical remarks we didn't intend to cause discouragment or disappointment but rather aimed to caution the interested reader that ATP is a field of high interest and potential which however has not yet reached the point of its ultimate perfection. And still, there are exciting new developments ahead... [12].

Acknowledgements:

The author thanks Profs. C. Joseph, C.P. Enz and M. Jacob for their kind interest and encouragements.
The author also thanks the CERN Theoretical Physics Division, where part of this work was done, for its kind hospitality.

References

1) B. Humpert
"Theorem Proving with First-Order Predicate Logic: I."
Proc. of the 8th Warsaw Symposium on Elementary Particle Physics (1985), Warsaw University Press, (Ed. Z.Ajduk)

2) B. Humpert
"Theorem Proving with First-Order Predicate Logic: II."
Proc. of the 9th Warsaw Symposium on Elementary Particle Physics (1986), Warsaw University Press, (Ed. Z.Ajduk)

3) L. Wos, R. Overbeek, E. Lusk and J. Boyle
"Automated Reasoning: Introduction and Application"
Prentice Hall (1984)

4) R.S. Boyer and J.S. Moore -
"A Computational Logic"
Academic Press, NY (1979)

5) H.J. Ohlbach and M. Schmidt-Schauss
"The Lion and the Unicorn"
Journ. Autom. Reasoning 1 (1985) 327

6) H.J. Ohlbach
"Predicate Logic Hacker Tricks"
Journ. Autom. Reasoning 1 (1985) 435

7) E. Lusk and R. Overbeek
"Non-Horn Problems"
Journ. Autom. Reasoning 1 (1985) 103

8) M.E. Stickel
"Schubert's Steamroller Problem: Formulations and Solutions"
Journ. Autom. Reasoning 2 (1986) 89

9) C. Walther
"A Mechanical Solution of Schubert's Steamroller by Many-Sorted Resolution"
Artificial Intelligence 26 (1985) 217

10) A.G. Cohn
"On the solution of Schubert's Steamroller in many-sorted Logic"
Proc. 9th IJCAI, Los Angeles, CA (1985) 1169

11) C. Walther
"Schubert's Steamroller - A case Study in Many Sorted Resolution"
Universität Karlsruhe (1984)

12) CADE-8 Conference, Oxford, 1986

13) L. Carroll
"Symbolic Logic"
Publ. Clarksen N. Potter, Inc. [Ed. W.W.Bartley III]

Table Captions

Table 3.1 : Person-to-job coordinations of the complex job-assignment problem.

Table 4.1 : Days of truth and non-truth of the lion and unicorn problem.

Table 10.1 : A particular placing of the domino-stones in the checkerboard problem.

Table 10.2 : The domino-stone covering of a modified checkerboard consisting of 26 squares.

Table 12.1 : Number of billiard balls in the $\{hls, hs, ls, s\}$ -classes after a weighing has taken place.

	R	T	S	P
Ch	n	y	n	n
Gu	y	n	n	n
Nu	n	n	y	n
OP	n	n	n	y
Po	n	n	y	n
Te	y	n	n	n
Ac	n	n	n	y
Bo	n	y	n	n

Table 3.1

	Lion	Unicorn
MO	N	T
TU	N	T
WE	N	T
TH	T	N
FR	T	N
SA	T	N
SU	T	T
MO	N	T

Table 4.1

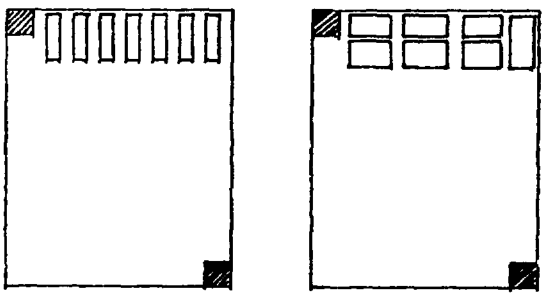

Table 10.1

Table 10.2

	hls - class	hs-class	ls - class	s - class
balance	xhls-(yhls+zhls)	xhs-(yhs+zhs)	xls-(yls+zls)	xs+yhls+zhls+yhs+zhs+yls+zls
tips left	0	zhls+zhs	yhls+yls	xs+zls+yhs+(xhls-yhls-zhls) +(xhs-yhs-zhs)+(xls-yls-zls)
tips right	0	yhls+yhs	zhls+zls	xs+zhs+yls+(xhls-yhls-zhls) +(yhs-yhs-zhs)+(xls-yls-zls)

Table 12.1

Precision Tests of the Electroweak Theory*

J. H. KÜHN

Max-Planck-Institut für Physik und Astrophysik
- Werner-Heisenberg-Institut für Physik -
P.O.Box 40 12 12, Munich (Fed. Rep. Germany)

ABSTRACT

The present status and further perspectives for precision tests of the electroweak theory are discussed with emphasis on future experiments at e^+e^- colliders. Ambiguities in the theoretical predictions for the W mass and the left-right asymmetry are scrutinized and the interplay between QED and QCD corrections is studied in detail. It is shown that the theoretical predictions are well under control at the precision level envisaged for future experiments. Various methods to determine the weak couplings of heavy quarks are compared. Asymmetries on a toponium resonance are free from hadronic uncertainties. They could be measured to an accuracy sensitive to electroweak radiative corrections.

*Lectures presented at the "X. Warsaw Symposium on Elementary Particle Physics", Kazimierz, Poland, May 25-29, 1987, and at the "Workshop on Topical Problems of Testing the Stanford Model in High Energy Reactions", Budapest, Hungary, June 15-19, 1987.

TABLE OF CONTENTS

1. Introduction

One of the central aims of future high energy experiments will be to fix the basic parameters of the GSW and to measure with comparable precision other observables which are then predicted by the theory. Thus some of the most basic aspects of the theory namely the quantum corrections will be tested and through the virtual corrections information may be obtained on heavy degrees of freedom not yet accessibly with present energies. More specifically, one measures three quantities which allow the determination of the $SU(2)$ and $U(1)$ gauge couplings g and g' and the Higgs field vacuum expectation value v. Many observables of the theory (like the boson masses, asymmetries in e^+e^- annihilation or neutrino scattering cross sections) can be calculated in lowest order from g, $g'$and v only. They depend only weakly through radiative corrections on the remaining parameters of the theory, the Higgs self-coupling (or m_H), the Yukawa couplings (fermion masses and mixing angles) or on the couplings of further, not yet discovered heavy particles. Two of these "basic" experimental input parameters are the fine structure constant, determined e.g. from the Thompson scattering cross section, and G_μ, as calculated from the muon lifetime.

$$
\begin{aligned}
\alpha &= 1/137.03604(11) \qquad \frac{\delta\alpha}{\alpha} = 0.82 \times 10^{-6} \\
G_\mu &= 1.16637(2) \times 10^{-5}\ \mathrm{GeV}^{-2} \qquad \frac{\delta G_\mu}{G_\mu} = 17 \times 10^{-6}.
\end{aligned}
\tag{1.1}
$$

These are known with extremely high precision and will retain their role for a long time.

As a third input quantity one of the two gauge boson masses, their ratio or information from neutrino scattering like $R_\nu \equiv \sigma_{NC}\,(\nu N)/\sigma_{CC}\,(\nu N)$ or $\sigma(\nu e)/\sigma(\bar\nu e)$ can be used. Within the standard model all these quantities serve to determine the weak mixing angle θ_W. The actual choice depends on the (time dependent!) precision of experiments (and should not be confused with the choice of a renormalization scheme).

Up to now the most precise value came from deep inelastic neutrino-nucleon scattering [1] $\sin^2\theta_W = 0.233 \pm 0.003 \pm 0.005$ (with the definition $\sin^2\theta_W \equiv 1 - M_W^2/M_Z^2$ and assuming $m_t \leq 100$ GeV, $m_H \leq 1$ TeV). The systematic error which originates from the uncertainty in the theoretical treatment of the hadronic system limits any further improvement of this measurement. The determination of $\sin^2\theta_W$ from M_W (or M_Z) in conjunction with α and G_μ starts to compete [2]

$$\begin{pmatrix} M_W = 80.2 \pm 0.6 \pm 0.5 \pm 1.3 \text{ GeV} \\ M_Z = 91.5 \pm 1.2 \pm 1.7 \end{pmatrix} \xrightarrow[\alpha,\, G_\mu]{} \sin^2\theta_W = 0.232 \pm 0.003 \pm 0.008 \quad (1.2)$$

whereas the determination from the W-Z mass ratio suffers still from significant statistical and systematical errors of about 0.025 and 0.01 respectively. In the near future this ratio will be determined at the $p\bar{p}$ collider [3] to an accuracy of $\pm 0.003 \pm 0.002$, which translates into an error of twice this size for $\sin^2\theta_W$. The Z-mass determination at the e^+e^- colliders LEP (and SLC) with an ultimate goal of $\delta M_Z = 20/50$ MeV (with/without transverse beam polarization for the energy calibration) will lead to a drastic improvement. This translates into a prediction for M_W and $\sin^2\theta_W$

$$M_W^2 = M_Z^2\frac{1}{2}\left(1 + \sqrt{1 - \frac{4\pi\alpha}{\sqrt{2}M_Z^2 G_\mu(1-\Delta r)}}\right) \quad (1.3)$$

$$\sin^2\theta_W = \frac{1}{2}\left(1 - \sqrt{1 - \frac{4\pi\alpha}{\sqrt{2}M_Z^2 G_\mu(1-\Delta r)}}\right) \quad (1.4)$$

[Δr incorporates the radiative corrections discussed below] with an error from δM_Z

$$\begin{aligned} \delta M_W &= \frac{M_W}{M_Z}\frac{\cos^2\theta_W}{\cos^2\theta_W - \sin^2\theta_W}\delta M_Z \approx 1.2\delta M_Z = 24/60 \text{ MeV} \\ \delta\sin^2\theta_W &= \left|\frac{2\sin^2\theta_W^2\cos^2\theta_W^2}{\sin^2\theta_W^2 - \cos^2\theta_W^2}\right|\frac{\delta M_Z}{M_Z} \approx 0.6\cdot\frac{\delta M_Z}{M_Z} = 1.31/3.3\times 10^{-4} \end{aligned} \quad (1.5)$$

(where the entries refer to $\delta M_Z = 20$ and 50 MeV respectively). An important quantity to be measured in e^+e^- annihilation is the left right asymmetry A_{LR}, defined as the asymmetry in the production cross sections for right-handed and left-handed polarized electron beams σ_L and σ_R

$$A_{LR} \equiv \frac{\sigma_L - \sigma_R}{\sigma_L + \sigma_R} = \frac{2(1-4\sin^2\theta_W)}{(1-4\sin^2\theta_W)^2 + 1} \approx 2(1-4\sin^2\theta_W) \quad (1.6)$$

It can be predicted from M_Z to an accuracy of

$$\delta A_{LR} \approx 8\,\delta\sin^2\theta_W = 1.1/2.7\times 10^{-3}. \quad (1.7)$$

To achieve an experimental precision of $\delta M_W \approx 100$ MeV and $\delta A_{LR} \approx 3 \times 10^{-3}$ is presently considered to be a reasonable experimental goal [4, 5] and we will in the following concentrate on these two measurements. Other observables of interest like the forward backward asymmetry, [6] $\sigma(\nu e)/\sigma(\bar{\nu} e)$ [7] or A_{LR} on toponium [8] will be measured with less precision, nevertheless also they might lead to important tests of the standard model and could be sensitive to new physics.

2. Windows to "New Physics"

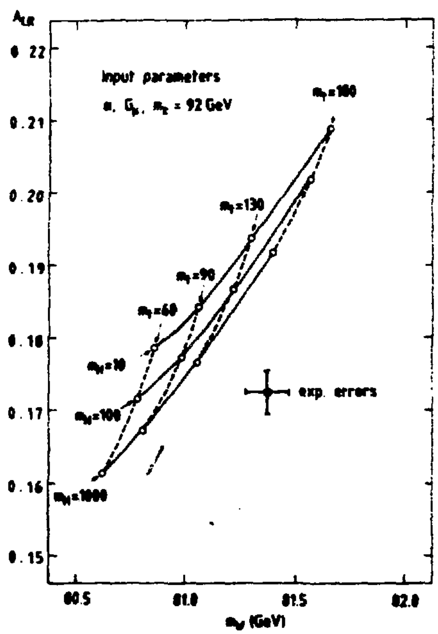

Fig. 2.1: Variation of the prediction for the left-right asymmetry A_{LR}, and for M_W, as a function of m_t and m_H in comparison with the expected experimental precision. (From Ref. [9]).

The theoretical predictions for M_W as a function of α, G_μ and M_Z to lowest order and including one loop corrections differ by about 1 GeV such that the effect of quantum corrections will be clearly visible. Since these corrections depend on m_t and m_H, a combined measurement of M_W and A_{LR} would lead to restrictive bounds on the Higgs boson and top quark masses or even to a crude determination of these parameters if both particles are beyond the kinematic limits of LEP. "New physics", like a fourth heavy quark doublet with large mass splitting, a fourth (even mass-degenerate) generation or contributions from SUSY particles all lead to radiative corrections at a level observable in experiments. Of course, to disentangle the combined effects of such contributions and identify their source, could well be difficult.

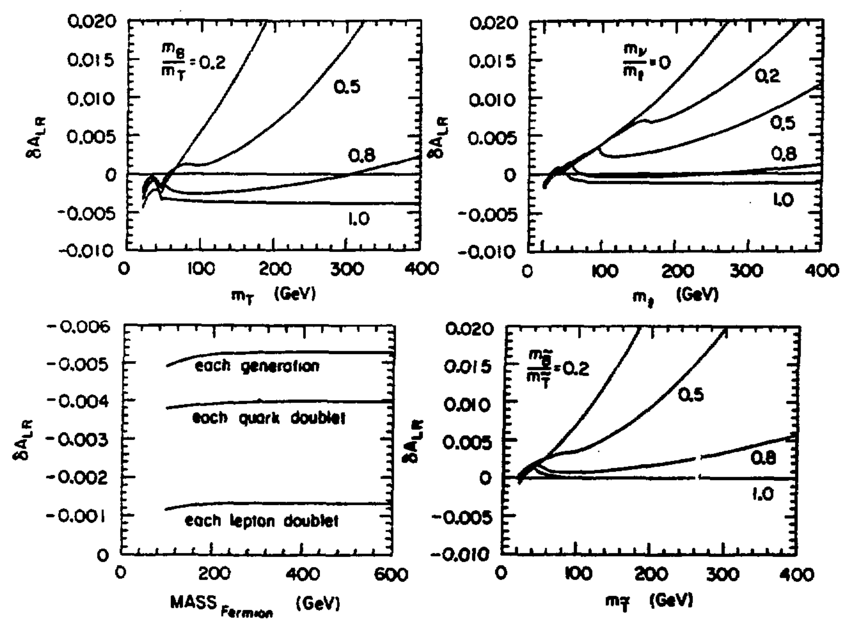

Fig. 2.2: Variation of the prediction for the left-right asymmetry A_{LR} for a fourth quark doublet (a) a fourth lepton doublet (b) with large mass splitting, mass degenerate fermion multiplets (c) and squark multiplets with large splittings (d). (From Ref. [10]*).*

3. Uncertainties in the Theoretical Predictions

When planning measurements a relative precision of $O(10^{-3})$, the study of uncertainties in the theoretical predictions is mandatory. These originate from uncalculated higher order electroweak corrections, from the hadronic contribution to the vacuum polarization and from hadronic initial or final state corrections, if one allows for hadrons in the initial or final state. Initial state radiation plays an important and special role for the M_Z determination.

3.1. Weak Corrections

The most thoroughly studied example is provided by the $M_Z - M_W$ mass relation (1.3). An error $\delta\Delta r$ in the radiative correction translates into an error in M_W and $\sin^2\theta_W$ through

$$\begin{aligned} \frac{\delta M_W}{M_W} &= \frac{1}{2}\frac{\sin^2\theta_W}{\cos^2\theta_W - \sin^2\theta_W}\delta\Delta r \\ \delta\sin^2\theta_W &= \frac{\sin^2\theta_W\cos^2\theta_W}{\cos^2\theta_W - \sin^2\theta_W}\delta\Delta r \end{aligned} \tag{3.1}$$

The hadronic contribution to Δr has been estimated on the basis of experimental results for $\sigma(e^+e^- \to \mathit{hadrons})$ at low and intermediate energies together with some theoretical input, namely asymptotic freedom at high energies and dispersion relations. An error on Δr of 0.0013 from this source has been quoted [11] which translates into an uncertainty of 17 MeV on M_W and of 4×10^{-4} on $\sin^2\theta_W$.

A full calculation to $O(\alpha^2)$ has not been performed to date. The dominant correction, however, originates from terms of the form $(\frac{\alpha}{\pi}\ln\frac{M}{m_f})^n$. These are fixed by renormalization group arguments and are incorporated already in (1.3). The second term in this series leads to a shift of M_W by 80 MeV and is thus comparable to the envisaged experimental accuracy.

Corrections of the form $\alpha^2 \ln M/m_f$ are calculated in Ref. 12. They are all contained in the corrections to the fermionic vacuum polarization (Fig. 3.1).

This amounts to multiplication of the leptonic part of Δr by $(1+\frac{3}{4}\frac{\alpha}{\pi})$ and thus to an increase of Δr (M_W) by $6\cdot 10^{-5}$ (1 MeV). The corresponding corrections to the hadronic part are, in any case, dominated by the uncertainty in the experimental input and are in principle absorbed in the evaluation of Δr from $\sigma(e^+e^- \to \mathit{hadrons})$.

Fig. 3.1: Leading correction of $\mathcal{O}(\alpha^2 \ln M_Z/m_f)$ to the mass relation.

The remaining not yet calculated $\mathcal{O}(\alpha^2)$-terms do not involve large logarithms and the resulting uncertainty is therefore a few MeV at most.

Once a complete calculation to order α^n has been performed, predictions within different renormalization schemes differ in general by terms of order α^{n+1}. After the forementioned $\alpha^2 \ln^2 M/m_f$ and $\alpha^2 \ln^1 M/m_f$ terms have been incorporated into a full $\mathcal{O}(\alpha)$ calculation, the remaining "scheme dependence" should therefore be of the same magnitude as the not yet calculated $\mathcal{O}(\alpha^2)$ terms, i. e. a few MeV*.

3.2. M_Z-DETERMINATION AND INITIAL STATE RADIATION

In view of the large Z_0 width around 3 GeV it will be a formidable experimental task to determine M_Z to a precision of 20 MeV and information from the peak of the resonance and from its wings will be required. This is complicated by the effects of initial state radiation which leads to a reduction of the cross section on top of the resonance, to a shift and a strong distortion of the line shape.

Terms of the form $(\alpha \ln M_Z/m_f)^n$ have been incorporated [14, 15] into the $\mathcal{O}(\alpha)$ result [16]. Recently also a complete $\mathcal{O}(\alpha^2)$ calculation has been performed [17]. The difference between $\mathcal{O}(\alpha)$ and $\mathcal{O}(\alpha^2)$ results is sizeable. The peak cross section is reduced by 26 % (29%) if the $\mathcal{O}(\alpha)$ ($\mathcal{O}(\alpha^2)$) result is compared with the Born prediction. The location of the maximum is raised by 184 MeV (96 MeV). The difference between the $\mathcal{O}(\alpha^2)$ and the exponentiated versions of the $\mathcal{O}(\alpha)$ and $\mathcal{O}(\alpha^2)$ calculations is about 20 MeV and should be indicative of the remaining theoretical uncertainty (Fig. 3.2.)

*For slightly larger estimates of this uncertainty see Ref. 13. These do not incorporate terms of $\mathcal{O}(\alpha^2 \ln^1 M/m_f)$.

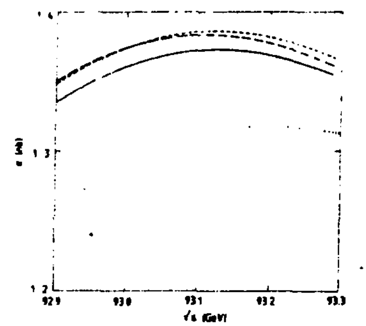

Fig. 3.2: The total cross section for $e^+e^- \rightarrow \mu^+\mu^-$ around the peak with $M_Z = 93$ GeV. The dotted line represents the $\mathcal{O}(\alpha)$ corrected cross-section. The curve with large dashes represents the $\mathcal{O}(\alpha^2)$ corrected cross-section. The other dashed line is the $\mathcal{O}(\alpha)$ exponentiated form, the solid line represents the $\mathcal{O}(\alpha^2)$ exponentiated expression. (From Ref. 17).

3.3. M_W Determination

No theoretical study for W pair production of comparable precision exists up to date. Initial and final state radiation, electroweak radiative corrections and finite width effects have to be controlled at the same time. Happily enough, since the planned experimental precision on M_W is only about 100 MeV, the requirements on the theory are less stringent. The M_W determination through an analysis of the distributions of $e\nu$ and/or $q\bar{q}$ final states will be straightforward since the connection between the distribution of the W decay products and M_W (defined through the location of the pole of the W propagator) is evident.

To determine M_W through the energy dependence of $\sigma(e^+e^- \rightarrow W^+W^-)$ is conceptually more complicated: The width of W amounts to about 2.5 GeV and hence the threshold is smeared over a region of several GeV. The cross-section depends on M_W *directly* through kinematics and *indirectly** through the dependence of the weak couplings g and g' on M_W, if one adopts the standard model and keeps e.g. α and G_μ fixed. Since the form of this second indirect dependence relies heavily on the standard model, this approach is no longer applicable in extensions of the model and would be invalidated by an anomalous magnetic moment of the W or by

*The compensation between these two effects leads to the insensitivity of the cross section to the value of M_W several GeV above threshold [4]. This, however, is an artifact of the choice of input parameters.

non-standard ZWW couplings expected e. g. from composite models. It is, however, possible to choose an energy region very close to threshold, say $1 - 2$ GeV above $2M_W$ where the neutrino t-channel exchange dominates the rate and the shape of the cross- section depends only weakly on the model [18, 19]. (Fig. 3.3).

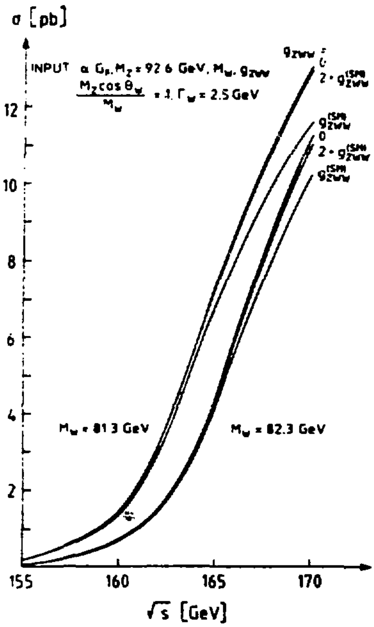

Fig. 3.3: The cross section for W pair production in the threshold region and its dependence on the ZWW coupling g_{ZWW} for two values of M_W. $g_{ZWW}^{(SM)}$ denotes the prediction of the standard model for g_{ZWW}. (From Ref. 18.*)*

4. A_{LR} From Hadronic Final States*

Once the parameters of the standard model are fixed through the determination of M_Z, the measurement of A_{LR} could well lead to the most precise test of the standard model, apart from the measurement of M_W. To arrive at a statistical error in the asymmetry of $3 \cdot 10^{-3}$ about $4 \cdot 10^5$ events are required, assuming an average polarization of 0.5. Hadronic final states with their large production rate will thus be of prime importance, at least in the first round of experiments. In such

*Sections 4.2-4.5 of this chapter are based on work done in collaboration with S. Jadach, G.G. Stuart and S. Wąs [20]. For a related discussion see also Ref. 21.

a situation large and uncalculable corrections from hadron physics could appear in principle. There is, furthermore, a complicated interplay between QED corrections and hadronic effects such that both have to be controlled simultaneously. Section 2 of this chapter will therefore be concerned with QCD corrections to A_{LR} for massless and massive quarks. The effect of initial state radiation on A_{LR} will be discussed in section 3. Section 4 is devoted to a discussion of $Z-\gamma$ and $\gamma-\gamma$ box diagrams and their influence on the cross section and the asymmetry. It will be shown that their influence is small on top of the Z. The discussion on helicity nonconserving spin configurations in section 5 concludes this chapter. In view of the importance of these measurements the brief discussion of the experimental setup in section 1 may be justified.

4.1. THE EXPERIMENTAL SETUP

Polarized electron beams have been produced and accelerated by the linear accelerator at SLAC since long ago. The main task for SLC will be to preserve the electrons' polarization on their complicated way from the source through the accelerator, the damping and the bending rings to the interaction region and to measure the degree of plarization with sufficient precision. ($\delta A_{LR} = A_{LR}\delta P/P$, such that an experimental accuracy on A_{LR} of $3 \cdot 10^{-3}$ requires the determination of P to about 10^{-2}.) The positrons remain unpolarized. Since the cross section for electrons and positrons with opposite spins vanishes in the ultra relativistic limit, this configuration is sufficient for a A_{LR} measurement.

At LEP, like at any other e^+e^- storage ring, the Sokolov-Ternov effect may be exploited. Synchrotron radiation from electrons and positrons flips their respective spins, such that their magnetic moments are aligned with the external field of the bending magnets. This leads to transverse polarization of e^+ and e^- with opposite relative sign. Spin rotators will then transform these to electrons and positrons with longitudinal spins pointing into opposite direction. This is most easily understood as a consequence of CT invariance (Fig. 4.1). Let us assume a set of spin rotators (consisting of a sequence of magnetic fields) which turns the transversely oriented spins (say in direction $s_\perp$) of electrons with momenta $\vec{p}$ into longitudinally oriented spins of direction $s_\parallel$ at the interaction region and back to their original direction afterwards. A CT operation leaves the magnetic fields of the spin rotators invariant, but changes the electrons into positrons of opposite momenta $-\vec{p}$ and opposite spins $-s_\perp$ and $-s_\parallel$ respectively. The cross section for such a configuration vanishes in the ultrarelativistic limit, assuming for the moment the idealized case of 100% polarization. To arrive at an interesting measurement, some of the (four electron and four positron) bunches have to be depolarized. A particularly elegant scheme* is provided by depolarizing the electron bunches number 1 and 2 and the positron bunches number 1 and 3. One can then measure at each interaction region the cross sections with the electron-positron spin configurations** $(\rightarrow, \leftarrow)$, (u,u), $(\rightarrow, u)$ and $(u, \leftarrow)$. The ratio between the first two rates provides the calibration for the polarization, the last two measurements determine A_{LR}.

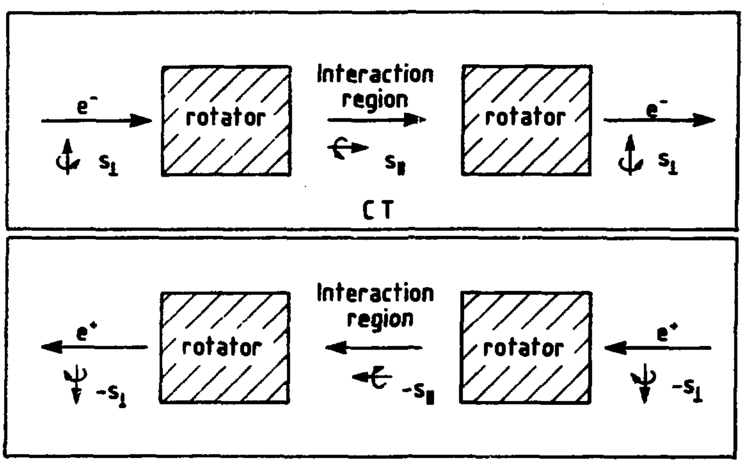

Fig. 4.1: Schematic description of the operation of spin rotators on polarized electron beams and their behaviour under a CT operation.

*For a more detailed discussion see [5].

**u stands for unpolarized.

4.2. QCD Corrections to the Left-Right Asymmetry

Calculations of the total hadronic cross section in e^+e^- annihilation are subject to large corrections, compared to the quark parton model predictions. For massless quarks, the correction factor has been calculated to $\mathcal{O}(\alpha_s^2)$ and is given [22] by $(1 + \alpha_{\overline{MS}}(Q^2)/\pi + 1.41(\alpha_{\overline{MS}}(Q^2)/\pi)^2)$ for $n_f = 5$. Numerically it amounts to about 1.05 on top of the Z^0. For massive quarks, in particular close to threshold, the corrections are even larger and are subject to a substantial uncertainty. For the left-right asymmetry, the situation is much more favourable. On top of the resonance, Z and γ Born amplitudes do not interfere and the square of the photon amplitude can be neglected to a good approximation. (The small corrections from this last contribution are discussed below). The dominant Z^0 contribution leads to an asymmetry, $2v_ea_e/(v_e^2 + a_e^2)$, (v_e, a_e are defined below) independent of the final state [23]. The Z–γ interference can no longer be neglected even slightly, say, 0.1GeV off resonance, and predictions for the asymmetry depend on the final state. The size of this effect can be calculated in the parton model. As long as we are concerned with massless quarks, all relevant hadronic vacuum polarization functions are modified by QCD corrections by the same factor to order α_s^2, which cancels for the asymmetry. (The parton model predictions even for the small corrections are therefore applicable up to this order). The question arises at which order of α_s the parton model will cease to apply. To simplify the discussion, only the Born terms in the electroweak interaction will be considered. The amplitude for the reaction $e^+e^- \underset{\gamma,Z}{\longrightarrow} h$, a hadronic final state, is then given by

$$\begin{aligned}\mathcal{A}(e^+e^- \to h) = &\langle h|J_\mu^{em}|0\rangle \frac{e^2}{s}\bar{v}Q_e\gamma^\mu u \\ &+ \langle h|J_\mu^V + J_\mu^A|0\rangle \frac{e^2}{s - M_Z^2 + iM_Z\Gamma_Z}\bar{v}\gamma^\mu(v_e - a_e\gamma_5)u\end{aligned} \tag{4.1}$$

with

$$Q_e = -1 \qquad v_e = \frac{I_e^3 - 2Q_e\sin^2\theta_W}{2\sin\theta_W\cos\theta_W} \qquad a_e = \frac{I_e^3}{2\sin\theta_W\cos\theta_W} \tag{4.2}$$

The total cross section with polarized beams is

$$\sigma_{\{{R \atop L}\}} = \frac{4\pi\alpha^2}{3s}\Big[(v_e \mp a_e)^2\Big|\frac{s}{s-M_Z^2+iM_Z\Gamma_Z}\Big|^2(r^{(V,V)}+r^{(A,A)}) + 2Q_e(v_e \mp a_e)\mathrm{Re}\Big(\frac{s}{s-M_Z^2+iM_Z\Gamma_Z}\Big)r^{(em,V)} + Q_e^2 r^{(em,em)}\Big] \tag{4.3}$$

The $r^{(i,j)}$ are defined as the transverse part of $\sum_h \langle 0|J^i|h\rangle\langle h|J^j|0\rangle$, and are generalizations of the familiar $R \equiv \sigma_{had}/\sigma_{point}$. Explicitly

$$r^{(i,j)}(P^2) = \frac{1}{p^2}\Big(\frac{P_\mu P_\nu}{P^2} - g_{\mu\nu}\Big)(2\pi)^2\sum_h (2\pi)^4\delta^4(P_h - P)\langle 0|J_\mu^i(0)|h\rangle\langle h|J_\nu^j(0)|0\rangle \tag{4.4}$$

$r^{(V,A)}$ and $r^{(em,A)}$ vanish upon summation over the final states as a consequence of charge conjugation invariance. The remaining r's are given in the massless parton model by

$$r^{(V,V)} = \sum_f v_f^2 \qquad r^{(A,A)} = \sum_f a_f^2 \qquad r^{(em,em)} = \sum_f Q_f^2 \qquad r^{(em,V)} = \sum_f Q_f v_f \tag{4.5}$$

On the basis of these equations the deviations from the parton model predictions for A_{LR} will be investigated. Evidently these are closely related to corrections to $r^{(i,j)}$ which cannot be absorbed in a global factor and the relative weight of such terms. The first and dominant $|Z|^2$ term in eq. (3) leads to the familiar result $2v_e a_e/(v_e^2+a_e^2)$ for the asymmetry. The last $|\gamma|^2$ term contributes differently to A_{LR} depending on the final state. This effect, however, amounts only to 1–2×10^{-3} and is thus already below the planned accuracy. This statement is somewhat modified in the presence of initial state radiation, see Section 3. Furthermore it can be be calculated quite reliably. (For massless quarks one expects non-trivial QCD corrections of order $(\alpha_s/\pi)^3$, such that the uncertainty from the contribution is completely negligible.) The interference term vanishes for $s = M_Z^2$, if and only if $r^{(em,V)}$ is real, a requirement evidently fulfilled in the parton model, independent of the quark mass. As long as all quark masses are identical (which means in practice, as long as $m_f^2/M_Z^2 \ll 1$), $r^{(em,V)}$ can be shown to be real by using $SU(n)$ flavour invariance. The argument is particularly simple if these light flavours are grouped into weak isospin doublets. say (u,d) plus (c,s). The electromagnetic and vector current are decomposed into weak isospin singlet (=hypercharge) and nonsinglet parts.

$$\begin{aligned} J^V &= 2(1-2\sin^2\theta_W)J^3 - 2\sin^2\theta_W J^Y \\ J^{em} &= \qquad\qquad J^3 + \qquad \frac{1}{2}J^Y \end{aligned} \tag{4.6}$$

$$\begin{aligned} r^{(em,V)} = {} & 2(1-2\sin^2\theta_W)r^{(3,3)} - \sin^2\theta_W r^{(Y,Y)} \\ & + (1-2\sin^2\theta_W)r^{(Y,3)} - 2\sin^2\theta_W r^{(3,Y)} \end{aligned} \tag{4.7}$$

The first two terms are evidently real, the remainder vanishes as a consequence of isospin invariance†. In case we have to consider incomplete multiplets of say, (u,d) plus s or (u,d), (c,s) plus b, one expands the electromagnetic and the neutral current in terms of $SU(n)$ generators with *real* coefficients ($n = 3$ or 5 in our case). As a consequence of $SU(n)$ invariance only diagonal elements contribute to $r^{(em,V)}$, such that $r^{(em,V)}$ is real also in this more general case. $\mathrm{Im}\, r^{(em,V)}$ thus originates from singlet–nonsinglet mixing due to different quark masses, denoted by m_{f_1} and m_{f_2} in the following.

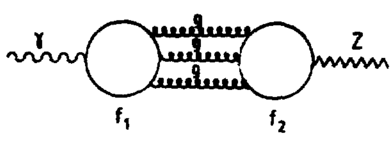

Fig. 4.2: Leading diagram responsible for the difference in $r^{(i,j)}$ for singlet and nonsinglet currents and for $\mathrm{Im}\, r^{(em,V)}$ if $m_{f_1} \neq m_{f_2}$.

Two gluon intermediate states are forbidden by C–invariance. The leading contribution to $\mathrm{Im}\, r^{(em,V)}$ and thus to the Z–γ interference on top of the Z^0 originates from the diagrams depicted in Fig. 4.2, is thus of order $(\Gamma_Z/M_Z)(\frac{\alpha_s}{\pi})^3\left(\frac{m_{f_1}^2-m_{f_2}^2}{M_Z^2}\right)$ and can be safely ignored. A similar line of reasoning applies *off resonance* where all four functions $r^{(i,j)}$ play an equally important role. As long as quark mass effects can be ignored, the leading (and not yet calculated) corrections to the parton model prediction are of order α_s^3. The argument is slightly more involved for the contribution from $r^{(A,A)}$ since flavour singlet states e.g. two gluons, can contribute

† Isospin breaking effects like ρ–ω mixing are induced by QED, and are thus part of the electroweak corrections.

already at order α_s^2. These terms, however, cancel within one isospin doublet, again up to mass terms, such that the leading (uncalculated) correction off resonance are of order $(\frac{\alpha_s}{\pi})^2\left(\frac{m_{f_1}^2-m_{f_2}^2}{s}\right)$. However, off resonance there are also other uncalculated corrections of order $\alpha_s^2 m_f^2/M_Z^2$ and even the uncertainty in the definition of the quark mass (say of a heavy top) plays an important role, such that these are the leading effects which limit the accuracy of an asymmetry measurement off resonance.

Massive Quarks The contribution from massive quarks, say top quarks, can be cast into a form similar to eq. (5). In the parton model

$$\begin{aligned} r^{(V,V)} &= \beta(3+\beta^2)/4\ v_t^2 \\ r^{(em,em)} &= \beta(3+\beta^2)/4\ Q_t^2 \\ r^{(em,V)} &= \beta(3+\beta^2)/4\ Q_t v_t \\ r^{(A,A)} &= \beta^3\ a_t^2 \end{aligned} \tag{4.8}$$

and the $\mathcal{O}(\alpha_s)$ QCD correction factors R^V and R^A for vector ($i,j=V$ or em) and axial vector ($i=j=A$) current induced production read [24]

$$\begin{aligned} R^V &= \left\{1+\frac{4}{3}\alpha_s\left[\frac{\pi}{2\beta}-\frac{3+\beta}{4}\left(\frac{\pi}{2}-\frac{3}{4\pi}\right)\right]\right\} \\ R^A &= \left\{1+\frac{4}{3}\alpha_s\left[\frac{\pi}{2\beta}-\left(\frac{19}{10}-\frac{22}{5}\beta+\frac{7}{2}\beta^2\right)\left(\frac{\pi}{2}-\frac{3}{4\pi}\right)\right]\right\} \end{aligned} \tag{4.9}$$

QCD corrections to the asymmetry are now in general of order α_s, their size, however, is small. Close to the peak the dominant uncertainty originates from the uncertainty in m_t and is shown in table 1 for some characteristic cases. A knowledge of m_t to ± 1 GeV is evidently sufficient to keep the resulting uncertainty in A_{LR} below the required level of 3×10^{-3}.

4.3. QED Corrections

Initial State Radiation

As for QED corrections we shall understand, if not stated otherwise, the $\mathcal{O}(\alpha)$ corrections with real and virtual photon emission (vertices with a photon line) from initial and final state fermions for both γ and Z^0 s-channel exchanges. Box diagrams with at least one photon are included. No vacuum polarization and no genuine electroweak correction are included. Fermions masses are assumed to be small.

$E_{beam} - \frac{M_Z}{2}$	$-2.5GeV$	$-0.5GeV$	0	$+.13GeV$	$+0.5GeV$	$+2.5GeV$
$\delta m_t = -1GeV$	−502	−89	−16	−4	33	103
$\delta m_t = +1GeV$	590	114	19	−2	−42	−126
$\delta m_t = -5GeV$	−1892	−331	−65	−12	17	383
$\delta m_t = +5GeV$	−	734	101	−30	−330	−990
$\delta A_{RL}(QCD)$	30	24	3	−8	−28	−114
$\lvert A^0_{RL} - A^1_{RL}\rvert$	440	95	23	8	26	93

Tab. 4.1: Variation in the asymmetry in units of 10^{-4} *from a variation of* m_t*, from inclusion of the QCD correction and from a variation of the QCD corrections as described in Ref.* 25.

As was stated in above, A_{LR} is least dependent on the properties of the final state due to pure QCD corrections at $\sqrt{s} = M_Z$ and it is thus particularly suited for a precision test of the standard electroweak theory. Initial state radiation, however, smears the effective energy and raises the energy of minimal sensitivity (EMS) to a slightly higher value. Also the maximum of the cross section is located about 200 MeV† above M_Z. With somewhat (over-) simplifying assumption it can be shown that the EMS is raised by roughly the same amount. The cross section as a function of s is given by

$$\sigma(s) = \int ds' f(s')\sigma_{Born}(s - s') \tag{4.10}$$

where the resolution function f incorporates the smearing from initial state radiation and from the beam energy spread. If f were strongly peaked and its width small compared to the Z^0 width, Γ_Z, then one would prove this coincidence rigorously. Under the above assumption the integral is dominated by the region close to the peak. σ_{Born} may be then expanded around M_Z^2

$$\sigma_{Born}(M_Z^2) + \frac{1}{2}\frac{d^2\sigma}{ds^2}\Big|_{s=M_Z^2}(s - M_Z^2)^2 + \ldots \tag{4.11}$$

†Result for single photon bremsstrahlung.

The folded cross section is then given by

$$\sigma(s) = \int ds' f(s') \left[\sigma_{Born}(M_Z^2) + \frac{1}{2}\frac{d^2\sigma}{ds^2}\bigg|_{s=M_Z^2}(s - s' - M_z^2)^2 + ...\right] \qquad (4.12)$$

and at the new maximum s_{max} the first derivative vanishes, which implies

$$\frac{d}{ds}\sigma(s)\bigg|_{s=s_{max}} = \int (s_{max} - s' - M_z^2) f(s') = 0 \qquad (4.13)$$

such that any term in σ_{Born} which vanishes linearly at $s = M_Z^2$ does not contribute to the corrected cross section at $s = s_{max}$. In practice, however, this can only be considered as a qualitative line of reasoning because the radiative tail extends through the whole Z^0 peak region and the presented argument is not strictly valid. For example, using the $\mathcal{O}(\alpha)$ exact result for the initial state bremsstrahlung [26] one finds the peak at $M_Z + 0.23$ GeV and the EMS at $M_Z + 0.32$ GeV. In Fig. 4.3a it is shown that also after the corrections from the initial state radiation are incorporated, the asymmetry at the EMS ($=M_Z$+0.32 GeV) is practically equal to the uncorrected asymmetry at M_Z and that at this point it is again independent of the final state fermion flavour‡. It should be noted, however, that to obtain this result the pure s-channel photon contribution had to be switched off (Fig. 4.3a). It affects the asymmetry differently for different final states, as can be seen in Fig. 4.3b. Without initial state radiation this difference amounts to about 10^{-3}. Inclusion of the initial state radiation up to the kinematical limits enhances the difference by a factor of about 3†, that is at a level relevant for experiments. However, a sizeable fraction of this effect originates from final states with a very hard photon plus a fermion pair of rather low invariant mass. This contribution is easily eliminated by a rather loose cut on the photon energy, say $k \leq 0.9$ which corresponds to $m(f\bar{f}) \geq 30$ GeV (cf. the dash-dotted line in Fig. 4.3b for $f = \mu$). Nevertheless these contributions seem to be large at first glance, since the leading Z^0-exchange amplitude is of $\mathcal{O}(\alpha^0)$ on

‡It should be noted, however, that A_{LR} at $s = M_Z^2$ is strongly affected by initial state radiation and furthermore becomes strongly dependent on the final state. This conclusion differs from the one of Ref. 21

†The resonant $|Z|^2$ contribution is depleted through the shift of the effective energy to a lower value, the $|\gamma|^2$ contribution is enhanced.

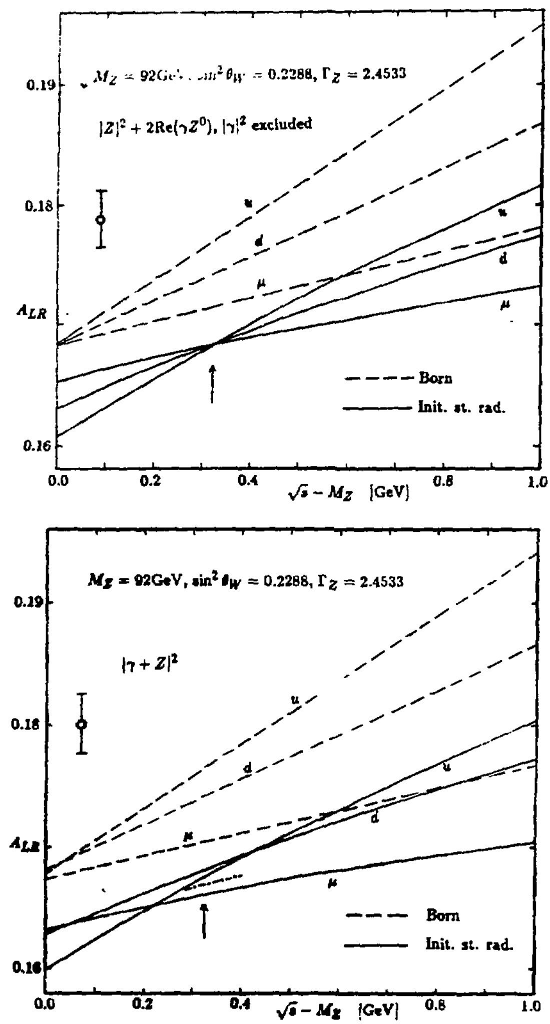

Fig. 4.3: Influence of initial state radiation (to order α) on A_{LR}, a) excluding, b) including the pure s-channel photon contribution for muon pair production. The arrow at $M_Z = 0.320GeV$ indicates the energy of minimal sensitivity. The short dashed dotted curve in b) represents the result $k_{max} = 0.9$.

the top of Z^0 while the photonic amplitude is of $\mathcal{O}(\alpha^1)$ and the non-interfering $|\gamma|^2$ correction is thus of $\mathcal{O}(\alpha^2)$. It should be noted, however, that the Z^0-amplitude is supressed by the large Z^0 width — a consequence of the large number n_f of open fermionic channels — such that its magnitude is characterized by α^0/n_f. No corresponding suppression operates for the photon, so that the alleviation of the α^2 suppression is easily understood.

Initial/Final State QED Interferences and Box Diagrams

Final state QED bremsstrahlung by itself is not able to influence A_{LR} because it factorizes off the cross section‡. The interference of the QED bremsstrahlung from initial and final state fermions and the interference of photonic box diagrams with the Born amplitude involve the couplings of the photon to the final state fermions and is therefore sensitive to the final state flavour. This dependence may, in principle, show up in the integrated cross sections and therefore in A_{LR}. One generally does not expect these contributions to be large because, at the level of the differential cross sections, they do not contain large logs of the type $\frac{\alpha}{\pi}\ln(s/m_e^2)$, however, the integration over the photon spectrum in the presence of the Z^0 resonance might perhaps produce $\frac{\alpha}{\pi}\ln(M_Z^2/\Gamma_Z^2)$ terms.

Technically, in the one-loop/single-bremsstrahlung calculations, an infrared free result is obtained by adding the contributions from box diagrams (in fact their interference with Born amplitude) to the corresponding initial/final state hard bremsstrahlung interference contribution integrated over the photon energy up to some maximum value, possibly up to the phase space limit. These two contributions, virtual and real, correspond to two possible ways of cutting across one generic diagram, see Fig. 4.4. We shall consider four QED interferences shown in Fig. 4.4 which correspond to four assignments for s-channel exchanges. They are denoted in the following as $(Z\gamma)\otimes Z$, $(Z\gamma)\otimes\gamma$, $(\gamma\gamma)\otimes Z$ and $(\gamma\gamma)\otimes\gamma$. The last one is, however, trivially equal zero due to charge conjugation invariance.

Most of ingredients necessary for numerical evaluation of the above QED interferences can be found in the literature. The relevant exact analytical expressions

‡ A very small influence $\sim 10^{-4}$ may arise for strong cut-off on photon energy due to competition of the initial and final state hard photon emission, see later in this section.

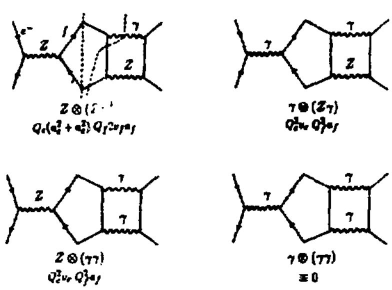

Fig. 4.4: Four diagrams corresponding to four types of QED initial/final state interference. Combinations of the coupling constants relevant for the contribution to A_{RL} are marked below the corresponding diagrams.

for the $\gamma\gamma$ contribution to the differential cross section may be found in Refs. 27, 28 and the corresponding one for the $Z\gamma$ box in Ref. 29. The analytical expression for the differential cross section, $d\sigma/dk$ (where k is the photon energy energy in units $\sqrt{s}/2$) from the initial/final state real hard bremsstrahlung interference contribution was calculated recently in Ref. 28 and later confirmed independently in Ref. 25. The total contribution to the cross section is obtained by integration of the box contributions over the scattering angle and of the real photon part over the photon momentum. The integrations can be performed either analytically, following Ref. 25, or numerically. (In principle, these are also calculable using the existing M.C. programs [30, 31] but this is technically difficult due to smallness of the result. Here the first two methods were employed. The Monte Carlo approach was only used for additional tests on the hard bremsstrahlung.)

The first result is based on analytical integration. $(\sigma_L - \sigma_R)/\sigma_Z^{Born}$ is shown for muon pair final states in Fig. 4.5. The cross section σ_A, where $A = R, L$ denotes the electron polarization (positrons unpolarized), is calculated for each type of the interference using the following compact expressions

$$\sigma_A^{(Z\gamma)\otimes Z} = \frac{6\alpha}{\pi} Q_e Q_f \frac{-\epsilon_A \beta_A^{e\,2}}{(\beta_L^{e\,2} + \beta_R^{e\,2})} \frac{(\beta_L^{f\,2} - \beta_R^{f\,2})}{(\beta_L^{f\,2} + \beta_R^{f\,2})} I^{(Z\gamma)\otimes Z}\left(\frac{M_R^2}{s}, k_{max}\right) \sigma_Z^{Born} \quad (4.14)$$

$$\sigma_A^{(Z\gamma)\otimes\gamma} = \frac{6\alpha}{\pi} Q_e^2 Q_f^2 \frac{-\epsilon_A \beta_A^{e}}{(\beta_L^{e\,2} + \beta_R^{e\,2})} \frac{(\beta_L^{f} - \beta_R^{f})}{(\beta_L^{f\,2} + \beta_R^{f\,2})} I^{(Z\gamma)\otimes\gamma}\left(\frac{M_R^2}{s}, k_{max}\right) \sigma_Z^{Born} \quad (4.15)$$

$$\sigma_A^{(\gamma\gamma)\otimes Z} = \frac{6\alpha}{\pi} Q_e^2 Q_f^2 \frac{-\epsilon_A \beta_A^{e}}{(\beta_L^{e\,2} + \beta_R^{e\,2})} \frac{(\beta_L^{f} - \beta_R^{f})}{(\beta_L^{f\,2} + \beta_R^{f\,2})} I^{(\gamma\gamma)\otimes Z}\left(\frac{M_R^2}{s}, k_{max}\right) \sigma_Z^{Born} \quad (4.16)$$

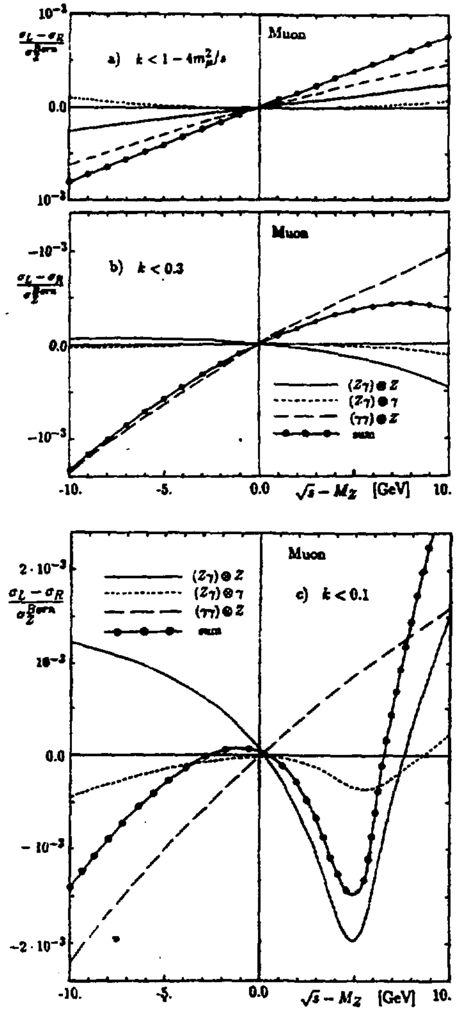

Fig. 4.5: Contributions to A_{LR} for muon pair final states from three types of the final/initial state QED interferences and their sum plotted as a function of $\sqrt{s}$ for three photon energy cut-offs a) $k_{max} = 1 - 4m_\mu^2$ b) $k_{max} = 0.3$ c) $k_{max} = 0.1$. They are normalized to the pure Z^0 Born cross section σ_Z^{Born}. Neither initial nor final state bremsstrahlung are included.

where $A = R, L$, $\epsilon_R = 1$, $\epsilon_L = -1$ and

$$I^{(Z\gamma)\otimes Z}(z, k_{max}) = \tag{4.17}$$
$$\mathrm{Re}\Big[z(z+1)\ln\frac{k_{max}+z-1}{z} + (z-1)(1-k_{max})\Big] - \ln|z| - 2\ln k_{max}$$

$$I^{(Z\gamma)\otimes\gamma}(z, k_{max}) = \tag{4.18}$$
$$\mathrm{Re}\Big[(1-z^*)\Big(z(z+1)\ln\frac{k_{max}+z-1}{z} + (z-1)(1-k_{max}) - \ln(z) - 2\ln k_{max}\Big)\Big]$$

$$I^{(\gamma\gamma)\otimes Z}(z, k_{max}) = \mathrm{Re}(1-z)\Big(-2\ln k_{max} + k_{max} + \frac{1}{2}\Big) \tag{4.19}$$

for which,

$$k = 2E_\gamma/\sqrt{s} < k_{max} \qquad M_R^2 = M_Z^2 - iM_Z\Gamma_Z \tag{4.20}$$

$$\sigma_Z^{Born} = \frac{\pi\alpha^2}{3s}\left|\frac{s}{s-M_R^2}\right|^2 ({\beta_L^e}^2 + {\beta_R^e}^2)({\beta_L^f}^2 + {\beta_R^f}^2) \tag{4.21}$$

β_L^e and β_R^e denote respectively the left and right hand couplings of the Z^0 to the electron in units of $e = \sqrt{4\pi\alpha}$.

$$\beta_L^e = \frac{I_3^e - \sin^2\theta_W Q_e}{\sin\theta_W\cos\theta_W} \qquad \beta_R^e = \frac{-\sin^2\theta_W Q_e}{\sin\theta_W\cos\theta_W} \tag{4.22}$$

β_L^f and β_R^f denote the corresponding quantities for the outgoing fermion. The expression for $\sigma^{(Z\gamma)\otimes\gamma}$ can be obtained directly from $\sigma^{(Z\gamma)\otimes Z}$ (c.f. Ref. 25) by suitably modifying the couplings and propagators. For $\sigma^{(\gamma\gamma)\otimes Z}$ the situation is slightly different since there are two $\gamma\gamma$ box diagrams compared to four $Z\gamma$ boxes. Hence one must return to the amplitude level and resum the contributing diagrams appropriately.

In Fig. 4.5 the size of the interference contribution is shown and the relative importance of the three terms is compared. Three different cut-offs k_{max} are applied. The quantity plotted in Fig. 4.5 is normalized with respect to σ_Z^{Born} and represents roughly the influence of each of the three terms on A_{LR}. The normalization with respect to σ_{tot}, the total cross section, with photonic corrections, integrated up to k_{max}, will be used in all other plots†. The following conclusions can be drawn from Fig. 4.5:

---

†The advantage of the normalization with respect to σ_Z^{Born} in Fig. 4.5 is that the figure can be easily reproduced using eqs. (15)–(16).

1. The smallness of the interference contribution is striking. For a cut-off of 0.3 and in the range $\sqrt{s} = M_Z \pm 10$ GeV the contributions are smaller than 10^{-3} i.e. below experimental precision level. They are below 10^{-4} for a looser cut-off and closer to the Z^0 position.

2. The smallest term originates from $(Z\gamma) \otimes \gamma$ and the other two, $(Z\gamma) \otimes Z$ and $(\gamma\gamma) \otimes Z$, are of comparable magnitude. It should be noted that the smallness of the vector coupling constant $v_e = v_\mu$ suppresses equally strongly all three terms. *(For the relevant combinations of the coupling constants see Fig. 4.4.)* This is different for quarks, as shown in the next figure.

3. All three terms increase strongly when the cut-off k_{max} is decreased from its maximum value $1 - m_\mu^2/s$ to 0.3 and further to 0.1. This reflects very strong cancellations among the real and virtual photon contributions.

Similar results are presented in Fig. 4.6 for u-quarks. Here the emphasis is on the cut-off dependence and $(\sigma_L - \sigma_R)/\sigma_{tot}$ is plotted separately for each value of k_{max}, for each type of interference and for the sum. The unpolarized cross section σ_{tot} includes initial and final state photon emission integrated numerically up to k_{max}. Each interference contribution and also their sum is again below the experimental accuracy, particularly close to the Z^0. Due to the different Z^0 coupling constants the contribution from $(Z\gamma) \otimes Z$ interference is now dominant.

The figures that follow display the combined influence of the final state bremsstrahlung together with the three interference terms dicussed before. The result for muons is presented in Fig. 4.7, the analogous result for u and d quarks in Fig. 4.8. The photon energy cut-off varies from $k_{max} = 0.1$ to 1. The combined influence on A_{LR} is very small, of the order 10^{-4}. It is so small, that many other phenomena are expected to influence A_{LR} at the same level. Even final state bremsstrahlung alone (no interferences) has a similar influence on A_{LR} as can be seen from one of the curves included in Fig. 4.7. This phenomenon results, in combination with initial state radiation, from the fact that switching on/off final state bremsstrahlung (modulus squared) influences slightly the relative strength of the initial state bremsstrahlung and thus indirectly also A_{LR}. It has also been checked that the inclusion of the imaginary part of the photonic vacuum polarization — formally an order α^2 correction on top of the Z^0 — affects A_{LR} near M_Z by a similar amount. At this

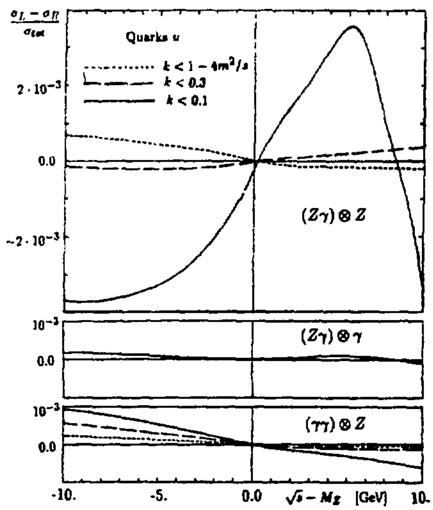

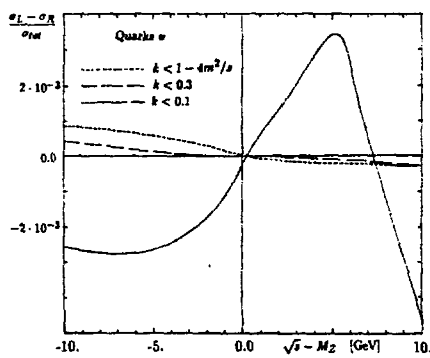

Fig. 4.6: Contributions to A_{LR} for u-quark pair final states a) from three types of the final/initial state QED interferences and b) their sum, plotted as a function of $\sqrt{s}$ for three photon energy cut-offs: $k_{max} = 1 - 4m^2/s$, 0.3 and 0.1. They are normalized to the integrated cross section $\sigma_{tot}(k_{max})$ which includes initial and final state bremsstrahlung with $k < k_{max}$.

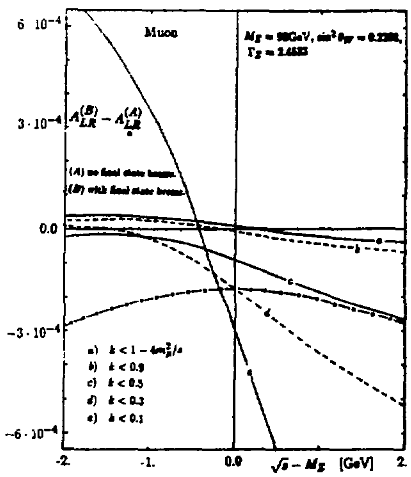

Fig. 4.7: Influence of the QED final state and initial/final state interferences bremsstrahlung on A_{LR}. Plotted is the difference $A_{LR}^{(B)} - A_{LR}^{(A)}$ where (A) includes only initial state QED bremsstrahlung and (B) includes final state QED bremsstrahlung with inital/final state interferences. The four curves a) – e) represent results for gradually stronger photon energy cut-off. The additional dashed-dotted curve represents the exclusive influence of the final state radiation (no interferences) for $k_{max} = 0.3$.

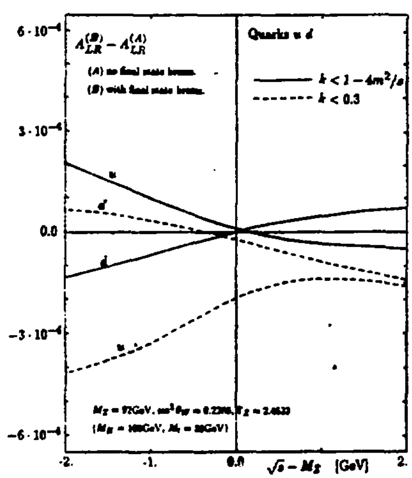

Fig. 4.8: As in Fig. 4.7 for u and d quarks.

order of magnitude most probably other higher order QED corrections come into play.

The following comments should be added:

The relative size of the interference contributions is given by $v_f a_f Q_f$ for $\sigma_{(Z\gamma)\otimes Z}$ and by $Q_f^2 a_f$ for $\sigma_{(Z\gamma)\otimes\gamma}$ and $\sigma_{(\gamma\gamma)\otimes Z}$. Neglecting mass terms these contributions vanish upon summation over all members of one generation as a consequence of anomaly cancellation. Of course, when measuring the cross section experimentally, the members of one generation (neutrino, heavy quark) will not be included with equal weight to allow for the exact cancellation.

All the contributions from initial/final state interference vanish for $s = M_Z^2$ or are at most of order $\frac{\alpha}{\pi}(\Gamma_Z/M_z)^2$ as compared to the Born cross section. This feature holds true also for general hadronic states. The reason for this is easily seen for $\sigma_{(Z\gamma)\otimes Z}$. The momentum flow in one of the two interfering Z-propagators remains unaffected by photon emission and the corresponding amplitude is thus purely imaginary for $s = M_Z^2$. To assure interference with the remaining contribution (the box amplitude for virtual and the amplitude with initial state radiation for real photon emission), the phase space of the photon is strongly restricted, namely to $|E_\gamma| \leq \Gamma_Z/2$ for real and to $|E_\gamma - k^2/2M_Z| \leq \Gamma_Z/2$ for virtual emission.

To summarize: QED initial/final state interference contributions to A_{LR} around the Z-peak are for loose cuts an order of magnitude below $3 \cdot 10^{-3}$, the anticipated precision of future experiments.

4.4. Bremsstrahlung and Helicity Nonconserving Beam Polarizations

Tests of electroweak theory by means of the measuring left-right asymmetry with an experimental error $3 \cdot 10^{-3}$ will require the beam polarizations to be measured with a precision of 10^{-2}. In LEP/SLC experiments this will be achieved either by means of Compton backscattering† off a polarized laser beam [33] and by scattering $e^{\pm}$ beams with four sets of polarizations (some of them zero) [34] where the polarization can be deduced indirectly from the four measured cross sections. Helicity conservation is an important ingredient in this analysis and will be inspected more closely now.

† For QED corrections to this method cf. Ref. 32.

Helicity is conserved for incoming $e^{\pm}$ beams up to (tiny) terms of order m_e^2/M_Z^2 in Born approximation. This implies that the cross section with arbitrary polarizations p_1 of e^- and polarization p_2 of e^+ may be expressed in terms of only two elementary cross sections σ_{RL} and σ_{LR},

$$(1+p_1)(1-p_2)\sigma_{RL} + (1-p_1)(1+p_2)\sigma_{LR}, \tag{4.23}$$

where first index in σ_{AB} denotes e^- the polarization R or L (helicity +1/2 or -1/2) and the second the corresponding e^+ polarization and U stands for an unpolarized beam. In Born approximation the helicity nonconserving cross sections σ_{RR} and σ_{LL} are of order m_e^2/s and are totally negligible by LEP/SLC standards. This allows not only σ_{RL} and σ_{LR} but also the degree of polarization to be determined from the measurement of σ_{RR}, σ_{RU}, σ_{UR} and σ_{UU}. In the presence of the QED bremsstrahlung, however, the helicity nonconserving cross sections σ_{RR} and σ_{LL} are of order α/π, they do not vanish for $m_e \to 0$ [35], are thus not *a priori* negligible.

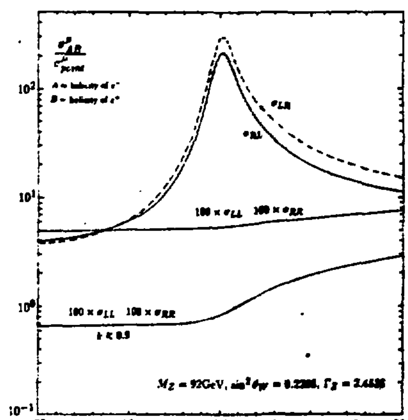

Fig. 4.9: Comparison of helicity conserving (σ_{LR} and σ_{RL}) and helicity nonconserving (σ_{RR} and σ_{LL}) cross sections into muon pairs in the Z^0 region. In σ_{AB} the index $A = R, L$ denotes the helicity of the electrons beam and $B = R, L$ the helicity of the positrons. σ_{AB} includes the complete single photon bremsstrahlung over the total phase space. The cross sections are divided by the pointlike muon cross section $\sigma^{\mu}_{point} = 4\pi\alpha^2/3s$. The helicity nonconserving cross sections are multiplied by a factor 100 and are shown for the cut-offs $k_{max} = 1 - m_\mu^2/s$ and 0.9.

In Fig. 4.9 the helicity conserving and nonconserving cross sections are compared as a function of the energy in the neighbourhood of the resonance. including initial state radiation. The helicity nonconserving contribution can be derived from Ref. 28:

$$\sigma_{RR} = \sigma_{LL} = \frac{2\alpha}{\pi} \int_{k_{min}}^{k_{max}} dk k(1-k)\sigma[s(1-k)] \tag{4.24}$$

As can be seen from Fig. 4.9 the helicity nonconserving cross sections do practically not affect the naïve result (23) through additional terms of the form $(1+p_1)(1+p_2)\sigma_{RR} + (1-p_1)(1-p_2)\sigma_{LL}$ since the ratios of σ_{RR} and σ_{LL} to σ_{RL} and σ_{LR} near top of Z^0 are clearly far below 10^{-3}. In fact most of the contributions to this tiny helicity nonconserving cross section originate from very hard bremsstrahlung (k close to one) and can easily be eliminated by a moderate cut on k as also shown in Fig. 4.9. However, such effects could become important if similar measurements were planned outside the Z^0 peak where they are of the order 10^{-2}. The smallness of the helicity nonconserving cross sections follows from the absence of infrared and (electron) mass singularities in eq. (24). (A logarithm of the form $\ln(1-k_{max})$ is present, however.) Furthermore, the additional relative suppression around $\sqrt{s} = M_Z$ is due to the fact that this cross section does not show a resonance peak but rather a mild step. The reason is that for helicity nonconserving beam helicities the fragmentation function of the electron into an electron and a photon (24) has a zero at $k = 0$ (instead of the usual infrared $1/k$ singularity.) When this fragmentation function is convoluted with the Born cross section the Z^0 resonance peak is effectively washed out.

5. Heavy Quark Couplings from e^+e^- Annihilation Experiments

In the previous chapters only precision tests involving light fermions were considered. However, experiments which are sensitive to the weak coupling of fermions with masses comparable to the weak scale are interesting in their own right. They could be sensitive to the Higgs-fermion Yukawa coupling through the diagrams depicted in Fig. 5.1, a feature practically absent in neutrino scattering, e^+e^--annihilation into light fermions or the muon decay rate (and thus in the $Z - W$ mass relation (1.3)). Not all measurements involving heavy fermions are equally suited for this purpose. The left-right asymmetry on top of the Z with heavy quarks as final states for example is practically insensitive to their couplings, as discussed in chapter 4.

The forward backward asymmetry exhibits this sensitivity, it is, however, subject to QCD corrections and in practice such a measurement may also depend on details of the quark decay, as discussed below in section 5.1. This leaves us with the left-right asymmetry on a toponium resonance. QCD corrections are largely absent in this case and a precision measurement is at hand (sect. 5.2).

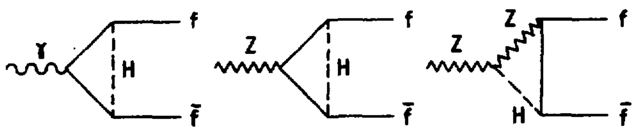

Fig. 5.1: Feynman diagrams relevant for $e^+e^- \to f\bar{f}$ involving the Higgs-fermion coupling.

5.1. THE FORWARD BACKWARD ASYMMETRY

It is straightforward to calculate the forward backward asymmetry of heavy quarks* in the parton model in closed form (see e.g. Refs. 37, 38). Since it depends on the quark mass it is subject to the corresponding uncertainty and in addition to QCD corrections which are available to $\mathcal{O}(\alpha_s)$ [39]. To perform this measurement the heavy meson has to be reconstructed or at least the the proper combination of jets or prompt leptons has to be collected. (Fig. 5.2.) Any such measurement will therefore depend to some extent on nonperturbative physics from hadronisation and jet reconstruction.

To avoid these complications one might look right away for asymmetries of the decay products, e.g. of prompt leptons, as has been done for $e^+e^- \to b(\to e^-)+\bar{b}(\to e^+)$. However, compared to the $b\bar{b}$-case the boost is far smaller which then leads to a large spillover of decay products into the opposite hemisphere. These lepton asymmetries will in addition depend strongly on quark spin asymmetries through correlations between the lepton direction and the quark spin such that the sign of quark and lepton asymmetries is in some cases even reversed (Fig. 5.3.). A cut on

*For a detailed discussion of the forward backward asymmetry with light quarks and polarized beams see Ref. 36.

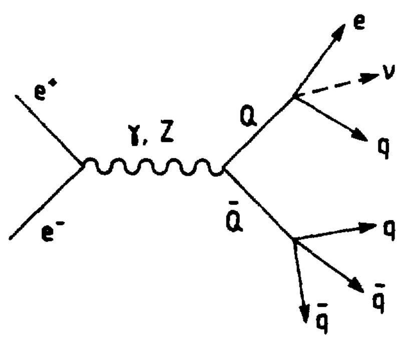

Fig. 5.2: Production and subsequent decay of heavy quarks in e^+e^--annihilation.

lepton energies reduces the spill-over, it leads, however, to a distortion of the asymmetry at the same time [40]. The measurement of the forward backward asymmetry with heavy quarks will therefore lead to interesting results on heavy quark decay properties and hadronization and a crude determination of quark couplings, but will not test radiative corrections.

5.2. ASYMMETRIES ON TOPONIUM

The situation is far more favourable for asymmetry measurements on a toponium resonance. The relative strength of electromagnetic and neutral current amplitudes is independent of the toponium wave function and of QCD corrections, such that a true precision test is at hand. Various measurements have been proposed which however, all determine basically the same quantity:

1. The left-right asymmetry A_{LR} that can be measured with polarized beams [41].
2. The forward backward asymmetry in μ-pairs A^{μ}_{FB} or in other fermion-pairs that is given by $A^{\mu}{}_{FB} = \frac{3}{4}A^2_{LR}$.
3. The forward backward asymmetry of leptons from the semileptonic decay of a quark inside toponium. These leptons may serve to analyse the polarization ($= A_{LR}$) of the bound state which is given by $\frac{1}{2}\frac{1+f}{2}A_{LR}$ with $f = \frac{1}{2}$. [42].

Depending on the toponium mass, on potential technical developments to reduce the beam energy spread and on the integrated luminosity available for toponium

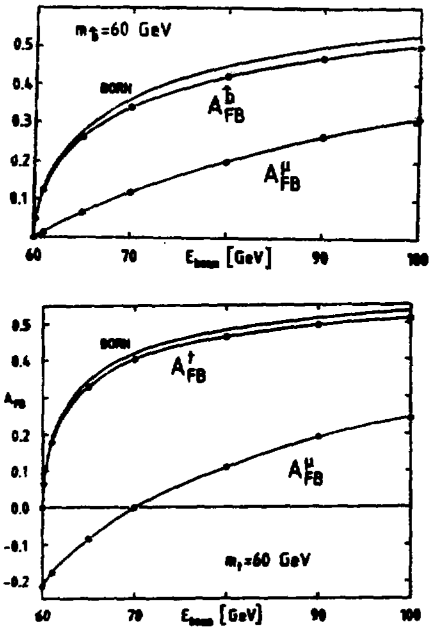

Fig. 5.3: Asymmetry parameters for top and b', with and without initial state radiation. Also shown is the asymmetry of prompt muons from the quark decay. (From [40].)

physics the asymmetry A_{LR}^{θ} can be determined to an accuracy between 0.02 and 0.1 [43, 38]. This suggests that radiative corrections are of relevance for this reaction. The following results have been obtained [8]:

The corrections do depend on the Yukawa couplings through the diagrams depicted in Fig. 5.1. The corrections to the lowest order result can be written in the form

$$A_{RL}^{\theta} = A_{RL}^{\theta}(\text{Born})(1 + \alpha f(m_W, m_Z, m_H, m_t) + \alpha\alpha_s\, \hat{f}(m_W, m_Z, m_H, m_t)) \quad (5.1)$$

and the function f has been calculated. The corrections are typically a few $\times 10^{-2}$, and so is the dependence on m_H (Fig. 5.4).

The next term in the expansion is of order $\alpha\alpha_S$ and originates from the combined electroweak and QCD corrections and has not been calculated. These corrections originate from diagrams like the one depicted in Fig. 5.5 and do not lead to large logarithms. Pure QED corrections from initial or final state radiation do not affect the result.

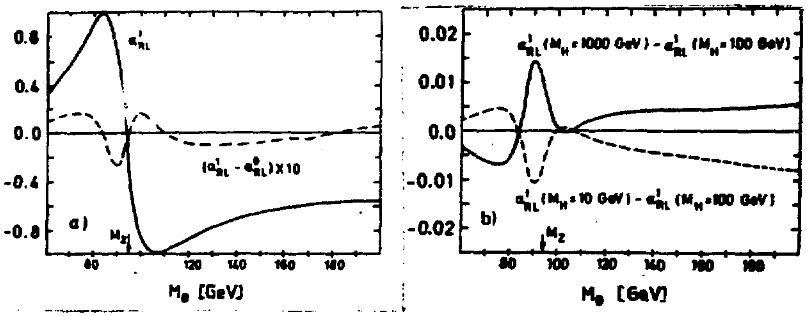

Fig. 5.4: (a) Prediction for the polarization asymmetry as a function of the toponium mass for M_H = 100 GeV and M_Z = 94 GeV. Solid line: full one-loop correction. Dashed line: difference between first-order and lowest order prediction.

(b) Change in the asymmetry, $\alpha_{RL}(M_H) - \alpha_{RL}(100\ \mathrm{GeV})$, for a Higgs mass of 1000 GeV (solid line) and 10 GeV (dashed line), including the variation of the Weinberg angle.

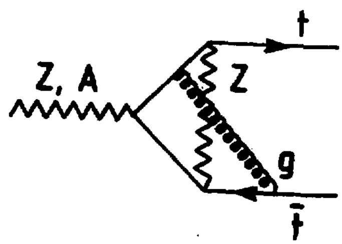

Fig. 5.5: Generic diagram giving rise to corrections of order $\alpha\alpha_s$.

6. Summary

The determination of M_W to 100 MeV and of A_{LR} to 3×10^{-3} accuracy would be complementary to the precision planned for M_Z. Theoretical predictions are under control to this level of accuracy, also for hadronic final states. The optimal place for an accurate determination of heavy quark coupling is toponium. Such a measurement is sensitive to physics not accessible anywhere else.

ACKNOWLEDGEMENTS

I am indebted to B. Grządkowski, Z. Hioki, S. Jadach, P. Krawczyk, R. Stuart, Z. Wąs and P. Zerwas for enjoyable collaborations on various topics treated in this report. Instructive discussions on experimental techniques at LEP with A. Blondel and W. Blum have strongly stimulated my interest in this field. Last but not least I would like to thank the organizers of the "X. Warsaw Symposium on Elementary Particle Physics" at Kazimierz and of the "Workshop on Topical Problems of Testing the Standard Model" at Budapest for their kind hospitality.

REFERENCES

[1] A. Sirlin, Plenary Talk at the International Symposium on Lepton and Photon Interactions at High Energies, Hamburg 1987.

[2] P. Jenni, Plenary Talk at the International Symposium on Lepton and Photon Interactions at High Energies, Hamburg 1987.

[3] P. Jenni, invited talk at the LEP 200 Workshop, Aachen 1986.

[4] P. Roudeau, Report of the W Mass Study Group, LEP 200 Workshop, Aachen 1986, J. Bijnens et al., Orsay preprint LAL 87-07.

[5] G. Alexander et al., Polarized e^+ and e^- Beams at LEP, Working Group Report, CERN/LEPC/87-6.

[6] G. Altarelli et al., in "Physics at LEP", CERN Report 86-02 (1986).

[7] CHARM II proposal, G. Busi et al., CERN/SPS C/83-24 (1983).

[8] B. Grzadkowski, P. Krawczyk, J.H. Kühn and R.G. Stuart, *Phys. Lett.* **163 B** (1985) 247, *Phys. Lett.* **176 B** (1986) 456, *Nucl. Phys.* **B 281** (1987) 18.

[9] Report of the Study Group on "Electroweak Radiative Corrections at LEP Energies", LEP 200 Workshop, A. Barroso et al., CERN-EP/87-70.

[10] B. Lynn, M. Peskin and R.G. Stuart, in "Physics at LEP", CERN Report 86-02 (1986).

[11] F. Jegerlehner, *Z. Phys.* **C 32** (1986) 195.

[12] A. Sirlin, *Phys. Rev.* **D 29** (1987) 89.

[13] F. Hollik and W. Timme, *Z. Phys.* **C 33** (1986) 125,
F. Jegerlehner, *Z. Phys.* **C 32** (1986) 425.

[14] E.A. Kuraev and V.S. Fadin, Sov. J. Nucl. Phys. 41 (1985) 466.

[15] G. Altarelli and G. Martinelli, in "Physics at LEP", CERN Report 86-02 (1986).

[16] G. Bonneau and F. Martin, *Nucl. Phys.* **B 27** (1971) 381.

[17] F.A. Berends, G.J.H. Burgers and W.L. van Neerven *Phys. Lett.* **185 B** (1987) 395.

[18] B. Grzadkowski, Z. Hioki and J.H. Kühn, Preprint MPI-PAE/PTh 47/87.

[19] K. Hagiwara and D. Zeppenfeld, Preprint KEK-TH-1963.

[20] S. Jadach, J.H. Kühn, R.G. Stuart and Z. Was, Preprint MPI-PAE/PTh 71/87.

[21] B. W. Lynn and C. Verzegnassi, *Nuovo Cimento* **94A** (1986) 15;
B. W. Lynn and C. Verzegnassi, *Phys. Rev.* **D 35** (1987) 3326.

[22] D.W. Duke and R. G. Roberts, *Phys. Rep.* **120C** (1985) 277.

[23] B.W. Lynn and R.G. Stuart, *Nucl. Phys.* **B 253** (1985) 216;
B.W. Lynn, M.E. Peskin and R.G. Stuart, In "Physics at LEP", CERN 86–02, eds. J. Ellis and R. Peccei. (1986) 90;
M. Böhm, W. Hollik and H. Spiesberger, *Z. Phys.* **C27** (1985) 523.

[24] S. Güsken, J.H. Kühn and P.M. Zerwas, *Phys. Lett.* **155 B** (1985) 185.

[25] J. H. Kühn and R.G. Stuart, MPI-PAE/PTh 53/87.

[26] G. Bonneau and F. Martin, *Nucl. Phys.* **B 27** (1971) 381.

[27] I. B. Kriplovich, *Sov. J. Nucl. Phys.* **17** (1973) 298;
R.W. Brown, V.K. Cung, K.O. Mikaelian and E.A. Paschos, *Phys. Lett.* **43 B** (1973) 403.

[28] Z. Wąs, Cracow Preprint TPJU-11/86; to appear in *Acta Phys. Polon.*

[29] M. Böhm and W. Hollik, *Nucl. Phys.* **B 204** (1982) 45;
R. W. Brown, R. Decker and E. A. Paschos, *Phys. Rev. Lett.* **52** (1984) 1192.

[30] S. Jadach, R. G. Stuart and Z. Wąs, KORALZ, Monte Carlo program for τ and μ pair production at LEP/SLC, (August 1987) unpublished.

[31] R. Kleiss, B. W. Lynn, R. G. Stuart, BREMUS Monte Carlo program, (January 1987) unpublished.

[32] R.G. Stuart and A. Góngora-T., MPI-PAE/PTh55/87, July 1987.

[33] C. Y. Prescott, SLAC Technical note SLAC-TN-73-1 (1973).

[34] ALEPH Collaboration, In "Polarized e^+e^- Beams at LEP", unpublished report CERN/LEPC/87 - 6 (1986).

[35] T.D. Lee and M. Nauenberg, Phys. Rev. **133** (1964) 1549.

[36] A. Blondel, B.W. Lynn, F.M. Renard and C. Verzegnassi, preprint Montpellier PM/87-14 (1987).

[37] J.H. Kühn, A. Reiter and P.M. Zerwas, *Nucl. Phys.* **B 272** (1986).

[38] P. Igo-Kemenes et al., Report of the Study Group on Heavy Quarks and Leptons, LEP 200 Workshop, Aachen 1986, CERN-EP/87-49.

[39] J. Jersak, E. Laermann and P.M. Zerwas, *Phys. Lett.* **98 B** (1981) 363.

[40] S. Jadach and J.H. Kühn, *Phys. Lett.* **191 B** (1987) 313.

[41] I.I.Y. Bigi, J.H. Kühn and H. Schneider, Preprint MPI-PAE 28/78 1978; J. Bernabèu and P. Pascual, *Nucl. Phys.* **B 172** (1981) 93; L.M. Sehgal and P.M. Zerwas, *Nucl. Phys.* **B 183** (1981) 417.

[42] J.H. Kühn and K.H. Streng, *Nucl. Phys.* **B 198** (1982) 71.J. H. Kühn and R. G. Stuart, *Phys. Lett.* **190 B** (1987) 208.

[43] W. Buchmüller et al., Study Group on "Toponium Physics at LEP", MPI-PAE/PTh 85/85 and CERN Report 86-02.

New Results from the UA5/2-Experiment[1]

Ch. Geich-Gimbel

Physikalisches Institut der Universität Bonn, Fed. Rep. of Germany

1. Introduction

This talk will cover recent results from the investigation of $p\bar{p}$-interactions at $\sqrt{s} = 200$ and 900 GeV with a streamer chamber detector (UA5/2-experiment) [1] at the CERN SPS Collider. Last year at the same occasion results on cross section measurements, diffraction dissociation, multiplicity distributions, forward-backward multiplicity correlations and on the search for Centauro-like events were presented [2].

Meanwhile the UA5-Collaboration has published the results on cross section measurements [3], diffraction dissociation [4] and the Centauro question [5]. The investigation of multiplicity distribution is not finalized, for the time being there is no new information available. Hence I will concentrate on correlation studies, i.e. forward-backward correlations and two-particle pseudorapidity correlations, on strange particle production, strangeness suppression and on the 'typical' event, i.e. the particle composition of an average non-single diffractive (NSD) event.

The data these preliminary results are based upon were taken during a very successful run of the pulsed $p\bar{p}$-Collider at CERN in spring 1985. The UA5/2 detector [6] took 115.000 streamer chamber pictures and 500.000 electronic events (i.e. only containing information from the trigger hodoscopes and the hadron calorimeter), mainly at the flat bottom at 100 GeV beam energy and the four seconds flat top at 450 GeV of the cycle, see fig. 1.

The UA5/2-detector consists of two large streamer chambers ($6 \times 1.25 \times 0.5\,m^3$ visible volume), placed above and below the 2 mm thick beryllium beam pipe[2], see fig. 2. The azimuthal coverage of the chambers is 95% for a pseudorapidity [3] $|\eta| \leq 3$. At each end of the chamber there is a pair of trigger hodoscopes covering a pseudorapidity range of $2 < |\eta| < 5.6$. For further details of the UA5 detector system see [1,6].

2. Correlation Studies

For any finite positive value of the parameter k of a *Negative Binomial Distribution* (NegBin)[4]

$$P(n;\bar{n},k) = \binom{n+k-1}{n} \left(\frac{\bar{n}/k}{1+\bar{n}/k}\right)^n \frac{1}{(1+\bar{n}/k)^k} \tag{2.1}$$

the dispersion

$$D_2^2 = \bar{n}(1+\frac{\bar{n}}{k}) \tag{2.2}$$

[1] Bonn-Brussels-Cambridge-CERN-Stockholm Collaboration

[2] For part of the run, an additional photon converter plate was introduced between the beam pipe and the upper streamer chamber to increase the photon detection efficiency at large production angles.

[3] $\eta = -\ln\tan\Theta/2$

[4] where confusion could arise we distinguish k_{cl} and k_{NB}, denoting cluster sizes k and the shape parameter k of the negative binomial distribution by appropiate subscripts.

is larger than that for a pure Poisson distribution where $D_2^2 = \bar{n}$. It has been found that at Collider energies charged multiplicity distributions may well be described by NegBins, obtaining values for the parameter k of 4.6 ± 0.4, 3.69 ± 0.09 and 3.2 ± 0.2 at $\sqrt{s} = 200$, 546 and 900 GeV, resp. [7].

Thus one may conclude onto the presence of *correlations* in the production of charged particles, which broaden the multiplicity distribution. Also, the investigation of correlations may provide a deeper understanding of the dynamics of multi-particle production.

2.1. *Forward-Backward Multiplicity Correlations*

The problem of forward-backward correlations concerns the fluctuations in the number of particles going to either c.m.s hemisphere, n_F and n_B, at an overall charged multiplicity

$$n_S = n_F + n_B \quad . \tag{21.1}$$

The two-dimensional n_F versus n_B distributions of minimum bias $p\bar{p}$ data are shown in fig. 3 for $\sqrt{s} = 200$, 546 and 900 GeV [8,9].

There are two equivalent ways to measure the correlation strength: one may compute the average number of backward going particles at a fixed number of forward going particles to obtain the correlation coefficient b by a straight line fit

$$< n_B(n_F) > = a + b \cdot n_F \, . \tag{21.2}$$

Alternatively, the linear regression (with unit weight to all events) leads to the correlation coefficient

$$b = \frac{\mathrm{cov}(n_B, n_F)}{\sqrt{\mathrm{var}(n_B)\mathrm{var}(n_F)}} = \frac{< (n_F - < n_F >) > \cdot < (n_B - < n_B >) >}{\sqrt{< (n_F - < n_F >)^2 > \cdot < (n_B - < n_B >)^2 >}} \, . \tag{21.3}$$

The linear relation (eq. 21.2) remarkably well describes the $p\bar{p}$ data at the Collider, see fig. 4 [8,9].

Equation (21.3) may further be developed, such that the correlation coefficient b only depends on the second moments (fluctuations) of the marginal distribution of the combined multiplicity n_S [8,10], finally leading to (eq. 21.5) below, as follows.

Formally, for each combined charged multiplicity n_S there exists a distribution $f_S(n_F)$ and its moments, describing the probability of finding events with n_F going into the forward region F, where as an appropiate choice

$$F := (0 \leq \eta \leq 4) \, , \; B := (-4 \leq \eta \leq 0) \, . \tag{21.4}$$

As an example, fig. 5 shows the $f_{12}(n_F)$ distribution, obviously excluding a binomial distribution, which would follow, if each *single* particle has a probability $p = 1/2$ to fall into either hemisphere, from random emission of *individual* particles along the (pseudo-) rapidity axis. This holds true at all Collider energies; an *assumed binomial* distribution is too narrow to describe the data.

Averaging over all n_S, with D_S^2 as the variance of the multiplicity distribution and $d_S^2(n_F)$ being the variance at a given value of n_S, the following identity emerges[5]

$$b = \frac{\frac{1}{4}D_S^2 - < d_S^2(n_F) >}{\frac{1}{4}D_S^2 + < d_S^2(n_F) >} \, . \tag{21.5}$$

[5] *If in eq. (21.3) one first sums over all events at fixed n_S, then over the n_S-distribution, formula (21.5) results [11].*

As in an ISR analysis [12] also at $\sqrt{s} = 546$ GeV [13,14] a different definition of the forward and backward regions was applied, namely

$$F := (1 \leq \eta \leq 4), \; B := (-4 \leq \eta \leq -1), \quad (21.6)$$

leaving a central gap of $\delta\eta = 2$ between the two regions. The motivation was to decouple this correlation study from short range correlation effects, which trivially may arise from *resonances*, emitting their decay products simultaneously into either region.

Quantitatively, the condition (21.6) lowers the correlation coefficient to $b = 0.41 \pm 0.01$, instead of getting $b = 0.54 \pm 0.01$ at $\sqrt{s} = 546$ GeV [13], when the two regions are in contact (condition 21.4). The corresponding values at the other Collider energies [8] are given in table 1, including an updated figure for b at $\sqrt{s} = 546$ GeV, based on a roughly doubled number of events[6].

Table 1	Correlation Strength b		
η-interval	$\sqrt{s} = 200$ GeV	$\sqrt{s} = 546$ GeV	$\sqrt{s} = 900$ GeV
$\lvert\eta\rvert \leq 4$	0.48 ± 0.02	0.58 ± 0.01	0.63 ± 0.02
$1 \leq \lvert\eta\rvert \leq 4$	0.32 ± 0.02	0.44 ± 0.01	0.49 ± 0.02

In fact, it is the presence of a positive correlation strength even in the case of a gap between the control regions (condition 21.6), which calls for the existence of so-called *long range correlations* in rapidity space in the particle production. The strength of these correlations increases with c.m. energy, see fig. 6, about linearly, i.e. $b = d + c \cdot \ln s$. *They were already seen at highest ISR energies in experiment* R701 [12], though with a much smaller correlation strength.

The correlation coefficient cannot exceed 1 by definition. To test for deviations from linearity we therefore also tried adding a quadratic term, i.e. $b = \alpha + \beta \cdot \ln s + \gamma \cdot \ln^2 s$. The contribution of the quadratic term however is small in the energy range considered. Consequently, up to $\sqrt{s}$ 900 GeV the rise of the correlation strength with c.m. energy is still compatible with a linear ln s behaviour, *indicating no saturation*. The result of a least squares fit for the linear parametrisation is $d = -0.184 \pm 0.016$, $c = 0.061 \pm 0.002$ for the full range and $d = -0.380 \pm 0.019$, $c = 0.065 \pm 0.002$ when a gap is introduced [8] (s in units of GeV^2).

2.2. Correlations and the Cluster Model

For the physical interpretation of the correlations observed different assumptions may be distinguished. In the case of independent *single* particle production, i.e. having a binomial distribution with $p = 1/2$ for a particle to fall into either hemisphere, one obtains $d_S^2(n_F) = p(1-p)n_S = 1/4\, n_S$, and with the measured values of $< n_S > = 16.0 \pm 0.2$ and $D_S = 8.8 \pm 0.1$ (for a $\delta\eta = 2$ gap at 540 GeV [15]), thus $b = 0.66$, in contradiction to a measured slope parameter of $b = 0.42 \pm 0.01$.

If instead of single particles, *groups* of them, or small-sized *clusters* [16] (tacitly including resonances resonances[7]), are randomly emitted, a *much better description of the data* may be reached[8].

[6] In this more recent analysis of $p\bar{p}$ data at $\sqrt{s} = 546$ GeV corrections were made for acceptance and trigger efficiency. The net effect of these corrections is smaller than 0.02 in terms of the slope parameter b [8,9].

[7] which on their own would not be sufficient to explain the measured mean charged cluster size $< k >$ of about 2.2, since from the spectrum of low-mass resonances (and prompt hadrons) one obtains $< k >$ of about 1.4 [8]

[8] Independent of multiplicity correlation studies it had been argued from several experiments that the final state particles in hadronic interactions are likely to group in 'Clusters' over a relatively small range of rapidity [17-19].

Assuming a fixed cluster size k one would get $d_S^2(n_F) = p(1-p)kn_S = 1/4\,kn_S$, or

$$k = 4\,d_S^2(n_F)/n_S \quad , \tag{22.1}$$

hence

$$b = \frac{D_S^2/<n_S> - k}{D_S^2/<n_S> + k} \quad . \tag{22.2}$$

This picture is still unrealistic, as the cluster size may vary, at least due to various decay multiplicities of known resonances. Under the assumption of clusters of mixed size the cluster size k in eq. (22.2) turns into an effective cluster size k_{eff} [20]

$$k_{eff} = <k> + \mathrm{var}(k)/<k> \quad , \tag{22.3}$$

which is a function of the first two moments of the (unknown) cluster decay multiplicity. Equation (22.2) finally becomes

$$b = \frac{D_S^2/<n_S> - k_{eff}}{D_S^2/<n_S> + k_{eff}} \quad . \tag{22.4}$$

This quantity $4\,d_S^2(n_F)/n_S = k_{eff}$ is plotted in fig. 7 for different c.m. energies and different spans $\Delta\eta$, in dependence of the overall charged multiplicity n_S in the intervals considered. It appears that, provided the multiplicity n_S is large enough as well as the interval $\Delta\eta$, the effective cluster size saturates at $k_{eff} \simeq 2.5$, also independent of the c.m. energy. As for smaller intervals and/or smaller multiplicities the relative probability for clusters to emit particles outside the control regions (leakage effects) is enhanced, naturally smaller values for k_{eff} emerge.

The curves in fig. 7 represent the results of Monte Carlo simulations, based on independent cluster emission (UA5 Cluster-Monte-Carlo [6,21]). There for the charged cluster decay multiplicity a truncated Poisson distribution was input, with $<k> \simeq 1.8$, resulting in $k_{eff} \simeq 2.6$.

This result ties in with the conclusions drawn from the analysis of two-particle pseudorapidity correlations [22] at $\sqrt{s} = 540$ GeV and also with earlier ISR results [23], where compatible values for k_{eff} were obtained.

2.3. Variation of the Central Gap Size and Position

A further investigation of the nature of long range multiplicity correlations has been carried out by determining the slope b between two regions in pseudorapidity that are one unit wide ($|\,\eta_2^{F,B} - \eta_1^{F,B}\,| = 1$) and separated by a central gap $\delta\eta^{F,B} = |\,\eta_1^F - \eta_1^B\,|$ of varying size. Furthermore we have studied the behaviour of the correlation coefficient for fixed forward/backward intervals of one unit in η decoupled by a gap of fixed size of 2 units in η, and moving the center of the separating gap from η=0 towards η=2.

As is shown in figure 8, where the slope b is plotted as a function of the size of the central pseudorapidity gap for 200, 546 and 900 GeV, the correlation strength decreases monotonically as the gap size is increased. The observed behaviour of b for different gap sizes are in agreement with model predictions [24,25], and is also well reproduced by the UA5 cluster Monte Carlo program [6,21] (illustrated by the curves in figure 8). In this Monte Carlo program first the charged multiplicity of the event is drawn from a negative binomial distribution and then the cluster decay multiplicity from a Poisson distribution with a mean value of ~2.3 charged particles/cluster, whereas the number of clusters is determined by the charged multiplicity of the event and the clusters are randomly distributed along the rapidity axis. Therefore the observed long range multiplicity correlations can be understood in our cluster Monte Carlo program as a result of correlated cluster emission. whereas the correlations between clusters are forced by the multiplicity distribution.

Figure 9 shows the correlation coefficient as a function of the central gap (being two units of pseudorapidity wide) position at 200, 546 and 900 GeV. The correlation strength decreases when shifting the center of the gap towards 2, but does not vanish. Thus we observe strong positive correlations of long range within one c.m. hemisphere.

2.4. Two-Particle Pseudorapidity Correlations

A different approach to correlations in particle production is obtained by the study of *two-particle (pseudo-) rapidity correlations* [16,26]. This approach requires the introduction of some supplementary variables.

Besides the one-particle pseudo-rapidity density

$$\rho^1(\eta) = 1/\sigma \, d\sigma/d\eta \,, \tag{24.1}$$

one similarly defines a two-particle pseudorapidity density *

$$\rho^2(\eta_1,\eta_2) = 1/\sigma \, d^2\sigma/d\eta_1 d\eta_2 \tag{24.2}$$

with the normalisations

$$\int_{-\infty}^{+\infty} \rho^1(\eta)\, d\eta = < n_{ch} > \tag{24.3}$$

$$\int_{-\infty}^{+\infty}\int_{-\infty}^{+\infty} \rho^2(\eta_1,\eta_2)\, d\eta_1 d\eta_2 = < n_{ch}(n_{ch}-1) > \,. \tag{24.4}$$

The definition of the *correlation parameter* (i.e. the second Mueller moment [27])

$$f_2 = < n_{ch}(n_{ch}-1) > - < n_{ch} >^2 \tag{24.5}$$

then leads to the construction of the *two-particle correlation function*

$$C(\eta_1,\eta_2) = \rho^2(\eta_1,\eta_2) - \rho^1(\eta_1)\rho^1(\eta_2) \,. \tag{24.6}$$

For the case of uncorrelated particle production the two-particle density factorizes

$$\rho^2_{uncorr.}(\eta_1,\eta_2) = \rho^1(\eta_1)\rho^1(\eta_2) \,, \tag{24.7}$$

whence $C(\eta_1,\eta_2)$ (eq. 24.6) vanishes likewise.

In connection with this correlation analysis it should be remembered that the multiplicity distributions were well described by negative binomials [7], where

$$f_2 = < n_{ch} >^2 / k \tag{24.8}$$

and for the shape parameter k *finite* (and positive) values were obtained.

In the past this formalism has been used in various analyses at the ISR [12,23,28], proving the existence of both short range and long range correlations in particle production. In terms of specific cluster models their relevant parameters, i.e. the decay multiplicity and decay width became accessible [16,29].

---

* *read rho-two for* ρ^2

2.4.1. *Inclusive Charged Particle Rapidity Correlations*

The inclusive correlation function $C(0, \eta_2)$ (η_1 fixed at $\eta = 0$) for $\sqrt{s} = 200$, 546 and 900 GeV is shown [1] in fig. 10a and for comparison the analogous quantity for $\sqrt{s} = 63$ GeV [19,23a] is included.

The striking increase of the height of the correlation function is to be expected as $D^2/ < n >$ (hence $D^2 - < n > = f_2$) has been found to increase strongly with the c.m. energy [7,30] – a behaviour which was discussed as a *broadening* of the multiplicity distribution (and KNO scaling violations).

Originally, in the context of two-component models [16,29,31,32], the correlation function was broken down into terms for intrinsic correlations within each component and a 'crossed' term from the mixing of components. When summing over a range of charged multiplicities n_{ch}, i.e. mixing events of different multiplicities, the inclusive correlation function similarly may be split like [31]

$$C(\eta_1, \eta_2) = C_S(\eta_1, \eta_2) + C_L(\eta_1, \eta_2) \tag{241.1}$$

where the 'short range' correlation term

$$C_S = 1/\sigma \sum_n \sigma_n C_n(\eta_1, \eta_2) \tag{241.2}$$

is related to the semi-inclusive function C_n at fixed multiplicity and where a 'long range' correlation term

$$C_L = 1/\sigma \sum_n \sigma_n [\rho^1(\eta_1) - \rho^1_n(\eta_1)] [\rho^1(\eta_2) - \rho^1_n(\eta_2)] \tag{241.3}$$

arises from the mixing of events, which have different pseudorapidity densities. In these formulae the index n denotes a fixed charged particle multiplicity and the corresponding one-particle densities.

The long range contribution, shown in fig. 10b as $C_L(0, \eta_2)$, only sums the products of the differences between the inclusive and semi-inclusive one-particle densities, and consequently depends on the shape of the multiplicity distribution. This term differs from zero even in absence of 'true' correlations [23a]. It broadens the correlation function and is often (misleadingly) called 'long-range' correlation term, masking dynamical correlations, which are present only in the C_S-term ('short-range'), as it is the only one which contains two-particle densities (eq. 241.2).

The determination of the pure short range correlation component wanted, $C_S(\eta_1, \eta_2)$, see fig. 10c, which is sharply peaked (hence 'short-range'), proceeds via a measurement of semi-inclusive pseudorapidity densities to obtain $C_L(\eta_1, \eta_2)$ (eq. 241.3). Then one may calculate [2], according to eq. (241.1),

$$C_S(\eta_1, \eta_2) = C(\eta_1, \eta_2) - C_L(\eta_1, \eta_2) \; . \tag{241.4}$$

The remaining short range contribution is usually fitted by the sum of a Gaussian and a residual background term proportional to the product of single particle densities,

$$C_S(\eta_1, \eta_2) = \frac{< k(k-1) >}{< k >} \cdot \frac{\rho^1(\frac{\eta_1+\eta_2}{2})}{2\sqrt{\pi}\delta} \cdot \exp\left(-\frac{(\eta_1 - \eta_2)^2}{4\delta^2}\right) - A \rho^1(\eta_1)\rho^1(\eta_2) \, , \tag{241.5}$$

where, within the framework of a cluster model, k is related to the decay multiplicity of the clusters and δ their decay width.

---

[1] corrected for streamer chamber and trigger acceptance [6]

[2] This is one reliable way to measure C_S, as it avoids the uncertainties in correcting measured semi-inclusive two-particle densities, which were needed if one followed eq. (241.2) and eq. (24.6) in its semi-inclusive form to measure C_S. The results of the alternative procedure, see the next section, are given in table 3.

In such an inclusive investigation of two-particle correlations one obtained for the cluster decay moment $\frac{<k(k-1)>}{<k>}$, which is linked to the effective cluster size k_{eff} (eq. 22.3) by

$$\frac{<k(k-1)>}{<k>}+1 = \frac{<k^2>-<k>^2+<k>^2}{<k>} = <k> + \mathrm{var}\, k/<k> = k_{eff} \qquad (241.6)$$

a value of ≈ 1.5 and for the decay width $\delta \approx 0.7$ at $\sqrt{s} = 546$ GeV [33]. These figures agreed quite well to ISR results at $\sqrt{s} = 53$ GeV [23b], and even to corresponding investigations at the FNAL [34]. The respective inclusive results on δ and $k_{eff} = \frac{<k(k-1)>}{<k>}+1$ at $\sqrt{s} = 200$ and 900 GeV and updated ones at $\sqrt{s} = 546$ GeV [8] are given in table 2.

Table 2	Inclusive Short Range Correlation Fits	
$\sqrt{s}$	δ	$k_{eff} = \frac{<k(k-1)>}{<k>}+1$
ISR 53 GeV	0.67 ± 0.05	2.24 ± 0.20
SPS 200 GeV	0.81 ± 0.08	2.65 ± 0.11
SPS 546 GeV	0.75 ± 0.03	2.65 ± 0.06
SPS 900 GeV	0.74 ± 0.04	2.84 ± 0.10

2.4.2. Semi-Inclusive Charged Particle Rapidity Correlations

The complementary semi-inclusive investigation of two-particle correlations is ideally performed at a given fixed multiplicity, where the C_L part in eq. (241.1) vanishes. On account of limited event statistics a narrow multiplicity band has to be chosen in practice.

In the framework of cluster models [16,29,31] the semi-inclusive correlation functions would also be expressed by a gaussian distribution and a background term (similar to eq. 241.5), being connected to cluster model parameters by

$$\begin{aligned} C_n(\eta_1,\eta_2) \; = \; & \left.\frac{<k(k-1)>}{<k>}\right|_n \cdot \rho_n^1\left(\frac{\eta_1+\eta_2}{2}\right)\cdot \frac{1}{2\sqrt{\pi}\delta_n}\cdot \exp\left(-\frac{(\eta_1-\eta_2)^2}{4\delta_n^2}\right) \\ & - \frac{\rho_n^1(\eta_1)\rho_n^1(\eta_2)}{n}\cdot\left(1+\left.\frac{<k(k-1)>}{<k>}\right|_n\right) \end{aligned} \qquad (242.1)$$

The parameters of the fits (242.1), $k_{eff}-1$ and δ, are shown in fig. 11 and 12, as function of the normalized multiplicity $z = n_{ch}/<n_{ch}>$ for all three Collider energies. For comparison, two sets of semi-inclusive ISR-results on two-particle correlations [23a,23b] at $\sqrt{s} = 44$ and 63 GeV have been added to these figures. A set of examples of such fits to Collider data at $\sqrt{s} = 900$ GeV is shown in fig. 13 for charged multiplicities between 34 and 38, and for fixed η_1 values, subsequently increased in steps of 0.4 units of pseudo-rapidity.

It appears that neither parameter of the Gaussian shaped fits (eq. 242.1, respectively eq. 241.5), describing short range two-particle correlations significantly varies with the overall charged multiplicity (or the normalized multiplicity z), and secondly, perhaps more important, they have – if at all – only slightly increased from ISR to Collider energies, see also tables 2 (for inclusive results) and 3 (weighted averages of semi-inclusive figures). Hence it appears fair to conclude that the clustering mechanism has not changed qualitatively between ISR and Collider energies.

Table 3	Semi-inclusive Fits, averaged	
$\sqrt{s}$	δ	$k_{eff} = \frac{<k(k-1)>}{<k>} + 1$
ISR 44 GeV	≈ 0.7	≈ 2.2
ISR 63 GeV	≈ 0.6	≈ 2.2
SPS 200 GeV	0.81 ± 0.05	2.56 ± 0.15
SPS 546 GeV	0.75 ± 0.03	2.65 ± 0.09
SPS 900 GeV	0.73 ± 0.04	2.63 ± 0.11

2.5. Conclusions on Correlation Studies

The complementary (and independent) analyses of *forward-backward multiplicity correlations* (section 2.1.) and of *two-particle pseudorapidity correlations* (section 2.4.) may jointly be interpreted in terms of a cluster model [16], which assumes independent emission of small sized clusters (which partially may consist of resonances). But these clusters should not be identified with resonances alone, as the mean charged multiplicity of known, light resonances is only in the order of 1.4. Thus, besides resonance production other short range order effects, such as local quantum number compensation, *must be present*.

The average cluster size (charged particles) k_{eff}, being about 2.6 from the forward-backward multiplicity correlation analysis agrees quite well with the results obtained in the (semi-inclusive) two-particle rapidity correlation study, namely $\frac{<k(k-1)>}{<k>} \approx 1.6$ as

$$k_{eff} - 1 = \frac{< k(k-1) >}{< k >} . \tag{25.1}$$

The decay width δ of the clusters (in units of rapidity) is of course not accessible via forward-backward multiplicity correlations, though the size of the gap required for the separation of the two control regions to prevent spill-over from decay products from the same cluster offers some estimate for the decay width.

The apparent approximate energy independence of the cluster size k_{eff} has an implication on the correlation parameter b, as to be seen from eq. (22.2)

$$b = \frac{D_3^2/ < n_s > - k_{eff}}{D_3^2/ < n_s > + k_{eff}} . \tag{25.2}$$

If k_{eff} is about constant (see fig. 11), most of the variation of b with the c.m. energy, see fig. 6, must arise from a variation of $D_3^2/ < n_s >$ with energy, as discussed in [35,36].

In final consequence one would state, as advocated in the introductory remarks to this chapter, that the shape of the multiplicity distribution (broader than Poisson) and positive correlations are two facets of the same phenomenon, whose underlying dynamical origin is well represented by the Cluster model.

3. Kaon Production

In an analysis [37] of kaon production at $\sqrt{s} = 546$ GeV the UA5 collaboration has found a large increase of the average transverse momentum of kaons compared to expectations from ISR data, while other features of kaon production seemed to agree well with extrapolations from lower energies.

From models based on Quantum Chromodynamics (QCD) one would expect [38] that the production of heavier quark pairs would be suppressed relative to lighter pairs. At Collider energies however there is a chance that these mass differences are less important and suppression of heavy quark production would become less pronounced.

For the present analysis a sample of 5162 (3113) events at 900 (200) GeV c.m. energy has been used, allowing for an analysis of strange particle production in $p\bar{p}$ interactions over a large range of c.m. energies with small systematic uncertainties.

Although there was no magnetic field in the streamer chambers, the kinematics of the decay processes $K^0_s \to \pi^+\pi^-$ and $K^\pm \to \pi^\pm\pi^+\pi^-$ can be fully determined using measured angles only. In the present study 192 (60) K^0_S decays have been analysed at 900 GeV (200 GeV) in the rapidity range $|\eta| \leq 3.5$ and 38 (18) $K^\pm$ decays in the range $|\eta| \leq 2.5$.

In fig. 13 we show the corrected lifetime distributions of K^0_S in the rapidity range $|\eta| \leq 3.5$ at $\sqrt{s} = 200$ GeV and 900 GeV. The data are consistent with an expected slope of one as represented by the straight lines and thus provide a useful check of our procedures.

Fig. 14 shows the corrected inclusive transverse momentum spectra (normalized to the number of non single-diffractive events) for kaon data in the range $|y| \leq 2.5$ at three Collider energies. The dependence of inclusive cross sections on p_T is often parametrized by a combination of simple exponentials in p_T. However at the Collider it has been found that the inclusive spectra of hadrons [39-41] and pions [40,41] follow nicely a QCD inspired power law $p_0^n/(p_0 + p_T)^n$ up to very high transverse momenta. Detailed studies of the low p_T part ($p_T \leq 500$ MeV/c) of transverse momentum spectra of pions at the ISR [42] show that they are best described by an exponential in transverse mass $\exp(-bm_t)$, where $m_t^2 = m^2 + p_T^2$. It has also been argued on theoretical grounds [43] that this form is more likely to be correct than an exponential in transverse momentum at low p_T. The lines shown in fig. 14 are minimum χ^2-fits to the form (for details see [48])

$$\frac{1}{\sigma_{NSD}} \cdot \frac{d\sigma}{dp_T^2} = \begin{cases} A \cdot \exp(-b \cdot m_t) & \text{for } p_T \leq 0.4 \text{ GeV/c} \\ A' \cdot \left(\frac{p_0}{p_T + p_0}\right)^n & \text{for } p_T > 0.4 \text{ GeV/c}\,. \end{cases} \tag{3.1}$$

From the fits we calculate the average transverse momenta to be (0.50 ± 0.04) GeV/c at 200 GeV and (0.63 ± 0.03) GeV/c at 900 GeV. These are to be compared with the value of (0.57 ± 0.03) GeV/c found previously [37] at 546 GeV.

The variation of the average transverse momentum with c.m. energy is shown in fig. 15a. We compare lower energy pp data with Collider energy $p\bar{p}$ data - as at Collider energies one expects no difference between pp and $p\bar{p}$ data (as suggested e.g. by the convergence of the total cross sections). One notes that our data suggest an increase with ln s, which is faster than that expected on the basis of ISR data alone. This trend can also be observed when comparing recent UA1 results [44] for the $\langle p_T \rangle$ of charged particles with lower energy pion data.

In non single-diffractive events for K^0_S we find $\rho(0)_{NSD} = 0.14 \pm 0.02$ at $\sqrt{s} = 200$ GeV and 0.19 ± 0.02 at 900 GeV. Correcting for a single diffractive component as described in [37] the central rapidity density of kaons in inelastic $p\bar{p}$ interactions is estimated to be:

$$\rho(0)_{\mathrm{inel}} = \begin{cases} 0.12 \pm 0.02 & \text{at } \sqrt{s} = 200\,\mathrm{GeV} \\ 0.17 \pm 0.02 & \text{at } \sqrt{s} = 900\,\mathrm{GeV}\,. \end{cases}$$

The energy dependence of the central rapidity density of K^0_S in inelastic events is shown in fig. 15b. The lower energy data and our point at $\sqrt{s} = 546$ GeV (0.15 ± 0.02) are taken from [37] and references therein. The central rapidity density is seen to rise slowly with energy. The straight line in fig. 15b shows the result of a linear fit in ln s, given by (units in GeV^2)

$$\rho(0) = (-0.035 \pm 0.002) + (0.015 \pm 0.001)\ln s \quad (\chi^2/NDF = 31.1/14)$$

In table 4 we display the average number of kaons per event and the kaon cross section at 200 and 900 GeV together with our earlier result [37].

Table 4	K^0_S - Production		
	200 GeV	546 GeV	900 GeV
$\langle n_{K^0_S}\rangle_{NSD}$ ($\lvert y\rvert \le 3.5$)	0.73 ± 0.11	0.92 ± 0.07	1.21 ± 0.10
$\langle n_{K^0_S}\rangle_{NSD}$	0.78 ± 0.12	1.10 ± 0.10	1.51 ± 0.13
$\sigma_{\mathrm{inel}}(K^0_S)$ [mb]	(30 ± 5)	(49 ± 5)	(66 ± 7)
$\langle n_{K^0_S}\rangle_{\mathrm{inel}}$	0.72 ± 0.12	1.00 ± 0.10	1.31 ± 0.14

These results, together with data from inelastic pp and $p\bar{p}$ interactions at lower energies and our result at $\sqrt{s} = 546$ GeV (from [37] and refs. therein), are shown in fig. 15c. The curve is a fit to pp data in the range 10 GeV to 63 GeV and to the UA5 results, using a quadratic form [3] in ln s (in units of GeV^2),

$$\langle n\rangle K_{\mathrm{inel}} = (-0.013 \pm 0.011) + (-0.012 \pm 0.003)\ln s + (0.0076 \pm 0.0001)\ln^2 s\,.$$

3.1. The K/π Ratio

The K/π ratio is defined as the ratio of one kind of kaon (e.g. K^0_S) to one kind of pion (e.g. π^0, which is taken as $\frac{1}{2}(\pi^+ + \pi^-)$). It has been found earlier [37] that the K/π ratio rises with c.m. energy, with the ratio estimated in the region $|y| \le 3.5$. The number of pions has been derived using the measured charged particle yield [45,46] in $|\eta| \le 3.5$ from which we subtract the measured rates of $K^\pm$ and estimated yields of $p/\bar{p}$, $\Sigma^\pm$, $\overline{\Sigma^\pm}$, Ξ^-, $\overline{\Xi^-}$ and the contribution from Dalitz pairs.

The K/π ratio has been found to be

$$\begin{aligned} & 0.092 \pm 0.015 \quad \text{at } \sqrt{s} = 200\,\mathrm{GeV} \\ \text{and } & 0.105 \pm 0.010 \quad \text{at } \sqrt{s} = 900\,\mathrm{GeV}. \end{aligned}$$

These results are compared to our result at 546 GeV (0.095 ± 0.009) and to lower energy data [37] and references therein in fig. 15d. Though the situation at the ISR seems somewhat unclear, the K/π ratio appears to rise very slowly with c.m. energy.

[3] It should be mentioned that the form used in fig. 15c may be simply motivated by the fact that both the width and the height of the rapidity distribution increase roughly like ln s.

Finally we give an estimate of the strange quark suppression factor λ, which is defined as the ratio of the numbers of produced $s\bar{s}$ to $u\bar{u}$ or $d\bar{d}$ pairs. Using our K/π ratios and the formulae of Anisovich and Kobrinsky [47] we find at 200 GeV $\lambda = 0.29 \pm 0.05$ and at 900 GeV $\lambda = 0.33 \pm 0.03$ to be compared to our result at 546 GeV of 0.30 ± 0.03 [37].

3.2. Strangeness Suppression and $B^0 - \bar{B}^0$ Mixing

The measured $\lambda_{s\bar{s}}$ value has implications on the conclusions drawn from the recently discovered evidence for substantial $B^0 - \bar{B}^0$ mixing by the UA1 experiment [49] at the Collider and by the ARGUS experiment [50] at DORIS[4]. At this conference $B^0 - \bar{B}^0$ mixing observed at the Collider was discussed by A. Roussarie [54].

Defining the degree of mixing r as

$$r = \frac{\mathrm{Prob}\,(B^0 \to \bar{B}^0)}{\mathrm{Prob}\,(B^0 \to B^0)} \tag{32.1}$$

one approximately has [5,6]

$$r \approx \left(\frac{\Delta M}{\Gamma}\right)^2 \Big/ \left(2 + \left(\frac{\Delta M}{\Gamma}\right)^2\right), \tag{32.2}$$

where

$$\Delta M = m(B^0_{\mathrm{Heavy}}) - m(B^0_{\mathrm{Light}}) \tag{32.3}$$

and

$$\Gamma = \frac{1}{2}\left(\Gamma(B^0_{\mathrm{Heavy}}) + \Gamma(B^0_{\mathrm{Light}})\right), \tag{32.4}$$

$B^0_{\mathrm{Heavy}}, B^0_{\mathrm{Light}}$ being the mass eigenstates.

Oscillations may dominantly occur due to the well known box diagrams [56] with the help of $Q = 2/3$ quarks (u,c,t) between the different neutral B-meson species

$$B^0_d = (\bar{b}d) \leftrightarrow \bar{B}^0_d = (b\bar{d}) \tag{32.5}$$

and

$$B^0_s = (\bar{b}s) \leftrightarrow \bar{B}^0_s = (b\bar{s}). \tag{32.6}$$

In the calculation [57] of the mass differences ΔM_i ($i = d, s$), entering the mixing rate (eq. 32.2), different elements of the (Cabibbo-)Kobayashi-Maskawa matrix [58,59] are involved, namely V_{td} for case (32.5) and V_{ts} for case (32.6), once only the dominant different contributions to ΔM_i are retained, such as t quark exchange.

As V_{ts} is large compared to V_{td}, their ratio being in the order of $1/\lambda$, $\lambda \approx \sin\Theta_c \approx 0.23$ (Cabibbo angle), B^0_s oscillations are likely to be more prominent than B^0_d oscillations. Recent calculations [60] rendered

$$\frac{\Delta M/\Gamma\,(B^0_s)}{\Delta M/\Gamma\,(B^0_d)} = 10 \ldots 40 \ . \tag{32.7}$$

---

[4] Upper bounds for $B^0 - \bar{B}^0$ mixing have been given from the CLEO experiment at Cornell [51], the MARK-2 [52] and the JADE [53] experiments at PETRA.

[5] $\Delta\Gamma(B_H, B_L) \ll \Delta M(B_H, B_L)$ assumed and CP violation neglected.

[6] This formula holds for time integrated quantities, as the time dependence of possible beauty oscillations appears not to be measurable with the present experimental resolution [55]. For maximal mixing i.e. the 'observation' (decay) time $\tau_{decay} = 1/\Gamma$ being much larger than the oscillation time $\tau_{osc} = 1/\Delta M$, the degree of mixing r approaches unity.

From the observed numbers of like and unlike sign dimuons for the parameter χ

$$\chi = \frac{(B^0 \to \bar{B}^0)}{(B^0 \to \bar{B}^0) + (B^0 \to B^0)} . \tag{32.8}$$

the UA1 experiment has obtained $\chi = 0.121 \pm 0.047$ [49b]. The other commonly used variable r (eq. 32.1) is connected to χ by

$$r = \frac{\chi}{1-\chi} . \tag{32.9}$$

Full mixing would correspond to $\chi = 1/2$ or $r = 1$.

Any measured χ-valne (at the Collider) reflects a combination of B_d and B_s transitions, which presumably have quite different oscillation rates (see relation 32.7):

$$\chi = \frac{1}{< BR >} [BR_d\, f_d\, \chi_d + BR_s\, f_s\, \chi_s] \tag{32.10}$$

or

$$\chi = f_d\, \chi_d + f_s\, \chi_s , \tag{32.11}$$

assuming equal branching ratios into muons. The factors f_s, f_d ($f_d = 1/2(1-f_s)$ if $f_d = f_u$, $f_{c,b,t} = 0$) denote the probability for a $\bar{b}$ quark (or a b quark) to pick up a strange or down quark to form a B_s^0 or a B_d^0 meson (resp. antiparticles). These quantities are related to the $\lambda_{s\bar{s}}$ parameter, as e.g. measured by UA5 or by the SFM experiment at the ISR [62], by

$$\lambda_{ss} = \frac{f_s}{\frac{1}{2}(1 - f_s)} . \tag{32.12}$$

As discussed before at the Collider the UA5 experiment has obtained a value of $\lambda_{s\bar{s}} = 0.30 \pm 20\%$, which appears to be quite energy-independent over the $p\bar{p}$ Collider range (including statistical and systematical uncertainties). From lower energies, at the ISR [62a], but at high values of the fragmentation variable z ($z = E_i/\Sigma E_{Had}$), a value of $\lambda_{ss} = 0.50 \pm 0.05$ is inferred by [62b] [7]. Converting these results into f_s values one ends up with $f_s = 0.13 \pm 0.02$, respectively with $f_s = 0.20 \pm 0.02$.

Some effect originates from the f_s, f_d values for the case of inclusive $B^0 - \bar{B}^0$ mixing rates χ, which have to be broken down according to eq. (32.11) into χ_d and χ_s parts. In fig. 16, which is adopted from [55], the central UA1 result ($\chi = 0.121 = f_d\, \chi_d + f_s\, \chi_s$ and one S.D. bands are shown, together with the newest ARGUS result [50] for the two extreme sets of f_s, f_d values [8]. As the intercept on the χ_s axis is χ/f_s, the UA1 result comes closer to the ARGUS result concerning χ_d for smaller f_s values [9].

For completeness the combined results of the UA1 analysis (with the larger f_s value), the ARGUS, CLEO and MARK-2 [49-52] experiments [10] are displayed in fig. 17, taken from [54,55]. The dotted line, first shown by [55] originates from the unitarity bound of the CKM matrix [64], constraining $|V_{td}|$ and $|V_{ts}|$ within in standard model of three families [11]. The remaining allowed region is dotted in fig. 17, demanding almost maximal amount of $B_s^0 - \bar{B}_s^0$ mixing – but being still compatible with three fermion families – unless χ_s will be found to be smaller than say 0.4.

[7] Arguments have been put forward [63] that in connection with $B^0 - \bar{B}^0$ mixing the c.m. energy may be less important for the usefulness of the measured λ_{ss} than the kinematical environment, i.e. the z region, as the produced B-mesons carry, due to their large mass, a substantial fraction of the energy of the surrounding jet [49,55].

[8] In [49,55] 10% of the produced beauty quarks are allowed to hadronize into B-baryons, hence one has $f_s + 2 f_d = 0.9$.

[9] The ARGUS experiment, being the susceptible to B_d^0 oscillations only, as studying B mesons from the $\Upsilon_{4S}(10575)$ decay, which is below $B_s^0\bar{B}_s^0$ threshold, may give results only for χ_d.

[10] The JADE result [53] is less tight on the same quantity as measured by MARK-2.

[11] Implications of $B^0 - \bar{B}^0$ mixing to non-standard models are discussed in [65], see also references therein.

4. The Average Event

Here the knowledge obtained so far on the particle composition of a typical event in inelastic (non-single diffractive, to be precise) $p\bar{p}$ collisions at Collider energies will be summarized.

The information is most complete from the first runs at $\sqrt{s} = 546$ GeV, the corresponding figures from the data taking at $\sqrt{s} = 200$ and 900 GeV are coming in, as the methods to determine inclusive cross sections for specific particles, total multiplicities for charged particles and the like are known and tested. For the UA5 experiment, for which one goal was a rapid survey on particle production at Collider energies [66,67], these methods have been described in various publications, the Monte Carlo programs involved are presented in a dedicated article [21].

Many of the figures given in table 5 (abbreviated from [61]), which contains rates for individual kinds of particles in non-single diffractive events at the Collider, and for comparison, at highest ISR energies, are deduced by indirect methods. This will be explained in detail later, together with individual references. As far as data from the Collider are concerned, they were obtained with the UA5 detector [6,68], unless explicitely stated otherwise. We have to warn the reader that some figures presented in table 5 might well be updated in between now and the printing of these proceedings.

Leading particles (i.e. one baryon and anti-baryon per event, with equal probabilities for proton and neutron) are always excluded from that table. Throughout isospin symmetry is assumed, e.g. to infer $\sigma(p + \bar{p})$ from $\sigma(n + \bar{n})$ measurements. Finally the average number of charged pions is estimated by subtracting all other sources of charged particles from the total charged multiplicity

From table 5 one may notice a discrepancy between $\frac{1}{2}\sigma(\pi^{\pm})$ and $\frac{1}{2}\sigma(\gamma)$ ($= \sigma(\pi^0)$ - assuming all photons originate from π^0 decays). One possible origin of this discrepancy is the production of η mesons, which on average deliver 2.65 more photons than charged pions when decaying. The number of η's given in table 5 has been adjusted to account for the photon excess at each energy [1]. One can not, of course, exclude other sources for this excess of photons, or the interesting case, that for unknown reasons there are more primary π^0's produced than π^+ or π^-.

In the last row of table 5 we have given estimates for the average number of stable particles produced in total, which is at least *fifty* particles at highest Collider energies. Into the term 'stable particles' we have included K, p, n, Λ, Σ, Ξ (and their anti-particles), η and π if not coming from the decay of η mesons. As the Ξ, Σ, Λ and nucleon rates are given inclusively, i.e. not corrected for hyperon decay, one could remove about two particles (nucleons and pions) from the stable particle count.

In a very first approximation, the relative abundance of the different kinds of particles does not change between $\sqrt{s} = 53$ and 900 GeV, if it were not for baryons, whose contribution is quite small at ISR energies, see also table 6.

In table 6 rates for some kinds of particles and particle ratios in their dependence on the c.m. energy are collected. One may notice that surprisingly the relative kaon content in the final state remains constant (within errors) at a level of about 9% - or, when compared to 'direct pions' (as from the bottom part of table 5) does not change much, either.

[1] Concerning the number of η's estimated this way the measured photon yield at $\sqrt{s} = 546$ GeV [69,70] now appears rather high, when compared with the corresponding figures at the other Collider energies, see table 5. The probable reason lies in the photon detection system of the UA5 apparatus itself. The data on which the former photon analysis was based originated from conversions in the corrugated steel beam pipe only, whilst for the newer photon analysis [71] one could make use of a photon converter plate [72,73], which was added in view of the Centauro question.

Table 5	Particle Composition of a Typical $p\bar{p}$ Event				
	ISR	SPS - Collider			
$\sqrt{s}$ [GeV]	53	200	546	900	
Particle Type	$\langle n \rangle$	$\langle n \rangle$	$\langle n \rangle$	$\langle n \rangle$	Remarks
All charged	10.5 ± 0.2	20.4 ± 0.8	28.1 ± 0.9	33.6 ± 1.2	a), b)
$K^+ + K^-$	0.74 ± 0.11	1.34 ± 0.28	2.24 ± 0.16	2.52 ± 0.30	c), d)
$K^0 + \overline{K^0}$	0.74 ± 0.11	1.34 ± 0.28	2.24 ± 0.16	2.52 ± 0.30	e), f)
γ	11.2 ± 0.7	~ 20	33.0 ± 3.0	~ 34	g), h)
$p + \bar{p}$	0.3 ± 0.05	0.63 ± 0.15	1.45 ± 0.16	1.50 ± 0.22	i), j), k), l)
$\Lambda + \overline{\Lambda} + \Sigma^0 + \overline{\Sigma^0}$	~ 0.13	0.41 ± 0.06	0.53 ± 0.11	0.84 ± 0.08	m), n)
$\Sigma^+ + \Sigma^- + \overline{\Sigma^+} + \overline{\Sigma^-}$		0.20 ± 0.03	0.27 ± 0.06	0.42 ± 0.04	o)
$\Xi^- + \overline{\Xi^-}$			0.10 ± 0.03		p)
$e^+ + e^-$	0.14 ± 0.01	~ 0.25	0.41 ± 0.04	~ 0.4	q)
$\pi^+ + \pi^-$	~ 9.2	~ 17.8	23.6 ± 1.0	~ 28.7	r)
η	0.75	0.85	3.5	2.0	s)
$\pi^\pm$ (not from η)	8.8	17.3	21.6	27.6	
π^0 (not from η)	4.4	8.7	10.8	13.8	
Stable particles	~ 16	~ 31	~ 44	~ 53	t)

a) For leading baryons 1.0 has been subtracted.
b) ISR data from [74], compare also [75], $\langle n \rangle = 10.3 \pm 0.1$, resp.; Collider data from [7].
c) Generally we take $\sigma(K^+ + K^-) = \sigma(K^0 + \overline{K^0})$. At $\sqrt{s} = 546$ GeV this relation was experimentally verified [37].
d) ISR data from [76].
e) Collider data at $\sqrt{s} = 546$ GeV from [37].
f) Collider data at $\sqrt{s} = 200$ and 900 GeV from [48].
g) ISR data from [74].
h) Collider data at $\sqrt{s} = 546$ GeV from [6,69], other estimates preliminary [71].
i) Generally we take $\sigma(p + \overline{p}) = \sigma(n + \overline{n})$.
j) ISR (pp) data from [76], *for non-leading protons/anti-protons the measured anti-proton rate was doubled.*
k) Collider data at $\sqrt{s} = 546$ GeV ($p/\overline{p}$) from UA2 [77], extrapolated to full phase space [6].
l) Collider data at $\sqrt{s} = 200$ and 900 GeV from [78], preliminary *values for neutron/anti-neutron production.*
m) $\Sigma^0(\overline{\Sigma^0})$ included in $\Lambda(\overline{\Lambda})$ values from *the Collider* [6,79].
n) *The value given for* $\sqrt{s} = 53$ GeV is estimated from [80].
o) Taking $\sigma(\Sigma^+ + \Sigma^0 + \Sigma^-) = \sigma(\Lambda)$, which includes Σ^0.
p) From [81], assumed same rate for neutral Xi's.
q) Estimated number of Dalitz pairs, calculated from the photon yield and relative branching ratios of π^0.
r) All other (known) sources subtracted from the total charged multiplicity.
s) Calculated from the excess of photons *over* $\pi^\pm$, as suggested in [69,70].
t) Long lived particles including the products of strong decays; hadrons from hyperon decays not subtracted.

The expected increase of heavier flavour production however is provided by a rise of the relative abundance of strange particles, when including hyperons, see table 6. This rise is mostly due to increased strange baryon production, which in turn proceeds in parallel to the baryon production taken as a whole.

So, the most significant variation of the particle content of a typical event, when going from ISR to SPS Collider energies, is the considerable increase of (non-leading) baryon production, while the mechanism of baryon production appears not to be very well understood.

Table 6	Strange Particle and Baryon Content of the Typical Event				
	ISR	SPS - Collider			
$\sqrt{s}$ [GeV]	53	200	546	900	Remarks
	Percentages of Stable Particles				a), b)
Kaons	9.1%	8.8%	10.2%	9.5%	
Baryons	4.9%	6.4%	8.8%	8.6%	
Hyperons	1.2%	2.3%	2.3%	2.9%	c)
	Particle Ratios				d)
Strange Particles/Stable Particles	0.10	0.11	0.12	0.13	
Hyperons/Baryons	0.25	0.36	0.26	0.34	e)
Kaons/Direct Pions	0.11	0.11	0.14	0.12	

a) Into 'Stable Particles', as from table 5, we have included K, p, n, Λ, Σ, Ξ, η and π (if not coming from η).
b) Typical uncertainty 20% of percentages given.
c) Larger uncertainties due to estimates on S = -2 Baryons.
d) Typical uncertainty 20%, except for Hyperon/Baryon ratio.
e) Error at least 30%, see remark c).

5. Summary

In this review of recent UA5 results from $p\bar{p}$-interactions at $\sqrt{s}$ = 200, 546 and 900 GeV, obtained at the CERN SPS Collider, the following points were discussed:

- The findings on correlations strongly favour the independent production of clusters (of mixed size) of particles, giving rise to multi-particle production. For the effective cluster size, which is defined by the first two moments of the cluster decay multiplicity, a value of about 2.5 charged particles is estimated.
- It appears that the strength of 'long-range' multiplicity correlations still increases linearly with ln s; 'short-range' correlations, when interpreted in terms of a cluster model only slightly change between ISR and Collider energies, i.e. the cluster size and decay width are little energy dependent.
- Kaon production has been investigated at all available Collider energies. The average mean transverse momentum rises with c.m. energy, faster than suggested from extrapolations of lower energy data (and faster than with ln s).
- From the K/π ratio (which is found to rise slowly with the energy) for the inclusive strangeness suppression factor $\lambda_{s\bar{s}}$ a value of 0.3 is calculated at Collider energies. This figure has been discussed in the context of beauty oscillations.
- In the investigation of the 'average event', i.e. the final state particle content of non-single diffractive events, it turned out that most remarkably the fraction of baryons amongst the stable particles has about doubled when compared to ISR energies.

References

[1] CERN/SPSC/82-75, SPSC/P184, UA5-Collaboration, 15 October 1982.
[2] C. Geich-Gimbel, IX. Warsaw Symposium on Elentary Particle Physics, Kazimierz, Poland, May 25-31, 1986, Proc., p. 173.
[3] G.J. Alner et al., UA5-Collaboration, Z. Phys. C 32 (1986), 153.
[4] R.E. Ansorge et al., UA5-Collaboration, Z. Phys. C 33 (1986), 175.
[5] G.J. Alner et al., UA5-Collaboration, Phys. Lett. B 180 (1986), 415.
[6] G.J. Alner et al., UA5-Collaboration, submitted to Physics Report.
[7] G.J. Alner et al., UA5-Collaboration, Phys. Lett. B 167 (1986), 476.
[8] UA5-Collaboration, 'Charged Particle Correlations at the Collider', in preparation for submission to Zeitschrift für Physik C, 1987.
[9] B. Holl, UA5-Collab., 6th Int. Conf. on $p\bar{p}$ Physics, Aachen, Germany, June 30 - July 4, 1986; Proc. p. 500.
B. Holl, PhD-Thesis, Bonn University, in preparation.
[10] G. Ekspong, 3rd Top. Workshop on $p\bar{p}$ Collider Physics, Rome, Italy, January 12-14, 1983; eds. C. Bacci and G. Salvini, CERN 83-04 (Yellow Report), 1983; p. 112.
[11] G. Ekspong, UA5-Collaboration, UA5-Memo A, Oct. 1982.
[12] S. Uhlig et al., Nucl. Phys. B 132 (1978), 15.
[13] K. Alpgård et al., UA5-Collaboration, Phys. Lett. B 123 (1983), 361.
[14] B. Eckart, XVIII. Rencontre de Moriond, La Plagne, March 19-25, 1983; ed. J. Tran Thanh Van, Editions Frontières, Gif-sur-Yvette, 1983; p.155.
[15] G.J. Alner et al., UA5-Collaboration, Phys. Lett. B 160 (1985), 193.
[16] E.L. Berger, Nucl. Phys. B 85 (1975), 61.
[17] G. Giacomelli and M. Jacob, Phys. Rep. 55 (1979), 1.
[18] J. Whitmore, Phys. Rep. 27 (1976), 187.
[19] L. Foa, Phys. Rep. 22 (1975), 1.
[20] G. Ekspong, Proc. of the 3rd Topical Workshop on Proton-Antiproton Collider Physics, CERN Yellow Report 83-04, 1983, p. 112.
[21] G.J. Alner et al., UA5-Collab., CERN-EP/86-213, Dec. 1986 ('The UA5 High Energy $p\bar{p}$-Simulation Program'); Nucl. Phys. B 291 (1987), 445.
[22] B. Eckart, XVIII. Rencontre de Moriond, La Plagne, March 19-25, 1983; ed. J. Tran Thanh Van, Editions Frontières, Gif-sur-Yvette, 1983; p.155.
K. Böckmann and B. Eckart, XV. Int. Symp. on Multiparticle Dynamics, Lund, Sweden, June 10-16, 1984; Bonn University, BONN-HE-84-22.
[23] S.R. Amendolia et al., Nuovo Cimento 31A (1976),17.
D. Drijard et al., Nucl. Phys. B 155 (1979),269.
W. Bell et al., Z. Phys. C 22 (1984),109.
[24] A. Capella and J. Tran Thanh Van, Z. Phys. C 18 (1983), 85.
[25] Meng Ta-chung et al., Phys. Rev. D 27 (1983), 2640.
Meng Ta-chung et al., Phys. Rev. D 33 (1986), 1287.
[26] For further references on 'Two-Particle Rapidity Correlations' see refs. [1,2] of ref. [16].
[27] A.H. Mueller, Phys. Rev. D 4 (1971), 150.
[28] K. Eggert et al., Nucl. Phys. B 86 (1975), 201.
[29] J. Benecke and J. Kühn, Nucl. Phys. B 140 (1978), 179.
[30] G.J. Alner et al., UA5-Collaboration, Phys. Lett. B 160 (1985), 199.
[31] A. Bialas, Proc. IVth INT. Symp. Multiparticle Hadrodynamics, Pavia 1973, Italy; p. 93.
[32] P. Pirilä and S. Pokorski, Phys. Lett. B 43 (1973), 302.
[33] K. Böckmann and B. Eckart, XV. Int. Symp. on Multiparticle Dynamics, Lund, Sweden,

June 10-16, 1984; Bonn University, BONN-HE-84-22, Sept. 1984.
[34] T. Kafka et al., Phys. Rev. D 16 (1977), 1261.
[35] G. Ekspong, 3rd Top. Workshop on $p\bar{p}$ Collider Physics, Rome, Italy, January 12-14, 1983; eds. C. Bacci and G. Salvini, CERN 83-04 (Yellow Report), 1983; p. 112.
[36] P. Carlson, UA5-Collab., XI. Int. Winter Meeting on Fundamental Physics, Toledo, Spain, April 11-16, 1983.
[37] G.J. Alner et al., UA5-Collab., Nucl. Phys. B 258 (1985), 505.
[38] A. Casher et al., Phys. Rev. D 20 (1979), 179.
[39] G. Arnison et al., UA1 Collab., Phys. Lett. B 118 (1982), 167.
[40] M. Banner et al., UA2 Collab., Z. Phys. C 27 (1985), 329.
[41] M. Banner et al., UA2 Collab., Phys. Lett. B 122 (1983), 322.
[42] K. Guettler et al., Nucl. Phys. B 116 (1976), 77.
[43] R. Hagedorn, Rev. Nuovo Cim. 6 (1983) no. 10.
[44] G. Ciapetti, UA1-Collab., Proc. of The Quark Structure of Matter, Karlsruhe-Strasbourg 1985; p. 455.
[45] G.J. Alner et al., UA5-Collab., Phys. Lett. B 167 (1986), 476.
[46] R.E. Ansorge et al., UA5-Collab., in preparation.
C. Fuglesang, UA5 Collab., Proc. of the 17th Symposium on Multiparticle Dynamics, Seewinkel, Austria (1986), p. 553.
[47] V.V. Anisovich and M.N. Kobrinsky, Phys. Lett. B 52 (1974), 217.
[48] R.E. Ansorge et al., UA5-Collab., 'Kaon Production at 200 and 900 GeV c.m. Energy', to appear in Phys. Lett. B.
[49] C. Albajar et al., Phys. Lett. B 186 (1987), 237.
C. Albajar et al., Phys. Lett. B 186 (1987), 247.
[50] H. Albrecht et al., ARGUS Coll., Phys. Lett. B 192 (1987), 245.
[51] A. Bean et al., PRL 58 (1987), 183.
[52] T. Schaad et al., Phys. Lett. B 160 (1985), 188.
[53] W. Bartel et al., Phys. Lett. B 146 (1984), 437.
[54] A. Roussarie, at this conference.
[55] K. Eggert and H.G. Moser, UA1-Coll., 1st Int. Symp. on the 4th Family of Quarks and Leptons, Santa Monica, USA, Feb. 26-28, 1987; RWTH Aachen, PITHA 87-10, Juni 1987; see also: K. Eggert, Proc. of 'New Particles 1985', Wisconsin, ed. by V. Barger et al., WSPC, p. 207; K. Eggert, Proc. 21th Rec. de Moriond, Les Arcs, France, 1986, 'Progress in Electroweak Interaction', Ed. Frontières, p. 369; H.G. Moser, Proc. 21th Rec. de Moriond, Les Arcs, France, 1986, 'Strong Interactions and Gauge Theories', Ed. Frontières, p. 331.
[56] M.K. Gaillard and B.W. Lee, Phys. Rev. D 10 (1974), 897.
[57] A.J. Buras, W. Slominski and H. Steger, Nucl. Phys. B 245 (1984), 369.
A.J. Buras, W. Slominski and H. Steger, Nucl. Phys. B 238 (1984), 529.
J.S. Hagelin, Nucl. Phys. B 193 (1983), 123.
[58] N. Cabibbo, Phys. Rev. Lett. 10 (1963), 531.
[59] M. Kobayashi and T. Maskawa, Progr. Theor. Phys. 49 (1973), 652.
[60] A. Ali, Desy 85-107.
A. Ali and C. Jarlskog, Phys. Lett. B 144 (1984), 266.
V. Barger and R.J.N. Phillips, Phys. Lett. B 143 (1984), 259.
V. Barger and R.J.N. Phillips, Phys. Rev. Lett. 55 (1985), 2752.
I.I. Bigi and A.I. Sanda, Nucl. Phys. B 193 (1981), 85.
I.I. Bigi and A.I. Sanda, Phys. Rev. D 29 (1984), 1393.
[61] C. Geich-Gimbel, 'Particle Production at Collider Energies', University of Bonn, in preparation (1987).

[62] A. Breakstone et al., Phys. Lett. B 135 (1984), 510.
W.M. Geist, 22th Renc. de Moriond, Les Arcs, France, March 15-21, 1987.
[63] K. Eggert. UA1-Coll., private communication, June 1987.
[64] G. Altarelli and P.J. Franzini, CERN-TH.4745/87, May 1987.
[65] K. Kleinknecht and B. Renk, Z. Phys. C 34 (1987), 209.
[66] UA5-Proposal CERN/SPSC/78-70/P 108, and addenda.
[67] UA5/2-Proposal CERN/SPSC/82-75/P 184.
[68] Bonn-Brussels-Cambridge-CERN-Stockholm Collaboration, presented by J.G. Rushbrooke, Phys. Scr. 23 (1981), 642.
[69] K. Alpgård et al., UA5-Collab., Phys. Lett. B 115 (1982), 71.
[70] Th. Müller, Ph.D.Thesis, Bonn University, BONN-IR-83-21, Aug. 1983.
[71] UA5-Collaboration, 'Photon Production at 200 and 900 GeV c.m. energy', in preparation for submission to Zeitschrift für Physik C, 1987.
[72] K.A. French, C. Geich-Gimbel, W. Pelzer, M.A.H. Tucker and D.R. Ward, UA5-Collab., CERN/EP/SCE-R703T/UA5/P84-7, July 1984.
[73] W. Pelzer, UA5-Collab., Dipl. Thesis, Bonn Univ., BONN-IR-85-39, Dec. 1985.
[74] K. Alpgård et al., UA5-Coll., Phys. Lett. B 112 (1982), 183.
[75] W. Thomé ,Ph.D. Thesis RWTH Aachen, PITHA 80/4, Feb. 1980.
[76] A.M. Rossi et al., Nucl. Phys. B 84 (1975), 269; and references therein.
[77] M. Banner et al., UA2-Coll., Phys. Lett. B 122 (1983), 322.
[78] R.S. DeWolf, UA5-Collab., Thesis, University of Cambridge, Dec. 1986.
L. Burow, UA5-Collab., Thesis, Bonn University, BONN-IR-87-25, July 1987.
[79] UA5-Collaboration, 'Hyperon Production at 200 and 900 GeV c.m. energy', in preparation, 1987.
[80] S. Erhan et al., Phys. Lett. B 85 (1979), 447.
[81] G.J. Alner et al., UA5-Coll., Phys. Lett. B 151 (1985), 309.

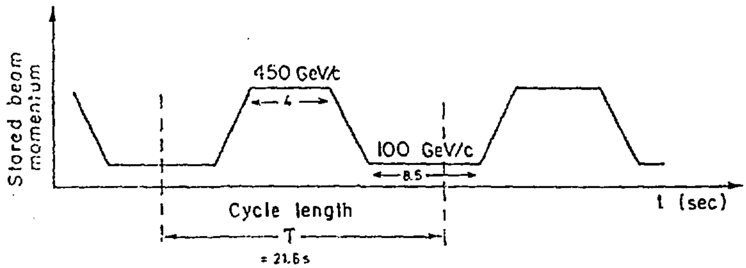

Fig. 1 The cycle of the pulsed SPS Collider

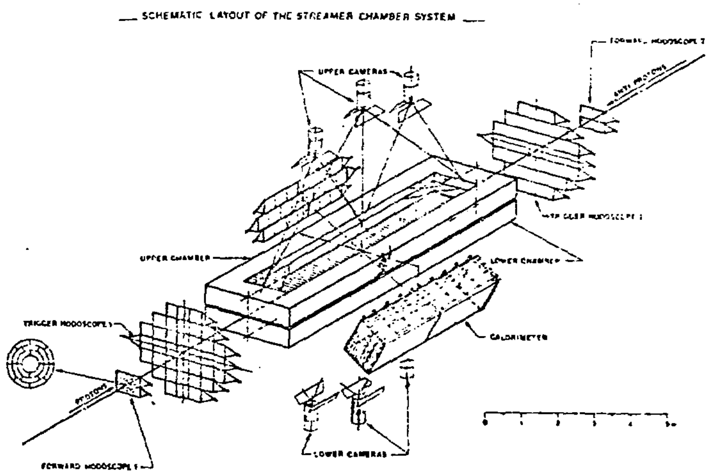

Fig. 2 Schematic layout of the UA5/2 Streamer Chamber Detector

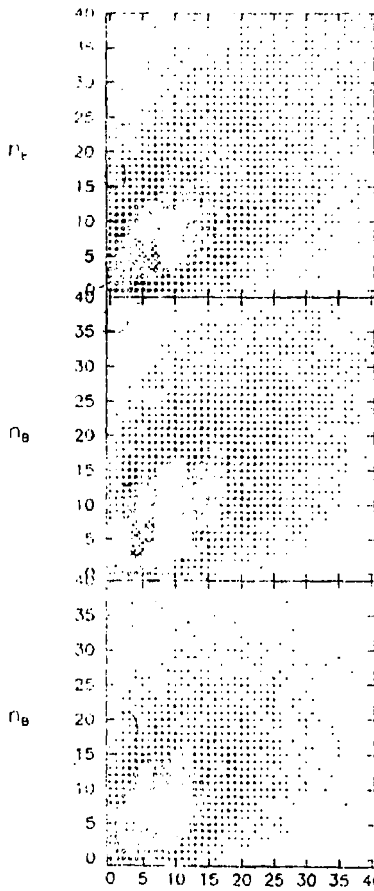

FIG.3

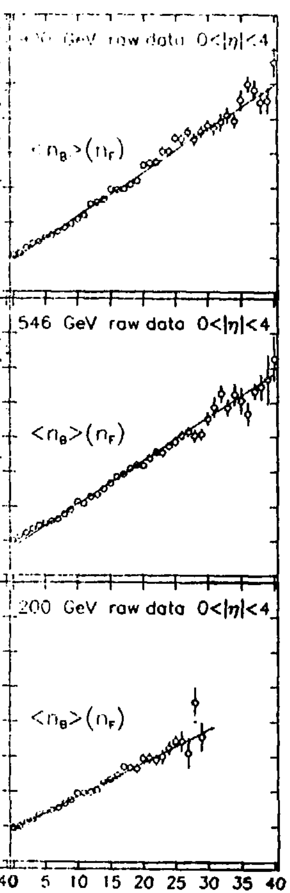

FIG.4

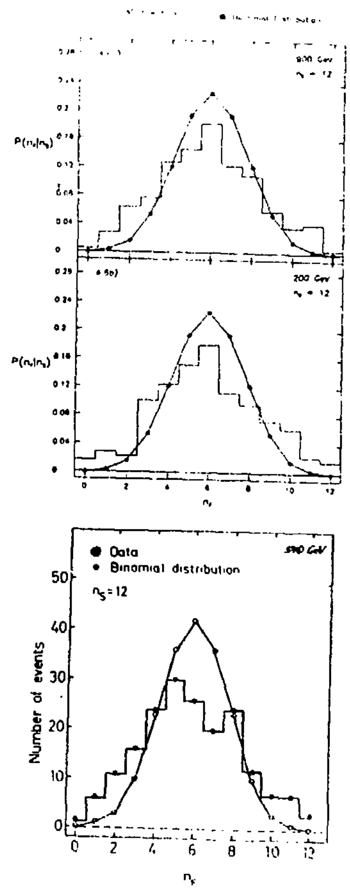

FIG.5

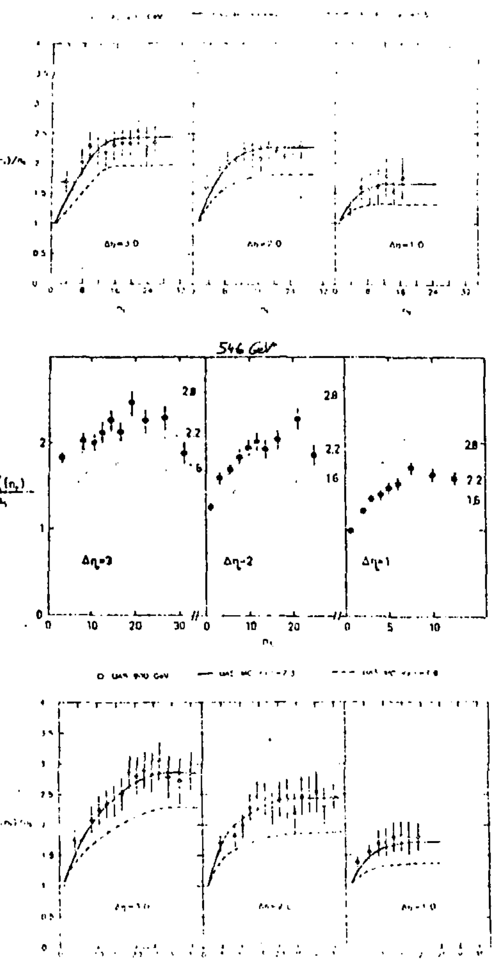
546 GeV
Δη=3
Δη=2
Δη=1
2.8
2.2
1.6
Δη=3.0
Δη=2.0
Δη=1.0

FIG.7

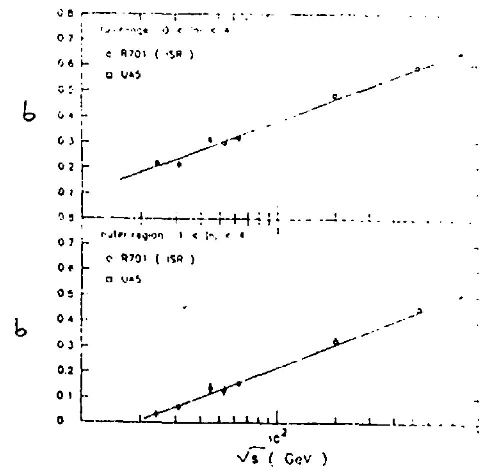
b
R701 (ISR)
UA5
b
R701 (ISR)
UA5
10^2
$\sqrt{s}$ (GeV)

FIG.6

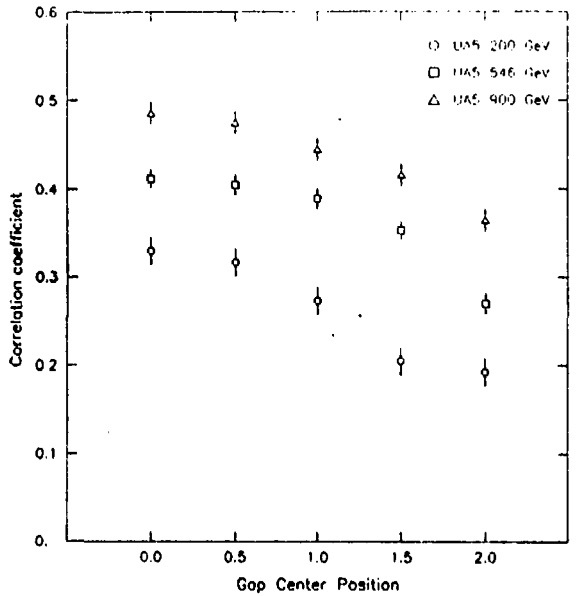
Correlation coefficient
Gap Center Position
UA5 200 GeV
UA5 546 GeV
UA5 900 GeV

FIG.9

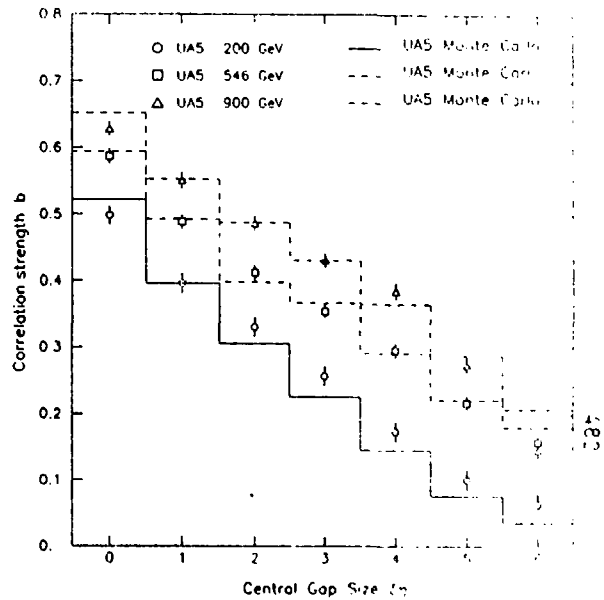
Correlation strength b
Central Gap Size
UA5 200 GeV
UA5 546 GeV
UA5 900 GeV

FIG.8

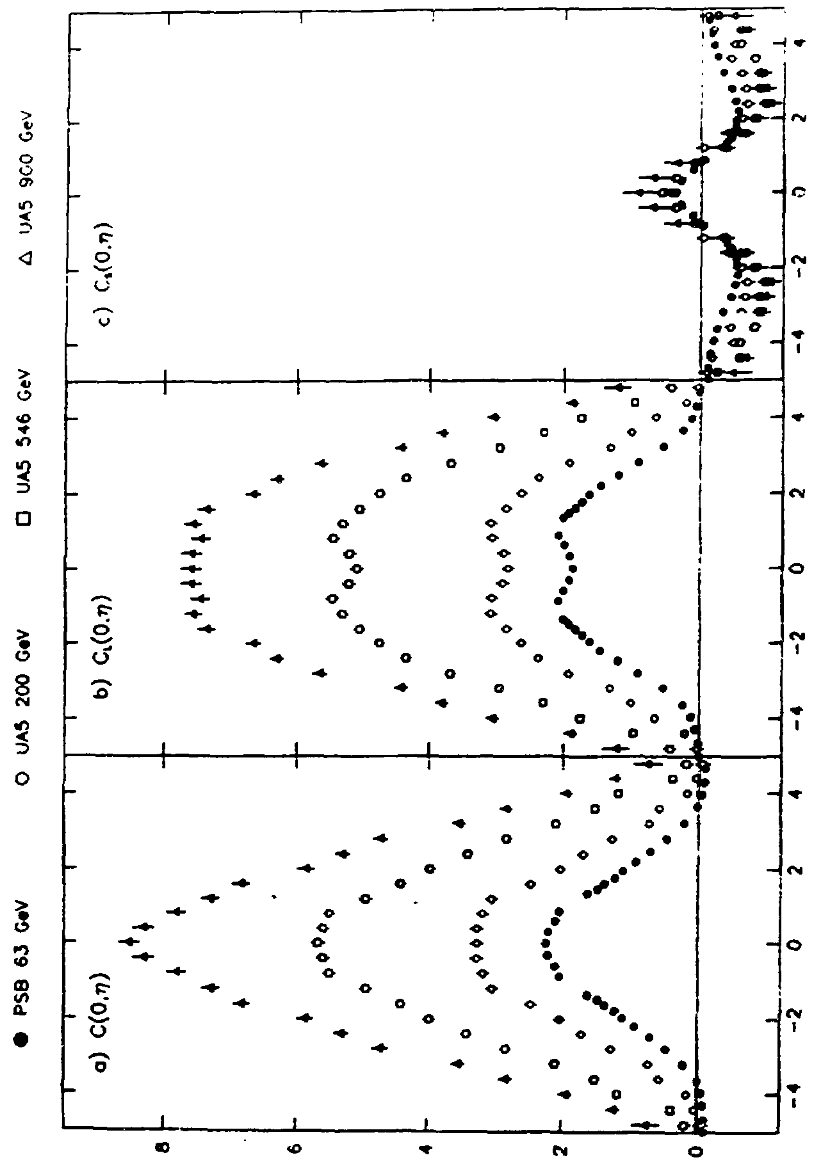

PSB 63 GeV
UA5 200 GeV
UA5 546 GeV
UA5 900 GeV
a) C(0,η)
b) C_L(0,η)
c) C_s(0,η)
η
η
η

FIG.1o

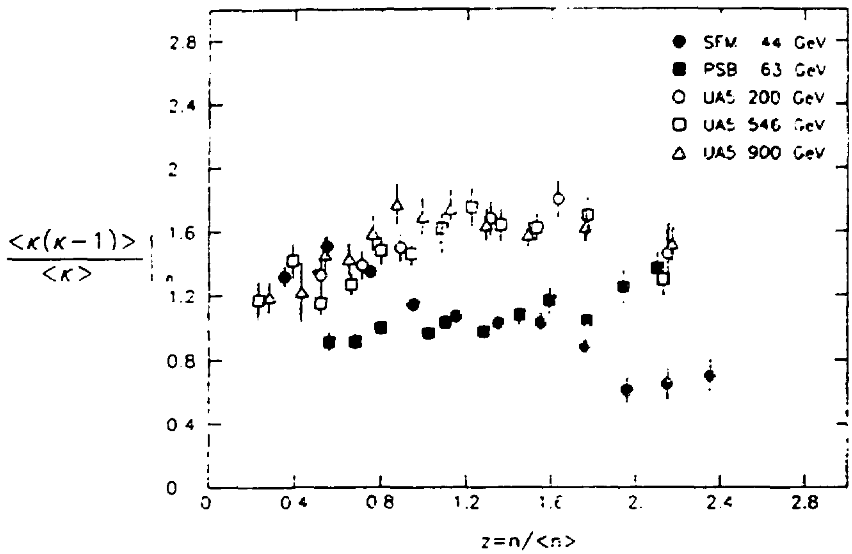
SFM 44 GeV
PSB 63 GeV
UA5 200 GeV
UA5 546 GeV
UA5 900 GeV
$\frac{\langle \kappa(\kappa-1)\rangle}{\langle \kappa \rangle}$
$z=n/\langle n\rangle$

FIG.11

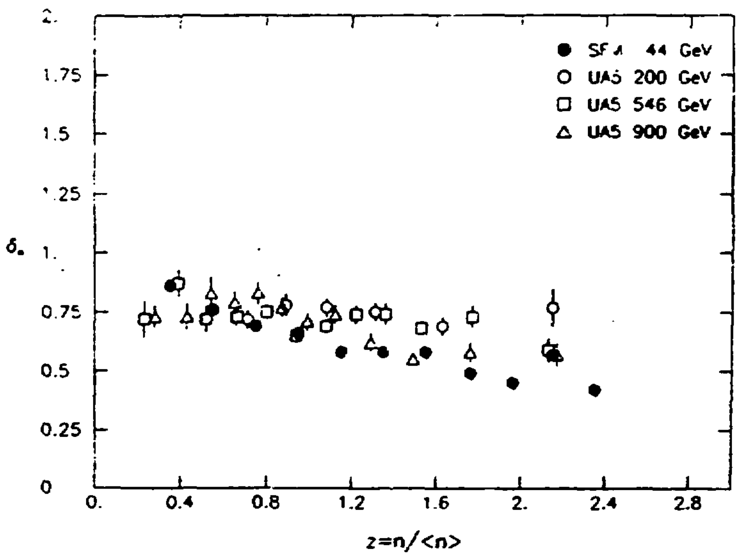
SFM 44 GeV
UA5 200 GeV
UA5 546 GeV
UA5 900 GeV
δ_*
$z=n/\langle n\rangle$

FIG 12

Figure 15

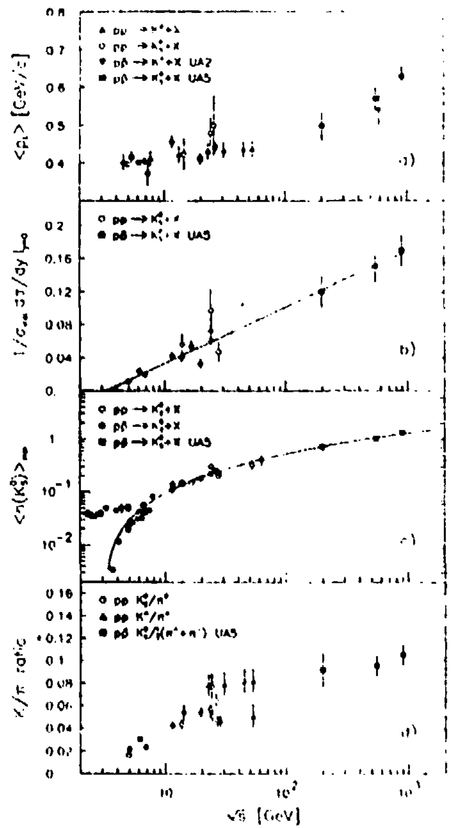

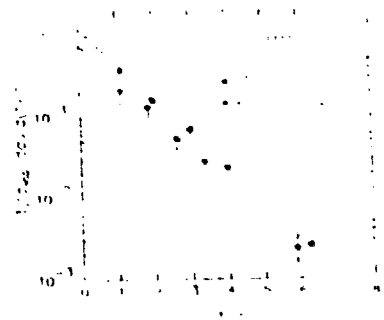

FIG.13

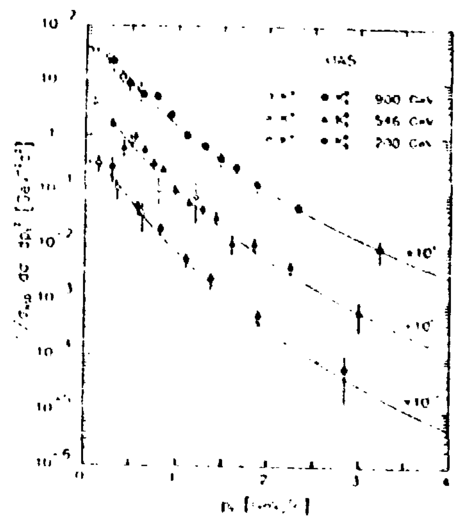

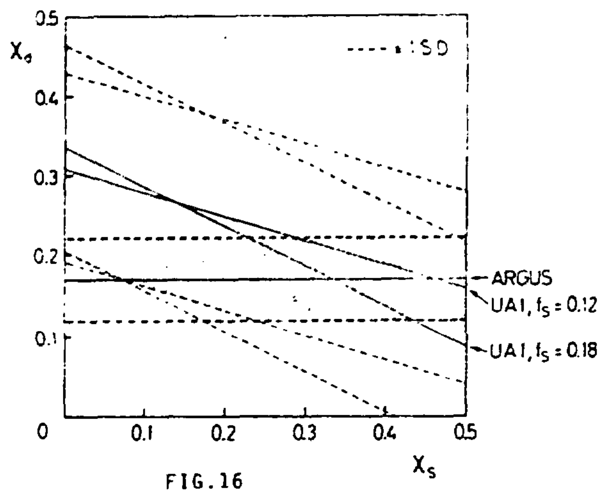

X_d
X_s
ISD
ARGUS
UA1, f_s = 0.12
UA1, f_s = 0.18

FIG.16

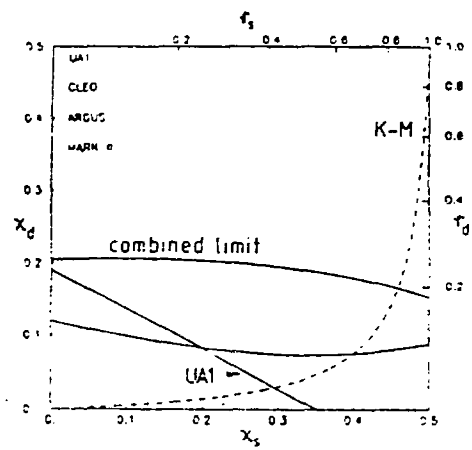

f_s
x_d
f_d
x_s
K-M
combined limit
UA1

FIG.17

QUARK FRAGMENTATION in SOFT K^+p COLLISIONS AT 250 GeV/c

EHS–NA22 Collaboration

E.A. De Wolf
Department of Physics, University of Antwerpen, Belgium

ABSTRACT

Inclusive data are presented on ρ^0, ρ^+, ω, $K^{*0}(892)$ and $\Phi(1020)$, produced in K^+p interactions at 250 GeV/c, for ρ^+ and ω for the first time in a K^+p experiment. In the forward c.m. hemisphere, the ρ^+, ρ^0 and ω differential production rates are equal within errors, and remarkably similar to muon-inelastic scattering data on ρ^0 and ω at 280 GeV/c. In the K^+ fragmentation region, $x > 0.2$, the ratio of ϕ to $K^{*0}(892)$ is used to estimate the strangeness suppression factor λ, with the result $\lambda = 0.17 \pm 0.02$ (stat) ± 0.01 (syst). We see no evidence for an energy dependence of λ in the c.m. energy range $7.8 \leq \sqrt{s} \leq 21.7$ GeV.

1 Quark Fragmentation in Soft Collisions ?

In this talk I shall discuss new data on production characteristics of resonances in soft K^+p collisions, and their interpretation in terms of quark fragmentation.

The subject of "quark fragmentation" is most naturally studied in point-like processes: e^+e^- annihilations, deep-inelastic scattering. For such reactions, QCD prescribes the dynamics at its earliest stage in terms of quarks and gluons. The fragmentation of these coloured objects enters in the evolution of the "primordial" final state towards the observable world of hadrons. Such a two-stage picture is remarkably successful in spite of some basic theoretical difficulties. It would be surprising indeed if nature has not invented a smoother and more elegant procedure than the abrupt transition from quantum mechanics to Monte Carlo, as imagined in present-day phenomenology !

Returning to soft hadron hadron interactions, it is well known that these share many similarities with point-like processes. Similarities, however, are more surprising than the observed differences, since the dynamics is apriori more complicated in the former. In a soft hadronic collision, ensembles of valence quarks and gluons of beam and target most of the time interact at relatively large distances. Final state hadrons emerge in "jets" collimated along the line of flight of the colliding objects. However, experiment reveals that the inclusive production properties along and transverse to these axes resemble strikingly those found in point-like processes along the direction of the fragmenting quark (or diquark) systems. Are such similarities the reflection of common hadronisation dynamics or are they accidental ? At present, the former explanation seems prefered, but clear-cut evidence is still lacking. If we adopt an optimistic point of view and assume that quark hadronisation is "universal", then we should address the question of the fate of valence quarks in a soft hadron hadron interaction.

Consider a K^+p collision as an example. A beam of $\bar{s}$ and u valence quarks and gluons interacts with a proton composed of three valence quarks and gluons. In a first class of models, one imagines that the collision is initiated by gluonic interactions. The valence quarks loose some energy but essentially behave as spectators. The original valence quarks may either "recombine" into a "fast" particle or fragment independently. In the first case, we expect the beam fragmentation region to be populated mainly by particles or resonances with the quantum numbers of the K^+ beam: K^+'s, $K^{*+}(892,1420)$. In the second case, the $\bar{s}$ and u valence quarks fragment and produce roughly equal amounts of K^+'s and K^0's, K^{*+}'s and K^{*0} etc. Naively, we expect the momentum distributions to be softer in the latter case since two valence quarks have to share the available beam momentum.

In a second class of models, the interaction is viewed as a collison of one of the valence quarks (say the u quark of the K^+) with proton constituents. This quark looses most of its energy whereas the $\bar{s}$ quark continues as a spectator carrying its original momentum. Forward particle production is then dominated by the hadronisation of a single ($\bar{s}$) quark. Alternatively, if the $\bar{s}$ quark interacts, we observe the fragmentation of the u quark. This picture implies that particle production in the K^+ fragmentation region is a superposition of $\bar{s}$- and u-quark hadronisation.

Which of these alternatives is chosen by nature ? This question has been the subject of several investigations with K^+ and (more recently) π^+ beams. The reactions studied are:

$$K^+p \rightarrow K^{*+}_{892,1420} + X, \quad (1)$$
$$\rightarrow K^{*0}_{892,1420} + X; \quad (2)$$

at 32[1,2,3] and 70 GeV/c[4], and

$$K^+p \rightarrow K^+X, \quad (3)$$
$$\rightarrow K^0_S + X; \quad (4)$$

at 70 GeV/c[5], and

$$K^+p \rightarrow \rho^0 + X, \quad (5)$$
$$\rightarrow \rho^+ + X; \quad (6)$$

at 250 GeV/c[6].

What has been learned from these studies can be summarized as follows:

- The total and differential cross sections of the pairs of reactions (1-2), (3-4), (5-6) are very similar in absolute value and in shape. This excludes an important contribution from so-called "two-valence recombination".
- The data are well reproduced by a simple model which assumes that hadron production in the beam fragmentation region results from a superposition of single quark hadronisation, whereby the fragmenting quark carries most of the momentum of the incident meson.

We therefore conclude that the second class of models (see above) comes closest to a description of the hadronic final state in soft hadron hadron collisions. This further implies that the soft meson-proton interaction can be used as a tool to study quark fragmentation. With kaon beams, this gives us the possibility to study s-quark fragmentation with better precision than is possible in other types of interactions.

In the rest of this talk, I shall briefly describe the data now being analyzed by the EHS–NA22 collaboration (sect.2). In sect.3, I present new results on ρ^+, ρ^0 and ω resonances and a comparison with recent EMC data. Sect. 4 is devoted to a discussion of a new measurement of the strangeness suppression using data on Φ and K^{*0} resonances in K^+p collisions.

2 The Experiment

The experiment (NA22) has been performed at CERN in the European Hybrid Spectrometer (EHS), equipped with the Rapid Cycling Bubble Chamber (RCBC) as an active vertex detector and exposed to a 250 GeV/c tagged positive meson enriched beam. In data taking, a minimum bias interaction trigger has been used. The experimental set up and the trigger conditions are described in [7] and references therein.

The detector consists of RCBC embedded in a 2T magnetic field and a downstream spectrometer composed of an additional 1T magnet, a wire-chamber and six drift chambers. Charged particles are measured over the full solid angle with the momentum resolution $(\Delta p/p)$ varying from 2.5% at 30 GeV/c to 1.5% above 100 GeV/c. Particle identification is supplied by RCBC, the Čerenkov counters SAD and FC, the ionization sampling device ISIS and the transition radiation detector TRD[7]. The photon detection in the intermediate and forward gamma detectors, IGD and FGD, is described in detail in [8]. The combined acceptance of the γ detectors allows to measure π^0's for $x(\pi^0) \geq 0.025$. The acceptance for ρ^+ and ω is then restricted to $x \geq 0.06$. For the ρ^+ the signal to background ratio is very small for $x < 0.2$ and we have to limit ourselves to the region $x > 0.2$.

In this analysis, events are accepted when the measured and the reconstructed multiplicity n are consistent, charge balance is satisfied, no electron is detected and the number of badly reconstructed tracks is less than $n/3$ and smaller than 4. There are 36300 such inelastic K^+p events, corresponding to a sensitivity of 2.05 events/μb. Charged particles for which the χ^2-probability of the best mass-hypothesis is at least 10 times larger than that for any other mass hypothesis are considered "uniquely identified". To these we add protons and π^+'s with laboratory-momentum smaller than 1.2 GeV/c, identified in RCBC by ionization. All other particles are considered unidentified and taken to be pions.

3 Inclusive $\rho^{+,0}$ and ω production

In spite of its importance for parton models, little is known about similarities or differences in the production of $\rho^{\pm}$, ρ^0 and ω. This is mainly due to difficulties in the identification and measurement of neutral pions.

In deep-inelastic lepton-nucleon scattering, ρ^0 and ω production are measured for the first time in the same experiment by the European Muon Collaboration[9]. The authors conclude that, in u-quark fragmentation, the differential production rates of ρ^0 and ω are equal within errors.

Here we present data on inclusive ρ^0, ρ^+ and ω production in the reactions

$$\begin{aligned} K^+p &\rightarrow \rho^0 + X, & (7)\\ &\rightarrow \rho^+ + X, & (8)\\ &\rightarrow \omega + X, & (9) \end{aligned}$$

at 250 GeV/c, the highest momentum so far reached for K^+ induced reactions.

In $K p$ interactions, ρ production is less affected by diffraction than in πp collisions. Moreover, low-p_T models lead us to expect that, in the forward c.m. hemisphere, non-strange vector mesons are mainly produced from K^+ u-valence quark fragmentation and should therefore resemble those in deep-inelastic scattering.

The data are obtained in the full Feynman-x range for reaction (7), $x \geq 0.2$ for reaction (8) and $x \geq 0.06$ in reaction (9). Reaction (7) has previously been studied at 32 [10] and 70 GeV/c [11]. No other data on reactions (8) and (9) are available.

The invariant $\pi^+\pi^-$, $\pi^+\pi^0$ and $\pi^+\pi^-\pi^0$ mass distributions are shown in Fig. 1 for $x \geq 0.2$ and $x \geq 0.5$. To account for the limited geometrical acceptance for the π^0 in reactions (2) and (3), we consider only events with $\cos\theta_J(\pi^0) \geq 0$, where $\cos\theta_J = -\vec{n}_{targ} \cdot \vec{n}_{\pi^0}$, with $\vec{n}$ unit-vectors in the resonance rest frame. The reflection of the (strong) $K^{*0}(892)$ and $\overline{K}^{*0}(892)$ resonances into the $\pi^+\pi^-$ mass distribution, and of the $K^{*+}(892)$ into the $\pi^+\pi^0$ mass distribution is treated as described in [12], where detailed results on meson resonance production will be presented.

The resonance cross sections are obtained by fitting the invariant mass spectra by the function $d\sigma/dM = BG(1 + \alpha BW)$, where BW is a relativistic P-wave Breit-Wigner for $\rho^{+,0}$ and a Gaussian for ω. For the $\pi^+\pi^-$ mass spectrum, a D-wave Breit-Wigner has been added to account for the f_2 signal. The background is taken as

$$BG = a(M - M_{th})^b \exp(-cM - dM^2), \qquad (10)$$

with M_{th} the corresponding threshold mass; a,b,c,d and α are fit parameters. The natural width Γ_N and mass of $\rho^{+,0}$ are taken from the PDG tables[13]. The total width Γ is taken as the sum of Γ_N and Γ_R, where Γ_R is the width (FWHM) of the experimental resolution function, measured to be 12 and 15 MeV for ρ^0 and ρ^+, respectively. For the ω, the mass and width of the Gaussian are left as free parameters. The fitted width is consistent with the experimental resolution of 29 MeV. The fits are shown by solid curves in Fig. 1 and describe the data reasonably well. The signal to background ratio for all resonances improves significantly at larger Feynman-x.

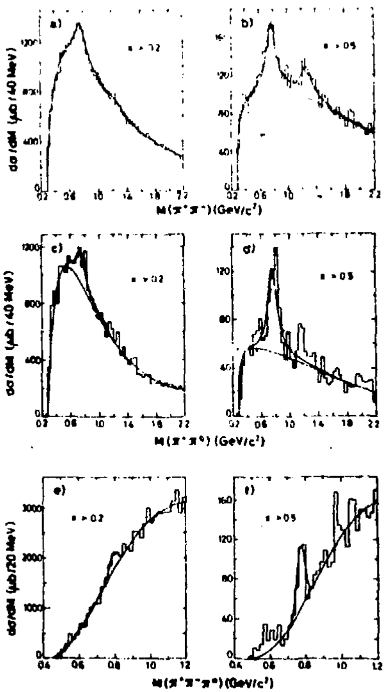

Fig.1 Invariant $\pi^+\pi^-$ (a,b), $\pi^+\pi^0$ (c,d) and $\pi^+\pi^-\pi^0$ (e,f) mass distributions in the indicated interval of Feynman-x. The curves are the results of fits as described in the text.

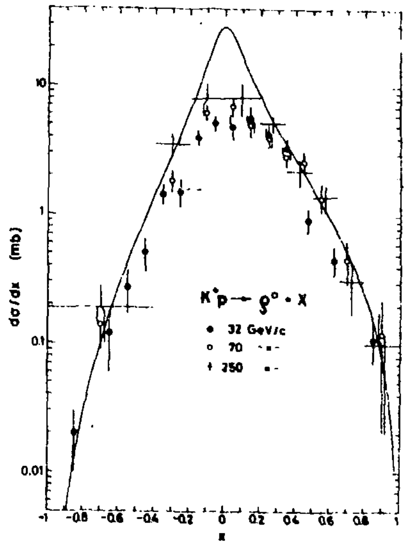

Fig.2 Inclusive $d\sigma/dx$ distributions of ρ^0 in reaction (1) at 250, 32 GeV/c and 70 GeV/c. The solid line is the prediction of the Dual Parton Model at 250 GeV/c.

The total inclusive ρ^0 cross section is found to be (5.4 ± 0.6)mb. The average multiplicity $< n(\rho^0) >$ per inelastic collision is 0.31 ± 0.04 Assuming a rise with c.m. energy, $\sqrt{s}$, according to

$$< n(\rho^0) >= a + b\ln(s/s_0), (s_0 = 1\text{GeV}^2), \tag{11}$$

and using the data at 32 GeV/c[10], 70 GeV/c[11] and our result, a slope $b = 0.04 \pm 0.02$ is obtained. These values are significantly smaller than the values $< n(\rho^0) >= 0.53$ and $b = 0.14$ predicted by the quark-combinatorics model of Anisovich et al.[14,15]. Furthermore, the Lund string fragmentation model[16,17,18] and one of the latest versions of the Dual Parton Models (DPM)[19] predict too large cross sections. $\sigma(\rho^0) = 9.3$ mb and 9.2 mb, respectivey, and too large b-values. A similar conclusion can be drawn for the Lund model from leptoproduction (see [9] and refs. therein).

The $d\sigma/dx$ distribution for inclusive ρ^0 production in reaction (1) at 250 GeV/c is presented in Fig. 2 and compared with data at lower energies. The spectra scale between 70 and 250 GeV/c in the fragmentation regions $|x| \geq 0.2$. The rise with energy of the total ρ^0 cross section occurs in the central region. The Dual Parton Model[19] (solid curve in Fig. 2) agrees with the data in the fragmentation regions, but overestimates the central region. The Lund model[16,17,18] gives a similar result.

The inclusive ρ^0, ρ^+ and ω cross sections in the kaon fragmentation region $x \geq 0.2$ are:

$$\sigma(\rho^0) = (1.36 \pm 0.14)\,\text{mb}, \tag{12}$$

$$\sigma(\rho^+) = (1.28 \pm 0.36)\,\text{mb}, \tag{13}$$

$$\sigma(\omega) = (1.37 \pm 0.35)\,\text{mb}. \tag{14}$$

A comparison of the forward ρ^0, ρ^+ and ω $d\sigma/dx$ distribution is made in Fig. 3a. For $x > 0.2$, also the differential production rates of these mesons are seen to be equal within errors.

In Fig. 3b we compare the $d\sigma/dx$ spectra for the ρ^0 and ω to the EMC-data[9]. The latter are scaled to the total inelastic K^+p cross section at $\sqrt{s} = 13.3$ GeV, the average hadronic energy $< W >$ in the μp experiment. Despite the difference in total energy, we observe an interesting similarity of ρ^0 and of ω production in the two types of collision. Such a similarity is not merely accidental. Indeed, a detailed comparison of our data with low-p_T models, presented elsewhere[12], shows that the production of $\rho^{+,0}$ and ω in the K^+ fragmentation region ($x > 0.2$) is dominated by the hadronization of the K^+ u-valence quark, and is therefore expected to be similar to μp deep-inelastic scattering.

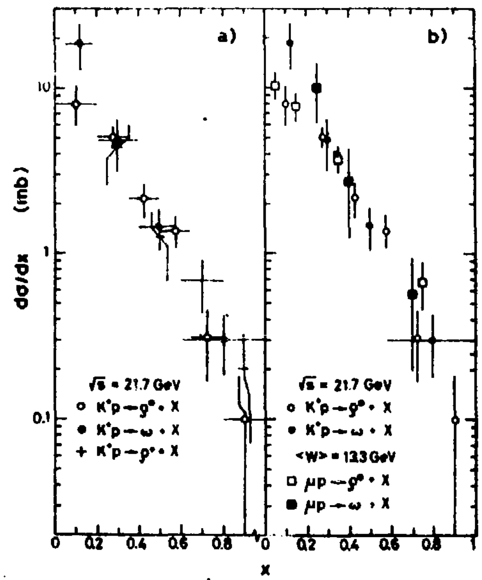

Fig.3 Inclusive $d\sigma/dx$ distributions of ρ^0, ρ^+ and ω in reactions (1)—(3) at 250 GeV/c (a); comparison of $d\sigma/dx$ distributions for ρ^0 and ω in μp and K^+p interactions (b).

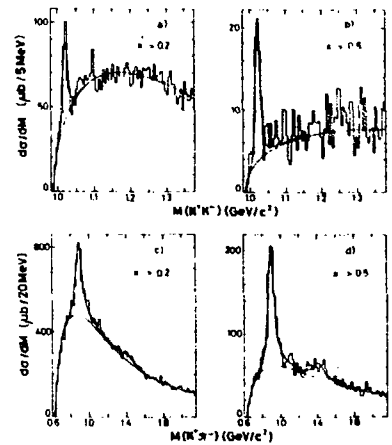

Fig. 4 Invariant K^+K^- (a,b) and $K^+\pi^-$ (c,d) mass distributions in the indicated intervals of Feynman-x. The curves are the results of fits to the Breit-Wigner functions and background.

4 Strangeness Suppression

It is known since long that strange hadrons are less copiously produced than non-strange hadrons, in hadron-hadron collisions, and in deep-inelastic processes. Precise knowledge about the suppression of strange quark-pair creation is important for topics such as quark fragmentation, heavy flavour production or the observation of a quark-gluon plasma. It plays a critical rôle in present phenomenology of $B_{d,s} - \overline{B}_{d,s}$ mixing[20].

To characterize this violation of SU(3) symmetry, the strangeness suppression parameter λ is introduced and defined as the ratio of the probabilities of producing an $s\bar{s}$-pair to that of producing a $(u\bar{u})$- or $(d\bar{d})$-pair in the hadronic vacuum. If related to finite energy mass effects, one may expect[21] an increase of λ at sufficiently large energies. If explained as a quantum tunneling effect, as in QCD[16,17], the suppression is expected to be independent of energy provided the field energy density is constant.

Recent analyses based on K/π ratio's from lepton-hadron collisions[22,23] give a λ-value of ≈ 0.2, while a value around 0.3 is obtained for e^+e^- annihilation[24,25].

For hadron-hadron collisions, λ may be mildly increasing at low $\sqrt{s}$ to reach an average of 0.20 ± 0.03 at $\sqrt{s} = 20$ GeV[26]. However, considerably higher values are reported from the collider[27] and, in particular, for high p_T jets at the ISR[28]

The NA22 collaboration has obtained data on inclusive $\phi(1020)$, $K^{*0}(892)$ and $\overline{K^{*0}}(892)$ production in the reactions

$$\begin{aligned} K^+p &\rightarrow \phi(1020) + X, & (15)\\ K^+p &\rightarrow K^{*0}(892) + X, & (16)\\ K^+p &\rightarrow \overline{K^{*0}}(892) + X; & (17) \end{aligned}$$

at 250 GeV/c. Reactions (15) and (16) are particularly well suited to determine the strangeness suppression directly from the data, while reaction (17) helps to estimate central $K^{*0}(892)$ production.

At lower energies, reactions (1)—(3) were systematically studied by the Mirabelle collaboration at 32 GeV/c[1,2,29,3] and by the BEBC collaboration (WA27) at 70 GeV/c[30,4]. High statistics data on ϕ-production in K^+Be interactions at 120 and 200 GeV/c were recently presented by the ACCMOR collaboration for the Feynman-x range $0 \leq x \leq 0.3$[31].

From Drell-Yan production at relatively low Q^2, it is known that the longitudinal momentum distribution in the K^+ is harder for the $\bar{s}$-valence quark than for the u-valence quark[32]. This implies that K^+ beam fragmentation at moderately large Feynman-x is mainly due to strange flavour fragmentation. Additionally, model calculations indicate that for $x \geq 0.2$, the K^* and ϕ fragmentation functions for u-quark jets are about an order of magnitude smaller than those for $\bar{s}$-quark jets.

In reaction (1), the ϕ-meson is dominantly produced through $\bar{s}$ fragmentation via the creation of an $(s\bar{s})$ quark pair from the vacuum. Furthermore, there is no experimental evidence that the observed ϕ-meson is a decay product of higher mass resonances.

As to $K^{*0}(892)$, besides prompt production through $\bar{s}$- quark fragmentation, via $(d\bar{d})$ pair production, other contributions must be considered. As discussed below, they are relatively small in the fragmentation region $x \geq 0.2$ and can be subtracted.

The cross sections for reactions (1)–(3) are determined by fitting the invariant K^+K^-, $K^+\pi^-$ and $K^-\pi^+$ mass distributions by the expression

$$d\sigma/dM = BG(M)(1 + \beta_1 BW_1(M) + \beta_2 BW_2(M)), \tag{18}$$

where $BW_1(M)$ and $BW_2(M)$ are relativistic P- and D-wave Breit-Wigner functions, β_1 and β_2 fit-parameters (β_2 is fixed to 0 in the absence of a tensor meson signal). The background function $BG(M)$ is parametrized as

$$BG(M) = \alpha_1 (M - M_{th})^{\alpha_2} \exp(-\alpha_3 M - \alpha_4 M^2). \tag{19}$$

The α_i are free parameters and M_{th} is the threshold mass.

To account for the reflection of a given resonance into the distribution of another invariant-mass combination due to K/π misidentification, we use the methods developed in[30,4] and discussed in detail in[12].

The total width of K^{*0} and $\overline{K^{*0}}$ is taken to be the sum of the natural width (Γ_N) and the width (FWHM) of the resolution function $\Gamma_R = 25$ MeV/c^2. For the narrow ϕ-signal, the natural width is folded with a Gaussian for the experimental resolution with a FWHM = 14 MeV/c^2. For illustration, we show the K^+K^- and $K^+\pi^-$ invariant mass distributions in Fig. 4 for $x \geq 0.2$ and $x \geq 0.5$. They exhibit clear ϕ, $K^{*0}(892)$ and $K_2^{*0}(1430)$ signals. The signal-to-noise ratio improves significantly as $x \to 1$. The best-fit results (solid lines) are seen to describe the experimental spectra. With our statistics and means of particle identification, we are able to determine the x-spectrum for K^{*0} in the full x-range and for ϕ in the region $x \geq 0$. For $\overline{K^{*0}}$, we present a total inclusive cross section only.

The inclusive cross sections of $K^{*0}(892)$, $\overline{K^{*0}}(892)$ and ϕ are summarized in

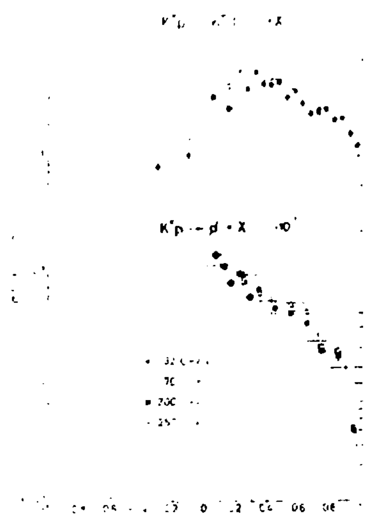

Fig. 5 Differential cross section $d\sigma/dx$ of ϕ and K^{*0} in reactions (1); (2) at 250 GeV/c compared with lower energies.

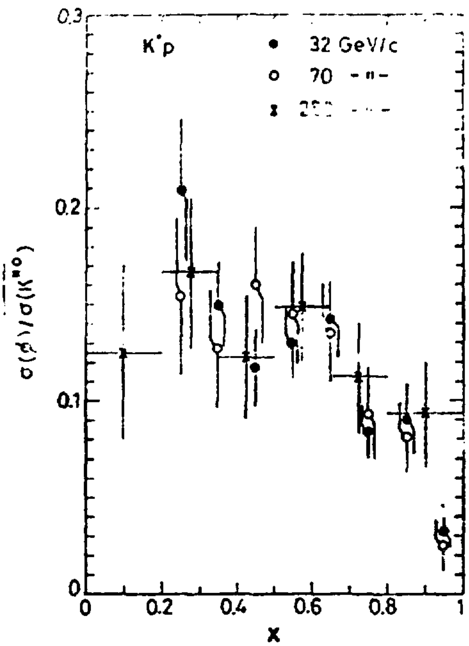

Fig. 6 The ratio of the ϕ to $K^{*0}(892)$ $d\sigma/dx$ distributions at 32, 70 and 250 GeV/c.

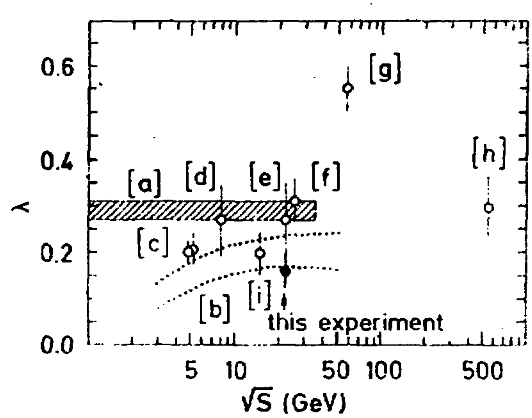

Fig. 7 A comparison of λ for different experiments (see text for refs.).

Table 1, together with measurements at 32 and 70 GeV/c.

Table 1. Cross sections (mb), ϕ/K^{*0} ratios and λ-values at 32, 70 and 250 GeV/c.

	x-range	32 GeV/c	70 GeV/c	250 GeV/c
$\sigma(K^{*0}(892))$	all x	3.2 ± 0.4	4.0 ± 0.5	5.07 ± 0.49
$\sigma(\overline{K}^{*0}(892))$	all x	0.1 ± 0.2	0.7 ± 0.2	2.49 ± 0.48
$\sigma(K^{*0}(892))$	> 0.2	2.32 ± 0.07	2.64 ± 0.09	2.54 ± 0.12
$\sigma(\phi)$	> 0.2	0.308 ± 0.019	0.334 ± 0.028	0.348 ± 0.037
$\phi/K^{*0}(892)$	> 0.2	0.133 ± 0.009	0.127 ± 0.012	0.137 ± 0.017
λ	> 0.2	$0.16 \pm 0.01 \pm 0.01$	$0.15 \pm 0.02 \pm 0.01$	$0.17 \pm 0.02 \pm 0.01$

The $\overline{K}^{*0}(892)$ has no valence-quark in common with beam or target and can only be produced from sea-quarks. The largest part of its cross section, (2.40 ± 0.34) mb is concentrated in the interval $|x| < 0.2$. Since central K^{*0} and $\overline{K}^{*0}$ production may be assumed to be equal we can attribute the rise of the K^{*0} cross section mainly to central production. This is indeed confirmed by inspection of the K^{*0} $d\sigma/dx$ spectrum. For $x > 0.2$, the K^{*0} cross section is practically energy independent between 32 and 250 GeV/c. As seen from Table 1, this is also true for the ϕ-cross section.

The differential cross section $d\sigma/dx$ for ϕ and $K^{*0}(892)$ in reactions (1) and (2) at 250 GeV/c is shown in Fig. 5 together with data at lower energies. Within errors it is independent of the c.m. energy of the collision, for ϕ in the measured x-range and for $K^{*0}(892)$ above $x > 0.2$. For the latter we observe an increase between 70 and 250 GeV/c in the central region $|x| < 0.2$.

The shape of the ϕ and the $K^{*0}(892)$ $d\sigma/dx$ spectrum is remarkably similar over the entire x-range, except for the highest x-values where the ϕ cross section falls faster. This is more clearly seen in Fig. 6, where the ratio of ϕ to K^{*0} differential cross sections at 32, 70 and 250 GeV/c is displayed. The high statistics data at 32 GeV/c show a significant drop of the ϕ/K^{*0} ratio for $x \geq 0.9$. We attribute this effect to diffractively produced systems decaying into $K^{*0}(892)$ but not into ϕ.

The previous discussion leads us to conclude that the ϕ/K^{*0} ratio for $x > 0.2$ provides an excellent and direct measure of the strangeness suppression. This ratio is given in Table 1 for K^+p collisions at 32, 70 and 250 GeV/c incident momentum.

Comparable data exist for K^-p interactions at 10 and 16, 32 and 110 GeV/c, where the ratio $\phi/\overline{K^{*0}}$ is found to be 0.12 ± 0.02[33], 0.18 ± 0.03[34,35] and 0.20 ± 0.04[36], respectively.

To obtain a proper estimate of λ, account has to be taken of the "non-prompt" component of the K^{*0} cross sections due to $K_2^{*+,0}(1430)$ decays and diffractive production. The $K_2^{*0}(1430)$ cross section at 250 GeV/c amounts to (1.04 ± 0.27) mb for $x > 0.2$[12]. Assuming equal $K_2^{*+}(1430)$ and $K_2^{*0}(1430)$ cross sections, as observed at lower energies[1,29,4], and taking into account branching fractions to $K^{*0}(892)$, yields a cross section for $K_2^{*0,+}(1430) \to K^{*0}(892) + X$ of (0.35 ± 0.09) mb. Diffractive $K^{*0}(892)$ and ϕ production was measured to be $(232 \pm 15)\mu$b[37] and $(17 \pm 5)\ \mu$b[3], respectively at 32 GeV/c. We assume these to be energy independent between 32 and 250 GeV/c. After removal of the $K_2^{*+,0}(1430)$ and diffractive contributions, we estimate λ, the ratio of "prompt" ϕ to "prompt" $K^{*0}(892)$, to be equal to $0.17 \pm 0.02(\mathrm{stat}) \pm 0.01(\mathrm{syst})$. The corresponding λ-values at 32 and 70 GeV/c are given in Table 1. Within errors, no energy dependence of the strangeness suppression is observed in the c.m. energy range $7.8 \leq \sqrt{s} \leq 21.7$ GeV.

A detailed comparison of the λ-values determined in this and in the two lower energy K^+p experiments with other recent measurements will be presented elsewhere[12]. A compilation of λ-measurements is shown in Fig. 7. It is seen that the recent νp, $\bar{\nu}p$ and μp measurements give a value in agreement with our result. Measurements from e^+e^- annihilation tend to favour a somewhat larger value.

Many estimates, in particular those extracted from measured K/π-ratios, are based on model comparisons. Adopting similar techniques to describe our K^{*0} and ϕ data, we find $\lambda = 0.16 \pm 0.02$ from the Statistical Quark Model[38] and $\lambda = 0.18 \pm 0.03$, using either the Dual Parton Model[39,40] or the Lund Fritiof model[41]. The latter two models describe the data at 32, 70 and 250 GeV/c with the same λ-value. All model-based values are seen to be in good agreement with the model-independent estimate presented above.

In summary, in the kinematical region $x > 0.2$, $K^{*0}(892)$ and ϕ mesons are predominantly produced off the strange valence-quark of the beam by creation of a $(d\bar{d})$-, respectively $(s\bar{s})$-pair from the vacuum. This allows us to estimate the strange quark suppression factor, an important parameter in present hadronization phenomenology. We obtain $\lambda = 0.17 \pm 0.02 \pm 0.01$ at 250 GeV/c, in good agreement with results at 32 and 70 GeV/c, indicating that the energy dependence of λ, if any, is very weak in the energy range considered

References

[1] I.V.Ajinenko et al. *Z. Phys.*, **C26**:103, 1984.

[2] P.V.Chliapnikov et al. *Phys. Lett.*, **130B**:432, 1983.

[3] I.V.Ajinenko et al. *Sov. J. Nucl. Phys.*, **39**:914, 1984.

[4] M.Barth et al. *Nucl. Phys.*, **B223**:296, 1983.

[5] E.A.De Wolf et al. *Z. Phys.*, **C31**:13, 1986.

[6] M. Adamus et al. *Phys. Lett.*, **183B**:425, 1987.

[7] M.Adamus et al. *Z. Phys.*, **C32**:475, 1986.

[8] NA22 Collaboration: M.Adamus et al. *Inclusive π^0 Production in π^+p, K^+, and pp Interactions at 250 GeV/c*. 1987. *Z. Phys.* **C** (in press).

[9] EMC Collaboration: M. Arneodo et al. *Z. Phys.*, **C33**:167, 1986.

[10] P.V. Chliapnikov et al. *Nucl. Phys.*, **B176**:303, 1980.

[11] M.Barth et al. *Nucl. Phys.*, **B223**:296, 1983.

[12] NA22 Collaboration:. *Inclusive Meson Resonance Production in K^+p Interactions at 250 GeV/c*. to be submitted to *Z. Phys.* **C**.

[13] Particle Data Group: M.Aguilar-Benitez et al. *Phys. Lett.*, **B170**:1, 1986.

[14] V.V.Anisovich, M.Kobrinsky, J.Nyiri. *Yad. Fiz.*, **34**:195, 1981.

[15] V.V.Anisovich, M.Kobrinsky, J.Nyiri. *Yad. Fiz.*, **35**:151, 1982.

[16] B.Andersson et al. *Nucl. Phys.*, **B178**:242, 1981.

[17] B.Andersson et al. *Phys. Reports*, **C97**:31, 1983.

[18] T.Sjöstrand. *Comp. Phys. Comm.*, **27**:243, 1982.

[19] A.V.Batunin, A.K.Likhoded, A.N.Tolstenkov. *Yad. Fiz.*, **42**:424, 1985.

[20] A.Ali. Dileptons, Electroweak Charge Asymmetry and $B-\overline{B}$ Mixings. In J.Grunhaus, editor, *Proceedings XVIth Int. Symp. on Multiparticle Dynamics*, page 645. Editions Frontières (Gif-sur-Yvette) and World Scientific (Singapore), 1985.

[21] V.V. Anisovitch, V.M.Shekhter. *Nucl. Phys.*, **B55**:455, 1973.

[22] G.T.Jones et al. *Z. Phys.*, **C27**:43, 1985.

[23] R.Windmolders. *Recent Results from the EMC collaboration.* In *Proc. Xth Warsaw Symposium on Elementary Particle Physics , Kazimierz, Poland*, 1987.

[24] W.Bartel et al. *Z. Phys.*, **C20**:187, 1983.

[25] H.Aihara et al. *Phys. Rev. Lett.*, **53**:2378, 1984.

[26] A.Wróblewski. *Acta Phys. Pol.*, **B16**:379, 1985.

[27] G.J.Alner et al. *Nucl. Phys.*, **B258**:505, 1985.

[28] A.Breakstone et al. *Phys. Lett.*, **135B**:510, 1984.

[29] I.V.Ajinenko et al. *Z. Phys.*, **C5**:177, 1980.

[30] M.Barth et al. *Phys. Lett.*, **117B**:267, 1982.

[31] H.Dijkstra et al. *Z. Phys.*, **C31**:375, 1986.

[32] J.Badier et al. *Phys. Lett.*, **B93**:354, 1980.

[33] P.Sixel et al. *Nucl. Phys.*, **B199**:381, 1982.

[34] Yu.Arestov et al. *Z. Phys.*, **C6**:101, 1980.

[35] Yu.Arestov et al. *Z. Phys.*, **C8**:283, 1981.

[36] S.Banerjee et al. *Z. Phys.*, **C31**:401, 1986.

[37] P.V.Chliapnikov et al. *Z. Phys.*, **C12**:113, 1982.

[38] V.Shekhter, L.Scheglova. *Yad. Fiz.*, **27**:1070, 1978.

[39] A. Capella. In R.T. Van de Walle, editor, *Europhysics Study Conf. on Partons and Soft Hadronic Interactions (Erice)*, page 199, World Scientific, Singapore, 1982.

[40] E.A.De Wolf. In G.Gustafson, editor, *Proc. XVth Int. Symp. on Multiparticle Dynamics (Lund)*, page 2, World Scientific, Singapore, 1984.

[41] B.Andersson, G.Gustafson, B.Nillson-Almqvist. *Nucl. Phys.*, **B281**:289, 1987.

Experimental Results on QCD from e^+e^- Annihilation

W. de Boer *

Max-Planck-Institut für Physik und Astrophysik,
Werner-Heisenberg-Institut für Physik, D 8000 Munich 40
and
Stanford Linear Accelerator Center
Stanford University, Stanford, CA 94305

Abstract

A review is given on QCD results from studying e^+e^- annihilation with the PEP and PETRA storage rings with special emphasis on jet physics and the determination of the strong coupling constant α_s.

1 Introduction

This paper reviews the progress on the theory of hadronic interactions during the eight years of PEP and PETRA physics. This is an appropriate time, since a new generation of e^+e^- storage rings is underway (SLC and LEP) or ready (TRISTAN), which will extend the maximium centre of mass energies reached sofar to the Z^0 mass and beyond, thus opening a whole new field of physics. I will restrict myself to results from hadronic events from e^+e^- annihilation and neglect QCD results from two photon physics. The emphasis will be on newer results about the determination of the strong coupling constant, since other topics, like searches for new phenomena, jet properties, heavy quark fragmentation, and gluon fragmentation have been discussed in detail elsewhere [1].

In order to appreciate how much progress was made, let us review what was known some 10 years ago[2] :

- In 1972 Quantum Chromodynamics (QCD) was proposed by Fritzsch and Gell-Mann[3] as a gauge invariant field theory of the strong interactions: the gauge bosons are 8 coloured gluons, which are responsible for the strong forces between the quarks very much like the exchange of photons yields the electromagnetic force between charged particles.

*Work supported in part by the Department of Energy contract DE-AC03-76SF00515
Mailing address: SLAC (Bin 61), P.O. Box 4349, Stanford, CA 94305, USA
Bitnet address: user WDB at node SLACVM

- QCD was given an enormous boost by the discovery of asymptotic freedom by Gross and Wilczek[4] and Politzer[5], the subsequent observation of scale invariance which offers a justification for the highly successful quark parton model (QPM), and the observation of logarithmic deviations from this invariance as predicted by QCD.

- The discovery of the J/Ψ in 1974 at SLAC[6] and Brookhaven[7] and the proof that it corresponded to a bound state of $c\bar{c}$ quarks completed the quark picture and left little doubt to the idea that the mathematical objects originally proposed by Gell-Mann[8] and Zweig[9] to classify the hadrons were real, existing quarks.

- The charmed quark fitted beautifully into the $SU(2) \otimes U(1)$ unified theory of the electroweak interactions, proposed by Glashow, Salam and Weinberg[10] and proven to be renormalizible by 't Hooft[11], since in this model the matter fields are arranged in left-handed doublets and right-handed singlets, so there was an 'empty' slot in the doublet structure of this so-called Standard Model for the charmed quark. Actually from the absence of stangeness changing neutral currents Glashow, Iliopoulos and Maiani (GIM) had predicted the existence of the charmed quark[12].

- After 1974 a new heavy lepton (called τ) with its own neutrino was discovered by Perl and collaborators at SLAC[14] and a new quark (called bottom) was discovered by Lederman's group at Fermilab[13]. Given the succes of the Standard Model, one was in the same situation of having an 'empty' slot for a new quark (called top) in a thirth generation of quarks and leptons. So by the time of proposal writing for the PETRA experiments the quark picture was well established and the detectors were all optimized to do 'top' physics.

However, what was going to be one of the major discoveries at PETRA, namely the discovery of the gluon, was not even considered in the proposals as a physics topic. The main reason is that jet physics at that time was not very advanced, for the simple reason that the jet energies were too small to see jets on an event by event basis, so the idea that one might observe gluons as jets was not obvious, although it was proposed by several theorists[15]. The main evidence for jets in e^+e^- annihilation at that time came from the MARK-I Collaboration[16], who observed a deviation of the sphericity of hadronic events from phase space. Furthermore, the beams at SPEAR turned out to be polarized, which yielded an azimuthal variation of the sphericity axis, as expected for spin 1/2 quarks.

The outline of this paper is as follows:

- After summarizing the predictions of the Standard Model we discuss the main features of jet physics. We will be short, since this topic has been reviewed many times.

- We then proceed to the discussion of the more ambitious task of the determination of the strong coupling constant α_s. Note that within QCD the coupling between all quarks and gluons is supposed to be the same, so there is only one coupling constant to be determined.

- We conclude with a summary.

2 Standard Model Predictions

Even at present energies the effects of Z^0 exchange are noticeable, so one has to take the complete Standard Model of $SU(3)_C \otimes SU(2)_L \otimes U(1)$ into account. This model has 4 fundamental parameters (aside from masses and mixing angles) : three coupling constants for SU(3), SU(2) and U(1), respectively, and the vacuum expectation value of the Higgs doublet. If the model contains Higgs representations other than doublets, the theory has an additional parameter, usually parametrized by the ρ-parameter. To make comparisons with experiments easier, one should use parameters closely related to physical processes. Two of the parameters can be chosen as follows: the fine structure constant $\alpha = 1/137.036$ as obtained from the Josephson effect, and the Fermi coupling constant $G_F = 1.16637\ 10^{-5} GeV^{-2}$, as derived from the muon lifetime after applying the appropriate radiative corrections. As a third parameter one can take either mass of the neutral gauge boson M_Z or the electroweak mixing angle θ_W defined by $\cos\theta_W = M_W/M_Z$, where M_W is the mass of the charged gauge bosons. In both cases M_W is predicted in case $\rho = 1$, else one has to use $\cos\theta_W = M_W/(\rho M_Z)$. M_Z and θ_W are related via α and G_F by:

$$\frac{G_F(1-\Delta r)M_Z^2}{8\sqrt{2}\pi\alpha} = \frac{1}{16\sin^2\theta_W\cos^2\theta_W} \tag{1}$$

Here $\Delta r \approx 0.07$[17] are one-loop radiative corrections, which have not been absorbed in G_F. They depend on the unknown top- and Higgs mass. E.g. they vary from ≈7 % to 6 % (3%, 0%) for top masses varying from 45 GeV to 90 (180, 240) GeV and for a Higgs mass equal to the Z^0-mass. The fact that these corrections are so large comes mainly from the fact that α has been renormalized at low energy and its value increases by about 7% if it is calculated at the W-mass.

Of course, one could use different choices of parameters, e.g. M_W, but experimentally the previous choices can be better determined. The fourth parameter is either the value of the running strong coupling constant α_s at a given energy or the QCD scale parameter Λ, which determines the running of α_s and can be used to calculate α_s for a given energy.

2.1 Lowest order predictions

From the Feynman diagram for the production of quarks, as shown in Fig. 1a, one obtains the lowest order differential cross-section for the production of a pair

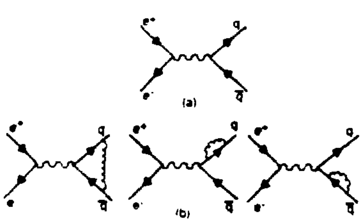

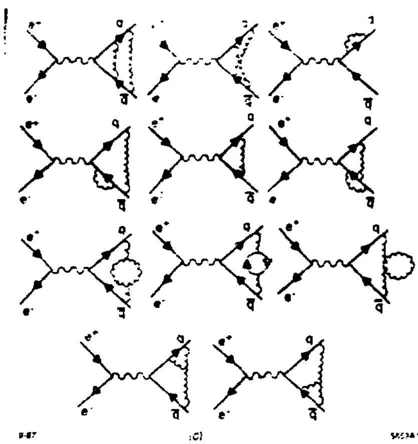

Fig. 1: a) Feynman diagrams for the production of 2-jet events in e^+e^- annihilation; b) first order QCD corrections; c) second order QCD corrections.

of quarks with charge e_q:

$$\frac{d\sigma}{d\Omega}(e^+e^- \rightarrow q\bar{q}) = N_c e_e^2 e_q^2 \frac{\alpha^2}{4s}\beta(1+\cos^2\theta + (1-\beta^2)\sin^2\theta) \qquad (2)$$

where θ is the scattering angle between the e^+ and the quark, and $\beta = \sqrt{1 - 4m_q^2/s}$ is the quark velocity. N_c=3 is the *colour factor*. Evidence for the colour of quarks comes from[2]:

- The Ω^- has spin 3/2 and is built up from three identical strange quarks. However, the Pauli principle does not allow spin 1/2 particles to be in the same state. To get the total wave function antisymmetric, one has to assume that each quark inside the Ω^- has an additional internal quantum number, called colour (red, green and blue quarks).
- The hadronic cross section of Eq. 2 would be a factor 3 too low compared with data, if the factor N_c was not introduced.
- The π^0 decays electromagnetically into two photons via a quark loop. Clearly the decay rate depends on the number of quarks in the loop and the experimentally observed decay rate requires N_c=3.

At higher energies the effect of the Z^0-exchange has to be included. In this case Eq. 2 becomes (if we use $\beta = 1$):

$$\frac{d\sigma}{d\cos\theta}(e^+e^- \rightarrow q\bar{q}) = N_c\frac{\pi\alpha^2}{2s}[C_1(1+\cos^2(\theta)) + C_2\cos(\theta)] \qquad (3)$$

with

$$\begin{aligned} C_1 &= e_e^2 e_q^2 + 2e_e e_q v_e v_q \Re(\chi) + (v_e^2 + a_e^2)(v_q^2 + a_q^2)|\chi|^2 \\ C_2 &= 4e_e e_q a_e a_q \Re(\chi) + 8v_e a_e v_q a_q |\chi^2| \end{aligned} \quad (4)$$

$$\begin{aligned} v_q &= 2(I_3^L + I_3^R) - 4\, e_q \sin^2\theta_W \\ a_q &= 2(I_3^L - I_3^R) \end{aligned} \quad (5)$$

and

$$\chi = \frac{\rho G_F}{8\sqrt{2}\pi\alpha} \frac{sM_Z^2}{s - M_Z^2 + iM_Z\Gamma_Z} \frac{1-\Delta r}{1-\Delta r'} \quad (6)$$

Here I_3^L and I_3^R are the 3th components of the weak isospin (see Table 1). In Eq. 6 the $1-\Delta r'$ term represents the loop corrections to the Z^0 propagator. Since $\Delta r' \approx \Delta r$ we can neglect both corrections in the fits to the hadronic cross section. Note that R-values are not corrected for $1-\Delta r'$, although asymmetry values are sometimes corrected for this factor in an indirect way[1]. In this case one has to apply only the correction factor $1-\Delta r$[18]. Then Eq. 6 becomes equal to its $\sin^2\theta_W$ parametrization (using Eq. 1):

$$\chi = \frac{G_F(1-\Delta r)}{8\sqrt{2}\pi\alpha} \frac{sM_Z^2}{s - M_Z^2 + iM_Z\Gamma_Z} \approx \frac{1}{16\sin^2\theta_W \cos^2\theta_W} \frac{s}{s - M_Z^2 + iM_Z\Gamma_Z} \quad (7)$$

A summary of these radiative corrections can be found in Ref.[19].

The terms proportional to $\Re(\chi)$ represent the interference between Z^0 and γ exchange and the terms proportional to $|\chi|^2$ the direct Z^0 exchange. The ratio of the total cross section contributions from Z^0 and γ exchange ($(C_1 - e_f^2)/e_f^2$) is shown in Table 1 for the various matter fields together with the coupling constants.

fermion	I_3^L	I_3^R	a	v	e_f	$\frac{C_1-e_f^2}{e_f^2}$	A
neutrino	1/2	0	1	1	0	∞	0.12
μ,τ *lepton*	−1/2	0	−1	$-1+4\sin^2\theta_W = -0.08$	−1	1.2%	−0.15
u,c,t *quarks*	1/2	0	1	$+1-\frac{8}{3}\sin^2\theta_W = 0.39$	+2/3	1.8%	−0.23
d,s,b *quarks*	−1/2	0	−1	$-1+\frac{4}{3}\sin^2\theta_W = -0.69$	−1/3	11.0%	−0.41

Table 1: Summary of couplings and asymmetry for M_Z=92 GeV and $\sin^2\theta_W$ =0.23 at $\sqrt{s}$=44GeV

From Eq. 3 the total cross section is found to be $N_c C_1 4\pi\alpha^2/3s$ and the forward-backward asymmetry in the differential cross section equals:

$$A = \frac{\int_0^1 \frac{d\sigma}{d\cos\theta} d\cos(\theta) - \int_{-1}^0 \frac{d\sigma}{d\cos\theta} d\cos(\theta)}{\int_0^1 \frac{d\sigma}{d\cos\theta} d\cos(\theta) + \int_{-1}^0 \frac{d\sigma}{d\cos\theta} d\cos(\theta)} = \frac{3}{8}\frac{C_2}{C_1} \quad (8)$$

For leptonic final states the vector coupling v is small and only the interference term needs to be taken into account at PETRA energies. In this case the asymmetry in Eq. 8 depends only on the axial vector couplings. However, for quarks the vector couplings are large and the direct Z^0-exchange term ($\propto |\chi|^2$) is larger than the interference term at the highest PETRA energies.

[1] The loop corrections and the initial state radiative corrections for the Z^0-exchange have an opposite sign and are similar in magnitude at PETRA energies, so if one neglects them both, the remaining contribution is negligible[18] and one can forget about the $1-\Delta r'$ correction.

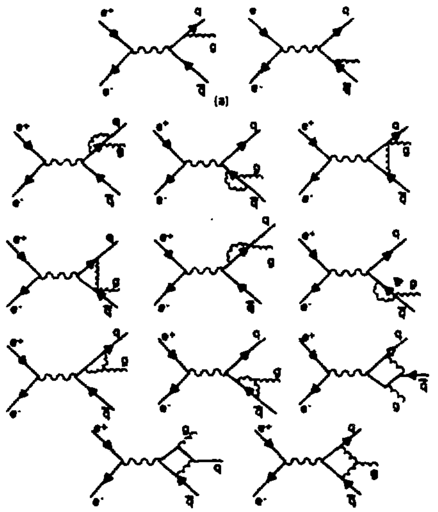

Fig. 2: a) Feynman diagrams for the production of 3-jet events in e^+e^- annihilation; b) second order QCD corrections.

2.2 First order QCD predictions

In first order the quark production is modified by gluon radiation as shown by the diagrams of Fig. 2a. The properties of the gluon are the following:

- the mass is 0.
- the spin parity $J^P = 0^-$.
- gluons are colour octet states. There exist $2N_c - 1 = 8$ different gluons. At the gluon-quark vertex the colour of a quark is changed, e.g. a red-blue gluon g_{rb} transforms a red quark into a blue one. (see Fig. 3a).
- The gluon-quark coupling is independent of the colour and quark flavour, so it is the same for all quarks and gluons.
- In contrast to photons, which are electromagnetically neutral, gluons carry a colour charge. As a result, the gluons interact with themselves, which lead to the presence of three and four gluon vertices in the theory (see Fig. 3b).

The differential cross section for gluon emission is given by[15]:

$$\frac{d^2\sigma(q\bar{q}g)}{\sigma(q\bar{q})dx_1dx_2} = \frac{\alpha_s}{2\pi}C_F\frac{x_1^2+x_2^2}{(1-x_1)(1-x_2)} = \frac{\alpha_s}{2\pi}C_F\left(\frac{y_{23}}{y_{13}} + \frac{2y_{12}}{y_{13}y_{23}} + \frac{y_{13}}{y_{23}}\right) \quad (9)$$

with 1, 2, 3 cyclic permutations. The Casimir operator $C_F = (N_c^2-1)/2N_c = 4/3$ for 3 colours and $x_i = E_i/E_{beam}$ are the fractional parton energies with $x_1 + x_2 +$

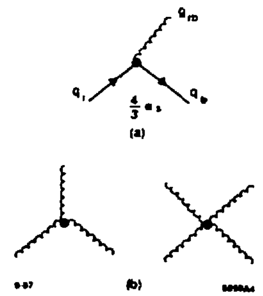

Fig. 3: a) Quark-gluon interaction: a red quark is transformed into a blue quark by emitting a red-blue gluon. The coupling strength=$4\alpha_s/3$.
b) Three - and four gluon vertices.

$x_3 = 2$ and $y_{ij} = (p_i + p_j)^2/s$ are the scaled invariant masses; the subscripts 1 and 2 refer to the quarks and 3 to the gluon. This formula neglects quark masses, in which case $y_{ij} = (p_i+p_j)^2/s = 2p_ip_j/s = 1-x_k$ with i, j, and k cyclic permutations.

The coupling constant α_s between quarks and gluons determines the rate of gluon emission, which follows a typical bremsstrahlung spectrum: it diverges for soft gluons (x_1 and $x_2 \approx 1$, so double pole) and collinear gluons (x_1 or $x_2 \approx 1$). The sum of the 2- and 3-jet cross sections is finite, since if the first order virtual corrections to the 2-jet cross section are taken into account (see Fig. 1b) the divergencies in the 3-jet cross section are canceled. This corresponds to the Kinoshita-Lee-Nauenberg theorem in QED[20], which guarantees that if one sums over all collinear and soft photons, the total cross section will be finite. Furthermore, the cross section stays finite for massless particles (no mass singularities).

Eq. 9 gives the cross section for bare partons. In order to calculate an observable cross section one has to take into account the finite jet resolution, which implies that one observes only jets 'dressed' by the accompanying soft gluons. The situation is similar to QED: the observed cross section $\sigma(e^+e^- \to \mu^+\mu^-)$ contains also that part from the radiative cross section $\sigma(e^+e^- \to \mu^+\mu^-\gamma)$ for which the photon is either too soft or too collinear to be detected. Correspondingly, the observable 2-jet cross section contains that part of the 3-jet cross section for which the gluon jet is irresolvable from the quark jets (dressed jets).

Two criteria have been used to define the jet resolvability:

- ϵ, δ cuts. In this case two partons are considered to be irresolvable if either one or both partons are too soft, i.e. have a parton energy less than $\epsilon \frac{\sqrt{s}}{2}$ or the partons are collinear, i.e. the angle between the partons is less than δ.

- y-cuts. In this case 2 partons are considered to be irresolvable if their scaled invariant mass is below a certain minimum: $(p_i + p_j)^2/s \leq y_{min}$. It should be noted that y cuts are Lorentz invariant, while the ϵ, δ cuts are not, so the ϵ, δ cuts refer to the centre of mass system.

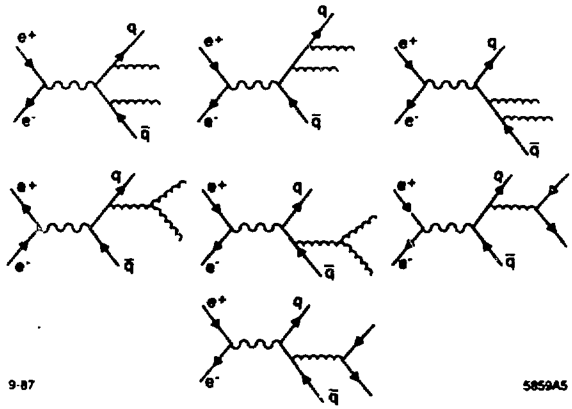

Fig. 4: Leading order Feynman diagrams for the production of 4-jet events in e^+e^- annihilation.

2.3 Second order QCD predictions

In second order QCD one has to take into account the production of 4-jets, as shown by the graphs in Fig. 4 and the virtual corrections to the 3-jet cross section as shown in Fig. 2b. Again, the observable jet cross sections have to include the contributions from higher order graphs with irresolvable partons, so schematically one gets in second order QCD:

$$\sigma^{obs}_{2-jet} = \sigma^{tree}_{2-jet} + \sigma^{virt}_{2-jet}[O(\alpha_s)] + \sigma^{virt}_{2-jet}\left[O(\alpha_s{}^2)\right] + \sigma_{3-soft} + \sigma_{4-soft} \tag{10}$$

$$\sigma^{obs}_{3-jet} = \sigma^{tree}_{3-jet} + \sigma^{virt}_{3-jet}\left[O(\alpha_s{}^2)\right] + \sigma'_{4-soft} \tag{11}$$

$$\sigma^{obs}_{4-jet} = \sigma^{tree}_{4-jet} \tag{12}$$

In these equations σ_{3-soft} and σ_{4-soft} are the 3- and 4 jet cross sections with irresolvable partons, which have to be integrated over the corresponding region of phase space and then added to the 2- or 3-jet cross section. These definitions are exemplified in Fig. 5 for the 3-jet case: σ_{3-soft} is the 3-jet cross section integrated over the shaded area with $y_{ij} \leq y_{min}$, while σ^{tree}_{3-jet} is the cross section integrated over the remaining part of phase space. As can be seen from Eqs. 10 to 12 the 2-jet cross section is the most elaborate one to calculate, but in actual Monte Carlos the 2-jet cross section is defined as the difference between the total cross section and the dressed 3- and 4-jet cross sections, which all have been calculated. Also the 2-jet cross section was calculated recently, which allows a check of the consistency of the calculations[21].

The 4-jet cross sections in second order has only contributions at the tree level(see Eq. 12), which have been calculated by various groups and all agree[22].

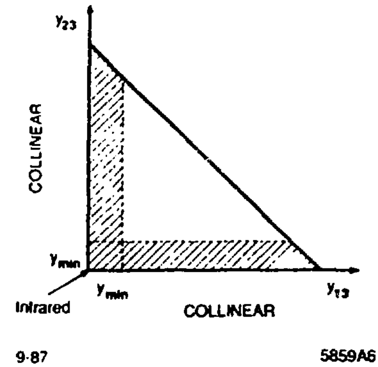

Fig. 5: $q\bar{q}g$ **phase space. The shaded area with** $y_{ij} \leq y_{min}$ **is counted as part of the 2-jet cross section .**

However, the 3-jet cross sections in second order requires virtual corrections (see Eq. 11 and Fig. 2b), which were calculated by several groups (denoted by the first letters of the author names): GKS[23], ERT[24], and VGO[25]. Originally the conclusions were rather different: The last 2 groups claimed the second order virtual corrections to be large, while the first group claimed these corrections to be small. It is now understood that these different conclusions came from the different jet-resolution criteria[26]: The first group included jet resolution ('dressed jets'), while the other groups calculated the cross section for bare partons. In the latter case the 4-jet cross section dominates and the 3-jet cross section becomes negative. An example of these cross sections as function of the jet resolution is shown in Fig. 6[27]. As can be seen, for small y-cuts (i.e. 1/y large) large cancelations occur corresponding to large second order corrections.

Insisting on a positive 3-jet cross section requires the y-cut to be above ≈ 0.01 (depending on α_s). On the other hand one should not take too large y-cuts, since in this case most of the 3-jet events are recombined to 2 jets. Reasonable cuts are in the range 0.01 to 0.05, although some experimental distributions prefer values closer to 0.01.

The GKS matrix element has been implemented in the LUND Monte Carlo and the ERT matrix element has been made suitable for Monte Carlo generators by Zhu[28] from the MARK-J Collaboration by complementing it with a jet dressing scheme along the lines of Ali[29] and Kunszt[30]. It was implemented in the LUND Monte Carlo by Csikor[31].

For the actual Monte Carlo implementations the GKS matrix element gives a lower 3-jet cross section than the ERT matrix element as shown in Fig. 7: at y=0.02(0.04) ERT gives a factor 2.5 (1.5) larger second order contribution, which corresponds to a 12(7) % increase in the total 3-jet rate for α_s=0.15. Possible

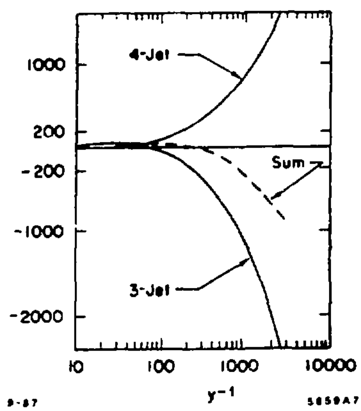

Fig. 6: The 3- and 4-jet cross section as function of the jet resolution parameter 1/y.

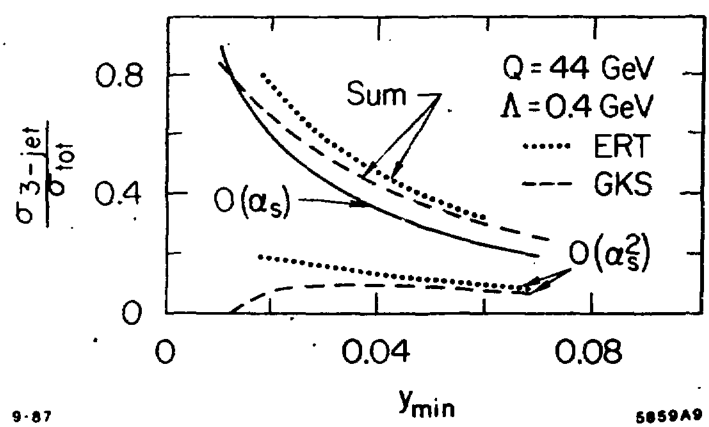

Fig. 7: The 3-jet cross sections as function of the y-cut for the ERT- and GKS matrix elements.

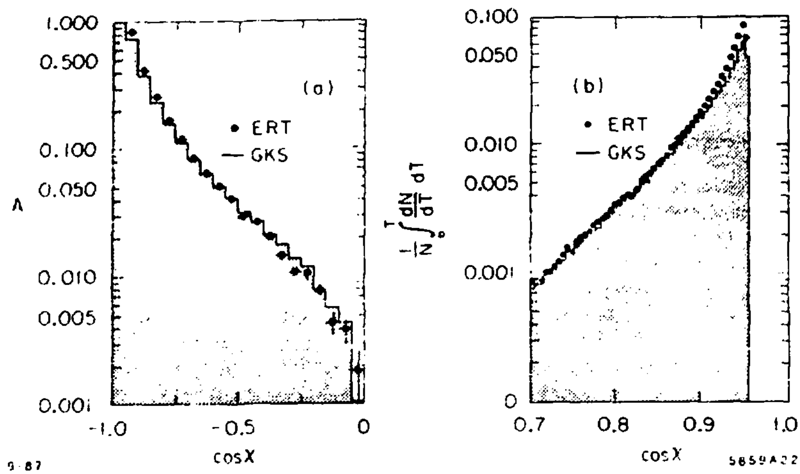

Fig. 8: Integrated thrust (a) and integral of the AEEC (b) for the 2 different matrix elements ERT(solid dots) and GKS(histogram). Both distributions are plotted at the parton level for $\sqrt{s}$=44 GeV, $\Lambda_{\overline{MS}}$=400 MeV and y_{min}=0.02.

causes for the differences are the approximations made in the GKS calculations and the ambiguity concerning the treatment of soft gluons in 4-jet events:

- In the ERT implementation the irresolvable partons are recombined with the nearest parton either by summing the 3-momenta or 4-momenta (momentum and energy schemes, respectively). The nearest parton is the one which yields the smallest invariant mass. The difference between the energy- and momentum scheme is small [28].

- In the GKS implementation with y-cuts the recombination scheme is similar to the previous one. However, if ϵ, δ cuts are used, the partons failing the δ cuts are recombined, but the partons failing the ϵ cuts are discarded and the energy of the remaining partons is rescaled, so here the energy of the soft partons is distributed over all partons, while in the previous scheme it was added to the nearest parton.

The difference between the various recombination schemes has been studied in detail[28,32]. Unfortunately, no clear-cut theoretical argument can be given for either of the dressing schemes, but the differences concern mainly soft gluons. So if one studies gluons only in the perturbative regime, the differences between the matrix elements are small, especially if one uses y-cuts (implying similar dressing schemes). This is demonstrated in Fig. 8 for the integrated parton thrust for dressed 3-jet events and the asymmetry in energy weighted angular correlations

(AEEC, see Sect. 5.3). Low thrust values and large angles correspond to regions where the hard gluons dominate. For thrust values integrated up to 0.9 the difference is negligible. For larger values ERT is ≈25% higher. For the AEEC the difference depends on the angular range considered: for $\cos\chi > -0.7$ the GKS prediction is somewhat above ERT while for the small angle region ERT is higher. A fit of the QCD calculation in the range $\cos\chi > -0.7$ yields less than 30 MeV difference in the QCD scale parameter between the two matrix elements.

TASSO [33] studied the differences between the matrix elements using ϵ, δ cuts (implying different dressing schemes). They find from the AEEC a difference in α_s of ≈ 15% even after correcting for some of the missing diagrams in the implementation of the GKS matrix element.

MARK-II [34] studied the difference between GKS and a new matrix element by Gottschalk and Shatz, which is also based on analytic formulae [26], but it does not use the approximations made by GKS. They find a 10% lower value of α_s with this new matrix element, if they fit the AEEC for $\cos\chi > -0.88$.

So it is important in the comparison of results to keep in mind which matrix element was used and which variable was fitted in what range.

2.4 Definition of the running coupling constant

The coupling constant is not constant, but varies with Q^2 both in QED and in QCD. However, in QED the coupling constant increases as function of Q^2, while in QCD the coupling constant decreases. A simple picture for this behaviour is the following:

- In QED the coupling constant decreases with increasing energy, since the photons which make up the electric field around an electric charge can be transformed into e^+e^- pairs. These e^+e^- pairs are oriented in the electric field (=polarized) and provide an effective shielding of the 'bare' electric charge. If the electric charge is probed at higher energies (or shorter distances), one penetrates the shielding from the vacuum polarization deeper and observes more of the bare charge, or equivalently one observes a larger coupling constant.

- In QCD the situation is more complicated: the colour charge is surrounded by a cloud of gluons and virtual $q\bar{q}$ pairs, but since the gluons themselves carry a colour charge, one has two contributions: a shielding of the bare charge by the $q\bar{q}$ pairs and an increase of the colour charge by the gluon cloud. The net effect of the vacuum polarization is an increase of the total colour charge, provided not too many $q\bar{q}$ pairs contribute (number of generations < 16, see hereafter). If one probes this charge at smaller distances, one penetrates part of the 'antishielding', thus observing a smaller colour charge at higher energies. So it is the fact that gluons carry colour themselves which make the coupling decrease at small distances (or high energies).

The effect of the virtual pairs surrounding an electric charge or colour charge can be calculated from the diagrams in Fig. 9. These diagrams are divergent for

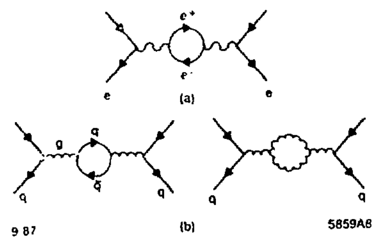

Fig. 9: The lowest order vacuum polarization diagrams leading to a renormalized electric - (a) and colour charge (b).

large Q^2. A theory is renormalizable if one can absorb all divergencies in the bare coupling constants. The first step in such calculations is the regularization of the divergencies, which is usually done with the dimensional regularization scheme of 't Hooft and Veltman[35]. In $n = 4 - 2\epsilon$ dimensions the bare coupling constant has the dimension of a mass. In order to make it dimensionless, one introduces an arbitrary parameter μ with the dimension of a mass and defines the coupling as $g(\mu^2) = \mu^\epsilon g$ and $\alpha_s = g^2/4\pi = \alpha_s(\mu^2)$ The diagram in Fig. 9a contributes a term $\approx \frac{\alpha(\mu^2)}{3\pi} ln\frac{Q^2}{\mu^2}$ to the cross section, if $Q^2 >> \mu^2$. In QED it is customary to choose for μ the electron mass m_e. In this case one can absorb the divergent vacuum polarization in an effective coupling constant by modifying the fine structure constant $\alpha = e^2/4\pi$ as follows:

$$\alpha(Q^2) = \alpha(1 + \frac{\alpha}{3\pi} ln\frac{Q^2}{m_e^2}) \tag{13}$$

If one sums more loops, this yields terms $(\frac{\alpha}{3\pi})^n(ln\frac{Q^2}{m_e^2})^m$ and retaining only the leading logarithms (i.e. n=m), the addition of these terms yields:

$$\alpha(Q^2) = \frac{\alpha}{(1 - \frac{\alpha}{3\pi} ln\frac{Q^2}{m_e^2})} \tag{14}$$

since

$$\sum_{n=0}^{\infty} x^n = \frac{1}{1-x}. \tag{15}$$

Of course, the total Q^2 dependence is obtained by summing over all possible fermion loops in the photon propagator.

The diagrams of Fig. 9b yield similarly:

$$\alpha_s(Q^2) = \alpha_s(\mu^2)\left[1 - \frac{\alpha_s(\mu^2)}{4\pi}\left(11 - \frac{2N_f}{3}\right) ln\frac{Q^2}{\mu^2}\right] \tag{16}$$

Note that α_s decreases with increasing Q^2 if $11 - \frac{2N_f}{3} > 0$ or $N_f < 16$, thus leading to asymptotic freedom at high energy. This is in contrast to the Q^2 dependence of $\alpha(Q^2)$ in Eq. 13, which increases with increasing Q^2. Since α_s becomes infinite at small Q^2, one cannot take this scale as a reference scale, as was done in the case of QED.

A physical quantity should not depend on the spurious parameter μ, at least if one calculates it to all orders. If one calculates only up to a finite order, one can minimize the higher order terms by a suitable choice of μ. In lowest order μ is arbitrary, but in higher orders the loop calculations contain terms $ln\frac{Q^2}{\mu^2}$ and to keep these terms small, it is best to choose μ^2 to be of the same order as Q^2, where Q^2 is the relevant physical scale of the process.

The higher order corrections are usually calculated with the renormalization group technique, which yields for the μ dependence of α_s :

$$\mu\frac{\partial \alpha_s}{\partial \mu} = \beta_0\alpha_s^2 + \beta_1\alpha_s^3 + \beta_2\alpha_s^4 + ... \tag{17}$$

The first two terms in this perturbative expansion are renormalization-scheme independent and given by:

$$\beta_0 = -\frac{1}{2\pi}\left[11 - \frac{2N_f}{3}\right] \tag{18}$$

$$\beta_1 = -\frac{1}{4\pi^2}\left[51 - \frac{19N_f}{3}\right] \tag{19}$$

Higher order terms depend on the renormalization prescription. In the $\overline{MS}$ scheme β_2 has been calculated [36]:

$$\beta_2 = -\frac{1}{64\pi^3}\left[2857 - \frac{5033N_f}{9} + \frac{325N_f^2}{27}\right] \tag{20}$$

Eq. 17 can be integrated as follows (retaining only the first two terms):

$$\int_{\mu_0}^{\mu}\frac{d\mu}{\mu} = \int_{\alpha_s(\mu_0)}^{\alpha_s(\mu)}\frac{d\alpha_s}{\alpha_s^2(\beta_0 + \beta_1\alpha_s)} \tag{21}$$

Here μ_0 is a reference mass scale. Instead of introducing two separate lower bounds in the integrals in Eq. 21, one usually combines them by choosing for μ_0 the QCD scale Λ, which fulfills the boundary condition $\alpha_s(\mu = \Lambda) = \infty$. Following the discussion after Eq. 16, we choose again $\mu^2 = Q^2$. In this case the solution of Eq. 21 is:

$$\frac{1}{\alpha_s(Q^2)} = -\frac{\beta_0}{2}ln\frac{Q^2}{\Lambda^2} + \frac{\beta_1}{\beta_0}ln(1 + \frac{\beta_0}{\beta_1\alpha_s(Q^2)}) \tag{22}$$

The last term in this equation can be approximated by $ln(1/\alpha_s) \approx ln(ln\frac{Q^2}{\Lambda^2})$, if $Q^2 >> \Lambda^2$. One can then write a functional form for α_s:

$$\frac{1}{\alpha_s(Q^2)} = -\frac{\beta_0}{2}ln\frac{Q^2}{\Lambda^2} + \frac{\beta_1}{\beta_0}ln(ln\frac{Q^2}{\Lambda^2}) \tag{23}$$

which is approximated in the Particle Data Book [37] as:

$$\alpha_s(Q^2) = \frac{12\pi}{(33-2N_f)ln\frac{Q^2}{\Lambda^2}}\left[1-6\frac{153-19N_f}{(33-2N_f)^2}\frac{ln(ln\frac{Q^2}{\Lambda^2})}{ln\frac{Q^2}{\Lambda^2}}\right] \tag{24}$$

The approximations in Eqs. 23 and 24 both introduce an error of $\approx 15\%$ in Λ for a given α_s, but they are of opposite sign and largely cancel each other, *so we will use Eq. 24 hereafter.*

In the $\overline{MS}$ scheme N_f is the number of flavours with mass $m_q < \mu$ (not $2m_q < \mu$). If μ becomes larger than m_q at a certain energy, one has to increase N_f. With the previous definition of α_s, this would give a discontinuity in α_s, since α_s depends explicitly on N_f. Such a discontinuity is unphysical, since only the running of the coupling constant can change if more quarks contribute to the vacuum polarization, not its value. This can be remedied in the previous formula either by the use of a different Λ for each number of flavours (as is usually done) or one has to incorporate explicitly a counter term in the definition of α_s. E.g. if Λ_5 is defined for 5 flavours, then for $m_c < Q < m_b$ Eq. 24 becomes[38]:

$$\alpha_s(Q^2) = \frac{12\pi}{(33-2N_f)ln\frac{Q^2}{\Lambda^2}}\left[1-\frac{\frac{462}{625}ln(ln\frac{Q^2}{\Lambda^2}) - \frac{2}{25}\left(ln\frac{m_b^2}{\Lambda_5^2}+\frac{963}{575}ln(ln\frac{m_b^2}{\Lambda_5^2})\right)}{ln\frac{Q^2}{\Lambda^2}}\right] \tag{25}$$

Alternatively, one can neglect the last term in the brackets and use for $m_c < Q < m_b$ a different Λ_4 defined by[38]:

$$\frac{\Lambda_4}{\Lambda_5} \approx \left[\frac{m_b^2}{\Lambda_5^2}\right]^{\frac{1}{25}}\left[ln\frac{m_b^2}{\Lambda_5^2}\right]^{\frac{963}{14375}} \tag{26}$$

This ratio varies from 1.57 to 1.47(1.41) for Λ_5 varying from 100 to 200(300) MeV.

In summary one can absorb the divergent vacuum polarization diagrams in the coupling constant, which then becomes dependent on Q^2. Instead of quoting a coupling constant at a given Q^2, one can use the scale parameter Λ, which is independent of Q^2 and can be defined by the boundary condition requiring $\alpha_s(\mu = \Lambda) = \infty$.

2.5 The total hadronic cross section

The normalized total cross section for multihadron production from e^+e^- annihilation is defined as the ratio R

$$R \equiv \frac{\sigma[e^+e^- \to \gamma, Z^0 \to hadrons]}{\sigma[e^+e^- \to \gamma \to \mu^+\mu^-]} \tag{27}$$

where the numerator is the hadron production cross section corrected for QED radiative corrections. The denominator is just a calculated quantity equal to the pointlike QED cross section: $4\pi\alpha^2/3s$.

At the highest PETRA energies Z^0 exchange and, to a lesser extent, the interference between the photon and Z^0 exchange becomes important. The prediction of the Standard Model can be written as:

$$R = R_0\left[1 + \frac{\alpha_s(s)}{\pi} + C_2\left(\frac{\alpha_s(s)}{\pi}\right)^2\right] \tag{28}$$

with (see Eq. 3)

$$R_0 = 3\sum_q \left[e_e^2 e_q^2 + 2e_e e_q v_e v_q \Re(\chi) + (v_e^2 + a_e^2)(v_q^2 + a_q^2)|\chi|^2\right] \tag{29}$$

Here we have neglected quark mass effects. At the lowest PETRA energies (14 GeV) the effect of m_b is 1%, which has been taken into account in the fits described hereafter[39]. The constant C_2 depends on the renormalization scheme chosen to minimize the higher order corrections. In the $\overline{MS}$ scheme it is given by[40]:

$$C_2 = 1.986 - 0.115N_f \tag{30}$$

provided the scale μ of α_s is taken to be $\sqrt{s}$. If another renormalization point is chosen, e.g. $\mu = x\sqrt{s}$, one obtains a different R, α_s, and C_2[41,42,43,44]:

$$R' = R + O(\alpha_s{}^3) \tag{31}$$

$$\alpha_s{}' = \alpha_s + \frac{\beta_0}{\mu}\alpha_s{}^2 d\mu + O(\alpha_s{}^3) \tag{32}$$

$$C_2' = C_2 + \frac{\partial C_2}{\partial \mu} d\mu \tag{33}$$

Eq. 33 is just by definition and Eq. 32 follows from Eq. 17. If one neglects terms of $O(\alpha_s{}^3)$ one obtains by simply equating $R' = R$:

$$\frac{\partial C_2}{\partial \mu} + \frac{\pi\beta_0}{\mu} = 0 \tag{34}$$

or

$$C_2' = C_2 - \pi\beta_0 \ln x \tag{35}$$

and

$$R = R_0\left[1 + \frac{\alpha_s(x^2 s)}{\pi} + C_2'\left(\frac{\alpha_s(x^2 s)}{\pi}\right)^2\right] \tag{36}$$

This last expression differs from Eq. 28 only by the constant C_2 and the renormalization point, so one sees that changing the renormalization point is equivalent to changing renormalization schemes (implying different coefficients C_2).

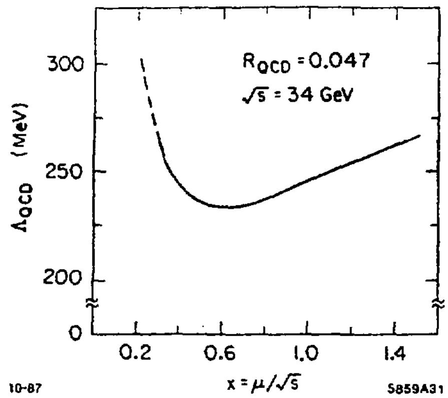

Fig. 10: The dependence of the QCD scale Λ on the renormalization point μ (normalized to $\sqrt{s} = 34GeV$) given a QCD contribution to R of 0.047. The curve was obtained by choosing x, then calculating the value of α_s for a given R from Eqs. 35 and 36, and then determining Λ from Eq. 22.

2.6 Choice of renormalization scheme

Physical quantities do not depend on the renormalization scheme (RS) or renormalization point (μ in Sect. 2.3), if they are calculated to all orders in perturbation theory. However, if one calculates only up to order n, thus neglecting terms of $O(n+1)$, then different RS's can also differ by terms of $O(n+1)$. Stevensen[42] proposed to choose for each process a renormalization point such that the observable shows minimal sensitivity to the RS, i.e. $\partial\Re/\partial(RS)=0$ or $\partial\Re/\partial ln\mu=0$.

This 'principle of minimal sensitivity' (PMS) can be easily applied to the measurement of R and we will then compare it to other renormalization schemes. For a given value of R one can study the dependence on μ with Eqs. 35 and 36 and one can determine the resulting variation of α_s as function of $x = \mu/\sqrt{s}$ or more easily Λ as function of x, since Λ is independent of μ. Fig. 10 shows this dependence. The PMS value of x is obtained by requiring

$$\frac{\partial R}{\partial ln\mu} = \frac{\partial R}{\partial\alpha_s}\frac{\partial\alpha_s}{\partial ln\mu} + \frac{\partial R}{\partial C_2'}\frac{\partial C_2'}{\partial ln\mu} = 0 \tag{37}$$

The partial derivatives are easily calculated from Eqs. 17, 35 and 36 and inserting them into Eq. 37 yields:

$$\left(\frac{1}{\pi} + 2\frac{\alpha_s}{\pi^2}C_2'\right)\alpha_s^2(\beta_0 + \beta_1\alpha_s) - \beta_0\frac{\alpha_s^2}{\pi} = 0 \tag{38}$$

or for $C_2' = C_2^{opt}$ corresponding to the PMS criterion

$$C_2^{opt} = -\frac{\pi\beta_1}{2\beta_0\left[1+\frac{\beta_1}{\beta_0}\alpha_s\right]} \approx -\frac{\pi\beta_1}{2\beta_0} \tag{39}$$

This corresponds to an optimum scale μ^{opt} given by $x^{opt} = \mu^{opt}/\sqrt{s}$ (from Eq. 35):

$$ln\ x^{opt} \approx \frac{1.41}{\pi\beta_0} + \frac{\beta_1}{2\beta_0^2} \tag{40}$$

The value of $x^{opt} \approx 0.59$ corresponds to the minimum of the curve in Fig. 10, since for this line R is constant, so Eq. 37 is automatically satisfied if $\partial\Lambda/\partial\mu=0$[43]. The difference in $\Lambda_{\overline{MS}}$ (defined for $x = 1$) and Λ at x^{opt} is less than 5% for the example shown in Fig. 10.

Other renormalization schemes absorb different factors in the coupling constant, yielding different values of Λ; they are related to each other by a one-loop calculation as was first pointed out by Celmaster and Gonsalves[45].

However, the ratio $\frac{\mu}{\Lambda}$ is similar in each RS[42][2], so instead of varying Λ one can study the RS dependence by studying the μ dependence as mentioned also in the previous section. From Fig. 10 one sees that Λ varies less than 15% for $0.5 < x < 1.5$, so the uncertainty from the renormalization scheme dependence is of this order of magnitude.

It is interesting to note that $C_2' = 0$ for $x = 0.69$, so if one chooses as scale $0.69\sqrt{s}$, the second order corrections become zero.

Note also that one cannot choose x below $\approx$0.20, since in that case the second order contribution becomes so large and negative that no positive solution for the QCD contribution to R can be found.

2.7 How to compare the Standard Model with data?

Not well determined in the SM are:

- the Higgs sector
- the strong coupling constant
- the weak properties of heavy quarks

In e^+e^- annihilation one gets a handle on the last two points, since

- The strong coupling constant can be either determined from the increase in the total hadronic cross section due to gluon bremsstrahlung or from the determination of the number of 3-jet events. The first one has the advantage, that it is theoretically very clean, but the effect is not large, (≈ 5 % increase in R at 34 GeV), so the experimental errors dominate. In the case of the multijet analysis uncertainties from uncalculable fragmentation effects dominate the error.

[2]The optimum value of μ/Λ is an RS invariant.

- Above threshold one can study both heavy and light quarks in contrast to e.g. deep inelastic lepton nucleon scattering, where only the electroweak properties of light quarks can be studied.

Several strategies can be followed in the analysis:

- Determine the vector and axial vector coupling constants of the individual quarks separately. The axial coupling constants can be determined from the asymmetry, which contains the product $a_e a_q$ (see Eq. 8). The asymmetry can be determined for a specific quark flavour by a suitable flavour tagging technique (high p_t leptons or heavy meson identification) or averaged over all quarks. All asymmetry measurements sofar have been found to be in agreement with the Standard Model, although the errors are large[46]. Therefore we will accept in the following the basic assumption that all matter fields belong to weak isospin doublets, which then fixes uniquely the axial vector couplings of all leptons and quarks, since it is given by the position in the doublet ($a = I_3^L - I_3^R$).
- With the axial vector couplings of quarks and leptons fixed, one can proceed to determine the vector couplings from the total hadronic cross section. These depend on the single parameter $\sin^2\theta_W$, once the weak isospin structure has been fixed (see Eq. 5). The consistency of the vector couplings with the Standard Model can be checked by comparing the fitted $\sin^2\theta_W$ value with the world average.

The Higgs bosons are difficult to search for, since the mass is unknown and the production cross sections are small. The ρ parameter can deviate from 1 in case of a more complicated Higgs sector. From an analysis of data on neutral current interactions ρ is constrained to 0.998 ± 0.009[47]. Therefore we will assume the standard Higgs structure with $\rho = 1$ in what follows.

3 Jet Physics

Since free quarks have not been observed, QCD has to be complemented by the hypothesis that physical states are colour singlets, so if energetic quarks are produced, they are converted into hadrons by the strong forces. This hadronization can be described by simple phenomenological models, in which the hadrons are created with limited transverse momenta. This automatically leads to jet production at high energies: since the multiplicity is only rising slowly with energy ($n_{ch} \propto lns$) the jets become more and more collimated. The cone angle of the jet will decrease roughly as:

$$\delta \approx \frac{< p_\perp >}{< p_\parallel >} \approx \frac{< p_\perp >}{s / < n_{ch} >} \propto \frac{lns}{s} \tag{41}$$

Therefore only at high energies will one be able to resolve the jets in multijet events. When PETRA started operating around 30 GeV, 2-jet events were very

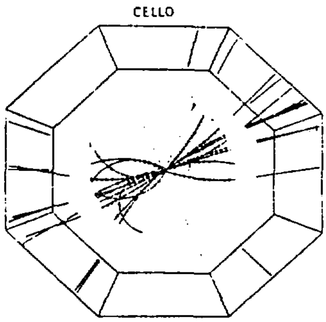

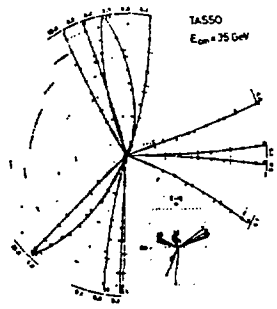

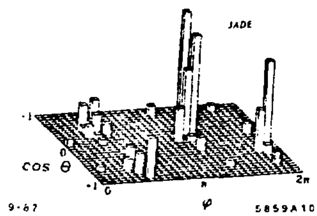

Fig. 11: Example of a 2- , 3- , and 4-jet event. The first two are shown in the projection perpendicular to the beam axis, while the last one is a 'LEGO' plot of azimuthal versus polar angle.

obvious just by visually scanning the events, so one did not need statistical methods. Furthermore, a sizeable fraction of events showed a clean 3-jet structure and sometimes 4-jets were observed. Fig. 11 shows some examples.

Several methods have been used to classify multijet events, e.g. cluster algorithms yielding directly the number of jets, the sphericity, aplanarity, thrust, oblateness, spherocity, triplicity and others. Most of them have been incorporated as utility routines in the LUND Monte Carlo, so the interested reader can consult the descriptions there[48]. Detailed studies showed that:

- From the angular distribution of two jet events it is clear that the original partons have spin 1/2, as shown in Fig. 12 by the characteristic $1 + a\cos^2\theta$ distribution of the sphericity axis: the best fit yields $a = 1.01 \pm 0.1$, which is close to the expected value of $a = 1$ for spin 1/2 quarks and far from the value of $a = -1$ for spin 0 quarks.

- The 3-jet events are planar and originated from a bremsstrahlung spectrum. Two typical plots are shown in Figs. 13 and 14. The first one shows that the broadening of the transverse momentum in a jet takes place mainly in the event plane, while $< p_t^{out} >$ hardly changes as function of energy, thus excluding the possibility that the p_t broadening is caused by an energy dependent fragmentation effect. The second plot shows that the oblateness is only well described by the Monte Carlo if gluon radiation is included.

- The angular distributions of the jets relative to each other in 3-jet events depend on the spin of the gluon. A simple distribution was proposed by Ellis

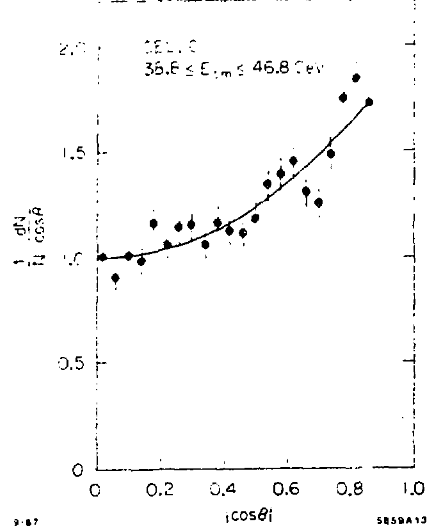

Fig. 12: **The angular distribution of the sphericity axis of multihadronic events. The curve is the fitted $1 + a\cos^2\theta$ distribution with $a = 1.01 \pm 0.1$.**

Fig. 13: **The transverse momenta in a jet as function of centre of mass energy. The data at lower energies (top) can be described by $q\bar{q}$-production while the events at high energies develop a planar event structure, as expected for $q\bar{q}g$ production. Note that the transverse momentum distribution perpendicular to the event plane, shown on the left-hand side, is found to be similar for both energies.**

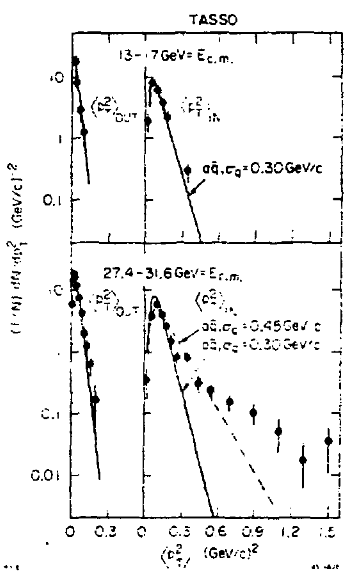

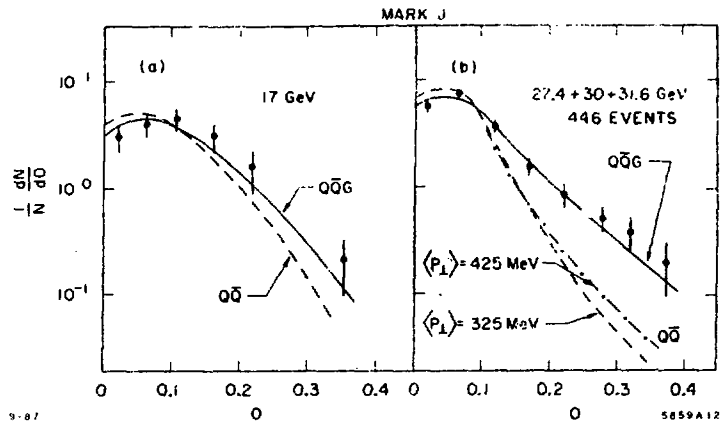

Fig. 14: The oblateness compared with a Monte Carlo simulation with and without gluon radiation.

and Karliner[49]: in the rest frame of the hardest jet the angle between the remaining jets is given by:

$$\cos\tilde{\theta} = \frac{x_2 - x_3}{x_1} = \frac{sin\theta_2 - sin\theta_3}{sin\theta_1} \tag{42}$$

The relation between the angles and fractional energies is given by energy momentum conservation for massless partons:

$$x_i = \frac{sin\theta_i}{sin\theta_1 + sin\theta_2 + sin\theta_3}. \tag{43}$$

Here θ_i is the angle between the 2 jets opposite to jet i. The scalar theory does not fit the data as shown by TASSO[50] (see Fig. 15).

Another simple way to test the gluon spin is the determination of the energy of the most energetic cluster in 3-jet events, which is simply x_1 for three partons. For a vector gluon x_1 is determined by the differential distributions given in Eq. 9. For a scalar gluon it is[27]:

$$\frac{d^2\sigma}{\sigma^{(2)}dx_1dx_2}(e^+e^- \rightarrow q\bar{q}g) = \frac{\tilde{\alpha}_s}{2\pi}C_F\frac{x_3^2}{(1-x_1)(1-x_2)} + 1,2,3\ cyclic\ perm. \tag{44}$$

Here $\tilde{\alpha}_s$ is the coupling constant for the scalar theory. This distribution has been checked by many experiments [51] and they all find much better agreement for a spin-1 gluon as shown in Fig. 16.

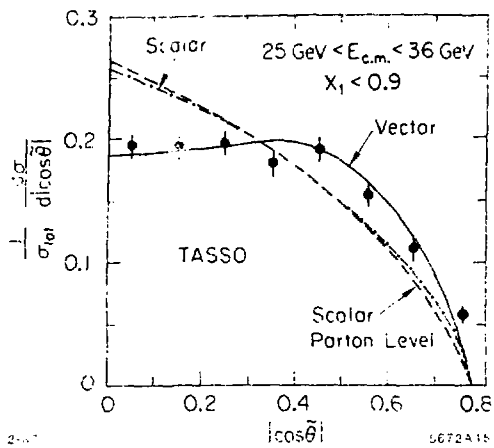

Fig. 15: **The observed distribution of the Ellis-Karliner variable for events in the 3-jet region defined by $x_1 < 0.9$. The full curve shows the prediction to $O(\alpha_s)$ for vector gluons, the dashed curves the predictions for scalar gluons at the parton and hadron level. These almost coincide, thus showing that fragmentation effects are not important for the shape of these curves.**

4 How to compare Jets with Partons ?

One of the basic difficulties with testing QCD quantitatively is the fact that QCD deals with calculations at the parton level, while experiments observe hadrons. The transition from partons to hadrons cannot be calculated at present, since this belongs to the 'non-perturbative' region of QCD. Therefore one has to use phenomenological models to describe the transition from partons to hadrons. This transition is usally called hadronization or fragmentation.

4.1 Fragmentation models

Several fragmentation models are on the market:

- Independent fragmentation models. In this case the original description of Field-Feynman[52] for single quarks is extended to each parton individually. The gluon is either treated as a quark (Hoyer et al.[53]) or split into two quarks according to the Altarelli-Parisi splitting functions (Ali et al.[54]). Due to the enforcement of energy-momentum conservation after the fragmentation of each parton, correlations between the outgoing jets are imposed, which depend on the rather arbitrary choice of the energy-momentum conservation mechanism, as will be discussed below.
- String fragmentation. In this case the hadrons are formed along a string stretched between the outgoing partons. The string tension represents the

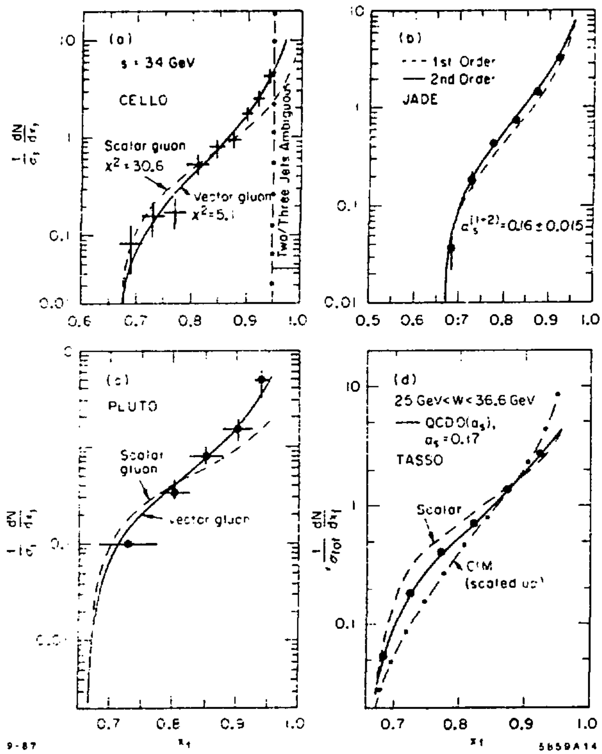

Fig. 16: The distribution of the fractional momentum of the highest energy jet in 3-jet events compared with various models. A vector gluon describes the data, while a scalar gluon does not. Also the second order QCD calculation fits better than the first order one (JADE) and the constituent interchange model (CIM) is excluded (TASSO).

strength of the colour field (growing linearly with distance) and as soon as the tension becomes large enough, the energy is converted into mass by the formation of $q\bar{q}$ pairs at the breakpoints of the string. Such a model introduces explicitly correlations between the outgoing partons, which are experimentally testable, as will be discussed later. The string fragmentation has been implemented in a widely used program written by T. Sjöstrand[48].

- Parton shower generation. In this case leading log calculations are used to generate events with many partons in the initial state in contrast to the previously mentioned Monte Carlos, which generate states with at most 4 partons ($O(\alpha_s^2)$). Because of the leading log approximation, the hard gluon production does not correspond to the exact QCD first or second order matrix element. Therefore one has to do a joining of the exact matrix element and the leading log approximation, but one has to be careful to avoid double counting. This joining of the first order QCD and leading log matrix elements has been implemented in the new Monte Carlo of the LUND group[48]. Furthermore, this version JETSET6.3 has the possibility to switch on and off interference effects between the initial partons, which were among the differences of earlier versions of shower Monte Carlos by Gottschalk[55] and Webber[56].

4.2 Can one distinguish between the models?

The main difference between independent fragmentation (IF) and string fragmentation (SF) is in the different treatment of the gluon. So a difference can only be observed in 3-jet and 4-jet events. The parameters used for the description of 2-jet events are the same: a fragmentation function to describe the longitudinal momentum spectra of the hadrons, the variance of the gaussian used to generate limited transverse momenta, the ratio of vector to pseudoscalar mesons, the amount of s- and c-quarks generated during fragmentation, amount of diquarks (yielding baryons), and others.

In the SF model the gluon is part of a string stretched between the quarks. If the gluon is soft, the main effect will be to give some transverse momentum to the string, but the event remains 2-jet like. If the gluon is hard and at a large angle, it will give a large p_t to the string and generate a 3-jet-like event. However, since the gluon is connected via a string to both quarks it will drag both string pieces in the direction of the gluon, thus depleting the particle density on the other side. (see Fig. 17).

This string effect was first observed by JADE and later confirmed by several other experiments[57]. It is shown in Fig. 18: After selecting the hardest jet in 3-jet events, the particle density with respect to this direction (0° in Fig. 18) is clearly higher in the region between the most energetic and least energetic jet as compared to the particle density in the region between the two most energetic jets. The least energetic jet has the highest probability to be the gluon jet. It is compared with several models: clearly the string fragmentation model describes the data, while the independent fragmentation model does not. However, some

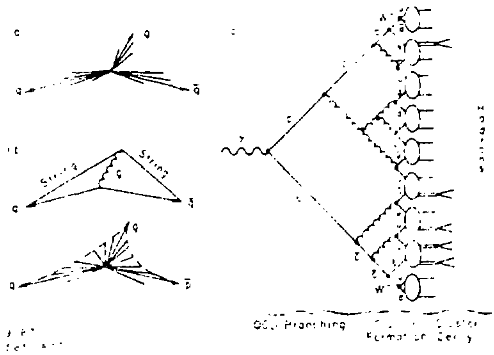

Fig. 17: Schematic picture of independent fragmentation(a) string fragmentation(b) and shower cascade Monte Carlo models(c).

parton shower models do reproduce the data too. Two effects contribute here:

- at the parton level a depletion of the $q\bar{q}$ region does occur if interference effects of multiple soft gluon emission are taken into account. This was first calculated by Azimov et al.[58] and proposed as an explanation why the fragmentation models based on the classical string picture describe the data
- After generating partons, they are combined into clusters which then fragment into hadrons. If this is done via the string fragmentation model, it is hard to distinguish how much of the coherence effect is due to the interference and how much is due to the string fragmentation, since both introduce a coherence between the final state particles[59]. However, if one has no interference and no string fragmentation, so no coherence effects at all, the model cannot describe the data as shown by the curve from the Gottschalk Monte Carlo in Fig. 18b. Also in the Webber model the 'string' effect disappears, if the clusters are allowed to decay isotropically[60].

To test coherence effects in a model independent way, a nice experiment was proposed by Azimov et al.[58]. They consider the radiation from a $q\bar{q}$ pair, which can either radiate photons or gluons. In case of a gluon interference effects occur, while they are absent in case of a photon. So the coherence effects can be studied by comparing $q\bar{q}g$ events with $q\bar{q}\gamma$ events. This was first done by the TPC and MARK-II and recently by JADE[61]. Fig. 19 shows the ratio of the particle density in the $q\bar{q}$ region for $q\bar{q}g$ and $q\bar{q}\gamma$ events, where the $q\bar{q}$ region in the $q\bar{q}g$ events is defined as the region between the 2 most energetic jets. This ratio should be 1 if no coherence effects would be present, since the gluon and photon energies were chosen such that the kinematical configurations of both event types were similar.

One can argue that the IF fragmentation models can be discarded, since they do not describe the string effect. However, this affects only a small number of

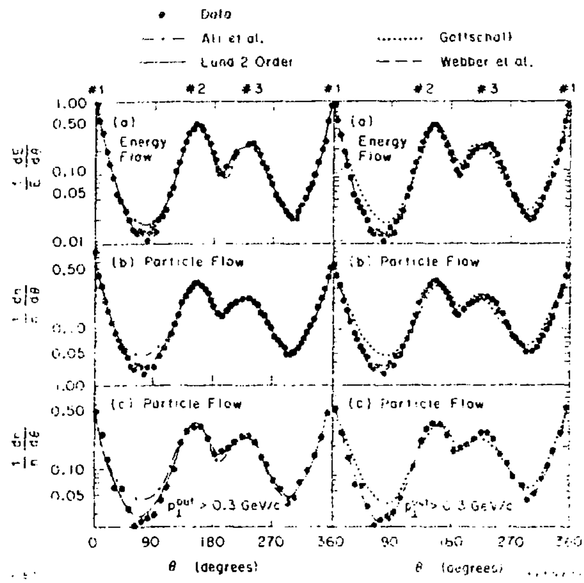

Fig. 18: The hadron flow in the plane of 3-jet events compared with different Monte Carlo models. Only the LUND and Webber Monte Carlos reproduce the depletion of particles between the two most energetic jets (around 70°). The effect is enhanced for particles with a large momentum out of the plane (see (c)), as expected if the effect occurs through a boost for which the relevant quantity is $m^2 + p_t^2$.

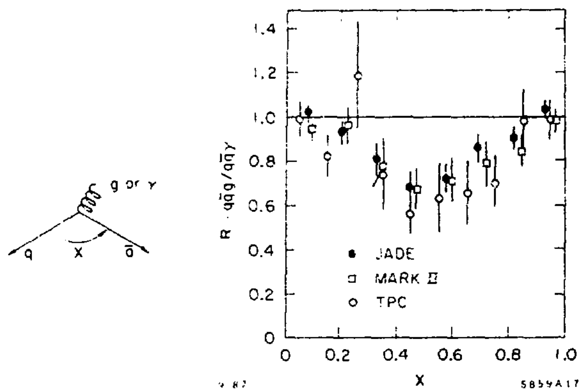

Fig. 19: The ratio of particle densities in $q\bar{q}g$ and $q\bar{q}\gamma$ events as function of the normalized angle $x = \phi/\phi_{q\bar{q}}$. The horizontal line at r=1 is the prediction if no interference effects occur in $q\bar{q}g$ events.

preferentially low momentum tracks in the 3-jet sample, so the effect is small. Disagreements at this level are also present in the LUND Monte Carlo up to $O(\alpha_s^2)$, e.g. in the 4-jet fraction of events[62] or the gluon fragmentation function[63].

Fig. 20a shows the fraction of multijet events as function of the jet resolution parameter from JADE data[62]. One sees that especially the 4-jet fraction is poorly described by the second order Monte Carlo. The shower Monte Carlos do a better job, but the leading log models shown do not reproduce the 3-jet cross section well for small invariant masses. This is remedied in the new LUND shower Monte Carlo, which incorporated the exact QCD matrix element for the radiation of the first gluon. In this case all the jet fractions are well described as shown by the preliminary TASSO data in Fig. 20b[64].

It was recently pointed out by Kramer and Lampe[44] that if one uses the PMS criterion (see Sect. 2.6) to find the optimum scale for the different multijet cross sections, the 4-jet rate comes out appreciably larger in the second order QCD calculations.

MARK-II[63] studied in a very nice way the properties of gluon jets by selecting symmetric 3-jet events ('MERCEDES' events) and determined the jet energies from the angles between the jets (see Eq. 43). Then they compare the momentum distribution of charged particles in these 3-jet events at 29 GeV with 2-jet events at 19 GeV. The average jet energies at 19 GeV are the same as the jet energies of the 2 quarks and gluon at 29 GeV. By taking the ratio of these distributions systematic effects largely cancel and one can compare a sample of 3-jet events, of which one is a gluon, with a sample of quark jets at the same averaged jet energy.

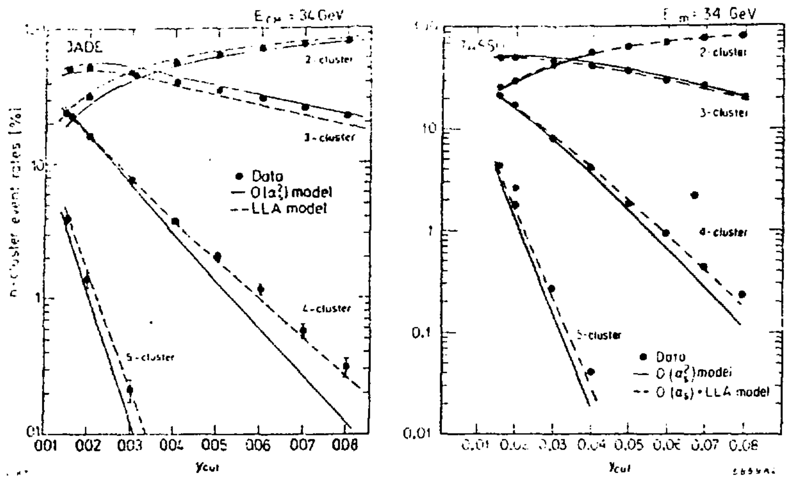

Fig. 20: **The fraction of multijet events as function of the jet resolution (invariant jet mass y_{min}) compared with various models. Only the LUND shower model using the Leading Log Approximation for the shower cascade combined with the exact first order QCD matrix element for the first gluon can describe all jet multiplicities at the same time as shown by the curve $O(\alpha_s) + LLA$ through the preliminary TASSO data[64].**

As can be seen from Fig. 21, this ratio is larger than one for small values of the scaled particle momentum $x_i = P_i/E_{jet}$, thus proving a softer distribution in the gluon enriched sample. A softer gluon fragmentation is expected in a non-abelian model, where the gluon carries colour. From the model predictions in Fig. 21 one sees that at high gluon momentum the spectrum of the LUND second order Monte Carlo is too hard; the shower models do reproduce the data better. JADE studied the transverse momentum of jets in 2- and 3-jet events and concluded that the transverse momentum is larger for gluon jets than for quark jets, indicating also a softer gluon fragmentation [65]. Recent summaries about the properties of gluon jets were given by Dorfan, Saxon and Sugano[1].

A recent comparison of the various Monte Carlo models with data at 29 GeV has been made by MARK-II[60]. They find that the LUND shower model using the correct $O(\alpha_s)$ matrix element for the first gluon and the leading log approximation for the soft gluons provides the most reasonable description of the data($\chi^2 \approx 2$ per point for 450 points), while the Webber shower Monte Carlo can be improved considerably if the phase space fragmentation of the clusters is replaced by string fragmentation. The Caltech-II Monte Carlo gives a considerably worse overall description of the data.

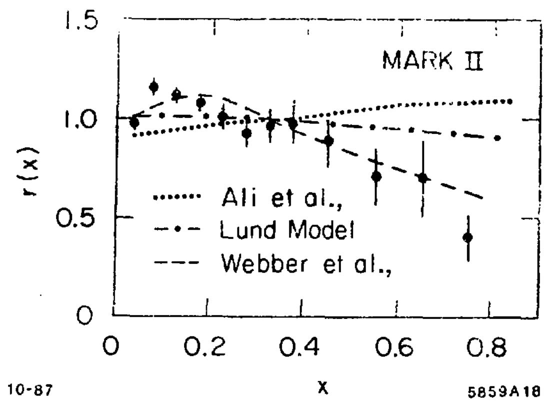

Fig. 21: The ratio of the inclusive charged particle distribution for three-fold symmetric 3-jet events at $\sqrt{s}$ = 29 GeV and 2-jet events at $\sqrt{s}$ = 19.3 GeV together with various model predictions.

5 Determination of α_s

Several methods have been used to determine the strong coupling constant α_s. Among them are:

- Event shape studies.
- Energy dependence of various quantities.
- Energy weighted angular correlations.
- Fits to the total hadronic cross section.

Here follows a summary of these results.

5.1 Shape variables

A study of variables which are sensitive to the event shapes or 'jettiness' can be used to determine the fraction of events with a hard gluon. Among the variables used are jet masses, sphericity, thrust, oblateness, and others or one uses cluster algorithms. which directly determine the number of 3-jet events. The problem with these variables is, that they are not only sensitive to α_s, but also to other 'knobs' in the Monte Carlo program, e g. the transverse and longitudinal momentum spectra, the fraction of vector mesons etc. Therefore we will not consider these quantities further here.

5.2 Energy dependence

One can try to study the influence of fragmentation effects on α_s by determining the energy dependence of various quantities, since fragmentation effects will decrease with energy, while gluon radiation effects become more prominent as the energy increases. Such a study was first done by PLUTO[66]. However, the energy dependence is model dependent. Therefore it was suggested by Field[67] to use only the sign of the fragmentation effect and choose quantities for which the fragmentation is assumed to contribute either positively or negatively in the following way:

$$F = F_1\left[\alpha_s(1 + C\alpha_s)\right] + F_2(fragmentation) \tag{45}$$

Here F_1 is the known QCD prediction for the variable F, while F_2 represents the unknown fragmentation contribution. If one neglects F_2, one obtains an upper limit for α_s , if $F_2 > 0$ and a lower limit if $F_2 < 0$. Fig. 22a shows the α_s values from JADE[68] obtained from a fit of Eq. 45 to several variables and neglecting F_2. The variables studied are:

- The scaled average jet mass of the jet with the largest jet mass (M_h^2/E_{vis}^2). The heavy jet mass is proportional to α_s at the parton level and the coefficients have been calculated by Clavelli[69]. It can be seen that the fitted value of α_s from the jetmass decreases with energy as expected from the fact that fragmentation effects decrease with energy. Since all Monte Carlo models predict $F_2 < 0$, this variable can be used to obtain an upper limit (solid line). Since the energy dependence is not known, JADE did not make a fit to all points, but toke the best point (44 GeV), which gives a 95% C.L. upper limit on $\Lambda_{\overline{MS}}$ of 400 MeV.

- The thrust variable, plotted as $1 - T$, shows a similar behaviour, but gives less tight limits.

- The asymmetry of the energy weighted angular correlations (AEEC, see next Sect.), integrated between 45° and 90° is also shown in Fig. 22a. It shows little energy dependence.

For most models the AEEC has $F_2 < 0$, so it can be used to get a lower limit as shown by the $\Lambda = 25$ MeV curve in Fig. 22a. However, the sign of F_2 is not uniquely predicted: e.g. the Hoyer model gives $F_2 > 0$ for the integration range of 45° to 90°, so this model would give a somewhat lower Λ . However, the effect is small and if the integration range is enlarged, the sign of F_2 becomes also negative for the Hoyer model. This is the reason why CELLO[70] used an integration range of between 30° and 90°. They fit the energy dependence of the scaled average heavy jet mass and the AEEC and find $\Lambda_{\overline{MS}}$ to be bound between 55 and 450 MeV at the 95 % C.L. The results are shown in Fig. 22b. The Λ limits given for both experiments correspond approximately to

$$0.10 < \alpha_s(1156\ \mathrm{GeV}^2) < 0.16$$

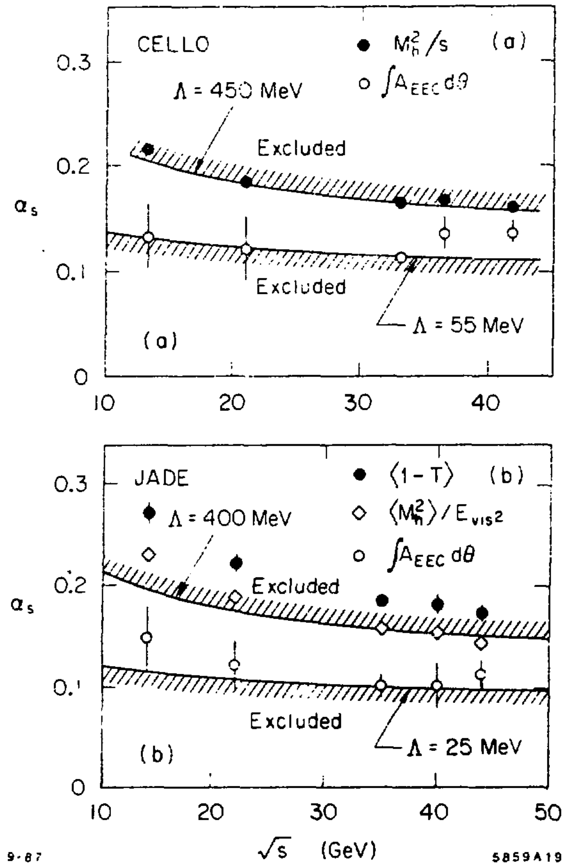

Fig. 22: **Limits on α_s as function of centre of mass energy computed from various observables. Since the fragmentation term has been neglected, one gets lower limits from observables with a negative fragmentation contribution (AEEC) and upper limits from observables with a positive fragmentation contribution (M_h^2 and $1-T$). The error bars for the JADE data correspond to 2σ, so the solid lines drawn through the endpoints of the error bars of the 'best' point (the point at 44 GeV in this case) represent the 95% C.L. limit. The solid lines through the CELLO data represent the best fit of Eq. 45 with $F_2 = 0$. From the fitted values of α_s the indicated 95% C.L. limits on Λ were determined.**

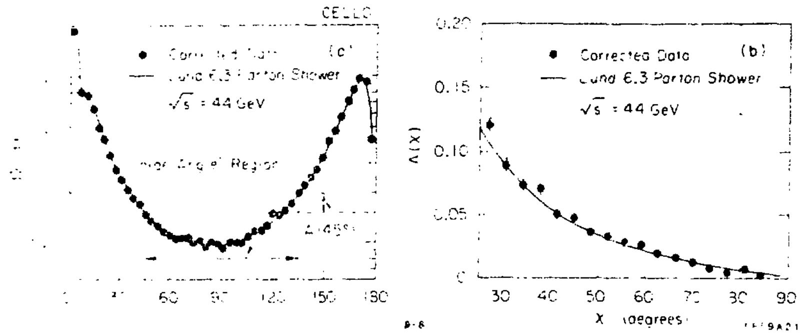

Fig. 23: An example of the energy-energy correlation (a) and asymmetry (b). The asymmetry $A(\chi)$ for 45°, defined as the difference between the EWAC at 135° and 45° is indicated in a).

5.3 Angular correlations

The energy weighted angular correlations (EWAC) were calculated first by Basham et al.[71], and later in higher order by other groups [72]. The way it is used by experimentalists, is simply producing a histogram of the angle χ_{ij} between any pair of particles or energy deposits in the detector with each entry weighted with the product of the two normalized energies of the pair. An example of the normalized EWAC is shown in Fig. 23a. The two peaks near 0° and 180° show the predominant 2-jet character of the events: the peak near 0° corresponds to the small angles between the many particles within a jet, while the peak near 180° corresponds to the angles between particles belonging to opposite jets. The EWAC distribution shows an asymmetry around 90° as shown e.g. for χ = 45° by the dashed lines in Fig. 23a. Such an asymmetry is not expected for 2-jet events, but 3-jet events automatically yield such an asymmetry, since a $q\bar{q}g$ event has usually one small angle and two large angles, so one gets more entries at the large angle side than at the small angle side. For $q\bar{q}$ events the asymmetry is negligible in the large angle region outside the cone of an average jet. The determination of α_s from the asymmetry has several advantages:

- One can sum over all events, so *no* special jet axis determination or cluster algorithm has to be applied beforehand
- The AEEC has been calculated in $O(\alpha_s^2)$[72] and the second order corrections were found to be small at the parton level ($O(10\%)$).
- The energy weighting makes it an infrared stable quantity implying it to be insensitive to the specific cut-off parameters used to separate the 2-,3-, and

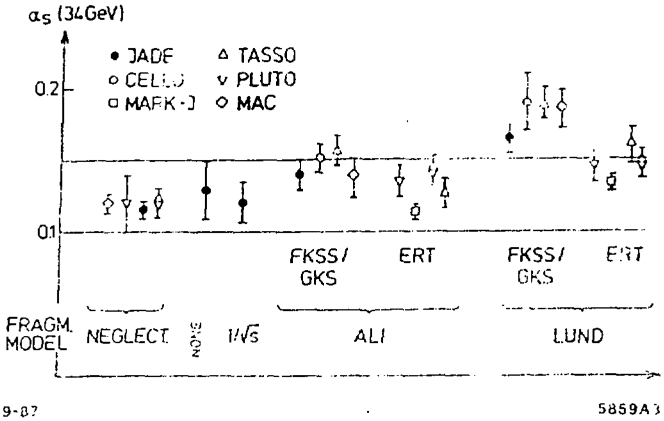

Fig. 24: A summary of the α_s values from the asymmetry in the energy energy correlations (see text).

4-jet events.

- The contribution from $q\bar{q}$ fragmentation largely cancels in the asymmetry.

In spite of this impressive list of nice properties, the resulting α_s values found by the various groups still have a wide range of 0.12 to 0.19, as shown in Fig. 24[73].

The α_s values indicated as fragmentation models 'neglected' come from a fit of Eq. 45 with $F_2 = 0$, 'none' corresponds to the limits given in the previous section, and $\frac{1}{\sqrt{s}}$ assumes this energy dependence for F_2 in Eq. 45. The indication Ali+ERT corresponds to the Ali Monte Carlo with the ERT matrix element, while Ali+GKS corresponds to the independent fragmentation option in the Lund Monte Carlo.

For the LUND Monte Carlo the α_s values range from 0.14 to 0.19, if summed over the matrix elements. Since the ERT matrix element gives a larger 3-jet cross section than the GKS one (see Fig. 7 in Sect. 2.3), this spread is usually attributed to the different matrix elements. However, this conclusion is premature, since the AEFC is very similar for both matrix elements, at least if y-cuts are used, as shown before in Fig. 8. From this figure it is clear that the ERT matrix element actually gives a somewhat higher value of α_s , if one restricts the fits to the large angle range ($\cos\chi > -0.7$), since in this range ERT gives a lower parton asymmetry than GKS [3].

The differences are unlikely to originate from problems with the data, since in this case the values indicated as 'neglect' in Fig. 24 would show a similar spread. Possible differences come from the different tuning and/or different versions of the Monte Carlos or the different range of χ used in the fit.

[3] An actual fit to the CELLO data with both matrix elements in this range yielded indeed a larger α_s value for ERT, but the difference is less than 0.002[74].

The influence of various fragmentation models on the AEEC has been summarized in Fig. 25 as function of α_s for $\sqrt{s}$ = 44 GeV. The curves labeled Ali and Hoyer were generated with the options for independent fragmentation in the LUND program, so they all use the same GKS matrix element. It can be seen that the Hoyer model increases the asymmetry of the hadrons as compared to the parton asymmetry (line labeled partons), while the other models (Ali and LUND) decrease the asymmetry compared with the value at the parton level. Consequently, the observed asymmetry requires for the Hoyer model a lower value of α_s than for the Ali and LUND models. As can be seen from Fig. 25 from the averaged data at 44 GeV from CELLO[74], JADE[68] and TASSO[75] one finds:

$$\frac{\alpha_s^{Lund}}{\alpha_s^{Hoyer}} \approx 1.4 \tag{46}$$

while the ratio

$$\frac{\alpha_s^{Lund}}{\alpha_s^{Ali}} \approx 1.1 \tag{47}$$

is appreciably smaller.

The large difference between the two independent fragmentation models Ali and Hoyer comes mainly from the different mechanism of energy momentum conservation (EMC), as was first discovered by CELLO[76] and later studied in more detail by Sjöstrand[77]. In IF models the partons fragment independently, so energy and momentum cannot be conserved simultaneously, because one generates a massive jet from a massless parton. One then has to apply an EMC mechanism to the ensemble of the jets *after* fragmentation. The difference between Ali and Hoyer can be qualitatively explained as follows: The fragmentation of each parton is stopped below a certain energy, say 1 GeV. Then overal energy momentum conservation can be imposed in several ways:

- In Hoyer it is done by rescaling the jet energy of each jet separately in such a way that the jet directions are not changed, so the hadrons follow the original parton directions.
- In Ali it is done by performing first a boost in the direction of the missing momentum and then rescaling the energies.

For 2-jet events the effects are not important, since on the average the missing momemtum in opposite jets compensates. However, in case of 3-jet events, the missing momentum in the 2 opposite jets still compensates on the average, so the missing momentum tends to point in the direction of the third jet (usually the gluon jet). In the Hoyer case more energy is then given to the gluon to compensate the missing momentum, thus increasing the 3-jettiness. In the Ali case a boost is performed in the direction of the missing momentum, which is preferentially the gluon. This has a similar effect as the boost of the strings in the LUND program, namely it decreases the average angle between the quark and gluon jet. Since the bremsstrahlung spectrum of the gluon is a steep function of this angle, one should not be surprised to find α_s to be sensitive to such effects in fragmentation models.

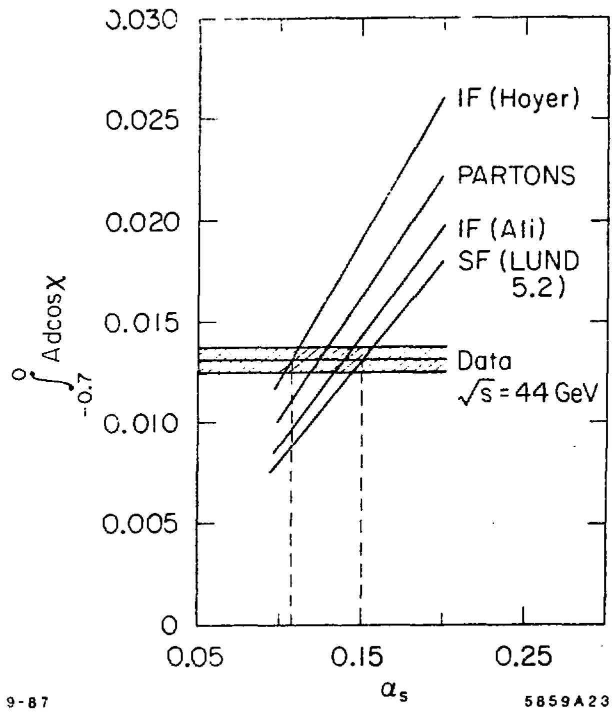

Fig. 25: Fragmentation model dependence of the integral of the AEEC as function of α_s. The curve labeled partons corresponds to the QCD prediction at the parton level. The other curves show the deviation after fragmentation for different models. The horizontal band indicates the averaged data from CELLO, JADE and TASSO at 44 GeV.

5.4 Conclusion on the asymmetry in angular correlations

What should be the conclusion of all this? Different collaborations give different answers. MARK-J[78] and PLUTO[79] maintain that one can determine α_s well from the AEEC. However, they estimate the systematic uncertainty from fragmentation models by cleverly picking the models which give very similar results: Ali and Lund, thus ignoring the Hoyer model.

JADE[80], MAC[81] and MARK-II[34] find a large difference in the α_s values between SF and IF models, but they find that IF models describe the data badly. However, this must be partly due to a poor tuning, since CELLO[76] and TASSO[33] find that their IF models describe the data reasonably well, at least in the angular range of interest [4].

The comparison of data with the Hoyer model is shown in Fig. 26 for CELLO and JADE data. JADE's tuning of the IF model disagrees everywhere, while the CELLO tuning of IF describes the data as well as SF in the angular range of interest (30° to 150°). The angles near 180° are not well described by the IF model, since $y_{min} = 0.03$ was used in that case, while for SF y_{min}=0.015 was used. The SF model would not describe the 'inside jet' region either with y_{min}=0.03[80].

However, it is difficult to use such a small y_{min} for the IF model, since in that case most events would have a soft gluon of a few GeV and IF models are not designed to fragment partons of a few GeV. The SF model has the nice property to absorb such soft gluons in the string, so their only effect is to generate some transverse momentum.

Note that even a small y_{min} of 0.015 eliminates already most angles below 20° at the parton level, so one should not be surprised to find disagreements in the 'inside jet' region at the hadron level. It is somehow fortuitous, that one can find a y_{min} for the SF model such that the 'hole' at the parton level is filled by the hadrons moved into this range by the string effect.

In conclusion, since all models can be tuned to describe the bulk of the data (the 2-jet and hard 3-jet events) reasonably well, there seems to be no convincing arguments to eliminate some models in the estimate on the systematic uncertainties of α_s. Therefore, the uncertainty in α_s from fragmentation models is appreciably larger than the uncertainties from the different matrix elements and the different parton dressing schemes (see Sect. 2.3). Especially, the two most widely used matrix elements (ERT and GKS) give the same results for the AEEC in the large angle region, if y-cuts are used.

Considering the HOYER model and LUND model to be extremes, one finds from Fig. 25 for the α_s determinations at $\sqrt{s} = 44$ GeV:

$$0.11 < \alpha_s(1936\ \mathrm{GeV}^2) < 0.16$$

[4] One obvious difference between the tuning used by the different experiments is that JADE, MAC and MARK-II all use a very small y_{min} cut of 0.015, while CELLO and TASSO use larger values. A y_{min} of 0.015 implies that most events have a gluon of a few GeV and fragmenting such low energy jets requires a delicate tuning. Furthermore, the last 2 experiments use the Petersen fragmentation function for heavy quarks, while the others use the LUND fragmentation function for heavy and light quarks, thus having less degrees of freedom.

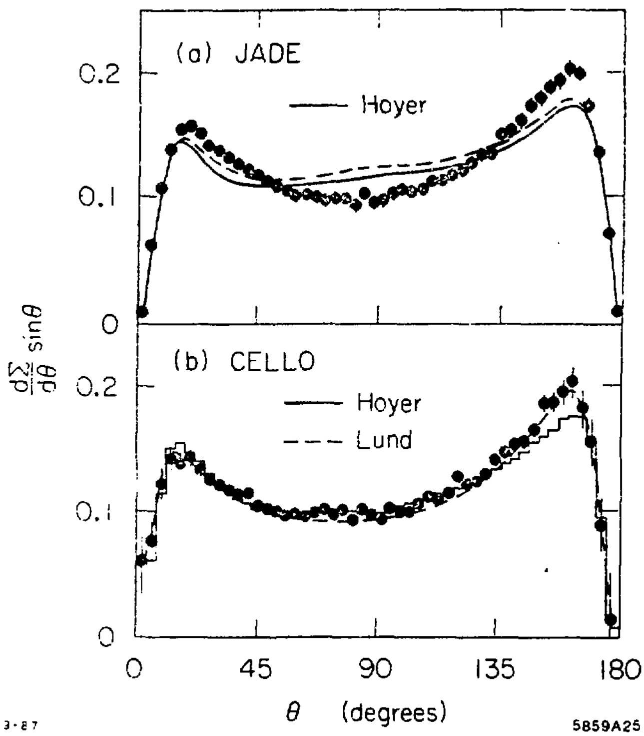

Fig. 26: Energy-energy correlation for different tunings of the Hoyer independent fragmentation model compared with JADE - (a) and CELLO data (b). The JADE figure at $\sqrt{s}$=34 GeV is from Ref.[80]. The main parameters of the Hoyer tuning describing the CELLO data at $\sqrt{s}$=44 GeV are: $\Lambda_{\overline{MS}}$=50 MeV; y_{min}=0.03; a=2.6 and b=1 in the Lund fragmentation function for light quarks, ϵ = 0.08 and 0.015 in the Petersen fragmentation function for c and b quarks; the transverse momentum in a quark(gluon) jet is generated by a gaussian with a variance of σ =400(600) MeV.

5.5 Triple energy correlations

Instead of angular correlations between 2 particles, Csikor et al.[82] proposed to use planar triple energy correlations (PTEC).

Obvious advantages are: a) One selects only planar particle combinations, thus one is able to suppress the contribution from multijet events. b) The acceptance corrections to the PTEC are less sensitive to the precise Monte Carlo tuning [83].

The PTEC was first studied by MARK-J[84] and recently also by CELLO[74]. The results have been summarized in Table 2. The α_s values are very similar to the ones from the AEEC; both matrix elements ERT and GKS give the same results (at least if y-cuts are used) and the fragmentation model dependence is as large as shown in Fig. 25 for the AEEC.

Experiment	*Model*	$\sqrt{s}(GeV)$	α_s
MARK − J	*Lund + ERT*	35	0.147 ± 0.005
[84]	*Ali + ERT*	35	0.112 ± 0.005
CELLO	*Lund + GKS*	35	$0.151 \pm 0.003 \pm 0.006$
[74]	*Lund + GKS*	44	$0.145 \pm 0.004 \pm 0.006$
	Lund + ERT	44	$0.143 \pm 0.004 \pm 0.006$
	Hoyer + GKS	35	$0.103 \pm 0.002 \pm 0.006$
	Hoyer + GKS	44	$0.100 \pm 0.004 \pm 0.006$

Table 2: Summary of α_s values from planar triple energy correlations.

5.6 α_s from the total hadronic cross section

The fragmentation dependence of α_s as discussed above, does not occur in the α_s determination from R, since one needs Monte Carlos only to determine the acceptance of the detector (including radiative corrections), but not to determine the event shape. For 4π detectors the acceptance is not strongly dependent on the Monte Carlo model used. Furthermore, this determination of α_s is not plagued by theoretical uncertainties, 'higher twist' effects, large second order corrections, or a strong renormalization scheme dependence, which are among the caveats in other determinations of α_s[41].

The disadvantage is that the QCD contribution to R is only 5 %, so one has to combine several experiments to get a good determination of R. In this case one has to study the systematic errors in detail. This was recently done by CELLO[39], who combined data from all experiments for $\sqrt{s}$ between 14 and 48 GeV and took the full error correlation matrix into account. More details about the method can be found in Ref.[85]. Fig. 27 shows an update of this analysis after including new data from TRISTAN at 50 and 52 GeV[86] and data below $\sqrt{s} < 10$ GeV[87]. The result of the fit is:

$$\alpha_s(1156\,\mathrm{GeV}^2) = 0.141 \pm 0.021 \text{ and } \sin^2\theta_W = 0.240 \pm 0.019$$

or

$$\Lambda_{\overline{MS}} = 245^{+250}_{-150}\mathrm{MeV}.$$

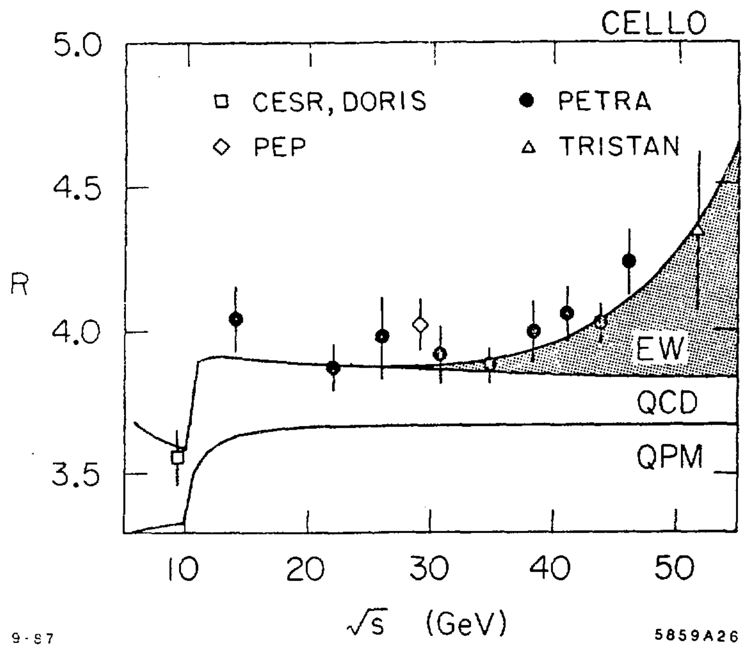

Fig. 27: R-values as function of centre of mass energy. The error bars include both systematic and statistical errors, which were obtained by combining the data in small intervals and fitting the averaged value, thus taking into account the correlations. The solid line is the result of the best fit with $\sin^2\theta_W = 0.23$.

This value of $\sin^2\theta_W$ is in good agreement with the world average of 0.23 [85]. We used as additional input only G_F and α, so this value of $\sin^2\theta_W$ is determined only by the vector couplings of the quarks and has no large loop corrections, because of the Δr cancelations in Eq. 6. Since the quark couplings are apparently in agreement with the Standard Model expectations, we can keep $\sin^2\theta_W$ fixed at the world average of 0.23. Refitting yields:

$$\alpha_s(1156\ \mathrm{GeV}^2) = 0.145 \pm 0.019$$

or

$$\Lambda_{\overline{MS}} = 290^{+350}_{-160}\mathrm{MeV}.$$

The value of α_s including the data around and below the Υ-region is somewhat lower than the result from the fit restricted to the energy above 10 GeV[39]. However, since the difference is within one standard deviation and both fits give an excellent χ^2 of about 0.7 per degree of freedom, there seems to be no reason to exclude part of the data.

Several points are worth mentioning:

- The result of the global fit describes well the single experiments. For example a fit of the normalization factor of each experiment was always compatible with the quoted normalization error.

- No correlations between different experiments were assumed, but the effect of an hypothetical common correlation error was estimated by introducing a correlated normalization error of 1% for all experiments in the full error correlation matrix. The effect on the fitted parameters was found to be small.

- Within one experiment , the measurements at different c.m. energies are certainly correlated. However , how much of the systematic error has to be considered common normalization error and how much point-to-point systematic error is not defined precisely. Therefore, the amount of splitting between normalization and point-to-point error was varied by $\pm 50\%$. The resulting change in the parameters is small as can be seen from the different error contours in Fig. 28.

  Note that these error contours correspond to $\chi^2_{min} + 1$. The extremes of the error contours, projected onto each axis correspond to $\pm 1\sigma$, i.e. 68% C.L. for each of the parameters (not to be confused with the C.L. inside the contour, which is 39% [46].)

- The value of α_s from R is in agreement with recent α_s values from deep inelastic scattering [88] and quarkonium decays[89] (see Table 3) and from limits on α_s presented in the previous section.

- The numerical value of α_s depends on the renormalization scheme. To give an experimental value of the QCD contribution independent of the renormalization scheme, it was fitted by a linear expression

$$R = R_{EW}(a + b(E - 34GeV)).$$

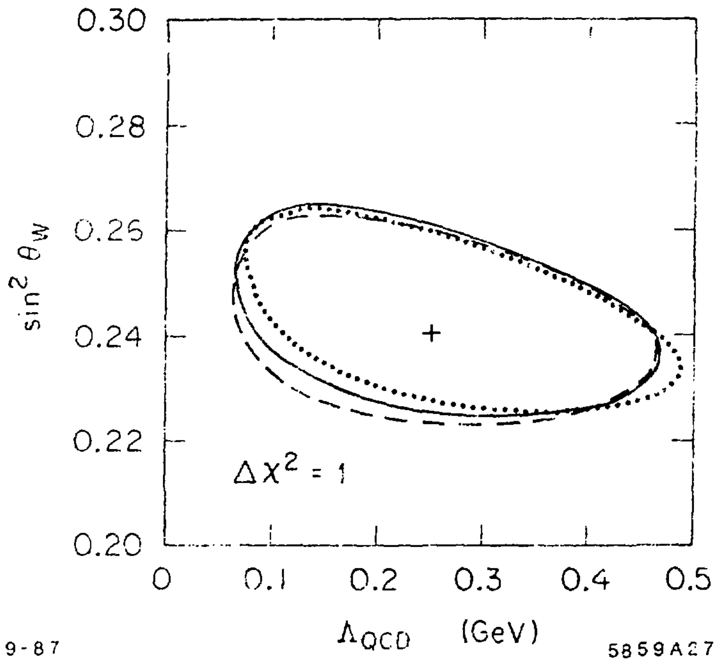

Fig. 28: Contour plots of α_s versus $\sin^2 \theta_W$ for different assumptions on the splitting between systematic and point to point errors.

Here R_{EW} represents the electroweak contribution to R. For $\sin^2\theta_W$ =0.23 this yields a = 1.000 ± 0.011 and b = (−0.55 ± 0.62) $10^{-3} GeV^{-1}$. The term b gives a direct measurement of the running of the strong coupling constant. This result implies an 80% probability for α_s to run with a negative slope, and the absolute value is compatible with the one expected from QCD ($b = -1.3\ 10^{-3}\ GeV^{-1}$) for $\alpha_s = 0.15$. Recently JADE concluded from the study of the energy dependence of the relative 3-jet rates are in excellent agreement with a running coupling constant and that an energy independent coupling is unlikely[90]. Also the values in Table 3 are consistent with a running coupling constant.

- The scale for α_s was chosen to be $Q = \sqrt{s}$. Changing scales is equivalent to changing renormalization schemes and uncertainties from this contribute only to $O(\alpha_s{}^3)$, so these are expected to be negligible. The effect of different scales can be studied by choosing as scale $Q = x\sqrt{s}$ and using the modified formula for R (see Eqs. 35 and 36). For x between 0.5 and 1.5 the fitted value of α_s was found to vary ≈ ± 3% (as expected from Fig. 10), so this is small compared with the total systematic error of 15%, which is dominated by the systematic uncertainties.

- Note that the quoted Λ value is the one for 5 flavours, even although one includes also data below $b\bar{b}$ threshold. This is consistent with the $\overline{MS}$ prescription, that N_f should be changed at $Q = m_q$ and not at $Q = 2m_q$ [38]. Nevertheless, if one chooses a different scale, say $\sqrt{s}/2$, one comes in the region where $N_f = 4$. If one fits Λ one has to use in this region the more complicated formula for α_s (see Eq. 25), which takes into account that the value of α_s does not change if one passes a new threshold, but only the running becomes slower, if N_f increases (it becomes ≈ 0 for N_f=16). Since the running of α_s does not change strongly by going from $N_f = 5$ to $N_f = 4$ in the small energy range below 10 GeV, this is a negligible effect as was checked from actual fits.

- The experimental data has not been corrected for more than one photon radiated in the initial state, since these calculations have become available only recently [91]. Previously the effect was estimated to be at the % level and a reduction of all R-values by 1% would reduce α_s by 15%[39]. However, a preliminary estimate with the exact calculations indicates that the effect is appreciably smaller since the radiative corrections are only important at high energies, so it lowers $\sin^2\theta_W$ somewhat, but hardly changes α_s. More definite statements require a Monte Carlo simulation, because the higher order corrections depend on the maximum allowed photon energy.

Process	Q	N_f	α_s	$\Lambda_{\overline{MS}}(GeV)$
$\frac{\Gamma(\Upsilon\to\gamma gg)}{\Gamma(\Upsilon\to ggg)}$ [89]	5	4	$0.180^{+0.009}_{-0.008}$	$0.182^{+0.033}_{-0.032}$
deep inel. μC[88]	10	4	$0.160 \pm 0.003 \pm 0.01$	$0.230 \pm 0.020 \pm 0.060$
$R(e^+e^-)$	34	5	0.141 ± 0.021	$0.245^{+0.250}_{-0.150}$

Table 3: Comparison of a few recent α_s values in different processes at different values of Q^2 (Q in GeV). The $\Lambda_{\overline{MS}}$ value from R was calculated for 5 flavours. The other $\Lambda_{\overline{MS}}$ values were calculated for $N_f = 4$, which can be compared with the value for five flavours by multiplying them by ≈0.7 (see Eq. 26). Note that all Λ values are based on Eq. 24 and not on Eq. 23, which would give an ≈15% lower value. A compilation of older or more debatable α_s determinations can be found in Refs.[41,88,89] and Sect. 5 of this report.

6 Conclusion

Comparing our present knowledge about QCD with what was known some 10 years ago, it is fair to say that we learned a lot from PEP and PETRA physics, namely:

- At high energies partons become observable as jets on an event by event basis, thus starting the era of studying *parton dynamics* instead of *particle dynamics*.
- First evidence for gluons came from the observation of clear 3-jet events. This unexpected discovery of the 'heart' of QCD is of equal importance as the discovery of the carriers of the weak force, namely the W and Z bosons.
- From angular distributions quarks were found to be spin 1/2 particles and gluons to be spin 1 particles, as expected for matterfields and gauge bosons in the Standard Model.
- From the total hadronic cross section one observes:
  - Quarks come in 3 colours and their electric charges agree with the standard fractional charge assignments.
  - A clear contribution from the direct Z^0-exchange is observed at the highest energies ($40 < \sqrt{s} < 52$ GeV).
  - A fit to the hadron cross section data above $\sqrt{s}$=8 GeV yields:

$$\alpha_s(1156\,\mathrm{GeV}^2) = 0.141 \pm 0.021 \text{ and } \sin^2\theta_W = 0.240 \pm 0.019$$

- The scale (or renormalization scheme) dependence of the as determination from R was studied in detail and found to be small. Also the sensitivity to the number of flavours used in the formula for α_s was found to be small, as long as care was taken that only the running of α_s could change for a different number of flavours, not is value (see Eqs. 25 and 26).
- The couplings of quarks to the Z^0 are in agreement with the Standard Model expectations, as is apparent from the above value of $\sin^2\theta_W$, which is completely determined by the vector couplings of the quarks to the Z^0 with the parametrization of the cross section in terms of G_F (see Eq. 6).

The fact that QCD is able to provide a consistent picture for so many unrelated topics - asymptotic freedom, deep inelastic lepton-nucleus scattering, multijet structure in e^+e^- and $p\bar{p}$ scattering - has promoted it from the 'candidate' theory to the only acceptable theory of strong interactions.

Acknowledgements

Many thanks go to Therese Tymieniecka and the Organizers of this Conference for inviting me to such a pleasant place.

I wish to thank my colleagues at PEP and PETRA for providing me their latest results, especially Andreas Dieckman, Klaus Gamerdinger, Jochen Hansmeyer, Luis Labarga, and F. Ould-Saada.

Thanks also to Gerrit Burgers for providing a program to calculate the second order radiative corrections, to Giulio D'Agostini, Günter Grindhammer and Wolfgang Hollik for the many stimulating discussions and to Siegfried Bethke, Jonathan Dorfan and Luis Labarga for their comments on the manuscript.

I thank the SLAC Directorate for the hospitality I am enjoying at SLAC and last but not least I want to thank my wife and children for their patience during the time of writing this review, which coincided with the time of moving to another continent.

References

[1] P. Söding and G. Wolf, Ann. Rev. Nucl. Sci. 31(1981) 231
Sau Lan Wu, Phys. Rep. 107(1984) 59
H. Yamamoto, Proc. of 1985 SLAC Summer Inst. Stanford (1985)
F. Barreiro, Fortschr. Phys. 34 (1986) 503
D.H. Saxon, Int. School of High Energy Phys., Duilovo-Split, Yugoslavia, (1986), RAL-86-057
W. de Boer, Proc. of 17th Int. Symp. on Multiparticle Dyn., Seewinkel, Austria (1986), MPI-PAE/Exp.El. 167
J. Dorfan, Proc. of 1986 SLAC Summer Inst., Stanford (1986)
K. Sugano, Proc. of Phys. in Collision VI, Chicago (1986)

P. Mättig, DESY Report 86-161, Cracow School of Theor. Phys., Zakopane, Poland, 1986
J. Chrin, DESY Report 87-040

[2] Details and ref. can be found in standard text books:
F.E. Close, An Introduction to Quarks and Partons, Academic Press (1979)
L.B. Okun, Leptons and Quarks, Noth Holland Publ. Comp. (1982)
K. Huang, Quarks, Leptons and Gauge Fields, World Scientific, (1982)
C. Quigg, Gauge Theories of the strong, weak and electromagnetic Forces, Benjamin-Cummings Publ. Comp. Inc. (1983)
J.E. Dodd, The ideas of Particle Physics, Cambridge Univ. Press (1984)
F. Halzen and A.D. Martin, Quarks and Leptons, An introductory course in Modern Particle Physics, John Wiley and Sons, Inc. (1984)
D.H. Perkins, Introduction to High Energy Physics, Addison Wesley Publ. Comp. (1987)

[3] H. Fritzsch and M. Gell-Mann, 16th Int. Conf. on High Energy Physics, Chicago (1972)
H. Fritzsch, M. Gell-Mann and H. Leutwyler, Phys. Lett. **47B** (1973) 365

[4] D.J. Gross and F. Wilczek, Phys. Rev. Lett. **30** (1973) 1343

[5] H.D. Politzer, Phys. Rev. Lett. **30** (1973) 1346

[6] G.S. Abrams et al., Phys. Rev. Lett. **33** (1974) 1452

[7] J.J. Aubert et al., Phys. Rev. Lett. **33** (1974) 1404

[8] M. Gell-Mann, Phys. Lett. **8** (1964) 214

[9] G. Zweig, CERN report 8419TH 412 (1964)

[10] S. Weinberg, Phys. Rev. Lett. **19** (1967) 1264
A. Salam, Elem. Part. Theory: Relativistic Groups and Analyticity (8th Nobel Symposium), Ed. N. Svartholm et al. (1968) 367
For a historical account, see S. Coleman, Science **206** (1979) 1290

[11] G. 't Hooft, Nucl Phys. **B 35** (1971) 167

[12] S.L. Glashow, J. Iliopoulos and L. Maiani, Phys. Rev. **D2** (1970) 1285

[13] S.W. Herb et al., Phys. Rev. Lett. **39** (1977) 252

[14] M. Perl et al., Phys. Rev. Lett. **35** (1975) 1489; Phys. Lett. **63B** (1976) 366

[15] J. Ellis, M.K. Gaillard, and G.G. Ross, Nucl. Phys. **B111** (1976) 253; ibid. **B130** (1977) 516;

[16] Mark-I Coll., G. Hanson et al., Phys. Rev. Lett. **35** (1975) 1609

[17] A. Sirlin, Phys. Rev. **D22** (1980) 891
W.J. Marciano and A. Sirlin, Phys. Rev. **D29** (1984) 945

[18] W. Hollik, DESY Report 86-049 , Proc. 21st Renc. de Moriond. Les Arcs, France (1986)
M. Böhm et al., Fortsch. Phys. **34** (1986) 687

[19] A. Barroso et al., CERN-EP/87-70, presented by F. Dydak at LEP200 ECFA Workshop, Aachen (1986)

[20] T. Kinoshita, J. Math. Phys. **3** (1962) 650
T.D. Lee and M. Nauenberg Phys. Rev. **D133** (1964) 1549

[21] G. Kramer and B. Lampe, DESY Reports 86-103 and 86-119

[22] A. Ali et al., Nucl. Phys. **B167** (1980) 454; Phys. Lett. **82B** (1979) 285
J.G. Körner et al., Nucl. Phys. **B185** (1981) 365
K.J.F. Gaemers and J.A.M. Vermaseren, Z. Phys. **C7** (1980) 81
O. Nachtmann and A. Reiter, Z. Phys. **C14** (1982) 47; ibid. **C16** (1982) 45

[23] F. Gutbrod, G. Kramer, G. Schierholz, Z. Phys. **C22** (1984) 235

[24] R.K. Ellis, D.A. Ross, E.A. Terrano, Phys. Rev. Lett. **45** (1980) 1225;
Nucl. Phys. **B178** (1981) 421

[25] J.A.M. Vermaseren, K.J.F. Gaemers, S.J. Oldham, Nucl. Phys. **B187** (1981) 301

[26] T.D. Gottschalk, Phys. Lett. **109B** (1982) 331
T.D. Gottschalk and M.P. Shatz, CALT-68-1172,-1173,-1199; Phys. Lett. **150B** (1985) 451

[27] G. Kramer, DESY Report T-83-01 and Theory of Jets in Electron-Positron Annihilation, Springer Tracts in Modern Physics, Vol. 102 (1984)

[28] R.Y. Zhu, Ph. D. Thesis, MIT (1983)

[29] A. Ali, Phys. Lett **110B** (1982) 67

[30] Z. Kunszt, Phys. Lett. **99B** (1981) 429; ibid. **107B** (1981) 123

[31] F. Csikor, private communication

[32] G. Rudolph, Habilitationsschrift, Innsbruck (1986)
F. Gutbrod et al., DESY Report 87-047

[33] TASSO Coll., M. Althoff et al., Z. Phys **C26** (1984) 157

[34] MARK-II Coll., D.R. Wood et al., SLAC-PUB 4374, to be published

[35] G. 't Hooft and M. Veltman, Nucl. Phys. **B44** (1972) 189

[36] O. Tarasov, A. Vladimirov, and A. Zharkov, Phys. Lett. **93B**(1980)429

[37] Particle Data Group, M. Aguilar-Benitez et al., Phys. Lett. **B170** (1986) 78

[38] W.J. Marciano, Phys. Rev. Lett. **29** (1983) 580

[39] CELLO Coll., H.J. Behrend et al., Phys. Lett. **B183** (1987) 400

[40] M. Dine, J. Sapirstein, Phys. Rev. Lett. **43** (1979) 668
A.L. Kataev, F.V. Tkachov, Phys. Lett. **B85** (1979) 277
W. Celmaster, R.J. Gonsalves, Phys. Rev. Lett. **44** (1980) 560

[41] D.W. Duke, R.G. Roberts, Phys. Reports **120** (1985) 275

[42] P.M. Stevenson, Phys. Rev. **D23** (1981) 2916

[43] G. Grindhammer, F. LeDiberder and J. Haissinski, CELLO Note O-83

[44] G. Kramer and B. Lampe, DESY Report 87-106

[45] W. Celmaster and R.J. Gonsalves, Phys. Rev. **D20** (1979) 1420; Phys. Rev. Lett. (**42** (1979) 1435

[46] R. Marshall, RAL-87-031 (1987)

[47] U. Amaldi et al., UPR-0331T (1987)

[48] B. Andersen et al. Phys. Rep. **97** (1983) 31
T. Sjöstrand, Computer Phys. Comm. **27** (1986) 243
T. Sjöstrand, Computer Phys. Comm. **28** (1986) 229
T. Sjöstrand, Computer Phys. Comm. **39** (1986) 347
T. Sjöstrand and M. Bengtsson, Computer Phys. Comm. **43** (1987) 367

[49] J. Ellis and I. Karliner, Nucl. Phys. **B148** (1979) 141

[50] TASSO Coll., R. Brandelik et al. Phys. Lett. **97B** (1980) 453

[51] CELLO Coll., H.J. Behrend et al. Phys. Lett. **110B** (1982) 329
JADE Coll., W. Bartel et al. Phys. Lett. **119B** (1982) 239
PLUTO Coll., Ch. Berger et al., Phys. Lett. **97B** (1980) 459
P. Söding, AIP Conf. Proc., APS-meeting, Santa Crus (1981)

[52] R. D. Field and R.P. Feynman, Nucl. Phys. **B136** (1978) 1

[53] P. Hoyer et al., Nucl. Phys. **B161** (1979) 349

[54] A. Ali et al. Phys. Lett. **93B** (1980) 155

[55] T.D. Gottschalk, Nucl. Phys. **B214** (1983) 201; ibid **B239** (1984) 349
T.D. Gottschalk and D. Morris, Nucl. Phys. **B288** (1987) 729

[56] G. Marchesini and B.R. Webber, Nucl. Phys. **B238** (1984) 1

[57] JADE Coll. W. Bartel et al., Z. Phys. **C21** (1983);
Phys. Lett. **134B** (1984) 275; ibid. **157B** (1985) 340
TPC Coll., M. Aihara et al., Z. Phys. **C28** (1985) 31
TASSO Coll., M. Althoff et al., Z. Phys. **C29** (1985) 29

[58] Y.I. Azimov et al., Phys. Lett. **165B** (1985) 147

[59] M. Bengtsson and T. Sjöstrand, Nucl. Phys. **B289**(1987)810

[60] MARK-II Coll., A. Petersen et al., SLAC-PUB-4290, submitted to Phys. Rev. D

[61] TPC Coll., M. Aihara et al.,Phys. Rev. Lett. **57** (1986) 945
MARK-II Coll., P. Sheldon et al.;Phys. Rev. Lett. **57** (1986) 1398
JADE Coll., W. Bartel et al., Contr. to Int. Symp. on Lepton and Photon Int., Hamburg (1987)

[62] JADE Coll., W. Bartel et al., Z. Phys. **C33** (1986) 23

[63] MARK-II Coll., A. Petersen et al., Phys. Rev. Lett. **55** (1985) 1954

[64] TASSO Coll., Contr. to Int. Symp. on Lepton and Photon Int., Hamburg (1987)

[65] JADE Coll., W. Bartel et al., Phys. Lett. **123B** (1983) 460

[66] PLUTO Coll., Ch. Berger et al., Z. Phys. **C12**(1981) 297

[67] R.D. Field, Proc. Int. Symp. on Lepton and Photon Int., Cornell (1983)

[68] A. Dieckmann, Ph.D. thesis, Heidelberg (1987)

[69] L. Clavelli and D. Wyler, Phys. Lett. **103B** (1981) 383

[70] J. Hansmeyer, Ph.D. thesis, Karlsruhe (1987)

[71] C.L. Basham et al., Phys. Rev. **D17**(1978)2298

[72] A. Ali and F.Barreiro, Phys. Lett **118B** (1982) 155; Nucl. Phys. **B236** (1984) 269
D.G. Richards, W.J. Stirling, Nucl. Phys. **B229** (1983) 317

[73] S. Bethke, Proc. of 23th Conf. on High Energy Phys., Berkeley (1986)
B. Naroska, Phys. Rep. **148** (1987) 67

[74] K. Gamerdinger, Ph.D. thesis, Karlsruhe, in preparation

[75] TASSO Coll., W. Braunschweig et al., DESY Report 87-081

[76] CELLO Coll. H.J. Behrend et al., Nucl. Phys. **B218** (1983) 269;
Phys.lett. **138B** (1984) 311

[77] T. Sjöstrand, Z. Phys. **C26** (1984) 93

[78] MARK-J Coll., B. Adeva et al., Phys. Rev. Lett.**54** (1985) 1750

[79] PLUTO Coll., Ch. Berger et al., Z. Phys. **C28** (1985) 365

[80] JADE Coll., W. Bartel et al., Z. Phys. **C25** (1984) 231

[81] MAC Coll., E. Fernandez et al., Phys. Rev. **D31** (1985) 2724

[82] F. Csikor et al., Phys. Rev. **D31** (1985) 1025

[83] M. Chen and L. Garrido, Phys. Lett. **180B** (1986) 409

[84] MARK-J Coll., B. Adeva et al., Phys. Lett. **180B** (1986) 181

[85] W. de Boer, Proc. of 17th Int. Symp. on Multiparticle Dyn., Seewinkel, Austria (1986);
MPI-PAE/Exp.El. 167
G. D'Agostini, Proc. of Renc. de Moriond, (1987) to be published

[86] Results on R from the AMY-, TOPAZ- and VENUS-Coll. were presented by S. Ozaki at the Int. Symp. on Lepton and Photon Interactions, Hamburg (1987)

[87] Crystal Ball Coll., Int. Symp. on Lepton and Photon Interactions, Hamburg (1987)
CLEO Coll., R. Giles et al., Phys. Rev. **D29** (1984) 1285
CUSB Coll., E. Rice, Ph. D. thesis, Columbia University (1982)
DASP2 Coll., S. Wescler, Diploma thesis, University of Heidelberg (1981)
DASP2 Coll., H. Albrecht et al., DESY Report 82-037 (1982), unpublished
DESY-Hamburg-Heidelberg-MPI Munich Coll., P. Bock et al., Z. Physik **C6** (1980) 125
LENA Coll., B. Niczyporuk et al., Z. Physik **C15** (1982) 299
PLUTO Coll., L.Criegee and G. Knies, Phys. Rep. **83** (1982) 151

[88] A.C. Benvenuti et al., CERN-EP/87-101, submitted to Phys. Lett. B

[89] Kwong et al., EFI 87-31, Chicago, 1987

[90] JADE Coll., Int. Symp. on Lepton and Photon Interactions, Hamburg (1987)

[91] F. Berends et al., Phys. Lett. 185B (1987) 395

ULTRA RELATIVISTIC HEAVY ION COLLISIONS

W. Heck and H. Ströbele
University of Frankfurt; GSI, Darmstadt and CERN, Geneva

NA35 Collaboration

In ~~this contribution~~ the first experimental results from the CERN heavy ion program are presented. A short introduction into the field of high energy heavy ion collisions is given, ~~which should be considered~~ as an experimentalist's approach to ~~simplify an otherwise~~ complex and far reaching subject. A ~~more professional~~ introduction into the field can be found in references [1]. At the ~~end of the introduction~~ we outline briefly the history of the CERN heavy ion program. The second part of this contribution is devoted to the experimental results. During the oral presentation the authors showed data from various experiments. However, we decided to reproduce here only NA35 data, since we believe that the use of preliminary data from other groups should remain at their discretion. Here we rather give the available references.

1. INTRODUCTION

Astrophysics and Cosmology deal with, among other subjects, several phenomena which are closely connected to the notion of compressed nuclear matter. Looking as far in time as the beginning of the Universe with the big bang, or in space as far as to the "dark" spots in the galaxies, which might be black holes or neutron stars, leads to the assumption that nuclear matter can be compressed to many times its normal density. Accepting this one has to ask for the laws governing the corresponding dynamical processes. It is unlikely that Nuclear Physics provides all the means to find these laws, because at high density the nucleon-nucleon distance in nuclear matter may become much smaller than the nucleonic size implying that the constituents must play an important rôle. Thus the study of compressed nuclear matter leads to an extension of nuclear physics in direction to particle physics. On the other hand, in particle physics, one of the unsolved problems is the long range forces between the constituents of hadrons. It is conceivable that nuclear medium effects will help to understand better this part of the underlying Quantum-Chromo-Dynamics. This becomes even more obvious if one considers the aspect of the long range problem which addresses the question of the physical versus perturbative vacuum. It has been mentioned already a long time ago that the vacuum is not uniquely defined and that its features may depend on its surrounding[2]. The question of how to explain the confinement of quarks and gluons in the hadrons is the continuation of a problem formulated more than ten years ago.

Apart from indirect evidence from cosmological studies nuclear compression can be looked at only in collisions between energetic nuclei. This had been done so far either only in rare cosmic ray events with its limited statistical significance or at relatively low beam energies (2-4 AGeV) which leads to a compression of only ~ 2 times normal density. With the advent of 200 AGeV oxygen and sulphur beams from the CERN SPS much higher nuclear densities are expected.

However, before one can address the related fundamental questions the experimenters have to cope with the special features of heavy ion interactions at high energies. These are:

- in each reaction many particles are involved. Whereas it is impossible to separately detect and identify each particle (which is a severe limitation) their large number is an advantage in so far as the fluctuations due to unseen or unidentified particles are reduced.

- enormous amounts of energy are in principle available in the collision. Fixed target 200 AGeV ^{32}S - ^{32}S interactions have a nominal 640 GeV c.m. energy. This energy is distributed over large volumes in configuration space.

Once the experiments can handle the large multiplicities and catch a significant amount of the liberated energy, the following specific questions may be asked:

- Are ^{32}S + ^{32}S interactions different from an appropriate convolution of (d + d) (we know already that N + Fe $\neq$ N + d). If indeed a difference is found the density dependence of the strong interaction can be studied by varying projectile mass and/or energy.

- To what degree is thermal and chemical equilibrium reached in the reaction zone?
- Is the confinement of the nucleon's constituents locally modified or even suspended? This would result in a hot plasma of quarks and gluons.

The Quark-Gluon Plasma or Quark Matter is a fictitious or expected, (depending on your point of view!) new state of matter with the following features (an experimentalists simplified point of view).

In an extended (reaction) volume, which is large compared to the size of a nucleon, quarks and gluons
- are in (near) equilibrium,
- move freely, i.e. unaffected by the physical vacuum,
- and contribute individually to the available degrees of freedom.

Lattice QCD[3] predicts a transition temperature, at which the hadrons "melt" into partons, of 200-250 MeV at energy densities of ~ 3.5 GeV/fm^3.

On the basis of these predictions simple quark counting gives an estimate of the required beam energy to produce the Q.G. Plasma: in the initial state 3 quarks per nucleon are present at normal nuclear density. In order to triple the density in the final state 6 more quarks per nucleon have to be created each with a temperature of 250 MeV or better an average energy of 750 MeV; thus around 7 GeV per nucleon incident energy would suffice if its conversion into thermal energy and quark production is perfect. At 200 AGeV the c.m. energy per nucleons is 10 GeV.

Even if one is now ready to believe that the Q.G. Plasma can be produced it still remains open how it will manifest itself and what are its signals. Without going into the details we just mention in table I the most popular predictions together with the corresponding references. To conclude this section we have to point out at least some of the principal problems connected with the detection of Quark Matter:
- the deconfined fraction of the reaction volume will vary event by event
- the transition from the plasma to the hadron state will alter most observables in the final state by an unknown amount.

- It is a priori unknown whether the experimental results are representing more normal hadronic or unusual plasma behaviour. Or, turning the argument around, there is no clear prediction of how the results should look in case there is no plasma formed.

Before turning to the experimental results we give an outline of the history of the heavy ion program at CERN.

The first detected signal was a study of Haseroth in 1977/78 [4] on light ions in the PS. This triggered a proposal from R. Stock and others for ^{16}O experiments at the PS in 1980 [5]. The feasability of such a program was confirmed in January 1983 [6] and the original proposal approved in September of this same year. After some delay other groups joined the heavy ion program and, triggered by technical reasons, the SPS was taken into consideration which lead to a SPS programme with oxygen at 60 and 200 AGeV. The ion source, provided by GSI and LBL, was installed in January 1986. Two months later a 12 AMeV beam emerged from LINAC I. In the two following months the Booster (280 AMeV) and the PS (10 AGeV) had their turn until finally the 9th September 1986 the SPS accelerated an oxygen beam to the envisaged energy of 200 AGeV. The physics run then took place in November 1986, with a ^{32}S beam for physics being scheduled for September 1987.

2. EXPERIMENTAL RESULTS

Instead of describing the experimental setup of the various collaborations with our own words we include here as reference the corresponding descriptions from the official CERN List of Experiments [7], in the appendix.

Figure 1 shows an artist's view of NA35's experimental setup. The major components are the Streamer Chamber in the 1.5 Tesla Vertex Magnet, the mid-rapidity calorimeters consisting of electromagnetic and hadronic parts, and the Veto calorimeter covering laboratory angles between 0° and 0.3°.

High multiplicity events show large measuring losses also in the forward cone corresponding to rapidities between 4 and 6. With these restrictions the Streamer Chamber detector is well suited to yield information about transverse momentum spectra and rapidity distributions, for negative particles, the rapidity being calculated assuming the pion mass thus neglecting admixtures of kaons and antiprotons. Electrons from π^0 decay into 2γ's and subsequent conversion in the target are corrected for. A first result on proton spectra is obtained by subtracting from the distributions of positively charged particles (P, K^+, π^+) the appropriate distribution of negatively charged particles (K^-, π^-) neglecting possible differences between the π^+ and π^- yields.

2. 1. 2. Results

Figure 2 shows the distribution $1/p_t\, dN/dp_t$ for central collisions of ^{16}O + Au at 200 AGeV. The solid line represents the corresponding results from p + p collisions at 240 GeV in the interval $0 < p_t < 1$ GeV/c. Above 300 MeV/c the agreement is surprisingly good. The deviation from the straight line (note the log-scale!) for momenta above 1 GeV/c is also similar to the findings in pp collisions[8]. Below 300 MeV/c the ^{16}O + Au data exhibit a significant enhancement, which is also seen in p + Au collisions (fig. 3). We can conclude from both figures, that there is no difference in the spectral shape of negative, i.e. produced, particles between p + Au and ^{16}O + Au collisions at 200 AGeV beam momentum. Above 300 MeV/c the transverse momentum spectra reproduce the finding of a previous pp experiment.

It is interesting to see how our results fit into the systematics of different projectiles and energies. Instead of comparing spectral shapes we look at the mean transverse momentum of pions as function of beam momentum (figure 4). The solid line is an eyeball fit to results from low energy AA collisions and α-α, α-p data from the ISR[9]. The two crosses are our findings at 60 AGeV and 200 AGeV. No drastic deviation from the common behaviour is observed. At 200 AGeV ^{16}O + Au interactions produce very few nucleon pairs, therefore the transverse momenta of protons are well suited to study the dynamics of the interaction or, more specifically, the process of transforming the initially longitudinal momentum of the nucleons in the projectile and target nuclei into transverse momentum. Figure 5 shows the proton transverse momentum spectrum of ^{16}O + Au collision at 60 AGeV.

The corresponding mean transverse momentum is 630 MeV/c which, in a thermal picture, corresponds to about the same temperature as found for the pions.

Figs. 6a,b show the rapidity distributions of pions in central ^{16}O + Au interactions at 200 and 60 AGeV. The qualitative finding is that the mean of the distributions is shifted to values lower than the position of the mean in pp collisions. Simple kinematical considerations correlate the mean rapidity (or the velocity of the centre-of-mass system) to the number of participating target nucleons (assuming that all nucleons of the projectile participate which is a reasonable assumption in central collisions). From the positions of the means of the distributions in figures 6a ($\langle y \rangle = 2.4$) and b ($\langle y \rangle = 2.0$) we infer that at 200 AGeV 55 nucleons and at 60 AGeV 40 nucleons from the target participate in the interaction. From this we conclude that the slowing-down of the interacting fireball at 200 AGeV is at least as effective as at 60 AGeV. The width of the rapidity distribution provides another piece of information about the nuclear stopping power. In pp collisions pions exhibit a rather pronounced plateau in the rapidity distribution which is not reproduced in ^{16}O + Au interactions. Comparing the full-width-half-maximum values at 200 AGeV (60 AGeV) for A + A and pp yields 3.2 and 3.5.(2.4 and 2.8). Thus ^{16}O + Au interactions yield significantly smaller widths than pp interactions if the rapidity distributions of pions are considered. Whether this difference is of a dynamical nature or originates from an appropriate convolution of pp interaction remains to be seen.

The NA35 Calorimeters

Results from calorimetry of the NA35 experiment at the CERN SPS for ^{16}O + A at 200 and 60 AGeV on transverse energy spectra for different targets and a comparison of p + Au with ^{16}O + Pb will be given after a description of the relevant detector parts. Fig. 8 shows the experimental setup[10]. Targets of Al, Cu, Ag, Au, and Pb (1% interaction length thickness) were mounted in front of the streamer chamber.

A set of electromagnetic and hadronic calorimeters measured the reaction products. The angular domain $\theta < 0.3°$ (nuclear projectile fragmentation) is covered by a 4-segment "Veto" calorimeter. The subsequent interval, 0.3° - 2.2°, is seen by a continuous single-cell EM + hadronic calorimeter. The larger angle domain is covered by a Photon Position Detector (PPD) consisting of alternating layers of lead and planes of proportional tubes read out by 3072 ADC channels, backed up by a Ring Calorimeter divided into 240 cells (24 in azimuth and 10 in radius with ring sizes chosen to cover equal units of pseudorapidity). This set of calorimeters is movable: at 200 AGeV it covered approximately a 2.3° - 12.5° angular range corresponding to $2.2 < \eta < 3.8$, and at 60 AGeV it covered a 4.3° - 20.5° range corresponding to $1.7 < \eta < 3.3$. Two principal trigger modes were employed. Both worked reasonably well with and without the field of the vertex magnet. From the Veto Calorimeter various levels of projectile energy degradation could be selected, ranging from "minimum bias" to "central collision", the later requiring $E_{veto} < 0.1\ E_{beam}$. The other trigger was obtained from the transverse energy of the produced π°s, recorded as photons in the PPD. At incident energies of 60 and 200 AGeV, a total of about 2,500,000 calorimeter events were recorded. In addition, data were taken for 200 GeV incident protons and π^{+}. First results have been published[11].

2. 2. 2. Results

Transverse Energy Distribution

Figure 9 shows the differential transverse energy (E_T) distribution for ^{16}O + Pb at 200 AGeV, as summed from the PPD and Ring calorimeters, with the magnetic field off[11]. The value of E_T is calculated for each event as the appropriately weighted sum of the energies found in individual PPD and Ring Calorimeter channels. The data points with $E_T < 50$ GeV were obtained with additional streamer chamber information. Systematic uncertainties in the E_T scale and normalization are estimated to be about 10%. The range of pseudorapidities included in the data is approximately $2.2 < \eta < 3.8$. The HIJET Prediction is also shown in figure 9 for comparison. This distribution is much narrower. The peak near 50 GeV arises in this model from impact parameters $b < 4$fm. The data exhibit the same "central collision" peak.

A variety of models has been used to describe the measured E_T spectra[12,13,14].

Dependence of E_T on $A_{projectile}$

In order to understand the E_T spectra further, the same measurement was made for p + Au, using a tagged 200 GeV proton beam. To eliminate surface interactions the value of E_{Veto} was required so be less than 150 GeV, corresponding to a p-Au cross section of 1.3 barns, or impact parameter b < 6fm. The result is described by an analytic fit $d\sigma/dE_T = 0.173.E_T^{2.36}$ $\exp(-0.727.E_T)$ barn/GeV. A 16-fold convolution of this analytic function is shown in figure 9, where it provides a fit to the "central collision" peak, both as regards position and shape at high E_T. The difference between Au and Pb for the purpose of this convolution is not expected to be significant.

Dependence of E_T on Beam Energy

Figure 10, shows the E_T spectra measured for ^{16}O + Au at 60 AGeV ($2.0 < \eta < 3.5$) and at 200 AGeV ($2.2 < \eta < 3.8$). The energy calibration is revised upwards from that of figure 2., but is still preliminary. The mean E_T for central collisions is approximately 45 and 90 GeV at 60 and 200 AGeV respectively. To have a scale for these values, we consider the total c.m. energy available ($\sqrt{s}$) in the 16 + 50 system consisting of the projectile nucleus and the tube of participant nucleons in the target nucleus for a central collisions. This is 318 and 582 GeV respectively. An upper limit for E_T might be the value for an isotropic emission of that energies, i.e., $\pi/4 * E_{cm}$: 250 and 457 GeV respectively. Since the experimental acceptance is about one half, these values would be reduced to 125 and 229 GeV. The average E_T for central collisions is therefore, at both energies, about 40% of the value for an isotropic fireball. It is also interesting to note that the observed E_T is approximately proportional to $\sqrt{s}$.

Estimate of Energy Density

From the E_T measurement we can make an estimate of the energy density in the interaction volume, using the formula of Bjorken[16]:

$$\epsilon \sim {}^{\Delta E_T}/_{\Delta\eta} / (\pi r^2 \tau)$$

where ΔE_T is the transverse energy observed in the pseudorapidity interval $\Delta\eta$, r is the radius of the ^{16}O nucleus and τ is the time that has elapsed since the beginning of the collision. For τ = 1fm/c, and the observed ΔE_T = 90 GeV in $2.2 < \eta < 3.8$ at 200 AGeV, we find an energy density of 2.0 GeV/fm^3.

It should be remarked, however, that the expression used for the energy density is very schematic, and at present has only qualitative utility.

Dependence of E_T on A_{target}

Figure 11 shows the E_T spectrum measured in the PPD (which is sensitive primarily to the electromagnetic component) for various targets at 200 AGeV. In the Au spectrum the "central collision peak" is not so evident as in the complete E_T measurement. For lighter targets this effect is compounded by the fact that central collisions form a smaller fraction of the total than for Au. Because of these effects detailed calculations will be needed to explain these spectra. Figure 12 shows that the electromagnetic E_T that is produced in central collisions is proportional to $A^{½}$.

Freeze-out density

The possibility to do pion interferometry (HBT), see figure 13, with the abundant information on pairs from the analysis of streamer chamber pictures, will lead to an estimate of the energy density at the instant of "pion freeze-out" when combined with $dE_T/d\eta$ information from the calorimeters.

Conclusions

First results from the ^{16}O run at the CERN SPS in 1986 have been presented. Most of them are preliminary, but some qualitative conclusions can be drawn:

- A superposition of 16 p-nucleus central collisions describes the "central collision" peak in the E_T spectrum for ^{16}O + Au at 200 AGeV.

- For the target nuclei Al, Cu, Ag, and Au the value of E_T, where for central collisions the differential cross section has dropped to 10% of the plateau value of ^{16}O + Au, is proportional to $A^{½}$, (as seen in the electomagnetic part of the transverse energy)

- For central ^{16}O + Au collisions E_T roughly doubles between 60 and 200 AGeV as does the available energy, i.e., we find similar stopping for both energies.

- With the Bjorken formula one finds that energy densities for average central collisions in ^{16}O + Au at 200 AGeV are of the order of 2 GeV/fm^3.

- Pion interferometry (HBT) can be used to study the size of the "freeze-out" volume.

- We look forward to the upcoming run in September/October 1987 when a ^{32}S beam will be used.

REFERENCES

[1] Proceedings of 5. Quark Matter conf., Asilomar 1986. And references therein.

[2] T.D. Lee: Abnormal nucleon states; Rev. Mod. Phys. 47, 267, 1975.

[3] J.B. Kogut, Nucl. Phys. A418 (1984) 381c. H. Satz ibid. p. 447c.

[4] Haseroth et al. CERN/PS/MU 77-25 (1977).

[5] R. Stock et al. Letter of Intent to the PSCC-1980.

[6] H. Haseroth CERN/PS/LI/83-7 (1983).

[7] Experiments at CERN in 1986; Geneva, November 1986.

[8] Van Hal, Nijmegen thesis 1987.

[9] R. Szwed, CERN-EP/84-125.

[10] A. Sandoval et al., Nucl. Phys. A461 (198) 465c.

[11] A. Bamberger et al . Phys. Lett., B184 (1987) 271.

[12] A.D. Jackson, H.Bøggild NORDITA - 87/11N preprint.

[13] G. Baym, P. Braun Munzinger, V. Ruuskanen, preprint (1987).

[14] J. Ranft, Phys. Lett, B188 (1987) 379.

[15] M. Gyulassy CERN - TH. 4794 preprint.

[16] J.D. Bjorken, Phys. Rev. D27 (1983) 140.

FIGURES CAPTIONS

Fig. 1 Artist's view of the NA35 experimental setup.

Fig. 2 Transverse momentum spectrum 1/pt dn/dpt of π^- for ^{16}O + Au events at 200 AGeV. The data were obtained with a hard veto trigger, i.e. they represent central collisions. The solid line is the result from pp interactions at 240 GeV/c.

Fig. 3 Same as fig. 2 but for p + Au events.

Fig. 4 Compilation of mean transverse momentum of π's as function of beam momentum.

Fig. 5 Difference of the transverse momentum spectrum of positive minus negative particles representing some approximation of the proton spectrum.
The data come from ^{16}O + Au interaction at intermediate impact parameters at 60 AGeV.

Fig. 6 Rapidity distribution of π^- for central ^{16}O + Au collisions.

Fig. 7 Same as Fig. 6, but for p + Au.

Fig. 8 The NA35 experimental setup.

Fig. 9 E_T distribution for ^{16}O + Pb at 200 AGeV in the acceptance $2.2 < \eta < 3.8$. The full line is a 16-fold convolution of the E_T distribution for inelastic p + Au collisions at 200 GeV, measured with the same apparatus. The dashed curve gives the HIJET prediction. A gamma function has been fitted to the p + Au data, the analytic 16-fold convolution gives $d\sigma/dE_T \propto E_T^{52.8} e^{-0.727 E_T}$ for the central collision peak for ^{16}O + Pb.

Fig. 10 Transverse energy distributions for ^{16}O + Au at 60 AGeV ($2.0 < \eta < 3.5$) and at 200 AGeV ($2.2 < \eta < 3.8$). The energy calibration (still preliminary) is different from Fig. 9.

Fig. 11 Transverse energy found in the PPD for $^{16}O \rightarrow$ Al, Cu, Ag, Au, at 200 AGeV. The horizontal line indicates 10% of the plateau value for ^{16}O + Au (see Fig. 12).

Fig. 12 PPD E_T at 10% of the ^{16}O + Au cross section plateau versus A_{target} (see Fig. 11).

Fig. 13 Two-pion correlation function with Gaussian fit projected onto the $Q_\perp$ - axis for 200 AGeV ^{16}O + Au, central events.

TABLE I

SIGNALS FOR THE Q. G. PLASMA

TEST	INFORMATION
lepton pair production, direct photons	state of the primordial environment at T>Tc
strange particle production	"chemical" potential of the chromoplasma
Pt - spectra	transition temperature
meson- baryon- momentum distributions and fluctuations	hydrodynamic expansion
interferometry	"fire ball" size
resonance fade out	chiral symmetry restauration
J/ψ suppression	Debey radius in the Plasma
$\bar{\Lambda}$ polarization	$\bar{\Xi}$ production

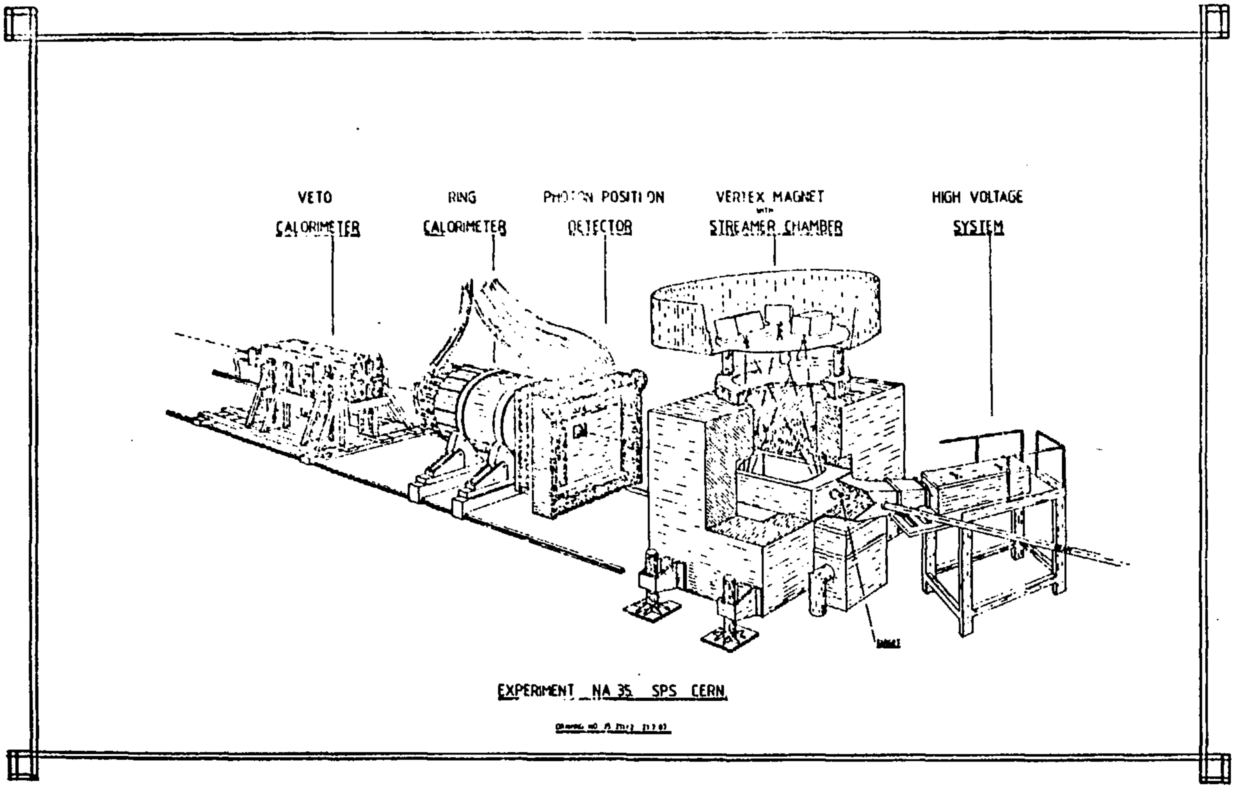
VETO CALORIMETER
RING CALORIMETER
PHOTON POSITION DETECTOR
VERTEX MAGNET with STREAMER CHAMBER
HIGH VOLTAGE SYSTEM
EXPERIMENT NA 35 SPS CERN

Fig. 1

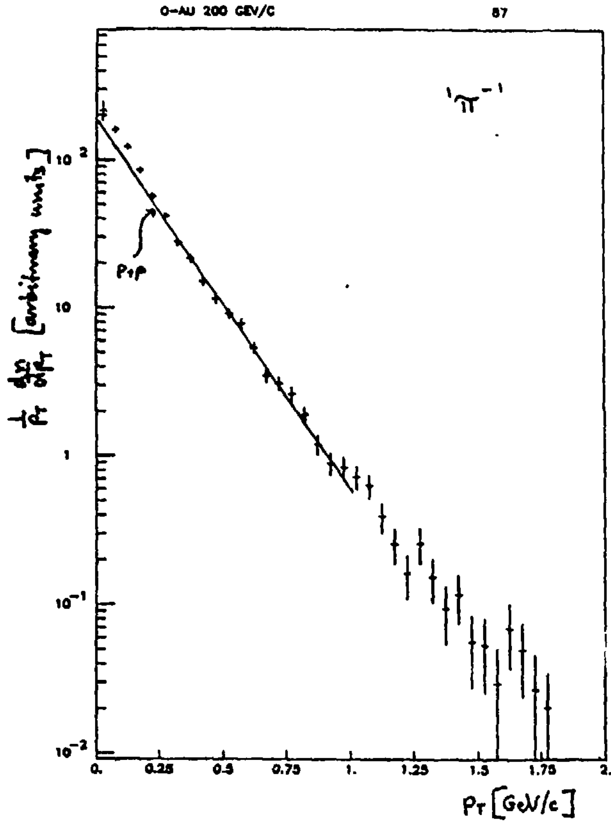
O-AU 200 GEV/C
87
'π^-'
p+p
$\frac{1}{p_T}\frac{dn}{dp_T}$ [arbitrary units]
p_T [GeV/c]
0. 0.25 0.5 0.75 1. 1.25 1.5 1.75 2.
10^2 10 1 10^-1 10^-2

Fig. 2

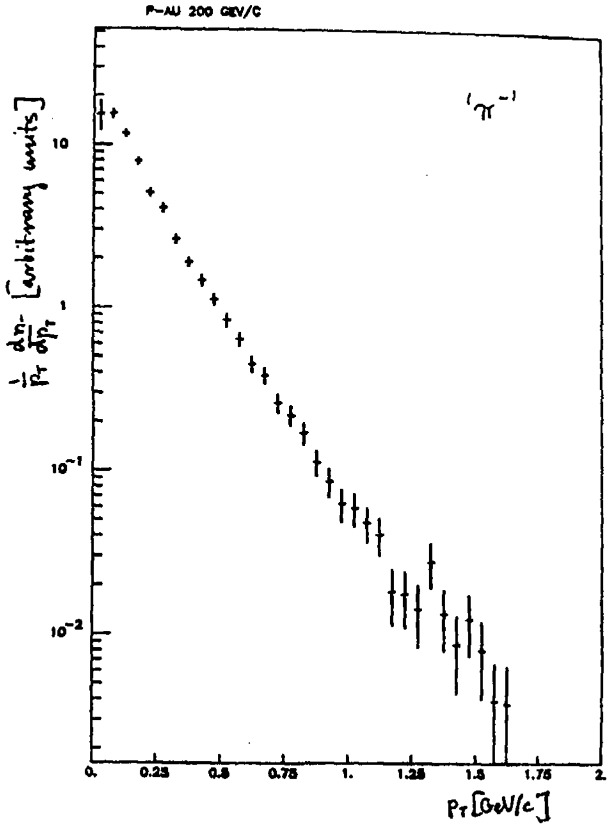
P-AU 200 GEV/C
'π^-'
$\frac{1}{p_T}\frac{dn^-}{dp_T}$ [arbitrary units]
p_T [GeV/c]
0. 0.25 0.5 0.75 1. 1.25 1.5 1.75 2.
10 1 10^-1 10^-2

Fig. 3

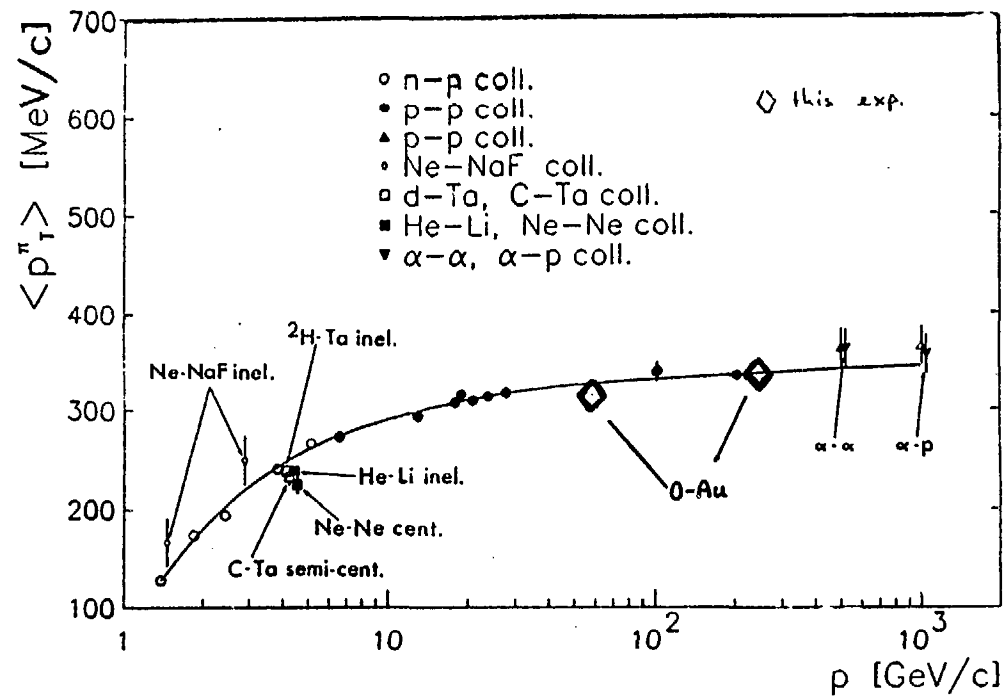
$\langle p^{\pi}_{T} \rangle$ [MeV/c]
700
600
500
400
300
200
100
1
10
10^2
10^3
p [GeV/c]
n−p coll.
p−p coll.
p−p coll.
Ne−NaF coll.
d−Ta, C−Ta coll.
He−Li, Ne−Ne coll.
α−α, α−p coll.
this exp.
Ne·NaF inel.
^{2}H·Ta inel.
He·Li inel.
Ne·Ne cent.
C·Ta semi-cent.
0-Au
α·α
α·p

Fig. 4

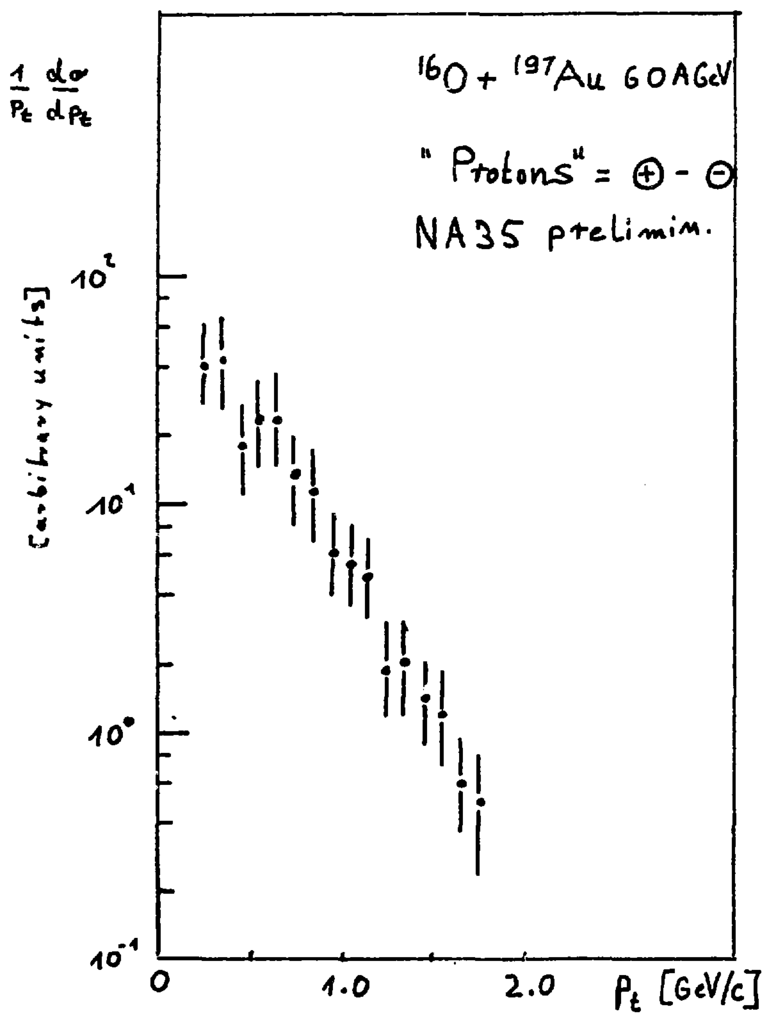

$\frac{1}{p_t}\frac{d\sigma}{dp_t}$
[arbitrary units]
$^{16}O + ^{197}Au$ 60 AGeV
"Protons" = ⊕ - ⊖
NA35 prelimin.
10^2
10^1
10^0
10^{-1}
0
1.0
2.0
p_t [GeV/c]

Fig. 5

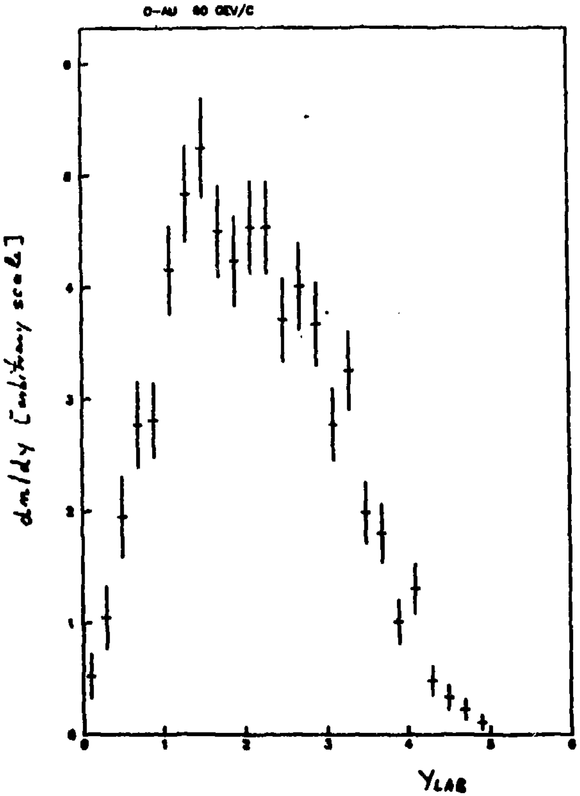

Fig. 6

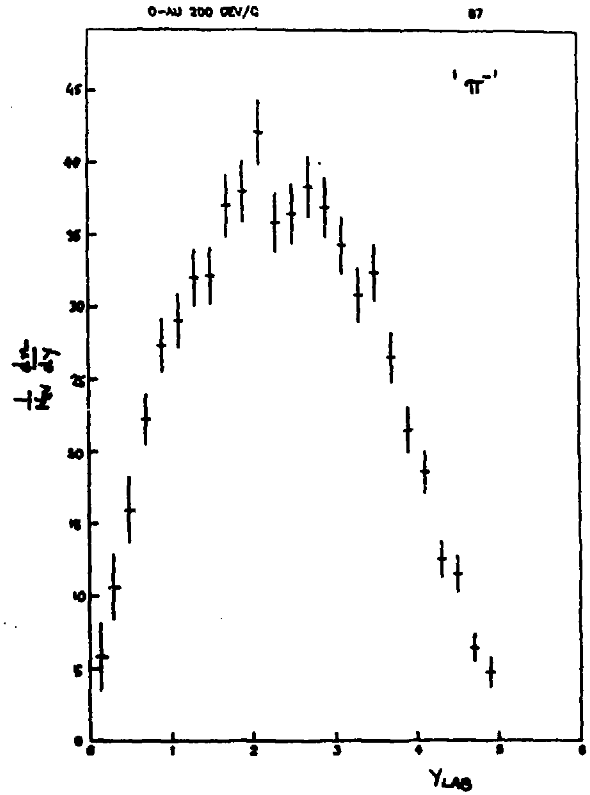

Fig. 7

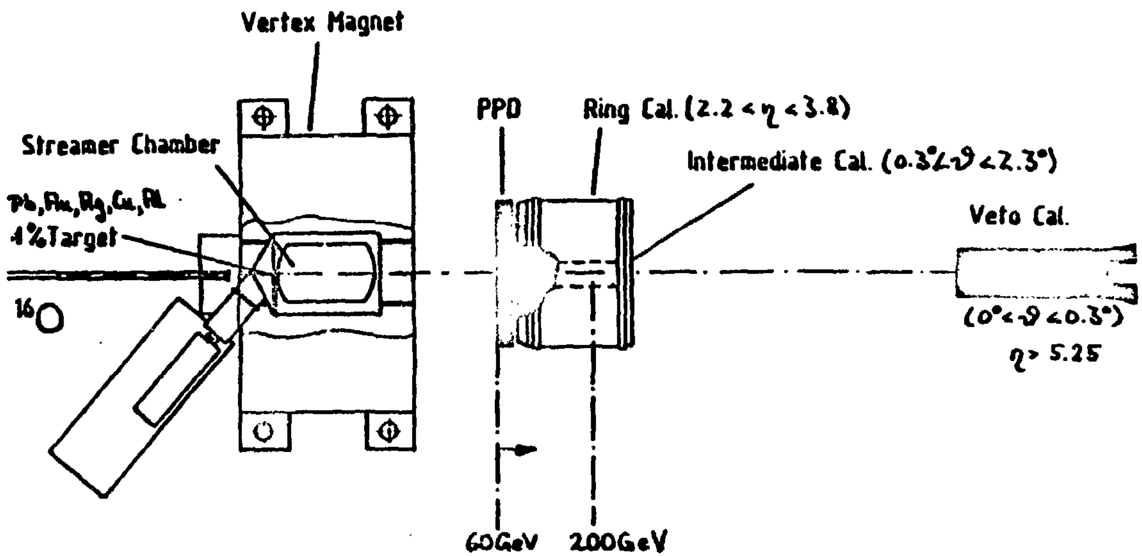

Vertex Magnet
Streamer Chamber
Pb, Au, Ag, Cu, Al
1% Target
^{16}O
PPD
Ring Cal. (2.2 < η < 3.8)
Intermediate Cal. (0.3° < ϑ < 2.3°)
Veto Cal.
(0° < ϑ < 0.3°)
η > 5.25
60GeV
200GeV

Fig. 8

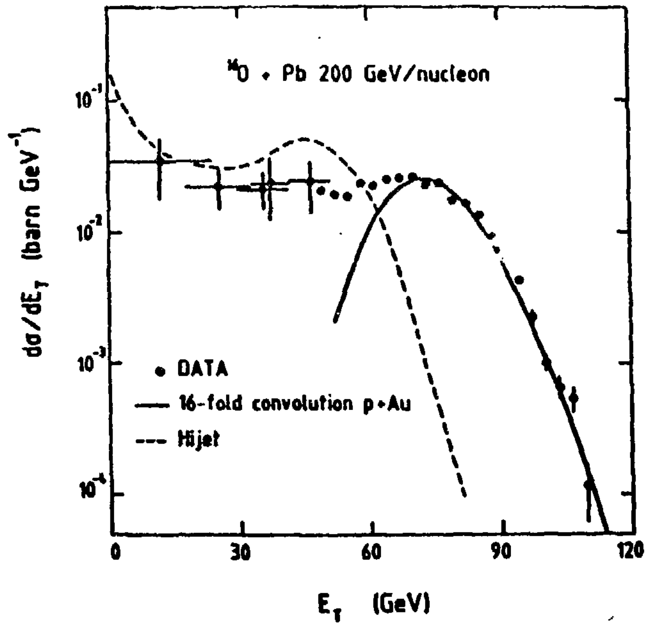

^{16}O + Pb 200 GeV/nucleon
dσ/dE$_T$ (barn GeV^{-1})
E$_T$ (GeV)
• DATA
— 16-fold convolution p+Au
--- Hijet

Fig. 9

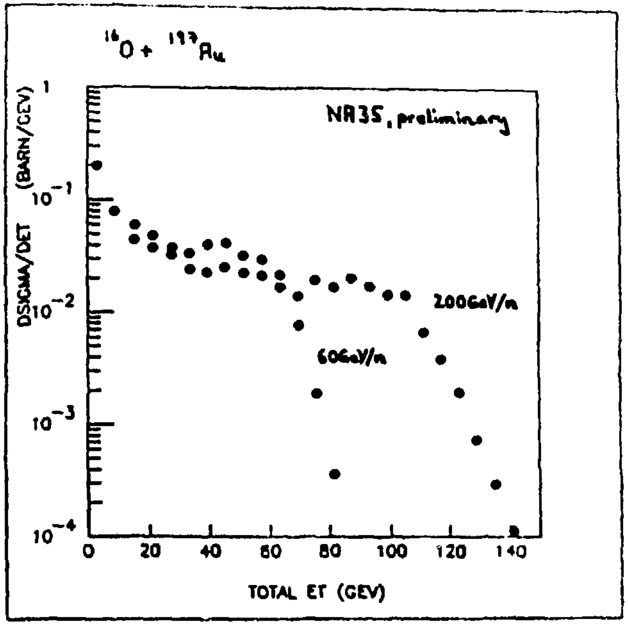

^{16}O + ^{197}Au
NA35, preliminary
DSIGMA/DET (BARN/GEV)
TOTAL ET (GEV)
200GeV/n
60GeV/n

Fig.10

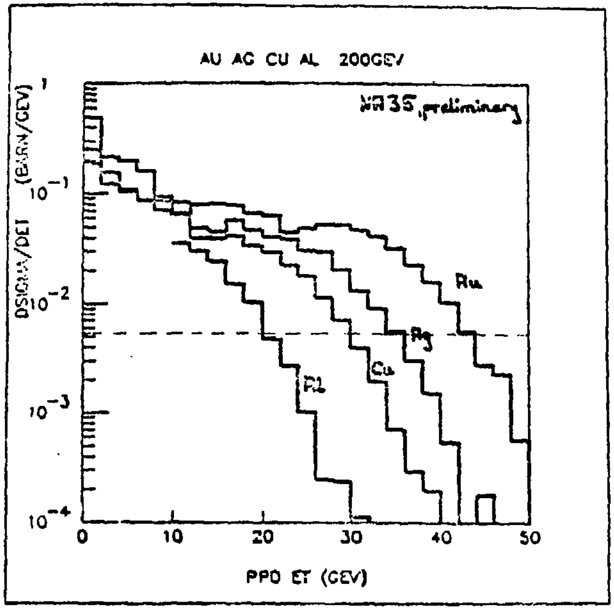

AU AG CU AL 200GEV
NA35, preliminary
DSIGMA/DET (BARN/GEV)
1
10^-1
10^-2
10^-3
10^-4
0
10
20
30
40
50
PPD ET (GEV)
Au
Ag
Cu
Al

Fig.11

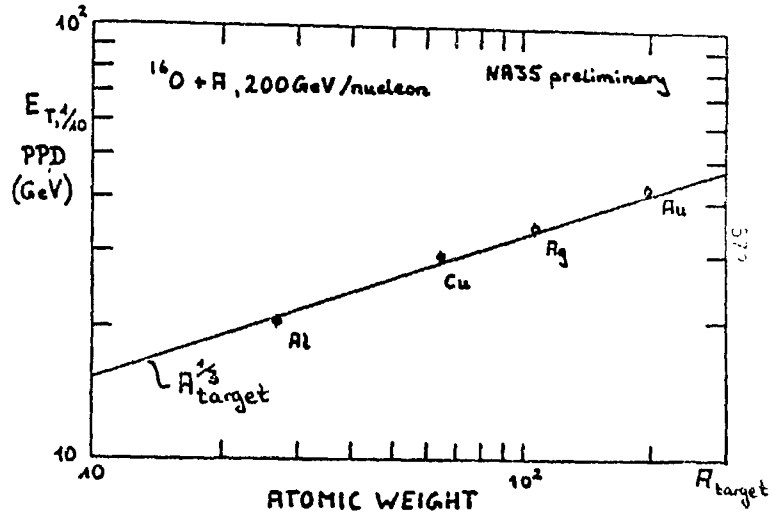

16O + A, 200GeV/nucleon
NA35 preliminary
E T,1/10
PPD
(GeV)
10^2
10
10
10^2
A target
ATOMIC WEIGHT
Al
Cu
Ag
Au
A^1/3 target

Fig.12

$$C(Q_\perp, Q_\parallel, Q_0) \propto 1 + \lambda e^{-Q_\perp^2 R_\perp^2/2 - Q_\parallel^2 R_\parallel^2/2 - Q_0^2 \tau^2/2}$$

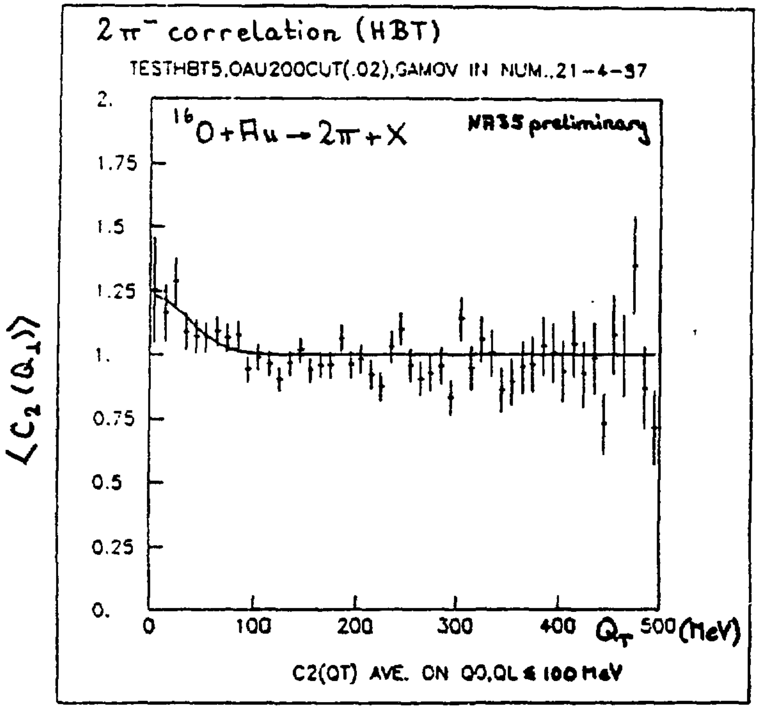

from 28 "central trigger" events :
in CM-frame "16 + 50"

$$R_T = 5.5 ^{+1.4}_{-1.0} \text{ fm}$$

$$R_\parallel = 2.4 ^{+0.8}_{-0.4} \text{ fm} \qquad \lambda = 0.29 ^{+.11}_{-.07}$$

$$\tau = 0.4 ^{+1.0}_{-0.4} \text{ fm}$$

Fig.13

PHENOMENOLOGY BASED ON SUPERSTRING INSPIRED E_6 GROUP

N.G. Deshpande
Institute of Theoretical Science
Eugene, OR 97403
USA

ABSTRACT

We present mass limits and properties of extra gauge bosons that might occur at low energy in superstring inspired E_6 models. Both rank 5 and rank 6 cases are considered. We then present the properties of the quark singlets that also occur in these models.

I. Introduction

Recent work on superstring theories has led to the interesting possibility that the $E_8 \times E_8'$ heterotic superstring theory in 10 dimensions yields, after compactification, a four-dimensional E_6 gauge group coupled to N = 1 supergravity.[1-4] Furthermore, the breaking at large scales is done by expectation values of order parameters which are in the adjoint representation. The low-energy gauge group that emerges must be larger than the standard $SU(3) \times SU(2) \times U(1)$, and should contain at least one extra U(1) gauge factor. If the low-energy model contains only one additional U(1), (the rank 5 case) the couplings of the extra Z boson to quarks and leptons are uniquely determined[5], in the absence of Z, Z′ mixing. The phenomenological implications of this extra Z boson are first considered and we discuss limits on its mass that emerge from a fit to low-energy neutral-current data and the measured W, Z masses. We also give constraints on the mass of extra Z from non-observation of high-mass e^+e^- pairs in $p\bar{p}$ collider experiments. We shall generalize this to rank 6 subgroup in a later section.

II. Limits on Extra Z of Rank 5 Subgroup

We can write the neutral current part of the Lagrangian as:

$$L_{NC} = e A_\mu J^\mu_{em} + g_Z Z_\mu J^\mu_Z + g' Z'_\mu J^\mu_{Z'} , \tag{2.1}$$

where J^μ_{em} and $J^\mu_Z \left(\equiv J^\mu_3 - x_W Q_\mu\right)$ are the usual electromagnetic and Z boson currents and $J^\mu_{Z'} = \bar{f}_L \gamma^\mu \tilde{Q} f_L$. The fermion fields belong to a $\underline{27}$ representation of E_6, and their decomposition into SO(10), SU(5), and SU(3) multiplets as well as the fermion quantum numbers Q (charge), I_{3L} (weak isospin), and $\tilde{Q}$ (extra U(1) charge) are given in Table 1. The coupling constant g′ with our normalization of $\tilde{Q}$ charges takes the value

$$g' = \frac{e}{\sqrt{1 - x_W}} \tag{2.2}$$

Table 1. Decomposition of $\underline{27}$ and fermion quantum numbers.

$SO(10)$	$SU(5)$	Left-handed state	$SU(3)$	Q	I_{3L}	$\tilde{Q}$
16	5^*	d^c	3^*	$\frac{1}{3}$	0	$-\frac{1}{6}$
		e^-	1	-1	$-\frac{1}{2}$	$-\frac{1}{6}$
		ν_e	1	0	$\frac{1}{2}$	$-\frac{1}{6}$
	10	e^{-c}	1	1	0	$\frac{1}{3}$
		d	3	$-\frac{1}{3}$	$-\frac{1}{2}$	$\frac{1}{3}$
		u	3	$\frac{2}{3}$	$\frac{1}{2}$	$\frac{1}{3}$
		u^c	3^*	$-\frac{2}{3}$	0	$\frac{1}{3}$
	1	N^c	1	0	0	$\frac{5}{6}$
10	5^*	h^c	3^*	$\frac{1}{3}$	0	$-\frac{1}{6}$
		E^-	1	-1	$-\frac{1}{2}$	$-\frac{1}{6}$
		ν_E	1	0	$\frac{1}{2}$	$-\frac{1}{6}$
	5	h	3	$-\frac{1}{3}$	0	$-\frac{2}{3}$
		E^{-c}	1	1	$\frac{1}{2}$	$-\frac{2}{3}$
		N_E^c	1	0	$-\frac{1}{2}$	$-\frac{2}{3}$
1	1	n	1	0	0	$\frac{5}{6}$

and g_Z is given as usual by

$$g_Z = \frac{e}{\sqrt{x_W}\sqrt{1 - x_W}}, \tag{2.3}$$

where $x_W = \sin^2\theta_W$. The assumption in (2) is that the evolution of the two U(1) factors from the grand unification scale to M_W is the same up to normalization constants. This assumes that the masses of all fermions in the 27 (and their superpartners) are low (in the TeV range). The fields Z_μ and Z'_μ are in general not mass eigenstates. In superstring theories the Higgs that is responsible for breaking of the low-energy group are also in the 27 representation, which has only $SU(2)_L$ doublets and singlet fields. If v_1, v_2 are the vacuum expectation values of the two doublets required in supersymmetric theories and χ that of the singlet, the mass matrix is

$$M^2 = M_Z^2 \begin{bmatrix} 1 & \sqrt{x_W}\,\dfrac{\left(4v_1^2 - v_2^2\right)}{3\left(v_1^2 + v_2^2\right)} \\ \sqrt{x_W}\,\dfrac{\left(4v_1^2 - v_2^2\right)}{6\left(v_1^2 + v_2^2\right)} & x_W\,\dfrac{16\,v_1^2 + v_2^2 + 25\,\chi^2}{9\left(v_1^2 + v_2^2\right)} \end{bmatrix} \tag{2.4}$$

where $M_Z^2 \equiv M_W^2 / (1 - x_W)$. The low-energy theory[6] then is described by the effective Lagrangian (of the same form as in Refs. 7,8)

$$L_{eff}^{NC} = \frac{G_F}{\sqrt{2}}\left[\left(\rho_1 J_Z\right)^2 + \left(\rho_2 J_Z + \eta J_{Z'}\right)^2\right] \tag{2.5}$$

where ρ_i,η are dependent on the mass matrix and the coupling constants. For our case, using Eqs. (2.2 - 2.4),

$$\rho_1 = 1 \tag{2.6a}$$

$$\frac{\rho_2}{\eta} = \frac{(v_2^2 - 4\,v_1^2)}{3(v_1^2 + v_2^2)} \tag{2.6b}$$

$$\frac{\rho_2^2 + 1}{\eta^2} = \frac{16\,v_1^2 + v_2^2 + 25\,\chi^2}{9(v_1^2 + v_2^2)} \tag{2.6c}$$

Determination of x_W, ρ_2 and η from experiment then yields limits on M_{Z_1} and M_{Z_2} which are the eigenvalues of the mass matrix. The low-energy parameters in neutrino-quark and neutrino-electron scattering and the parameters involved in atomic parity violation and asymmetry in electron-deuteron scattering for our Lagrangian are listed in Table 2, where we use the same notation as Kim et al..[9] For $e^+e^- \rightarrow \mu^+\mu^-$ we use the exact form for the cross section with Z-resonance contributions and the Z - Z′ mixing angle given by $\tan 2\theta = -2\rho_2\eta \,/\left(1 + \rho_2^2 - \rho_2\,\eta\right)$

We fit simultaneously all the low-energy data to determine x_W, ρ_2 and η. We impose the restriction $-\frac{4}{3} < \frac{\rho_2}{\eta} < \frac{1}{3}$ coming from Eq. (2.6b). There are 53 data points used in the analysis. Data from the following categories are taken from Ref. 7: νN (18 data points), νe (7 data points), and A_{eD} (11 data points). We have also included low-energy data from atomic parity violation (1 data point from Ref. 10) and $e^+e^- \rightarrow \mu^+\mu^-$ (12 data points from the compilation of Ref. 11). The measured W mass gives a constraint on x_W through the radiatively corrected[12] relation $M_W = 38.65\ \mathrm{GeV} / \sqrt{x_W}$. The measured Z mass gives a constraint on the lowest mass eigenstate, M_{Z_1}. The Z-mass eigenstates are related to the Lagrangian parameters by

Table 2. Parameters of effective Lagrangian.

$\alpha \equiv 1 + \rho_2^2 - \frac{1}{3}\rho_2\eta\,,$	$\beta \equiv \rho_2\eta - \frac{1}{3}\eta^2$
$\gamma \equiv 1 + \rho_2^2 + \frac{2}{3}\rho_2\eta\,,$	$\delta \equiv \rho_2\eta + \frac{2}{3}\eta^2$
$\epsilon_L^u = (\frac{1}{2} - \frac{2}{3}x_W)\alpha + \frac{1}{3}\beta$	
$\epsilon_R^u = (-\frac{2}{3}x_W)\alpha - \frac{1}{3}\beta$	
$\epsilon_L^d = (-\frac{1}{2} + \frac{1}{3}x_W)\alpha + \frac{1}{3}\beta$	
$\epsilon_R^d = (\frac{1}{3}x_W)\alpha + \frac{1}{6}\beta$	
$g_V^e = (-\frac{1}{2} + 2x_W)\alpha - \frac{1}{2}\beta$	
$g_A^e = -\frac{1}{2}\alpha + \frac{1}{6}\beta$	
$C_1^u = (-\frac{1}{2} + \frac{4}{3}x_W)\alpha$	
$C_1^d = (\frac{1}{2} - \frac{2}{3}x_W)\alpha - \frac{1}{2}\beta$	
$C_2^u = (-\frac{1}{2} + 2x_W)\gamma - \frac{1}{2}\delta$	
$C_2^d = (\frac{1}{2} - 2x_W)\alpha + \frac{1}{2}\beta$	

$$M^2_{Z_{1,2}} = \frac{1}{2} M_Z^2 \left[1 + x_W (1 + \rho_2^2)\eta^2 \pm \sqrt{\left[1 - x_W (1 + \rho_2^2)\eta^2\right]^2 + 4 x_W \rho_2^2 \eta^4}\,\right] \qquad (2.7)$$

The following W, Z mass data values[13] are used in the fit:

$$M_W = 83.1 \pm 3.2 \text{ GeV}, \quad M_{Z_1} = 93.0 \pm 3.4 \text{ GeV} \quad \text{(UA1 collaboration)};$$

$$M_W = 81.2 \pm 1.7 \text{ GeV}, \quad M_{Z_1} = 92.5 \pm 2.0 \text{ GeV} \quad \text{(UA2 collaboration)}.$$

The analysis gives the following best fit values (χ^2 / D.O.F. = 31/50)

$$x_W = 0.222^{+0.017}_{-0.012} \qquad \rho_2 = 0.08^{+0.07}_{-0.24} \qquad \eta = 0.26^{+0.22}_{-0.26}\,. \qquad (2.8)$$

where an average radiative correction to the low-energy x_W of -0.013 is included. The one and two standard deviation limits on M_{Z_2} are

$$\begin{aligned} M_{Z_2} &> 1.13\, M_Z = 105 \text{ GeV} \qquad (1\sigma) \\ &> 1.02\, M_Z = 95 \text{ GeV} \qquad (2\sigma). \end{aligned} \qquad (2.9)$$

The mixing angle between Z and Z′ is $\theta = -0.02 \pm 0.06$ radians.

The fact that e^+e^- pairs from the Z_2 have not yet been detected at the CERN $\bar{p}p$ collider also puts a limit on the Z_2 mass. An extra Z with standard-model couplings is excluded[13] below 200 GeV. The application of this constraint depends both on the Z_2 / Z_1 production and branching fraction ratios. Adjusting for the different couplings of the Z_2 to the u and d quarks, the Z_2 / Z_1 cross-section ratio in $p\bar{p}$ collisions at $\sqrt{s} = 630$ GeV is approximately

$$\frac{\sigma Z_2}{\sigma Z_1} = 0.28 \exp\left[-0.033\left(M_2 - M_1\right)\right]. \tag{2.10}$$

The partial widths for $Z_2 \rightarrow f\bar{f}$ decays are

$$\Gamma\left(Z_2 \rightarrow f\bar{f}\right) = \left[x_W M_2 / M_1\right](1.412 \text{ GeV})\, c_f\left(1 - 4m_f^2 / M_2^2\right)^{\frac{1}{2}}$$

$$\cdot \left\{g_V^2\left(1 + 2m_f^4 / M_2^2\right) + g_A^2\left(1 - 4m_f^2 / M_2^2\right)\right\} \tag{2.11}$$

where $c_f = 1$ for leptons and $c_f = 3.12$ for quarks; the g_V and g_A couplings can be deduced from the $J^{\mu}_{Z'} = \bar{f}\gamma^{\mu}\left(g_V - g_A\gamma^5\right)f$ and Table 1. The major difference from the corresponding expression for the Z_1 partial width (aside from different g_V, g_A) is the factor $x_W M_2 / M_1$. Typical partial widths are given in Table 3, for the case in which decays to the exotic fermions are (are not) phase-space-suppressed (i.e. $m_f < 30$ GeV); supersymmetric particles are assumed to be heavy. Results for W partial widths are also given in the table.

The ratio of the e^+e^- branching fractions is

$$B\left(Z_2 \rightarrow e^+e^-\right) / B\left(Z_1 \rightarrow e^+e^-\right) \cong 0.45\ (1.3) \tag{2.12}$$

for no (complete) phase-space suppression of Z_1 and Z_2 decays into three generations of exotic fermions.

Figure 1 shows the $Z_2 \rightarrow e^+e^-$ production rate relative to $Z_1 \rightarrow e^+e^-$ for the above two extreme cases. Also shown in the CERN limit[13] which requires at 90% C.L.

Table 3. Partial widths for Z, W decays to exotic fermions, assuming no phase-space suppression; note that the Z_2 partial widths scale with M_2/M_1. Total widths assume $m_t = 40$ GeV and three generations of exotics with no (complete) phase-space suppression.

Channel	Γ_{Z_1} (GeV)	$(M_1/M_2)\Gamma_{Z_2}$ (GeV)	Channel	Γ_W (GeV)
$h\bar{h}$	0.02	0.23	$\bar{\nu}_E E^-$	0.24
$E^- E^+$	0.11	0.07	$\bar{N}_E E^-$	0.24
$\nu_E \bar{\nu}_E$	0.18	0.004		
$N_E \bar{N}_E$	0.18	0.07		
$N\bar{N}$	0	0.11		
$n\bar{n}$	0	0.11		
Total width	4.22 (2.75)	2.27 (0.50)		4.16 (2.71)

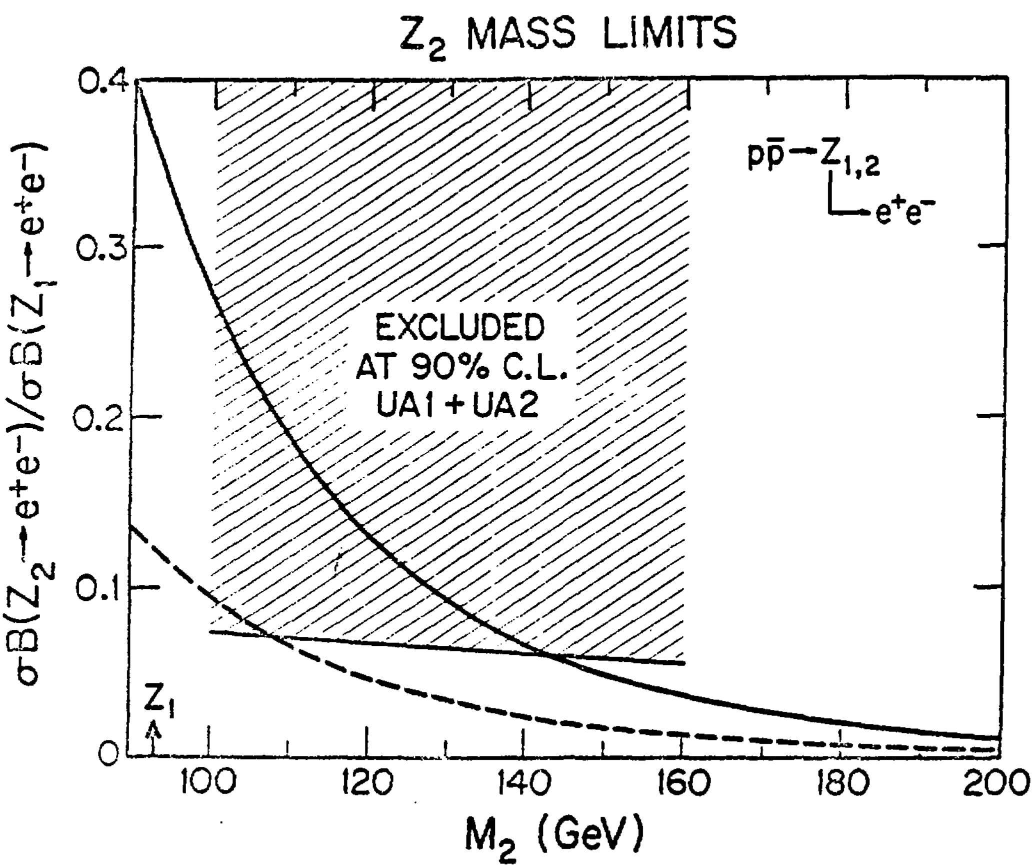

Z2 MASS LIMITS
0.4
0.3
0.2
0.1
0
σB(Z2→e+e−)/σB(Z1→e+e−)
pp̄→Z1,2
→e+e−
EXCLUDED
AT 90% C.L.
UA1 + UA2
Z1
100
120
140
160
180
200
M2 (GeV)

Fig. 1

$$M_{Z_2} > 107 \text{ GeV } (143 \text{ GeV}) \tag{2.13}$$

for unsuppressed (completely suppressed) decays to exotic fermions.

III. Extra Z in Rank 6 Subgroup

To analyze the effects of an extra neutral gauge boson in E_6, consider the breakdown[14-15] $E_6 \to SO(10) \times U(1)_\psi \to SU(5) \times U(1)_\chi \times U(1)_\psi$. If there is one light extra Z boson it will be a linear combination of the two extra U(1)'s: $Q(\alpha) = Q_\psi \cos\alpha + Q_\chi \sin\alpha$. The Z boson associated with this generator will be called $Z(\alpha)$. If E_6 is broken to a rank 6 group the mixing angle α is unconstrained. However, if E_6 is broken to a rank 5 group, α is uniquely determined and has the value $\alpha = \tan^{-1}(\sqrt{3/5})$ (we call this special case the Z′). In addition to the cases $\alpha = 0$ (Z_ψ) and $\alpha = \pi/2$ (Z_χ) there is the special value $\alpha = \tan^{-1}(-\sqrt{5/3})$ (Z_I) corresponding to an extra SU(2) group at electroweak energies.

In an E_6 theory, each generation of fermions belongs to a 27 representation. The decomposition of the 27 into SO(10) and SU(5) multiplets and the extra U(1) charge ($\tilde{Q}$) are given in Table 4 note that $\tilde{Q}$ depends on the mixing angle α. In addition to the usual fermions $\overset{(-)}{u}$, $\overset{(-)}{d}$, $e^\pm$ and ν_e there is a charge $-\frac{1}{3}$ quark isosinglet h, charged leptons $E^\mp$ and neutral leptons ν_E, N_E, N_e and n.

The neutral current Lagrangian for the E_6 models with one extra Z at low energies is $L_{NC} = eA_\mu J^\mu_{em} + g_Z Z_\mu J^\mu_Z + g' Z(\alpha)_\mu J^\mu_{Z(\alpha)}$ where J^μ_{em} and $J^\mu_Z \left(\equiv J^\mu_3 - x_W Q^\mu\right)$ are the usual electromagnetic and Z boson currents and $J^\mu_{Z(\alpha)} = \frac{1}{2}\Sigma_f \bar{f} \gamma^\mu (1-\gamma_5) \tilde{Q} f$. Note that the couplings of a left-handed charge conjugate state give right-handed couplings of opposite sign. The coupling constants are $g' = g_Z \sqrt{x_W} = e/\sqrt{1-x_W}$, where $x_W = \sin^2\theta_W$. In general, Z and $Z(\alpha)$ may mix, but fits to low-energy neutral-current data for the rank 5 value of α ($\tan\alpha = \sqrt{3/5}$) show that this mixing is very small.[6] Hence we shall ignore $Z - Z(\alpha)$ mixing in our analysis.

The partial width for the decay of $Z(\alpha)$ into a fermion-antifermion pair in the limit $m_f << M_{Z(\alpha)}$ is $\Gamma\left(Z(\alpha) \to f\bar{f}\right) = \alpha_{em} M_{Z(\alpha)} \left[6\,(1 - x_W)\right]^{-1} \left(g_L^2 + g_R^2\right) c_f$, where g_L

Table 4. Decomposition of 27 and fermion quantum numbers. The $\tilde{Q}$ charges a_i are given as an amplitude times a factor which varies with α over the range -1 to $+1$.

$SO(10)$	$SU(5)$	Left – handed state	$\tilde{Q}$
16	10	e^{-c}, d, u, u^c	$a_1 = 1/3\left(\sqrt{5/8}\cos\alpha + \sqrt{3/8}\sin\alpha\right)$
	5^*	d^c, e^-, ν_e	$a_2 = 2/3\left(\sqrt{5/32}\cos\alpha - \sqrt{27/32}\sin\alpha\right)$
	1	N_e^c	$a_3 = \sqrt{10}/3\left(1/4\cos\alpha + \sqrt{15}/4\sin\alpha\right)$
10	5^*	h^c, E^-, ν_E	$a_4 = 2/3\left(-\sqrt{5/8}\cos\alpha + \sqrt{3/8}\sin\alpha\right)$
	5	h, E^{-c}, N_E^c	$a_5 = 2/3\left(-\sqrt{5/8}\cos\alpha - \sqrt{3/8}\sin\alpha\right)$
1	1	n	$a_6 = \sqrt{10}/3\cos\alpha$

and g_R are the left- and right-handed couplings which can be read off from Table 4, and c_f is 1 for leptons and 3 for quarks. We take the fine structure constant to be $\alpha_{em}^{-1}(M_W) = 128.5$. If n_G generations of exotic fermions contribute fully (i.e., with no phase space suppression) in $Z(\alpha)$ decays then the total width is

$$\Gamma(Z(\alpha)) = \alpha_{em} M_{Z(\alpha)} \left[2\left(1 - x_W\right)\right]^{-1}$$

$$\left[10\, a_1^2 + 5\, a_2^2 + n_G \left(5 - 10\, a_1^2 - 5\, a_2^2\right) / \; 3\right]. \tag{3.1}$$

If $n_G = 3$ the width is independent of the mixing α: $\Gamma(Z(\alpha)) = 0.025\, M_{Z(\alpha)}$. Figure 2a shows the $Z(\alpha)$ width versus $\cos\alpha$ when the $Z(\alpha)$ decays to all exotic fermions are inaccessible. Figures 2b and 2d show $Z(\alpha)$ branching ratios versus $\cos\alpha$ in the two extreme cases $n_G = 0$ and $n_G = 3$. The e^+e^- branching fraction varies from 3.3% to 6.7% (0.7% to 3.0%) for $n_G = 0$ (3). Exotic fermion branching fractions for $n_G = 3$ are given in Fig. 2c.

The differential cross section for the reaction $q\bar{q} \to \mu^+\mu^-$ (or e^+e^-) in a model with two Z bosons in the limit of negligible fermion masses can be written

$$d\sigma^{q\bar{q}} / d\cos\theta^* = \pi\, \alpha_{em}^2 / \left(2m^2\right)^{-1} \left[S_q\left(1 + \cos^2\theta^*\right) + A_q\, 2\cos\theta^*\right] \tag{3.2}$$

where θ^* is the angle of the outgoing μ^- with respect to the quark q in the $q\bar{q}$ center of mass, m is the lepton-pair mass and

$$S_q, A_q = \sum_{j\,k} \left(g_j / e\right)^2 \left(g_k / e\right)^2 m^4$$

$$\left[\left(m^2 - M_j^2\right)\left(m^2 - M_j^2\right) + M_j M_k \Gamma_j \Gamma_k\right] D_j^{-1} D_k^{-1} \tag{3.3}$$

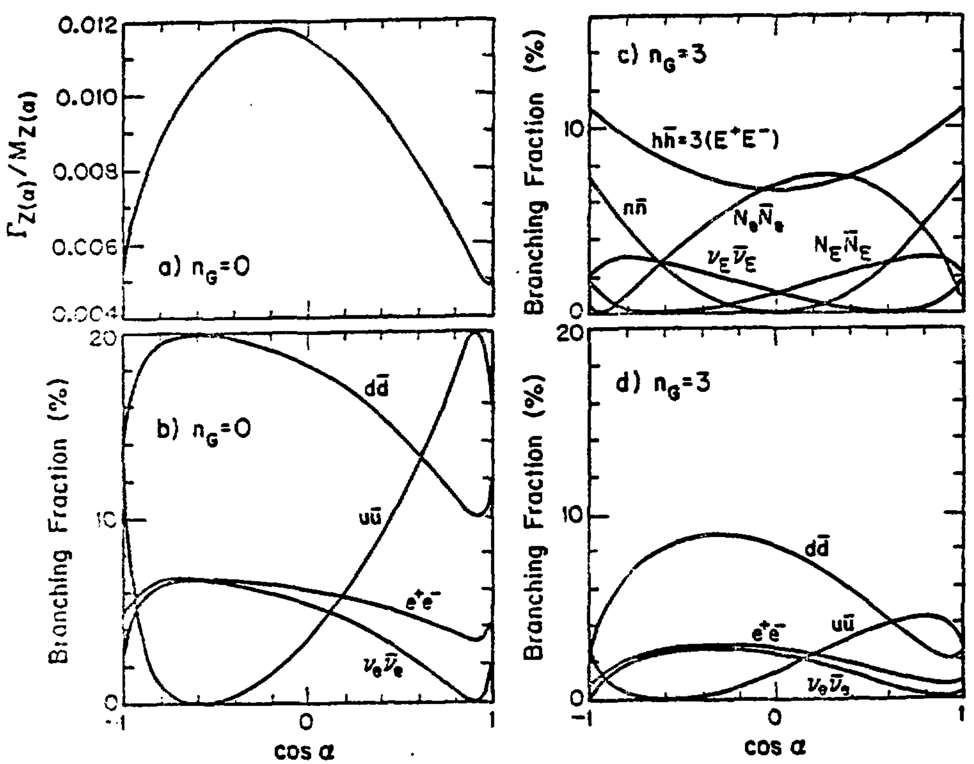

Fig. 2. Properties of Z(α) decays versus cos α.

$$\times \left[g_L^j(\mu)\, g_L^k(\mu) \pm g_R^j(\mu)\, g_R^k(\mu)\right]\left[g_L^j(q)\, g_L^k(q) \pm g_R^j(q)\, g_R^k(q)\right] / 4$$

where g_j, M_j, Γ_j are the gauge boson coupling strengths, masses and widths, respectively and the Breit-Wigner denominators are $D_j = \left(m^2 - M_j^2\right)^2 + M_j^2\Gamma_j^2$. For the photon (j,k = 0), $g_0 = e$, $M_0 = \Gamma_0 = 0$ and the photon couplings to a fermion f are $g_L^0(f) = g_R^0(f) = Q_f$. The hadronic cross section for $A + B \to \mu^+\mu^- X$ is easily found by folding Eq. (3.2) with the quark distribution functions. In our calculations we use the structure functions of Ref. 16, except where noted otherwise, and sum over u, d and s quark contributions. We also include an m^2 dependent K factor as discussed in Ref. 17.

To study the helicity structure of the $Z(\alpha)$ couplings, as exhibited by the coefficients S_q and A_q in Eq. (3.2) one may look at the forward-backward asymmetry as a function of y

$$A^{FB}(y) = \frac{d\sigma^F/dy - d\sigma^B/dy}{d\sigma^F/dy + d\sigma^B/dy}$$

$$\frac{3}{4}\frac{\left[g_R(\mu)^2 - g_L(\mu)^2\right]}{\left[g_R(\mu)^2 + g_L(\mu)^2\right]}\frac{\sum_q\left[g_R(q)^2 - g_L(q)^2\right] G_q^-}{\sum_q\left[g_R(q)^2 + g_L(q)^2\right] G_q^+} \tag{3.4}$$

Forward (backward) is defined in the $z(\alpha)$ rest frame as $\theta^* < \frac{\pi}{2}\left(\theta^* > \frac{\pi}{2}\right)$ and $G_q^{\pm}(y, m^2, \sqrt{s}) = f_{q/A}(x_A)\, f_{\bar{q}/B}(x_B) \pm f_{\bar{q}/A}(x_A)\, f_{q/B}(x_B)$, where $f_{q/A}(x_A)$ is the distribution of q in hadron A. Exact double zeroes in A^{FB} occur when $a_1 = \pm a_2$ ($\cos\alpha = \sqrt{3/8}, \pm 1$) because for those α values $g_R(\mu)^2 - g_L(\mu)^2 = g_R(d)^2 - g_L(d)^2 \to 0$ and the u quark, which always has an axial vector coupling to $Z(\alpha)$, does not contribute to the numerator in Eq. (4). $A^{FB}(y)$ is even (odd) in y for $p\bar{p}$ (pp) machines. For $p\bar{p}$ reactions, an A^{FB} integrated over y can be obtained from Eq. (3.4). For pp reactions the appropriate quantity is

$$A^{FB} = \frac{\left(\int_0^{\sqrt{s}/m} dy - \int_{-\sqrt{s}/m}^{0} dy\right)\left(d\sigma^F / dy - d\sigma^B / dy\right)}{\left(\int_0^{\sqrt{s}/m} dy + \int_{-\sqrt{s}/m}^{0} dy\right)\left(d\sigma^F / dy + d\sigma^B / dy\right)} \tag{3.5}$$

$p\bar{p}$ colliders. We calculate the production cross section of $Z(\alpha)$ at $\sqrt{s} = 630$ GeV for the CERN $p\bar{p}$ collider using the structure functions of Ref. 18. Figure 3a shows the lower limit on $M_{Z(\alpha)}$ versus cos α deduced from the combined UA1-UA2 upper limit[19] of $\sigma B \leq 3$ pb on an extra Z boson in its e^+e^- decay channel, for the cases $n_G = 3$. Also shown is the lower bound on $M_{Z(\alpha)}$ deduced from fits to neutral-current data. All limits are at the 90% confidence level.

The $p\bar{p}$ total cross section and lepton pair signal are shown in Fig. 3b versus $M_{Z(\alpha)}$ at $\sqrt{s} = 2$ TeV. The shaded bands correspond to variations with the mixing angle α. This dependence on α is shown in Fig. 3c for specific values of the $Z(\alpha)$ mass. In Fig. 4a the integrated forward-backward asymmetry computed using Eq. (3.4) is shown. With an annual luminosity $\int L = 1\text{pb}^{-1}$ one expects from 1 to 20 events in each dilepton channel for $M_{Z(\alpha)} = 300$ GeV.

pp colliders.

A high luminosity pp collider will be an excellent source for producing the $Z(\alpha)$ boson. We calculate $d\sigma/dm$ for $pp \to Z(\alpha)\,X$, $Z(\alpha) \to \mu^+\mu^-$ at $\sqrt{s} = 40$ TeV as a function of dilepton mass m; the results are shown in Fig. 4a for $M_{Z(\alpha)} = 0.5$ and 1 TeV. The $Z(\alpha)$ peaks are shown for the two extreme cases $n_G = 0$ and $n_G = 3$. The total $Z(\alpha)$ production cross sections and cross section times leptonic branching ratio as a function of $Z(\alpha)$ mass are given in Fig. 5b; the α dependence is shown in Fig. 5c for $M_{Z(\alpha)} = 0.5$ and 1 TeV. The forward-backward asymmetry defined in Eq. (3.4) is shown in Fig. 4b versus y for

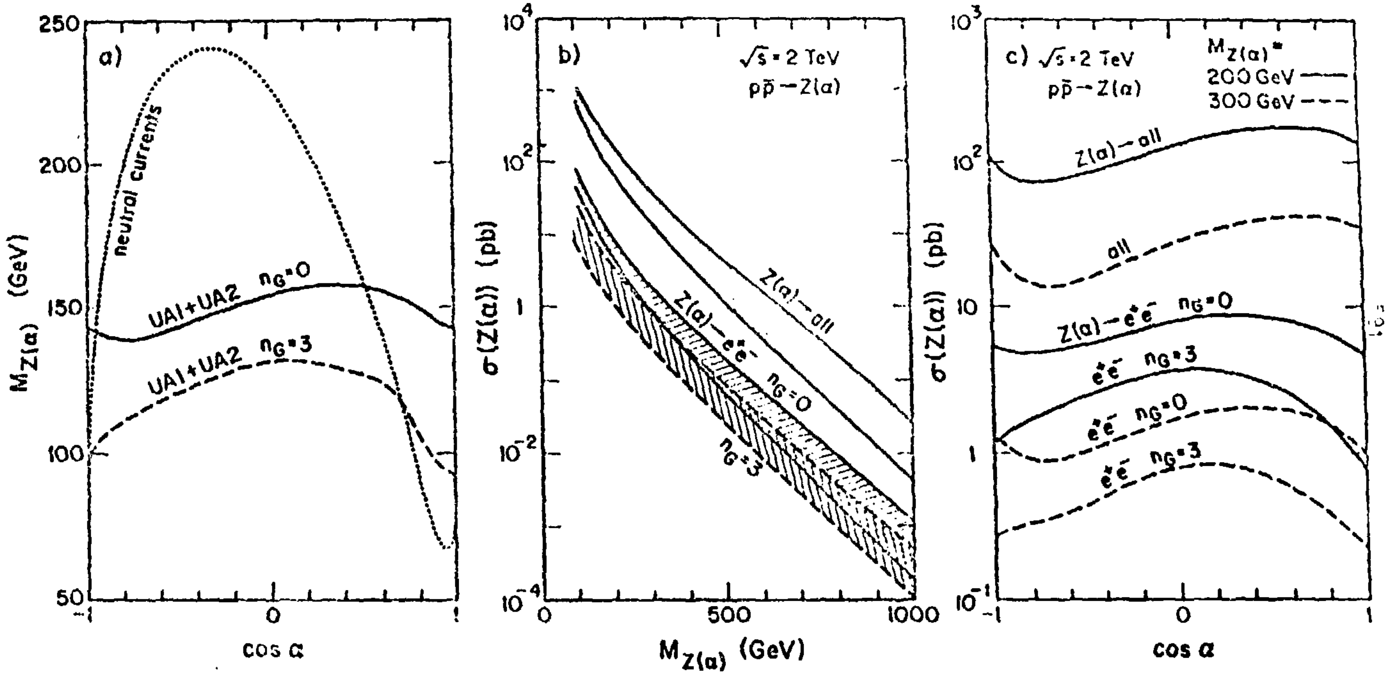

Fig. 3. (a) Lower bounds on mass of extra Z boson versus cos α deduced from UA1/UA2 searches for $Z\to e^+e^-$ at $\sqrt{s}=630$ GeV. The solid (dashed) curve assumes $n_G = 0(3)$. The dotted curve denotes the lower bound on $M_{Z(\alpha)}$ from neutral-current data. Predictions for Z(α) production at the 2 TeV Fermilab $p\bar{p}$ collider: (b) σ of Z(α) and σB(Z(α) → e^+e^-) versus $M_{Z(\alpha)}$, for the two extreme cases $n_G = 0$ and 3 exotic fermions. The shades regions correspond to the range allowed by varying α. (c) σ and σB for $M_{Z(\alpha)}$ = 200 and 300 GeV shown versus cos α.

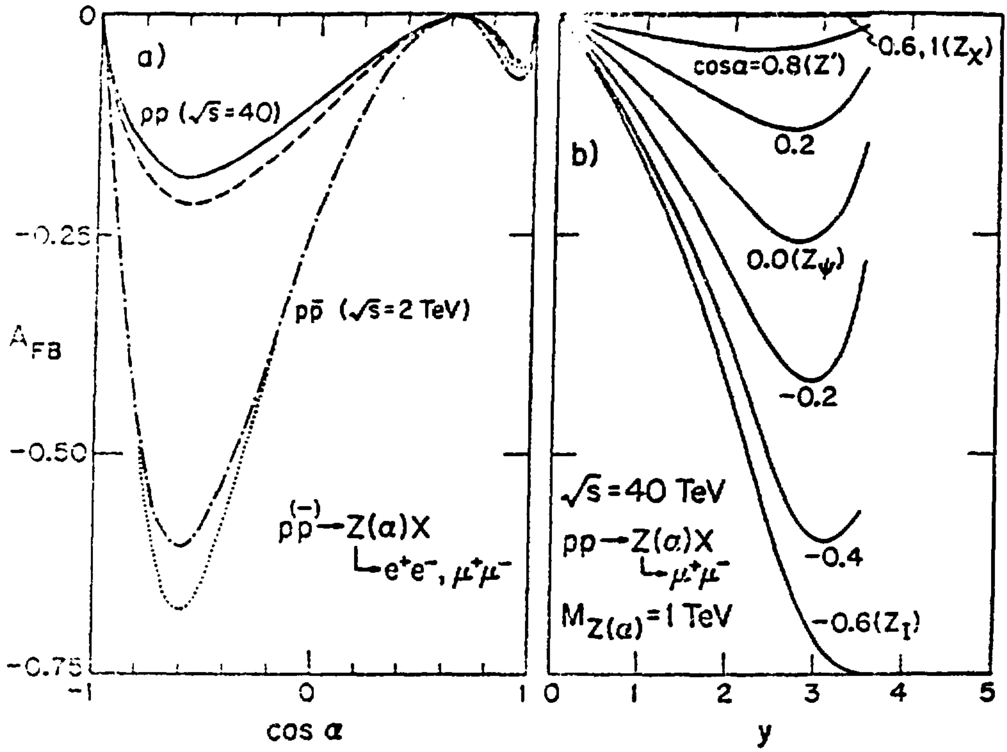

Fig. 4. Forward-backward asymmetries for the reactions $p\overset{(-)}{p} \to Z(\alpha)X$, $Z(\alpha) \to e^+e^-$ or $\mu^+\mu^-$: (a) asymmetry integrated over y versus cos α for $p\bar{p}$ at $\sqrt{s}$ = 2 TeV, $M_{Z(\alpha)}$ = 200 (dot-dash curve) and 300 GeV (dotted), and pp at $\sqrt{s}$ = 40 TeV, $M_{Z(\alpha)}$ = 0.5 (solid) and 1 TeV (dashed); (b) asymmetry versus y for representative cos α for pp at $\sqrt{s}$ = 40 TeV, $M_{Z(\alpha)}$ = 1 TeV.

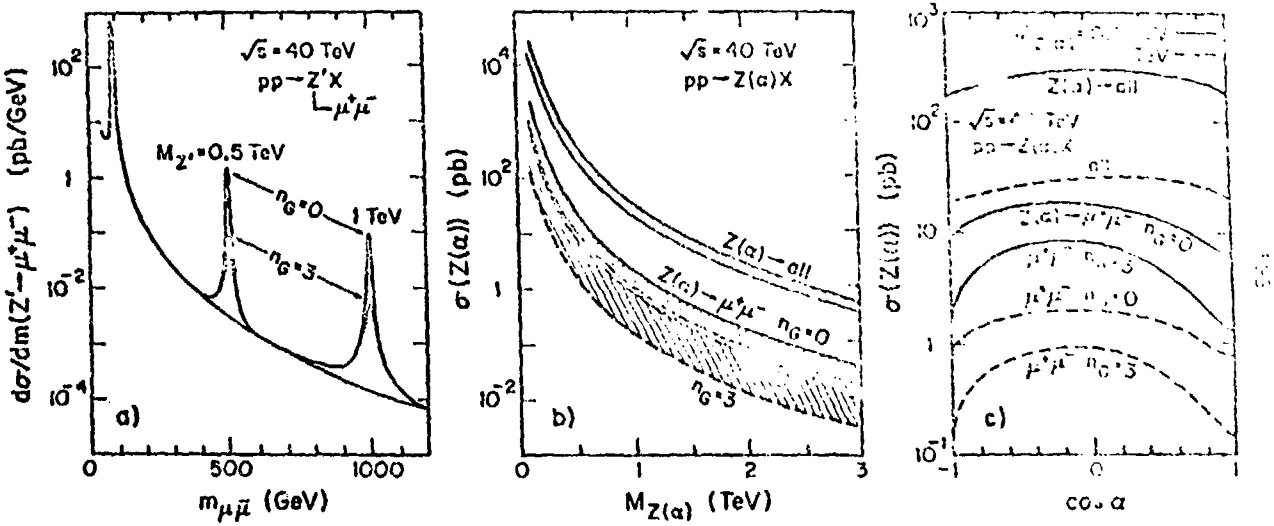

Fig. 5. Predictions for Z′ (cos α = $\sqrt{5/8}$) production in a pp collider at $\sqrt{s}$ = 40 TeV: (a) dσ/dm(pp → e^+e^- X) versus dilepton invariant mass for $M_{Z'}$ = 0.5 and 1 TeV; the solid (dotted) curves correspond to n_G = 0(3); (b) σ and σB(Z(α) → e^+e^-) for producing Z(α) versus $M_{Z(\alpha)}$; the shaded regions correspond to the range allowed by α; (c) σ and σB(Z(α) → e^+e^-) for $M_{Z(\alpha)}$ = 0.5 and 1 TeV versus cos α.

various values of cos α, for $M_{Z(\alpha)}$ = 1 TeV; the integrated asymmetry of Eq. (3.5) is given in Fig. 4a as a function of cos α.

For masses below 4 TeV the Z(α) boson of E_6 theories should be easily detectable through its leptonic decays in a pp machine at √(s) = 40 TeV with integrated luminosity $\int L \sim 10^4\ pb^{-1}$, irrespective of the mixing angle α or the exotic fermion masses. If the exotic fermion decay channels of the Z(α) are kinematically inaccessible then even higher Z(α) masses may be probed. The Z(α) mass and production cross section will provide some information on α. For no phase space suppression of exotic fermions in Z(α) decays, accurate measurements of forward-backward asymmetries in pp → Z(α) X, Z(α) → $\mu^+\mu^-$ and Z(α) branching ratios will further constrain α for Z(α) masses below about 1 TeV; if the exotic fermion decays are kinematically suppressed, a good determination of α may be possible if $M_{Z(\alpha)} \leq 1.5$ TeV.

IV. Properties of Quark Singlet from E_6[20]

We restrict ourselves to the E_6 model inspired by superstring theory with no intermediate mass scale. All the 27 superfields should then be light (≤ TeV) and we may expect to find them at present or future colliders.[21] We assume that the low energy group is rank 5, $SU(3)_c \times SU(2)_L \times U(1)_Y \times U(1)_\eta$. However, the extra gauge boson is not especially relevant to our discussion here. The fermions belong to the 27 representation of E_6. The 27 of E_6 can be decomposed according to SO(10) {SU(5)} and has the left-hand fermion content

$$27 = 16\left\{10\begin{bmatrix} & l^c \\ (u,d) & u^c \end{bmatrix}_{1/3} + 5^*\begin{bmatrix}(\nu, l) \\ d^c\end{bmatrix}_{-1/6} + 1\begin{bmatrix}N^c\end{bmatrix}_{5/6}\right\}$$

$$+ 10\left\{5\begin{bmatrix}(E^c, \nu_E^c) \\ h\end{bmatrix}_{-2/3} + 5^*\begin{bmatrix}(\nu_E, E) \\ h^c\end{bmatrix}_{-1/6}\right\} + 1\begin{bmatrix}n\end{bmatrix}_{5/6}. \qquad (4.1)$$

Here the upper entries are color singlets and the lower ones color triplets. The subscripts outside the square brackets are the Z' charges of the extra $U(1)$. We focus our attention on the new weak SU(2) singlet charge $-\frac{1}{3}$ particles h and their supersymmetric partners $\tilde{h}_L$ and $\tilde{h}_R$.

The most general low energy superpotential involving $\tilde{h}$ is [22]

$$
\begin{aligned}
W = {} & \lambda_1^{ijk}\, \tilde{h}_i^c \left(\tilde{\nu}_j \;\; \tilde{l}\right) \begin{pmatrix} \tilde{d}_k \\ -\tilde{u}_k \end{pmatrix} + \lambda_2^{ijk}\, \tilde{h}_i\, \tilde{e}_j^c\, \tilde{u}_k^c + \lambda_3^{ijk}\, \tilde{h}_i\, \tilde{N}_j^c\, \tilde{d}_k^c \\
& + \lambda_4^{ijk}\, \tilde{h}_i \left(\tilde{u}_j \;\; \tilde{d}\right) \begin{pmatrix} \tilde{d}_k \\ -\tilde{u}_k \end{pmatrix} + \lambda_5^{ijk}\, \tilde{h}_i^c\, \tilde{u}_j^c\, \tilde{d}_k^c + \lambda_6^{ijk}\, \tilde{h}_i\, \tilde{h}_j^c\, \tilde{n}_k
\end{aligned}
\tag{4.2}
$$

where the superscript labels $i,j,k = 1,2,3$ on the couplings refer to generations and the twiddles denote the scalar superpartners of the corresponding fermions. The couplings λ_a are arbitrary parameters. There are three possible choices of h quantum numbers and couplings that insure baryon stability at low energies[23]

A) leptoquark h: $B(h) = 1/3,\ L(h) = 1 \quad \lambda_4 = \lambda_5 = 0$

B) diquark h^c: $B(h) = -2/3,\ L(h) = 0 \quad \lambda_1 = \lambda_2 = \lambda_3 = 0$

C) quark h: $B(h) = 1/3,\ L(h) = 0 \quad \lambda_1 = \lambda_2 = \lambda_4 = \lambda_5 = 0.$

Case C is ruled out in the rank 5 model by the predicted decay of K^+ into π^+ and a pseudo-Goldstone boson. The assignment A) or B) may be realized with a discrete symmetry of the compactified 6-dimensional space.[22-24] Here we shall assume that such symmetry indeed exists in nature and examine the consequences of scenarios A) and B). In these two cases we can assign even R-parity for u,d,ν_e,e,N (S(10) 16 states) and odd for h, E, ν_E, n, (SO(10) 10 and 1 states) with the opposite assignments for their supersymmetric scalar partners. In particular, fermions h_i are R-odd whereas scalars $\tilde{h}_i$ are R-even.

The $\tilde{h}_i$ and h_i acquire masses from the vacuum expectation values $<n_{\tilde{\nu}}>$. With three families there are three Dirac mass eigenstates ψ_i and six scalar mass eigenstates ϕ_i; the latter are mixtures of the $\tilde{h}_i$ and $\tilde{h}_i^c$. For example with one generation only the scalar mass eigenstates are related to the $\tilde{h}_i$ by

$$\begin{pmatrix} \phi_1 \\ \phi_2 \end{pmatrix} = \begin{pmatrix} \cos\xi & \sin\xi \\ -\sin\xi & \cos\xi \end{pmatrix} \begin{pmatrix} \tilde{h}_{1L} \\ \tilde{h}_{1R} \end{pmatrix}. \tag{4.3}$$

We redefine the couplings λ_i $(i = 1,2,...,5)$ in the mass eigenstate basis and concentrate on the lightest mass eigenstates in each sector, ϕ_1 and ψ_1; hencefore we often denote ϕ_1 by $\tilde{h}_1$ and ψ_1 by h_1.

e^+e^- production:

The electroweak gauge interaction for h_1 and $\tilde{h}_1$ production has the form

$$L = -ee_h\left(A^\mu - \tan\theta_W Z^\mu\right)\left(\bar{\psi}_1 \gamma_\mu \psi_1 + i\,\phi_1^* \bar{\partial}_\mu \phi_1\right) \tag{4.4}$$

$$\bar{\psi}_1 \gamma_\mu \psi_{1L} + \frac{1}{6}\bar{\psi}_1 \gamma_\mu \psi_{1R} + \left(-\frac{2}{3}\cos^2\xi + \frac{1}{6}\sin^2\xi\right)\left(i\,\phi_1^* \bar{\partial}_\mu \phi_1\right)$$

where $e_h = -\frac{1}{3}$. The Z' coupling to ϕ_1 depends on the $\tilde{h}_i$, $\tilde{h}_i^c$ mixing because $\tilde{h}_i$ and $\tilde{h}_i^c$ have different $U(1)_\eta$ quantum numbers. For the present we shall neglect Z, Z' mixing effects, which are constrained to be small. Then the e^+e^- production cross sections at $\sqrt{s} << M_{Z'}$ are

$$\begin{aligned} \frac{d\sigma}{d\cos\theta}\left(e^+e^- \to h_1 \bar{h}_1\right) &= \sigma_{pt}\frac{1}{8}\beta\left(2 - \beta^2\sin^2\theta\right)\Sigma\,, \\ \frac{d\sigma}{d\cos\theta}\left(e^+e^- \to \tilde{h}_1 \tilde{h}_1^*\right) &= \sigma_{pt}\frac{1}{16}\beta^3\sin^2\theta\Sigma\,, \end{aligned} \tag{4.5a}$$

where $\sigma_{pt} = (4\pi\alpha^2/3s)$, $\beta = (1 - 4m^2/s)^{\frac{1}{2}}$, and

$$\Sigma = 1 + \frac{bs^2 - 2as\left(s - M_Z^2\right)}{\left(s - M_Z^2\right)^2 + M_Z^2\Gamma_Z^2} \tag{4.5b}$$

with $a = \left(\frac{1}{4} - x_W\right) / \left(1 - x_W\right)$, $b = \left(\frac{1}{8} - \frac{1}{2}x_W + x_W^2\right) / \left(1 - x_W\right)^2$, and $x_W = \sin^2\theta_W$. We note that there is no forward-backward asymmetry. On the Z-resonance the total cross sections (in terms of $k = (2.6\ \text{GeV}/\Gamma_Z)^2$ with $x_W = 0.23$) are

$$\begin{aligned}
\sigma\left(e^+e^- \to Z \to h_1\,\bar{h}_1\right) &= \tfrac{1}{3}\sigma_{pt}\left(b\,M_Z^2/\Gamma_Z^2\right)\beta\left(\tfrac{3}{2} - \tfrac{1}{2}\beta^2\right) \\
&= (0.52\ \text{nb})\,k\beta\left(\tfrac{3}{2} - \tfrac{1}{2}\beta^2\right)
\end{aligned} \tag{4.6}$$

$$\sigma\left(e^+e^- \to Z \to \tilde{h}_1\,\bar{\tilde{h}}_1\right) = \tfrac{1}{12}\sigma_{pt}\left(b\,M_Z^2/\Gamma_Z^2\right)\beta^3 = (0.13\ \text{nb})\,k\beta^3$$

to be compared with $\sigma\left(e^+e^- \to Z \to \mu^+\mu^-\right) \equiv (1.86\ \text{nb})\,k$.

Decays of a Z' resonance produced in e^+e^-, $p\bar{p}$ or pp collisions could be a copious source of h_1 and $\tilde{h}_1$. The partial widths are

$$\begin{aligned}
\Gamma\left(Z' \to h_1\,\bar{h}_1\right) &= \frac{\alpha M_{Z'}}{1 - x_W}\,\frac{\beta\left(27 + 41\beta^2\right)}{288} \\
\Gamma\left(Z' \to \tilde{h}_1\,\bar{\tilde{h}}_1\right) &= \frac{\alpha M_{Z'}}{1 - x_W}\,\frac{\beta^3}{4}\left(-\tfrac{2}{3}\cos^2\xi + \tfrac{1}{6}\sin^2\xi\right)
\end{aligned} \tag{4.7a}$$

giving in the limits $\beta \to 1$, $\xi \to 0$ the branching fractions

$$B\left(Z' \to h_1\,\bar{h}_1\right) = 0.23\,f,$$

$$B\left(Z' \to \tilde{h}_1 \tilde{\bar{h}}_1\right) = 0.11\, f. \tag{4.7b}$$

The factor $f = (M_{Z'} / M_Z) / \Gamma_{Z'} / \mathrm{GeV})$ is estimated[20] to be of order 0.3 to 1.7 with the exact value dependent on the exotic and supersymmetry particle decay channels that are accessible.

$p\bar{p}$, pp and ep production:

In hadron collisions $h\bar{h}$ and $\tilde{h}\tilde{\bar{h}}$ pairs are strongly produced via gluon-gluon and quark-antiquark fusion. The $h\bar{h}$ cross sections are the same as for heavy quark production and the $\tilde{h}\tilde{\bar{h}}$ cross sections are the same as for squark pair produciton. The $\tilde{h}$ may also be singly produced with significant rates[25] in ep collisions (scenario A) or in pp, $p\bar{p}$ collisions (scenario B) via their Yukawa couplings, provided that these couplings are not too small.

Scalar $\tilde{h}$ decays:

The lighter of $\tilde{h}_1$ and h_1 can only decay via Yukawa couplings. In four-component Dirac notation, the Lagrangian for the decay couplings is

$$\begin{aligned}
-L = {} & \lambda_1 \left[\tilde{h}_R^* \left(\overline{\nu^c}\, d_L - \overline{\ell^c}\, u_L \right) + \bar{h} \left(\tilde{\nu}_L d_L - \tilde{\ell}_L u_L \right) + \nu_L \tilde{d}_L - \ell_L \tilde{u}_L \right] \\
& + \lambda_2 \left[\tilde{h}_L \left(\bar{\ell} u_L^c \right) \right] + \lambda_2^* \left[\bar{h} \left(\tilde{\ell}_R u_R \right) + \ell_R \tilde{u}_R \right] \\
& + \lambda_3 \left[\tilde{h}_L \left(\bar{N} d_L^c \right) \right] + \lambda_3^* \left[\bar{h} \left(\tilde{N}_R d_R \right) + N_R \tilde{d}_R \right] \qquad (4.8) \\
& + \lambda_4 \left[\tilde{h}_L \left(\overline{u^c}\, d_L - \overline{d^c}\, u_L \right) + \overline{h^c} \left(\tilde{u}_L d_L - \tilde{d}_L u_L \right) + u_L \tilde{d}_L - d_L \tilde{u}_L \right] \\
& + \lambda_5 \left[\tilde{h}_R^* \left(\bar{u}\, d_L^c \right) + \bar{h} \left(\tilde{u}_R^* d_L^c + u^c \tilde{d}_R^* \right) \right] + \text{h.c.}
\end{aligned}$$

with i,j,k generation indicies (in the order of the three fields in each entry) suppressed but understood; here $u^c_L = (u^c)_L$, etc. In absence of any data, the h couplings are arbitrary, although a weak bound can be placed[26] on some of them from precision measurements, since they affect β-decays, $\pi \to e\nu$, $K \to \pi\nu\bar{\nu}$, $\mu \to e\,\gamma$, $K^0 - \bar{K}^0$ and $B^0 - \bar{B}^0$ mixings, etc. We shall assume that all the Yukawa coupling λ are small, consistent with such bounds.

First we consider the decays of the scalar $\tilde{h}_1$. Neglecting the masses of the final state fermions, the partial widths are of the generic form

$$\Gamma\left(\tilde{h}_1 \to f_j\, f'_k\right) = \left|\lambda_a\right|^2 K(\xi)\, M_1 / (16\pi)\,, \tag{4.9}$$

where M_1 is the $\tilde{h}_1$ mass. The λ_a and K values for the various modes are

$$\begin{array}{lll}
\Gamma\left(\tilde{h}_1 \to \nu_{jL}\, d_{kL}\right) = \Gamma\left(\tilde{h}_1 \to l_{jL}\, u_{kL}\right) & \lambda_1^{1jk} & \sin^2\xi \\
 & & \\
\Gamma\left(\tilde{h}_1 \to l_{jR}\, u_{kR}\right) & \lambda_2^{1jk} & \cos^2\xi \\
 & & \\
\Gamma\left(\tilde{h}_1 \to N_{jR}\, k_{kR}\right) & \lambda_3^{1jk} & \cos^2\xi \\
 & & \\
\Gamma\left(\tilde{h}_1 \to \bar{u}_{jR}\, \bar{d}_{kR}\right) = \Gamma\left(\tilde{h}_1 \to \bar{d}_{jR}\, \bar{u}_{kR}\right) & (2)^{\delta_{jk}}\,\lambda_4^{1jk} & 2\cos^2\xi
\end{array} \tag{4.10}$$

$$\Gamma\left(\tilde{h}_1 \rightarrow \bar{u}_{jL}\, \bar{d}_{kL}\right) \qquad\qquad \lambda_5^{1jk} \quad 2\sin^2\xi$$

where δ_{jk} is the Kronecker delta. Since in general the couplings λ^{1jk} will be generation dependent, one expects violations of flavor university, including violations of e, μ universality.

In scenario A) the leptoquark $\tilde{h}_1$ decay signatures are spectacular: either a hard lepton or large missing p_T accompanied by a jet. The decay distributions from single production will have a Jacobian peak shape. In scenario B) the two-jet signatures of the decays would be much more difficult to experimentally identify because of QCD backgrounds.

Fermion h decays:

The decays $h_1 \rightarrow f\tilde{f}'$ of a *fermion* h_1 have partial widths of the generic form

$$\Gamma\left(h_1 \rightarrow f_j\, \tilde{f}'_k\right) = \left|\lambda_a^{1jk}\right|^2 K(\xi)\, M_1 \left(1 - \tilde{M}^2 / M_1^2\right)^2 / (32\pi)\,, \qquad (4.11)$$

where $\tilde{M}$ is the mass of the supersymmetric particle in the final state. The values of λ_a and K are similar to those in Eq. (4.10). Here we have assumed that $M_1 > \tilde{M}$; otherwise the supersymmetric particle is virtual and the h_1 decay is three-body. In either case the Yukawa couplings lead us to expect flavor non-universality in the decay products.

h or $\tilde{h}$ decays via neutralinos:

The heavier of h_1 and $\tilde{h}_1$ may decay into the light one plus a neutralino $\tilde{\chi}^0$

$$h \rightarrow \tilde{h}_1\, \tilde{\chi}^0 \text{ or } \tilde{h}_1 \rightarrow h_1\, \tilde{\chi}^0$$

via gauge couplings, if kinematically allowed. Since h is an isosinglet, there are no decays into charginos. In the current basis the neutralino couplings are

$$L = -\sqrt{2}\, e e_h \left(\bar{\psi}_{\tilde{\lambda}} - \tan\theta_W\, \bar{\psi}_{\tilde{Z}}\right)\left(\cos\xi\, \psi_{1L} - \sin\xi\, \psi_{1R}\right)\phi_1^* + \text{h.c.} \quad (4.12)$$

The $\tilde{Z}'$ contribution should also be taken into account if $\tilde{\chi}^0$ has a significant $\tilde{Z}'$ component.

Two-body decays of the top quark:

If $\tilde{h}_1$ is lighter than the top quark, then the two body decay modes $t \to \tilde{h}_1 \bar{l}_j$ or $t \to \tilde{\bar{h}}_1 \bar{d}_j$ may dominate over the usual three-body modes $t \to b\bar{l}\,\nu$ and $t \to bq\bar{q}'$ so long as $\lambda \geq G_F m_t^2/\pi = 0.5 \times 10^{-2}\,(m_t/40\ \text{GeV})^2$. (A less likely possibility is $t \to h_1 \tilde{\bar{l}}$ or $t \to \bar{h}_1 \tilde{\bar{d}}_1$) decays since these are likely to be phase space suppressed.) The t-decay partial widths have the generic form

$$\Gamma\left(t \to \tilde{h}_1 \bar{l}_j \text{ or } \tilde{\bar{h}}_1 \bar{d}_j\right) = |\lambda_a|^2 K(\xi)\, m_t \left(1 - M_1^2 / M_t^2\right)^2 / (32\pi), \quad (4.13)$$

with the λ_a and K values

$$\Gamma\left(t \to \tilde{h}_1 \bar{l}_R\right) \qquad \lambda_1^{1j3} \qquad \sin^2\xi$$

$$\Gamma\left(t \to \tilde{h}_1 \bar{l}_L\right) \qquad \lambda_2^{1j3} \qquad \cos^2\xi \quad (4.14)$$

$$\Gamma\left(t \to \tilde{\bar{h}}_1 \bar{d}_R\right) \qquad \lambda_4^{13j} + \lambda_4^{1j3} \quad 2\cos^2\xi$$

$$\Gamma\left(t \rightarrow \tilde{\bar{h}}_1 \, \bar{d}_L\right) \qquad\qquad \lambda_4^{13j} \quad 2 \, \sin^2 \xi$$

The $\tilde{h}_1$ or $\tilde{\bar{h}}_1$ would further decay with the rates in Eqs. (9) and (10).

In scenario A) the top decay signatures are

$$t \rightarrow \ell_i^+ \tilde{h}_1 \rightarrow \ell_i^+ \ell_j^- u_k \text{ or } \ell_i^+ \nu_j d_k \, .$$

The decays into two different leptons and a jet would be spectacular. Note that due to flavor non-universality there is no assurance that the signal for one particular type of lepton would be strong. The $t \rightarrow \bar{\ell} \, \nu \, d$ decays would bear some resemblence to $t \rightarrow \bar{\ell} \, \nu \, b$, but have different kinematic distributions due to the two body intermediate step. The other decay possibilities in scenario A) are

$$t \rightarrow \tilde{\ell}_i^+ h_1 \rightarrow \left(\ell_i^+ \tilde{\chi}^0\right)\left(\ell_j^- u_k \, \tilde{\chi}^0 \text{ or } \nu_j d_k \, \tilde{\chi}^0\right).$$

but these modes are less likely from phase space considerations.

In scenario B) the t-decay chains would be

$$t \rightarrow \tilde{\bar{h}}_1 \, \bar{d}_k \rightarrow \left(u_i \, d_j\right) \bar{d}_k$$

or

$$t \rightarrow \bar{h}_1 \tilde{\bar{d}}_k \left(u_i \, d_j \, \tilde{\chi}^0\right) \left(\bar{d}_k \, \tilde{\chi}^0\right).$$

The first decays above would be essentially impossible to search for at a hadron collider but the second may be detected through the missing transverse momentum.

Gluino decays:

If the masses should satisfy the inequality

$$m_{h_1} + m_{\tilde{h}_1} < m_{\tilde{g}} < m_{\tilde{q}}$$

then the two body decays

$$\tilde{g} \to \bar{\tilde{h}}_1 \, h_1 \quad \text{or} \quad \tilde{h}_1 \, \bar{h}_1$$

via the strong interaction should be dominant and swamp all conventional gluino signals. This would totally alter strategies for gluino detection at hadron colliders.

In summary we have pointed out several surprising effects which arise form the exotic quark singlet of E_6, such as flavor non-universality and two body decays of the top quark. Most new particles expected in straight-forward extensions of the standard model (such as fourth generation quarks and leptons, superpartners of ordinary matter and gauge bosons) decay via gauge interactions that preserve e, μ, τ universality. Even heavy Higgs particles would decay predominantly into heavy fermions or weak bosons and then e, μ universality still holds for the final decay products. Consequently the observation of e, μ universality violation would indicate the existence of totally new interactions, such as those obtained in superstring theory from the compactification of hidden dimensions.

REFERENCES

1. E. Witten, Phys. Lett. 155B, 151 (1985); Nucl. Phys. **B258**, 75 (1985).
2. P. Candelas, G.T. Horowitz, A. Strominger, and E. Witten, Nucl. Phys. **B258**, 46 (1985).
3. J.D. Breit, B.A. Ovrut and G. Segre, Phys. Lett. 158B, 33 (1985).
4. A. Sen, Phys. Rev. Lett. 55, 33 (1985).
5. J. Rosner, Comments on Nuc. and Part. Phys. 15, 195 (1986); R. Robinett, University of Massachusetts report UMHEP-239 (1985).
6. V. Barger, N.G. Deshpande, K. Whisnant, Phys. Rev. Letts **56**, 30 (1986); E. Cohen, J. Ellis, K. Enquist, and D.V. Nanopoulos, CERN report TH4222/85; L.S. Durkin and P. Langacker, Phys. Lett. **166D**, 436 (1986).
7. V. Barger, E. Ma, and K. Whisnant, Phys. Rev. **D26**, 2378 (1982).
8. V. Barger, E. Ma, and K. Whisnant, Phys. Rev. **D28**, 1618 (1983).
9. J.E. Kim, P. Langacker, M. Levine, and M.M. Williams, Rev. Mod. Phys. **53**, 211 (1981).
10. M.A. Bouchiat et al., Phys. Lett. **134B**, 463 (1984).
11. G. Barbiellini and C. Santoni, CERN Report EP/85-117.
12. A. Sirlin, Phys. Rev. **D29**, 89 (1984); W.J. Marciano and A. Sirlin, Phys. Rev. **D29**, 945 (1984).
13. L. Di Lella and C. Rubbia, talks at Kyoto Conference (1985).
14. D. London and J.L. Rosner, Phys. Rev. **D34**, 1530 (1986); P. Langacker, R.W. Robinett and J.L. Rosner, Phys. Rev. **D30**, 1470 (1984).
15. V. Barger, N.G. Deshpande, J. Rosner, K. Whisnant, Phys. Rev. **D35**, 2893 (1987).
16. E. Eichten, I. Hinchliffe, K. Lane and C. Quigg, Rev. Mod. Phys. **56**, 579 (1984).

17. V. Barger, p. 95, Proceedings of the Oregon Meeting, Eugene, OR (1985), published by World Scientific.

18. D.W. Duke and J.F. Owens, Phys. Rev. **D30**, 49 (1984).

19. S. Geer, report at the XXIII International Conference on High Energy Physics, Berkeley, CA (1986).

20. This section is based on V. Barger, N. Deshpande and K. Hagiwara, Univ. of Wisconsin preprint MAD/PH/347.

21. V. Barger, N.G. Deshpande, and K. Whisnant, Phys. Ref. Lett. **56**, 30 (1086); Phys. Rev. **D33**, 1912 (1986); J. Ellis, K. Enqvist, D.V. Nanopoulos and F. Zwirner, Nucl. Phys. **B276**, 14 (1986) and Mod. Phys. Lett. **A1**, 57 (1986); R. W. Robinett, Phys. Rev. **33**, 1908 (1986); J.L. Hewett, T.G. Rizzo, and J.A. Robinson, ibid **D33**, 1476 (1986)

22. B. Campbell, J. Ellis, M.K. Gaillard, D.V. Nanopoulos and K. Olive, Phys. Lett. **B180**, 77 (1986).

23. V. Barger, N.G. Deshpande, J.F. Gunion et al., in Proceedings of 1986 Snowmass Workshop, p. 216.

24. M. Mangano, . Phys. **C28**, 613 (1985); A. Joshipura and U. Sarkar, Phys. Rev. Lett. **57**, 33 (1986); P. Binetruy, S. Dawson, I. Hinchliffe and M. Sher, Nucl. Phys. **B273**, 501 (1986); B. Greene, K. Kirlin, P. Miron and G.G. Ross, Nucl. Phys. **B278**, 667 (1986); M. Drees and X. Tata, UW Madison report MAD/PH/344 (1987).

25. V.D. Angelopoulos, J. Ellis, H. Kowalski, D.V. Nanopoulos, N.D. Tracas and F. Zwirner, CERN-TH.4578 (1986).

26. A. Masiero, D.V. Nanopoulos and A. I. Sanda, Phys. Rev. Lett. **57**, 663 (1986); W. Buchmuller and D. Wyler, Phys. Lett. **B177**, 377 (1986); S.M. Barr and A. Masiero, Phys. Rev. Lett. **58**, 187 (1987); Y. Kizukuri, Phys. Lett. **B185**, 183

(1987); B.A. Campbell, J. Ellis, K. Enqvist, M.K. Gaillard and D.V. Nanopoulos, CERN-TH.4473 (1986).

PRECISION MEASUREMENTS OF STANDARD ELECTROWEAK MODEL PARAMETERS IN LEP

Alain BLONDEL
CERN, Geneva, Switzerland

ABSTRACT

A combined knowledge of the Z mass, the W mass, and the fermion couplings to the Z will be obtained in the Large Electron-Positron storage ring (LEP) with unprecedented accuracy, providing information about physics beyond our energy scale. The question of the feasibility in LEP of longitudinally polarized beams, which are essential for accurate measurements of the couplings at the Z, is briefly considered.

1. EXPECTED PERFORMANCE OF THE LEP MACHINE

Details of the Large Electron-Positron storage ring can be found in the LEP design report [1]. The operation of LEP should begin in 1989, at centre-of-mass energies around 100 GeV, with conventional radio frequency (RF) power. Higher energies, up to the nominal limit of 110 GeV per beam, can only be obtained with the adjunction of superconducting RF cavities, which should gradually reach the WW pair creation threshold about 4-5 years after start-up [2].

The design peak luminosity is shown in Fig. 1 and gives the rates represented in Fig. 2. One can see that high-statistics measurements should mostly come from the running at the Z peak, where one can contemplate the prospect of event samples of 10^7 Z decays. The higher energy region will offer a unique exploratory power, and allow the study of the WW pair-production mechanism and W-mass measurement, with more limited statistics however.

2. DEFINITION OF PARAMETERS

In Born approximation, the Standard Electroweak Model (SEM) is fully described by α, G_μ, and one more parameter, which can be chosen as $\sin^2\theta_W$, m_W, or m_Z; the measurement of any of these is sufficient to predict the other two, as well as the couplings of the various particles. This works very well within the present experimental accuracy [3].

Small deviations from this simple picture can occur if the SEM is only a low-energy approximation of a broader theory, as is now commonly suspected; more certainly, small deviations are expected when radiative corrections are taken into account.

Radiative corrections can be separated into three classes [4].

i) Photonic corrections: these correspond to adding a real or virtual photon to any charged leg of the interaction diagram. These are substantial; they can be very large indeed in the LEP regime (Fig. 2), and must certainly be taken into account. They carry, however, no real physics content.

ii) Vertex corrections and box diagrams: these are generally small and we will omit them from the reasoning here even though they must certainly be taken into account in carrying out experiments.

iii) Loop corrections to the photon, W and Z propagators (see Fig. 3).

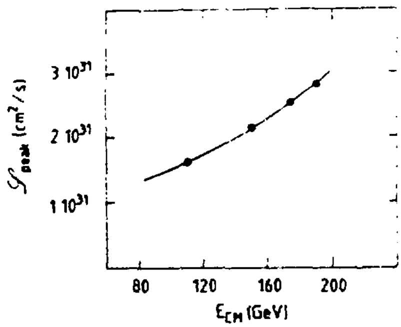

Fig. 1 Expected peak luminosity in LEP as a function of centre-of-mass energy (from Ref. [2]).

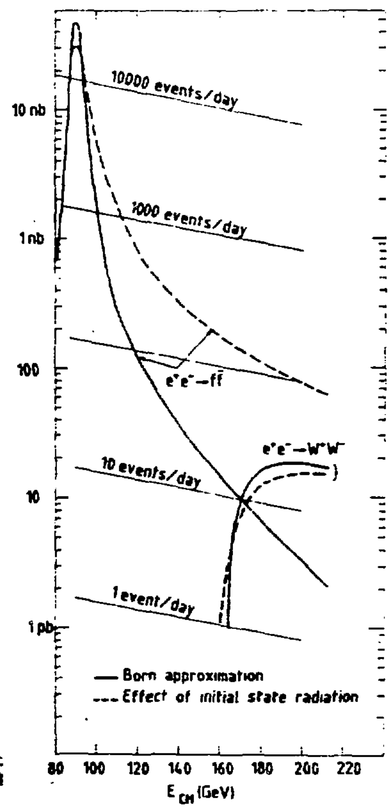

Fig. 2
Typical cross-sections and event rates for the processes considered in this report.

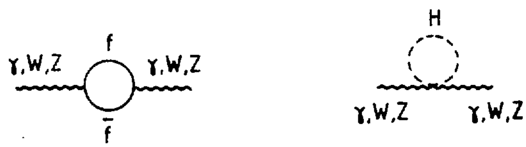

Fig. 3 Loop correction to the γ, W, and Z propagators.

These loop corrections induce large shifts in the W and Z masses compared to the lowest order prediction using $\sin^2\theta_W$. These have been discussed extensively in Ref. [5]. They turn out to be sensitive to the fermion masses, in particular the top mass, and to the mass of the Higgs. The great interest of loop corrections lies in the fact that, other than in QED, particles heavier than the W and Z do not decouple and their effect can be felt.

The effects of heavy particles in 'loop physics' have been classified by Lynn and Kennedy [6]. In order to do this, they introduced the following definition of $\sin^2\theta_W$:

$$\sin^2\theta_W = e_*^2/g_*^2\,(m_Z^2) \equiv s_*^2 \ ,$$

where $e_*\,(m_Z^2)$ and $g_*\,(m_Z^2)$ are the *effective* electromagnetic and weak running coupling constants, taken at the Z mass scale. The real W and Z masses are given by:

$$m_W^2 = \frac{e_*^2}{s_*^2}\,\frac{1}{4\sqrt{2}\,G_{\mu *}}\bigg|_{m_W^2} \ .$$

$$m_Z^2 = \frac{e_*^2}{s_*^2\,c_*^2}\,\frac{1}{4\sqrt{2}\,G_{\mu *}\,\rho_*}\bigg|_{m_Z^2} \ .$$

In the following we will ignore the small and calculable differences in effective variables evaluated at m_W^2 and m_Z^2. The values of $e_*^2\,(m_Z^2)$ and $s_*^2\,(m_Z^2)$ are straightforwardly related to α and $s_*^2\,(0)$, by the renormalization group equations, in a way which is independent of heavy particles; the effect of heavy particles is felt in $G_{\mu *}$ and ρ_*. We thus have three unknown variables:

- s_*^2 is completely arbitrary, but predicted, for instance, in Grand Unification Models.
- ρ_* is only different from 1 if week isospin SU(2) is violated: this occurs in the $\binom{t}{b}$ doublet, or more generally for any new

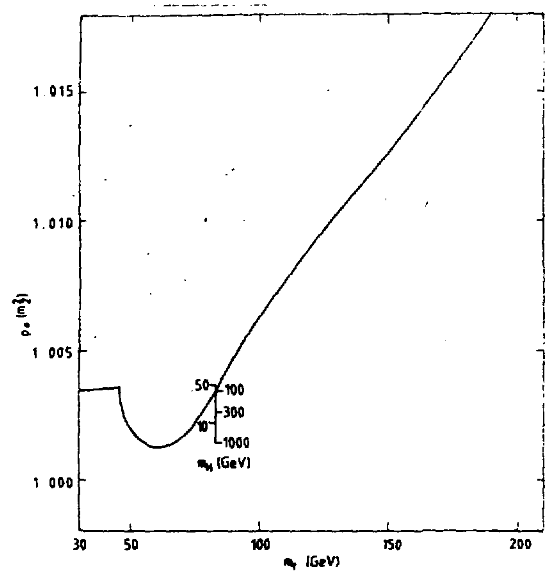

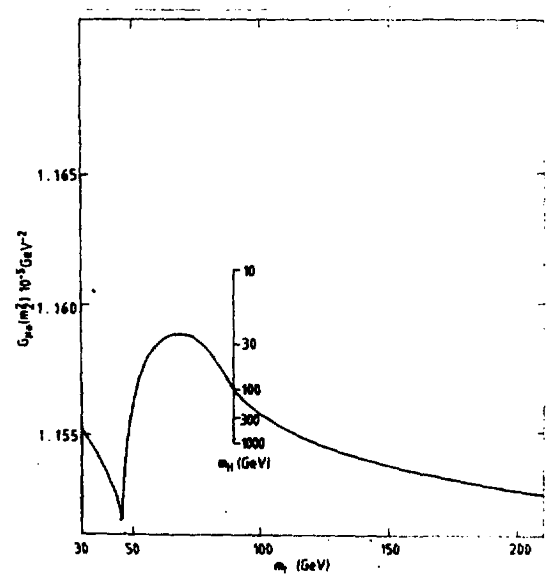

Fig. 4 Variation of the radiative correction parameters $\varrho_e(m_Z^2)$, $G_{\mu e}(m_Z^2)$ with m_H and m_t (for m_Z = 92 GeV).

family of fermions with large isotopic splitting. This can also occur for certain configurations of Higgs triplets; ϱ_* is only weakly and indirectly dependent on the Higgs mass because of the W-Z isotopic splitting; the contribution to ϱ_* from new particles which respect weak isospin (unsplit doublets) vanishes.

- $G_{\mu *}$ receives contributions that are common to the W and Z masses, such as the effect of the Higgs mass, and contributions from unsplit doublets of fermions or further Higgs particles.

The values of ϱ_* and $G_{\mu *}$ are shown as functions of m_H and m_t in Fig. 4.

We will describe in the following paragraphs how LEP should be able to measure the W mass, the Z mass, and $\sin^2\theta_W$ with unprecedented precision.

3. MEASUREMENT OF THE Z MASS

The statistical and systematic errors on a measurement of the Z mass from the Z resonance line shape (Fig. 5) have been estimated

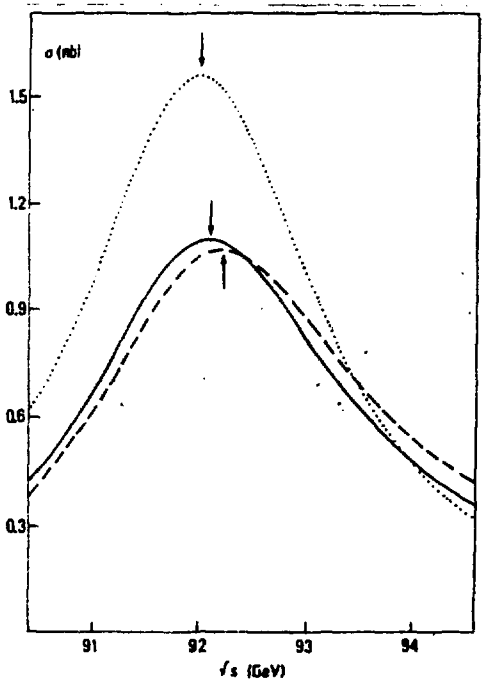

Fig. 5 The Z line shape; dotted line Born approximation; dashed-line leading-logarithmic approximation; full line next-to-leading logarithmic approximation. m_Z = 92 GeV, $\sin^2\theta_W$ = 0.23, Γ_Z^{tot} = 2.628 GeV (from Ref. [16]).

Table 1

Errors on the Z mass measurement

	Δm_Z (MeV)	
Statistics: 13 points from 82 to 106 GeV, 2 pb^{-1} per point, $e^+e^- \to \mu^+\mu^-$ (γ) channel only	± 10	
Systematics on luminosity: Variation with $\sqrt{s}$ of the luminosity monitor calibration by 0.2%/GeV	± 10	
Uncertainty in QED radiative correction: Displacement by ~ 100 MeV ($\pm$10%) of the peak due to initial-state radiation	± 10	
Uncertainty in centre-of-mass energy: Knowledge of the field integral in LEP to $\pm$ 3 x 10^{-4}	± 30	
Improvement with depolarizing resonance method if transverse polarization is available		± 10
Total	± 35	± 20

in Ref. [7], and are summarized in Table 1, which calls for the following comments:

i) The authors of Ref. [7] have restricted themselves to the channel $e^+e^- \to \mu^+\mu^-$, which is only 3% of all Z decays. One could probably convince oneself that all Z decays can be used, under the argument that the main theoretical uncertainty, initial-state radiation, is independent of the final state. In this case the Z-mass measurement would be limited by systematics after only 1 pb^{-1} of data, one day at nominal luminosity!

ii) Initial-state radiation is extremely important and requires theoretical calculation up to $O(\alpha^2)$ and exponentiation of soft photons [8].

iii) The possibility of reducing the uncertainty on the centre-of-mass energy by the depolarizing resonance technique [23] is an advantage of LEP compared to the Stanford Linear Collider (SLC), and strongly argues in favour of an early polarization programme at LEP.

The Z mass should be measurable to $\pm$20 MeV in LEP, very soon after start-up.

4. MEASUREMENT OF THE W MASS

Pair production of real W's offers the only substantial source of W's in the LEP energy range. The measurement of the W mass can be obtained from two different methods: i) from the threshold behaviour of $e^+e^- \to W^+W^-$ (Fig. 6), and ii) from the analysis of events at the cross-section maximum. An analysis of statistical and systematic errors was done in Ref. [9] and is summarized in Table 2.

The W pair events can be divided experimentally into three classes:

i) Class 0; both W's decay leptonically:
$e^+e^- \to \ell_1\nu_1 + \ell_2\nu_2 + \gamma$'s (9% of the events);

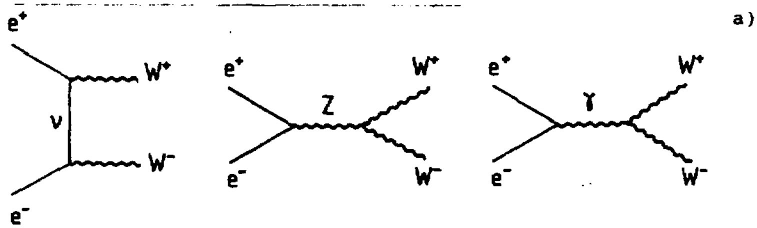

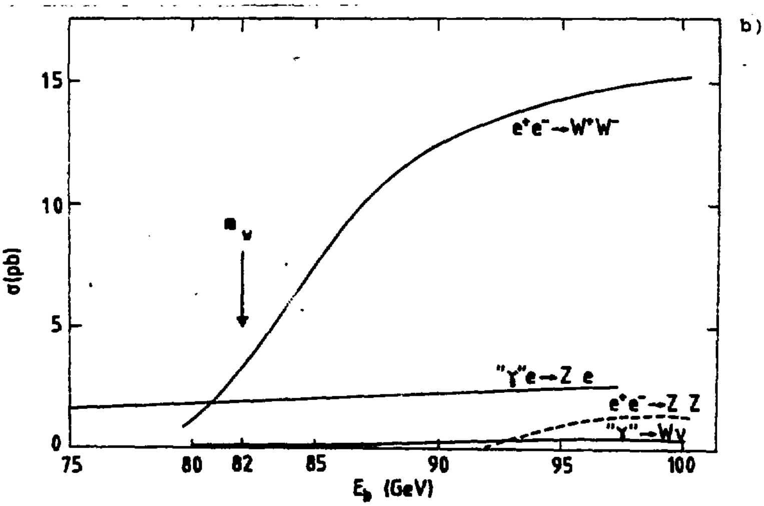

Fig. 6 a) W pair production lowest order diagrams,
b) W and Z pair production cross-sections (from Ref. [9]).

Table 2

Projected uncertainties in the measurement of m_W (for m_W = 82 GeV)

	Δm_W (MeV)
Method I: Measurement of W pair threshold	
Statistics ($\int\mathcal{L}dt$ = 500 pb^{-1})	$\pm$ 90
Systematics:	
Background	$\pm$ 60
Luminosity and detection efficiency ($\pm$5% absolute)	$\pm$120
Total	$\pm$160
Method II: Event reconstruction at maximum cross-section	
Statistics ($\int\mathcal{L}dt$ = 500 pb^{-1} at $\sqrt{s}$ = 190 GeV)	$\pm$ 60
Systematics:	
Shift due to initial-state radiation ($\approx$ 300 MeV)	$\pm$ 30
Detector hadronic energy calibration ($\pm$2%) (Calibration on $e^+e^- \to \gamma$ Z events)	$\pm$ 70
Total	$\pm$100

ii) Class 1; one W decays leptonically:

$e^+e^- \to \ell\nu + (q\bar{q} + g's) + \gamma's$ (42% of the events);

iii) Class 2; both W's decay hadronically:

$e^+e^- \to (q\bar{q} + g's) + (q\bar{q} + g's) + \gamma's$ (49% of the events).

The presence of frequent radiative emission of photons and gluons makes life somewhat difficult, especially when trying to reconstruct W's by, say, jet-jet masses. Fifty per cent of the class 2 events have more than four jets. This does not affect the detection procedure for identifying an $e^+e^- \to W^+W^-$ event, and thus the total cross-section measurement needed for the threshold measurement.

The mass measurement from the analysis of $e^+e^- \to W^+W^-$ events at cross-section maximum requires a correct assignment of the particles to each W; for this reason class 1 events -- which ideally appear as a high-energy (20 to 60 GeV) lepton, a missing neutrino, and jets -- are the most useful. When reconstructing the W mass in these events one can apply kinematical constraints unique to an e^+e^- collider: the beam energy is known, and the energy of each W is equal to it.

An exposure of 500 pb^{-1} would yield 7500 W pairs at cross-section maximum, and about 1600 useful class 1 events for mass determination. The low cross-section (15 pb at cross-section maximum) will make the W mass measurement at LEP II a very time-consuming enterprise. It will, however, be somewhat cleaner than what can be done, for instance, in $p\bar{p}$ experiments, which are (conservatively) expected to yield $\Delta m_W = \pm 350$ MeV [10].

Altogether at LEP II, which is expected to be in operation around 1995, the W mass should be measured, one way or another, with a precision of $\Delta m_W \simeq \pm 100$ MeV, after a substantial amount of running.

It would not be fair to leave this section on W pairs without mentioning that total cross-section measurements at the highest energies and the study of angular distribution should also provide important tests of the SEM, as studied in Refs. [11, 12].

5. MEASUREMENTS OF $\sin^2\theta_W$ AT THE Z POLE

Impressive statistics will be available at the Z pole. The total cross-section is $\approx$ 30 nb and this results in the rates given in Table 3 for a 100 pb^{-1} exposure, assuming $m_t > 45$, $m_Z = 92$, $\sin^2\theta_W = 0.23$, $\alpha_s/\pi = 0.033$, and including QED radiative corrections.

This will permit very precise measurements to be performed in the fields of strong interactions and fragmentation, heavy flavour decays, and neutral-current couplings. Only the later will be considered here.

Table 3
Event rates at the Z peak

Decay modes	Branching fraction $Z \to f\bar{f}$ (%)	Cross-section (nb)	Events for 100 pb^{-1} exposure
$\nu\bar{\nu}$ (3 families)	6.7		
e^+e^-, $\mu^+\mu^-$, or $\tau^+\tau^-$	3.4	1.25	125 000
$u\bar{u}$ or $c\bar{c}$	11.9		437 500
$d\bar{d}$, $s\bar{s}$ or $b\bar{b}$	15.3		562 500
Visible	79.9	29.4	2.94×10^6

The fermion couplings are related to s_*^2 in the following way:

$$a_f = 2I_{3f} ,$$

$$v_f = a_f - 4Q_f s_*^2 ,$$

where I_{3f} is the third component of weak isospin for fermion f and Q_f is its charge. A frequently encountered quantity is

$$\mathcal{A}_f = 2v_f a_f/(v_f^2 + a_f^2) ,$$

which is related to the parity violation in the Z-f coupling. Numerical values of a_f, v_f and $\mathcal{A}_f$ are given in Table 4.

Table 4

Standard Model coupling constants

(Numerical values for $\sin^2\theta_W = 0.23$)

$a_f = 2I_3^f$

$v_f = a_f - 4Q_f \sin^2\theta_W$

	a_f	v_f	$\mathcal{A}_f = \frac{2a_f v_f}{v_f^2 + a_f^2}$	$\frac{\partial \mathcal{A}_f}{\partial \sin^2\theta_W}$
ν	+1	+1	1	0
e	-1	-0.08	+0.16	-7.9
u	+1	+0.39	+0.67	-3.5
d	-1	-0.69	+0.94	-0.6

Measurable quantities at the Z pole are:

i) the partial width of $Z \to f\bar{f}$

$$\Gamma_{f\bar{f}} = C \left\{\frac{s}{12\pi} \frac{e_*^2}{s_*^2 c_*^2} \left[a_f^2 + v_f^2\right]\right|_{M_Z^2}$$

with

$$C = 1 \text{ for leptons}$$

$$C = 3(1 + \frac{\alpha_s}{\pi} + \ldots) \text{ for quarks} ;$$

ii) the forward-backward asymmetry with unpolarized beams,

$$A_{FB} = \frac{\sigma_F - \sigma_B}{\sigma_F + \sigma_B} \simeq \frac{3}{4} \mathcal{A}_e \mathcal{A}_f \ , \qquad (1)$$

where σ_F and σ_B represent the cross-sections for the emitted fermion in the forward and backward hemispheres, with respect to the incident electron.

iii) If the polarization of the outgoing fermion can be measured, its average value is

$$\langle P_f \rangle = \mathcal{A}_f \ .$$

iv) If longitudinal beam polarization is available, the angular distribution in $e^+e^- \to f\bar{f}$ is given by [13]

$$\frac{d\sigma(e^+e^- \to f\bar{f})}{d\cos\theta} = \sigma_u^f[(1+\mathcal{P}\mathcal{A}_e)(1+\cos^2\theta) + 2\cos\theta(\mathcal{P}+\mathcal{A}_e)\mathcal{A}_f]\ \frac{3}{8}\ (1-P^+P^-)\ ,$$

where σ_u^f is the total cross-section for this channel at the top of the resonance, P^+ and P^- are the longitudinal polarizations of the e^+ and e^- respectively (P is positive when the spin is parallel to the particle velocity), and $\mathcal{P}$ is the polarization of the e^+e^- system, i.e. $\mathcal{P} = (P^+ - P^-)/(1 - P^+P^-)$.

By taking data with opposite beam helicities and measuring the corresponding cross-sections σ^+ and σ^- and $\sigma_F^{\pm}$ and $\sigma_B^{\pm}$, one can measure the longitudinal polarization asymmetry (or left-right asymmetry) [14]

$$A_{LR} = \frac{1}{\mathcal{P}} \frac{\sigma^+ - \sigma^-}{\sigma^+ + \sigma^-} = \mathcal{A}_e \qquad (2)$$

and the polarized forward-backward asymmetry [15]

$$A_{FB}^{pol,f\bar{f}} = \frac{1}{\mathcal{P}} \frac{(\sigma_F^+ - \sigma_B^+) - (\sigma_F^- - \sigma_B^-)}{\sigma^+ + \sigma^-} = \frac{3}{4} \mathcal{A}_f \ . \qquad (3)$$

The precision obtainable in measurements without polarized beams has been studied in Refs. [7, 16-18] and summarized in Table 5. The measurement of the partial and total widths also permits interesting tests of universality and neutrino counting.

Table 5

Errors on partial width and asymmetries obtainable from a scan of the Z with 26 pb^{-1} (for the widths) and a 100 pb^{-1} exposure at the Z (for $\Gamma_{\mu\mu}/\Gamma_{ee}$, R, $A_{FB}^{\mu\mu}$, and P_τ) compiled from Refs. [7, 16-18]

Quantity	Error	Equiv. error in $\sin^2\theta_W$
Γ_{ee}	$\Delta\Gamma_{ee}/\Gamma_{ee}$ = 1.8%	0.005
Γ_{tot}	$\Delta\Gamma_{tot}$ = 20 MeV	0.0025
$\Gamma_{\mu\mu}/\Gamma_{ee}$	$\dfrac{\Delta(\Gamma_{\mu\mu}/\Gamma_{ee})}{\Gamma_{\mu\mu}/\Gamma_{ee}}$ = 1.5%	0.004
$\Gamma_{hadron}/\Gamma_{\mu\mu}$ = R	$\Delta R/R$ = 1%	0.008
$A_{FB}^{\mu\mu}$	Statistics: $\Delta A_{FB}^{\mu\mu}$ = 0.3%	
	Systematics:	
	Δm_Z = 20 MeV 0.2%	
	Detection eff. 0.2%	
	QED rad. corr. 0.12%	
	Total 0.4%	0.002
$\langle P_\tau\rangle$	Statistics ΔP_τ = 1.2%	
in $\tau\to\pi\nu$ decay	Background 0.8%	
	Total 1.5%	0.0018

The measurement of the muon forward-backward asymmetry is, in principle, very precise. Unfortunately,

$$A_{FB}^{\mu\mu} = \frac{3}{4}\mathcal{A}_e\mathcal{A}_\mu \simeq \frac{3}{2}\,(1-4\,s_*^2)^2$$

has a reduced sensitivity to s_*^2 if s_*^2 is close to 0.25. In addition, it is a very steeply varying function of $\sqrt{s}$ across the Z resonance (Fig. 7). This results in a great sensitivity to initial-state radiation effects and to the precise knowledge of the Z mass.

The polarization asymmetry is a linear function of $\sin^2\theta_W$, $\mathcal{A}_\ell = 2\,(1-4\,s_*^2)$ for leptons, but it is measurable in practice for τ decays only; the most sensitive channel is the $\tau\to\pi\nu$ decay and this reduces the statistics further.

Measurements at the Z without polarized beams provide a precision of $\Delta\,s_*^2 \approx 0.0015$. This does not quite match the precision required for sensitivity to, say, the Higgs mass: $m_H = 10^{2\pm1}$ GeV corresponds to $\delta s_*^2 = {}^{+0.0013}_{-0.0009}$.

The improvement obtainable with longitudinally polarized beams is clearly brought to light when comparing Eqs. (1), (2), and (3). With A_{LR} and A_{FB}^{pol}, one measures directly $\mathcal{A}_e$ and $\mathcal{A}_f$ instead of measuring their product. In addition, a major breakthrough comes from the fact that A_{LR} *is the same for all final states*. All decay modes can be used, providing impressive statistical power. There is a simple heuristic argument for this: A_{LR} is the asymmetry for *producing* a Z from opposite beam helicities, and thus depends only on the electron coupling, and not on the decay mode of the Z. Consequently, A_{LR} is also insensitive to final-state QCD and QED corrections.

The final-state couplings, at the same time, are nicely isolated in A_{FB}^{pol}, with increased sensitivity if the polarization $\mathcal{P}$ is greater than $\mathcal{A}_e \simeq 0.15$. The measurement of $\mathcal{A}_f$ being limited for unpolarized beams by the knowledge of A_e itself ($\Delta\, s_*^2 = 0.002$ corresponds to $\Delta\, A_e/A_e = 10\%$), this limitation would disappear if longitudinally polarized beams were used. Table 6 taken from

Table 6

Accuracy for the fermion vector coupling constants: From present experimental information and the estimated precision, which can be achieved with 10^5 events at the SLC with and without polarization

	Present Accuracy		No Polarization $10^5 Z^0$		$P = 45\%$ $10^5 Z^0$	
Fermions	Reaction	Δv_f	Reaction	Δv_f	Reaction	Δv_f
e	$\nu_\mu e \to \nu_\mu e$ (1) $ee \to ee$ (2)	0.1	τ-polarization asymmetry.	0.05	${}^{all}A_{LR}$	0.005
μ	$\mu N \to \mu X$ (3) $\Gamma(Z^0 \to \mu\mu)/\Gamma(Z^0 \to ee)$ (4)	0.3	v_e and ${}^{\mu}A_{FB}$	0.08	${}^{\mu}A_{FB}$	0.02
τ	τ-polarization (5) at PETRA	2.8	v_e and ${}^{\tau}A_{FB}$ mean τ-polarization	0.05	${}^{\tau}A_{FB}$	0.02
u, d, s ...	eD (6) νN (7)	0.04	$\Gamma(Z^0 \to q\bar{q})/\Gamma(Z^0 \to ee)$	0.04	$\Gamma(Z^0 \to q\bar{q})/\Gamma(Z^0 \to ee)$	0.04
c	$R_{c\bar{c}}$ (8) at PETRA/PEP	~ 3.	v_e and ${}^{c}A_{FB}$ $\Gamma(Z^0 \to c\bar{c})/\Gamma(Z^0 \to ee)$	0.2	${}^{c}A_{FB}$	0.10
b	$R_{b\bar{b}}$ (9) at PETRA/PEP	~ 1.	v_e and ${}^{b}A_{FB}$ $\Gamma(Z^0 \to b\bar{b})/(Z^0 \to ee)$	0.1	${}^{b}A_{FB}$	0.05

Ref. [19] shows the improvement brought by polarization to the measurement of the fermion couplings.

An interesting feature of the polarization asymmetries is their slow variation in energy; this has the consequence that both A_{LR} and A_{FB}^{pol} are quite insensitive to initial-state radiation and to the precise knowledge of the beam energy.

On the other hand, $A_{LR} \simeq 8\ (0.25-s_*^2)$ is a very sensitive measurement of s_*^2, and is thus sensitive to weak effects, as shown in Fig. 7.

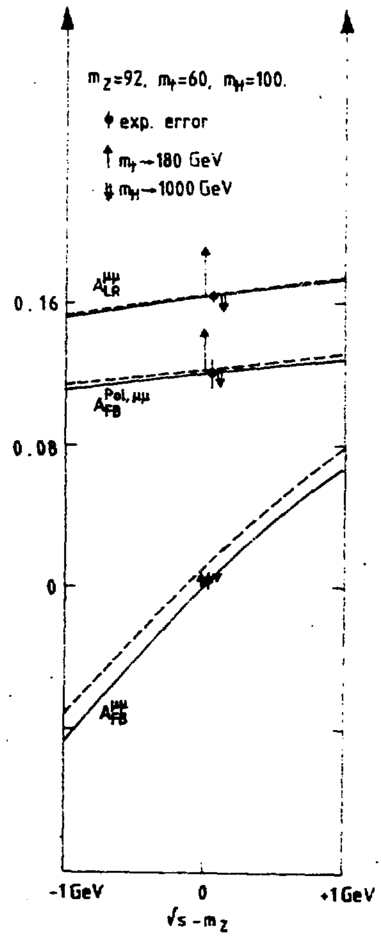

Fig. 7
Behaviour of various asymmetries around the Z pole:

$A_{FB}^{\mu\mu}$: muon unpolarized forward-backward asymmetry.

$A_{LR}^{\mu\mu}$: left-right or polarization asymmetry.

$A_{FB}^{pol,\mu\mu}$: muon polarized forward backward asymmetry.

Full line: only geometrical cuts ($\theta > 20°$).
Dashed line: effect of an acolinearity cut of 2°.
Error bars: expected experimental accuracy.
Full arrow: effect of a heavy top (m_t = 180 GeV).
White arrow: effect of a heavy Higgs (m_H = 1000 GeV).
Exposure of 100 pb^{-1} (unpolarized) or 40 pb^{-1} with 50% longitudinal polarization.

Having described the attractive features of polarization measurements, I will now describe how one can hope to obtain polarization in LEP.

6. POLARIZATION IN LEP

Polarization at LEP was not considered a priority until recently. In view of its potential, a study was made [20, 21] and the LEP Experiments Committee recommended a design study to be conducted by the Machine Division. An overview of how one can hope to get longitudinally polarized beams in LEP will be outlined in the following. The reader interested in more rigour and details is referred to Ref. [22].

Transverse polarization builds up in an electron storage ring by the Sokolov-Ternov effect: synchrotron-radiation emission has a small spin-flip probability, with a large asymmetry in favour of orienting the particles' magnetic moment along the magnetic field. In a perfect machine a large asymptotic polarization (92.4%) builds up slowly. The typical build-up time τ_p for the LEP machine is 5 h at 46 GeV beam energy, but is strongly energy dependent [Fig. 8]. This is clearly unacceptable when compared with a luminosity lifetime of ~ 3 h. This can be cured by introducing wiggler magnets in the machine.

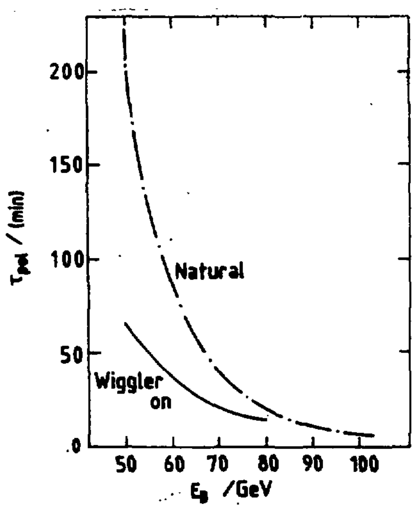

Fig. 8 Polarization build-up time in LEP with and without wigglers (from Ref. [23]).

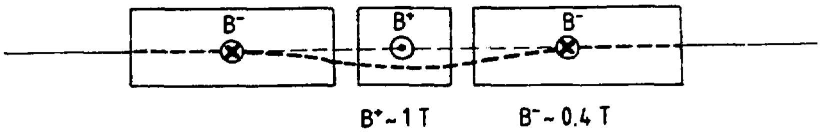

Fig. 9 Sketch of a wiggler magnet foreseen for LEP.

A sketch of a wiggler magnet is shown in Fig. 9. The field integral is zero, but the polarizing power is proportional to $\int B^3\, dl$ and is made different from zero by a large asymmetry between the strong central field, which is positive, i.e. parallel to the field in the Main Ring, and the weaker end field, which is negative. Wiggler magnets increase the synchrotron radiation and thus decrease the damping time -- this is why they are needed in the machine in any case -- as well as the polarization time. They also reduce the asymptotic polarization level to $P_{-}{'}_{\text{wigglers}} = P_{-}(B_{+}^2 - B_{-}^2)/(B_{+}^2 + B_{-}^2)$; the presently designed wigglers decrease the polarization to 75% of its value, but this drawback could be avoided for polarization runs by constructing dedicated wigglers with a larger asymmetry. What is unavoidable, however, is the increase in beam energy spread caused by the wigglers, which is suspected of worsening the depolarizing effects considerably, and constitutes a major limitation in the reduction of the polarization time. It is currently believed that the polarization time cannot be reduced to much less than 80 minutes at the Z.

Depolarizing effects cast doubt on the feasibility of a physics programme with polarized beams in an e^+e^- storage ring. The origin of this difficulty lies in the combination of three defavourable factors:

i) The extreme sensitivity of the polarization vector to transverse magnetic fields: at 46 GeV the precession of the polarization vector around a transverse field is $a\gamma \simeq 104$ times larger than the rotation of the particle. [$a = (g_e - 2)/2$ is the anomalous magnetic moment of the electron.]

ii) The extremely long 'polarization damping time' is equal to the polarization time of hours, meaning that the effect of imperfections will be 'memorized' by the polarization vector over typically 10^8 turns around the machine.

iii) Spin resonances, similar to Nuclear Magnetic Resonance, occur each time the precession frequency ($a\gamma$ per machine turn) is in phase with one of the basic motions of the particle: turn around the machine (integer resonance), betatron and synchrotron oscillation (betatron and synchrotron resonances). The precession effect being energy independent, the spacing in energy between spin resonances is constant, whereas the beam energy spread is a rapidly increasing function of energy. The spacing between integer spin resonances is 440 MeV, not comfortably large compared to the beam energy spread of ± 40 MeV expected at LEP I.

Despite these difficulties, polarization has been observed in every e^+e^- machine where it has been searched for. In SPEAR, in particular, high luminosity and a high degree of polarization were observed at the same time, leading to the observation [24] of the transverse polarization asymmetry of $e^+e^- \to$ hadrons typical of the production of spin 1/2 objects (quarks). In PETRA things turned out to be more difficult, as expected at higher energies, but procedures were developed to correct the orbit and optimize the polarization degree close to its theoretical asymptotic level. The difficulties in LEP should be bigger, and work is going on to simulate the spin motion in the machine accurately and to design correction procedures allowing the cancellation of depolarizing resonances. The outcome of these studies is as yet unknown. Preliminary estimates [25] indicate that an asymptotic polarization level between 50% and 70% could be obtainable at well-chosen energies.

Assuming that a stable polarization builds up in the machine, it will be aligned on the magnetic field, i.e. it will be transverse. In order to carry out experiments with non-zero helicity, one has to foresee spin rotators (S.R., Fig. 10) which

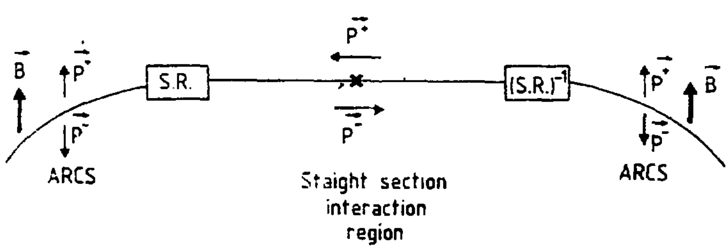

Fig. 10 Top view of the spin motion in the arc and in the interaction region, with Spin Rotators (SR); the positron ($\vec{P}^+$) and electron ($\vec{P}^-$) polarization vectors are indicated.

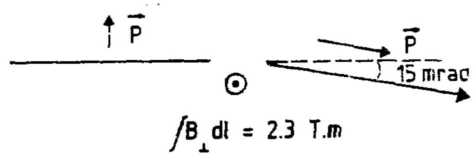

Fig. 11 Side view of the simplest 90° spin rotator at LEP energy (50 GeV).

rotate the spin from vertical in the arcs of the machine to horizontal in the straight sections and back to vertical (S.R.$^{-1}$). In engineering spin rotators one turns to an advantage the fact that the polarization vector precesses ~ 104 times more than the particle turns, as sketched in Fig. 11. This simple scheme does not work since it would bring the beam off orbit, and one must use more complicated arrangements of vertical and horizontal bends such as in Fig. 12, taken from Ref. [26].

One difficulty in designing spin rotators is again the depolarizing effects: after going through the interaction region, the spin must be brought back to vertical to a very good accuracy. and this holds for any particle energy or betatron phase, or else strong depolarization will occur. This results in complicated 'spin-matching' conditions which must be fulfilled by the string of spin rotator magnets in relation to the rest of the machine.

Another constraint for the design of the spin rotators is given by the conflicting requirements of minimizing depolarization (this requires weak bends and thus large vertical excursions) and finding space in the tunnel. Moreover, two of the experimental straight sections are occupied by RF cavities, which are incompatible with spin rotators. The solution to this problem is found in installing the rotators in the last section of the arcs, which also has the advantage that the normal horizontal bends can be used as part of the spin rotator system. The spin rotators are designed for one precise energy, since the rotations of the particle spin and trajectory have a different energy dependence. However, polarization is needed for precision measurements in long runs at discrete energies (Z peak, toponium peak, W pair production, Z', etc.) and not specially for scans, and this delicate adjustment does not need to be done too often.

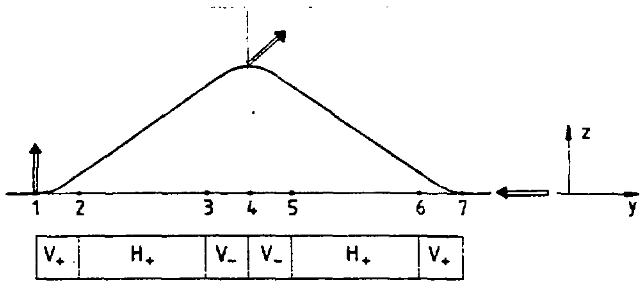

Separated-bend rotator; vertical orbit

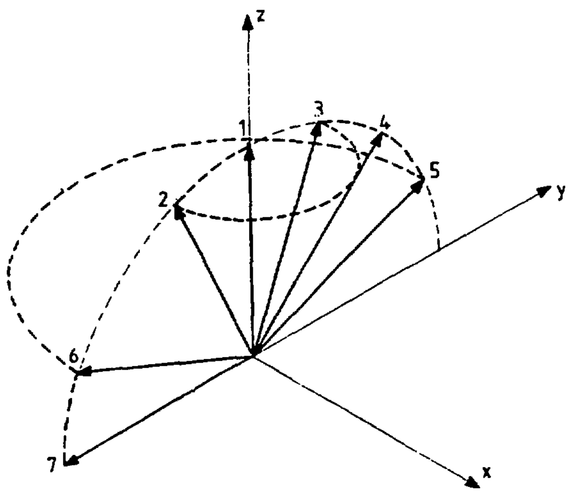

Separated-bend rotator, motion of spin vector

Fig. 12 Evolution of the orbit and of the spin vector in a spin rotator proposed in Ref. [26].

Assuming that all this has been successful, one would have both electrons and positrons polarized in the interaction point according to Fig. 10: P^+ and P^- have the same sign since they are counted as positive if aligned on the particles' momentum, and about equal. The Z production cross-section

$$\sigma = \sigma_u[1 - P^+P^- + A_{LR}(P^+ - P^-)]$$

is both independent of A_{LR} and considerably reduced; it even vanishes if $P^{+} = P^{-} = 1$. In order to obtain non-zero helicity at the interaction point it has been suggested [27] that some bunches be depolarized selectively and not the others.

The principle of the depolarizer [28] is to continuously excite an artificial spin resonance by applying a small (~ 1 G·m) transverse field in phase with the spin precession period. Because the field is small, the device can be gated and guarantees a polarization level of < 10^{-3} for any set of the eight bunches circulating in the machine. Depolarization is indeed much easier than polarization.

This facility can be used to obtain all combinations of helicities [29]: by depolarizing the electron bunches 1 and 3 and positron bunches 2 and 3, one obtains in turn in the experiment the following four combinations:

Electron bunches	1	$\vec{2}$	3	$\vec{4}$
Positron bunches	$\vec{1}$	2	3	$\vec{4}$
Cross-sections	σ_1	σ_2	σ_3	σ_4

$$\sigma_1 = \sigma_u(1 + P^{+} A_{LR})$$
$$\sigma_2 = \sigma_u(1 - P^{-} A_{LR})$$
$$\sigma_3 = \sigma_u$$
$$\sigma_4 = \sigma_u[1 - P^{+}P^{-} + A_{LR}(P^{+} - P^{-})]$$
$$P^{+} \simeq P^{-}$$

This is a very favourable experimental situation:

i) The total cross-sections are measured from data taken simultaneously, in the same detector and with beams circulating in the same machine: a nearly perfect cancellation of detector efficiency, luminosity systematics, etc., is expected; this is true up to possible small systematic differences from one bunch to another, the exact effect and monitoring of which is presently being scrutinized.

ii) The four equations above can be solved to extract A_{LR}, σ_u, P^{+}, and P^{-} from the data themselves, avoiding the need to rely on an independent external measurement of the polarization; this is in contrast with the situation in SLC [19] where positrons cannot be polarized, and only σ_1 and σ_2 are measurable, and where it is necessary to measure the beam polarization with an absolute precision of $\Delta P/P = \pm 1\%$ if one wants to match the statistical precision of 10^6 Z events, this being quite a challenge [30].

Even with the above four equations at our disposal, one would still need two polarimeters in LEP, one for e^+ and one for e^-, for the following reasons:

i) the need to monitor the time evolution of the polarization,

ii) the need to measure the relative polarizations of different bunches in the same beam.

The four cross-sections can then be used to derive the absolute calibration constant of the polarimeters, with the caveat that it is not affected by the small differences between bunches previously mentioned.

If all the conditions mentioned above can be fulfilled, which the detailed study will determine, the experimental precision on A_{LR} can reach $\Delta A_{LR} = 0.003$ [Table 7], for a 40 pb^{-1} exposure

Table 7

	Requirement	ΔA_{LR}
Statistics (for A_{LR}, $\langle P\rangle = 0.5$) Statistics (for $\Delta P/P$)	10^6 Z events 10^5 Z events	0.0020 0.0016
Relative luminosity: Monitoring of relative differences in beam divergence in transverse position	$< 1 \times 10^{-3}$ < 10 μrad < 20 μm	< 0.001
Residual polarization of depolarized bunches Error in difference of bunch polarizations	$< 3 \times 10^{-3}$ $< 5 \times 10^{-3}$	< 0.001 < 0.001
Event selection, background, uncertainty in c.m.s. energy, radiative corrections		< 0.001
TOTAL EXPERIMENTAL ERROR		0.003
α, G_μ, $m_Z \rightarrow A_{LR}$ owing to error in m_Z: owing to error in Δr:	$\delta m_Z = 20$ MeV	0.001 0.003
TOTAL THEORETICAL ERROR		0.003

(10^6 Z events), corresponding to $\Delta \sin^2 \theta_W = \pm 0.0004$. This matches the main theoretical error $\Delta \sin^2 \theta_W = \pm 0.0004$ encountered when predicting $\sin^2 \theta_W$ from m_Z. This uncertainty arises when estimating the electroweak radiative correction, Δr, $\Delta(\Delta r) = \pm 0.0013$ [31] and is mostly due to light quark loops. The corresponding contributions to Δr can be related to the measurement of $\sigma(e^+e^- \to \text{hadrons})$; the error is dominated by the experimental error in this cross-section, especially at low energies. A more precise measurement of this quantity would improve our knowledge of Δr by a factor of 2 [32] and would certainly be welcome.

Many problems still need to be studied in detail concerning measurements with polarized beams, and most of all much work is necessary to convince ourselves that stable operation of the machine with polarized beams and decent luminosity is more than a dream. The theoretical and experimental cleanliness of the polarization asymmetries and their sensitivity to physics beyond our energy scale make this work highly motivating.

7. CONCLUSION

Precision measurements, albeit difficult, are appealing if they produce fundamental results: the power of a combined measurement m_Z, m_W, and A_{LR}, with the above-mentioned precision, is emphasized in Fig. 13. The order of magnitude of the Higgs mass and the top quark mass, if it is not known then, would be severely constrained. The existence of physics beyond the SEM, such as Z' [33], charged Higgs [34], supersymmetric particles [35], and compositeness, would be likely to be visible or, in any case, severely constrained. The additional information gained from measurements of the individual weak couplings could be used to disentangle the various origins if a discrepancy were to be observed [36].

Altogether a very large improvement over existing measurements should be obtained from LEP data.

* * *

Acknowledgements

This conference offered me an excuse to set foot in Poland for the first time. It was a wonderful experience to live in this beautiful little village, walk along by the Vistula, and share the warm and fun-loving friendship of our hosts. To Halina Abramowicz in particular goes my deep gratitude.

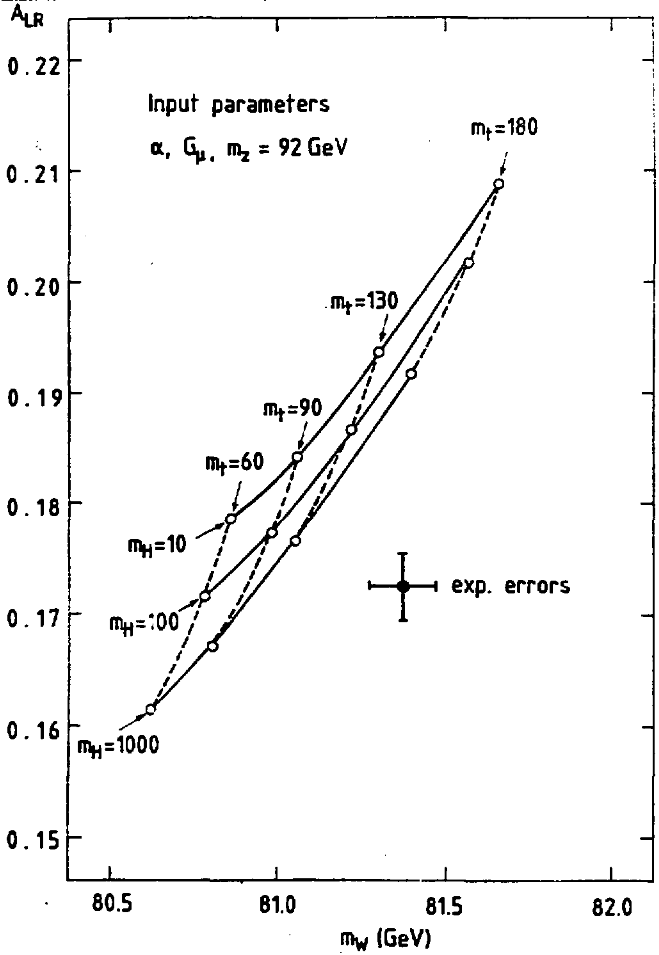

Fig. 13 Combined measurement of m_Z, m_W and A_{LR} constraining both m_t and m_H.

REFERENCES AND FOOTNOTES

[1] LEP design report, CERN-LEP/84-01 (1984).

[2] E. Keil, *in* Proc. ECFA Workshop on LEP 200, CERN 87-08, ECFA 87/108 (1987), p. 17.

[3] F. Dydak, preprint CERN-EP/86-121 (1986).
U. Amaldi et al., Pennsylvania preprint PRO331T (1987).
A. Blondel, preprint CERN-EP/87-174 (1987).

[4] F. Dydak et al., *in* Proc. ECFA Workshop on LEP 200, CERN 87-08 (1987), p. 157.

[5] B.W. Lynn, M.E. Peskin and R.G. Stuart, *in* Physics at LEP, CERN 86-02 (1986), p. 90.

[6] B.W. Lynn and R.C. Kennedy, SLAC-Pub 4039 (1987).

[7] A. Blondel, F. Dydak, A. Para and W. Blum, *in* Physics at LEP, CERN 86-02 (1986), p. 35.

[8] F.A. Berends, W.L. van Neerven and C.J.H..Burgers, preprint CERN-TH.4772 (1987).

[9] P. Roudeau et al., *in* Proc. ECFA Workshop on LEP 200, CERN 87-08, ECFA 87/108 (1987), p. 49.

[10] P. Jenni, ibid, p. 486.

[11] D. Treille et al., ibid, p. 414.

[12] M. Davier et al., ibid, p. 120

[13] M. Böhm and W. Hollik, Nucl. Phys. B204, 45 (1982).

[14] C.Y. Prescott, *in* Proc. 1980 Int. S. osium on High-Energy Physics with Polarized Beams and Polarized Targets, Lausanne, 1980, eds. C. Joseph and J. Soffer (Birkhaüser, Basle, 1981), p. 34.
B.W. Lynn and C. Verzegnassi, SLAC-Pub 3967 (1986).

[15] A. Blondel, B.W. Lynn, F.H. Renard and C. Verzegnassi, Montpellier preprint PM/87-14 (1987), to appear in Nuclear Physics.

[16] G. Altarelli, *in* Physics at LEP, CERN 86-02 (1986), p. 3.

[17] P. Baillon et al., ibid, p. 172.
Also M. Zentilin, Ecole Polytechnique, Palaiseau, France. Ph.D. Thesis, Université de Paris VI (1987), unpublished.

[18] C. Chauveau, *in* Physics at LEP, CERN 86-02 (1986), p. 177.

[19] D. Blockus et al., SLC Polarization Proposal, SLAC-SLC-Prop-1 (1986).

[20] G. Alexander et al., Working group report CERN/LEPC/87-6, LEPC/M81 (1987).

[21] J. Badier et al., ALEPH Note 87-17 (1987).

[22] B.W. Montague, Phys. Rep. 113, No. 1 (1984).
J. Buon, Orsay preprint LAL/RT/86-02 (1986).
B.W. Montague, CERN LEP-TH/86-19.
See also the Machine Section in Ref. [20].

[23] C. Bovet, B. Montague, M. Placidi and R. Rossmanith, *in* Physics at LEP, CERN 86-02 (1986), p. 58.

[24] R.F. Schwitters et al., Phys. Rev. Lett. 35, 1320 (1975).
G. Hanson et al., Phys. Rev. Lett. 35, 1611 (1975).

[25] J.-P. Koutchouk, CERN LEP Note 573 (1987).

[26] B.W. Montague, CERN LEP Note 256 (1980).

[27] M. Placidi and R. Rossmanith, CERN LEP Note 545 (1985).

[28] J. Buon and J.M. Jowett, CERN LEP Note 584 (1987).

[29] A. Blondel, ALEPH Note 168 (1986).

[30] H. Steiner, Berkeley preprint LBL-23452 (1987).

[31] C. Verzegnassi, Phys. Lett. 147B, 455 (1984).
B.W. Lynn, G. Penso and C. Verzegnassi, SLAC-Pub 3742 (1985).
F. Jegerlehner, Z. Phys. C32, 195 and 425 (1986).

[32] C. Verzegnassi, Trieste, private communication.
Measurement of very low energy e^+e^- data is foreseen at Novosibirsk (M. May, Brookhaven, private communication).

[33] W. Hollik, Z. Phys. C8, 149 (1981).
P. Franzini and F. Gilman, Phys. Rev. D32, 237 (1985), and SLAC-Pub 3932 (1986).
J. Bigi and M. Cvetič, Phys. Rev. D34, 1651 (1986).
F. del Aguila, M. Quiros and F. Zwirner, *in* Physics at future accelerators, CERN 87-07 (1987), Vol. 2, p. 165.

[34] W. Hollik, DESY 87-068 (1987).

[35] The effect of supersymmetric particles has been studied in Ref. [5] and in J. Ellis, S. Rudaz and N. Tracas, CERN TH.4657/87 (1987).

[36] S. Narison, CERN-TH.4700/87, PM87/19 (1987).

[37] M. Cvetič and B.W. Lynn, SLAC Pub 3900 (1986).
B.W. Lynn, F. Renard and C. Verzegnassi, Montpellier preprint PM 87/45 (1987).

Charm Lifetime Measurements from TASSO*

Geoffrey E. Forden
State University of New York
at
Stony Brook

Recent measurements by TASSO of the lifetimes of charmed mesons is reviewed. The lifetime reported for the D_s meson utilizes the entire data sample collected. The lifetime of the neutral charmed meson, D^0, is from a subsample of the total data set. Special emphases is given to the experimental procedures used.

The TASSO detector has taken a total of 140 pb^{-1} since the instillation of a gas vertex chamber[1] in the summer of 1983 and the shut down of the PETRA e^+e^- accelerator in late 1986. During that time it was used, in conjunction with the large cylindrical drift chamber, to measure the lifetimes of several long lived particles, including the tau lepton, the charmed mesons, D^0 and the D_s (formerly the F^+), and the average lifetimes of bottom hadrons. Over the same period the standard of a "high precision" vertex chamber has changed substantially, to the point were all modern detectors being built for the next generation of accelerators will use silicon "micro-vertex" chambers. These new chambers will have totally different characteristics and hence will require new analysis methods then those used at either PETRA or PEP. This report should therefore be viewed as something of a summary of the state of the art, at least as far as TASSO is concerned, at the end of an era. The measurements by TASSO of the lifetimes of both the D^0 and the D_s mesons are reviewed with emphases on the experimental procedures used. The theoretical implications, important as they are, are only briefly mentioned at the end of the paper.

---

1 D.M. Binnie *et al.*, Nucl. Inst. Meth. A228 (1985), 220

The samples of both the D^0 and D_s used for measuring their lifetimes were isolated by making use of decay modes whose widths are limited by the available phase space at some point in their decay chains. The neutral D^0 was tagged by restricting the search to only those charmed mesons resulting from the decay chain $D^{*+} \rightarrow D^0 \pi^+$; $D^0 \rightarrow K^-\pi^+$. The mass difference between the D^{*+} and the D^0 is only 145.45 MeV, just greater than the mass of the transition pion, as shown in Figure 1. The D^0 signal was isolated by using the standard technique of looking for the mass difference between the vector and the iso-scaler states. The low Q^2 of this decay produces a sharp mass difference plot, shown in Figure 2, and minimizes the dependence on the mass resolutions of either state. This is technique may be used even in cases where neither state is completely completely reconstructed, such as in the case of $D^{*+} \rightarrow D^0 \pi^+$; $D^0 \rightarrow K^-\pi^+ (\pi^0)$, where the π^0 is undetected. This is the so-called satellite state. A third D^0 decay chain was also used, $D^{*+} \rightarrow D^0 \pi^+$; $D^0 \rightarrow K^-\pi^+\pi^-\pi^+$. The mass difference technique was important to this decay since the width of the resolved mass peak increases as the number of final state particles increases. The D_s analysis used the decay chain $D_s^+ \rightarrow \phi\pi^+$; $\phi \rightarrow K^+K^-$. In this case it is the phi mass width that is limited by the available phase space, with $M(\phi)=1019.5$ MeV as compared 987 MeV, twice the kaon mass.

The TASSO D^0 lifetime analysis reviewed[1] here used a data sample of 47 pb^{-1} taken at an average center of mass energy of 42.2 GeV. The decays were reconstructed using tracks that had at least five digitalizations (out of a possible eight) in the vertex chamber as well as being reconstructed in three dimensions in the central drift chamber. All charged tracks for the D^0 decay were required to form a vertex.[2] Since the transition pion originated in the hadronic decay of the excited charm state it was not included in the vertex. A sophisticated kinematic fitter[3] was then used, on the totally charged final state decay modes, to constrain the mass

[1] D. Strom, "Proc. XXIII Inter. Conf. High Energy Phys.", vol. 1 (1986), 806

[2] D. H. Saxon, Nucl. Inst. Meth. 234 (1985), 258

[3] G. E. Forden, Nucl. Inst. Meth. A248 (1986), 439

to the D^0 value. These (*improved*) tracks were then combined with another track to reconstruct the D^* and the mass difference was calculated. A clean sample of D^0's was isolated by requiring that the mass difference was less than 150 MeV. This sample consists of 11 decays D^0 to $K^-\pi^+$, and two each of the other decays. No particle identification was used in this analysis since that would severely limit the detector acceptance and has not proved necessary. The final requirement was that the reconstructed D^0 have

$$x_{D^\circ} = \frac{E_{D^\circ}}{E_{beam}} > 0.5.$$

This final cut helps eliminate charmed mesons that have cascaded down from bottom hadron decays.

The D_S selection preceded in a similar fashion. Oppositely charged tracks, which had at least four digitalizations in the vertex chamber and reconstructed in three dimension in the large drift chamber, were paired together and constrained to come from the same (three dimensional) vertex. Their mass was calculated (assuming the kaon mass for both) using the vertex constrained tracks. A third track, assumed to be a pion, was combined with these two if the phi candidate was within ±15 MeV of the accepted phi mass. A three dimensional vertex constraint was then applied to this triplet of tracks and the two kaons were constrained to the phi mass. The lone pion's track parameters were also improved by this fit since the kinematic fitter that was used acted on all the track parameters for the vertex. The D_S candidate was accepted for the lifetime study if the resulting mass for the triplet was within ±40 MeV of the accepted D_S mass of 1970 MeV, provided $x_{D_S} \geq 0.6$. A total of 14 D_S candidates were found using this method of selection for the final data sample from 140 pb^{-1}. The resulting mass plot is shown in Figure 3. One of the curves represents the fitted plot with the expected $D^+ \rightarrow \phi\pi^+$ peak while the other curve has no such contribution.

The decay points of both the D^0 and the D_S were determined as by-products of the selection process as well as was the momentum

(and hence the boost) of the charmed meson. The lifetime measurement also needs an estimate of the production point. The method for determining the decay lengths for these measurements was based on determining the most probable production point within the beam spot. The the beam spot is the envelop in the plane perpendicular to the beam axis containing both beams, which is usually described by two Gaussians along the "X" and "Y" axes. These Gaussians are determined for each "run", the period between fills of the accelerator, by finding the average center of collisions between beam particles and gas in the beam tube and the widths of these distributions. The most probable decay length is then given by :

$$l = \frac{x\sigma_{yy}t_x + y\sigma_{xx}t_y - \sigma_{xy}(xt_y + yt_x)}{\sigma_{yy}t_x^2 - 2\sigma_{xy}t_xt_y + \sigma_{xx}t_y^2} .$$

Here σ_{ij} is the sum of the reconstructed error matrix and the beam spot envelop, t_j is the (three dimensional) direction cosine of the charmed meson's momentum along the j^{th} direction and x and y are the reconstructed vertex coordinates.

It has often been suggested that the other particles present in the event can be used to reconstruct the production point on an event-by-event basis. In practise this has proved difficult to do. The error of a reconstructed vertex, along the general direction of flight of several tracks, goes roughly as $(\sin\Omega)^{-1}$ where Ω is the opening angle of the tracks. The jets that charmed mesons are produced in are, in general, collimated in the direction of the charmed meson and hence produce the largest error precisely in the direction where the best accuracy is needed. There have been some lifetime measurements made that combine the beam spot and the fragmentation particles present[1] but these methods produce their best effects when an impact parameter method is used to determine the lifetimes. Full utilization of these fragmention

[1] See for example D. J. Mellor, "A Measurement of the Bottom Hadron Lifetimes in $e^+ e^-$ Annihilations", Ph.D. Thesis (Oxford), RAL-036

particles will have to wait until the next generation of vertex chambers.

The decay times of the individual charmed mesons in the samples, see Figure 4 for the D_s and Figure 5 for the D^0, were determined using the most probable decay length, as calculated above, but the average lifetimes of the samples had to use a maximum likelihood approach. The likelihood function took into account the background probability of an event being a random combination of fragmentation particles, a real charmed meson resulting from a cascading B decay, and a real primary charm meson but of the wrong type (eg. D^+ instead of a D_s.) The relative probabilities of these backgrounds have to be determined from Monte Carlo studies but in general can be normalized to the data through side bands. The overall background fraction for the D_s meson is 30%, as determined by the side bands. This includes, for example, 7% of the D_s candidates which are misidentified D^+'s, as determined by Monte Carlo.

The Monte Carlo contains assumptions about the production and decay of charmed (and bottomed) mesons which have been tuned as well as possible.[1] This was done by comparing other distributions of the data, such as mean charged multiplicity etc., with the Monte Carlo. Individual parameters in the Monte Carlo were varied by amounts corresponding to their uncertainty and the effects on the calculated lifetime were added in quadrature to determine the Monte Carlo's contribution to the systematic error of the measurements. The complete absence of the Cabibbo suppressed $D^+ \to \phi\pi^+$ peak, for instance, changes the D_s lifetime by 0.2×10^{-13} sec. and this was included in the reported systematic error.

The largest contribution to the systematic error of these lifetime measurements was the uncertainty about the <u>effective</u> resolution of the drift chamber system and the track finding/fitting routines in the environment of a hadronic event. This problem is exasterbated at TASSO by the large amount of material between the vertex and the central drift chambers.

[1] M. Althoff, TASSO Collaboration, Z. Phys. <u>C22</u> (1984), 307

necessitating a scattering angle in the middle of each track. The scattering between the two drift chambers has the effect of increasing the momentum dependency of the resolution function. In addition, the high probability of tracks crossing over each other in the vertex chamber reduces the number of digitalizations available to each track and hence degrading the resulting resolution. The appropriate resolution to use in track and vertex fitting was determined by observing the control samples for the different charmed mesons.

In the case of the D_s meson, track pairs whose mass is in the range: 1.05 GeV < $m(K^+K^-)$ < 1.15 GeV were used to construct false phi candidates and then combined with assumed pions to create control D_s combinations. The acceptable D_s mass range was increased to achieve a higher statistics sample. The same lifetime algorithm as that used for the D_s was repeatedly applied to this control sample assuming a series of vertex chamber resolution values between 100 and 150 microns. This range around the nominal value of 120 microns represents the limits where the assumed resolution increases the width of the control sample's lifetime distribution significantly. The average lifetime of this large statistics control sample was not effected by the assumed vertex chamber resolution. The limited D_s sample was effected when the same range of resolutions was used in the algorithm producing a contribution to the systematic uncertainty of $\pm 0.7 \times 10^{-13}$ sec. The dependence of the lifetime on this assumed resolution was not a smoothly varying function, as was the case for the control sample. Instead, there were sudden small jumps corresponding to individual digitalizations being deleted from tracks during the track and vertex fitting algorithms. It was determined from Monte Carlo studies that these discontinuities disappear for large enough samples. It is also true that for a larger hadronic sample the range of possible effective resolutions could have been reduced significantly.

In concluding the experimental discussion, the lifetimes of the charmed mesons, as measured by TASSO are, for the D^0:

$$\tau_{D^o} = 4.2^{+2.0}_{-1.4} \pm 0.8 \times 10^{-13} \text{ sec}$$

and for the D_s:

$$\tau_{Ds} = 5.7^{+3.6}_{-2.6} \pm 0.9 \times 10^{-13} \text{ sec.}$$

The systematic errors shown have had the contributions from uncertainties in background combinations and detector resolutions added in quadrature.

It is, by now, clear that the lifetime of the D^0 is about half that of the D^+. The naive spectator model, where the light valence quark does not participate in the decay of the charmed meson, is clearly wrong. The theoretical point of view has changed substantially since the summer of 1985 when the announcement of the observation[1] of $D^0 \to \phi K^0$ was interpreted as strong evidence for the spectator quark being annihilated by the exchange of a W boson. Now this particular decay is interpreted in terms of a rescattering[2] of the mesons resulting from the weak decay of the charmed quark. The lifetime difference between the charged and neutral charmed mesons is credited to a destructive interference between color states. The lifetime of the D_s meson will be a further tool in studying weak decays in this mass range. Confidence in our understanding of charm decays is very important when these ideas are applied to the bottom meson systems, where there have been recent observations[3] of substantial mixing in the $B_d{}^0$- $(B_d{}^0)_{bar}$ system.

---

[1] H. Albrecht *et al.*, Argus Collaboration, DESY 85-048 (1985)

[2] J. F. Donoghue, Phys. Rev. D33 (1986), 1516

[3] H. Albrecht *et al.*, Argus Collaboration, DESY 87--029

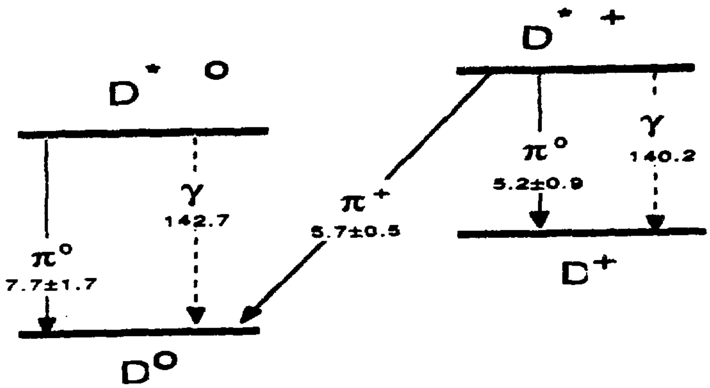

Figure 1. The allowable hadronic and elctromagnetic transitions from the vector excited states to the psudo-scaler ground states.

Figure 2. The reconstucted mass differences between $K^- \pi^+ \pi^+$ and $K^- \pi^+$. Accepted candidates have this difference less than 150 MeV.

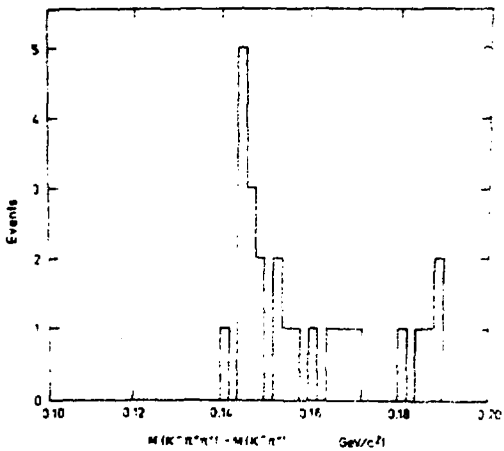

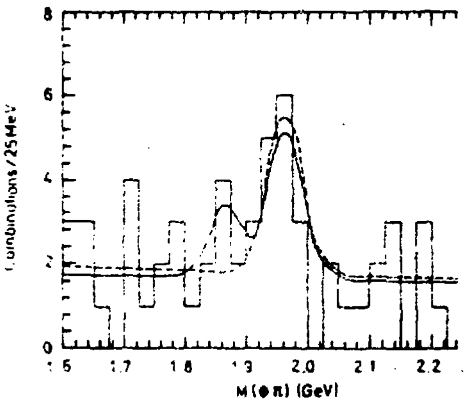

Figure 3. The reconstructed KKπ mass, after constraining the kaons to the phi mass. The solid curve represents the expectation for the Cabbibo supressed $D^+ \to \phi\pi^+$ decay while the dashed line is the fitted curve assuming no events in the D^+ channel.

Figure 4. The distribution of D_s decay times for the candidates. Each decay time is weighted by its experimental resolution. The curve respresents the measured lifetime folded in with the resolutions on an event-by-event basis.

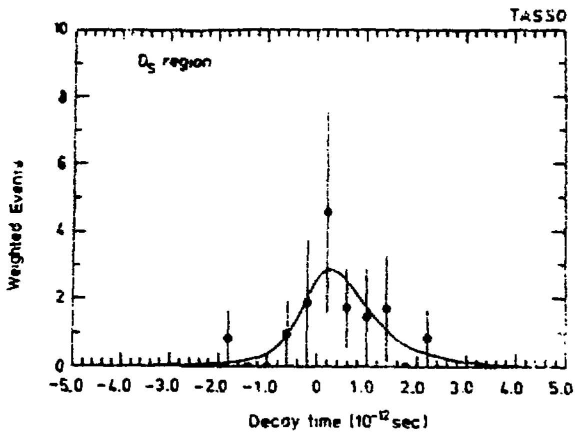

Figure 5. The distribution of D^0 candidate decay times. The curve represents the measured lifetime folded in with the experimental resolution.

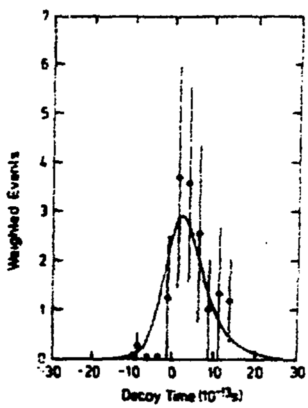

Appendix

LIST OF PARTICIPANTS

of the III Warsaw Symposium on Elementary Particle Physics

Jodłowy Dwór, May 22-28, 1980

1.Z.Ajduk - Warsaw
2.J.Bartelski - Warsaw
3.L.Becker - Zeuthen
4.G.Bellettini - Frascati
5.G.Białkowski - Warsaw
6.S.Brandt - Siegen
7.J.Branson - MIT Cambridge
8.J.Ciborowski - Warsaw
9.G.Cicuta - Milan
10.A.Czechowski - Warsaw
11.F.Dittmann - Hamburg
12.K.Doroba - Warsaw
13.P.Drijard - CERN Geneva
14.A.Dubnickova - Bratislava
15.F.Dydak - Heidelberg
16.P.Falkensteiner-Vienna
17.J.Finjord - Berne
18.H.G.Fischer - CERN Geneva
19.E.Floratos - Saclay
20.M.Gourdin - Paris
21.J.F.Gunion - Davis
22.F.Gutbrod - Hamburg
23.J.Gwiżdż - Warsaw
24.Z.Horvath - Budapest
25.B.Humpert - Geneva
26.A.Jachołkowska- Warsaw
27.A.Jachołkowski- Warsaw
28.M.Jeżabek - Cracow
29.M.Jędrzejczak - Warsaw
30.J.Kalinowski - Warsaw
31.R.Kirschner - Leipzig
32.W.Koch - Hamburg
33.P.Kosiński - Łódź
34.D.Kisielewska - Cracow
35.M.Krawczyk - Warsaw
36.P.Krawczyk - Warsaw
37.W.Krzyżanowski- Warsaw
38.M.Kuroda - Bielefeld
39.H.Lubatti - Seattle
40.L.Łukaszuk - Warsaw
41.P.Maślanka - Łódź
42.D.Mazurek - Warsaw
43.S.Mikocki - Cracow
44.C.Matteuzzi - CERN Geneva
45.S.Mrówczyński - Warsaw
46.P.Minkowski - Berne
47.R.Messner - Pasadena
48.J.Nassalski - Warsaw
49.B.Niczyporuk - Cracow
50.R.Nowak - Warsaw
51.A.Okopińska - Warsaw
52.M.Otwinowska - Warsaw
53.S.Pokorski - Warsaw
54.J.Rames - Prague
55.G.Ranft - Leipzig
56.J.Ranft - Leipzig
57.K.Redlich - Wrocław
58.J.Rembieliński - Łódź
59.E.Rondio - Warsaw
60.K.Rith - CERN Geneva
61.R.Rückl - Munich
62.I.Sakrejda - Cracow
63.W.G.Scott - CERN Geneva
64.R.Sosnowski - Warsaw
65.H.Spitzer - Hamburg
66.M.Staszel - Warsaw
67.J.Stepaniak - Warsaw
68.L.R.Sulak - Harvard
69.M.Szczekowski - Warsaw
70.L.Szymanowski - Warsaw
71.M.Święcki - Warsaw
72.K.Tanaka - Columbus
73.T.Taylor - Warsaw
74.U.Timm - Hamburg
75.S.Tkaczyk - Warsaw
76.L.Turko - Wrocław

77.A.Turski - Warsaw
78.J.Tymieniecka - Warsaw
79.S.Wolfram - Pasadena
80.A.Wróblewski - Warsaw
81.F.J.Yndurain - Madrid
82.J.Zakrzewski - Warsaw
83.A.Zieliński - Warsaw

Z-d Małej Poligr. U.W. zam. 1377/87 300 egz. K-6